269 Reg
2/26/68

ANL-7360

ANL-7360

Argonne National Laboratory

RADIOLOGICAL PHYSICS DIVISION

ANNUAL REPORT

JULY 1966 THROUGH JUNE 1967

DISTRIBUTION OF THIS DOCUMENT IS UNLIMITED

DISCLAIMER

This report was prepared as an account of work sponsored by an agency of the United States Government. Neither the United States Government nor any agency Thereof, nor any of their employees, makes any warranty, express or implied, or assumes any legal liability or responsibility for the accuracy, completeness, or usefulness of any information, apparatus, product, or process disclosed, or represents that its use would not infringe privately owned rights. Reference herein to any specific commercial product, process, or service by trade name, trademark, manufacturer, or otherwise does not necessarily constitute or imply its endorsement, recommendation, or favoring by the United States Government or any agency thereof. The views and opinions of authors expressed herein do not necessarily state or reflect those of the United States Government or any agency thereof.

DISCLAIMER

Portions of this document may be illegible in electronic image products. Images are produced from the best available original document.

The facilities of Argonne National Laboratory are owned by the United States Government. Under the terms of a contract (W-31-109-Eng-38) between the U. S. Atomic Energy Commission, Argonne Universities Association and The University of Chicago, the University employs the staff and operates the Laboratory in accordance with policies and programs formulated, approved and reviewed by the Association.

MEMBERS OF ARGONNE UNIVERSITIES ASSOCIATION

The University of Arizona
Carnegie Institute of Technology
Case Institute of Technology
The University of Chicago
University of Cincinnati
Illinois Institute of Technology
University of Illinois
Indiana University
Iowa State University
The University of Iowa
Kansas State University
The University of Kansas
Loyola University
Marquette University
Michigan State University
The University of Michigan
University of Minnesota
University of Missouri
Northwestern University
University of Notre Dame
The Ohio State University
Purdue University
Saint Louis University
Washington University
Wayne State University
The University of Wisconsin

LEGAL NOTICE

This report was prepared as an account of Government sponsored work. Neither the United States, nor the Commission, nor any person acting on behalf of the Commission:

A. Makes any warranty or representation, expressed or implied, with respect to the accuracy, completeness, or usefulness of the information contained in this report, or that the use of any information, apparatus, method, or process disclosed in this report may not infringe privately owned rights; or

B. Assumes any liabilities with respect to the use of, or for damages resulting from the use of any information, apparatus, method, or process disclosed in this report.

As used in the above, "person acting on behalf of the Commission" includes any employee or contractor of the Commission, or employee of such contractor, to the extent that such employee or contractor of the Commission, or employee of such contractor prepares, disseminates, or provides access to, any information pursuant to his employment or contract with the Commission, or his employment with such contractor.

Printed in the United States of America
Available from
Clearinghouse for Federal Scientific and Technical Information
National Bureau of Standards, U. S. Department of Commerce
Springfield, Virginia 22151
Price: Printed Copy $3.00; Microfiche $0.65

MASTER

ANL-7360
Biology and Medicine (TID-4500)
AEC Research and Development

ARGONNE NATIONAL LABORATORY

9700 South Cass Avenue
Argonne, Illinois 69439

RADIOLOGICAL PHYSICS DIVISION ANNUAL REPORT

July 1966 through June 1967

L. D. Marinelli, Division Director
R. E. Rowland, Associate Division Director

Preceding Report:
ANL-7220 - July 1965 through June 1966

LEGAL NOTICE

This report was prepared as an account of Government sponsored work. Neither the United States, nor the Commission, nor any person acting on behalf of the Commission:

A. Makes any warranty or representation, expressed or implied, with respect to the accuracy, completeness, or usefulness of the information contained in this report, or that the use of any information, apparatus, method, or process disclosed in this report may not infringe privately owned rights; or

B. Assumes any liabilities with respect to the use of, or for damages resulting from the use of any information, apparatus, method, or process disclosed in this report.

As used in the above, "person acting on behalf of the Commission" includes any employee or contractor of the Commission, or employee of such contractor, to the extent that such employee or contractor of the Commission, or employee of such contractor prepares, disseminates, or provides access to, any information pursuant to his employment or contract with the Commission, or his employment with such contractor.

DISTRIBUTION OF THIS DOCUMENT IS UNLIMITED

THIS PAGE

WAS INTENTIONALLY

LEFT BLANK

TABLE OF CONTENTS

RADIOLOGICAL AND HEALTH PHYSICS

1 Fluorescence Polarization Studies
W. R. ANDERSON, I. B. BERLMAN, AND H. O. WIRTH

4 Anomalous Fluorescence Characteristics of Fluoranthene and Some of Its Derivatives
I. B. BERLMAN, H. O. WIRTH, AND O. J. STEINGRABER

9 Hydrogen Flash Lamps
I. B. BERLMAN, O. J. STEINGRABER, AND M. J. BENSON

16 Energy Transfer by Drifting Electrons
JOSEPH C. BOWE

18 Drift Velocity and the Elastic Collision Cross Section for Electrons in Helium
JOSEPH C. BOWE AND R. K. LANGS

22 Production Rates of Neutrons in the Earth's Crust due to Natural Radioactivity
Y. FEIGE, B. G. OLTMAN, AND J. KASTNER

25 Tabulation of Luminescence Characteristics under the Influence of Intermolecular Energy Transfer
MITIO INOKUTI AND FUMIO HIRAYAMA

26 Sum Rule for the Bethe Inelastic-Scattering Cross Sections
MITIO INOKUTI, Y.-K. KIM, AND R. L. PLATZMAN

28 The Effects of Fast Neutron Exposure on the ^{7}LiF Thermoluminescent Response to Gamma Rays
B. G. OLTMAN, J. KASTNER, AND P. TEDESCHI

29 Thermoluminescent Microdosimetry in Dental Radiology

I. Technique
C. E. REHFELD, J. KASTNER, B. G. OLTMAN, H. M. ROSENBERG, AND D. E. DOYLE

II. Clinical Application
H. M. ROSENBERG, C. E. REHFELD, J. KASTNER, B. G. OLTMAN, D. E. DOYLE, AND D. J. HAUPTFUEHRER

30 The Oscillator Strength Distribution of the Negative Hydrogen Ion
YONG-KI KIM

34 Relative Risk of Injury in Different Organ Systems Following the Administration of Thorium Oxide with Particular Reference to the Hemopoietic System
L. D. MARINELLI

34 A Revised Estimate of the Maximum Permissible Burden for Sr^{90}
L. D. MARINELLI

37 Dosimetry in Relation to Epidemiology Its Implications in Radiogenic Leukemias and Bronchial Carcinoma: (Thorotrast)
L. D. MARINELLI

42 Thorotrast-Exposed Persons in the Chicago Area
HAROLD MAY AND EDWIN KINGSLEY

44 Photoionization Studies in the Vacuum Ultraviolet
JAMES C. PERSON

44 Isotope Effects in the Photoionization of Acetone, Butane, Ethylene and Ammonia
JAMES C. PERSON AND PAUL P. NICOLE

50 Specific Primary Ionization by High-Energy Electrons
F. F. Rieke and William Prepejchal

53 Multiple Elastic Scattering of Alpha Particles—Application of the Small-Angle Theory
Harvey A. Schultz

61 Synthesis and Properties of 2-Arylindoles
Hermann O. Wirth and Emily B. White

TOXICITY OF RADIOELEMENTS

68 Neutron Activation Analysis of Samples of Biological and Environmental Interest. Evaluation of the Experimental Method
D. N. Edgington and H. F. Lucas, Jr.

78 Division Delay in Irradiated Gametes of Sea Urchins
Patricia M. Failla

81 Excretion of ^{210}Pb and ^{226}Ra by Radium-Dial Painters
Richard B. Holtzman and Henry F. Lucas, Jr.

82 Concentrations of the Naturally-Occurring Radionuclides ^{210}Pb, ^{210}Po and ^{226}Ra in Aquatic Fauna
R. B. Holtzman

89 A Rapid and Precise Method for the Analysis of Calcium in Blood Serum
Frank H. Ilcewicz and R. B. Holtzman

93 Surface/Volume Ratios of Bone Determined by Computer Analysis of Microradiographs
Elizabeth Lloyd, R. E. Rowland, Donald Hodges, and J. H. Marshall

96 A Radon Removal System for the NASA Lunar Sample Laboratory: Design and Discussion
Henry F. Lucas, Jr.

104 Radon in Coal Mine Air. Part II
Henry F. Lucas, Jr.

105 Excretion and Retention of Lead-210 in Rats
Henry F. Lucas, Jr. and James E. Stanford

110 Radial Diffusion from Canaliculi: An Explanation for the Retention of Alkaline Earths in Adult Bone
John H. Marshall and Claude Onkelinx

114 Calcium Pools and the Power Function
John H. Marshall

123 Autoradiography of Radium Bone Sections by Means of Polaroid Film
R. E. Rowland

124 Rickets in Rats. A Progress Report
David J. Simmons

130 Skeletal Changes in Murine Runt Disease
David J. Simmons and Richard L. Simmons

131 Observation on the Deposition of Thorotrast in Rat Tissue
David J. Simmons, Helen Cummins, and Edwin Nirdlinger

144 Lead and Lead-210 in Rainwater
G. L. Ter Haar, R. B. Holtzman, and H. F. Lucas, Jr.

147 Air, Water, and Soil as Sources of Lead in Plants
G. L. Ter Haar, R. R. Dedolph, R. B. Holtzman, and H. F. Lucas, Jr.

METEOROLOGICAL STUDIES

149 Dewpoint Temperature Inversions
W. C. Ashby, Harry Moses, and Mary A. Bogner

160 Modifications of Cup Anemometer Design to Improve the Measurement of Mean Horizontal Wind Speeds in Turbulence
PAUL FRENZEN

167 Instrumentation for Atmospheric Turbulence Studies. IV.
PAUL FRENZEN AND RICHARD L. HART

169 Stack Design Parameters Influencing Plume Rise
HARRY MOSES AND JAMES E. CARSON

173 The Influence of Meteorological Conditions upon Radiation Doses Due to Inhalation Following a Maximum Credible Reactor Accident
HARRY MOSES, MARY A. BOGNER, CYNTHIA CHAMOT, AND FRANK C. KULHANEK

182 Publications

FLUORESCENCE POLARIZATION STUDIES

W. R. Anderson, I. B. Berlman, and H. O. Wirth

TESTING FOR HIDDEN ELECTRONIC TRANSITIONS

Data on changes in the degree of polarization of the fluorescence of an aromatic in the direction 90° to that of the exciting beam, as one scans the absorption spectrum of the molecule, are of help in deciding what electronic levels are involved in the transitions. So that such studies could be made by us, a polarization-analysis apparatus was set up. Figure 1 indicates schematically its operation. Exciting light travelling in the y direction, with x and z vibrational components, from the monochromator M (Bausch and Lomb High Intensity with 200–400 mμ grating and xenon source) is polarized with an x vibration by the polarizer P (Glan-Thompson prism) and is partially absorbed in the liquid fluorescent solution S (contained in a cylindrical cell of 1 cm path length). The fluorescent light travelling in the negative z direction falls on the photomultiplier PM after passing through the analyzer A (Glan-Thompson prism), which selects either the x or the y vibrational component. The photomultiplier signal is measured with an electrometer. Omitted in the diagram are two filters, the first between P and S, chosen to pass the excitation wavelength but to block longer-wavelength stray light of the monochromator, and the second between S and A, chosen to block light of the exciting wavelength scattered by the cell but to pass the band of longer wavelengths in the emission spectrum. Various stops for confining the beams are also omitted.

The degree of polarization of the fluorescent beam is defined as

$$\frac{I_x - I_y}{I_x + I_y}$$

where I_x and I_y are the relative intensities of the x and y components, respectively. Theory[1] shows that if no molecular rotation occurs between absorption and emission, a polarization of $+\frac{1}{2}$ results when the absorbing and emitting oscillators are parallel and $-\frac{1}{3}$ when they are perpendicular to each other. Rotation results in lower (absolute) values, and zero polarization, i.e., complete depolarization, results when considerable rotation has occurred. Because of this effect, satisfactory results with liquid solutions are obtainable only when the molecule has a short decay time[2] and when the solution is highly viscous. Table 1 gives values obtained by us for a few compounds tested with mineral oil as the solvent and the solution cooled to just above the solidification temperature. With reference to the first five compounds listed, it is apparent that the results are meaningful only for molecules with decay times in the neighborhood of one nanosecond. The other two entries in the table are discussed below.

INTRINSIC VISCOSITY STUDIES

It was pointed out by H. O. Wirth that our apparatus might also have certain capabilities in connection with the study of the intrinsic viscosity of the aromatic molecules (both this and that of the solvent presumably affecting rotation). In his possession were samples he had prepared of three binaphthyl derivatives (Number 6 of Table 1), all having the same chromophore but having different sizes of substituents attached. The structural formula is

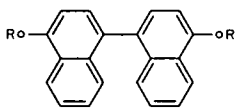

where R is either n-butyl, n-octyl, or n-undecyl. His thought was that perhaps the apparatus is capable of verifying the fact that the intrinsic viscosities are in the order of size of the substituent, i.e., in the order just stated above. An increase in length reduces the ease of both linear flow and rotation, and the latter should result in a polarization change. With reference to Table 1, a possible explanation for the lower value for PPO than for other molecules of similar decay time is its relatively short length.

Figure 2 gives the absorption and emission spectra for the three compounds. Also shown is the absorption for the mineral oil alone relative to that of the solute in the concentrations actually used. It was decided to test the three compounds at 330 mμ and

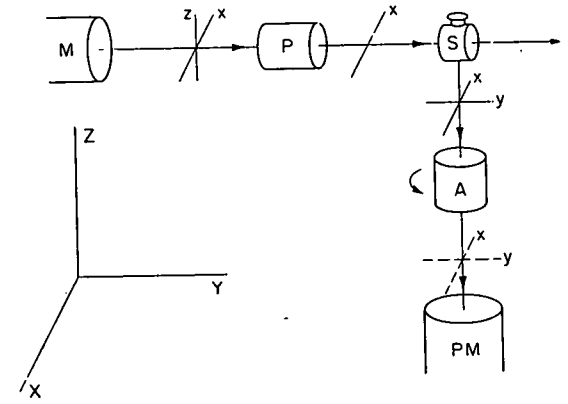

FIG. 1. Diagram showing operation of polarization-analysis apparatus.

at 340 mμ. Any errors from the fluorescence of the mineral oil alone at these wavelengths had been determined to be negligible. Concentrations making 330 mμ the approximate point of maximum signal were used. A calculation showed that this condition corresponded to an absorbance of 0.9 approximately.

Two difficulties have been encountered. First, the xenon light source has been found to be unsteady. The discharge shifts position, sometimes suddenly, producing a large intensity change. However, sets of reading during which this sudden shift takes place can usually be spotted and disregarded. Second, the solvent viscosity is very temperature-dependent, and the present apparatus does not include means for insuring temperature stability. This is not an important consideration when a marked effect, such as that produced by a shift of the oscillator by 90°, is involved, but it becomes a problem when small changes are to be detected. Cooling is by nitrogen gas which has flowed through a coil of tubing immersed in liquid nitrogen. An attempt was made to maintain a temperature just above that for solidification of the mineral oil (approximately −10°C) during the course of a set of readings through constant checking by sight and touch and readjustment of the nitrogen flow. However, as the results in Table 2 indicate, a small error in temperature can be responsible for a significant error in the polarization.

TABLE 1. POLARIZATION OF COMPOUNDS TESTED WITH MINERAL OIL AS THE SOLVENT

Compound[a]	Decay time, nsec	Wavelength, mμ	Approximate polarization
1. BBOT	1.1	395-373-353	0.39-0.38-0.39
2. PPO	1.4	334	0.21
3. POPOP	1.26	379-363-342	0.36-0.38-0.35
4. BPSB	1.4	377-358-344	0.41-0.41-0.41
5. 1,6-Diphenylhexatriene	12.4	374-354-337	0.09-0.09-0.10
6. 4,4′-Di(butyloxy-1)-1,1′-binaphthyl[b]	2.6	340-330	0.37-0.25
7. 9,12-Di(*n*-octadecyl-oxy)-benz[e]ace-phenanthrylene	6.0	395-354-339	0.33-0.25-0.20

[a] See pp. 251–253 of Reference 2 for names represented by the abbreviations.

[b] Or octyloxy or undecyloxy.

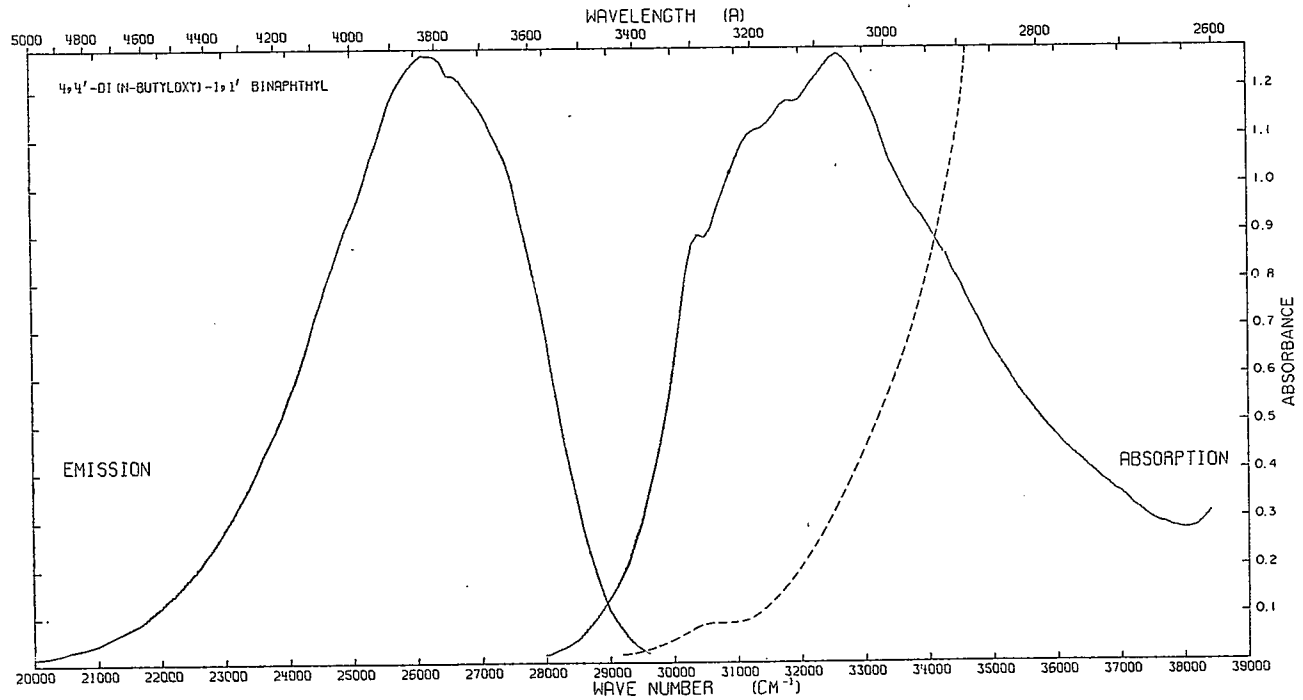

FIG. 2. Spectra of binaphthyl derivatives and of mineral oil (broken line)

Each trial consisted of four readings, two x and two y, as the analyzer was rotated 90° at a time through 360°. The average of the two x readings and the average of the two y readings were used in calculating the polarization. Five or more such trials were averaged in obtaining each result in Table 3. The standard deviation based on the variation in the five or more trials is indicated.

It is apparent that the expected pattern did not emerge, and one is tempted to conclude that the viscosity effect, at least in connection with the group of compounds tested, is of a lower order of magnitude than is the error due to temperature instability. A comparison of results at either of the wavelengths shows that the variation in polarization is of the order of 0.02, an amount equivalent to a temperature variation of perhaps 5 C°. A thermometer has since been added, and it is found that the range was undoubtedly at least this great. Improved temperature control, with the attendant increase in accuracy of results, could make the shift observable.

However, there is also a complication associated with the particular compounds used which in any event would tend to reduce the effect looked for. For the first five compounds listed in Table 1 no great variation was noted in the polarization across the portion of the absorption band tested; for Number 6, the group of binaphthyl derivatives, this is not true. A more complete scan shows that the polarization not only dips as one goes from 340 to 330 mμ, but it rises again at 320 mμ. This appears to indicate an intruding electronic level, one in which there is a 90° oscillator

TABLE 2. Effect of Solvent Temperature on Polarization

	Polarization	
	At 330 mμ	At 340 mμ
n-butyl at room temperature	0.15	0.22
n-butyl at just above solidification temperature	0.25	0.37
Approximate average change per degree C	0.004	0.006

TABLE 3. Comparison of Polarization of the Three Binaphthyl Derivatives

Compound	Polarization	
	At 330 mμ	At 340 mμ
n-butyl	0.249 ± 0.009	0.367 ± 0.009
n-octyl	0.271 ± 0.007	0.371 ± 0.004
n-undecyl	0.246 ± 0.006	0.355 ± 0.007

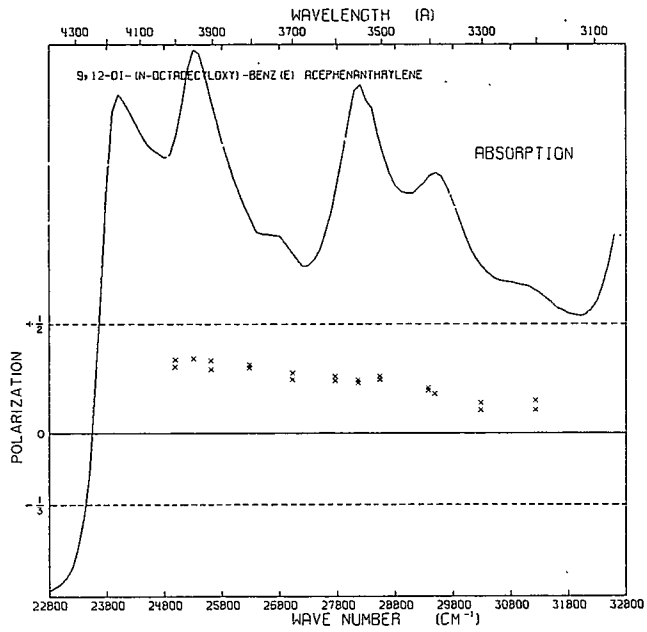

Fig. 3. Absorption spectrum of Compound 7 in Table 1 together with corresponding polarizations measured.

shift. The opposite polarizations tend to make the "undepolarized" as well as the depolarized values smaller than desirable and hence the variations smaller than they might be for another group of compounds.

That intrinsic viscosity is an important factor is demonstrated in our tests on another molecule. This long heavy molecule, Number 7 in Table 1, has the structural formula

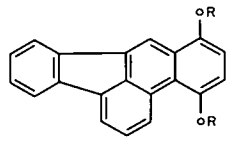

where R is octadecyl, $C_{18}H_{37}$. As Table 1 indicates, in spite of a relatively long decay time of 6.0 nanoseconds, polarizations as high as 0.33 were obtained, apparently permitted because of high intrinsic viscosity. Again, as for the binaphthyl derivatives, the polarization changes as the absorption spectrum is scanned, indicating overlapping electronic transistions. Figure 3 gives the absorption spectrum of this molecule and the corresponding polarizations found.

SELECTION OF SOLVENT

In an effort to find a more suitable vehicle than mineral oil, if one exists, several other solvents have been tested by us. The important requirements, in addition to high viscosity at reasonable temperatures,

TABLE 4. COMPARISON OF SOLVENTS

Substance	Dissolving power	Wavelength (mμ) at which absorbance is approx.		Approx. temp. at which used	Polarization for 20R-BFA at 395 mμ
		0.1	1.0		
Mineral oil	Good	320	290	−5°C	0.33
Cyclohexanol	Good	No test		Room	0.25
Silicone oil	Poor	310	265	−10°C	0.15
Decalin	Good	340	310	−10°C	0.31

are good dissolving power and transparency in the range of excitation wavelengths. In our tests, a single solute molecule, Number 7 in Table 1, was used, and in Table 4 our findings are compared. Cold mineral oil evidently provides the most viscous solution and remains the choice. Gläss-like solid solutions[3] would of course be ideal, but those solutions we have solidified have been found to be diffusing rather than transparent. However, further tests seem in order on cyclohexanol, which tends to become glassy on standing at room temperature.

REFERENCES

1. P. P. Feofilov. *The Physical Basis of Polarized Emission.* Consultants Bureau, New York, 1961, p. 39.
2. I. B. Berlman. *Handbook of Fluorescence Spectra of Aromatic Molecules.* Academic Press, New York, 1965, pp. 24–26.
3. F. Dörr, H. Gropper, and N. Mika. Influence of Heavy Substituents on the Polarization of the Triplet-Singlet Emission. Monohalogen Derivatives of Naphthalene. *Z. Naturforsch.* **18a**, 1025 (1963).

ANOMALOUS FLUORESCENCE CHARACTERISTICS OF FLUORANTHENE AND SOME OF ITS DERIVATIVES ☒

I. B. Berlman, H. O. Wirth, and O. J. Steingraber

INTRODUCTION

Fluoranthene (No. II in Table 5) is a nonalternate conjugated hydrocarbon and, therefore, has been of interest in theoretical and experimental studies.[1-3] We have studied the fluorescence characteristics of fluoranthene and several of its derivatives (III–V in Table 5) in a dilute cyclohexane solution and have found that most of these compounds have many anomalous characteristics. In particular, Compound II has four anomalous fluorescence characteristics: (1) the value of the fluorescence lifetime τ_{om} obtained from measuring the decay time, τ, and the quantum yield Q.Y., is many times greater than a calculated value τ_{oc} (Table 5), obtained by integrating over its long wavelength band; (2) its Stokes shift is very large; (3) it appears to be immune to concentration quenching and excimer formation; and (4) it is relatively resistant to oxygen quenching. It is our belief that the last two anomalies are unrelated to the first two.

Fluorescence measurements were made with equipment and according to procedures described elsewhere.[4] All measurements were made on dilute cyclohexane solutions in the concentration region of about 0.2 g/l, and the solute was excited directly by monochromatic radiation. The following data were obtained: the absorption spectrum, the fluorescence spectrum, the fluorescence decay time, τ, and the relative intensities of the fluorescence spectrum of a nitrogenated and an aerated solution, L_o/L. They are shown in Figure 4. From the data, calculations were made of (1) the quantum yield Q.Y., computed by integrating over the emission spectrum, (2) the natural fluorescence lifetime τ_o, computed[4] by integrating over the long wavelength absorption bands that are related to the transition leading to fluorescence, and (3) the Stokes shift. The results of these measurements and computations are given in Table 5.

It is immediately seen from the results of Table 5 that the fundamental relationship $\tau_o = \tau/\text{Q.Y.}$ is not satisfied. The discordance in this relationship requires for clarity that we distinguish between two τ_o parameters, τ_{oc} and τ_{om}, where τ_{oc} is obtained by integrating over the absorption bands and $\tau_{om} = \tau/\text{Q.Y.}$ Our experience has been that when $\tau_o \neq \tau/\text{Q.Y.}$, the difficulty can usually be traced to an improper evaluation of τ_o, namely when absorption bands not related to the fluorescence have been included in the integration.

L_o/L is a measure of the relative sensitivity of the first excited singlet state to quenching by oxygen. For aromatic molecules, a direct correlation has been found between the value of L_o/L and the value of the fluorescence decay time.

In addition to those on II, measurements were also made on derivatives of II, such as 3-phenyl fluoranthene

TABLE 5. Structural Formula, Time Constants (τ_o, Natural Lifetime, τ, Decay Time), Quantum Yield (Q.Y.), Stokes Shift, Susceptibility to Oxygen Quenching (L_o/L), Solubility (Sol. Toluene, 20°C) and Melting Point of Biphenyl, Fluoranthene and Some Fluoranthene Derivatives

Structural formula	No.	τ, nsec	Q.Y.	$\tau f(\tau_{oc})$, nsec	L_o/L	Stokes shift,	Sol., g/l	M.P., °C
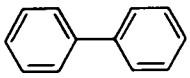	I	16.0	0.18	(2.8)	1.95	3300	414	71
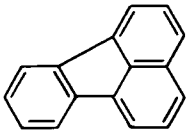	II	53.0	0.30	(16.4)	1.47	3970	>100	111
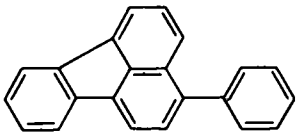	III	34.5	0.63	(11.0)	1.28	2950	>20	145
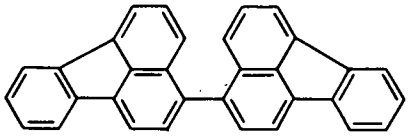	IV	8.0		(4.0)	1.16	2700	0.2	331
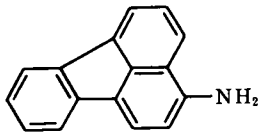	V	11.4	0.65	22.3	1.46	2700	10	117

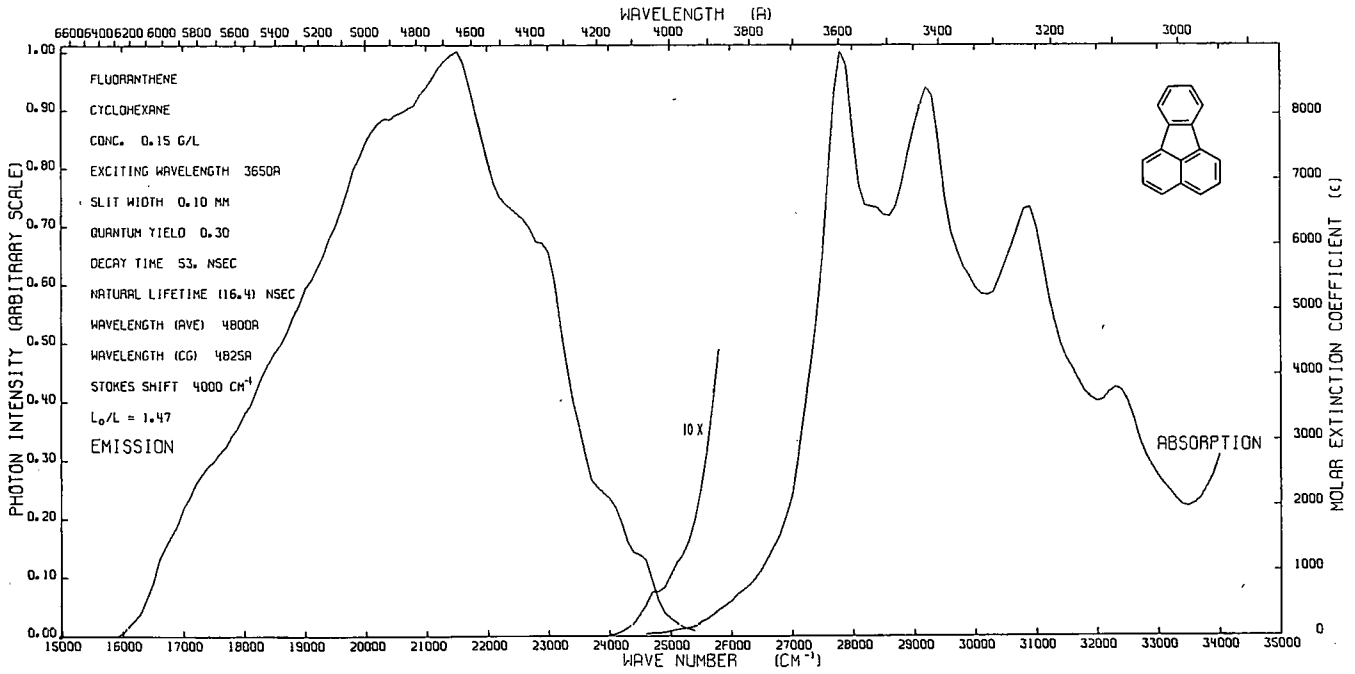

Fig. 4. Absorption and fluorescence spectra of fluoranthene. Technique and symbols are given in Ref. 4

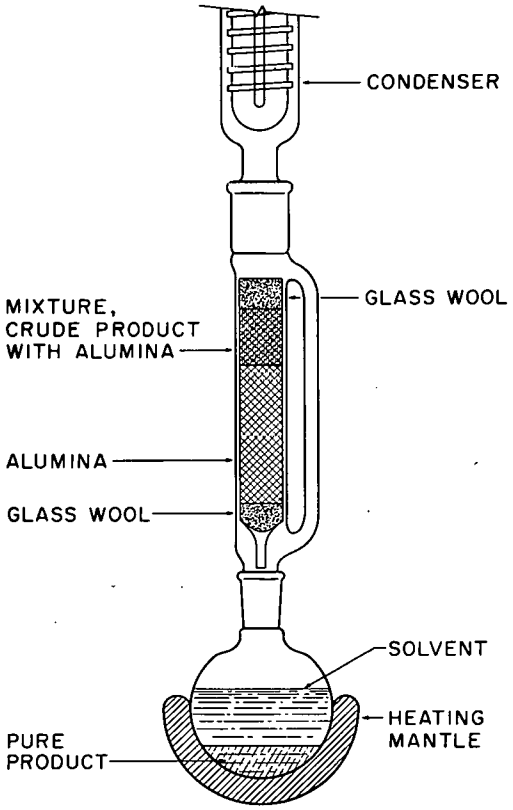

FIG. 5. Chromatographic column extractor

(III), 3,3′-bifluoranthenyl (IV), and 3-amino fluoranthene (V). The results of these investigations as well as the structural formulae of these compounds are also shown in Table 5.

SYNTHESIS AND PURIFICATION OF FLUORANTHENE DERIVATIVES

Although both 3,3′-bifluoranthenyl (IV) and 3-phenyl fluoranthene (III) were already known,[5] we were able to synthesize each of them in a different and (especially III) more efficient manner.

In both cases 3-iodofluoranthene (VI) was used as starting material. This compound was easily obtained by direct iodination[6] of fluoranthene (II) according to Eq. 1.

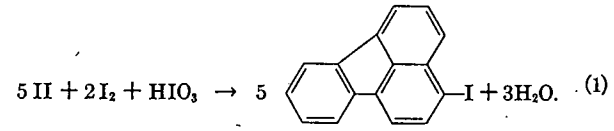

(VI)

The substitution of the iodine in the 3-position is according to expectation;[7] as far as electrophilic substitution is concerned, fluoranthene behaves as a biphenyl derivative. Compound VI was also known previously[8] but was obtained by a procedure involving several steps.

The Ullmann reaction with VI, according to Eq. 2, led to a fair yield of 52% of the bifluoranthenyl derivative, IV. Table 5 shows physical properties of this compound.

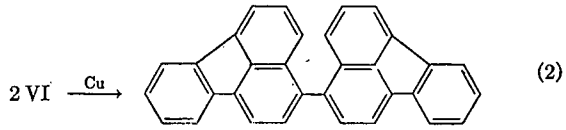

The synthesis of 3-phenyl fluoranthene (III) was achieved by a so-called mixed Ullmann reaction[9] with an excess of iodobenzene as indicated in Eq. 3. In this reaction, three compounds were actually formed, but by the application of excess iodobenzene, the formation

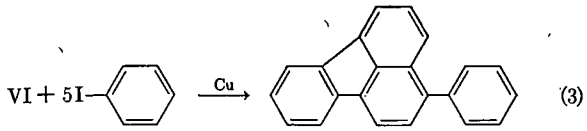

(III)

of one of these compounds, bifluoranthenyl, was strongly reduced and there remained only the problem of separation of biphenyl from the desired 3-phenyl fluoranthene. This problem was easily solved by taking advantage of the steam volatility of biphenyl. In Table 5 physical properties of III are listed.

Several techniques were applied to achieve the desired high purity necessary for luminescence studies. A chromatographic column extractor, as sketched in Figure 5, which is a simplified version of the adsorption-purification appartus developed by Sangster and Irvine,[10] proved to be very efficient. We found the extraction technique to be especially useful in the purification of poorly soluble compounds like IV. The use of alumina saturated with dry hydrogen chloride, as previously reported,[11] was also very effective in connection with the column-extraction technique. More details concerning this purification technique are presented elsewhere.[12]

EXPERIMENTAL

3-iodo fluoranthene (VI)

A mixture of 11.2 g fluoranthene, 5.0 g iodine, 2.0 g iodic acid (large crystals), 50 ml acetic acid, 5 ml water, 1 ml concentrated sulfuric acid (the last two mixed beforehand) and 5 ml carbon tetrachloride was heated and stirred at 80°C until the iodine was completely consumed (about 7 hours). The crude iodine compound was isolated (16.2 g) by the addition of water. A chromatographic process using benzene as solvent and

alumina as adsorbent, followed by crystallization from ethyl acetate/methanol (solution being cooled to −20°C) gave pure VI, 13.6 g, m.p. 112° (lit.: 110°C).[8]

3,3′-bifluoranthenyl (IV)

In a reaction apparatus described previously,[13] a mixture of 6.3 g 3-iodo fluoranthene (VI), 5.8 g copper powder,* about 100 mg mercury and 3 ml 3,3′-dimethyl biphenyl was heated in a nitrogen atmosphere and stirred first for 2 hours at 200°, then for 2 hours at 220°, and finally for 1 hour at 250°C. After cooling to room temperature, the reaction mixture was mixed with about the same volume of alumina and then extracted with chloroform in a Soxhlet apparatus or in the chromatographic column extractor (Figure 5); 2.1 g (52 % of the theoretical amount) of rather pure IV were isolated, m.p. 328–330°C. The final purification was achieved by chromatographic column extraction (Figure 5) with benzene as solvent and over alumina as adsorbent (half of it—the upper layer—saturated with dry hydrogen chloride gas), followed by crystallization from boiling triethylbenzene under conditions of slowly decreasing temperature (using a Dewar vessel). By this method, it was possible to obtain IV with a sharp m.p. of 331°C (lit.: 327–329°C).[5]

3-phenyl fluoranthene (III)

A mixture of 6.6 g 3-iodo fluoranthene (VI), 20.5 g iodobenzene, 30.6 g copper powder, 0.5 g mercury and 3 g biphenyl was reacted as described for IV. After the extraction, a steam distillation was performed to remove the biphenyl. The remainder was dissolved in benzene and the insoluble side-product (IV) filtered off. The dried benzene solution ($CaCl_2$) was then poured over an alumina column, the upper layer of which had been saturated with dry hydrogen chloride gas. After crystallization from ethyl acetate/methanol (cooling at −20°C) 2.5 g of III were obtained, m.p. 141–143°C. The final purification was effected by a chromatographic column extraction technique as described for IV but using petroleum ether (b.p. 30–60°C) as solvent; 1.9 g of pure III, m.p. 145°C (lit.: 144°C),[5] were obtained.

TESTING FOR ARTIFACTS

To make certain that our results were not governed by ubiquitous impurities, much effort was expended in purifying and testing our compounds, especially fluoranthene. Compound II was bought from several different suppliers, and various techniques of purification were employed, such as zone refining, recrystallization from various solvents, and column chromatography.

An additional test for detecting an impurity consisted of exciting the solution with radiation of different wavelengths in succession, recording the fluorescence spectrum each time, then looking for any major changes as a function of the exciting wavelength. This procedure is very sensitive in highlighting the presence of an impurity which has a different fluorescence spectrum. Except for minor variations, the fluorescence spectrum of II was independent of the wavelength of the exciting wavelength.

Excimer fluorescence has also been investigated by us as a source of the fluorescence anomalies of II and concentration studies were, therefore, made over a concentration range from 0.01 to 14 g/l. The fluorescence spectrum, the decay time, the quantum yield, and the degree of quenching by oxygen were found to be invariant with the concentration of the solute.

Fluorescence decay time measurements provided us with more information than just values of the decay time. The technique of exciting the solute directly by pulsed monochromatic radiation established the decay time as being single valued and exponential. It can be demonstrated that when the decay curve has more than one component, either a secondary process, such as excimer formation, has been initiated or an impurity is present. All of our measurements yielded decay curves which were exponential and single valued.

Further tests on II gave negative results. For example, varying the temperature of the solution over a temperature range of about 30° produced no significant change in the shape of the fluorescence spectrum. Also, measurements with either ethanol or benzene as solvent yielded only minor modifications in the position and shape of the absorption and fluorescence spectra. Because of these negative results, the presence of impurities or excimer formation can be discounted.

A PARTIALLY HIDDEN TRANSITION

In studies on fluoranthene,[1, 2] it has been suggested that a weak band at about 3,900 Å represents a transition from a level below that represented by the intense bands at 3,590 Å and 3,240 Å. Our findings, including the apparent large Stokes shift of about 4,000 cm^{-1}, provide confirming evidence for the existence of a partially hidden level. Furthermore, a long wavelength band at approximately 4,040 Å (Figure 4) corresponds to the band from which fluorescence takes place. On the basis of a natural fluorescence lifetime τ_{om} of 177 nsec and an assumed electronic level width equal to that for most molecules, we estimate the maximum value of the molar extinction coefficient of the most intense band associated with this transition to be $\epsilon_{max} = 270 \pm 40$. This low value of ϵ_{max} is consistent with the designation of the transition ^1L_b.

Anomalous fluorescence characteristics have been encountered and reported before in biphenyl (I in

*Purchased from the firm of Venus, Nuremberg, Germany.

Table 5).[14] The fluorescence decay time of I is abnormally long, its apparent Stokes shift is large, and it is immune to concentration quenching and excimer formation. Since biphenyl (I) is structurally related to fluoranthene (II) as shown in Table 5, it is not surprising that both have similar anomalies. The long decay time of I has already been explained[14] by postulating a hidden but weak transition as just described for II. The fluorescence spectrum of I possesses an apparent Stokes shift of 3,300 cm^{-1}, and such a large shift is consistent with the proposal of a hidden level. Steric hindrance in both the excited state and ground state is probably responsible for the lack of concentration quenching or excimer formation.

As shown in Table 5 compounds III and IV also exhibit anomalous characteristics, but to a lesser degree. Concentration studies were not made with these materials. The fluorescence characteristics of V appear to be normal in that $\tau_{om} \approx \tau_{oc}$. Also $L_o/L = 1.46$ is approximately the value that would be expected for a decay time value of 11.4 nsec. The reason that this latter compound conforms to the general rules of behavior may be found in its absorption spectrum wherein the band at 4,040 Å is more intense than its adjacent absorption band at about 3,700 Å.

OXYGEN QUENCHING

It has been shown[4, 15] that in the case of aromatic compounds, including biphenyl and its derivatives, the first excited singlet state is quenched by oxygen in proportion to the decay time of that state. This result is interpreted to mean that oxygen quenching is a diffusion-controlled process and that every encounter between an oxygen molecule and a molecule in an excited state leads to quenching of that state.

Fluoranthene is singularly different. It has a fluorescence decay time, τ, of 53 nsec, yet its ratio of L_o/L is only 1.17 (Table 5), whereas, for example, τ and L_o/L of 2-methyl naphthalene are 59 and 4.1 nsec, respectively.

The answer to the obvious question of why fluoranthene is relatively immune to oxygen quenching has not yet been resolved. Part of the uncertainty stems from our lack of knowledge concerning the mechanisms by which the first excited singlet state is quenched so effectively by oxygen. One possibility is that oxygen quenching can be explained in certain cases by an electron transfer reaction. We have not investigated this possibility. A second mechanism proposed for oxygen quenching is given by the expression

$$M^* + O_t \rightarrow M_t + O^*,$$

where M^* is a molecule in its first excited singlet state, O_t is an oxygen molecule in its ground state (triplet), M_t is a molecule in its lowest triplet state, and O^* is an oxygen molecule in its first excited singlet state. Since the energy difference between the states M_t and M is about 0.8 ev[16] and this is less than the energy required to produce a transition between the states O^* and O_t, which is about 1.0 ev, one may conclude that every encounter between an oxygen molecule and an excited fluoranthene molecule does not necessarily lead to quenching. Other factors may also contribute to a reduced sensitivity to oxygen quenching, e.g., steric hindrance. Further investigations are intended to clarify this problem.

We would like to thank Mr. J. Ostapowicz, Jr. for his skillful and generous assistance in constructing the chromatographic column extractor. Also our sincere thanks to Mr. W. R. Anderson for his many suggestions concerning the presentation of this paper.

REFERENCES

1. J. Koutechy, P. Hockman, and J. Michl. *J. Chem. Phys.* **40,** 2439 (1964).
2. E. Heilbronner, J. P. Weber, J. Michl, and R. Zahradnik. *Theoret. Chim. Acta* **6,** 141 (1966).
3. B. L. Van Duuran. *Anal. Chem.* **32,** 1436 (1960).
4. I. B. Berlman. *Handbook of Fluorescence Spectra of Aromatic Molecules.* Academic Press, Inc., New York, 1965.
5. J. v. Braun and G. Manz. *Ber. Deut. chem. Ges.* **70,** 1063 (1937).
6. H. O. Wirth, O. Königstein, and W. Kern. *Liebigs Ann. Chem.* **634,** 84 (1960).
7. E. Clar. *Polycyclic Hydrocarbons.* Academic Press, New York, 1964, Vol. 2, pp. 295 ff.
8. H. W. D. Stubbs and S. H. Tucker. *J. Chem. Soc. (London)* 2936, (1951).
9. H. O. Wirth, G. Waese, and W. Kern. *Makromol. Chem.* **86,** 139 (1965).
10. R. C. Sangster and J. W. Irvine, Jr. *J. Chem. Phys.* **24,** 672 (1956).
11. H. O. Wirth, W. Kern, and E. Schmitz. *Makromol. Chem.* **68,** 69 (1963).
12. H. O. Wirth and E. B. White. First International Congress on Heterocyclic Chemistry, University of New Mexico, Albuquerque, June 12–15, 1967. Proceedings to be published.
13. H. O. Wirth, K. H. Gönner, R. Stück, and W. Kern. *Makromol. Chem.* **63,** 30 (1963).
14. I. B. Berlman and O. J. Steingraber. *J. Chem. Phys.* **43,** 2140 (1965).
15. I. B. Berlman and T. A. Walter. *J. Chem. Phys.* **37,** 1888 (1962).
16. A. Weller. Private communication.

HYDROGEN FLASH LAMPS

I. B. Berlman, O. J. Steingraber, and M. J. Benson

INTRODUCTION

Hydrogen-filled lamps possess many favorable characteristics which make them desirable sources of pulsed radiation. The light flashes from these tubes can be made to be extremely fast (to decay in less than a nsec), and the spectral distribution of the radiation from these flashes contains a continuum from about 4000 Å to about 1600 Å. Several investigations concerning specific characteristics of hydrogen-filled lamps have already been made,[1-5] but they are of limited scope.

For many years a hydrogen-filled flash lamp has been used in our fluorescence decay-time apparatus as a source of fast radiation pulses to excite scintillation solutions. Since our equipment is well suited for measuring the decay time of very fast pulses and for making these measurements over a wide spectral range, we have studied the parameters which affect the speed and brightness of the flashes and the interrelationship of the characteristics of the radiation pulse. The purpose of these investigations has been to understand more clearly how the various parameters affect the operation of these tubes and, therefore, to be able to design an efficient and inexpensive flash tube. Furthermore, a troublesome feature of radiation pulses from flash tubes has been studied and minimized, viz., the slow component.

The characteristics were 1) the relative intensity of the flash as a function of wavelength, 2) the decay time of the pulse as a function of the gas pressure and type of gas, and 3) the relative intensity of the long component (the long tail). The parameters which were varied were the type of gas, the gas pressure, the gap spacing, the voltage across the thyratron, and the material of the electrodes. More than 50 flash tubes were assembled and tested.

EXPERIMENTAL TECHNIQUES

A diagram of our tubular flash tube with side window is shown in Figure 6. It is simple in design and relatively inexpensive to fabricate. The electrodes, of tungsten, are 0.080 inch in diameter, and have their gap ends machined and polished to a hemispherical shape. This configuration of tip has been found in previous studies to produce a stable and reproducible pulse shape. The body of the tube is of Pyrex tubing, 9 mm O.D., and a small extension is fabricated on the side to accomodate a window.

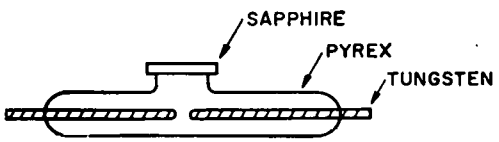

FIG. 6. A tubular flash lamp

During fabrication the tungsten electrodes become oxidized and discolored. To clean the electrodes, a NaOH solution is placed inside the tube and an electric current is maintained for a short interval between a third electrode and each of the tube electrodes. The inside of the tube is then rinsed with distilled water and dried, and the window is affixed to the body of the tube by means of epoxy.*

Since the epoxy softens at 80 to 100°C, the window is easily removed. We have found that the most convenient method of doing this is to balance the tube on its window on a warm hot plate until the epoxy softens. Worn-out flash tubes can be rejuvenated by removing the window, cleaning the electrodes, reattaching the window, and refilling with gas. To reduce attenuation in the short wavelength region, sapphire windows of 0.020 and 0.040 inch in thickness have been used.

For evacuation and gas filling, the flash tubes are attached, seven at a time, to a manifold, and the system is evacuated by means of a forepump and mercury diffusion pump. After the tubes have been evacuated to a pressure less than 10^{-5} mm of Hg for several days, a metal valve is employed to isolate the filling system from the pumping system, and hydrogen or deuterium gas is introduced into the system through heated palladium thimbles. The gas pressure is read on a Wallace and Tiernan Gauge.

A diagram of the electronic circuit for triggering the flash lamp is presented in Figure 7 and is somewhat simpler than that described earlier.[6] A free running multivibrator produces pulses (frequency variable from 2000 to 3000 cps) which triggers a thyratron. When the thyraton fires, its plate potential quickly drops toward ground potential, and this voltage drop triggers the hydrogen flash tube. A voltage of 3 to 8 kV can be applied across the thyratron circuit. To secure the shortest possible pulse, the tube is operated without any capacitance connected to it; stray capacitance alone suffices for energy storage.

* Baker Epoxy, Union Laboratories, Inc., Morganville, N. J.

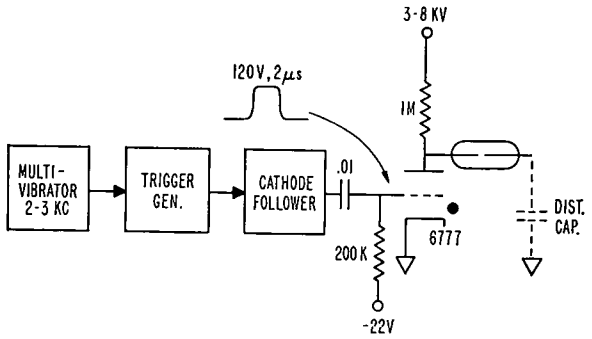

HYDROGEN THYRATRON DRIVER FOR FLASH TUBES

FIG. 7. Circuit for triggering flash lamp

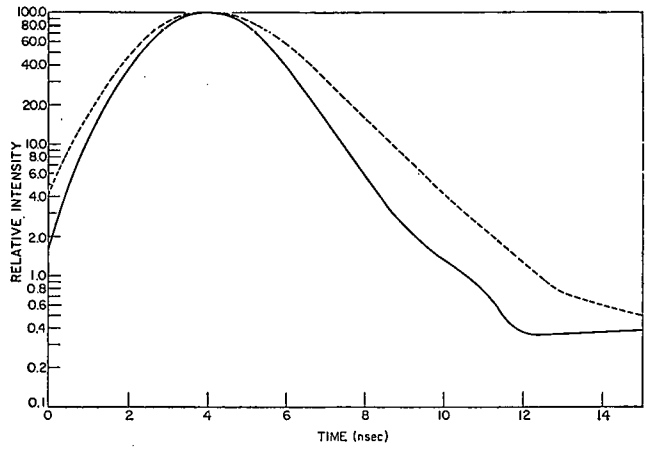

FIG. 8. Histograms of the pulse contours of the flashes from lamps with a 1-mm gap, filled to a gas pressure of 10 cm of Hg and operated at a voltage of 5,000 V. Solid curve, hydrogen gas; dashed curve, deuterium gas.

The stray capacitance is reduced by operating the tube single-ended as shown in the diagram.

An estimate has been made of the number of photons per flash using the formula

$$\text{Energy} = \tfrac{1}{2} CV^2,$$

where C is the capacitance and V, voltage. Assuming a stray capacitance of 1 pF, an average voltage of 5000 V, an average photon energy of 4 eV, and an efficiency factor[2] for converting electrical energy into light of 2×10^{-5}, the number of photons per discharge is about 4×10^8. Another determination which is of more immediate concern in the operation of the equipment is the number of photons/flash from the monochromator impinging on the sample. This latter number was obtained by comparing the size of the signal pulse (without sample) to noise. At a wavelength of 3500 Å and with a slit opening of 1 mm, there are approximately 50,000 photons/flash.

The equipment for detecting and recording the histogram of the pulse contours has been described elsewhere.[7] Briefly, the apparatus combines to advantage the desirable features of several units: the speed and high gain of a 56UVP photomultiplier tube, the fast rise time of a pulse-sampling oscilloscope, and the large storage capacity of a multichannel analyzer. The photomultiplier produces an electrical analogue of the light pulse, the pulse-sampling oscilloscope records its shape, and the multichannel analyzer stores the recorded information. A histogram of the sum of many stored pulses can be plotted on an X-Y recorder in semilog form. In Figure 8 are shown the recorded pulse contours from two flash tubes, one filled with hydrogen and the other deuterium. To our knowledge, the curve for deuterium is the first published pulse contour for that gas.

In the determination of the true decay times of the excited states of these gases, a correction must be made for the instrument response function of the system. Čerenkov radiation from Sr^{90} beta particles was used as a very fast radiation pulse, and the pulse contour of this radiation was assumed to be the instrument response function. Assuming an exponential decay for the excited states of the molecules, curves were generated for various decay times using a convolution integral, as described in Refs. 6 and 7. In Figure 8, approximately 2.7 nsec of the FWHM of each of the curves is due to the transit time spread of the electrons in the photomultiplier and the lamp, and other electronic effects.

RESULTS

Pulse Shape Versus Wavelength

If the lamp parameters, such as voltage and gas pressure, are kept constant, the measured pulse shape is not a function of the wavelength at which it is recorded. This result is surprising because all of the published pulse shapes from hydrogen-filled lamps have a large percent of long component as well as a short component. Our finding of a constancy of pulse shape with wavelength over a range from 1900 to 3500 Å can be interpreted to mean that the transitions involved in the radiation from the long tail are probably the same as those involved in the radiation associated with the fast component.

Minor exceptions to the rule of a constancy of pulse shape with wavelength occur at certain Hg lines where the pulse contour has a long tail. These exceptions are discussed further under "Anomalies."

Spectral Intensity Distribution

The intensity distribution as a function of wavelength of the radiation from a hydrogen-filled or deuterium-filled lamp contains a broad continuum extending from approximately 1600 to 4000 Å. Two

curves of the relative intensity versus wavelength over the wavelength range from 1700 to 3500 Å are shown in Figure 9. These data were taken with lamps having an electrode gap of 1 mm operated at 5000 V and a pressure of 12 cm of Hg. No correction has been made for the wavelength dispersion of our prism monochromator. The upper curve is composed of data from a deuterium-filled tube and the lower curve from a hydrogen-filled tube.

Since some of the radiation with wavelengths shorter than 2000 Å might be absorbed by the quartz faceplate of the photomultiplier, the radiation in the region from 1700 to 2600 Å was made to fall on a disk coated with sodium salicylate, and the resulting fluorescence from this phosphor was viewed by the photomultiplier. The use of sodium salicylate to convert all shorter wavelengths to a constant but longer band of wavelengths allows us to designate this phosphor as a heterochromatic converter. The fluorescence quantum yield of sodium salicylate is assumed[8] to be independent of the wavelength of the exciting radiation. Above 2600 Å the absorbance of sodium salicylate falls off sharply; therefore, for wavelengths greater than this, the disk was removed and the radiation was made to impinge directly on the quartz faceplate of the photomultiplier. The data with and without the phosphor were normalized at 2600 Å. Since no correction was made for the wavelength response of the photomultiplier in the region from 2600 to 3500 Å, the curves are, therfore, relative ones, not absolute

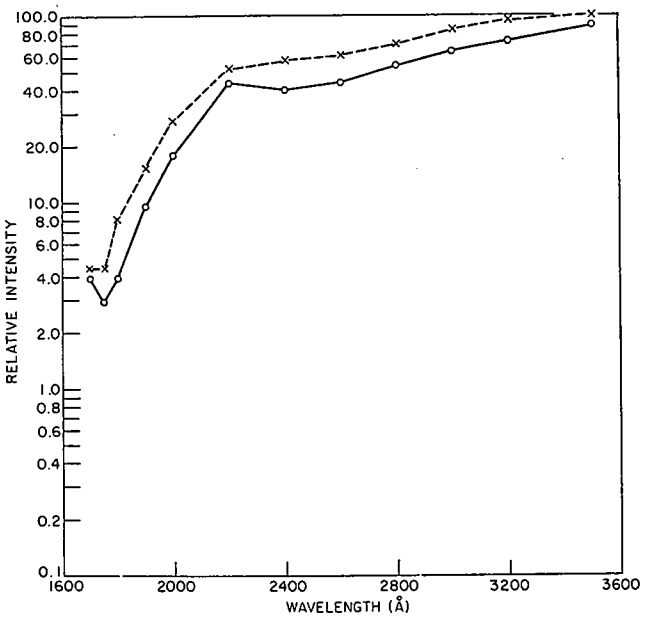

FIG. 9. Relative intensity distribution as a function of wavelength for lamps with a gap of 1 mm, a gas pressure of 12 cm of Hg, and voltage of 5,000 V. The upper curve is for a deuterium-filled tube and the lower for a hydrogen-filled tube.

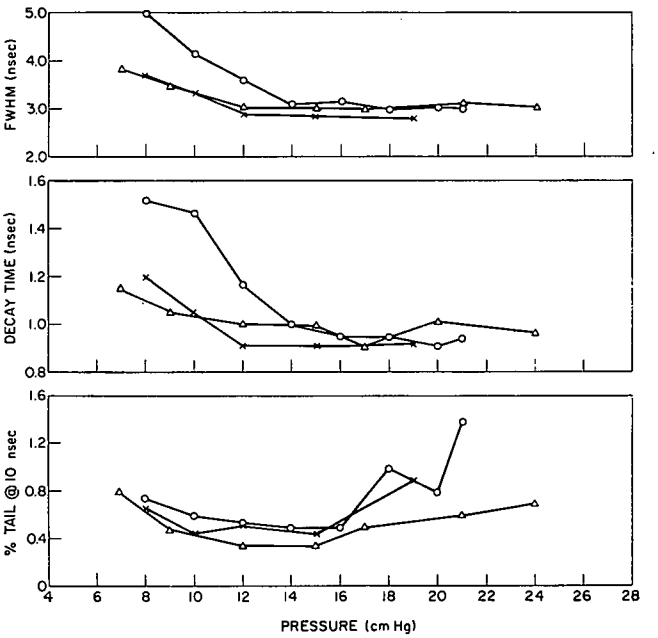

FIG. 10. The decay time of the pulse, the full width at half-maximum (FWHM), and the percent long component at 10 nsec after the peak as a function of gas pressure. ×——×, lamp with hydrogen and 1-mm gap; ○——○, lamp with deuterium and 1-mm gap; △——△, lamp with hydrogen and 2-mm gap.

curves. Furthermore, as with most instruments, our monochromator is troubled by stray light which becomes more annoying in the weaker regions of the spectrum; therefore, the data below 1850 Å are more susceptible to error than the data for longer wavelengths.

In this study of the intensity distribution as a function of wavelength, we have made use of the observation stated above that the pulse shape does not change with wavelengths. The peak height of each histogram was assumed to be representative of its area, i.e., its intensity.

Factors Contributing to an Enhanced Photon Yield

The radiation intensity and the pulse contour are modified by a change of each or a combination of the following parameters: (1) type of filling gas (H_2 or D_2), (2) the pressure of the filling gas, (3) the gap spacing, (4) the voltage across the tube, and (5) the charging capacitance. Only the first four parameters have been the concern of this report, each parameter being generally varied independently.

Gas Pressure.—Measurements were made over a range of gas pressures from 7 to 24 cm of Hg. The decay time of the pulse, the FWHM, and the percent of long tail were measured as a function of pressure, and the data are shown in Figure 10. Decay time is defined as the time interval for the pulse to reach

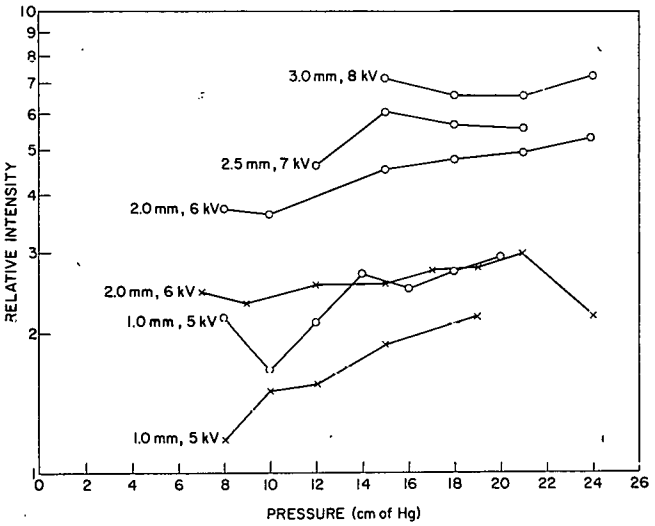

FIG. 11. Relative intensity of the flashes versus gas pressure. Sodium salicylate was used as a photon integrator. ×——×, hydrogen-filled lamps; ○——○, deuterium-filled lamps. Each datum represents an individual lamp.

a value $1/e$ of its maximum value. These values of decay time, as plotted in the above figure, are values which are read directly from the histograms and are not corrected for the instrument response function of the system. When a correction is made for the system response, the corrected values represent the decay times of the excited state(s) responsible for the emitted radiation, as discussed later. At pressures above 16 cm of Hg, the decay times have reached a limiting value imposed by the capabilities of our equipment. It is of interest to note the lower decay times at lower pressures of the hydrogen-filled lamps with 2-mm gaps than those of lamps with 1-mm gaps. A contributing factor toward smaller values of decay time may be the smaller percent of long component in lamps with wider gaps.

The FWHM is related to the decay time since a longer decay time leads to a greater value of the FWHM. At pressures above about 14 cm of Hg the pulse contour has assumed an instrument-limited shape, and the values should be judged accordingly.

All of the measurements in Figure 10 were made at a wavelength of 3000 Å. Generally each point on a graph represents a measurement on a single tube, but occasionally a point designates an average value for two or more tubes. The percent of long component is obtained from the histograms by noting the value in percent of the ordinate 10 nsec after the peak value of 100%.

Although the technique is capable of making measurements to within a few percent, the reproducibility of the results when tubes are changed is much poorer. The uncertainty has a twofold origin: 1) the experimental error introduced in aligning a tube at the proper distance from a focusing mirror, and 2) the inherent variations in the tubes themselves with the "same" tube parameters. We estimate a possible error of ±20% for each measurement. With an uncertainty this large, emphasis is on trends rather than on absolute values.

At low gas pressures, as the pressure is increased from 7 to 14 cm of Hg, the amplitude of the pulses is increased but the FWHM is decreased. In terms of total photon yield these variations would appear to cancel each other. By using sodium salicylate (coated on a quartz disk) as a photon integrator the effect of pressure on the total intensity has been measured and the data are shown in Figure 11. The decay time of sodium salicylate (about 7.5 nsec) is much longer than that of the flashes and is essentially not affected by a small variation in the decay time of the flash with pressure.

The FWHM apparently remains constant at the higher pressures of 14 to 24 cm of Hg; nevertheless, the intensity can be accurately measured by means of the sodium salicylate photon integrator: The data in Figure 11 were so measured.

Although there seemingly is a large amount of scatter in the data in Figure 11, there are some apparent trends. The number of photons per discharge from lamps with 1-mm gaps tend to increase appreciably with pressure. Pressure has less effect on tubes with slightly larger gaps and practically no effect on tubes with a 3-mm gap.

Voltage.—A certain minimum voltage is necessary to cause a lamp to fire. This value of voltage is dependent on the electrode tip configuration, the gas pressure, the gap distance, and the type of gas. The values of voltage used in obtaining the data in Figure 11 are well above the minimum value because it was necessary to have the tubes fire over the complete range of pressures.

The effect of voltage on the intensity is shown in Figure 12. At a fixed pressure and gap the voltage of a lamp was varied over a range from about 4 to 8 kV. By plotting the intensity as a function of the ratio E/p, where E is voltage and p is pressure in cm of Hg, the effect of these two parameters can be easily seen. What is not shown is the constancy of the percent of slow component with voltage.

Gap Distance.—As the gap distance is increased but the other parameters such as voltage and pressures are kept constant, the pulse shape is changed in the following manner: The peak intensity is increased, so is the FWHM, but, surprisingly, the percent of tail is decreased. By using sodium salicylate as a photon integrator and comparing the intensities of lamps

with different gaps at a wavelength of 2600 Å, the integrated intensity per pulse is measured. The data are plotted in Figure 11. Although the intensity per pulse is increased with a larger gap distance, the relative changes are not proportional. The spectral intensity distribution from tubes with different gaps is shown in Figure 13.

For a lamp with a larger gap to fire properly, a larger voltage is generally required. Here again, the pulse shape is modified by a change in voltage. By

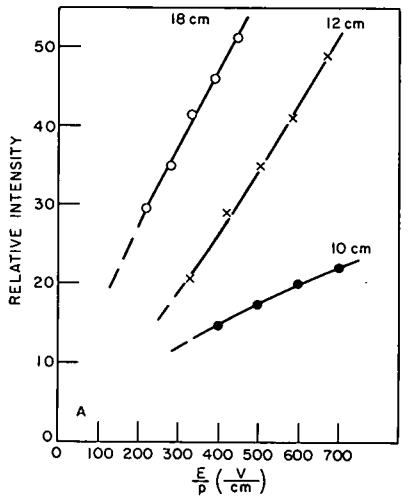

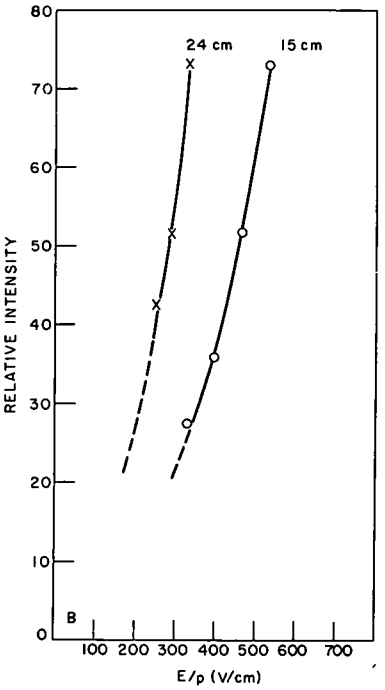

Fig. 12a. Relative intensity versus ratio E/p (Volts/cm of Hg). Each curve represents data from one tube with a 1-mm gap. Pressure was constant, voltage was varied.

Fig. 12b. Relative intensity versus ratio E/p (Volts/cm of Hg). Each curve represents data from one tube with a 3-mm gap. Pressure was constant, voltage was varied.

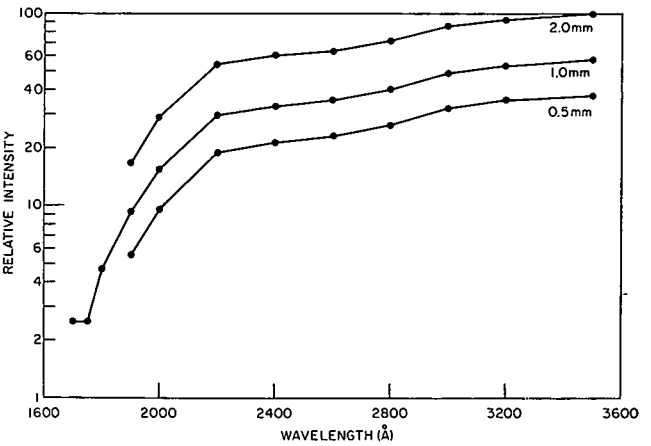

Fig. 13. Spectral intensity distribution of the radiation from tubes with different sized gaps.

the use of a sodium salicylate button in the fashion mentioned above, tubes with different gaps and voltages were compared. A tube with a 3-mm gap operated at 8 kV emits about 50% more photons per flash than a tube with a 2-mm gap operated at 6 kV. The latter tube has twice the emission intensity per discharge of a tube with a 1-mm gap operated at 5 kV. These data are shown in Figure 11.

Hydrogen versus Deuterium.—The intensity of light from deuterium-filled tubes is greater than from hydrogen-filled tubes if all other parameters are kept constant. Not only is the peak height of each pulse greater but so is the FWHM. The much greater FWHM would indicate that the decay time of the excited state of deuterium is longer than that of hydrogen. To compare intensities from H_2- and D_2-filled lamps, the sodium salicylate photon integrator must be used.

The curves in Figure 11 illustrate the fact that a deuterium-filled lamp with a 2-mm gap produces about (65 ± 10)% more light than a hydrogen-filled tube. Levikov and Shishatskaya[3] have also observed in their studies of lamps tested under steady (non-pulsed) conditions that deuterium-filled lamps emit more light than hydrogen-filled lamps.

Other authors[9] have indicated that below 1700 Å H_2-filled tubes may emit more radiation than D_2-filled tubes. Our equipment is not capable of making measurements below 1700 Å; hence, we cannot verify this. As shown in Figure 9, our measurements indicate that over the entire region from 1700 to 3500 Å deuterium-filled tubes emit more radiation than hydrogen-filled tubes.

Decay Time Measurements

As shown in Figure 10, the $1/e$ decay time of a pulse decreases with increasing pressure in the re-

gion from 7 to 17 cm of Hg. Above 17 cm of Hg no change in the decay time is recorded; obviously the frequency response of the system has been reached, and any further decrease in decay time cannot be detected.

Preliminary measurements have been made on the decay time of the excited H_2 and D_2 molecules as a function of gas pressure. The technique of making these measurements and calculations is very similar to that for making fluorescence decay time measurements, as described in Ref. 6, except that the instrument response function is obtained by means of Čerenkov radiation. We estimate that the decay time of a lamp filled with hydrogen to a pressure of 10 cm of Hg is about 0.8 ± 0.1 nsec, whereas that of a tube filled to the same pressure of deuterium is about 1.3 ± 0.1 nsec. At higher pressures the decay time of each gas becomes correspondingly less.

Anomalies

Impurities in the gas and on the electrodes produce some anomalies. Mercury vapor is present in our filling system in trace amounts, even though there is a liquid-nitrogen trap between the mercury diffusion pump and the filling system. The presence of mercury vapor in our lamps is evident from the fact that when one records the pulse shape at one of the mercury lines the pulse contour has a relatively large percentage of long component (large tail). Being aware of this trace impurity, we generally use wavelengths about 50 Å away from prominent mercury lines.

Tungsten is a porous material and occasionally after a lamp has been operated for ten hours or more, some impurity such as iron is diffused out onto the electrode tip. The net effect is to superimpose the intense line spectrum of the impurity on the continuum. Lines with intensities ten times that of the continuum have been observed. We have been able to identify only Fe and Fe^+ lines. The impurity lines generally are of a wavelength greater than 3500 Å, and the hydrogen continuum from tubes containing these lines is generally less intense than in tubes without impurities. In some applications, lamps with these impurities may be desirable since so much energy is concentrated at specific wavelengths. An interesting observation has been that the recorded pulse shape of any one of these iron lines displays a very fast component and a relatively low percentage of long component. The very fast component is probably caused by collision quenching between the excited atoms and hydrogen molecules. Thoriated tungsten electrodes are especially prone to produce anomalies. Not only does the spectral intensity distribution have a line structure superimposed on the continuum, but also the long component of the pulse is abnormal. Pulse shapes taken at the wavelengths of these lines have a large long component, of 7 to 15% (see definition above). Even the pulse shape taken at a wavelength on the continuum has a relatively large long component, 3%. Pfeffer et al.[5] have found that hydrogen-filled lamps containing water vapor produce a continuum with many lines superimposed thereon. Data from lamps with impurities on their electrodes have been excluded from the general results presented here.

TABLE 6. Percent Tail versus Electrode Diameter

Diameter, in.	Pressure, cm	Voltage, V	% of Tail at 10 nsec
0.040	12	3500	0.7
0.060	12	3500	0.8
0.100	12	3500	1.1
0.040	24	4000	0.7
0.060	24	4000	1.0
0.100	24	4000	1.0

Lamp gap was 0.022 inch.

Long Tail

Tubes with wide gap spacing have been found to have a relatively lower percentage of long tail than tubes with narrow gap distances. This observation can be explained by assuming that although most of the radiation intensity is generated in the gap some of the radiation appears to be generated at the end surfaces of the electrodes, and radiation from this latter region must be predominantly long component. To test this hypothesis, a series of lamps with the same small gap of about 0.55 mm were made with different diameter electrodes, and as shown in Table 6, the smaller diameter electrodes can be correlated with the smaller tail. Furthermore, tubes with electrodes which have their tips covered with an iron impurity as mentioned above, also emit pulses with very little tail.

We have found that a tube with a 1-mm gap but with an open window will operate very well if the lamp housing is filled with nitrogen (not air). An intense, fast, and many-lined spectrum appears superimposed upon a continuum. However, since we are reporting on H_2- and D_2-filled tubes, no further data will be given except that the percent of tail is again inversely related to the gap distance, being greater for a 0.5-mm gap than for a 1-mm gap. All these facts seem to support the assumption that the long tail is associated with a region near the surface of the electrodes.

DISCUSSION

A theory of the intensity distribution of the H_2 and D_2 spectra has been given by Coolidge and James.[9, 10] Their explanation, generally accepted, states that the spectrum is produced by transitions from lower vibrational levels of the $1s\sigma 2s\sigma^3 \sum_g$ state to a repulsive (unstable) $1s\sigma 2p\sigma^3 \sum_u$, i.e., the continuum is produced by transitions to a repulsive state, and the distribution in the short wavelength region is dependent on the probability of transitions from several low-lying vibrational levels of the upper state to this repulsive state. The transition probabilities from the lower vibrational levels of the upper state to the repulsive state are different for H_2 and D_2. The relative increase in the intensity at 1700 Å for the H_2 curve, as shown in Figure 9, appears to be real and is probably associated with a prominent peak at about 1600 Å. The slight increase at 2200 Å has also been found to be a characteristic of H_2-filled lamps.

The very fast decay times of less than a nsec are produced by collisions between excited and unexcited molecules. As the pressure in a tube is increased, the probability of added collisions is increased. Intensity quenching probably accompanies these collisions. An explanation as to why the intensity remains approximately constant with increasing pressure could be that more molecules are excited per discharge, but at the same time more of these excited molecules are quenched by collisions with unexcited molecules. A mechanism of quenching could be that the electronic energy of the excited molecule is transferred to a second molecule as potential energy, the latter energy being sufficient to break the H—H or D—D bond.

Our measurements indicate that the mean lifetime of D_2 molecules in their excited state is much longer than that of H_2 molecules, the difference becoming more dramatic at the lower pressures. This observation would appear to be contrary to the theoretical work of James and Coolidge[9] who predict that at low pressures the mean lifetimes of transitions producing the continuum is approximately the same for H_2 and D_2, about 11 nsec. Our observations would be in agreement with the results of the above authors if within our assumption of collision quenching there is the premise that excited H_2 molecules are quenched by H_2 molecules at a faster rate than excited D_2 molecules are quenched by D_2 molecules. The smaller number of photons per discharge and the faster decay of H_2 flashes would support this idea of greater concentration quenching for H_2.

Another possibility for explaining the greater intensity per discharge for D_2 lamps, is that the upper state in D_2 becomes more heavily populated than in H_2. This latter process would, however, not affect the decay time. Although both processes may occur during the discharge, we believe that at the pressures at which we are working concentration quenching is the dominant one.

Malmberg[2] has stated that the long tail is probably caused by the recombination of electrons and positively charged molecules. This explanation is in accord with our observation that the percent of long tail increases with pressure for pressures above 16 cm of Hg as shown in Figure 10. At higher pressures more excited molecules and ions are formed per discharge. However, concentration quenching predominately affects the excited molecules; therefore, the relative percent of long tail is increased. More excited molecules and ions per discharge can also be formed by higher voltage, pressure being kept constant, but since concentration quenching is not operative, the percent of slow component is not changed.

As noted above, the shape of a recorded pulse from a particular lamp is not a function of wavelength; this implies that the same transitions are involved in both components. The observation that the electrode tips provide a reactive surface to increase the percent of long tail is not well understood.

From our qualitative studies, we have been able to conclude that for high intensity a deuterium-filled lamp with a large gap should be used. If speed is also important, high pressures and high voltages should be employed.

The author would like to thank Drs. H. A. Schultz and J. C. Person for several informative discussions. We would also like to express our appreciation for the skillful assistance of Mr. S. Omiecinski in the construction of the flash lamps.

REFERENCES

1. M. K. Ivanova and A. V. Yakovleva. *Izv. Akad. Nauk SSSR*, Ser. Fiz. **14**, 561 (1950).
2. J. H. Malmberg. *Rev. Sci. Instr.* **28**, 1027 (1957).
3. S. I. Levikov and L. P. Shishatskaya. *Opt. Spectry. (USSR)* (English Trans.) **11**, 371 (1961).
4. M. N. Smolkin and N. B. Berdnikov. *Opt. Spectry. (USSR)* (English Trans.) **14**, 220 (1963).
5. G. Pfeffer, H. Lami, G. Laustriat, and A. Coche. *Nucl. Instr. Methods* **23**, 74 (1963).
6. I. B. Berlman and O. J. Steingraber, *IEEE Trans.* **NS 11**, 27 (1964).
7. O. J. Steingraber and I. B. Berlman. *Rev. Sci. Instr.* **34**, 524 (1963).
8. K. J. Nygaard. *J. Opt. Soc. Am.* **55**, 944 (1965).
9. A. S. Coolidge and H. M. James. *Phys. Rev.* **55**, 184 (1939).
10. A. S. Coolidge. *Phys. Rev.* **65**, 236 (1948).

ENERGY TRANSFER BY DRIFTING ELECTRONS

Joseph C. Bowe

INTRODUCTION

Comparison of experimental and computed values of the transport coefficients of electrons in gases has been developed into a technique whereby absolute values are obtained for the energy-dependent cross sections of atomic and molecular gases for collisions with electrons. The low energy limit of this method is about 0.001 eV, the limit being set by the temperature of liquid nitrogen. Computation of the transport coefficients can be carried out if the energy distribution of the electrons is known. In general, the energy distribution depends upon the value E/p_0, the elastic and inelastic processes between electrons and gas molecules, and the gas temperature T. Although it is possible, in principle, to obtain the energy distribution function by solving the Maxwell-Boltzmann transport equation, formidable practical difficulties are nevertheless encountered. These difficulties, however, become somewhat manageable with the aid of modern computers. As a result of such studies, a large body of experimental knowledge and computational results concerning the behavior of electron swarms in gases is now available.

This report sets out to look at the data on electron swarms in terms of energy balance in order to determine what information and insight these data might reveal about energy-loss processes. In this context, an attempt is made to account for the known energy input which the swarm absorbs from the electric field. It is known, for example, that only a very small portion of the absorbed energy is stored in the electron swarm itself, whereas the remainder is dissipated by elastic and inelastic collisions which the electrons make with the gas. It is interesting to determine, for example, the relative number of elastic and inelastic collisions that are involved in this division of energy. It is desired, moreover, that meaningful interpretation of swarm data should be possible without resorting to computers or without involving the mathematical complexities of the complete theory. The desired argumentative approach might be illustrated by the physical reasoning employed in the following example. Suppose that the drift velocity v_d in two different gases or mixtures of gases is compared at the same value of electric field strength E and gas pressure p_0. If it is realized that the larger of the two values of drift velocity is ascribable to a longer average time between collisions (hence, the electric field is more effective in producing drift motion), then the average energy loss that the electrons experience in each collision must be greater in that gas in which v_d is greater. This follows because in each gas, the electrons fall through the same potential difference per unit length of drift distance and, therefore, absorb the same amount of energy from the field. In the steady state, this energy is dissipated by collision. The electrons that have the greater value of v_d make, on the average, fewer collisions per second and, therefore, fewer collisions in a given drift distance; hence these electrons must lose more energy per collision than do the electrons in the gas for which v_d is smaller. The implications of this type of argument are particularly interesting in those cases where a small amount of impurity gas has a profound effect on the value of the drift velocity.

Again, consider two gases in which the drift velocity has the same magnitude but at different values of E/p. In this case, as a formula to be derived later will show, the ratio of effective electron collision frequencies is proportional to the ratio of the E/p values, where the larger collision frequency is proportional to the larger value of E/p.

MOMENTUM BALANCE

To develop a more quantitative description of energy balance, notice that the magnitude of the average drift velocity v_d of an electron in a swarm is given by

$$v_d = \frac{eE}{3mp_0} \frac{\int_0^\infty \frac{1}{NQ(v)} \frac{\delta f_0(v)}{\delta v} v^2 \, dv}{\int_0^\infty f_0(v) \, v^2 \, dv}, \qquad (1)$$

where $f_0(v)$ is the isotropic portion of the velocity distribution function obtained from the Maxwell-Boltzmann equation, $Q(v)$ is the cross section for momentum transfer due to elastic and inelastic collisions and $Np_0 = 3.54 \times 10^{16} \, p_0$ molecules-cm^{-3} is the gas density when p_0 is expressed in torr. Evaluation of the integrals in Eq. (1) assumes a priori knowledge of the cross sections $Q(v)$. For present purposes, it is convenient to adopt the viewpoint that the ratio of integrals is evaluated at each value of E/p_0 by the experimental value of v_d. Notice also that the ratio of integrals in Eq. (1) has the dimension of time and it is, therefore, convenient to define the "effective" frequency $\langle \nu_m \rangle$ for momentum transfer at unit pressure as

$$\langle \nu_m \rangle = \frac{\int_0^\infty f_0(v) \, v^2 \, dv}{3 \int_0^\infty \frac{1}{NQ(v)} \frac{\delta f_0}{\delta v} v^2 \, dv}. \qquad (2)$$

This quantity is the true frequency for momentum transfer $\nu_m = NQ(v) \cdot v$ only when $Q(v)$ is inversely proportional to velocity. Otherwise, consider $\langle \nu_m \rangle$ to be the "effective" frequency for momentum transfer defined by Eq. (2) and evaluated by the experimental values of v_d. Equation (1) may now be written as

$$eE = mv_d \langle p_0 \nu_m \rangle, \tag{3}$$

a form which expresses momentum balance. Notice that $\langle p_0 \nu_m \rangle$ is the correct average value of collision frequency which assures momentum balance. The bracket $\langle\ \rangle$ will hereafter be omitted.

ENERGY BALANCE

The average rate at which the electrons absorb energy from the electric field is obtained by multiplying both sides of Eq. (3) by v_d, i.e.,

$$eEv_d = mv_d^2 \, p_0 \nu_m . \tag{4}$$

The total energy that the electron absorbs from the electric field is obtained by integrating over τ, the time of drift; i.e., $eEv_d\tau = eV$, which is what is expected for electrons that fall through a uniform electric field that is established by a potential difference V.

The energy that the electrons absorb from the field between two successive collisions is then, on the average,

$$\frac{eEv_d}{p_0 \nu_m} = mv_d^2 = 2\, u_d , \tag{5}$$

where u_d is the energy of drift.

The energy exchanged in each collision with a gas molecule is $\lambda(\bar{u}_g - u)$ where $\bar{u}_g$ is the thermal energy of the gas, which can be taken as kT, u is the energy of the electron, and $\lambda = (2\ \mathrm{m/M})$, the average fractional energy loss if collisions are elastic. In these collisions, energy is gained or lost, depending upon the relative magnitudes of $\bar{u}_g$ and u. It is reasonable to assume that the rate of energy exchange by this process is obtained by multiplying the fractional energy loss per collision by the "effective" collision frequency $p_0 \nu_m$. If an energy level at u_1 is excited, the rate of energy loss in such collisions is $p_0 \nu_u u_1$, where ν_u is the number of excitation collisions per second. The net rate at which electrons gain energy from the electric field and through collisions is then given by

$$\frac{du}{dt} = 2u_d p_0 \nu_m + \lambda p_0 \nu_m \, (\bar{u}_g - u) - p_0 \nu_u u_1 , \tag{6}$$

and the solution is

$$u(t) = \frac{2u_d}{\lambda} + \bar{u}_g - \frac{\nu_u u_1}{\lambda \nu_m} + Ae^{-\lambda \nu_m p_0 t} \tag{7}$$

where A is an arbitrary constant and where the relaxation time for energy equilibrium is $(\lambda \nu_m p_0)^{-1}$. The equilibrium energy u_e is

$$u_e = \frac{2u_d}{\lambda} + \bar{u}_g - \frac{\nu_u u_1}{\lambda \nu_m} \tag{8}$$

and if $u = 0$ when $t = 0$, it follows that $A = -u_e$. Hence, when energy equilibrium is established, the energy $2u_d$ that the electrons absorb from the electric field between successive collisions [See Eq. (5)] is expended in elastic and inelastic collisions according to the following expression which is obtained from Eq. (8)

$$2u_d = \lambda(u_e - \bar{u}_g) + \frac{\nu_u}{\nu_m} u_1 . \tag{9}$$

If the drift time of the electrons in a uniform electric field is τ, then the energy that the electrons transmit to the gas is given by the sum of the following two integrals

$$\int_0^\tau p_0 \nu_m \lambda (u - \bar{u}_g)\, dt + \int_0^\tau p_0 \nu_u u_1 \, dt , \tag{10}$$

where u is given by Eq. (7). When the substitution and integration are carried out, it is found that the energy transmitted to the gas is $eV - u_e$. Thus, at a given value of E/p_0, irrespective of the voltage V that is impressed across the chamber or the value of pressure p_0 by which the value of E/p_0 is obtained (it is assumed, however, that energy equilibrium is established), the electron swarm retains only a constant amount of energy in the form of random energy u_e, and transmits the remaining energy $(eV - u_e)$ to the gas.

RESULTS

If inelastic collisions do not occur, $\nu_u = 0$ and Eq. (8) can be used to obtain the equilibrium energy u_e as a function of E/p_0. In helium, if λ is taken to be 2.4 m/M, the values of u_e obtained from our drift velocity measurements are in good agreement with the experimental measurements of the characteristic energy $u_k = D/\mu$ (D is the diffusion coefficient and μ is the electron mobility) that are reported in the literature. For the other noble gases, however, the magnitude of the equilibrium energy u_e does not correspond to either the characteristic energy D/μ or to the average energy $\bar{u}$ of the swarm. The equilibrium energy which is defined solely by the drift velocity and λ when all collisions are elastic [see Eq. (8)] is consistently lower than $\bar{u}$ by a factor of 1.5 to 2. It would seem that the difference could be accounted for by adjusting the value of λ which itself is an averaged quantity and is therefore related to the particular distribution of energy that the electrons have.

The variation of u_e with E/p_0, when plotted on a log-log graph, is linear for the noble gases over the region of E/p_0 where thermal motion of the gas and

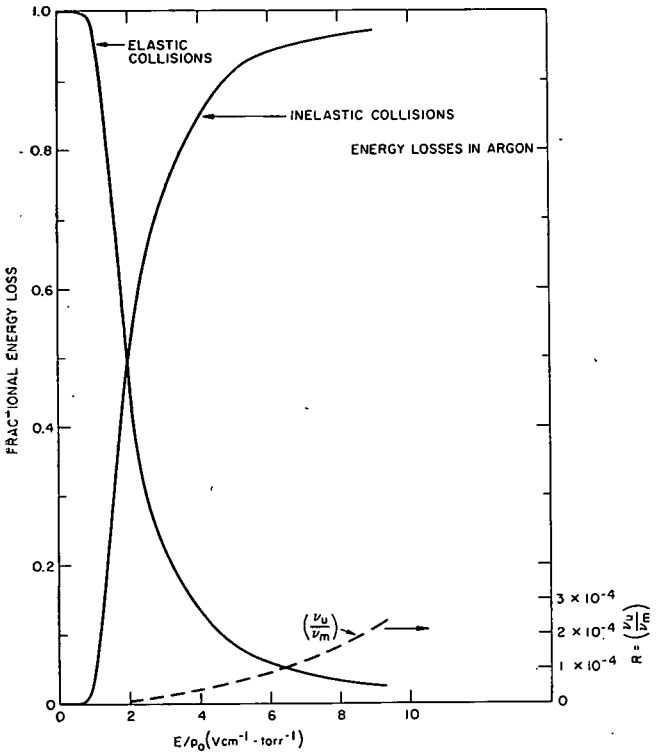

FIG. 14. Fractional input energy transmitted to argon atoms by elastic and inelastic collisions as a function of E/p_0. The dashed curve gives the ratio of the number of inelastic to elastic collisions that correspond to this division of energy.

inelastic collisions can both be neglected. For helium and neon the slope is about 1 and for argon, krypton, and xenon, the slope is about ½. At a higher value of E/p_0 that is characteristic of each gas, the slope changes quite abruptly to a value of about 2. This is interpreted as being caused by inelastic collisions, and energy losses due to inelastic collisions must now be taken into account in Eq. (8). There are no recent measurements of u_k in this region of E/p_0, but earlier work indicates that the energy stored in the swarm remains sensibly constant in the region immediately above the onset of inelastic collisions. Thus, by keeping u_e constant at its appropriate value, the ratio (ν_u/ν_m) in Eq. (9) can be evaluated when u_1 is known.

In Figure 14, the division of energy between elastic and inelastic collisions is shown for argon. The results are deduced, as outlined above, from drift-velocity data only. Also shown is the ratio of the number of inelastic to elastic collisions. It is interesting to note that the energy balance is thoroughly dominated by relatively few inelastic collisions, when they occur. The drift velocity and momentum balance, however, are still determined mainly by the elastic collision rate.

The literature was freely consulted in the preparation of this report. Because it is of a preliminary nature, individual papers are not cited. Instead, reference to several representative books on the subject is made. The author wishes to thank R. K. Langs for assembling the data and performing the computations.

REFERENCES

1. R. H. Healey and J. W. Reed. *The Behaviour of Slow Electrons in Gases*. Amalgamated Wireless Limited, Sydney, 1941.
2. L. B. Loeb. *Basic Processes in Gaseous Electronics*. University of California Press, Berkeley, California, 1955.
3. L. G. H. Huxley and R. W. Crompton. *Atomic and Molecular Processes*, Ed. D. R. Bates. Academic Press, New York, 1962, Ch. 10.
4. E. W. McDaniel. *Collision Phenomena in Ionized Gases*. John Wiley and Sons, New York, 1964.

*DRIFT VELOCITY AND THE ELASTIC COLLISION CROSS SECTION FOR ELECTRONS IN HELIUM**

Joseph C. Bowe and R. K. Langs

INTRODUCTION

We have recently repeated our measurements[1] of the drift velocity of electrons in helium and now report these results with particular reference a) to other existing measurements and b) to their relation to the collision cross section for slow electrons. The energy variation of the cross section $Q_m(u)$ in helium has been obtained from drift velocity measurements by both Frost and Phelps,[2] and by Crompton and Jory.[3] These cross sections are obtained by establishing agreement between calculated and measured values of electron drift velocity. In the numerical calculations that are carried out for this purpose, the cross section is treated as an adjustable parameter. It should be noted that this procedure embodies no a priori assumptions about the energy distribution function of the drifting electron swarm or about the mathematical form of the

* Paper presented at the 19th Annual Gaseous Electronics Conference, October 12–14, 1966, Atlanta, Georgia.

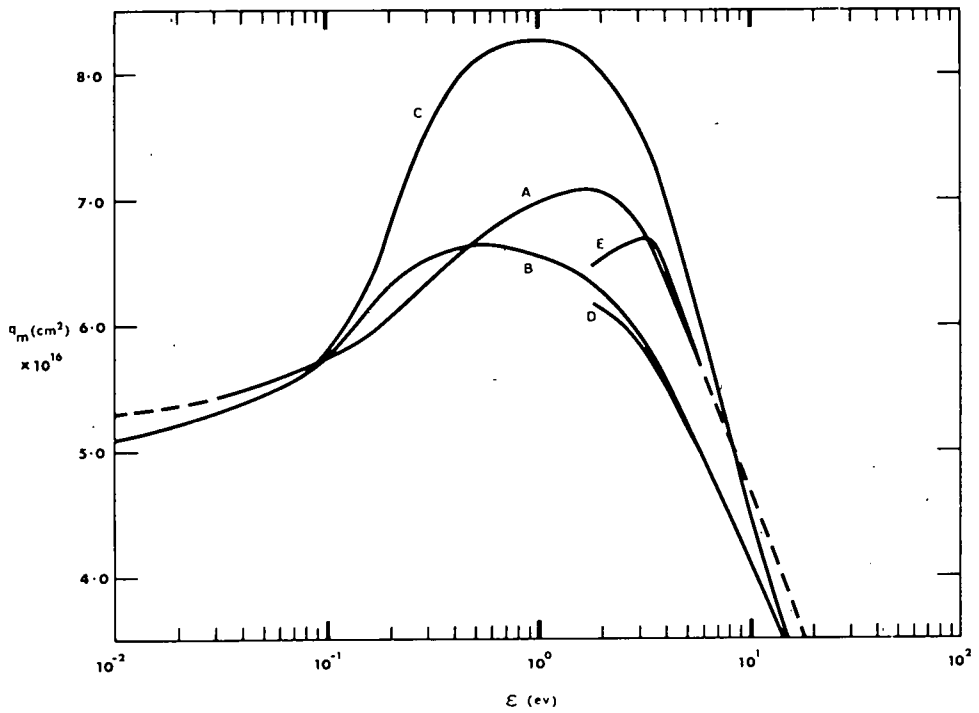

FIG. 15. Momentum transfer cross sections in helium: A, calculated from present drift-velocity data; B, Frost and Phelps; C from Bowe's data (Frost and Phelps); D, calculated from Bandel and Golden's beam data; E, calculated from Ramsauer and Kollath's data (Barbiere).

cross section as a function of energy. It follows, therefore, that a true energy dependence of the cross section is obtained. A basic limitation of this method, which Frost and Phelps[2] demonstrated, is the lack of energy resolution. The sensitivity of the drift velocity to the cross section can, however, be very great, as we shall see. Finally, it should be noted that analysis of swarm data leads directly to absolute values of cross section and no special calibration of the experimental apparatus is needed for this purpose.

SUMMARY OF CROSS SECTION MEASUREMENTS

We show in Figure 15 curves which were presented by Crompton and Jory[3] at the 1965 Conference in Quebec. The diffusion cross section for electrons in helium is plotted as a function of energy from 0.02 eV to about 10 eV. Curves A, B, and C are obtained from swarm measurements, whereas D and E are obtained from beam measurements of Ramsauer and Kollath[4] and from Golden and Bandel,[5] respectively. Crompton and Jory point out that the cross section around 2 eV (i.e., around the peak of the curve) is extremely sensitive to the drift velocity. On the other hand, the cross sections in the wings of the curve are much less sensitive to variation in the drift velocity. Crompton says that significant values are not obtained below 0.03 eV or above 7 eV.

The differences in curves A, B, and C are due solely to differences in the measurements of the drift velocity. This being the case, it would seem that better agreement should be possible. In this connection, we point out that curves A and B are derived from drift velocity data that are obtained by similar experimental techniques in which grids are employed as electrical shutters. In this method, the average current produced by a large number of drifting swarms is measured as a function of the frequency with which the shutters are opened and closed. These measurements generally require a correction for diffusion. On the other hand, the measurements that correspond to curve C are made by a method which we believe to be more direct and less complicated. In this method, which is due to Hornbeck,[6] we observe the transient current pulse induced by a *single* swarm of electrons that drift between two parallel plates. No grids are employed. The electrons that comprise the swarm are initially released from the cathode by a short burst of ultraviolet light. The current pulse which is subsequently observed on the oscilloscope, therefore, represents a time and space profile of a single swarm of drifting electrons. The width of the current pulse represents the time-of-flight of the electrons across the calibrated gap. These discrepancies in the literature values of drift velocity, therefore, raise the question of whether or not the two methods can, in fact, lead to equivalent values of drift velocity.

We, therefore, repeated our measurements using

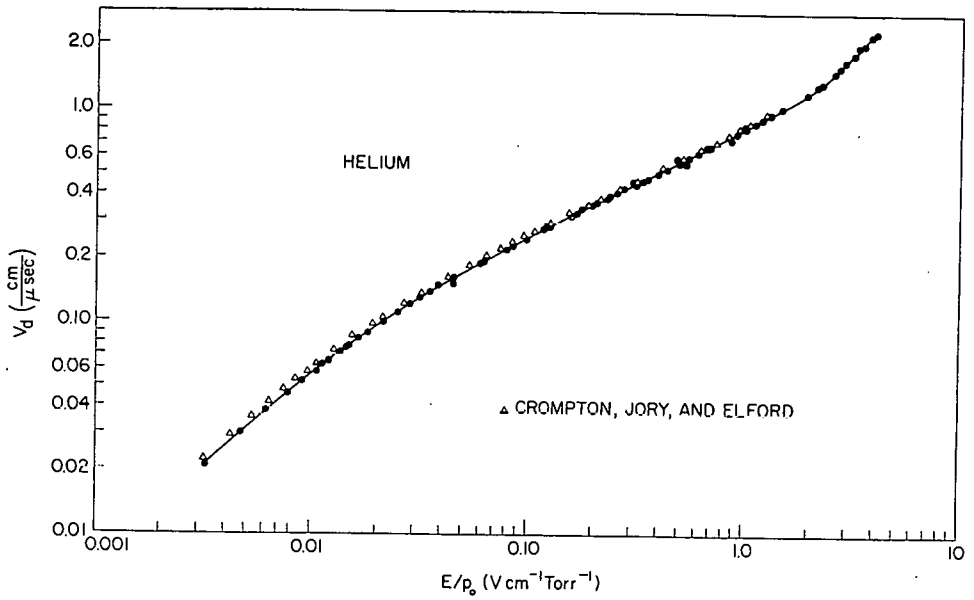

FIG. 16. Electron drift velocity in helium

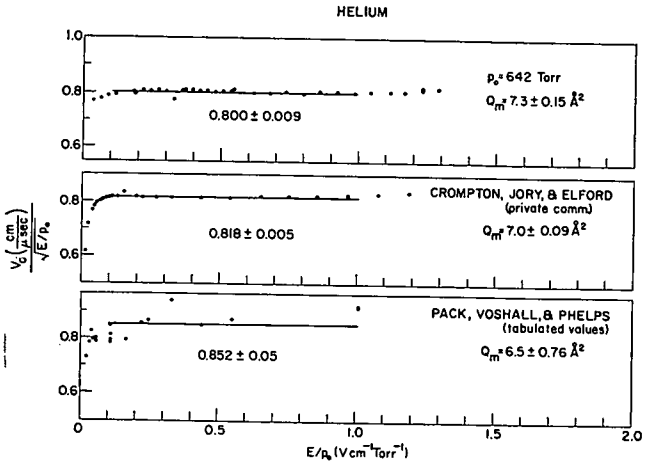

FIG. 17. Comparison of various drift velocity data

improved instrumentation. We constructed an improved light source that gives flashes of shorter duration, i.e., less than 50 nsec at half-maximum. We improved the signal-to-noise ratio of our wide band current amplifier by nearly a factor of ten (amplifier characteristics: rise time variable from 40 nsec to 1000 nsec, 7788 input tube in cascode with a 2N918 transistor). The oscillograms are read more accurately with the aid of a machine that digitizes the amplitude and time coordinates. In addition to these improvements, we made measurements over two drift distances and found, as we expected, that end corrections are not required. Measurements were carried out over a pressure range from 20 torr to 640 torr, and no pressure effect is observed. Finally, we also extended our measurements both to higher and lower values of E/p_0.

DRIFT VELOCITY MEASUREMENTS

In Figure 16 we compare our measurements with the most recent values of Crompton, Jory and Elford.[7] Here we plot the electron drift velocity in cm/μsec as a function of E/p_0. The open triangles represent the measurements of Crompton, Jory, and Elford. Although generally good agreement is obtained, there is nevertheless a small but definite difference in the two sets of data. We also point out that at the lower values of E/p_0, the electron swarm is in thermal equilibrium with the gas, whereas at the larger values of E/p_0, the swarm has sufficient energy to excite the gas. A striking feature of these data is that the drift velocity is proportional to $\sqrt{E/p_0}$ with a remarkable degree of precision in the range of E/p_0 from 0.1 to 1.0.

COMPARISON OF DATA

In Figure 17 we compare the constancy of the quotient $V_d/\sqrt{E/p_0}$ for different experimental data. The mean value of this quotient for the data of Pack, Voshall, and Phelps[8] is 0.852 with a standard deviation of ± 0.05 ($\sim 6\%$). The mean value for the data of Crompton, Jory, and Elford[7] is 0.818 with a standard deviation of about $\pm 0.6\%$. The mean value of the present measurements is 0.800 with a standard deviation somewhat larger than 1%. In this range of E/p_0 there is about a 2% difference between the ratio obtained by Crompton, Jory, and Elford and that obtained from the present measurements. This difference is outside the range of the assigned errors and might easily be due to a systematic error of some kind.

It is evident that the empirically constant value of the ratio $V_d/\sqrt{E/p}$ provides a convenient and sensitive

measure by which the various experimental data might be compared in this range. We also know that the formula for electron drift velocity given by Professor Allis[9] over 30 years ago shows that the drift velocity is proportional to $\sqrt{E/p}$ when the cross section is independent of energy, and when the thermal motion of the gas is neglected. The constant cross section that is consistent with the drift velocity data in the range E/p_0 from 0.1 to 1.0 is shown at the right of the figure. We see that the value of Crompton, Jory and Elford is very close to the mean of the other two values—one is about 5% higher and the other about 5% lower. We also have an example here of the sensitivity of the drift velocity to the cross section. A value of cross section that deviates by more than 1% from the value 7.0 Å^2 is no longer in agreement with the drift velocity measurements of Crompton, Jory and Elford. We do not, however, assign an energy range over which the cross section is constant because it is difficult to characterize the swarm accurately in terms of a "typical" electron. The behavior of the swarm is too complex to allow a description of all its properties in terms of a "typical" electron. Moreover, it is not clear that thermal motion of the swarm is indeed negligible in the range of E/p_0 from 0.1 to 1.0.

Whether or not the gas motion term in the formula for drift velocity can be neglected depends upon two factors. The first factor $(eE/NQ_m/2mu/M)$ compares the energy gain from the field between collisions to that lost in an elastic collision. The second factor $(eE/NQ_m/3kT)$ compares the energy gain between collisions with the kinetic energy of the gas atoms. It is not necessary that *each* factor *individually* be much greater than unity, but only that the *product* of these factors be much greater than unity in order that the thermal term should be negligible. It is simple enough to apply these criteria to a single electron that has a definite energy u, but it is not as simple and straightforward to decide whether or not thermal motion can be neglected for the swarm as a whole at a particular value of E/p_0. Thus at $E/p_0 = 0.1$ the product of the two above-mentioned terms has a value of about 2.5 if the swarm is characterized by an electron having *average* energy $\bar{u}$, or the product can have a value of about 6 if the swarm is represented by an electron that has the *characteristic* energy (D/μ) where D is the diffusion coefficient and μ is the mobility. This would seem to indicate that thermal motion is not entirely negligible at $E/p_0 = 0.1$. At $E/p_0 = 1.0$, the products of the ratios have corresponding values of 25 and 50. It would be interesting to make a careful comparison of drift velocity measurements at lower temperatures to assess the effect of thermal gas motion.

Our conclusions, therefore, are as follows: (1) A constant cross section is not altogether inconsistent with previous determinations if the energy range of constancy is properly restricted. (2) The two different methods that were used to measure the drift velocity seem to yield equivalent results. (3) The great disparity in the value of the cross section has been removed. (4) Calculations by Crompton and Elford[7] show that the drift velocity is about 5% lower at $E/p_0 = 0.1$ if the thermal motion term is retained in the formula when Q_m is energy independent. From this it follows that the cross section must decrease at lower electron energy.

We are indebted to Dr. Crompton for sending us his latest values prior to publication.

REFERENCES

1. J. C. Bowe. *Phys. Rev.* **117,** 1411 (1960).
2. L. S. Frost and A. V. Phelps. *Phys. Rev.* **136,** A1538 (1964).
3. R. W. Crompton and J. L. Jory. IVth Intern. Conf. on Physics of Electronic and Atomic Collisions, Université Laval, Quebec, August 2–6, 1965. Abstracts of Papers, Science Bookcrafters, Hastings-on-Hudson, N. Y., p. 118.
4. C. Ramsauer and R. Kollath. *Ann. Physik.* **12,** 529 (1932).
5. D. E. Golden and H. W. Bandel. *Phys. Rev.* **138,** A14 (1965).
6. J. A. Hornbeck. *Phys. Rev.* **83,** 375 (1951).
7. R. W. Crompton, private communication.
8. J. L. Pack, R. E. Voshall, A. V. Phelps. *Tables of Drift Velocities of Slow Electrons.* Research Report 62-928-113R1, Westinghouse Research Laboratories (1962).
9. P. M. Morse, W. P. Allis, and E. J. Lamar. *Phys. Rev.* **48,** 412 (1935).

PRODUCTION RATES OF NEUTRONS IN THE EARTH'S CRUST DUE TO NATURAL RADIOACTIVITY

Y. Feige, B. G. Oltman, and J. Kastner*

INTRODUCTION

Neutrons are produced in the earth's crust by (α,n) reactions involving mainly alpha rays of the uranium and thorium series impinging on the light elements, oxygen, sodium, magnesium, aluminum, and silicon. To estimate the neutron production rate, several compounds and elements were exposed to monoenergetic helium ions with energies ranging from 4.77 to 8.8 Mev. The following is an account of the experiment and the analysis of the derived relative neutron yield.

THE ENERGY DEPENDENCE OF (α,n) REACTIONS

Two important parameters which determine the cross sections of nuclear reactions induced by alpha particles are: (a) the reaction energy Q, defined for a $M_1(\alpha, n)\, M_2$ reaction as

$$Q = (M_1 + M_\alpha - M_2 - M_n)c^2, \qquad (1)$$

and (b) the height of the coulomb barrier B, which is approximately

$$B = \frac{2\,e^2 Z}{R} = \frac{2.88Z}{R}\ \text{MeV}, \qquad (2)$$

where $R = (1.4\ A^{1/3} + 1.2)\cdot 10^{-13}$ cm.

The threshold energy E_{th} for an alpha induced reaction is the minimum kinetic energy the impinging alpha particle must have (in the laboratory system) to make the reaction energetically possible.

For endothermic reactions, it is

$$E_{th} = -\frac{M_1 + M_\alpha}{M_1} Q. \qquad (3)$$

The threshold energy is zero for exothermic reactions (having a positive reaction energy Q).

Table 7 lists some data relevant to (α,n) reactions for the more abundant isotopes found in the earth's crust.

The highest energy of naturally emitted alpha particles is 8.78 MeV arising from the decay of Po^{212} (Th C'). Hence O^{16}, Si^{28} and Ca^{40}, which constitute some 75% of the earth's crust by weight (over 82% of the numbers of atoms),[1] cannot participate in the natural (α,n) reactions because of their high E_{th}, and similiarly the contribution of Mg^{24} (if any) will be negligible.

The cross sections of nuclear reactions induced by alpha particles are extremely small for low or intermediate alpha energies because the low transmission of the coulomb barrier prevents any appreciable interaction, even with nuclei for which (α,n) reactions are energetically possible. Furthermore, most alpha particles will be slowed down by coulomb interactions with the electrons of the medium before their first nuclear encounter. It follows that the isotopes for which $B > 8$ MeV, namely all the elements for which Z exceeds 16, cannot contribute significantly to the neutron yield considered here. The only target iso-

TABLE 7. THRESHOLD ENERGIES FOR NUCLIDES OF THE MORE ABUNDANT ELEMENTS

Element	Abundance in the earth's crust, % of weight[1]	B, MeV	Isotope	Relative abundance, %	$E_{th}^{(2)}/Q^{(3)}$, MeV
$_8$O	46.6	4.8	O^{16}	99.76	15.19
			O^{17}	0.0374	0 (+0.6)
			O^{18}	0.204	0.86
$_{14}$Si	27.7	7.3	Si^{28}	92.27	9.26
			Si^{29}	4.68	1.75
			Si^{30}	3.05	3.98
$_{13}$Al	8.13	6.9	Al^{27}	100	3.05
$_{26}$Fe	5.0	11.4	Fe^{56}	91.67	5.47
$_{20}$Ca	3.63	9.4	Ca^{40}	96.97	12.27
			Ca^{44}	2.06	2.37
$_{11}$Na	2.83	6.1	Na^{23}	100	3.48
$_{19}$K	2.59	9.1	K^{39}	93.08	7.90
			K^{41}	6.91	3.72
$_{12}$Mg	2.09	6.5	Mg^{24}	78.60	8.39
			Mg^{25}	10.11	0 (+2.65)
			Mg^{26}	11.29	0 (+0.04)
$_{15}$P	1.18	7.7	P^{31}	100	6.39
$_{25}$Mn	1.00	11.0	Mn^{55}	100	3.76
$_{16}$S	0.52	8.0	S^{32}	95	9.71
$_{22}$Ti	0.44	10.1	Ti^{48}	73.45	2.93
$_{17}$Cl	0.32	8.3	Cl^{35}	75.4	6.54
			Cl^{37}	24.6	4.31
$_6$C	0.32	3.9	C^{12}	98.9	11.35
			C^{13}	1.1	0 (+2.2)
$_9$F	0.30	5.25	F^{19}	100	2.36
$_3$Li	0.065	2.25	Li^6	7.3	6.64
			Li^7	92.7	4.38
$_4$Be	0.006	2.8	Be^9	100	0 (+5.71)
$_5$B	0.003	3.4	B^{10}	19.8	0 (+1.07)
			B^{11}	80.2	0 (+0.15)

* Visiting Scientist on leave from the Soreq Nuclear Research Centre, Yavne, Israel.

TABLE 8. Relative Neutron Yields for Thick Targets

Target	α energy in MeV						
	8.8	7.7	6.8	6.0	5.3	4.77	4.1[a]
Experimental							
SiO_2	15.7	8.3	4.3	2.3	1.00	0.46	0.07
Na_2CO_3	200	121	54	26.3	10.1	3.15	0.65
K_2CO_3	13.3	7.4	4.6	2.37	1.05	0.38	0.1
Al	223	116	51	20.2	6.8	1.81	0.28
Mg	169	100	55	27	13.4	4.9	0.93
Fe	31.4	6.3	0.71	0.25	0.068	0.017[a]	0.003
CaF_2	441	306	203	108[a]	52.5	25.4[a]	8.50
Calculated[b]							
Na	520	315	140	68.5	26.2	8.2	1.7
F	960	670	445	248	115	56	18.5

[a] Estimated by extrapolation.

[b] Assuming the (α,n) yield of a compound is simply the sum of the (α,n) yields of its atomic components, weighted by their relative mass stopping power.[11-15]

topes which seem of some importance for possible (α,n) reactions are aluminum and sodium (which are monoisotopic elements) and the less abundant isotopes of oxygen, magnesium, and silicon. The contribution of fluorine and other light elements like beryllium or boron, having a low coulomb barrier, may be detectable in geological formations in which their abundance is unusually high. Data for these light elements are included in Table 7 for comparison, as (α,n) reactions in light elements, induced by 5.3 MeV alpha particles of Po^{210}, have been extensively studied.[4-8]

EXPERIMENTAL PROCEDURES

Several targets of light elements, or their compounds, and one gold target for background determinations, were exposed to monoenergetic alpha-particle beams from the Argonne van de Graaf Tandem Accelerator. To obtain integral results, thick targets, about ⅛ in. in thickness and ¾ in. in diameter, were mounted on a mechanical target holder, which enabled easy and rapid change of targets, without loss of vacuum.[9] The targets were, respectively, a quartz disc (SiO_2), Al, Mg, and Fe metal discs, and tightly compressed pellets of analytically pure Na_2CO_3, K_2CO_3 and CaF_2 powder.

Relative neutron yields in the forward direction for six alpha energies, ranging from 4.77 to 8.8 MeV, were determined using a long counter 5 inches from the target. The long counter consisted of a He^3 proportional counter inside a directional paraffin moderator as described by Hanson and McKibben.[10] These targets allowed us to reconstruct 95% of the earth's crust by weight. The iron target was used to represent the "high" Z elements, while fluorine in CaF_2 represented the light element with relatively high (α,n) yields in the earth's crust.

TABLE 9. Relative Neutron Yields for the Th and U Series

Target	Th(α)	U(α)	Abundance in granite	Th(α)	U(α)
SiO_2	3.52	1.76	0.6950	2.45	1.22
Na_2CO_3	42.9	22.2	0.0678	2.91	1.51
K_2CO_3	3.34	1.64	0.0457	0.153	0.075
Al	42	19.4	0.0813	3.41	1.58
Mg	40.6	21.1	0.0209	0.85	0.44
Fe	3.64	0.84	0.0505	0.184	0.042
CaF_2	135	75.5	0.0006	0.081	0.045
Granite			1.0000	10.44	5.11
Na	111	58.6	0.0283		
F	296	165	0.0003		

RESULTS

The net counts per target, normalized to SiO_2 yield at 5.3 MeV are listed in Table 8.

In the energy ranges considered here, the atomic stopping power of each atom in a compound may be taken as independent of the presence of atoms of other types.[11] The values from sodium (α,n) yields were calculated from the Na_2CO_3 results neglecting any contribution from CO_3, in view of the low yields found for K_2CO_3. The (α,n) yields of fluorine were calculated from the CaF_2 results assuming the yield from Ca to be negligible.

The weighted average yields per alpha particle for the six alpha disintegrations of the Th^{232} series, and the eight alpha disintegrations of the U^{238} series, are shown for each of the targets in Table 9. The last

TABLE 10. Comparison of Relative Neutron Yields for 5.3-MeV Alpha Particles

Target	This experiment	Gorshkov[8]	Roberts[7]
SiO_2	1.00	1.00	1.00[a]
O	—	0.63	0.66
CaF_2	52.5	60.2	60.6
Na	26.2[a]	—	14
Mg	13.4	12.5	13.1
Al	6.8	7.1	6.9
Si	—	1.57	1.5
Fe	0.068	—	—
Granite	2.39[a]	2.23	—

[a] Calculated.

TABLE 11. Comparison of Experimental Data with Theoretical Predictions of Neutron Yields (Y)

Target	Y(Thα)/Y(5.3)		Y(Uα)/Y(5.3)		Y(Thα)/Y(Uα)	
	This experiment	Morrison and Pine's calculations[18]	This experiment	Morrison and Pine's calculations	This experiment	Morrison and Pine's calculations
SiO_2	3.5	2.9	1.8	1.7	2.0	1.7
Na	4.2	3.4	2.2	1.7	1.9	2.0
Mg	3.0	2.7	1.6	1.6	1.9	1.7
Al	6.2	4.2	2.9	2.1	2.2	2.0
Granite	4.4	3.7	2.1	1.8	2.1	2.0

two columns of Table 9 show how the weighted average (α,n) yield for granite (= the earth's crust) is derived. The composition of granite by weight, consistent with the data included in Table 7, is given in the preceding column.

SiO_2 (abundance of 69.5%) contributes less than 25% to the neutron yield of granite. The actual yield will depend mainly on the amount of Na and Al in the sample. The (α,n) yield per alpha particle of the Th series in sand (SiO_2) or granite is twice as high as that of the U series.

DISCUSSION

Table 10 compares our results at 5.3 MeV with the systematic studies undertaken by Gorshkov et al.[8] and by Roberts[7] of the neutron yields due to (α,n) reactions from light elements and granite, using Po^{210} alpha particles.

The agreement is excellent, considering the fact that our measurements are in the forward direction, whereas Gorshkov and Roberts' data are based on wide angle measurements. No corrections seemed necessary for the energy dependence of the neutron detection efficiency of the long counter.[16]

Angular distribution corrections might be indicated, although at the alpha energies used the compound nucleus will usually also decay to excited states of the residual nucleus through neutron emission, thus tending towards isotropic emission in the center of mass system.[17] We plan further experiments at different angles in order to elucidate this point.

Table 11 compares our results with calculations performed by Morrison and Pine,[18] who assumed (α,n) cross sections simply proportional to the coulomb barrier penetration probability. Their values are systematically somewhat lower than ours, usually about 25%, which would be expected if the (α,n) cross section continues to increase beyond the height of the potential barrier. This systematic difference may also be explained by the large extrapolation necessary to obtain the ThC′ (Po^{212}) and RaC′ (Po^{214}) yields from measured Po^{210} data.

CONCLUSIONS

Table 8 allows us to assign absolute values to our relative measurements if we accept Gorshkov's[8] determinations of

$$Y(SiO_2) = 10.7 \text{ n}/10^8 \ \alpha \text{ of } Po^{210}, \qquad (4)$$

10^{-6} g of Th^{232} emit $0.77 \cdot 10^6$ α particles per year; thus 1 ppm by weight will produce 0.29 n/g/year in sand (SiO_2) and 0.85 n/g/year in granite. And 1 ppm of U^{238} emits $3.11 \cdot 10^6$ α/year; thus it will produce 0.60 n/g/year in sand and 1.7 n/g/year in granite. An additional 0.48 n/g/year will be generated due to spontaneous fission in 1 ppm U^{238}.[19]

Assuming 3 ppm U^{238} and 11 ppm Th^{232} as representative of the upper earth's crust,[19, 20] a production rate of 6.4 n/g/year in soil and 16 n/g/year in granite is obtained. One should keep in mind that the upper layers of the soil may significantly differ in composition and in their uranium and thorium contents, or their radioactive decay products, from the underlying geologic structures.[21, 22]

The production rate of neutrons due to cosmic ray interactions in soil must be of the order of 1 to $2 \cdot 10^3$ n/g/year to account for the neutron flux of 5 to $10 \cdot 10^{-3}$ n/sec/cm^2 as observed on the earth's surface.[19, 23-26] Thus, in comparison to cosmic ray produced neutrons, (α,n) reactions cannot be of any significance in exposure rates of human populations. They may be of some interest to geologists, however, and be the main contributors to neutron fluxes in tunnels, deep caves or mines where the cosmic ray background is unusually low.

This problem was brought to our attention by Professor A. Nir of the Weizman Institute of Science, Rehovot, Israel. We are indebted to Dr. J. P. Schiffer

and Dr. A. J. Elwyn of the Physics Division for the valuable advice and use of facilities. We are grateful to R. Selman and E. Fudala of Central Shops and D. E. White, Metallurgy Division, for their help in the preparation of the various targets.

REFERENCES

1. *Handbook of Chemistry and Physics*, 45th Edition, (1964), p. F-81
2. R. J. Howerton, D. L. Braff, W. J. Cahill and Nanette Chazan. Thresholds of He^4-Induced Reactions. University of California Radiation Laboratory Report UCRL-14005 (1964).
3. W. Kunz and J. Schintlmeister. *Nuclear Tables, Part II. Nuclear Reactions*. Pergamon Press, Ltd., London, 1965.
4. E. Amaldi. The Production and Slowing Down of Neutrons. *Encyclopedia of Physics*, Ed. S. Flugge, Springer Verlag, Heidelberg, 1959, Vol. **37/2**, pp. 107–130.
5. A. D. Hanson. Radioactive Neutron Sources. *Fast Neutron Physics*, Ed. J. B. Marion and J. L. Fowler. Interscience Publishers, Inc., New York, 1960, Ch. I-A.
6. H. L. Anderson. Neutrons from Alpha Emitters. National Research Council, Nuclear Science Series, Preliminary Report No. 3, Washington, D. C. (1948).
7. J. H. Roberts. Neutron Yields of Several Light Elements Bombarded with Polonium Alpha Particles. U. S. Atomic Energy Commission Report MDDC-731 (1947).
8. G. V. Gorshkov, V. A. Zyabkin, and O. S. Tsvetkov. Neutron Yield from the Reaction (αn) in Be, B, C, O, F, Mg, Al, Si, and Granite Irradiated with Polonium Particles. *Atomnaya Energiya* **13**(1), 65 (1962).
9. A. J. Elwyn, A. Marinov, and J. P. Schiffer. Proton Reactions, Cross Sections and Strength Functions. *Phys. Rev.* **145**, 957–962 (1966).
10. A. O. Hanson and J. L. McKibben. A Neutron Detector Having Uniform Sensitivity from 10 keV to 3 MeV. *Phys. Rev.* **72**, 673–677 (1947).
11. R. D. Evans. *The Atomic Nucleus*. McGraw-Hill Book Co., New York, 1955, p. 646.
12. R. E. Tate and A. S. Coffinberry. Plutonium-Beryllium Neutron Sources, Their Fabrication and Neutron Yield. *2nd U.N. Intern. Conf. on the Peaceful Uses of Atomic Energy*, **14**, 427–431, (1958).
13. H. A. Bethe. Nuclear Dynamics. *Rev. Mod. Phys.* **9**, 211 (1937).
14. J. F. Janni. Calculation of Energy Loss, Range Pathlength, Straggling, Multiple Scattering and the Probability of Inelastic Nuclear Collisions for 0.1- to 1000-MeV Protons. Air Force Weapons Laboratory Report AFWL-TR-65-150 (1966).
15. J. F. Janni. Calculation of Energy Loss Range and Pathlength for 2- to 12-MeV Alpha Particles. Private communication (1967).
16. W. D. Allen. Flat Response Counters. *Fast Neutron Physics*, Ed. J. B. Marion and J. L. Fowler. Interscience Publishers, Inc., New York, 1963, Ch. III-A.
17. L. J. B. Goldforb. Angular Correlations and Polarization. *Nuclear Reactions*, Ed. P. M. Endt and M. Demeur. North-Holland Publ. Co., Amsterdam, 1959, Vol. I, Ch. IV, pp. 159–193.
18. P. Morrison and J. Pine. Radiogenic Origin of the Helium Isotopes in Rock. *Ann. N. Y. Acad. Sci.* **62**, 69–92 (1955).
19. *Radiation from Natural Sources*. UNSCEAR Report, A/6314, Annex A, Supplement No. 14. United Nations, New York, 1966, pp. 18–27.
20. J. A. S. Adams. Radioactivity of the Lithosphere. *Nuclear Radiation in Geophysics*, Ed. H. Israel and A. Krebs. Academic Press, New York, 1962, pp. 1–17.
21. A. B. Tanner. Radon Migration in the Ground. *The Natural Radiation Environment*, Ed. J. A. S. Adams and W. M. Lowder. University of Chicago Press, Chicago, 1964, Ch. IX.
22. W. S. Osburn. Primordial Radionuclides, Their Distribution, Movement, and Possible Effect within Terrestrial Ecosystems. *Health Phys.* **11**, 1275–1295 (1963).
23. J. Kastner, B. G. Oltman, L. D. Marinelli, and J. H. Klems. Measurement of the Cosmic Ray Fast Neutron Background. Argonne National Laboratory Radiological Physics Division Annual Report, July 1963 through June 1964. ANL-6938, (1964), pp. 71–76.
24. L. L. Newkirk. Calculation of Low Energy Neutron Flux in the Atmosphere by the Sn Method. *J. Geophys. Res.* **68**, 1875–1833 (1963).
25. J. A. Simpson. Neutrons Produced in the Atmosphere by Cosmic Radiation. *Phys. Rev.* **83**, 1175–1188 (1951).
26. J. A. Simpson and W. C. Fagot. Properties of the Low Energy Nucleonic Component at Large Atmospheric Depths. *Phys. Rev.* **90**, 1068–1072 (1953).

TABULATION OF LUMINESCENCE CHARACTERISTICS UNDER THE INFLUENCE OF INTERMOLECULAR ENERGY TRANSFER

*Mitio Inokuti and Fumio Hirayama**

School of Chemistry, University of Minnesota.

An extensive tabulation of donor luminescence characteristics, such as the yield and various decay times, as functions of the acceptor concentration under the influence of intermolecular energy transfer has been a long contemplated project designed to provide an extension of an earlier publication.[1] The completed compilation of numerical and tabular material should provide a sound quantitative basis for the analysis of experimental data on solid state luminescence and should eventually lead to recognition of the different mechanisms involved in energy-transfer processes.

Significant progress has been made towards comple-

tion of the tabulation, and several new points of view have been formed concerning methods of analysis with use of calculated data. A revised computer program now permits the computation of the $1/e$-decay time after steady-state excitation, τ_{es}, in addition to other decay times already discussed.[1] This quantity τ_{es} deserves considerable attention, because its accurate measurements seem feasible under interesting experimental situations, such as when the donor is a triplet state, and also because the variation of τ_{es} with the acceptor concentration depends fairly strongly on the type of energy-transfer processes.

Continued efforts are being made for the preparation of the final tabulation.[2]

REFERENCES

1. M. Inokuti and F. Hirayama. *J. Chem. Phys.* **43**, 1978 (1965).
2. M. Inokuti and F. Hirayama. Tables for Analyzing Luminescence Data in Energy-Transfer Studies, in preparation.

*SUM RULE FOR THE BETHE INELASTIC-SCATTERING CROSS SECTIONS**

Mitio Inokuti, Y. K. Kim, and R. L. Platzman†

We report a sum rule for the Bethe inelastic-scattering cross section[1] which makes possible an accurate theoretical calculation of the total cross section for inelastic scattering of any swiftly-moving charged particle by an atom or a molecule.

The Bethe cross section for an optically-allowed electronic transition to the states induced by a particle of charge ze and (nonrelativistic) velocity v is

$$\sigma_s = \frac{4\pi a_0^2 z^2}{T/R} \frac{f_s}{E_s/R} \ln (4c_s T/R), \qquad (1)$$

where a_0 is the Bohr radius, R the Rydberg energy, $T = mv^2/2$ (m being the *electron* mass), E_s is the excitation energy of the state s measured from the ground state, f_s the (dipole) oscillator strength for the transition, and c_s an atomic constant characterizing the particular transition. (If T exceeds about 10^4 eV, elementary corrections for relativistic kinematics are required.) For an optically-forbidden transition to the state s' (for which $f_{s'} = 0$) the corresponding expression is

$$\sigma_{s'} = \frac{4\pi a_0^2 z^2}{T/R} b_{s'}, \qquad (2)$$

where $b_{s'}$ is a corresponding atomic constant. The dimensionless constant $f_s R/E_s$, which will be denoted by M_s^2, embodies the contribution of "glancing" ("optical") collisions (small values of $\mathbf{K}\hbar$, the momentum change of the particle) and c_s, $b_{s'}$ the contribution of the "close" ("hard") collisions (large values of $\mathbf{K}\hbar$). The total inelastic-scattering cross section is then

$$\sigma_{\text{tot}} = \sum_s \sigma_s + \sum_{s'} \sigma_{s'} = \frac{4\pi a_0^2 z^2}{T/R} M_{\text{tot}}^2 \ln (4c_{\text{tot}} T/R), \qquad (3)$$

where the summations, which include integration over continua, refer to all optically-allowed and all optically-forbidden transitions, respectively.

Theoretical evaluation of formula (1) or (2) devolves upon calculation of f_s and c_s, or $b_{s'}$, all of which require accurate knowledge of the corresponding excited-state wave function. Such wave functions are inexactly known in all cases except atomic hydrogen, and indeed rather poorly known in most of them. It is this obstacle which has thus far crippled the general application of the Bethe formulae. In Equation (3), however, only the two atomic constants can be determined from the ground-state wave function alone. The factor M_{tot}^2 is an optical property, that is, is determined by the oscillator-strength distribution:

$$M_{\text{tot}}^2 = \sum_s M_s^2 = \sum_s f_s R/E_s . \qquad (4)$$

It can be computed either from the $f_s(E_s)$ according to Equation (4) or from the equivalent expression:

$$M_{\text{tot}}^2 = \sum_{j,k} \langle x_j x_k \rangle / a_0^2 , \qquad (5)$$

in which $\langle\ \rangle$ denotes an expectation value in the ground state. The constant c_{tot} has not hitherto been treated theoretically, apart from the one-electron case. We show that it, too, can be expressed exactly in terms of an optical property and ground-state expectation values:

* Abstract of a paper presented at the Fifth International Conference on the Physics of Electronic and Atomic Collisions, Leningrad, U.S.S.R., July 17–23, 1967. A few corrections have been made to the version printed in "Abstracts of Papers," Publishing House Nauka, Leningrad, 1967. A fuller account of the work appears in *Phys. Rev.* **164**, 55 (1967).

† Departments of Physics and Chemistry, The University of Chicago.

$$M_{\text{tot}}^2 \ln c_{\text{tot}} = -2 \sum_s M_s^2 \ln E_s/R + Z \int_0^1 S_{\text{inc}}(K)\, d(Ka_0)^{-2} - \int_1^\infty [M_{\text{tot}}^2 (Ka_0)^2 - ZS_{\text{inc}}(K)]\, d(Ka_0)^{-2}. \quad (6)$$

Here Z is the number of electrons in the atom and $S_{\text{inc}}(K)$, commonly called the incoherent scattering function, is defined by

$$S_{\text{inc}}(K) = \frac{1}{Z}\left[\sum_{j,k} \langle \exp i\mathbf{K}\cdot(\mathbf{r}_j - \mathbf{r}_k)\rangle - \left|\sum_j \langle \exp i\mathbf{K}\cdot\mathbf{r}_j\rangle\right|^2\right]. \quad (7)$$

APPLICATIONS

The content of the sum rule was utilized implicitly by Bethe in his treatment[1] of scattering by the hydrogen atom. Here the correlation terms in Equations (5) and (7) are absent and Equation (6) reduces to a very simple form. The values of the constants are[1, 2]

$$M_{\text{tot}}^2 = 1, \qquad \ln c_{\text{tot}} = 0.449469.$$

In the case of the helium atom a great variety of approximate wave functions of differing quality is available. Many values of M_{tot}^2 have, indeed, already been computed for other purposes from Equation (5): the definitive one is that of Pekeris,[3] 0.752498, but even as simple a function as the 6-parameter Hylleraas wave function gives a result only ¼% lower. We have performed numerous calculations of c_{tot} in order to examine its convergence as the wave function is improved, and to explore its dependence on various characteristics of the wave function. Apart from the importance for helium, this study is intended to provide a guide for the investigation of more complex atoms, for which the wave functions are less well known. The best values are

$$M_{\text{tot}}^2 = 0.75250, \qquad \ln c_{\text{tot}} = -0.5050,$$

the former from Pekeris and the latter computed from the 20-parameter Hylleraas wave function. The total inelastic-scattering cross section is, therefore,

$$\sigma_{\text{tot}} = \frac{z^2}{T}(3.603 \ln T - 6.229) \times 10^{-15} \text{ cm}^2, \quad (8)$$

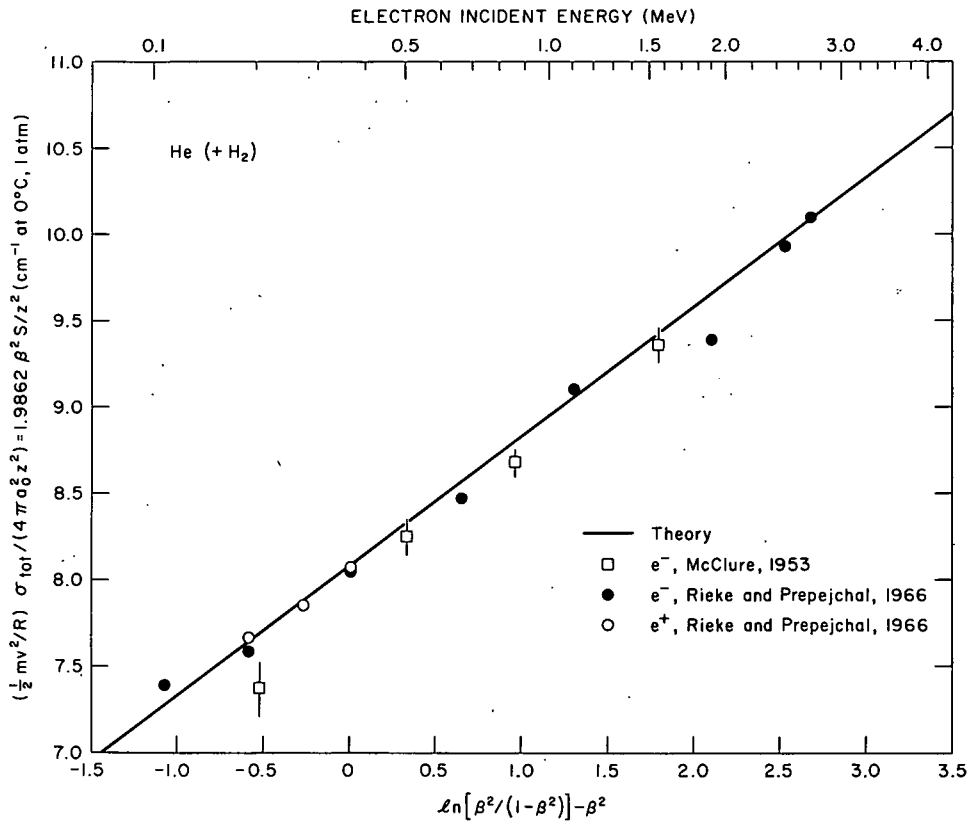

FIG. 18. The total cross section for inelastic scattering of charged particles by helium. The ordinate is $(\frac{1}{2}mv^2/R)\sigma_{\text{tot}}/(4\pi a_0^2 z^2)$. The horizontal scale at the bottom applies to all kinds of the particles; the nonlinear scale at the top is restricted to particles of mass m. The measurements, which yield the specific primary ionization S (number of primary ions per cm at 1 atm, 0°C) are in effect determinations of σ_{tot} because the helium contains a small admixture of hydrogen, which serves to convert each excitation event to an ionization.[4,5]

T being expressed in eV, or, for the relativistic case,

$$\sigma_{tot} = \left(\frac{z}{\beta}\right)^2 \left[1.410\left[\ln\left(\frac{\beta^2}{1-\beta^2}\right) - \beta^2\right] + 15.118\right] \times 10^{-20}\ \text{cm}^2, \quad (9)$$

where $\beta = v/c$. We estimate the uncertainty in these cross sections as smaller than 0.1 % for $T \gtrsim 2 \times 10^4$ eV. (In the relativistic region, T is defined as the product of the kinetic energy and m/M, where M is the mass of the incident particle.)

The Bethe formula becomes a straight line when plotted with $\frac{1}{2}mv^2\sigma_{tot}/4\pi a_0^2 z^2 R$ as ordinate and $\ln[\beta^2/(1-\beta^2)] - \beta^2$ as abscissa. (At nonrelativistic energies, it is more convenient to use the logarithm of the kinetic energy as abscissa; this differs only by a horizontal displacement.) Figure 18 presents such a plot of Equation (9), together with available experimental data. The agreement is excellent, and it should be noted that the uncertainty in the theoretical values is very likely as much as 100 times smaller than that in the measurements.

Calculations for neon and for argon using Hartree-Fock wave functions have also been made. Application to molecules, which requires averaging over the spatial anisotropy, is also promising and is under current study. In both cases useful values of M_{tot}^2 are already available in the literature, although their relevance to scattering phenomena has not been recognized.

Current theoretical and experimental information on absolute cross sections for inelastic scattering is highly undependable, being pervaded by innumerable uncertainties and errors. Use of the sum rule should aid greatly in improving knowledge of these cross sections. It will even bring benefits at low velocities, below the range of validity of the Born and Bethe approximations, for the total cross section there must approach the Bethe values as the velocity increases. Although its results will inevitably be less accurate, the more complex is the atom, this will tend to be compensated by the circumstance that less is known about the cross sections. The theoretical total cross section may also be exploited as a requirement of compatibility among the individual inelastic cross sections. It can serve to deduce total excitation cross sections from experimental ionization cross sections, which, when available, are usually far more trustworthy than excitation cross sections. When the ionization cross section is quite unknown it can be obtained in favorable cases by estimate of the excitation cross section.

REFERENCES

1. H. Bethe. *Ann. Physik.* **5**, 325 (1930).
2. M. Inokuti. Argonne National Laboratory Radiological Physics Division Summary Report, July 1962 through June 1963. ANL-6769, p. 7.
3. C. L. Pekeris. *Phys. Rev.* **115**, 1216 (1959).
4. G. W. McClure. *Phys. Rev.* **90**, 796 (1953).
5. F. F. Rieke and W. Prepejchal. Personal communication (1966).

*THE EFFECTS OF FAST NEUTRON EXPOSURE ON THE ^{7}LiF THERMOLUMINESCENT RESPONSE TO GAMMA RAYS**

B. G. Oltman, J. Kastner, P. Tedeschi

An experiment is described, the results of which indicate that the gamma-ray response of ^{7}LiF is diminished when the thermoluminescent dosimeter is exposed to fast neutrons in the range, 0.1 to 1 MeV. The diminution occurs regardless of whether the gamma-ray exposure is carried out before or during the neutron bombardment.

* Abstract of paper to be published in *Health Physics*.

THERMOLUMINESCENT MICRODOSIMETRY IN DENTAL RADIOLOGY. I. TECHNIQUE*

C. E. Rehfeld,† J. Kastner, B. G. Oltman, H. M. Rosenberg,‡ and D. E. Doyle†

Irradiation of lithium fluoride (LiF) crystals leads to an excited energy state due to the entrapment of freed electrons in the LiF crystal defects. The electrons remain trapped at room temperatures, but are released at higher temperatures, e.g. 200°C. When the irradiated LiF crystals are raised to a high temperature in a short time (15–30 seconds), de-excitation occurs with an emission of visible light. This emitted light is registered by an electronic phototube and recorded in the form of a glow curve on a strip chart. The integral of the curve is directly proportional to the ionizing radiation exposure.

Nine milligrams of annealed LiF powdered crystals are loaded into each section of a plastic tube measuring 1 × 10 mm in outside dimensions. Each section of loaded tube is heat-sealed to form one microdosimeter; it is small enough to be placed in a large dental cavity or in the dental supporting tissues. After x-ray exposure, the powder is emptied from the tube onto a small pan, heated to obtain a glow curve, and weighed as a final step. The integral of the glow curve is divided by the weight of LiF in the pan to determine the response per mg of LiF.

Calibration, in roentgens, is accomplished by exposing a number of microdosimeters to radioactive Ra or Co standards. The irradiation response per mg of the LiF exposed to Ra or Co provides the factor for conversion of response per mg of x-ray exposure to roentgens. Ionizing effects of beta, gamma, and x-ray radiation can all be measured equally well. The variation in 0.1 and 1.0 R readings is ±5% and ±2%, respectively.

* Abstract of a paper presented at the International Association of Dental Research (Radiology Section) held in Washington, D. C., March, 1967. Publication is planned for the *Journal of Oral Surgery, Oral Medicine and Oral Pathology.*

† Biological and Medical Research Division.

‡ University of Illinois College of Dentistry, Chicago.

THERMOLUMINESCENT MICRODOSIMETRY IN DENTAL RADIOLOGY. II. CLINICAL APPLICATION*

H. M. Rosenberg,† C. E. Rehfeld,‡ J. Kastner, B. G. Oltman, D. E. Doyle,† and D. J. Hauptfuehrer†

Lithium fluoride microdosimeters are being used to measure relative and absolute x-ray doses to skin, teeth, and other oral structures in dental patients. This pilot study was designed to develop a technique for the employment of these dosimeters in radiology.

Each microdosimeter is placed in one of three anatomical locations to be aligned in an x-ray beam. The dental films are processed to assure adequate exposure to produce routine x-ray images. The microdosimeters are read in the manner described by Kastner.[1]

The initial group consisted of 50 randomly selected patients. Eight primary dental x-ray examination areas on the right side of the face were selected, and two or three patients were employed for each area. Fixed wet specimens of maxillae and mandibles, from which no tissue had been removed, provided teeth for intradental measurements. Microdosimeters were placed in the pulp chambers and in the adjacent gum tissue of 20 teeth. All x-ray exposures were made at 90 kVp, 15 Ma at $\frac{1}{10}$ second, using a standardized reproducible technique.

This study demonstrates that lithium fluoride microdosimeters can provide total dose and dose ratio data. Approximately $\frac{1}{3}$ roentgen is required to produce an intraoral x-ray film. The average intradental dose was 142 millirads with a range of 126 to 153, and the gum level dose averaged 207 millirads with a range of 159 to 223.

* Abstract of a paper presented at the International Association of Dental Research (Radiology Section) held in Washington, D. C., March, 1967. Publication is planned for the *Journal of Oral Surgery, Oral Medicine and Oral Pathology.*

† University of Illinois College of Dentistry, Chicago.

‡ Biological and Medical Research Division.

REFERENCE

1. J. Kastner, R. Hukkoo, and B. G. Oltman. Argonne National Laboratory Radiological Physics Division Annual Report, July 1964 through June 1965. ANL-7060, p. 15.

THE OSCILLATOR STRENGTH DISTRIBUTION OF THE NEGATIVE HYDROGEN ION

Yong-Ki Kim

The oscillator strength distribution (OSD) of the H^- ion has been determined from currently available theoretical and experimental data, and the results are reported below. The oscillator strength distribution df/dE, where E is the excitation energy measured from the ground state in rydbergs, can in principle be deduced from the measurement of the photoabsorption cross sections. However, such experimental data on H^- are scarce and do not cover enough wavelengths to determine the OSD with sufficient accuracy.[1, 2] There are a few elaborate theoretical calculations of the OSD,[3-5] but the results do not agree with each other within the accuracy expected of such calculations.* Furthermore, none of the theoretical results has enough short wavelength data to reproduce accurately known values of the moments of the OSD

$$S(\mu) = \int (df/dE)\, E^{\mu}\, dE. \qquad (1)$$

The values of $S(\mu)$ for $\mu = -1$, 1, and 2 can be calculated accurately from the ground state wave function, and $S(0)$ is the number of electrons in the atom.† The values of $S(\mu)$ for some negative μ's can, in general, be determined from experimental data such as the dielectric constant, refractive index, and the Verdet constant.‡ [7] The dipole polarizability may also be used to determine $S(-2)$.[6, 9] (According to the calculation of K. T. Chung and R. P. Hurst the dipole polarizability of H^- is 205.874 ± 0.003 in atomic units[9].) No experimental data are available at present to determine the negative moments for H^-.

The theoretical values of $S(\mu)$ for H^- are accurately known for $\mu = -2$, -1, 0, 1, and 2 (cf. Table 12), and the comparison of $S(\mu)$ calculated directly from the OSD by Eq. (1) provides a rather sensitive test of the reliability of the OSD.§ There are no reliable data on the OSD at energies where the double excitations are possible ($E \gtrsim 0.806$ rydberg) but such data hardly affect the negative moments.

Due to the loosely bound nature of the H^- ion, it is expected that only the wave functions of utmost accuracy will produce reliable theoretical results, as may be inferred from the list of the total energy and $S(-1)$ (cf. Table 13) computed from ground state wave functions of various accuracies.

In the application of a sum rule for the Bethe inelastic-scattering cross section,[18] the derivative

$$L(\mu) = dS(\mu)/d\mu = \int (df/dE)\, E^{\mu} \ln E\, dE \qquad (2)$$

at $\mu = -1$ is needed, and it is desirable to find a reliable OSD to evaluate $L(\mu)$ directly. Other values of $L(\mu)$ are also important in various problems in atomic physics.[18] The values of $L(\mu)$ can also be determined graphically by taking the slope of the $S(\mu)$ curve, but such a method is less reliable than the direct computation using Eq. (2) because $S(\mu)$ varies rapidly near $\mu = -1$ in the case of the H^- ion.

TABLE 12. VALUES OF $S(\mu)$ AND $L(\mu)$ CALCULATED FROM VARIOUS SOURCES (ENERGY IN RYDBERGS)

μ	$S(\mu)$				$L(\mu)$
	Accurate[a]	Doughty[4]	Bell and Kingston[5]	Present work	Present work
2	5.514157			5.839	14.69
1	1.495015			1.500	0.6045
0	2			1.977	−1.742
−1	7.48425	7.1	7.35	7.486	−12.70
−2	51.469 ± 0.0008	50.5	51.25	51.21	−107.5
−3	500 ± 40	477.5	462.5	467.0	−1075
−4				4969	−12020

[a] The accurate values of $S(2)$, $S(1)$ and $S(-1)$ were calculated by C. L. Pekeris (Ref. 11), $S(-2)$ from the dipole polarizability (Ref. 9), and $S(-3)$ by C. Schwarz (unpublished, quoted in Refs. 3 and 4).

TABLE 13. TOTAL ENERGY AND $S(-1)$ CALCULATED FROM VARIOUS WAVE FUNCTIONS

Wave function	Total energy, rydbergs	$S(-1)$
Hartree-Fock[12]	−0.975858	6.2741
2-term Hyllerraas[13]	−1.01756	3.6548
Open-shell[14]	−1.02660	11.343
3-term Hyllerraas[13]	−1.0506	5.4507
6-term Hyllerraas[15]	−1.05292	5.9580
11-term Hyllerraas[16]	−1.055118	7.2001
20-term Hyllerraas[17]	−1.05528934	7.1139
444-term Pekeris[11]	−1.05550202	7.48425

* References to earlier theoretical works can be found in Refs. 3 and 4.

† The formulas for $S(\mu)$ are given in Ref. 6.

‡ Later references can be found in Ref. 8.

§ An investigation along this line was reported by A. Dalgarno and R. W. Ewart.[10] The values of $S(2)$ and $S(1)$ quoted in this reference are incorrect. Also, these authors did not use the moments to determine or adjust the oscillator strength distribution.

TABLE 14. OSCILLATOR STRENGTHS OF THE H^- ION

λ/a_0	E/R	$df/d(E/R)$	λ/a_0	E/R	$df/d(E/R)$
10	1.722083 + 002	1.048 − 007	2800	6.150297 − 001	1.001 + 000
20	8.610415 + 001	1.185 − 006	2900	5.938217 − 001	1.042 + 000
30	5.740277 + 001	4.899 − 006	3000	5.740277 − 001	1.082 + 000
40	4.305208 + 001	1.260 − 005	3100	5.555107 − 001	1.124 + 000
50	3.444166 + 001	2.555 − 005	3200	5.381510 − 001	1.165 + 000
60	2.870138 + 001	4.649 − 005	3300	5.218433 − 001	1.206 + 000
70	2.460119 + 001	7.620 − 005	3400	5.064950 − 001	1.247 + 000
80	2.152604 + 001	1.150 − 004	3500	4.920237 − 001	1.288 + 000
90	1.913426 + 001	1.640 − 004	3600	4.783564 − 001	1.330 + 000
100	1.722083 + 001	2.301 − 004	3700	4.654279 − 001	1.370 + 000
150	1.148055 + 001	7.944 − 004	3800	4.531797 − 001	1.412 + 000
200	8.610415 + 000	1.907 − 003	3900	4.415598 − 001	1.453 + 000
250	6.888332 + 000	3.738 − 003	4000	4.305208 − 001	1.495 + 000
300	5.740277 + 000	6.439 − 003	4500	3.826851 − 001	1.697 + 000
350	4.920237 + 000	1.017 − 002	5000	3.444166 − 001	1.900 + 000
400	4.305208 + 000	1.507 − 002	5500	3.131060 − 001	2.102 + 000
450	3.826851 + 000	2.131 − 002	6000	2.870138 − 001	2.304 + 000
500	3.444166 + 000	2.883 − 002	6500	2.649359 − 001	2.501 + 000
550	3.131060 + 000	3.784 − 002	7000	2.460119 − 001	2.696 + 000
600	2.870138 + 000	4.802 − 002	7500	2.296111 − 001	2.886 + 000
650	2.649359 + 000	5.974 − 002	8000	2.152604 − 001	3.072 + 000
700	2.460119 + 000	7.270 − 002	8500	2.025980 − 001	3.248 + 000
750	2.296111 + 000	8.715 − 002	9000	1.913426 − 001	3.421 + 000
800	2.152604 + 000	1.029 − 001	9500	1.812719 − 001	3.585 + 000
850	2.025980 + 000	1.199 − 001	10000	1.722083 − 001	3.740 + 000
900	1.913426 + 000	1.383 − 001	10500	1.640079 − 001	3.885 + 000
950	1.812719 + 000	1.588 − 001	11000	1.565530 − 001	4.025 + 000
1000	1.722083 + 000	1.778 − 001	11500	1.497464 − 001	4.152 + 000
1100	1.565530 + 000	2.214 − 001	12000	1.435069 − 001	4.272 + 000
1200	1.435069 + 000	2.676 − 001	12500	1.377666 − 001	4.383 + 000
1300	1.324679 + 000	3.160 − 001	13000	1.324679 − 001	4.488 + 000
1400	1.230059 + 000	3.654 − 001	13500	1.275617 − 001	4.578 + 000
1500	1.148055 + 000	4.158 − 001	14000	1.230059 − 001	4.651 + 000
1600	1.076302 + 000	4.669 − 001	14500	1.187643 − 001	4.715 + 000
1700	1.012990 + 000	5.180 − 001	15000	1.148055 − 001	4.761 + 000
1800	9.567128 − 001	5.679 − 001	15500	1.111021 − 001	4.794 + 000
1900	9.063595 − 001	6.162 − 001	16000	1.076302 − 001	4.810 + 000
2000	8.610415 − 001	6.608 − 001	16500	1.043687 − 001	4.813 + 000
2100	8.200395 − 001	7.056 − 001	17000	1.012990 − 001	4.804 + 000
2200	7.827650 − 001	7.480 − 001	17500	9.840475 − 002	4.769 + 000
2300	7.487318 − 001	7.912 − 001	18000	9.567128 − 002	4.716 + 000
2400	7.175346 − 001	8.335 − 001	18500	9.308557 − 002	4.644 + 000
2500	6.888332 − 001	8.753 − 001	19000	9.063595 − 002	4.554 + 000
2600	6.623396 − 001	9.173 − 001	19500	8.831195 − 002	4.452 + 000
2700	6.378085 − 001	9.593 − 001	20000	8.610415 − 002	4.330 + 000

TABLE 14. *Continued*

λ/a_0	E/R	$df/d(E/R)$	λ/a_0	E/R	$df/d(E/R)$
20500	8.400405 − 002	4.207 + 000	26500	6.498427 − 002	1.794 + 000
21000	8.200395 − 002	4.057 + 000	27000	6.378085 − 002	1.561 + 000
21500	8.009689 − 002	3.892 + 000	27500	6.262120 − 002	1.339 + 000
22000	7.827650 − 002	3.718 + 000	28000	6.150297 − 002	1.120 + 000
22500	7.653702 − 002	3.528 + 000	28500	6.042397 − 002	9.063 − 001
23000	7.487318 − 002	3.335 + 000	29000	5.938217 − 002	6.960 − 001
23500	7.328013 − 002	3.126 + 000	29500	5.837570 − 002	5.074 − 001
24000	7.175346 − 002	2.904 + 000	30000	5.740277 − 002	3.270 − 001
24500	7.028910 − 002	2.695 + 000	30500	5.646174 − 002	1.617 − 001
25000	6.888332 − 002	2.468 + 000	31000	5.555107 − 002	0.000 + 000
25500	6.753267 − 002	2.244 + 000			
26000	6.623396 − 002	2.018 + 000			

λ/a_0 = Wavelength in atomic units.
E/R = Excitation energy in rydbergs measured from the ground state.
$df/d(E/R)$ = Differential oscillator strength.
Columns 2 and 3 are given in FORTRAN notation, e.g., 1.048 − 007 = 1.048×10^{-7}.

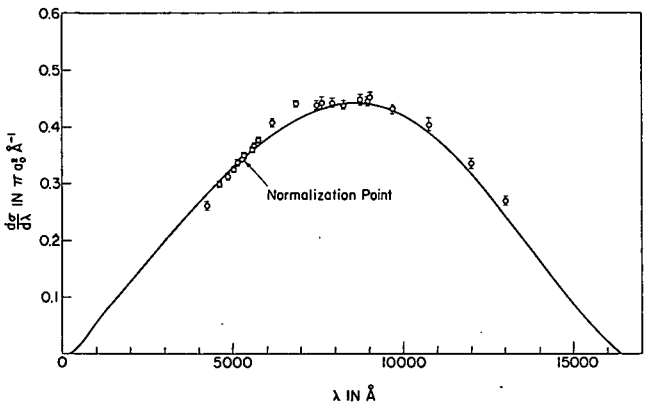

FIG. 19. Bound-free photoabsorption cross sections of H^-. The solid line is the result computed from the moment-adjusted oscillator strengths. The circles with dots (⊙) are the experimental values of Smith and Burch.[2] The experimental values were normalized at λ = 5280 Å to the calculated value of 0.342 πa_0^2 Å^{-1}.

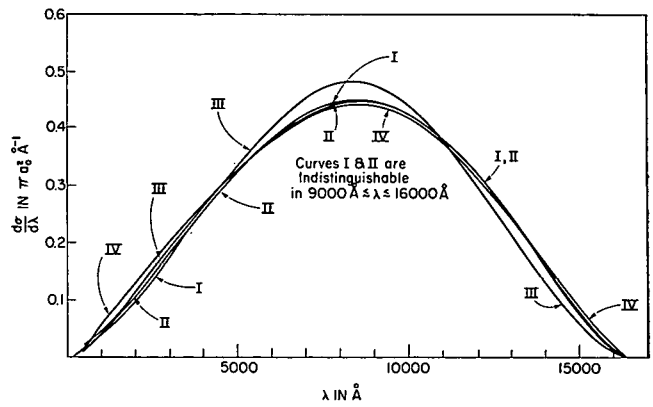

FIG. 20. Comparison of theoretical photoabsorption cross sections of H^-. Curve I is the cross section by Geltman,[3] II is by Doughty,[4] III is by Bell and Kingston,[5] and IV represents the moment-adjusted cross section.

To obtain a consistent OSD of H^-, the calculated distributions[3–5] were adjusted graphically to reproduce the known values of $S(\mu)$ closely. Table 14 contains the moment-adjusted OSD; the values of $S(\mu)$ and $L(\mu)$ calculated from various sources are listed in Table 12. The bound-free photoabsorption cross sections derived from the moment-adjusted OSD are plotted in Figure 19, along with the experimental data of Smith and Burch.[2] The experimental cross sections were normalized to our value 0.342 πa_0^2 (a_0 is the Bohr radius of the hydrogen atom) at 5280 Å.

In the medium to longer wavelength region ($\lambda \gtrsim$ 4000 Å), our OSD was adjusted to follow the distributions calculated by Geltman[3] and Doughty,[4] in view of their good agreement with each other and with the experimental data.[2] In the shorter wavelength region our OSD, however, is significantly different from those in Refs. 3, 4, and 5. The photoabsorption cross sections computed by other investigators are compared with ours in Figure 20.

Since the OSD can be determined uniquely from its moments only if all moments are known, our OSD is not expected to reflect any minute details in the actual OSD. For this reason, no effort was made to account for the double excitations explicitly.* Our data, instead,

* The double excitation thresholds are 0.806 rydberg ($H^* + e$) and 1.06 rydbergs ($H^+ + 2e$). Hence the uncertainty of df/dE in the threshold region is not amplified much ($E^\mu \sim 1$, $\ln E \sim 0$) in the calculation of $S(\mu)$ and $L(\mu)$ of the H^- ion, with our choice of the energy scale.

indicate a small broad maximum in the vicinity of the double ionization threshold (see Figure 20). As in the He atom,[11] we expect the asymptotic behavior

$$df/dE = 7.021E^{-7/2}. \quad (3)$$

There are, however, no experimental or theoretical data to indicate the region in which Eq. (3) is expected to be valid. It was found that the adjusted df/dE can smoothly be joined with the asymptotic form (3) for $E \gtrsim 50$ rydbergs.

Although it is difficult to estimate the accuracy of the moment-adjusted OSD, the quantities which depend on the over-all shape of the OSD such as $S(-4)$ and $L(\mu)$ are expected to be reasonably well represented except for $L(2)$. The moment-adjusted data in Tables 13 and 14 are given to 4 significant figures to assist in interpolating the data.

We have used $L(-1)$ in Table 12 to calculate the Bethe asymptotic electron-detachment cross section of H^- by electron bombardment* and found an excellent agreement (cf. Figure 21) with the experimental data of Dance, Harrison and Rundel.[19] As can be seen from Figure 21, the experimental result of Tisone and Branscomb[20] not only indicate larger cross sections but have an asymptotic slope that is very different from that predicted by the Bethe theory. According to the Bethe theory,[18] the asymptotic slope of the *total* inelastic-scattering cross section, when it is plotted as in Figure 21, is $S(-1) = 7.484$ for the H^- ion. The theoretical uncertainty of the slope is negligible, and the intercept is expected to be accurate within 10% or so, whereas the experimental uncertainty in both experimental data is of the order of 20%.

The experimental data in Figure 21 are not, strictly speaking, the total cross section predicted by the Bethe theory because neither experiment was designed to detect double-ionization events. The data of Dance et al.[19] in Figure 21 indicate that double ionization contributes little to the total cross section for an incident electron energy of a few hundred eV or higher. The agreement of our result with that of Ref. 19 also indicates that the Coulomb distortion, which is neglected in our treatment, is important only for low incident electron energies. Details of the application of the Bethe cross section sum rule to the H^- ion will be published in the near future.

The author wishes to thank Dr. M. Inokuti for suggesting this problem and for many helpful discussions, and Dr. M. Wilson for the Hartree-Fock data in Table 13.

* The total inelastic-scattering cross section calculated by the method described in Ref. 18 corresponds to the total electron detachment cross section including double ionization because H^- does not have any discrete excited state below the first ionization threshold.

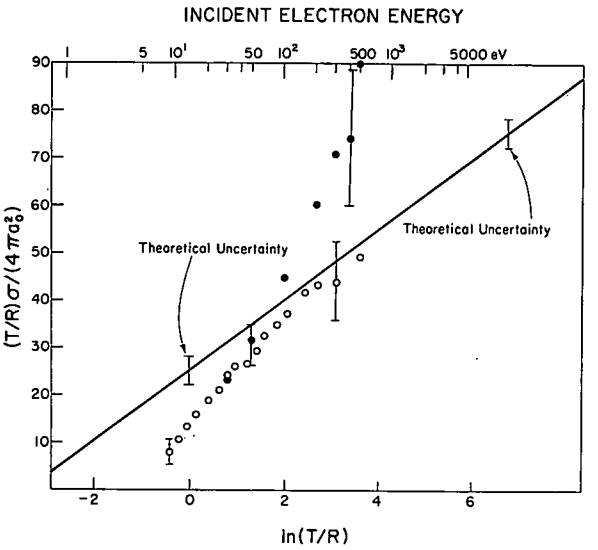

FIG. 21. The electron-detachment cross sections of H^- by electron bombardment. The solid line is the Bethe asymptotic cross section. The open circles (○) are the experimental data of Dance, Harrison, and Rundel,[19] and the solid circles (●) are those of Tisone and Branscomb.[20] The slope of the theoretical line is 7.484 and its intercept is 25.3. The ordinate is proportional to $(T/R) \times$ (total detachment cross section), and the abscissa is ln (T/R) where T/R is the incident electron energy in rydbergs. The experimental data represent the single ionization cross section only, whereas the theoretical cross section includes the double ionization cross section.

REFERENCES

1. L. M. Branscomb and S. J. Smith. *Phys. Rev.* **98,** 1028 (1955).
2. S. J. Smith and D. S. Burch. *Phys. Rev. Letters* **2,** 165 (1959); *Phys. Rev.* **116,** 1125 (1959).
3. S. Geltman. *Astrophys. J.* **136,** 935 (1962).
4. N. A. Doughty, P. A. Fraser and R. P. McEachran. *Monthly Notices Roy. Astron. Soc.* **132,** 255 (1966); also N. A. Doughty, Ph.D. Thesis, University of Western Ontario, London, Canada (1964).
5. K. L. Bell and A. E. Kingston. *Proc. Phys. Soc.* (*London*) **90,** 895 (1967).
6. H. A. Bethe and E. E. Salpeter. *Quantum Mechanics of One- and Two-Electron Atoms.* Springer Verlag, Berlin, 1957, p. 358.
7. A. Dalgarno and N. Lynn. *Proc. Phys. Soc.* (*London*) **A70,** 802 (1957); W. F. Miller, Ph.D. Thesis, Purdue University, West Lafayette, Indiana (1956).
8. R. J. Bell and A. Dalgarno. *Proc. Phys. Soc.* (*London*) **89,** 55 (1966).
9. K. T. Chung and R. P. Hurst. *Phys. Rev.* **152,** 35 (1966).
10. A. Dalgarno and R. W. Ewart. *Proc. Phys. Soc.* (*London*) **80,** 616 (1962).
11. P. K. Kabir and E. E. Salpeter. *Phys. Rev.* **108,** 1256 (1957). [For the expectation value $\langle\delta(r_2)\rangle$ of H^-, see C. L. Pekeris, *Phys. Rev.* **126,** 1470 (1962). The asymptotic formulas quoted in Ref. (10) contain misprints. The numerical factor 512/3 should read $128Z^2/3$ where Z is the nuclear charge.]
12. Michael Wilson. Argonne National Laboratory Chemistry Division. Private communication.

13. L. C. Green *et al. Phys. Rev.* **112,** 1187 (1958).
14. R. P. Hurst, J. D. Gray, G. H. Brigman, and F. A. Matsen. *Mol. Phys.* **1,** 189 (1958).
15. R. E. Williamson. *Astrophys. J.* **96,** 438 (1942).
16. L. R. Henrich. *Astrophys. J.* **99,** 59 (1944); *ibid.* **99,** 318 (1944).
17. A. Hart and G. Herzberg. *Phys. Rev.* **106,** 79 (1957).
18. M. Inokuti, Y.-K. Kim, and R. L. Platzman. *Phys. Rev.* **164,** 55 (1967). (Abstract in this report.)
19. D. F. Dance, M. F. A. Harrison, R. D. Rundel. *Proc. Roy. Soc.* (*London*) **A299,** 525 (1967).
20. G. C. Tisone and L. M. Branscomb. *Phys. Rev. Letters* **17,** 236 (1966); see also G. C. Tisone, Joint Institute for Laboratory Astrophysics Report JILA-73 (1966).

*RELATIVE RISK OF INJURY IN DIFFERENT ORGAN SYSTEMS FOLLOWING THE ADMINISTRATION OF THORIUM OXIDE WITH PARTICULAR REFERENCE TO THE HEMOPOIETIC SYSTEM**

L. D. Marinelli

Our knowledge of the dosimetry (dose rate and cumulative dose) involving the various organ systems of patients injected with colloidal ThO_2 is still incomplete, although vigorous efforts are being made to elucidate the very complicated problem with adequate precision.

The tissues most heavily involved and most extensively assayed have been the liver and spleen, and to a first approximation, they seem to be the ones most frequently affected by cancer and other pathological lesions. The dose distributed therein is spotty, and predominantly alpha radiation; no relevant comparison can be made with other irradiated human populations, with the exception, perhaps, of the survivors of weapon detonation, whose whole bodies, however, were instantaneously irradiated with smaller doses of gamma and neutron radiation.

The tissues irradiated by thorium and daughters at the next level are the marrow and the lung, for which some comparison can be drawn from other epidemiological studies. In these classes of patients, however, the quality factor (alpha vs. electron radiation), the rate of delivery and the homogeneity of the spatial irradiation differ considerably; a complicating factor which must be considered also is the co-carcinogenic effect of the ThO_2 colloidal particle per se.

Last, but not least, bone and kidney lesions may appear as a consequence of more or less uniform radiation dose rates of the order of 1–5 rads per year.

Since the rates under consideration are relatively close to the rates presumed by the ICRP to be tolerable during the working lifetime of men, the study of their effects deserves special attention; in many respects they may represent the only direct experience that will ever be available for the study of long-term effect of relatively constant and uniform doses to various organs in man.

* Abstract of paper presented at N.Y. Acad. Sci. Conf. on Distribution, Retention, and Late Effects of Thorium Dioxide, New York City, April 20–22, 1966.

*A REVISED ESTIMATE OF THE MAXIMUM PERMISSIBLE BURDEN FOR Sr^{90} **

L. D. Marinelli

The calculation of the maximum permissible burden (MPB) of Sr^{90} in man needs revision because of more extensive data kindly made available by Dr. M. P. Finkel.[1] Comparison of the oncogenic effects produced by Sr^{90} and Ra^{226} is possible by means of data given in Ref. 1, Figure 3, based on observations on osteosarcomas arising in several thousand mice.

By confining attention to an osteosarcoma expectancy of 0.2 down to 0.03 per mouse, one observes that roughly similar expectancies are obtained when the activity of Sr^{90} injected per unit weight is about 200 times that of radium expressed in the same units.* Since for a given

* Presented at ICRP Committee II Meeting, London, April 3–14, 1967; NCRP Committee II Meeting, Mayaguez, Puerto Rico, May 4–5, 1967.

* This statement has been challenged from different quarters. It will suffice to state here that if the Ra^{226} data from Dr. M. P. Finkel are connected by a line located *between* the experimental points and said line is transposed by factors of 200 and 400 to the right as in Fig. 22, one observes that 3

level of incidence the time sequence of osteosarcoma appearance is approximately the same for both radionuclides (Ref. 2, Figure 1), the absorbed doses relevant to the injected μCi/kg should be calculated for a single average latent period. To be on the safe side, I have chosen 600 days because it is the life expectancy of the control mice. Calculations for 800 days [approximately the latest time at which osteosarcomas have appeared in these animals (Ref. 2, Figure 5)] differ by only a few percent (vide infra). Extreme assumptions relating to shorter induction times will be considered later.

DOSES IN MICE

Ra^{226}

The dose to the skeleton of a female mouse injected at about 70 days has been calculated according to the equation (Ref. 3, confirmed in Ref. 4):

$$\text{Dose } (Ra^{226}) = I\,(3.22t^{0.72} + 0.5t^{0.935}) \text{ rads},$$

where I = the number of (1) μCi/kg injected and t is in days.
For $I = 1$,

$$t = 600 \text{ days} \qquad D^{Ra}_{600} = 520 \text{ rads}$$

$$t = 800 \text{ days} \qquad D^{Ra}_{800} = 655 \text{ rads}.$$

Sr^{90}

The retention of Sr^{90} in mice has been reported by many authors.[5-7] We have chosen Ref. 6 since it is the most relevant to the experiments in question.

The daily dose rate D_0 in an extended medium with a concentration of C μCi/kg is given by

$$D_0 = 51.2 \times \bar{E}_\beta \times C \text{ rads per day}.$$

In our case, $\bar{E}_\beta$ (the average energy in MeV per disintegration of $Sr^{90} + Y^{90} = 0.20 + 0.93 = 1.13$) must be multiplied by the fraction $\epsilon = 0.32$ of the energy absorbed by the average mouse skeleton.[8] Hence, $D_0(Sr^{90}$ in mice$) = 51.2 \times 1.13 \times 0.32 = 18.55$ rads/day per μCi/g of mouse skeleton. Since Sr^{90} is retained[6] in mouse bone according to

$$R = 0.75 \times t^{-0.3} \ (t \text{ in days})$$

and the weight of the mouse skeleton = 0.075 × the weight of the mouse,[8] the concentration $C(t)$ of Sr^{90} in the skeleton of the mouse, per μCi/kg injected will be:

$$C(t) = \frac{0.75}{75} t^{-0.3} = 10^{-2}t^{-0.3} \ \mu\text{Ci/g of mouse skeleton.}$$

It follows that the average absorbed dose D^{Sr}_t accumulated in the mouse skeleton will be

at $t = 600$ days,

$$\bar{D}^{Sr}_{600} = 18.55 \times 10^{-2} \int_0^{600} dt \cdot t^{-0.3}$$

$$= (0.186/0.7)(600)^{0.7}$$

$$= 23.3 \text{ rads per } \mu\text{Ci/kg injected};$$

at $t = 800$ days,

$$D^{Sr}_{800} = 28.5 \text{ rads per } \mu\text{Ci/kg injected}.$$

Then the ratio of the average absorbed doses to the skeleton, $D(\text{Sr})/D(\text{Ra})$—producing equal incidence of osteosarcoma in mice—comes to

$$D(\text{Sr})/D(\text{Ra}) = \frac{200 \times 23.3}{520} = 8.95 \qquad (t = 600 \text{ d})$$

$$D(\text{Sr})/D(\text{Ra}) = \frac{200 \times 28.5}{655} = 8.7 \qquad (t = 800 \text{ d}).$$

This number represents essentially the Modifying Factor (MF)* experimentally determined for Ra^{226} vs. Sr^{90} oncogenic effects in mouse bone.

It should be realized, however, that although the exponent b in the retention equation ($R = At^{-b}$) is about the same for both Ra and Sr in mice, the ratio of the average dose rates is not a constant in time, owing to the proportionately greater retention of radon with the passage of time; this fact does not change matters

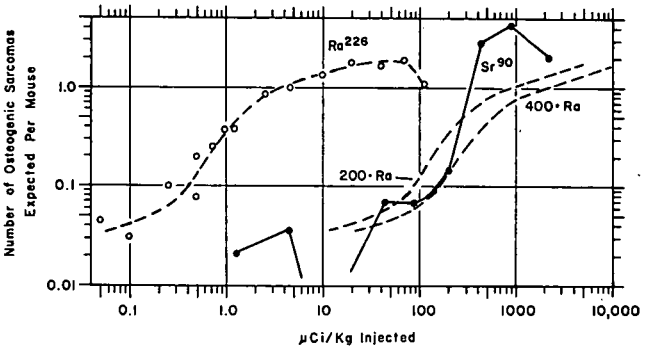

FIG. 22. Ra^{226} and Sr^{90} osteosarcomas in mice (from Ref. 1)

points of the Sr^{90} data can be considered to fall to the left of the 200·Ra curve (at 1.3, 4.5 and 44 μCi/kg) and the other 3 points (8.9, 88 and 200 μCi/kg) fall almost on or to the right of the 400·Ra line. This argument is not conclusive since the number of tumors available at these levels is insufficient to allow a firm choice within a factor of 2, and the control background dilutes the significance of the data still further. It seems reasonable, however, to proceed on the more conservative assumption while waiting for more data on the 10–200 μCi/kg Sr^{90} and the 0.05–1.0 μCi/kg Ra^{226} levels in mice and later results from the beagle.

* For definition of MF see Ref. 9; the term RBE is omitted from this discussion since it is reserved exclusively for radiobiological experiments wherein all experimental factors—exclusive of LET—are identical.

much, however, unless the absorbed dose responsible for oncogenesis is delivered in the first few T_0 days after injection. If this were the case, the MF would be higher: thus in the extreme case of $T_0 = 1$ day

$$\text{MF} = D(\text{Sr})/D(\text{Ra})$$

$$= \frac{(200 \times 0.186)/0.7}{(3.22 + 0.50)} = \frac{53.1}{3.72} = 14.3.$$

Hence, the value of MF = 8.8, calculated by neglecting the osteosarcoma induction period, is on the conservative side.

CALCULATION OF THE MPB IN MAN

If one assumes that the main risk of Sr^{90} contamination in the human skeleton is the production of osteosarcoma, and one assumes also that the magnitude of this risk in man, vis-a-vis the risk of Ra^{226}, is the same as in the mouse, namely equal to about 1/8.8, then the MPB for Sr^{90} in man follows from the product of the inverse ratios of the dose rates by the Modifying Factor.

The dose rates follow the average energy per disintegration: namely, 10.7 MeV for Ra^{226} (+ 30% Ra[B + C])[10] and $1.13 \times 0.88 = 0.99$ MeV for Sr^{90}. (The factor 0.88 is the average utilization of $Sr^{90} + Y^{90}$ β-ray energy in the human skeleton.)[8]

Hence, since MPB (Ra^{226}) = 0.1 μCi,

$$\text{MPB } (Sr^{90}) = 8.8 \times \frac{10.7}{0.99} \times \text{MPB } (Ra^{226})$$

$$= 95 \times 0.1\ \mu\text{Ci} = 9.5\ \mu\text{Ci}.$$

Note: If one considers the accumulation of Ra(D + E + F) found in Ra patients[11] the MPB (Sr^{90}) in man would be higher by about 10%.

DISCUSSION

The following data and/or comments are in order:

1. In dogs, preliminary estimates from Utah[12] indicate that the lowest skeletal doses producing osteosarcomas are 8100 rads from Sr^{90} in a dog dying 960 days after injection and 490 rads from Ra^{226} in a dog dying 4108 days after injection. The ratio of 16.5 between these values should be regarded provisionally as a maximum since: (a) it is based on minimal doses producing osteosarcomas at *widely different times*, and (b) the accumulated dose required for oncogenesis seems to be *inversely* related to the average latent period.[2, 13, 14]

2. Although MPB (Sr^{90}) = 9.5 μCi is conservative in some respects, it does not take into account the possible leukemogenic effect of $Sr^{90} + Y^{90}$ β-rays on the human blood-forming organs.

3. The MPB (Sr^{90}) calculated above is almost identical to that proposed by Spiers[15] on the basis of ICRP limits to bone marrow.

4. The Modifying Factor (Ra^{226}/Sr^{90} = 8.8) in mice does not seem to change very much, if the dose to endosteal cells instead of average dose to the skeleton were considered. (See Ref. 16, Figures 22 and 30 for Sr^{90} endosteal dose to femur and Ra^{226} endosteal dose to lumbar spine.)

5. In view of (2) and (3) above, consideration should be given to acceptance of a new level of MPB for Sr^{90} in man between 4 and 5 μCi. This value results from the assumption that following Sr^{90} intake, osteosarcoma and leukemia incidence in man are equally probable; this assumption is debatable, of course, but it has the merit of leading to the lower value.

6. The possibility of the MF being of the order of 400 instead of 200, and the simplicity and logic of Spiers' proposal[15] have tempted many observers to favor the latter without further question. It must be realized, however, that the greater risk for leukemia induction which is therein assumed—and is implied in the lower MPB for the blood-forming organs—is supported by evidence in man irradiated only at higher dose rates and/or over large parts of the body. No evidence exists that this greater susceptibility exists also in man irradiated preponderately by β-ray bone seekers. Current observations on experimental animals indicate that Sr^{90} irradiation of bone and marrow may produce either or both leukemia and osteosarcoma and that their relative incidence depends on injected amounts, age of the animal, species, subdivision of the dose, etc.

Since no definite conclusions can be drawn at this moment as to whether leukemia or osteosarcoma is the greater risk under conditions relevant to MPB's, the most conservative assumptions should prevail.

REFERENCES

1. M. P. Finkel and B. O. Biskis. Experimental Induction of Osteosarcoma. To be published in *Progress in Experimental Tumor Research*, Ed. F. Homburger, Vol. **10**.
2. M. P. Finkel and B. O. Biskis. The Induction of Malignant Bone Tumors in Mice by Radioisotopes. *Acta Unio Intern. Contra Cancrum* **15**(1), 99 (1959).
3. C. W. Mays, T. H. Cochran, and W. S. S. Jee. Radium and Radon Retention in Mice. *Health Phys.* **9**(6), 615 (1963).
4. C. E. Miller and A. J. Finkel. Radium Retention in Mice after Single Intravenous Injection. *Radiation Res.* **26**(2), 269 (1965).
5. T. W. Speckman and W. P. Norris. The Age Dependence of Strontium Retention in Rats and Mice. *Radiation Res.* **23**(3), 461 (1964).
6. M. P. Finkel, B. J. Tellekson, Juanita Lestina, and B. O Biskis. The Influence of Dosage Pattern upon the Toxicity of Sr^{90} in Mice. Argonne National Laboratory Biological and Medical Research Division Semiannual Report, January through June 1957. ANL-5732, p. 21.

7. M. Fujita and J. Iwamoto. Retention and Excretion of Strontium-85 in Mice, Rats and Rabbits—Extrapolation to Long-Term Retention in Humans. *Health Phys.* **11**(4), 271–281 (1965).
8. W. W. Parmley, J. B. Jensen, and C. W. Mays. Skeletal Self-absorption of Beta-Particle Energy. *Some Aspects of Internal Irradiation.* Pergamon Press, Oxford, 1962, p. 473.
9. *Recommendations of the International Committee on Radiological Protection.* ICRP Publication No. 6. Pergamon Press, Oxford, 1964, p. 7; also *Health Phys.* **9**, 357–384 (1963).
10. L. D. Marinelli, C. E. Miller, and H. F. Lucas, Jr. Retention of Radium in Man from Twenty to Twenty-nine Years after Intravenous Administration and Some of Its Physiologic Implications. *Radiology* **78**(4), 544–552 (1962).
11. R. B. Holtzman. RaD (Pb^{210}) in the Human Skeleton: Estimates of the Exponent of the Retention Function, the Skeletal Content, and the Dose Rate to High Radium People. *Radiology* **80**, 122–123 (1963); also *Health Phys.* **9**, 385–400 (1963), Table II; also H. Petrow, Radioactivity Studies, U. S. Atomic Energy Commission Report NYO-3086-1 (September 1, 1965), pp. 2.1 to 2.18.
12. T. F. Daugherty and Staff. Research in Radiobiology, Injection Tables. University of Utah Report COO-119-236 (March 1967).
13. R. D. Evans. The Effect of Skeletally Deposited α-Ray Emitters in Man. *Brit. J. Radiol.* **39**, 881–895 (1966).
14. T. F. Daugherty. Incidence of Bone Cancer in Internally Irradiated Dogs. *Some Aspects of Internal Irradiation.* Pergamon Press, New York, 1962, pp. 48–78.
15. F. W. Spiers. Dose to Bone from Sr^{90}: Implications for the Setting of the Maximum Permissible Body Burden. *Radiation Res.* **29**, 624 (1966).
16. J. H. Marshall and M. P. Finkel. Autoradiographic Dosimetry of Mouse Bones Containing Ca^{45}, Sr^{90}, and Ra^{226}. Argonne National Laboratory Radiological Physics Division Semiannual Report, July through December 1959. ANL-6104, pp. 48–65.

*DOSIMETRY IN RELATION TO EPIDEMIOLOGY: ITS IMPLICATIONS IN RADIOGENIC LEUKEMIAS AND BRONCHIAL CARCINOMA (THOROTRAST)**

L. D. Marinelli

Concern with the impact of the ever-expanding applications of nuclear fission to every-day life has focussed world-wide attention on some recent epidemiological studies, and in particular, on their quantitative, rather than their qualitative conclusions. The attention is well deserved since they have furnished international bodies such as ICRP and UNSCEAR with the data necessary to evaluate some radiation risks in dosimetric terms, such as osteosarcoma and leukemia incidence per man-rad per year.

Events of the last decade involving this controversial field suggest that estimates of radiation risks become more convincing to the layman when they are related to human experience and less abhorrent to the radiobiologist when epidemiological deductions find confirmation in the laboratory animal colony.

Radiation dosimetry has played, and will continue to play, an essential role in this important relation between laboratory and field observations, since its basic task is the same in both types of investigation, namely the task of supplying a measure of the atomic events initiating biochemical and cellular perturbations which lead ultimately to the observed effect.

Concern with the specification of dose, however, should include detailed information on the modalities of its administration and should not detract from the importance of describing accurately the status of the populations under comparison. The latter requirement becomes especially important in studies at low doses of radiation, when the influence of extraneous factors can easily obliterate the observation of a true radiation effect.

It is conceded that the ultimate accuracy in the evaluation of dosimetric factors in radioepidemiology should be comparable to that attainable in the description of biological effects; i.e., it need not be as high as that required in medical uses of radiation.

However, the attainable accuracy of the doses relevant to epidemiology depends not only on the precision of technical measurements, but also on the uncertainties introduced by variations in physiological and/or anatomical factors of the populations under scrutiny and, where applicable, also on additional uncertainties connected with sampling.

The technical approach to dosimetry varies considerably depending on whether the dose is due to internal or external radiation. With internal emitters the basic data require both radioactive and metabolic measurements, but the techniques vary somewhat with the study in question. Thus, in cases of luminous dial painters, the radium burden is assessed by whole-body counting, analysis of exhaled radon, and the measurement of excreta; it is then converted into

* Presented at the International Conference on Guidelines to Radiological Health, Montreal, Canada, August 17–21, 1967.

rads by means of extensive autoradiographic and radiochemical analysis. Long-term metabolic parameters which describe the change of radioactivity with time have been obtained from studies of patients previously treated with known amounts of Ra^{226} a few decades ago. In the case of the dial painters, as in other industrial exposures, the magnitude of the initial intake is unknown and may vary widely; hence the measurement of every individual under observation is necessary.

In the Midwest Epidemiological Survey,[1] which is concerned with the effects of a few picocuries of Ra in potable water supplies in a population of about a million, the dosimetric problem is theoretically relegated to the measurement of radioactivity of water and food, since the metabolism of Ra in man is fairly well known. However, the influence of population stability, the use of water softeners and other epidemiological, demographic and socioeconomical factors remain to be evaluated by judicious sampling.

In another study involving ThO_2 in colloidal form, documentation of the diagnostic techniques used in given institutions seems adequate for the estimate of the intake pertinent to various categories of patients. However, some radiobiologically essential dosimetric measurements, which depend upon detailed assessments of radioactivity throughout the body, still pose a sharp challenge to the investigator, mainly because the most energetic members of the chain that translocate in the body have inconveniently short natural lifetimes.

It is well to stress at this point that operational difficulties in the analysis of cause and effect of ThO_2 in man should stimulate rather than depress the meager measure of financial support that has been devoted to this epidemiological area. The present indecision in this regard recalls the official doubts that were expressed 20 years ago about the usefulness of the ABCC studies and the indifference that for almost a decade prevailed in many laboratories vis-a-vis the experimental study of effects of inhaled radioactive gases and particles. The direct relevance of epidemiological studies of ThO_2 patients to the topics of this Conference can best be illustrated by perusal of Table 15 where the yearly dose rates of alpha radiation absorbed by various tissues of the typical Thorotrast patient[2] are shown. It will be noted that, besides the well-known high levels accruing to the liver and spleen, dose rates of current concern accrue also to marrow, lung, and bone. As a rough guide, a fair mental picture of equivalent photon or beta radiation can be had by multiplying these values by 5 in order to account for an RBE of 10 and an average injection of 25 cc. It is obvious that in the case of the marrow and the lung, we are dealing with average dose rates in rems which are respectively 24 and 4 times the maximum levels considered to be permissible to those tissues by the ICRP. For obvious reasons, it is important to note that preliminary results indicate that in a pool of about 2,000 persons at risk for an average of 25 years, the leukemia incidence rate is roughly seven times normal (Table 16). The average radioleukemogenic risk in this group is of the order of 1.8 cases per million man-rad years. This figure should be compared to those mentioned by UNSCEAR and ICRP involving the Japanese survivors and the spondylitics[7] which are shown in the first two lines of Table 17.

Despite the obvious uncertainties due to statistics and the rough estimates of years at risk, it is useful to gather some of these epidemiological figures in one table, not so much to reach firm conclusions, but to consider what we may learn from studies of this type. In Table 18, by similar calculations, are gathered the epidemiological results on risk of osteosarcoma and

TABLE 15. MAXIMUM DOSE RATES PER 50 CC THOROTRAST INJECTION IN RADS YEAR^{-1}

Element	$T^{1/2}$	$K^{(a)}$	Liver	Spleen	Marrow	Bone	Kidney	Lung	Blood	Soft tissue
Th^{232}	1.4 10^{10}y	74.5	44.0	66.0	7.4	0.007	0.35	0.5	—	—
Ra^{228}	5.8y	—	—	—	—	—	—	—	—	—
Th^{228}	1.90y	100	26.3	34.0	5.0	0.30	0.2	0.7	0.08	0.14
Ra^{224}	3.64d	105	30.2	34.5	2.1	0.63	0.68	0.2	0.22	0.04
Thoron + ThA	51s; 0.16s	234	36.0	43.0	5.5	1.31	1.5	6.9	1.96	0.07
ThB (Pb^{212})	10.6 hr	—	—	—	—	—	—	—	—	—
Bi^{212} (ThC)	1 hr	38	2.8	4.0	0.9	0.21	0.4	1.0	0.50	0.05
Po^{212} (ThC′)	0.3μs	109	8.2	11.4	2.7	0.61	1.1	3.3	1.42	0.15
T^{208} (ThC″)	3m	—	—	—	—	—	—	—	—	—
Total			147	192	23.6	3.1	4.2	12.6	4.2	0.45

(a) Rads per year per nCi/g.

leukemia from high and low LET radiation delivered at high and low exposure rates. Obviously the separation of the effect of the two variables has not been achieved, but of tantalizing interest is the fact that the ratio of the leukemogenic to the osteosarcoma risk seems to be of the order of 5 for the combination of high dose rate and low LET radiation, but it could be only 0.5 for low dose rate, combined with high LET irradiation. Of peripheral interest is the fact that if the natural incidences of osteosarcoma and leukemia were all attributed to background radiation, one would obtain ϵ_O and ϵ_L values of 1.4 and 14, approximately.

Of equal interest and perhaps of greater urgency should be an estimate of the doses to various parts of the lung of these patients who exhale a considerable amount of thoron. Doses to various sections of the lung, as calculated by Muth and Grillmaier,[9] are shown in Table 19 and compared to similar calculations by Jacobi[10] on doses resulting from one WL (Working Level) atmosphere in mining operations. In view of the various uncertainties inherent to calculations of this sort, no great claim for accuracy can be made, especially for the various tracts of the respiratory tree; but the comparison has the merit of being based on similar physiological, diffusion and attachment constants. I may add that one assay of ThB in the lung made in our laboratory[11] yielded 12 rads/year for the average dose to alveoli and bronchioli, namely a value embarrasingly close to these figures. On an average of 25 years at risk, these patients have accumulated roughly an equivalent integral exposure of the order 1500, 3000, 40, and 2100 WLM (Working Level Month), respectively, in the alveoli, small bronchi, large bronchi and trachea, that is, doses which are wholly comparable to those experienced by the mining population mentioned in FRC Report ※8.[12] An inquiry into the incidence of bronchogenic carcinoma in Thorotrast patients was made by Faber as far back as 1961, and he concluded that the number of cases observed in the Danish material was the number to be expected taking age, sex, and time of observation into consideration. As of today, if one considers all the cases collected by Da Silva-Horta[5] and Okawara[13] (the latter includes the cases of Faber) as pertaining to the population of 2000 considered in Table 16, one calculates an incidence of 13 cases in roughly 30,000 to 50,000 man years. This figure is certainly not from 8 to 46 times the normal expected incidence which, according to FRC preliminary report ※8, is the case for the mining populations exposed to comparable doses of radiation to the respiratory tract. It is obvious, then, that these data are relevant to any inquiry as to the causation of bronchogenic carcinoma in underground uranium mines and that further study along these lines needs the immediate support of the agencies concerned and the attention of the best epidemiologists and radiological physicists.*

After this detailed demonstration of the necessity

TABLE 16. RADIOLEUKEMOGENIC RISK ϵ_L IN THOROTRAST SERIES

Source	N[a]	Tr	$\dot{D}$	n_L	$\epsilon_{L\times10^6}$[b]	Ref.
Denmark	514	25	10.7	6	3.1	3
Sweden	436	23	8.8	1	0.9	4
Portugal	930	26	13.1	9	2.0	5
Japan	187	26	15(?)	1	1.3	6

Average: For $\sim5 \times 10^4$ man year, No. of leukemias expected: $5 \times 10^4 \times 50 \times 10^{-6} \simeq 2.5$—cases found: 17 or $\sim7 \times$ normal.

[a] N = population; $\dot{D}$ = rads yr^{-1} $\simeq$ ½ ml injection; $\epsilon_L = 2n_L/\dot{D}\,N\,Tr^2$ (leukemia); Tr = years at risk; n_L = cases of leukemia.

[b] Average whole group $\epsilon_L \simeq 1.8$.

TABLE 17. RADIOLEUKEMOGENIC RISK ϵ_L FROM EXTERNAL SOURCES

Source and radiation	D[a]	$\dot{D}$	ϵ_L	Ref.
A.B.C.C. γ + neutrons	300	$>10^{13}$	1.6	7, p. 84
Spondylitis (x-rays)	850	$\sim3.2 \times 10^6$	1.3	8
Children in utero (x-rays)	1–10	$\sim10^7$	>5.0	7, p. 89
Radiologists[b] (x-rays)	600[c]	15[c]	0.5[c]	7, p. 85

[a] D = Total rads; $\dot{D}$ = Rads yr^{-1}; ϵ_L = Leukemia/10^6 man/rad/year.

[b] Protracted irradiation.

[c] May vary by a factor of 3 either way.

TABLE 18. APPROXIMATE ONCOGENIC RISK ϵ IN CASES PER $10^6 \times$ yr$^{-1} \times$ (MAN-RAD)$^{-1}$
O = osteosarcoma L = leukemia

Dose rate	High LET α-radiation		Low LET electron radiation	
	ϵ_O	ϵ_L	ϵ_O	ϵ_L
High	?	?	0.23 (Sp) ? (J)	1.5 (Sp)(J) 5.0 (f)
Low	? (T) 4.0 (D)	1.8 (T) 1.8 (D)	? (R) [<1.4] (B)	0.5 (R) [<14.3] (B)

(Sp) = Spondylitis;[8] (J) = Japanese survivors;[7] (T) = Thorotrast patients; (B) = Background; (f) = fetal irradiation; (R) = Radiologists;[7] (D) = Dial painters (Ra^{226}).[7]

* As to the role of the α-irradiation of the respiratory track caused by smoking,[14] it is pertinent to note that DaSilva-Horta[15] noted no bronchial carcinomas in 331 Thorotrast injected females and 5 cases in 590 males.

TABLE 19. DOSE RATE TO LUNGS

Exposure	Tissue	Millirads·yr^{-1}					Rems·yr^{-1}		
		External radiation	α-Radiation				Quality factor		
			Rn^{222} + d	Th^{228} + d	Internal[b] α	Total α	1	10	100
Mining operations[a]	Alveol.	5000	720	—	20	740	5.7	12.4	790
100 pCi/1 Rn +	Bronch.	5000	720	—	20	740	5.7	12.4	790
100 pCi/1 daughters	Bronch. (SQ)	5000	21000	—	20	21000	26.0	215	2100
	Trachea	5000	3800		20	3800	8.8	3	385
50 cc Thorotrast[c]	Alveol.	115	—	8000	—	8000	8.0	80	800
3.6×10^4 pCi min^{-1}	Bronch.	115	—	16000	—	16000	16	160	1600
	Bronch. (SQ)	115	—	5500		5500	5.5	55	550
	Trachea	115	—	55000	—	55000	55	550	5500
Cigarette smoker[d]	Bronch. epithelium	115	6.6	—	—	6.6	6.6 min.		

[a] Ref. 10, Table 5.
[b] ¼ Average dose to osteocytes (20 vs. 80% retention at continual intake).
[c] Ref. 9.
[d] Ref. 14.

of *sharpening* our skill in the radiation dosimetry of internal emitters, we turn to offer some comments on the assessment of the *relevant external* dose in epidemiology which presents a spectrum of difficulties and uncertainties wider, perhaps, than those just mentioned. On one extreme, one has the relatively easy task of assessing effects resulting from clinical irradiation. In these cases the investigator has all the factors and records necessary to establish with more than sufficient accuracy the exposure to a given anatomical field. From this information, using classical methods of radiological physics, the average dose to a given organ can be satisfactorily determined. Clinical records in representative institutions have successfully extended these estimates to 10^7 to 10^8 persons, as exemplified by the various surveys concerned with the average significant genetic dose to entire national populations. It is hoped that similar techniques will be employed on an international scale to calculate the incidence of late morbidity per man-rad year in patients successfully treated for cancer of the cervix and to obtain, at relatively low cost, a reference point on the effects of irradiation of a well-defined portion of the body to compare directly with the effects observed on irradiated spondylitics. It should be recalled, however, that contrasted to the relative ease with which absorbed dose can be evaluated, radioepidemiological studies based on clinical exposure face the dilemma of either choosing control populations of identical medical status which have not been exposed to radiation, or of establishing beyond doubt that whatever the immediate cause leading to irradiation, the irradiation only (and not the cause itself or its therapy) is responsible for the effects observed at a later date.

In the study of dose due to background radiation, circumstances change somewhat. Technically, difficulties arising from the smallness of the dose can be easily overcome by employing suitable organic scintillators, but the difficulty is shifted to the task of "sampling" the background exposure of the population in question. At last report our colleagues in Brazil seem to have coped with this problem by the judicious use of inconspicious personnel dosimeters.[15]

The sampling of the dose to a population becomes of itself difficult to implement when the source and/or the circumstances of exposure cannot be reconstructed. In this classification falls the calculation of the dose to the survivors of Hiroshima and Nagasaki. These dosimetric studies must evaluate the dose delivered to tens of thousands of individuals by radiation emanating from an asymmetrical, irreproducible source of neutrons and gamma rays whose flux is subject to the inverse square law of distance and to attenuation and scatter by the atmosphere and walls of different composition. The latest dosimetric report[16] augurs well in this regard, however, since activation analysis of cobalt impurities in iron structures and utensils, and thermoluminescent measurement of roof tiles seems to be connected directly wit the best estimates of radiation fluences of Augu 1945 and their azimuthal variations.

On the other extreme, we face the less expensive, but perhaps more perplexing task of assessing the

dose to the practicing radiologists of a few decades ago, on whom several epidemiological surveys have been, and for good reason, are still being done. To assess the average marrow dose pertinent to the leukemia incidence of this population, it is necessary to obtain its dose-distribution function; and only one function would be sufficient if the range of doses received within the entire group were small. It should be realized, however, that in this particular case, this range could be as high, or higher, than one thousand. Hence, to obtain a realistic appraisal of the leukemogenic risk of radiation, it is necessary to establish whether the average dose to the leukemia victims is not very different from the average dose to the rest of the population. The task appears tedious and demanding, but it may be accomplished, perhaps, if colleagues, technicians of the deceased, and the surviving members of the profession would contribute adequate information, not only on the radiological armamentarium and techniques prevailing in the epoch of interest, but also on the caution extant both in the profession in general, and in the leukemia group in particular.

In conclusion, I would like to stress the view that if we are facing a period of budgetary restriction in matters concerning radiological health, we should give a thoughtful look at priorities of support, especially at those studies involving long-term effects which cannot be postponed because of either natural extinction of the population or attrition of medical records, as in radioepidemiology. Mice and other laboratory animals will always be with us.

These decisions will require courage because, despite recognition of their valuable contributions by UNSCEAR and ICRP, radioepidemiological studies per se seem to be still the object of disdain on the part of certain coteries of investigators and administrators. Not extraneous to this attitude may be the human propensity to pursue the easiest path, unmindful of the urgency of the task, and the conceit inherent in the philosophy that true scientific effort should ignore social needs. Certainly it cannot be logic: For it has become abundantly clear that evaluation of radiation risks on man cannot be attempted within the foreseeable future without the aid of epidemiological study.

It is equally clear, moreover, that the interplay between laboratory and field observation is essential to the interpretation of epidemiological findings and to their extrapolation to different conditions of exposure, and that all this is impossible without dosimetric information.

REFERENCES

1. N. J. Peterson, L. D. Samuels, H. F. Lucas, and S. P. Abrahams. An Epidemiological Approach to the Problem of Low Level Ra^{226} Exposure. *Public Health Rept.* **81**(9), 805–814 (1966).
2. L. D. Marinelli. The Doses from Thorotrast and Migrated Descendants: Status, Prospects, and Implications. Argonne National Laboratory Radiological Physics Division Annual Report, July 1964 through June 1965. ANL-7060, p. 37.
3. M. Faber. Thorotrast in Man: The Carrier State and the Sequelae. *Some Aspects of Internal Irradiation.* Pergamon Press, New York, 1962, p. 473.
4. R. Blomberg, R. Larsson, B. Lindell, and E. L. Lindgren. Late Effects of Thorotrast in Cerebral Angiography. *Acta Radiol.* **1**(4), 995 (1963).
5. J. Da Silva-Horta, J. D. Abbott, L. Cayolla de Motta, and M. L. Roritz. Malignancy and Other Late Effects Following Administration of Thorotrast. *Lancet*, 201 (July 31, 1965).
6. S. Takahashi et al. Statistical Study of Thorotrast-Induced Cancer of the Liver. *Tohoku J. Exptl. Med.* **87**(2), 144 (1965).
7. UNSCEAR (1964). Reports of the United Nations Scientific Committee on the Effects of Atomic Radiation, Official Records, 19th Session, Suppl. No. 14 (A/5814), 1964; also Task Group Chairman R. S. Russell. The Evaluation of Risks from Radiation. *Health Phys.* **12**, 239-302 (February 1966).
8. W. M. Court-Brown and R. Doll. Mortality from Cancer and Other Causes after Radiotherapy for Ankylosing Spondylitis. *Brit. Med. J.* **2**, 1327 (1965).
9. H. Muth and R. Grillmaier. Doses from Thoron and Primary Thorotrast Deposits in Lungs. Paper presented at Symposium on Dosimetry and Toxicity of Thorotrast, Vienna, October 1965 (unpublished).
10. W. Jacobi. The Dose of the Human Respiratory Tract by Inhalation of Short-Lived Rn^{222} and Rn^{220} Decay Products. *Health Phys.* **10**, 1163 (1964).
11. R. Parr, H. F. Lucas, and M. Griem. Private communication (1967).
12. Federal Research Council. Staff Report (Preliminary) No. 8. Guidance for the Control of Radiation Hazards in Uranium Mining (May 1967).
13. S. Okawara. Studies on Thorotrast. Report No. 6: Sequelae Induced by Thorotrast. *Nippon Acta Radiologica* **25**(10), 1213 (January 25, 1966).
14. E. P. Radford and V. R. Hunt. Polonium-210—a Volatile Radioelement in Cigarettes. *Science* **143**, 247–249 (January 17, 1964).
15. E. Penna-Franca et al. Status of Investigations in the Brazilian Areas of High Natural Radioactivity. *Health Phys.* **11**, 699 (August 1965).
16. T. Hashizume et al. Estimation of the Air Dose from the Atomic Bombs in Hiroshima and Nagasaki. *Health Phys.* **13**, 149 (1967).

42

THOROTRAST-EXPOSED PERSONS IN THE CHICAGO AREA

*Harold May and Edwin Kingsley**

INTRODUCTION

Examination in the whole-body counter of four individuals containing colloidal Th^{232} and its daughter elements in the liver and spleen, accompanied by skeletal deposits resulting from translocation and redeposition, has been previously reported.[1] These individuals were referred to us from a large medical center in a neighboring state as part of a study to demonstrate the feasibility of a large-scale study of many persons known to have been injected with Thorotrast at this hospital. In the course of evaluating the significance of these measurements and the means for obtaining more detailed information from whole-body counting, certain conclusions have been reached. These are:

(a) The principal gamma rays observed originate in the decay of the daughter elements actinium-228, lead-212, bismuth-212, and thallium-208. Calculation of the burden of Bi^{212} based on the 1.62 and 2.2 MeV photons emitted is always in agreement with the Tl^{208} as calculated from the 2.62 MeV gamma ray. While a certain amount of simplification in the observed spectra results from coincidence or summing-coincidence modes of operation, these seem to offer no compelling advantage for the purposes of estimating total body burden.

(b) Accuracy in the quantitative measurement of Ac^{228} from gamma emission at 907 and 964 keV is significantly affected by the amount of potassium-40 present, since degraded photons resulting from Compton scattering of the 1.46 MeV radiation of K^{40} form an underlying continuum upon which the thorium contribution in the 900 to 960 keV region must be "stripped." The K^{40} content is, in turn, somewhat difficult to determine because of interfering radiation at 1.62 MeV from Bi^{212}. Normal metabolic processes, principally excretion of radium-224 (half-life of 3.6 days) and exhalation of radon-228 (thoron, half-life of 54 seconds), result in approximately 80% retention of the late daughter elements relative to the Ac^{228}. The relative amounts of each isotope are expected to differ with deposition site, being most nearly in radioactive equilibrium in the primary deposit. If the crystal detector is positioned some distance from the body so as to afford constant response to all locations, accuracy is impaired by the reduced number of events which may be detected in a time period limited by patient discomfort.

(c) Some success in estimation of skeletal burden from measurement over the tibiae and fibulae has been achieved. Information about the amounts of activity translocated to other organs such as the lungs and kidneys is desired. The close proximity of these organs to the primary deposits, as well as their much lower expected total burden, make this very difficult, and it remains to be seen whether direct, *in vivo* detection of these secondary sites is indeed possible.

Thus, the further application and improvement of procedures briefly outlined above call for improved spatial resolution and sensitivity, accompanied by freedom from, or at least some systematic and rational compensation for, normal variability in patient size, physique, and habitus, with the concomitant fluctuations in potassium-40 (and, to a constantly diminishing extent, of cesium-137) content, organ size and location, etc. Further development of measurement techniques and the application of sophisticated computer manipulation of data are desirable.

But in addition to these technical problems, there are logistic ones. We refer to the desirability, if not necessity, of having available for study some Thorotrast-exposed individuals who are accessible and cooperative. The first requirement may best be realized by residence within 40 or 50 miles of the Laboratory. It also requires that the persons be reasonably free to be called in at our convenience; i.e., that they not be employed full time. The cooperativeness of these individuals involves personality factors as well as age and physical condition.

The results of direct, *in vivo* measurements of activity translocated to secondary sites will be, at very best, of low accuracy. Therefore, these should eventually be correlated with measurements of individual tissue samples obtained at time of death and autopsy. The applicability of the above qualifications for this further phase of the investigation is obvious.

CHICAGO AREA SEARCH

Since Thorotrast has been used extensively as an x-ray contrast media in cerebral angiography, a search of medical records for the names of individuals undergoing such examination was undertaken. It was ascertained that of the many neurosurgeons in practice in the Chicago area during the period when use of Thorotrast was common, only two individuals em-

* Summer employee, 1966.

ployed it extensively. One of these is still active, and was able to furnish us with a log-book listing all angiographic examinations performed between 1942 and 1956, listed consecutively and summarized yearly. The other individual had retired from practice and left the state; however, it was known that most of his practice was done at one hospital. Since the hospital records of this institution were found to be exceptionally well organized, all of the pertinent records were located and examined with no difficulty.

The task of record search was carried out by the junior author, a medical school student of the University of Cincinnati employed in the Radiological Physics Division during the summer of 1966. It was found that the type of records kept, and their accuracy and completeness, differed greatly among the various institutions. The operative record sheet normally would contain spaces to record site of injection, type of contrast medium used, and amount injected. Frequently, these spaces were found blank, supplemented only by the cryptic remark "Usual dye injection made."

The results of this record search are summarized in Tables 20 and 21.

As the names of verified Thorotrast cases were obtained, search procedures were instituted, usually by reference to telephone and address listings, contact with the listed family physician or place of employment, or next of kin. In some cases, a personal visit to the last known address and interview with former neighbors was necessary. In view of the great mobility of most city-dwellers, and the rapid changes that have taken place in most of the city neighborhoods during the past two decades, it is a matter of great satisfaction that 90% of the patients on record have been either located or their death authenticated.

TABLE 20. Summary of Record Search

Source of records	Records examined	Use of Thorotrast verified
Hospital W	850	31
Hospital X	300	57
Hospital Y	40	4
Neurosurgeon Z	115	1
Miscellaneous	4	4

TABLE 21. Breakdown of Records Examined, Hospital W

Type of dye not specified	208
Diodrast employed	421
Thorotrast employed	31
Other contrast media used	63
Patient record not found—missing	53
atient record not found—error in admission number versus patient's name, etc.	62
Arteriogram not successful	12
	850

TABLE 22. Time Distribution, Known Thorotrast Cases

Year	All cases	Known deceased	Known living	Not located
1934	1		1	
1945	2			2
1946	3	2	1	
1947	3	2	1	
1948	6	5	1	
1949	3	1	2	
1950	4	4		
1951	8	4	3	1
1952	15	8	5	2
1953	18	12	6	
1954	10	5	4	1
1955	8	4	3	1
1956	5	3	1	1
1957	3	3		
1958	3	3		
1959	1	1		
Total	93	57	28	8
Date unknown	4	2	2	
Grand total	97	59	30	8

We had expected to find that Thorotrast was most frequently used around 1938–1941, but analysis of all verified cases reveals a much later peak date. A partial explanation for this lies in the statement of the neurosurgeon associated with hospital W, to the effect that the radioactivity of Thorotrast was known, and its possible hazards recognized; hence, it was used only after careful consideration of the patient's age and probable prognosis, with due consideration being given to the possible long-term radiation effects versus the immediate need for radiographs having optimum information content. The time distribution of injection for all records examined is summarized in Table 22.

A brief analysis of the ages of these patients reveals the following:

Age at injection, located (mean value)	47.9 years
Age at injection, known deceased (mean value)	51.8 years
Age at death (mean value)	55.0 years
Present age, located (mean value)	62.5 years

For individuals known to be dead, the average time elapsed between injection and death is 3.2 years, indicating that Thorotrast was the preferred contrast medium in cases of short life expectancy. By contrast, those located and hence still known to be living

have survived for an average period of 14.6 years. Many of these are approaching or have exceeded their normal life expectancy—four are in their 70's and nine more are between 65 and 70. If this small sampling can be considered representative of the situation in the entire United States, it is obvious that the majority of recorded Thorotrast-exposed individuals have already expired, and that prompt measures should be taken to examine those remaining.

It is impossible to mention all the persons that have been contacted and have made suggestions or have been of help in the patient search. Our special thanks go to Miss Rita Finnegan and Mrs. Yamaguchi, medical record librarians at the two hospitals where most of this work was done. Mr. Robert Xenos of the Security Division, ANL, was able to locate several of these persons when there were seemingly no leads at all. The unfailing interest and encouragement of Mr. L. D. Marinelli is also deeply appreciated.

REFERENCE

1. H. A. May and L. D. Marinelli. A Preliminary Study of Gamma Rays Emitted by Thorotrast Patients. Argonne National Laboratory Radiological Physics Division Annual Report, July 1964–June 1965. ANL-7060, pp. 93–99.

*PHOTOIONIZATION STUDIES IN THE VACUUM ULTRAVIOLET**

James C. Person

Recent results on the effects of deuterium substitution on the photoionization of gaseous molecules [1, 2] by photons with energies up to 11.7 eV are presented. The results in benzene and acetone indicate that preionization of superexcited states is an important ionization mechanism for these molecules, whereas the results in ammonia, *n*-butane, and ethylene indicate that direct ejection of an electron during the excitation act is the dominant ionization mechanism for these molecules. Ethylene is an especially interesting case, since the increase in the photoionization yield upon deuteration is caused by an isotope shift in the production of neutral excited states rather than by preionization. Another interesting result is the observation of chemi-ionization in acetone just below the ionization threshold.

* Abstract of an invited paper presented before the Lake Superior Section of the American Chemical Society, Duluth, Minnesota, April 27, 1967.

REFERENCES

1. James C. Person. *J. Chem. Phys.* **43**, 2553 (1965).
2. James C. Person and Paul P. Nicole. This report.

ISOTOPE EFFECTS IN THE PHOTOIONIZATION OF ACETONE, BUTANE, ETHYLENE, AND AMMONIA

James C. Person and Paul P. Nicole

INTRODUCTION

As a continuation of a program of studies of isotope effects on the photoionization of gaseous molecules,[1] we have studied the photoionization of acetone, *n*-butane, ethylene, and ammonia, together with their fully deuterated analogues. Measurements were made of the total absorption cross section, $\sigma(E)$, and the photoionization yields, $\eta(E)$, (this quantity is also called the photoionization efficiency and it is defined as the probability that photon absorption will produce an ion pair) as a function of photon energy, E, for $E \leqq 11.7$ eV.

From observations of an increase in $\eta(E)$ upon deuteration, one can determine some of the cases where the preionization of superexcited states makes a large contribution to the ionization, since the preionization processes, presumably invariant under isotopic substitution, compete with atomic rearrangement processes, such as dissociation, which are slower in heavier isotopic molecules.[2] Such an effect was observed in the photoionization of benzene,[1] and similar isotope effects ha been observed earlier in the cases where ionization was produced by collision with excited atoms,[3, 4] by β particles,[5] and by 70-eV electrons.[6]

EXPERIMENTAL APPARATUS AND MATERIALS

The experimental apparatus consisted of a hydrogen discharge light source, a McPherson Model 225 vacuum monochromator (used with a 1-Å band width), and a dual-beam detector system.[7] Ionization currents were collected by parallel-plate electrodes in the 5.1-cm-long ionization cell, and gas pressures in the cell, which had LiF windows, were measured with a MKS Baratron capacitive manometer.

The Matheson Company supplied the *n*-butane (instrument grade, stated purity 99.5+ %), the ammonia (stated purity 99.99+ %), and the nitric oxide (stated purity 99+ %), while the acetone was Matheson Scientific Company chromato-quality grade (stated purity 99+ %) and the ethylene was Phillips Petroleum Company research grade (stated purity 99.99+ %). The Volk Radiochemical Company supplied the deuterated materials which were stated to have the following minimum atom per cent deuterium: 99.5 for acetone-d_6, 99 for ethylene-d_4, and 98 for *n*-butane-d_{10} and for ammonia-d_3. Each gas was further purified by bulb-to-bulb distillation in the vacuum system.

EXPERIMENTAL DIFFICULTIES

The η values reported here are only preliminary values because of (a) difficulty in achieving ion current saturation, (b) the correction for the empty cell ion current, (c) the correction for extra ionization produced by photons reflected or scattered at the windows, and (d) the measurement of the absolute photon flux.

When the cell voltage is increased, the ion current first rises rapidly, then levels out to a broad maximum and then with a further increase in voltage, decreases by some 2 to 10 %. Also, the ion current changes slowly for several minutes after the cell voltage is changed, and the maximum ion current decreases when the light absorption is increased above about 99.5 %. These effects are evidently caused by unknown surface potentials on the insulator surfaces of the LiF windows and the glass walls, since these effects are not observed when using a new stainless steel cell with LiF windows covered by a high-transmission tungsten mesh. The data reported here were measured using the glass cell where the cell voltage was adjusted at each gas pressure to give an ion current in the region of the broad maximum.

Even in an empty cell (pressure $\sim 10^{-5}$ torr), there is still a photoion current of some 1 to 3 % of the current at complete absorption. This ion current is resumably due to electrons ejected from the cathode y photons which are scattered at the exit slit of the monochromator, the grid wires of the light splitter in the dual beam apparatus, or at the cleaved surfaces of the two LiF windows. When there is gas in the cell, some of these scattered photons will be absorbed along with some of the photons which are specularly reflected at the rear window. Most of these photons would not pass through the rear window even with no absorption, so they are not measured as photons absorbed by the gas and any ionization they produce must be subtracted. [The σ measurements are corrected for the small ($\sim$1 %) amount of light which is reflected twice so that it does pass through the rear window.] Assuming that this physical model is complete, the ion current due to these effects is estimated for each gas pressure and photon energy. However, only the values of the ion current measured for high absorptions (80 to 99.5 %) are used to calculate the η values, since the corrections are smaller at high absorptions.

The values of $\eta(E)$ for each gas were measured relative to the value of $\eta(E)$ for acetone—which is a convenient reference gas because of its rather constant value of $\sigma(E)$ and $\eta(E)$. The η values for acetone were then determined by comparison of the ionization in acetone with the ionization in nitric oxide whose η values have been measured by Matsunaga, *et al.*[8] The η values measured in this way showed a somewhat irregular pattern which repeated in different gases and which was eliminated by adjusting the NO η values. The data points in Figure 23 illustrate the irregular behavior of the photoelectron yield for a nickel surface while the line illustrates how the data were smoothed.

RESULTS AND DISCUSSION

The measurements of σ and η are illustrated in Figures 24, 26, 28, and 30 while Figures 25, 27, 29, and 31 show plots of the photoionization cross section, σ_i ($\sigma_i \equiv \eta\sigma$), and the neutral cross section, σ_N [defined as $\sigma_N = \sigma - \sigma_i = \sigma(1 - \eta)$]. In each figure the heavy and dashed

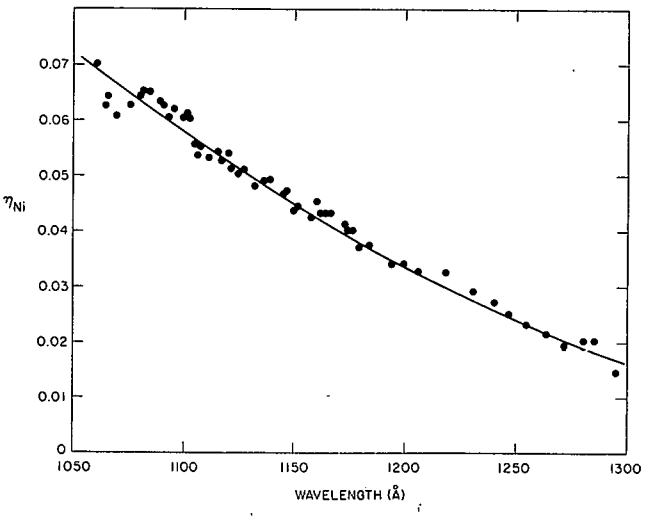

FIG. 23. Photoelectron yield of a nickel mesh as a function of photon wavelength.

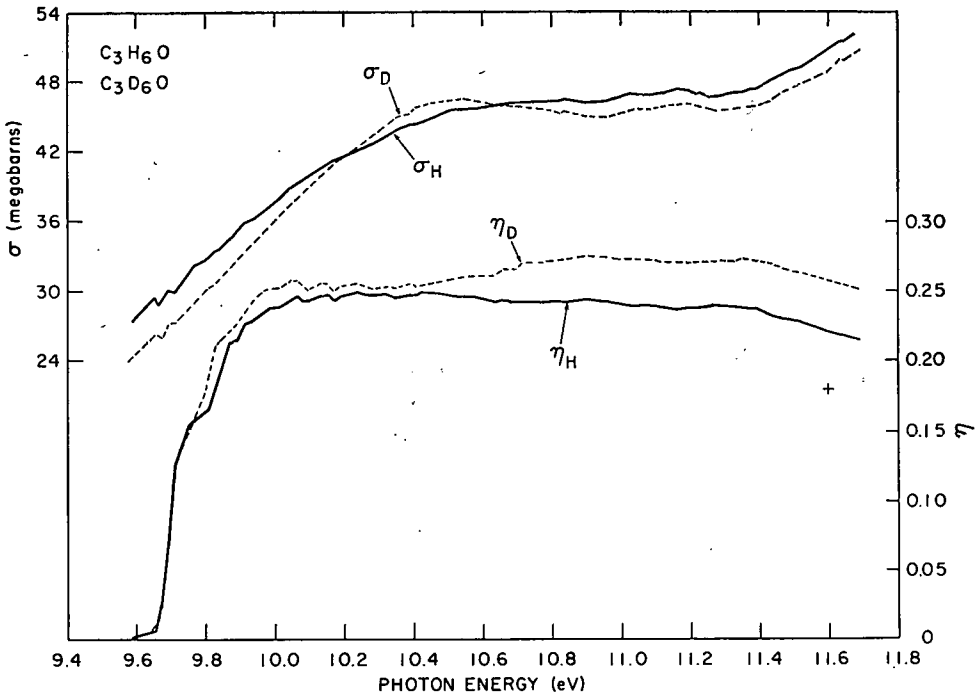

FIG. 24. Absorption cross sections and photoionization yields for acetone and acetone-d_6 as functions of photon energy. Th values for the collisional ionization yield (Reference 9) is plotted with + for η_{cH} .

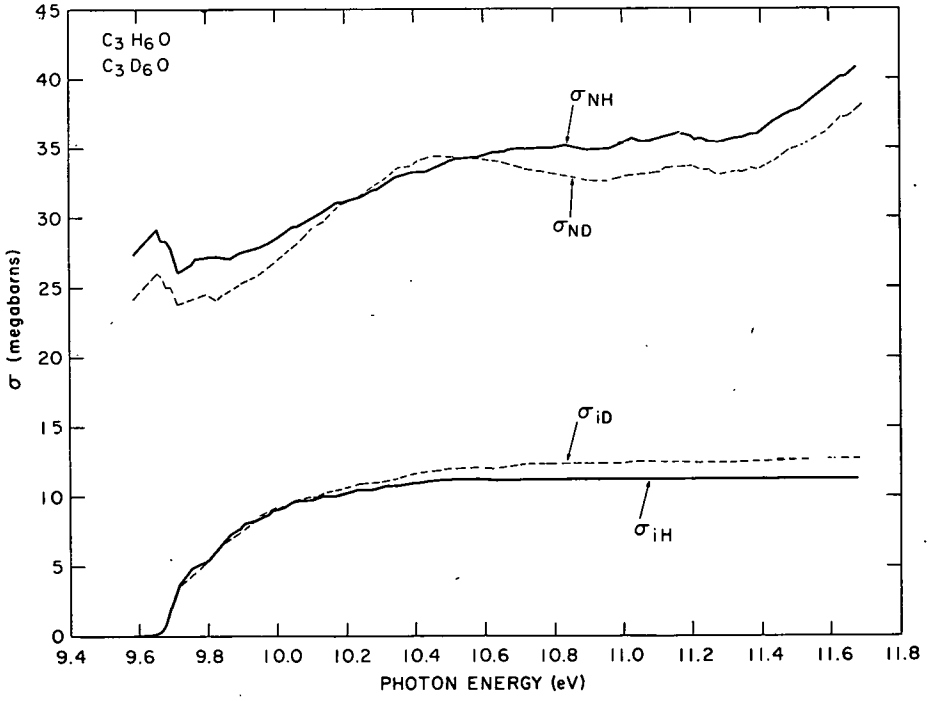

FIG. 25. Photoionization and neutral cross sections for acetone and acetone-d_6 as functions of photon energy.

lines refer respectively to the undeuterated and the deuterated species.

Acetone

Figure 24 shows that for acetone the $\eta(E)$ values increase rapidly in the first 0.4 eV above the ionization potential and then remain approximately constant at a value of ~0.23. This low value of η is in harmony wit the 0.18 value of the collisional ionization yield mea: ured by Hurst and coworkers[9] for acetone ionized by collision with excited argon atoms (excitation energy ~11.6 eV). The η_D (for C_3D_6O) values are generally

above the η_H (for C_3H_6O) values and the average η_D/η_H for the energy range of 10.42 to 11.6 eV is 1.10. Figure 25 shows that the photoionization cross section also increases upon deuteration. These facts, together with lack of evidence of any large shifts in energy thresholds, indicate that preionization of superexcited states is an important ionization mechanism in acetone.

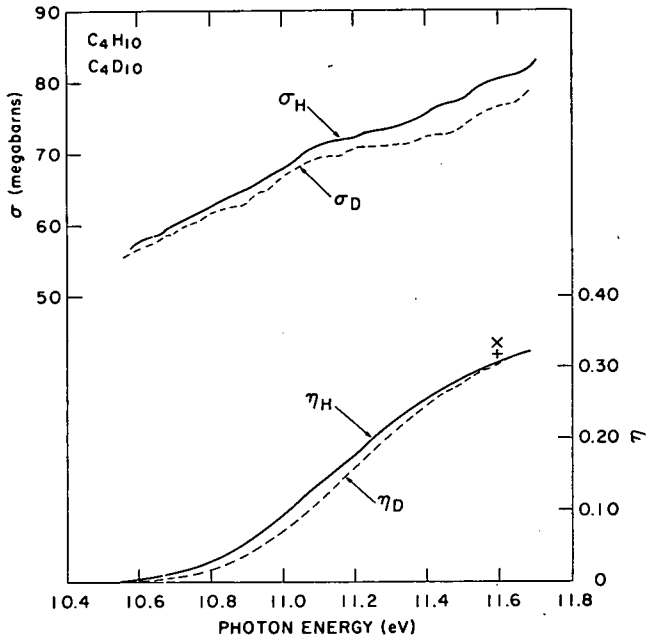

FIG. 26. Absorption cross sections and photoionization yields for n-butane and n-butane-d_{10} as functions of photon energy. Jesse's values for the collisional ionization yields (Reference 4) are plotted with + for η_{cH} and × for η_{cD}.

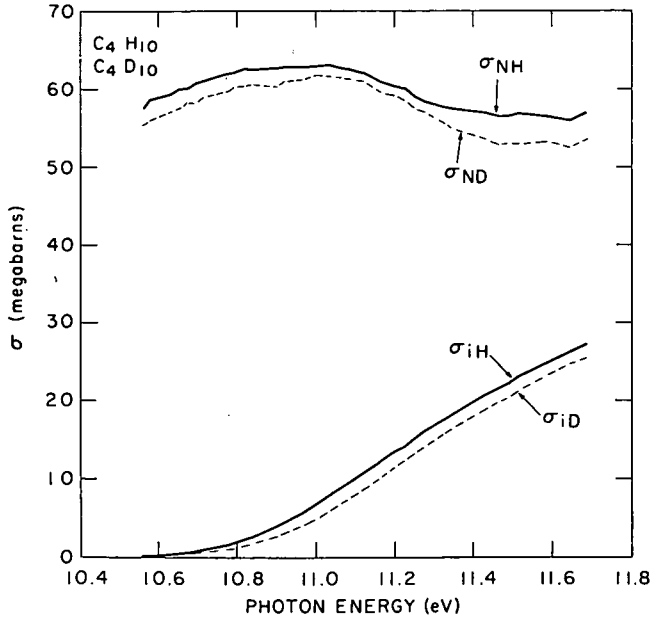

FIG. 27. Photoionization and neutral cross sections for n-butane and n-butane-d_{10} as functions of photon energy.

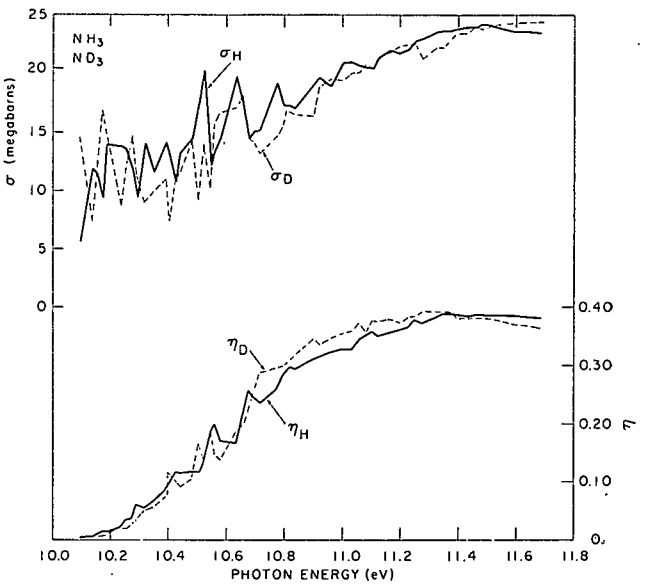

FIG. 28. Absorption cross sections and photoionization yields for ammonia and ammonia-d_3 as functions of photon energy.

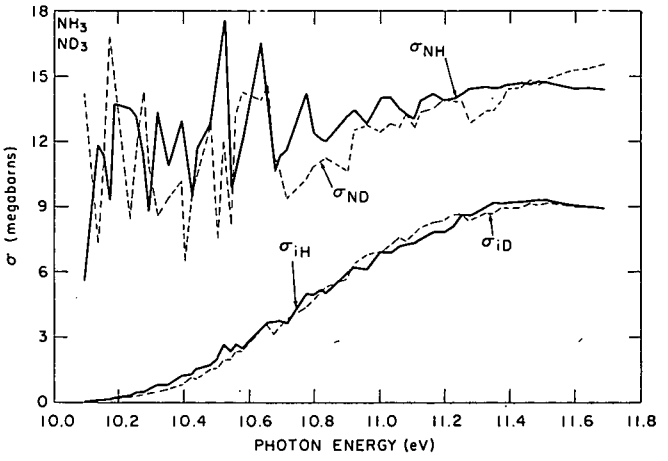

FIG. 29. Photoionization and neutral cross sections for ammonia and ammonia-d_3 as functions of photon energy.

The plots of σ_N for acetone and acetone-d_6 show a peak at ~9.65 eV—just below the ionization threshold. This peak presumably consists of transitions to highly excited ($n \geqq 13$) members of a rydberg series converging to 9.705 eV.[10]

Some ionization is observed in this energy region due to photoionization of molecules possessing vibrational energy in the ground state. However, the ion current per photon absorbed in this energy region first increases as the pressure is increased and then levels out at a constant value. Such a pressure dependence suggests that the increased ionization is the result of a chemi-ionization reaction of an excited acetone molecule with a ground state acetone molecule to form a dimeric ion.

In order to live long enough to undergo such a reaction, the excited state must have a radiative lifetime and not a lifetime limited by a rapid dissociation. Such chemi-ionization processes are well established for atomic[11] and diatomic[12] species and have been observed previously for acetylene.[13]

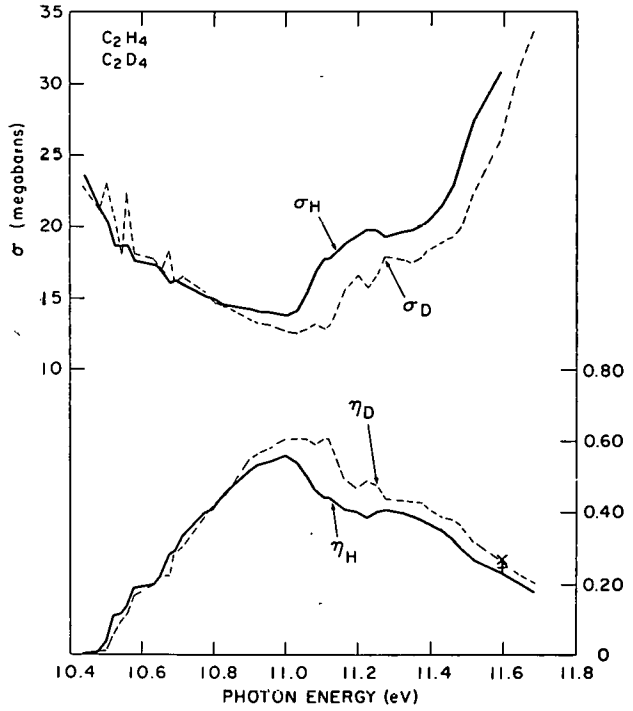

FIG. 30. Absorption cross sections and photoionization yields for ethylene and ethylene-d_4 as functions of photon energy. Jesse's values for the collisional ionization yields (Reference 4) are plotted with + for η_{cH} and × for η_{cD}.

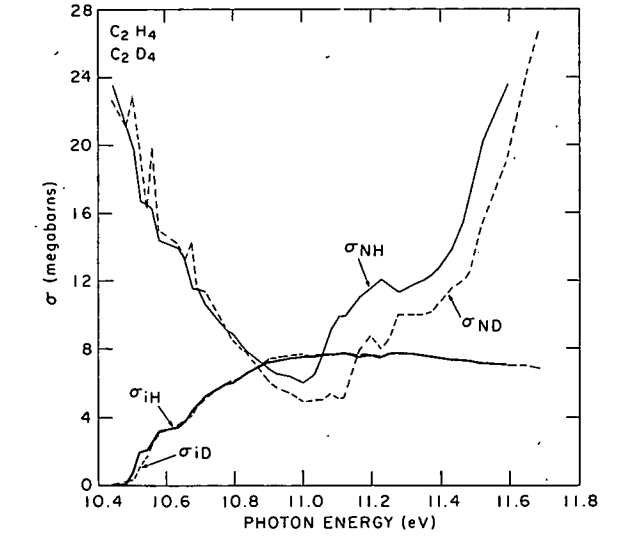

FIG. 31. Photoionization and neutral cross sections for ethylene and ethylene-d_4 as functions of photon energy.

Butane

Figures 26 and 27 illustrate the results in *n*-butane and *n*-butane-d_{10}. The $\eta_D(E)$ values here lie below the $\eta_H(E)$ values, and there seems to be a shift in the energy threshold for ionization. If there is a general energy shift of more than a few hundreths of an eV, then the data are no longer of use in determining the relative importance of preionization vs. direct ionization—unless one has further information concerning the magnitude of the energy shift. For example, in Figure 27, if the σ_{iD} curve is shifted to lower energies by about 0.07 eV or more, then the $\sigma_{iD}(E)$ would be equal to, or larger than, the $\sigma_{iH}(E)$ values. A similar energy shift has been observed when the $\sigma(E)$ values of C_4H_{10} and C_4D_{10} are compared in the energy region of 7.5 to 9.3 eV.[14]

The σ value which Schoen determined for C_4H_{10} at $E \approx 11.4$ eV agrees with our result, but Schoen's value of $\sim$0.18 for η_H at this energy is low.[15] Our measurements of η_H and η_D are in better agreement with the values obtained by Ausloos and Lias ($\eta_H = 0.32$; $\eta_D = 0.33$) using an argon resonance lamp producing a mixture of 11.63 and 11.82 eV photons,[16] and also with the values of the collisional ionization yield measured by Jesse[4] using excited argon atoms ($\eta_{cH} = 0.32$; $\eta_{cD} = 0.338$), although these workers obtained a higher value for the η_D/η_H ratio.

Ammonia

The results of the measurements on NH_3 and ND_3 are shown in Figures 28 and 29. The deuterium substitution changes the energy level spacings, but does not seem to produce any general increase in the η values, so that direct ionization seems to be the dominant ionization mechanism for ammonia. The lines connect the measurements at 55 photon energies, but still more points are needed in the regions with structure. In general, the data for NH_3 are in agreement with earlier measurements of σ and σ_i by Watanabe and Snood[17] and with many of the values of $\sigma(E)$ reported by Weissler and coworkers.[18, 19]

Ethylene

The results illustrate that an increase in η upon deuteration does not, in itself, imply that preionization is an important ionization mechanism in ethylene. Figure 30 shows the values of σ and η for C_2H_4 and C_2D_4, and the $\eta_D(E)$ values are clearly larger than the $\eta_H(E)$ values. Notice, also, that the $\sigma_H(E)$ values are larger than the $\sigma_D(E)$ values, so that the σ_i values are essentially identical, as Figure 31 shows. Figure 31 also shows that ethylene has a strong absorption peak above the ionization threshold, and that very few, if any, of the photons absorbed in this state form ions since the $\sigma_i(E)$ remains essentially constant even though the

$\sigma(E)$ values rise sharply as E increases above 11.2 eV. Evidently the energy threshold to reach this excited state is ~0.1 eV greater for C_2D_4 than for C_2H_4, and it is this energy shift that produces the isotope effect in η.

This observation that preionization is not an important ionization mechanism for ethylene at energies around 11.6 eV offers a simple explanation of the dilemma raised by Meisels[20] of reconciling the chemical evidence that H or H_2 fragments but not CH_2 radicals are formed in the argon-sensitized radiolysis of ethylene, while the magnitude of the isotope effect observed by Jesse in the collisional ionization yield[4] would indicate that if most of the ionization is from preionization, then most of the reactions which lead to neutral products involve the motions of two groups which both contain a carbon atom. However, since our results indicate that preionization is not an important ionization mechanism here, Jesse's results cannot be used to predict the dissociation products, and we may then assign the large peak in $\sigma_N(E \approx 11.6$ eV) to production of a state which rapidly dissociates to form H or H_2 fragments.

The σ_H values are in general agreement with most of the measurements of Zelikoff and Watanabe[21] and with the two values of Schoen,[15] but they are somewhat larger than the values reported by Walker and Weissler.[22] Schoen's measurement of η_H ($E \approx 11.4$ eV) ≈ 0.15 is lower than the present result; our measurements agree very well with Jesse's value of η_{cH} ($E \approx 11.6$ eV) = 0.245 and η_{cD} ($E \approx 11.6$ eV) = 0.266.[4]

The assignment of the neutral-producing process around 11.5 eV in ethylene to a dissociation producing H or H_2 fragments offers a possible explanation of the energy shift as the result of the lower zero-point vibrational energy in the ground state of the heavier molecule. For a zero-order explanation of this, consider that the vibrational energy of the dissociation products will be approximately the same in the upper electronic state as they would be if the lower electronic state dissociated into the same fragments; furthermore, the electronic energy of the excited state should be independant of the isotopic composition to a good approximation, so that if the different isotopic molecules each had the same vibrational energy in the lower electronic state, then the transition energy to the upper state would be the same. However, in the absence of vibrational excitation in the lower electronic state, the lower zero-point vibrational energy of the heavier isotopic species changes the transition energy required to reach the excited electronic state. As an example, the zero-point vibrational energy in C_2H_4 is 1.3 eV, while for C_2D_4, it is 0.9 eV—or the total difference in zero-point energy in the 12 vibrational modes is 0.4 eV. For a C_2H_3 fragment there are only 9 vibrational modes, so a first estimate of the difference in the zero-point energy for three vibrational modes no longer present after dissociation would be ($0.4 \times 3/12$ eV) = 0.1 eV. Notice that a large energy shift is not predicted for transitions to the ground vibrational levels of bound excited states because of the difference in the zero-point vibrational energy of these electronically-excited states.

If the increased absorption in ethylene between 11 and 12 eV is caused by transition to only a few electronic states, then the energy shift would be especially apparent.

REFERENCES

1. J. C. Person. *J. Chem. Phys.* **43**, 2553 (1965); Argonne National Laboratory Radiological Physics Division Annual Report, July 1964 through June 1965. ANL-7060, p. 3.
2. R. L. Platzman. *J. Chem. Phys.* **38**, 2775 (1963).
3. W. P. Jesse and R. L. Platzman. *Nature* **195**, 790 (1962).
4. W. P. Jesse. *J. Chem. Phys.* **41**, 2060 (1964).
5. W. P. Jesse. *J. Chem. Phys.* **38**, 2774 (1963).
6. S. Meyerson, H. M. Grubb, and R. W. Van der Haar. *J. Chem. Phys.* **39**, 1445 (1963).
7. J. C. Person. Argonne National Laboratory Radiological Physics Division Annual Report, July 1963 through June 1964. ANL-6936, p. 21.
8. K. Watanabe, F. M. Matsunaga, and H. Saki. *Appl. Opt.* **6**, 391 (1967).
9. C. E. Melton, G. S. Hurst, and T. E. Bortner. *Phys. Rev.* **96**, 643 (1954).
10. K. Watanabe. *J. Chem. Phys.* **22**, 1564 (1954).
11. F. Mohler, P. Foote, and R. Chenault. *Phys. Rev.* **27**, 37 (1926); F. Mohler and C. Boeckner. *J. Res. Natl. Bur. Std. (U.S.)* **5**, 51, 399 (1930). For recent work in this area see the following: Y. Lee and B. H. Mahan. *J. Chem. Phys.* **42**, 2893 (1965); **43**, 2016 (1965); R. E. Huffman and D. H. Katayama. *J. Chem. Phys.* **45**, 138 (1966).
12. W. A. Chupka and J. Berkowitz. Unpublished data.
13. I. Koyano, I. Tanaka, and I. Omura. *J. Chem. Phys.* **40**, 2734 (1964).
14. J. R. McNesby and H. Okabe. *Advan. Photochem.* **3**, 157 (1964).
15. R. I. Schoen. *J. Chem. Phys.* **37**, 2032 (1962).
16. P. Ausloos and S. G. Lias, *J. Chem. Phys.* **45**, 524 (1966).
17. K. Watanabe and S. P. Snood. *Sci. Light* **14**, 36 (1965).
18. W. C. Walker and G. L. Weissler. *J. Chem. Phys.* **23**, 1540 (1955).
19. H. Sun and G. L. Weissler. *J. Chem. Phys.* **23**, 1160 (1955).
20. G. G. Meisels. *Nature* **206**, 287 (1965).
21. M. Zelikoff and K. Watanabe. *J. Opt. Soc. Am.* **43**, 756 (1953).
22. W. C. Walker and G. L. Weissler. *J. Chem. Phys.* **23**, 1547 (1955).

SPECIFIC PRIMARY IONIZATION BY HIGH-ENERGY ELECTRONS

F. F. Rieke and William Prepejchal

When the preceding annual report was written, measurements with both electrons and positrons had been made on H_2, D_2, He, Ar, CH_4, CD_4, C_2H_6, and C_3H_8. Since then measurements have been made on Ne, Kr, Xe, N_2, CO, and NH_3. Improvements have been made in counting circuits, pressure calibrations, and data reduction. Measurements are being extended to other gases to which the method is applicable.

REDUCTION OF DATA

In preceding reports[1, 2] we have employed the relation

$$-\ln (1 - \epsilon') = SLp + b, \qquad (1)$$

where

S = Specific primary ionization in (atm cm)$^{-1}$,
ϵ' = observed efficiency of a gas-filled counter,
p = pressure of filling gas, in atm reduced to 0°C, and
L = length of path through the counter for a primary electron,

and the relation

$$1.9862\beta^2S^2 = M^2x + C, \qquad (2)$$

where

β = velocity of primary electron/speed of light,
x = $\ln (\beta^2/(1 - \beta^2)) - \beta^2$,
M^2 = sum of oscillator strengths squared, and
C = a second atomic constant.

Relation (1) was used to determine S, at each of a series of primary energies, from observations of ϵ' as a function of p. With the values of S so obtained, relation (2) was used to determine M^2 and C. Graphical or least-squares fits of (1) were made to obtain b as a function of p; then with a smoothed set of b's, (1) was fitted again to obtain S as a function of primary energy. By another least-squares solution, M^2 and C were obtained from (2).

By making a plausible assumption regarding the dependence of b on primary energy and some trivial manipulations, relations (1) and (2) can be combined into an equation of the form

$$z = c_1x_1 + c_2x_2 + c_3x_1x_3 + c_4x_2x_3, \qquad (3)$$

where

$$z = -\ln (1 - \epsilon')$$

$$x_1 = \frac{1}{\beta^2} \ln \frac{\beta^2}{1 - \beta^2} - 1$$

$$x_2 = 1/\beta^2 \qquad (x_1/x_2 = x \text{ of Eq. 2})$$

$$x_3 = 760\,p \qquad (x_3 \text{ in torr, } p \text{ in atm})$$

$$c_1x_1 + c_2x_2 = b \text{ of Eq. 1}$$

$$c_3 = \frac{LM^2}{1.9862 \times 760}$$

and

$$c_4 = \frac{LC}{1.9862 \times 760}.$$

All of the data from an experiment on a particular gas can be combined in one least-squares fit to equation 3 to determine M^2 and C. The new procedure has many advantages over the former one: the values of b are smoothed in an objective way, the observations are weighted more equitably, and a quantitative measure of the goodness of fit is given.

Typically, ϵ' is measured at at least four different pressures for each of eight different primary energies. Counting is usually continued until the statistical error in $1 - \epsilon'$ is 1 % or less; such data are given unit weight. If the statistical accuracy is less than 1 %, a proportionally lower weight is assigned.

Example

The following results were obtained with H_2 in an experiment made with the counting system in its present form. Hydrogen behaves very well as a counting gas; this set of data is the most self-consistent one that we have obtained.

Forty-three data points were observed, all with statistical uncertainty of 0.01 or less in z. The root mean square deviation (RMS) of the observed z's from those given by the fitted Eq. 3 is 0.010; counting statistics alone account for a RMS deviation of 0.006. The constants obtained, along with their standard deviations as given by least-squares formulas, are given in Table 23. Values of b obtained from least-squares fitting of Eq. 1 for individual primary energies are compared with $c_1x_1 + c_2x_2$ in Table 24.

PRESSURE CALIBRATION

Our Wallace & Tiernan gauge has been calibrated against a new Texas Instrument Co. fuzed quart Bourdon gauge that has a calibration traceable to th Bureau of Standards. The data sheet for the T. I. instrument indicates a maximum error of 0.01 torr for the pressure range 0–25 torr, 0.052 torr for the range

25–376 torr. The range of pressures in our experiments varies from 10 to 100 torr for H_2 and He to 3 to 12 torr for Xe and C_3H_8. The errors in S that result from inaccuracy of pressure measurement are, accordingly, less than ½%.

Because of distortion of the thin windows, the path length L depends, to a small degree, upon the gas pressure in the counter. The distortion has been measured and allowed for in the calculations by adding small corrections to the observed pressures.

COUNTING CIRCUIT

For gases other than hydrocarbons it has been necessary to employ the G-M mode of counting. To secure near-unity probability of detection for single electron events it is necessary to apply to the counter voltages well above threshold; that is, to operate far out on the plateau. Application of a large over-voltage, however, frequently results in what appears to be a continuous discharge; with external quenching it is observed that a new discharge follows immediately the restoration of above-threshold voltage to the counter, even in the absence of an external source of ionization. We have found, however, that the counter becomes stable if the quench pulse is made very long; in some cases it is necessary to hold the voltage below threshold for as long as ½ second in order to allow complete recovery from the preceding discharge. (It would be contrary to the purpose of the experiments to add a quenching agent such as ethyl alcohol to the counter gas in amount sufficient to stabilize the counter.)

Many variations of quenching circuit have been tried; the one that has proved by far the most satisfactory is illustrated in Figure 32, which also indicates the types of waveform that are involved. The resistance R_1, to some extent, acts as a normal quenching resistance; its effect is reinforced and sustained by the negative square wave applied through the direct-coupled vacuum tube

TABLE 23. LEAST-SQUARES ANALYSIS OF NOVEMBER 1966 DATA FOR H_2

	c_1	c_2	c_3	c_4
Constant	0.0055	0.021	0.000551	0.00660
Standard deviation	0.0016	0.002	0.000024	0.00003

$M^2 = 0.64 \pm 0.03$, $C = 7.70 \pm 0.03$ [$(1.986 \times 760/L) = 1168$].

TABLE 24. INTERCEPTS, $-\ln(1-\epsilon')$ VS. x_3 AT $x_3 = 0$

Primary energy, MeV	0.11	0.19	0.36	0.68	1.10	1.90	2.48	2.71
$10^3(c_1x_1 + c_2x_2)$	47	37	32	30	31	34	36	37
10^3b	38	41	35	31	33	33	30	37

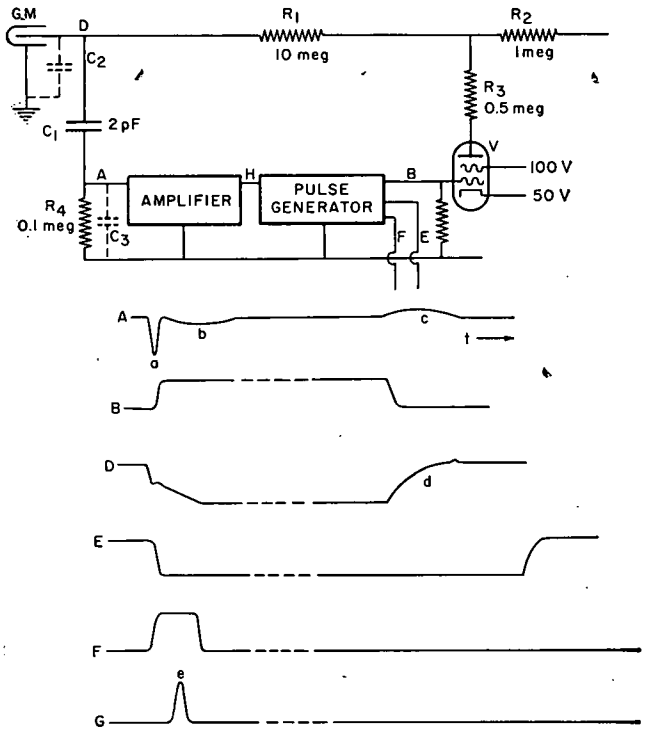

FIG. 32. Quenching circuit

V. The large disparity between the time constants $R_1(C_1 + C_2)$ and R_4C_3 serves to attenuate the quench pulse at the input to the amplifier. In the amplifier, additional discrimination against slow-rising pulses helps to isolate the input of the quenching circuit from its output. In consequence, it is possible to adjust the circuit so that it will trigger on a 1-mV pulse at A, apply a −300V quench pulse at D, and at the same time be stable against oscillation. Experience indicates that this high sensitivity is important even though the GM pulses normally saturate the amplifier. It appears that the circuit may lose control when a GM discharge occurs at the tail of the quench pulse, for then the voltage is only very slightly above threshold, as at d, and is too small to activate the quenching circuit.

In addition to B, the pulse generator supplies the two wave forms E and F. The square wave F is supplied to a coincidence circuit that registers coincidences between responses of the GM and silicon detectors; as normally adjusted it is eight microseconds long. The pulse G from the silicon detector is delayed four microseconds before entering the coincidence circuit. The square wave E is two hundred microseconds longer than B; it is supplied to an anticoincidence circuit to reject those pulses from the silicon detector that occur while the voltage on the GM counter is below its normal value: silicon pulses that fall within F are counted as coincidences; those outside of E as anticoincidence; the remaining ones are not counted at all.

With the quenching arrangement described above it is possible to secure data on He, Ne and Ar without adding to them several torr of hydrogen as had been necessary previously. Hydrogen stabilizes the counter by quenching rapidly the metastable atoms that are produced in a discharge and which otherwise regenerate the discharge as they slowly diffuse to the cathode and liberate electrons from it. The long quench pulse, by allowing ample time for diffusion to occur before full voltage is reapplied, eliminates the need for large amounts of added hydrogen. It is not certain, however, that liberation of electrons from the cathode by metastable atoms is the only mechanism that tends to regenerate the discharge in the absence of hydrogen, for the pulse length of quench pulse that is required for complete stability is considerably greater than the estimated time for diffusion; surface effects connected with the deposition of ions are suspect.

We have found that with very pure helium the GM discharge is much delayed, so that coincidences do not occur within the five microseconds allowed by the coincidence circuit. Addition of a very small amount of impurity, (0.01 torr) such as hydrogen or argon, eliminates the delay. We interpret this behavior to mean that photoionization in the gas is necessary for rapid avalanche-breeding, and that a very small amount of a component that can be photoionized by helium resonance radiation is effective. The amount of argon that is required to speed up the discharge is not great enough to have a significant effect on the observed primary ionization, however.

RESULTS

All the measurements that have been made, including those reported earlier, have been reduced according to the procedure described here and are summarized in Table 25. The second and third columns indicate whether, and in what amount, a foreign gas has been added to stabilize the counter. The method of calculation excludes direct ionization of the foreign gas and refers to the main component only. Table 26 contains values of x_1 and x_2 as functions of primary energy for convenience in deriving cross sections from the values of M^2 and C given in Table 25.

The standard deviation for M^2 and C given in columns 9 and 11 of Table 25 are derived from the RMS residual of the individual data points and coefficients from the least squares solution; they reflect random errors in counting, setting of the magnetic field in the analyzer, measurement of pressure, etc. In the most favorable cases they are about equal to what one would obtain from a least-squares fitting of equation 4 (see Table 26) to cross sections known with a standard deviation of 1.5% at each of the eight primary energies we have used. Systematic errors connected with the path length L and with energy and pressure calibrations may

TABLE 25. M^2 AND C FOR VARIOUS GASES

Gas	Additive		Data set	Pressure range, torr	No. data points	RMS residual	M^2		C	
	Pressure, torr	Gas					Value	S.D.	Value	S.D.
He	0.01	Ar	2/67	20–110	50	0.012	0.74	0.03	7.05	0.04
He	4.6	H_2	3/66	15–90	45	0.013	0.70	0.04	8.08	0.05
He	3.8	CH_4	4/66	15–125	50	0.014	0.75	0.04	7.06	0.05
Ne	0.01	H_2	3/67	10–65	46	0.010	2.02	0.05	18.18	0.07
Ne	3.8	H_2	5/66	10–50	33	0.018	2.09	0.13	18.50	0.20
Ar	0.9	H_2	4/66	2–35	22	0.018	3.66	0.25	38.6	0.3
Ar	—		1/67	7–30	32	0.012	3.96	0.19	38.4	0.2
Kr	3.8	H_2	6/66	4–20	33	0.012	6.03	0.22	52.4	0.3
Xe	3.8	H_2	7/66	4–15	35	0.019	7.36	0.52	74.9	0.7
H_2	—	—	2/65	38–185	40	0.010	0.70	0.03	8.11	0.04
D_2	—	—	2/65	35–185	47	0.013	0.57	0.03	8.38	0.04
H_2	—	—	1/66	35–110	51	0.015	0.61	0.05	8.10	0.07
D_2	—	—	1/66	35–125	40	0.014	0.69	0.04	8.19	0.04
H_2	—	—	11/66	18–110	43	0.010	0.64	0.03	7.70	0.03
D_2	—	—	4/67	18–125	37	0.018	0.64	0.05	8.40	0.07
N_2	3.8	H_2	9/66	7–30	47	0.024	3.6	0.6	35.3	0.6
CO	3.8	H_2	9/66	9–18	40	0.015	3.7	0.4	33.6	0.5
CH_4	—		3/65	5–35	70	0.022	3.8	0.2	41.9	0.3
CH_4	—		8/65	9–25	40	0.013	4.7	0.3	42.4	0.4
CD_4	—		8/65	5–25	42	0.014	4.4	0.2	43.8	0.3
C_2H_6	—		5/65	4–25	40	0.018	6.5	0.4	69.4	0.5
C_3H_8	—		6/65	3–20	56	0.015	10.7	0.5	115.7	0.7
NH_3	—		4/67	3–12	33	0.020	4.4	0.6	31.0	0.7

together contribute uncertainties of 4% to M^2 and 2% to C.

A remaining possible source of error, and one that is difficult to assess, is that connected with the reliability with which the gas-filled counter and associated circuitry indicates whether or not an ionization has occurred within the gas. The very close agreement between our results for He + 4.6 torr H_2 and the very accurate quantum-mechanical calculation by Inokuti, Kim and Platzman[2, 3] indicates that errors from this source are very small. This indication is not contradicted by the observation of lower values of C for He + 0.01 torr Ar and for He + 3.8 torr CH_4; the argument here is that:

1) In the presence of several torr of H_2, all excitations of He are converted into ionization;

2) with only 0.01 torr Ar, collisions of an excited He with Ar are too infrequent to permit appreciable conversion of He excitation into Ar ionization within the resolving time (a few microseconds) of the coincidence circuit; and

3) CH_4 is less efficiently ionized in collisions with excited He than is H_2.

A somewhat less encouraging result is the C value obtained from the 11/66 data set for H_2, which is 5% lower than that for the two preceding data sets. We are unable, at present, to account for so large a discrepancy.

TABLE 26. x_1 AND x_2 OF Eq. 2 AS FUNCTIONS OF ELECTRON ENERGY

T, MeV	x_1	x_2	T, MeV	x_1	x_2
0.001	−1421	256.2	0.45	0.298	1.394
0.01	−85.98	26.30	0.5	0.437	1.343
0.1	−3.810	3.327	0.6	0.668	1.268
0.12	−2.874	2.906	0.8	1.028	1.179
0.14	−2.234	2.606	1.0	1.311	1.129
0.16	−1.768	2.381	1.2	1.551	1.098
0.18	−1.416	2.207	1.4	1.761	1.077
0.20	−1.137	2.069	1.6	1.949	1.062
0.25	−0.641	1.821	1.8	2.120	1.051
0.3	−0.307	1.658	2.0	2.277	1.043
0.35	−0.060	1.544	2.5	2.622	1.030
0.40	+0.136	1.459	3.0	2.916	1.022

$$\frac{S\ (\text{cm atm})^{-1}}{1.9862} = \frac{\sigma(\text{cm}^2)}{5.34 \times 10^{-19}} = M^2 x_1 + C x_2 \qquad (4)$$

REFERENCES

1. F. F. Rieke and W. Prepejchal. Argonne National Laboratory Radiological Physics Division Annual Report, July 1964 through June 1965. ANL-7060, p. 33.
2. F. F. Rieke and W. Prepejchal. Argonne National Laboratory Radiological Physics Division Annual Report, July 1965 through June 1966. ANL-7220, p. 19.
3. M. Inokuti, Y. K. Kim and R. L. Platzman. Sum Rule for the Bethe Inelastic-Scattering Cross Sections. This report.

MULTIPLE ELASTIC SCATTERING OF ALPHA PARTICLES— APPLICATION OF THE SMALL-ANGLE THEORY

Harvey A. Schultz

INTRODUCTION

Multiple scattering may interfere with the measurement of the effect of pressure upon W, the average energy lost by a fast charged particle per ion pair produced. It is proposed to make the measurements in pure rare gases, especially neon and argon and to utilize alpha particles.[1] The paths of alpha particles in a gas are relatively straight lines, in contrast to the jagged tracks of electrons; however, a collimated beam will always tend to spread, and the spreading may be large enough to produce spurious ionization results, depending upon the size and shape of the ion chamber. This effect would be especially troublesome if, according to one design that has been considered, natural alpha particles were reduced in energy to 1 or 2 MeV and then admitted to a long thin ion chamber, there to be completely stopped by the gas.

No suitable scattering data for use in chamber design were found; accordingly, the theory of multiple scattering was consulted.

Multiple scattering appears to have been reported first in 1894 by Lenard, who observed cathode rays in air (reported in Ref. 2). The theoretical treatment was started as early as 1921[3, 4] and it has been refined and extended repeatedly until the present. All sorts of particles have been considered. Earlier investigators were interested in the scattering of alpha particles because the effect of multiple scattering interfered with the interpretation of single-scattering experiments; recent workers have been concerned more with other particles, e.g., protons, mesons, neutrons, electrons, or even photons.

Below is a discussion of those portions of the general theory of multiple scattering that apply to the lateral

spreading of a beam of alpha particles in a gas. Some numerical examples are given in the section on application of small angle theory.

THE THEORY OF LATERAL DISPLACEMENTS

The basic problem of the statistical theory for lateral displacements of fast particles is this: in Figure 33 the particles are projected along the positive OZ axis, and after a number of scattering collisions, each particle passes through the plane $z = z_0$ at some point (x,y,z_0); we wish to determine the relative density of these points as a function of x and y.

Fermi (reported in Ref. 5) seems to have been the first to present a theory for this distribution; his result is a Guassian approximation, and it does not take energy loss into account. Scott and Snyder[6] extended the theory and obtained a more realistic, non-Gaussian function. Molière showed how the energy loss of the particle could be taken into account (Ref. 9, p. 86). The principal references for this report are the comprehensive summary published by Scott in 1963,[7] three articles of Molière,[8-10] and an article of Bethe.[11]

The theory outlined here has the following characteristics: the scattering is treated in the small-angle approximation; the medium is taken as infinite, the energy loss of the alpha particles is taken into account—also their gain and loss of electrons; the single deflections are assumed to be elastic nuclear processes and the differential cross sections to be of the Rutherford type, with a modification because of the screening effect of the bound electrons. The initial beam of alpha particles is assumed to be infinitesimal in area and perfectly collimated; actual physical beams may be treated by a subsequent superposition process. To define the small-angle approximation, let θ be the angle between any tangent to the track and a line parallel to the initial tangent (Figure 33); in this approximation $\sin\theta$ is replaced by θ and $\cos\theta$ by 1, also the upper limit of θ is changed from π to ∞. Corresponding approximations are made when the x and y projections of θ are considered.

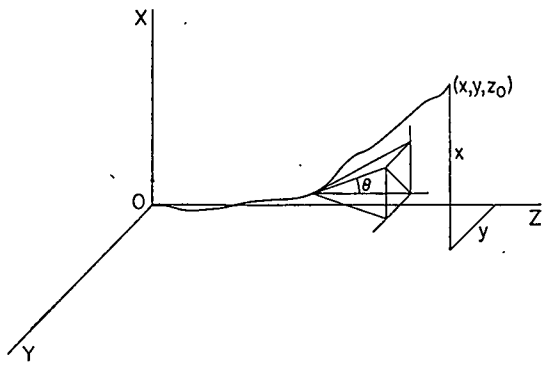

FIG. 33. The coordinate system, an alpha track and an instantaneous tangent angle or track angle, θ.

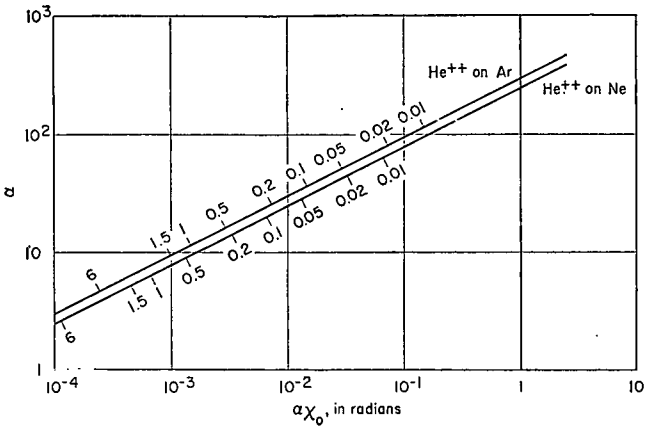

FIG. 34. Parameters α and $\alpha\chi_0$ (Eq. 1, 2) as a function of the energy of He^{++} particles in argon and neon. Energies in MeV are indicated along the curves.

Screening by Bound Electrons

Numerous formulas covering single elastic scattering in a screened nuclear field have been published (Ref. 7, pp. 255–265, 277–288). In general, the more recent publications present relations that were developed primarily for application to fast electrons; two earlier works, those of Williams[12] and Molière,[8] give results that may be used for alpha particles in most materials (atomic number Z about 10 or greater).

In Figure 34 the single collisions of 6-MeV He^{++} nuclei as they lose energy in neon and argon are characterized by points along straight lines. Bohr used a diagram of this type in a discussion of scattering in a general central field.[13] The parameters are defined as follows:

$$\alpha = ZZ_p e^2/\hbar v, \qquad (1)$$

(called the Born parameter) and

$$\alpha\chi_0 = ZZ_p e^2/mv^2 a' \qquad (2)$$

in which $Z_p e$ is the charge of the fast particle, m its mass and v its velocity, Ze is the nuclear charge of the scatterer, a' is the Thomas-Fermi radius, a measure of the radial distance at which the electronic screening becomes effective, and $\hbar$ is $1/2\pi$ times Planck's constant h. The angle χ_0 is $\lambda/2\pi\ a'$, in which λ is the de Broglie wavelength h/mv. We are interested here only in non-relativistic particles. The Thomas-Fermi radius a' is defined as

$$a' = 0.885\ a_0\ Z^{-1/3} \qquad (3$$

with a_0 as the Bohr radius.

Toward the end of an alpha track there are many

intervals during which one or two electrons are carried along by the particle. An appropriate allowance for this additional screening is made by using Bohr's relation[14] for $Z^{-1/3}$; Eq. 3 is replaced by

$$a' = 0.885\, a_0\, (Z^{3/2} + Z_i^{3/2})^{-1/2}, \qquad (3a)$$

where Z_i is the number of electrons attached to the fast particle. (The parameters used by Bohr were actually 2α and $2\alpha\chi_0$; the choice here conforms better with the papers of Scott[7], Molière,[8-10] and Williams.[11])

For the special case of a pure Coulomb field, the classical orbit theory is valid for deflections to all angles, provided $\alpha > 1$ and $\chi_0 = \lambda/2\pi a' \ll 1$ (see Figure 34); on the other hand, the Born approximation is valid for $\alpha < 1$, independent of λ. For the Coulomb field, both theories give the same result for $\alpha = 1$.

Williams gave separate treatments of screening for $\alpha \gg 1$ and $\alpha \ll 1$. For $\alpha \gg 1$, which is of interest here, he assumed that the particles move in classical orbits in a Thomas-Fermi field (discussed in Ref. 15). When the impact parameter is small, screening has very little effect upon the deflection because most of the momentum transfer occurs in the almost-Coulomb inner field. Williams assumed that, for the purpose of calculating the momentum transfer associated with any impact parameter, the particle could be considered to move uniformly in a straight line.

The computations are summarized by the solid curve in Figure 35, which shows $q(\chi)$ the ratio of the scattering cross section of an atom to that of a bare nucleus (as a function of χ the single scattering deflection). Williams' final step was to replace the gradual change of $q(\chi)$ shown in Figure 35 by a unit step at the angle χ_{min} defined so that the root-mean-square angle of single deflection would be correct; the defining equation may be written

$$\langle\chi^2\rangle = 2\pi \int_0^{\chi_m} \chi^2\, q(\chi) Q_R(\chi) \chi d\chi = 2\pi \int_{\chi_{min}}^{\chi_m} \chi^2 Q_R(\chi) \chi d\chi \qquad (4)$$

in which the Rutherford differential cross section $Q_R(\chi)$ is given in the small angle approximation by

$$Q_R(\chi) = (2ZZ_p e^2/mv^2)^2/\chi^4, \qquad (5)$$

and the upper limit χ_m is chosen large enough so that $q(\chi_m)$ is essentially unity. Williams' result is

$$\chi_{min} = 3.8(0.885)\alpha\chi_0\,. \qquad (6)$$

(According to the conventions followed here, Williams' θ becomes χ, θ' becomes $0.885\ \alpha\chi_0$, and θ_m becomes χ_{min}.)

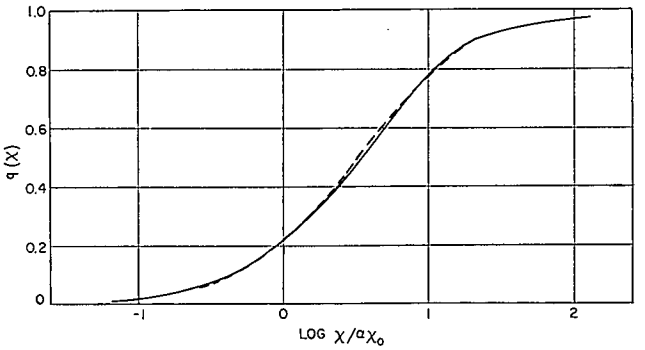

FIG. 35. Ratio, $q(\chi)$, of the actual cross section to the Rutherford cross section as a function of angle of deflection χ, for $\alpha \gg 1$. Solid curve from Williams[12] dotted curve from Molière.[8].

The Molière treatment of multiple scattering to be applied below actually uses only the angle χ_{min} ; however, it is necessary also to have information about the approach of $q(\chi)$ to unity, in order to establish that the Molière method is valid for the case that is being considered. Bohr pointed out that orbital pictures would be expected to fail for an impact parameter $\gg a'$, that is for $\chi/\alpha\chi_0 \ll 2$, but that this is exactly the region in which $q(\chi)$ falls to zero (Ref. 12, p. 20).

Molière's wave mechanical treatment of screening for $\alpha \gg 1$ and $\alpha\chi_0 \ll 1$ gave results that agree so closely with those of Williams that the difference might possibly be the result of rounding off in the computations.[8] The dotted curve for $q(\chi)$ in Figure 35 was obtained by reconstructing Molière's curve for $\alpha = 9.6$ from the tabulated constants (Ref. 8, p. 143). Molière's treatment of single scattering has been criticized by Nigam, Sundaresan, and Wu,[16] and the criticisms have been reconsidered by Scott (Ref. 7, p. 262). The objections relate primarily to the Molière derivations for $\alpha \ll 1$ and to the empirical relation for screening angle vs. α for all α (Ref. 8, Eq. 9.3; Ref. 11, Eq. 21). There are two criticisms that may also be valid for $\alpha \gg 1$: in the expansion of wavenumber in powers of $\alpha\chi_0$, the effect of the $(\alpha\chi_0)^2$ term was not investigated (Ref. 8, Eq. 1.2′) and, in considering the wave propagation beyond the scatterer, the phase shifts were found by only the first Born approximation (Ref. 8, p. 142; Ref. 7, pp. 258, 261).

Molière defined a screening angle χ_a, chosen so that when

$$q(\chi) = \chi^4/(\chi^2 + \chi_a^2)^{-2} \qquad (7)$$

is inserted into (4), one obtains the same integral as with the exact $q(\chi)$. (This "a" refers to "Abschirmung," i.e., screening; it has no direct relation to a'.)

Relation (7) gives the exact $q(\chi)$ for the special case in which the potential function

$$V(r) = (ZZ_p e^2/r) \exp(-r/r_0) \quad (8)$$

is used in conjunction with the Born approximation (r_0 is a constant).

The relation between χ_a and χ_{min} is

$$\chi_a = \chi_{min} \exp(-1/2), \quad (9)$$

and for $\alpha \gg 1$ (actually, for $\alpha = 9.6$), Molière obtained

$$\chi_a = (3.77)^{1/2} \alpha \chi_0, \quad (10)$$

so the Molière χ_{min} is 0.95 times the Williams value. This affects the average angle of multiple scattering of 6-MeV alpha particles in argon by about 1/2%.

Moliere's Method of Deriving Distribution Functions

To obtain a formal equation for the distribution function of track angles θ after successive scatterings, Molière[9] superimposed individual deflections in the manner of Wentzel.[4] Bethe showed that Molière's basic equation could be derived from the Boltzmann transport equation (Ref. 11 p. 1257). Molière devised an ingenious method of transforming the formal solution into one that is much easier to evaluate (Ref. 11, p. 1258), and Snyder and Scott[6] introduced a method for finding the distribution of various track characteristics other than the track angles; the chord angle is one such characteristic. They considered projections upon a plane parallel to OZ (Figure 36); since the deflections are assumed to have axial symmetry, there is a unique relation between the distribution function for spatial chord angles and that for projected chord angles Ψ_y. The y projection χ_{yi} of a single deflection at z_i will produce a contribution $y_i = (z_0 - z_i)\chi_{yi}$ to the final projected displacement y at z_0 : also, it will produce a contribution

$$\Psi_{yi} = (z_0 - z_i)\chi_{yi}/z_0$$

to the final projected chord angle.

Scott (Ref. 7, p. 272) gives a table of constants to be used in the determination of chord angles and various other track characteristics, but these are valid only if the particle energy is constant; otherwise it is necessary to utilize Molière's more general method. The Molière equations (Ref. 10, Eq. 3.9) are in fact more general than needed here because they were designed to establish a link between the new result and Fermi's Gaussian function for the joint distribution of track angles and chord angles.[5] To determine chord angles only, each deflection χ is just weighted by the coupling constant $a_2 = (z_0 - z)/z_0$.

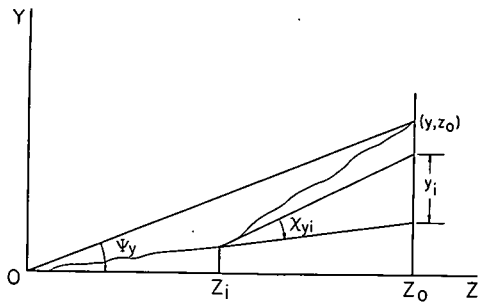

FIG. 36. Sketch showing the y projection of an alpha track that has a final spatial chord angle Ψ, of which the y projection is Ψ_y. At $z = z_i$, a deflection χ_i with y projection χ_{yi} produces a contribution y_i to the final y displacement.

The essential simplicity of Molière's distribution function is the result of the special procedure that he devised for determining this function from its Fourier transform after the transform had been found by the Wentzel method of considering individual collisions. Except for the absolute scale of the angles, Molière's distribution function depends only upon a single parameter denoted by B; furthermore, it depends upon B in a quite simple manner. (This B has no direct relation to the stopping number usually designated by B.)

In the Molière treatment all the essential information about the passage of the particle through the medium is collected into two numbers; for the present chord angle problem, the numbers are the characteristic chord angle Ψ_c and the mean chord angle of screening Ψ_a. The physical interpretation of Ψ_c is that throughout the entire path length l_0 there is on the average exactly one collision for which the square root of the sum of the squares of Ψ_{yi} and the corresponding x component

$$\Psi_{xi} = (z_0 - z_i)\chi_{xi}/z_0$$

is greater than Ψ_c. The angles Ψ_c and Ψ_a are found from the equations (Ref. 10, 3.9 with $s = 1$, $c = 0$)

$$\Psi_c^2 = \int_0^{l_0} dl\, a_2^2 \chi_c'^2(l) \quad (11)$$

$$\ln \Psi_a^2 = \Psi_c^{-2} \int_0^{l_0} dl\, a_2^2 \chi_c'^2(l) \ln[a_2^2 \chi_a^2(l)] \quad (12)$$

in which χ_a is the screening angle defined above [Eq. (7)], and

$$\chi_c'^2(l) = 4\pi N (ZZ_p e^2/mv^2)^2, \quad (13)$$

where N is the number of scatterers per cm^3. The quantities $\chi_c'^2$ and χ_a^2 depend upon l through mv^2, and χ_a^2 also depends upon l through a', according to Eqs. 9, 6, 2, and 3a. The integrals in (11) and (12) do not vary with the pressure of the gas, provided the initial and final energies are kept constant, because at any given energy not only $\chi_c'^2$ but also the stopping power is direct proportional to N. Strictly, dl is an increment of ar because N is the number of scatterers per cm^2 per cm of travel, but in the small-angle approximation no distinction is made between l and z.

Bethe established a criterion for determining whether the Molière method will give a valid result for a particular scattering problem (Ref. 11, p. 1258). Bethe's principle, rather than his exact statement, must be applied to the present problem because chord angles rather than path angles are considered here and because the screening angle varies along the path of the particle, and therefore the ratio q (Figure 35) depends upon l as well as upon χ. In approximate terms, Bethe's criterion requires that Ψ_c must be large relative to the maximum value of $a_2\chi_a$ along the path. In more specific terms, the Molière method is valid if it is possible to select a constant angle $\Psi_k \ll \Psi_c$ such that, for all points along the track, $q(\chi,l)$ is essentially unity for

$$\chi \geq \chi_k(l) = \Psi_k/a_2(l). \tag{14}$$

The Molière distribution function for chord angles Ψ in space at $z = z_0$ is given in terms of the new variable

$$\psi = \Psi/\Psi_c B^{1/2} \tag{15}$$

by the relation

$$F(\psi) = (2\pi)^{-1}[2 \exp(-\psi^2) + B^{-1}F^{(1)}(\psi) + B^{-2}F^{(2)}(\psi) + \cdots] \tag{16}$$

in which $F^{(1)}$ and $F^{(2)}$ are tabulated functions (Scott, Ref. 7, pp. 284–5, 297) and B appears only in the coefficients of the second and third terms. The numerical factor $(2\pi)^{-1}$ is shown so that $F(\psi)$ is normalized in accordance with the equation

$$2\pi \int_0^\infty F(\psi)\psi d\psi = 1. \tag{17}$$

The function $F(\psi)$ takes the above form only because, in the determination of F from its Fourier transform, Molière chose to make B equal to the larger root of the transcendental equation

$$B - \ln B = \ln(\Omega_0\gamma^2) - 1, \tag{18}$$

in which

$$\Omega_0 = \Psi_c^2/\Psi_a^2 \tag{19}$$

and $\ln\gamma$ is Euler's constant 0.5772 $\cdots$. (Euler's constant is here denoted by $\ln\gamma$[17] rather than γ,[18] to preserve the notation of Molière.) In general, B is of order 10 and the term in B^{-2} is very much less than the sum of the other two terms. Scott and associates[19] have derived empirical formulas for finding various characteristics of the distribution functions directly from Ψ_c, Ω_0 and B. In general, the first term of (16) is not a very good Gaussian approximation to the whole function.

Some other methods for finding distribution functions are summarized by Scott; (Ref. 7, pp. 267–269, 277–286); equations of the type (11) are used quite generally, but the method of averaging the screening angle given by (12) is specialized for the Molière treatment (Scott, Ref. 7, Eq. 7.7).

The alpha particles lose a negligible fraction of their energy in the elastic nuclear collisions considered above; essentially all of it is lost through inelastic collisions with bound electrons.[20] On the other hand, the inelastic electronic collisions do not contribute very much to the spreading of an alpha particle beam. It is estimated, on the basis of a study by Fano,[21] that the average chord angles calculated in the next section should be increased by about 1 or 2% to correct for this effect.

APPLICATION OF THE SMALL-ANGLE THEORY

The examples given here were calculated for argon as scatterer. The results are summarized in Table 27, and also in Figures 37 and 38 which will be discussed below. All angles are given in radians, accordingly the probability, per radian squared, that a single alpha particle track will have a final chord angle Ψ is

TABLE 27. CONSTANTS OF FOUR CALCULATIONS OF FINAL CHORD ANGLE FOR ALPHA PARTICLES IN ARGON AT 15°C

	Case			
	1	2	3	4
Initial energy, MeV	6.00	6.00	6.00	1.50
Final energy, MeV	3.83	0.05	0.05	0.05
Pathlength × pressure, cm-atm	2.45	4.80	4.80	0.70
Screening angle	[a]	[a]	[b]	[a]
Ψ_c, Radians	7.8×10^{-3}	1.33×10^{-2}	1.33×10^{-2}	2.6×10^{-2}
Ψ_a, Radians	4.6×10^{-4}	4.2×10^{-4}	1.04×10^{-4}	2.1×10^{-3}
$\Psi_c/(a_2\chi_a)_{max}$	16	27	107	11
B	7.5	9.0	12.0	6.8
$3^{1/2}$, Radians	2.1×10^{-2}	4.0×10^{-2}	4.6×10^{-2}	6.8×10^{-2}
$\langle\Psi\rangle$, Average in space, radians	2.1×10^{-2}	3.9×10^{-2}	4.4×10^{-2}	6.8×10^{-2}

[a] Screening angle according to Williams.
[b] Screening angle 0.25 of Williams' value.

$[\Psi_c^2 B]^{-1} F(\psi)$ in which ψ is written for $\Psi/\Psi_c B^{1/2}$, as above. Cases 1 and 2 in Table 27 represent two points along the path of a 6-MeV particle at 50% and 98% of the mean range of 4.90 cm. The ratio of path lengths is 1 to 1.96, of mean chord angles 1 to 1.83, and of the probability of exceeding 0.1 radian, 1 to 4.3. The relatively small effect of a change in screening angle from 100% to 25% of the Williams value is shown by Cases 2 and 3. If the initial energy is only 1.5 MeV, as in Case 4, the average Rutherford cross section is greater than in Cases 1 to 3, the average screening angle is also greater, and the path is much shorter. The net result is that the distribution function is broader.

A range-energy relation was needed; a composite was used, based upon (1) Whaling's formula and his table for mean range for energies of 6 to 2.5 MeV[22]; (2) Bertolini and Bettoni's experimental values for 2.0 to 0.25 MeV[23]; and (3) Cook, Jones and Jorgensen's range-energy measurements and Weyl's stopping power data for <0.25 MeV.[24, 25] Both a_2 and v decrease with increasing coordinate z, so the product $a_2^2 \chi_c'^2$ in (11) varies much less rapidly than either a_2^2 or $\chi_2'^2$.

To correct the screening angle for the gain and loss of electrons that an alpha particle experiences after its energy is reduced below 1.5 MeV, $\ln \chi_a^2$ in (12) was evaluated by using

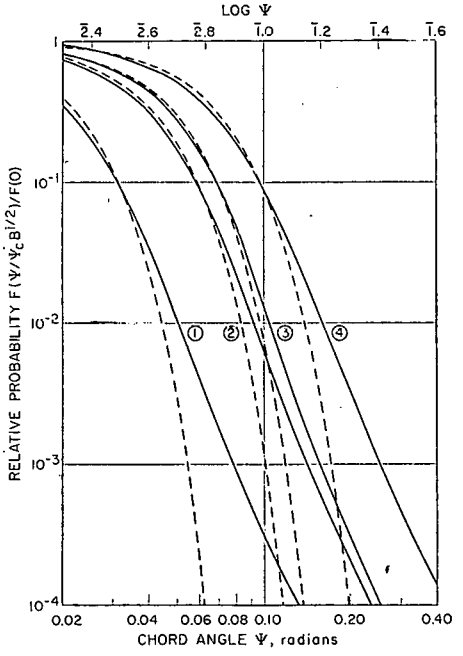

FIG. 37. Calculated chord angle distribution functions compared with normalized Gaussian functions having the same central maximum. Solid curves: relative probability $F(\Psi/\Psi_c B^{1/2})/F(0)$ as a function of chord angle Ψ. Dotted curves: each $F(\Psi/\Psi_c B^{1/2})/F(0)$ is replaced by exp $\{-[\pi F(0)/B\Psi_c^2]\Psi^2\}$. Conditions are given in Table 27.

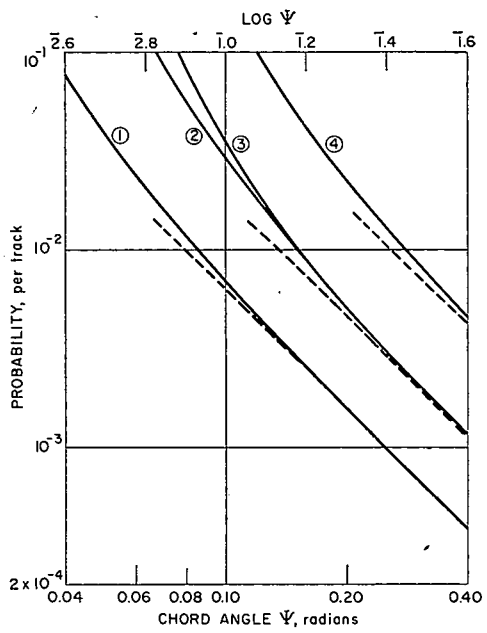

FIG. 38. Probability, per track, of a final chord angle greater than Ψ radians. Conditions are given in Table 27.

$$\ln \chi_a^2 = \sum_{i=0}^{2} F_{i\infty} \ln \chi_{ai}^2 \qquad (20)$$

in which i is the state of charge of the alpha particle, e.g., $i = 2$ for He^{++}; χ_{ai} is the screening angle, based upon (3a) with $Z_i = 2 - i$, and $F_{i\infty}$ is the fraction of the alpha particles in the i state when a beam is in equilibrium with argon. The $F_{i\infty}$ data came from Pivovar, Tubaev, and Novikov[26] for 1.5 to 0.2 MeV and from Barnett and Stier[27] for <0.2 MeV.

The characteristic tail of the distribution function $F(\psi)$ is shown in Figure 37 for the four cases of Table 27. The relative probabilities $F(\psi)/F(0)$ were plotted, and, for comparison, "Gaussian" probabilities

$$F_G(\psi)/F(0) = \exp\{-[\pi F(0)]\psi^2\} \qquad (21)$$

were added as dotted curves. The two disposable parameters of the Gaussian function were chosen so that $F_G(\psi)$ would have the same central maximum as $F(\psi)$ and would be normalized, as in (17). As Ψ approaches zero, all eight curves approach unity. At large Ψ, the solid curves approach the asymptotes (not shown),

$$F(\psi)/F(0) \sim [B/\pi F(0)](\Psi_c/\Psi)^4 \qquad (22)$$

(from the asymptotic expansion for $F^{(1)}(\psi)$; see the Appendix.)

The probabilities, per track, that the final chord angles are greater than ψ radians are shown in Figure 38. These probabilities approach unity as ψ approach zero and they approach the asymptotes,

$$[B\Psi_c^2]^{-1} \int_{\Psi}^{\infty} F(\psi)\, 2\pi\Psi d\Psi \sim (\Psi_c/\Psi)^2 \qquad (23)$$

for $\Psi \gg \Psi_c$. Cases 2 and 3 have the same asymptote because they have the same Ψ_c.

It is very probable that a particle that attains a large chord angle $\Psi \gg \Psi_c$ does so because of a single large deflection. The number of single chord angle contributions between Ψ' and $\Psi' + d\Psi'$ that are produced as the particle moves from $z = 0$ to z_0 is

$$\int_0^{z_0} N\, dz[\{(2ZZ_p e^2/mv^2)^2/\chi^4\}2\pi\chi d\chi]_{\chi'}$$

in which $\chi' = \Psi'/a_2$, the square bracket is the cross section at coordinate z for single scattering into the zone between Ψ' and $\Psi' + d\Psi'$, and the only restriction upon Ψ' is that it must be at least as great as the maximum value of $a_2\chi_{\min}$. The above integral is to be evaluated with Ψ' held constant, while a_2 and v vary with z. It may be rewritten as

$$(2d\Psi'/\Psi'^3)\int_0^{z_0} dz\, a_2^2\chi_c'^2 = (2d\Psi'/\Psi'^3)\,\Psi_c^2. \quad (24)$$

The average number of single contributions $\geq \Psi$ per track is

$$\psi_c^2\int_\Psi^\infty (2d\Psi'/\Psi'^3) = (\Psi_c/\Psi)^2. \quad (25)$$

Therefore, chord angle contributions $\Psi_1 > 30\Psi_c$ will occur in only one track in about 10^3, and two such contributions in only one track in about 10^6. If the contributions to the chord angle of a particular track consist of many random small ones and only one large one, Ψ_1, the most probable final chord angle will be Ψ_1, and the distribution of probable chord angles will be almost the same as if the particle had started out along the Ψ_1 direction and the single large deflection had been suppressed. Thus it is reasonable that if $\Psi_1 > 30\Psi_c$ the probability of a final chord angle $> \Psi_1$ is only slightly greater than the probability of a single contribution $> \Psi_1$ (see Figure 38). As a specific numerical example, let us consider Case 4 (Table 27 and Figure 38) at an argon pressure of 5 torr; at this pressure it is expected that only approximately 0.4 of all possible Ar_2^+ ions will be formed. Alpha particles having an initial energy of 1.50 MeV will travel on the average 106 cm as their energy is reduced to 0.05 MeV. As they travel this distance, 1% of them will attain a chord angle greater than 0.28 radians according to the small angle theory (Figure 38) that is to say, an ideally collimated beam of infinitesimal initial area will spread so that 1% of the particles will not pass through a plane circular diaphragm of 60 cm diameter perpendicular to, and centered upon, a line drawn and extended along the original flight path.

A change of gas (at the same pressure and temperature) changes the atomic number Z and the value of the coordinate z_0 that corresponds to a given energy loss. The characteristic angle Ψ_c is approximately proportional to Z^2 times the range of the alpha particle (Eqs. 11 and 13); accordingly the ratio Ψ_c^2 (neon)/Ψ_c^2 (argon), and consequently the ratio of the two inte

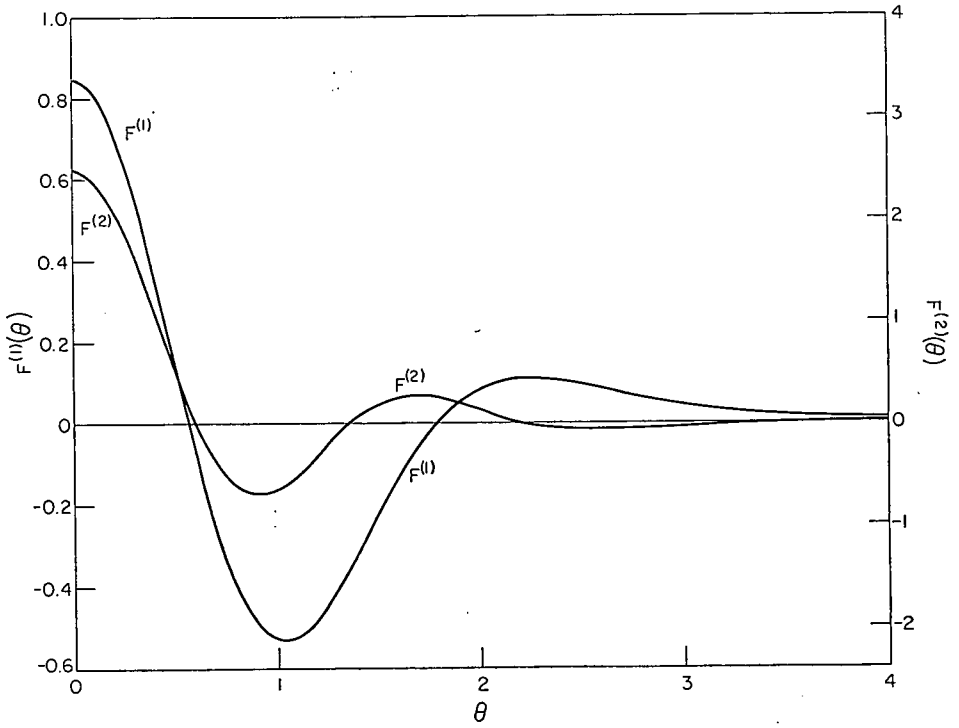

FIG. 39. The functions $2D_1(2,1,-\theta^2) = F^{(1)}(\theta)$ and $D_2(3,1,-\theta^2) = F^{(2)}(\theta)$ vs. θ

grated tail probabilities $(\Psi_c/\Psi)^2$, with Ψ constant, is approximately 50% (Eq. 23).

APPENDIX: THE FUNCTIONS $F^{(1)}$ and $F^{(2)}$

The functions

$$D_1(2,1,\ -\theta^2)\ =\ (1/2)F^{(1)}\ (\theta) \tag{26}$$

and

$$D_2(3,1,\ -\theta^2)\ =\ F^{(2)}\ (\theta) \tag{27}$$

oscillate for $\theta < 4$, as shown in Figure 39. To find the probability of exceeding θ, the integrals

$$\int_\theta^\infty D_n(n+1,1,\ -\theta^2)\theta d\theta = \frac{-\theta^2}{2} D_n(n+1,2,\ -\theta^2) \tag{28}$$

are needed, with $n = 1$ and 2. Scott has tabulated the functions in (26) and (27) for $\theta = 0$ to 13.0 (Ref. 7, p. 284). Presumably he has also computed $D_1(2,2,\ -\theta^2)$ and $D_2(3,2,\ -\theta^2)$ and deposited the tables with the American Documentation Institute, but we have not been able to obtain copies as yet.

For large values of θ, asymptotic formulas may be used (Scott, Ref. 7, p. 311):

$$D_1(2,1,-\theta^2) \sim \theta^4 \sum_{k=0}^{n} (k+1)!(k+1)\theta^{-2k} + R_{n+1} \tag{29}$$

$$D_1(2,2,-\theta^2) \sim -\theta^{-4} \sum_{k=0}^{n} (k+1)!\theta^{-2k} + R_{n+1} \tag{30}$$

$$D_2(3,1,-\theta^2) \sim -4\theta^{-6} \sum_{k=0}^{n} (k+2)!(k+1)(k+2) \times [\psi(R+2) - \ln\theta] + R_{n+1}\,. \tag{31}$$

$$D_2(3,2,-\theta^2) \sim 2\theta^{-6} \sum_{k=0}^{n} (k+2)!(k+1) \times [\psi(k+2+\psi(k+1) - 2\ln\theta] + R_{n+1} \tag{32}$$

The remainders R_{n+1} are approximately as large as the term with $k = n + 1$, for the range in which Eq. 29–32 are useful, and $\psi(k)$ is given by

$$\psi(k) = -0.5772\cdots + 1 + 1/2 + 1/3 + \cdots + 1/k$$

in which 0.5772 ··· is Euler's constant.

REFERENCES

1. H. A. Schultz. Argonne National Laboratory Radiological Physics Division Annual Report, July 1965 through June 1966. ANL-7220, pp. 20–21.
2. E. Breitenberger. *Proc. Roy. Soc.* (*London*) **A250**, 514–23 (1959).
3. W. Bothe. *Z. Physik* **4**, 161–177, 300–314; **5**, 65-69 (1921).
4. G. Wentzel. *Ann. Physik* **69**, 335–368 (1922).
5. B. Rossi and K. Greisen. *Rev. Mod. Phys.* **13**, 262–8 (1941).
6. W. T. Scott. *Phys. Rev.* **76**, 212–219 (1949); H. S. Snyder and W. T. Scott. *Phys. Rev.* **76**, 220–225 (1949).
7. W. T. Scott. *Rev. Mod. Phys.* **35**, 231–313 (1963).
8. G. Molière. *Z. Naturforsch.* **2A**, 133–145 (1947).
9. G. Molière. *Z. Naturforsch* **3A**, 78–79 (1948).
10. G. Molière. *Z. Naturforsch.* **10A**, 177–211 (1955).
11. H. A. Bethe. *Phys. Rev.* **89**, 1256–1268 (1953).
12. E. J. Williams. *Phys. Rev.* **58**, 29–306 (1940).
13. N. Bohr. The Penetration of Atomic Particles Through Matter, *Det Kgl. Danske Vidensabernes Selskab. Mathematisk-fysiske Middelelser* (*Copenhagen*), **18**(8), 5–35 (1948).
14. N. Bohr. *Phys. Rev.* **59**, 270–275 (1941).
15. N. F. Mott and H. S. W. Massey. *The Theory of Atomic Collisions*. Oxford University Press, London, 1952, pp. 188–191.
16. B. P. Nigam, M. K. Sundaresan, and T.-Y. Wu. *Phys. Rev.* **115**, 491-502 (1959).
17. E. Jahnke and F. Emde. *Table of Functions*, Dover Publications, Ann Arbor, Michigan, Fourth Ed., 1945, p. 2.
18. E. T. Whittaker and G. N. Watson, *A Course in Modern Analysis*. Cambridge University Press, Cambridge, Fourth Ed., 1952, pp. 235, 246.
19. W. T. Scott. *Phys. Rev.* **85**, 245–248 (1952); J. S. Goldberg, H. S. Snyder and W. T. Scott. *Phys. Rev.* **100**, 1013–1014 (1955).
20. H. A. Bethe and J. Ashkin. *Experimental Nuclear Physics*, Ed. E. Segre. John Wiley and Sons, New York, 1953, Vol. I, pp. 166–231.
21. U. Fano. *Phys. Rev.* **93**, 117–120 (1954).
22. W. Whaling. *Handbuch der Physik*, Ed. S. Flügge. Springer-Verlag, Berlin. 1958, Vol. **34**, pp. 193–216.
23. G. Bertolini and M. Bettoni. *Nuovo Cimento* **1**, 644–650 (1955).
24. C. J. Cook, E. Jones, and T. Jorgensen, Jr., *Phys. Rev.* **91**, 1417–1422 (1953).
25. P. K. Weyl. *Phys. Rev.* **91**, 289–296 (1953).
26. L. J. Pivovar, V. M. Tubaev, and M. T. Novikov. *Soviet Phys. JETP*, **14**, 20–23 (1962) [translated from *J. Exptl. Theoret. Phys.* (*USSR*) **41**, 26–31 (1961)].
27. C. J. Barnett and P. M. Stier. *Phys. Rev.* **109**, 385–390 (1958).

SYNTHESIS AND PROPERTIES OF 2-ARYLINDOLES*

Hermann O. Wirth† *and Emily B. White*

INTRODUCTION

These investigations were undertaken to study the self-quenching structure correlation in organic scintillator solutes.‡ No systematic work had been performed previously on this topic.

In Figure 40, typical self-quenching curves are shown for two scintillator solutes,[1] one of them being the very popular PPO (2,5-diphenyloxazole). There is a very significant decrease in the light yield with increasing concentration, especially with the indole derivative. In case of no self-quenching, the relative pulse height (RPH) vs. concentration curves would have reached a certain level which is independent of the concentration. The decrease in the light yield is actually caused by interactions between excited and unexcited molecules. The real goal of this whole project was to study the inherent steric conditions required for this interaction.

The 2-phenylindole was considered to be an ideal model substance for this study for two very clear and obvious reasons: 1) It shows very strong self-quenching and 2) it is easily amenable to structure variations. These structure variations are the primary subject of this paper.

SYNTHESIS OF 2-ARYLINDOLE DERIVATIVES

Program of Synthesis

Table 28 lists the compounds with which we dealt in this study. Some of them were previously known (I,§ II,[4] V,[5] VII,[6] VIII,[7] XI,* XIII,* XV,[8] XIX,[9] XX,[10] XXVI,[11]) but we have obtained a few of those by different methods of synthesis; of others we can report the high-grade purification procedure.

Our main interest in this 2-arylindole series was directed toward the N-alkyl and to a certain extent also toward the N-aryl derivatives. Some of these compounds we were able to obtain directly by Fischer indole syntheses using the corresponding hydrazines as starting material. The preparation of others has been possible through N-substitution reactions of the protonated basic compounds (R: hydrogen).

There were three important reasons for placing our main interest in the N-derivatives, especially those with alkyl groups: First of all, we considered the variation of both the size and structure of these alkyl groups a fine possibility for studying the steric requirements in the self-quenching process, in full accordance with the real goal of this work. Second, we saw in the substitution of these groups a provision for achieving the necessary solubility in order to study this quenching phenomenon at very high solute concentrations, since these groups exhibit a significant solubilizing effect. Last, but not least, the replacement of the nitrogen proton with the mentioned groups enabled us to enhance considerably the chemical, and especially the photochemical, stability of these compounds.

Problems of Synthesis

Mainly two types of Fischer indole synthesis were applied. Figure 41 shows a representative example in which use is made of a procedure first applied by Rogers and Corson.[12] In this case no isolation of the corresponding hydrazone is required. In addition, the reaction conditions are simple and mild. We obtained good results, yields in the range of 80% with cyclic ketones like benzosuberon (Figure 41). This method is not applicable, however, to ketones of the acetophenone type.

The second Fischer type indole synthesis which was used is based on the application of polyphos-

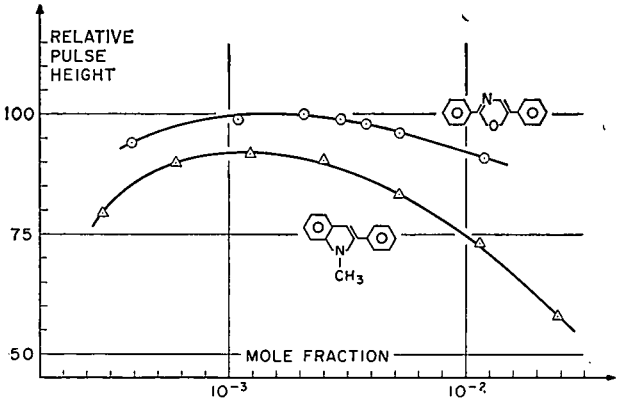

FIG. 40. Relative scintillation efficiency (Cs^{137} electron excitation) vs concentration (mole fraction) curves of two scintillator solutes in toluene as solvent.

* Presented at the First International Congress of Heterocyclic Chemistry, June 12–15, 1967, University of New Mexico, Albuquerque, New Mexico.

† Visiting scientist, formerly of the University of Mainz, ermany.

‡ A mutual project with Dr. D. L. Horrocks, Chemistry Division.[1, 2, 3]

§ Technical grade, purchased from Aldrich Chemical Co., Inc., Milwaukee, Wisconsin.

TABLE 28. LIST OF INVESTIGATED 2-ARYLINDOLES

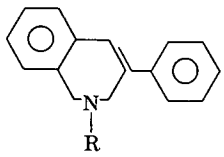	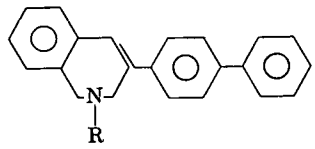	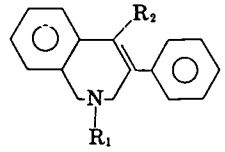
R: Hydrogen (I) : Methyl (II) : Neopentyl (III) : n-Hexyl (IV) : Phenyl (V) : 3-[N-(2-phenyl) indolyl]-propyl (VI)	R: Hydrogen (VII) : Methyl (VIII) : n-Butyl (IX) : 3-Methoxy-butyl (X)	R_1 : Hydrogen, R_2 : Methyl (XI) R_1 : Methyl, R_2 : Methyl (XII) R_1 : Hydrogen, R_2 : Phenyl (XIII) R_1 : Methyl, R_2 : Phenyl (XIV)
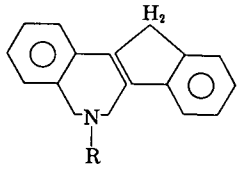	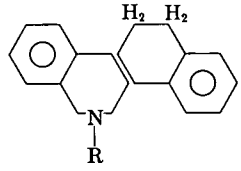	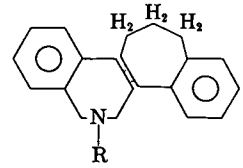
R: Hydrogen (XV) : Methyl (XVI) : Neopentyl (XVII) : Phenyl (XVIII)	R: Hydrogen (XIX) : Methyl (XX) : Ethyl (XXI) : n-Propyl (XXII) : n-Butyl (XXIII) : 3-Methyl-butyl (XXIV) : Phenyl (XXV)	R : Hydrogen (XXVI) : Methyl (XXVII) : Phenyl (XXVIII)

phoric acid as catalyst according to Witkop and coworkers[6] (Figure 42). The reaction conditions are explained with the synthesis of a biphenylyl indole derivative. Also in this case no isolation of the hydrazone is necessary. This method covers ketones of the acetophenone type as well, but in general the yields are lower and noticeable amounts of tarry side products are formed, which, in addition, render more difficult the isolation and purification of the indole derivatives.

A special problem in our program of synthesis was the N-alkylation of the 2-arylindoles by larger

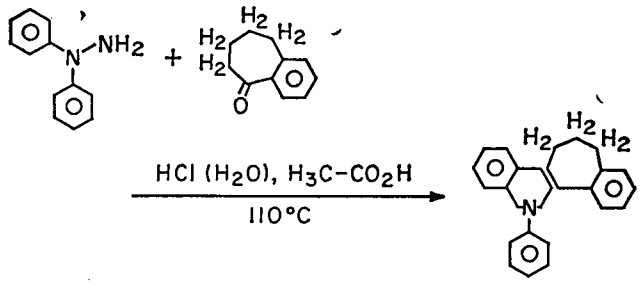

FIG. 41. Fischer type indole synthesis[12]

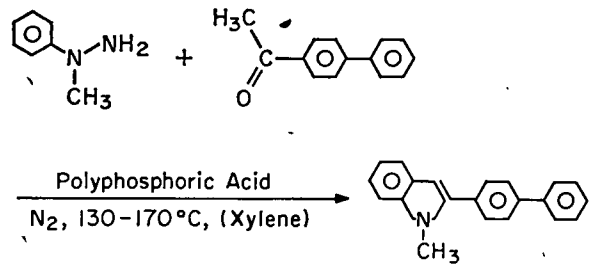

FIG. 42. Fischer type indole synthesis[6]

alkyl groups. (The N-methyl and also the N-phenyl derivatives were accessible by direct synthesis, using the corresponding, commercially available hydrazines.)

Nothing was reported in the literature on N-alkylations of 2-arylindoles until the appearance of a paper by Buchmann and Trautmann;[13] they succeeded in preparing N-alkyl derivatives of 2-phenylindole by a method with sodium in liquid ammonia. Th method, however, did not satisfy us.

In the course of our solubilization studies during the last few years we found a very favorable alkyla-

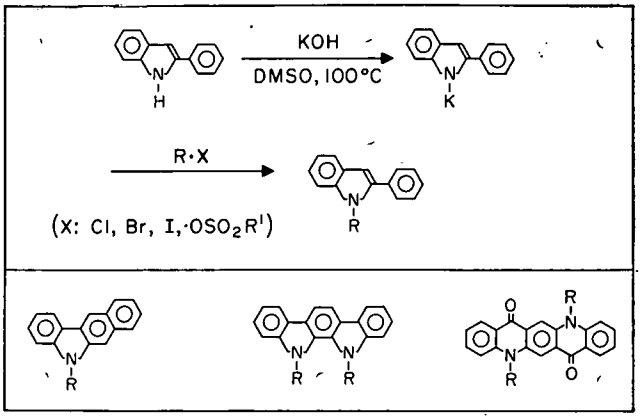

FIG. 43. N-Alkylations of heterocyclic compounds in dimethyl sulfoxide as solvent.

tion method based on dimethyl sulfoxide as solvent.* [14] It was especially developed for the alkylation of poorly soluble compounds like indanthrene and azo dyes or compounds shown in the lower part of Figure 43. This method also proved to be applicable to our 2-arylindoles. In Figure 43 it is explained in more detail. The reaction actually occurs in two steps. At 100°C a potassium salt is formed, and this conversion is accompanied by a characteristic color change (halochromy effect). This potassium salt reacts in the second step with the alkylating agent to yield, in most cases, quantitatively the N-alkyl derivative. The temperature required for this second step depends on the alkylating agent. Iodoalkyls react at 20°C; the same is true for sulfonic acid esters. Bromo- and also chlorine compounds need some heating (50 or 80°C, respectively). This alkylation method is limited, of course, to primary alkyls. Alkyls of the neopentyl type, although primary, are less reactive and need heating to higher temperatures (~100°C). According to our present knowledge this method seems to have a very broad applicability and we are considering this as our most important contribution to the field of heterocyclic chemistry. It should be mentioned also that the etherification of phenols can be carried out in the same manner.[14]

Purification Methods

For luminescence studies a very high purity of the compounds is of paramount importance. We found column chromatography over aluminum oxides a very useful purification method. Alumina saturated with dry hydrogen chloride gas as previously reported[16] proved also most efficient.

* The application of this solvent was first applied by Kuhn and coworkers;[15] their reaction conditions, however, were quite different.

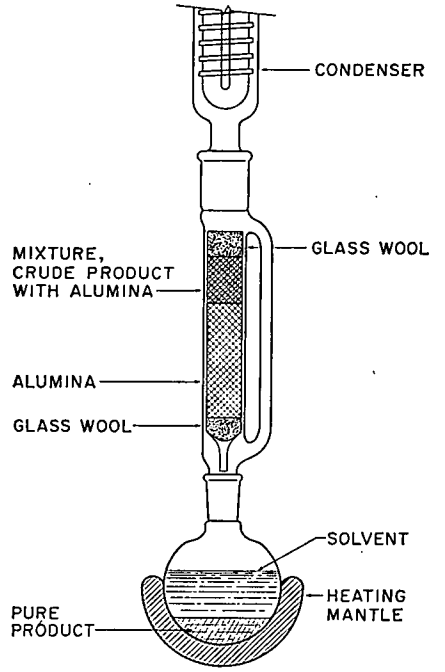

FIG. 44. Chromatographic column extractor

TABLE 29. SOLUBILITIES AND MELTING POINTS OF DIALKYL-p-QUINQUIPHENYLS

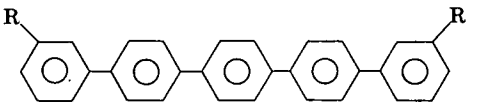

R	Solubility (Toluene, 20°C) g/l	Melting point °C
H	<0.003	395
Methyl	0.10	313
Ethyl	0.18	291
n-Butyl	0.48	268
n-Hexyl	0.52	259
n-Octyl	0.55	253
3-Amyl	8.6	236
5-Nonyl	34	177
7-Tridecyl	227	127
9-Heptadecyl	>500	80

For the purification of compounds with low solubility we applied a chromatographic column extractor as sketched in Figure 44.* [17] This extractor is a simplified type of the adsorption purification apparatus developed by Sangster and Irvine.[18] It turned out in the meantime that this column extractor is something like a multipurpose instrument, useful for

* We would like to thank Mr. J. Ostapowicz, Jr., for his skillful and generous assistance in constructing this apparatus.

TABLE 30. SOLUBILITY (TOLUENE, 20°C) AND MELTING POINTS OF ALKYL DERIVATIVES OF 2-ARYLINDOLES

General structural formula	R	Solubility, g/l	Melting point, °C
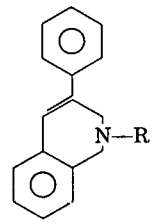	H	18	188
	$-CH_3$	>200	102
	$-CH_2-(CH_2)_4-CH_3$	Infinitely soluble	(Oil)
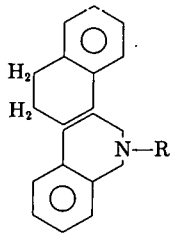	H	28	165
	$-CH_2-CH_3$	105	125
	$-CH_2-CH_2-CH(CH_3)-CH_3$	Infinitely soluble[a]	53
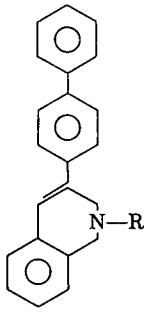	H	<0.1	300
	$-CH_2-(CH_2)_2-CH_3$	150	110
	$-CH_2-CH_2-CH(OCH_3)-CH_3$	Infinitely soluble[a]	85

[a] Because of forming supercooled melts.

any extraction and crystallization and purification problem.

PROPERTIES OF 2-ARYLINDOLE DERIVATIVES

Solubility Behavior

Since a high solubility was required for a comprehensive study of the self- or concentration quenching, some of these compounds had to be solubilized.

As a result of systematic studies on the correlation between solubility and melting point on the one hand and the chemical constitution on the other hand (especially in the oligophenylene series) an effective and widely generalizable principle of solubilization has been developed. A great deal of this investigation has already been published,[19, 20] but nevertheless a very impressive example taken from the p-oligophenylene series is shown in Table 29.

The p-quinquiphenyl is an interesting compound, particularly for luminescence studies. Unfortunately, its solubility is very poor. By substitution of longer, branched, and especially long-chain branched alkyl groups, its solubility can be greatly enhanced. One can even come into a range where it is impossible to measure exact values.

With increasing solubility a concomitant decrease in melting point can be observed. This is easily understandable since these properties are closely related to each other. It is of special interest to point out the enormous difference (>300°C) between the melting point of the heptadecyl derivative and the basi compound.

As had been expected this solubilization principle proved to be applicable also to our 2-arylindole series. It can be seen from Table 30, where, however,

only three examples are listed. The comparison of the solubility data of the alkyl derivatives with those of the corresponding basic substances shows clearly the strong solubilizing effect of such groups. We even succeeded in reaching the point of infinite solubility with two compounds due to their forming supercooled melts or supersaturated solutions. Thus, it was possible to extend self-quenching studies over the entire concentration range.

Melting and Crystallizing Behavior

In general, the groups which increase the solubility cause at the same time a decrease in melting point (Tables 29 and 30). Frequently this decrease in melting point is accompanied by a reduced tendency to crystallize, even to the extent that compounds may be obtained without any ability to crystallize. We obtained several 2-arylindole derivatives which also showed this behavior. Only one of them, (IV in Table 28), will be described in this paper; we have not yet succeeded in the purification of the remainder.

We found, in addition, quite a reasonable number of compounds which were crystallizable from solution; the recrystallization from the molten state, however, was delayed; in some cases it even seems that the recrystallization will never take place. In Table 31 a random selection of 4 compounds which form such supercooled (amorphous) melts is shown; these have lifetimes from one week to more than ten months, the present age of the samples.

There are some disadvantages of these supercooled melts. First of all, one can never realize this peculiarity with high certainty, especially not for compounds with very long lifetimes; quite often substances are obtained which either are no longer capable of crystallization or which recrystallize immediately after melting. In addition, the crystallization from solvents of such compounds exhibiting very long lifetimes is especially troublesome and usually only possible by applying special tricks.

We have already reported another technique for bringing compounds of this type to such an amorphous state with much higher certainty and—which is most interesting—without forfeiting the crystallization tendency.[20] The latter point is very important since crystallization is still the most efficient purification provision for compounds of a higher molecular weight. This technique is worth pointing out once more in this connection (Table 32).

By mixing different but crystallizable alkyl derivatives of the same basic molecule and melting them together one can obtain an eutectic-like system which no longer crystallizes. In Table 32 three examples are shown, including only one of the 2-arylindole series. According to our present knowledge this principle seems to have general applicability. As far as luminescence behavior is concerned, it doesn't make any difference whether there is a mixture or not, since the electronic properties of the basic molecules are not influenced by the size or structure of the alkyl groups.

The consistency of such systems, including the supercooled melts discussed above, depends mainly on the size or, better, rigidity of the basic molecules. Thus, one can get either a fluid liquid, a sticky glass-like mass, or even a brittle glass. Hence, it is possible to realize properties in a rather low molecular range (even below 1000) which are considered to be typical of high polymers.

TABLE 31. ARYLINDOLE DERIVATIVES THAT FORM SUPERCOOLED MELTS

Structural formula	Melting point, °C	Lifetime of supercooled state
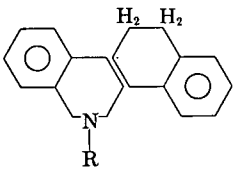 R: n-butyl	75	>10 months
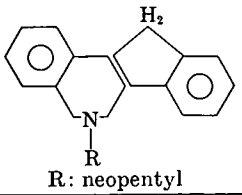 R: neopentyl	117	>10 months
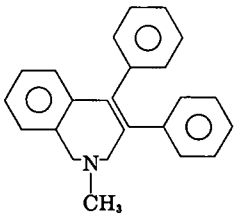	138	~1 month
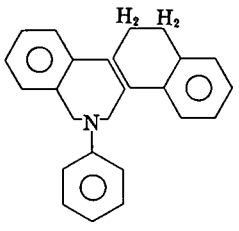	140	~1 week

TABLE 32. ALKYL DERIVATIVES OF HETEROCYCLIC COMPOUNDS FORMING A NONCRYSTALLIZING MIXTURE

General structural formula	Derivatives		Consistency of the noncrystallizable mixture of the alkyl derivatives at 20°C
	R	Melting points, °C	
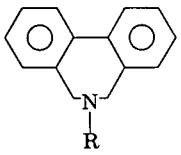	n-Octyl	22	Rather fluid liquid
	n-Decyl	12	
	i-Butyl	50	
	H	247	
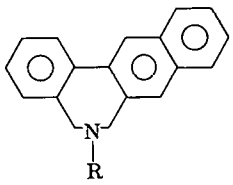	n-Hexyl	39	High viscous oil
	n-Tetradecyl	49	
	i-Propyl	110	
	H	335	
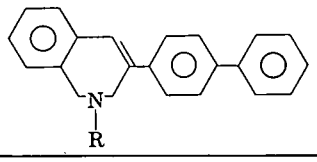	n-Butyl	110	Tar-like mass
	3-Methoxy-n-Butyl	85	
	H	300	

Scintillation Properties

Some of these supercooled melts were tested for their scintillation properties.[21] It was most surprising when we found that some of them convert electron excitation energy into fluorescent light more efficiently than the most commonly used liquid and plastic scintillators. Table 33 provides a comparison of the relative pulse heights of the supercooled melts of four 2-arylindole derivatives with some conventional liquid scintillators (including PPO as a standard, with the relative light yield under aerated conditions of unity). With the melt of one compound we even reached the value of the highly efficient toluene solution of dialkyloxy-*p*-quaterphenyl.[20]

Self-Quenching Studies

Finally it should be mentioned that we were able to clarify the correlation between chemical structure and self-quenching rather satisfactorily. We would like to summarize very briefly the most important results, some of which have already been published; others will be included in a comprehensive paper just in preparation.[3]

According to our findings, self-quenching occurs only when two molecules, one of which is in the excited state, can approach each other so that a mirror image overlay of the entire chromophoric systems is possible. We are quite sure that this approach is identical with the formation of the excimer state, and we are also convinced that self-quenching occurs always and only over the excimer state, as already assumed by Förster in 1954.[22]

As a consequence, structural provisions rendering more difficult, or preventing entirely, the close approach in the mentioned orientation of two molecules lead to a diminution or even to a complete lack in self-quenching.

This can be clearly seen from Figure 45.[2] On this graph are plotted the relative scintillation efficiencies (under β-excitation) as a function of concentration

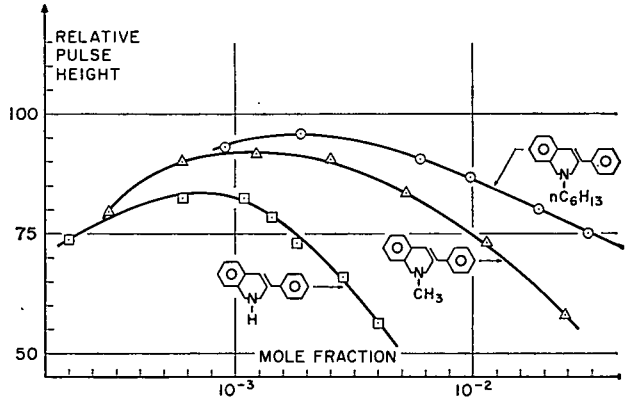

FIG. 45. Relative scintillation efficiency (Cs^{137} electron excitation) vs. concentration (mole fraction) curves of three 2-phenylindole derivatives.

(expressed in mole fractions) of three 2-phenylindole derivatives. There is a very significant decrease in self-quenching with increasing size of the substituents at the nitrogen atom. This graph shows, in addition, that self-quenching already can be affecting the scintillation efficiency curve in the low concentration range and, therefore, also the peak. Hence, a lack in self-quenching means finally an increase in light yield.

TABLE 33. COMPARISON OF THE SCINTILLATION PROPERTIES OF COMMONLY USED SCINTILLATOR SOLUTES WITH THOSE OF THE SUPERCOOLED MELTS OF 2-ARYLINDOLE DERIVATIVES

Structural formula	Relative pulse height	Optimal conc., g/l	
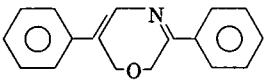 (PPO)	1.00 (Standard)	3	
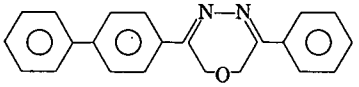 (PBD)	1.28	10	
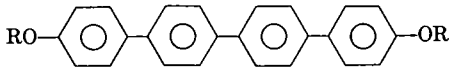 R: 2-butyloctyl (1)	1.41	16	
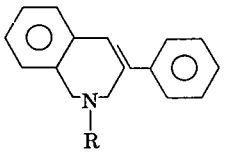 R: n-hexyl	0.66		SUPERCOOLED MELTS
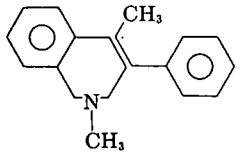	0.87		
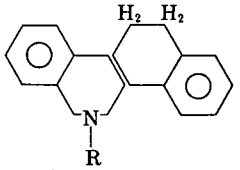 R: phenyl	1.20		
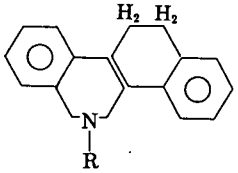 R: i-amyl	1.41		

Stimulating discussions with Dr. D. L. Horrocks and Dr. I. B. Berlman are gratefully acknowledged. We also feel very much indebted to Mr. M. J. Benson for helpful assistance.

REFERENCES

1. D. L. Horrocks and H. O. Wirth. *Molecular Crystals.* Proc. Intern. Symp. on Organic Scintillators, Argonne, Illinois, 1966. In press.
2. D. L. Horrocks. *Developments in Applied Spectroscopy,* 18th Ann. Mid-America Symp. on Spectroscopy, Chicago, Illinois, 1967. Soc. Appl. Spectroscopy, Chicago Section, Plenum Press. In press.
3. D. L. Horrocks and H. O. Wirth. Paper in preparation.
4. J. Culmann. *Ber. Deut. chem. Ges.* **21,** 2596 (1888).
5. Huang-Hsinmin and F. G. Maun. *J. Chem. Soc.* [*London*] 2903 (1949).
6. H. M. Kissman, D. W. Farnsworth, and B. Witkop. *J. Am. Chem. Soc.* **74,** 3948 (1952).
7. F. Brown and F. G. Mann. *J. Chem. Soc.* [*London*] 847 (1948).
8. F. S. Kipping. *J. Chem. Soc.* [*London*] **65,** 494 (1894).
9. C. U. Rogers and B. B. Corson. *Org. Synth.* **30,** 90 (1950).
10. N. P. Buu-Hoï and P. Jacquignen. *J. Chem. Soc.* [*London*] 1515 (1956).
11. N. P. Buu-Hoï and N. D. Xuong. *J. Chem. Soc.* [*London*] 2225 (1952).
12. C. U. Rogers and B. B. Corson. *J. Am. Chem. Soc.* **69,** 2910 (1947); see also Ref. 9.
13. G. Buchmann and P. Trautmann. *J. prakt. Chem.* **1** (4), 25 (1966).
14. H. O. Wirth. Unpublished investigations.
15. R. Kuhn, H. Trischmann, and I. Löw. *Angew. Chem.* **67,** 32 (1955); R. Kuhn and H. Trischmann. *Chem. Ber.* **94,** 2258 (1961); R. Kuhn and H. Trischmann. *Monatsh. Chem.* **95,** 457 (1964).
16. H. O. Wirth, W. Kern, and E. Schmitz. *Makromolekulare Chem.* **68,** 69 (1963).
17. I. B. Berlman, H. O. Wirth, and O. J. Steingraber. *J. Am. Chem. Soc.* In press.
18. R. C. Sangster and J. W. Irvine, Jr. *J. Chem. Phys.* **24,** 672 (1956).
19. H. O. Wirth. *Proc. Intern. Symp. on Luminescence.* Karl Thiemig Verlag, Munich, 1966, p. 141; also unpublished investigations.
20. H. O. Wirth, F. U. Herrmann, G. Herrmann, and W. Kern. *Molecular Crystals.* Proc. Intern. Symp. on Organic Scintillators, Argonne, Illinois, 1966. In press.
21. D. L. Horrocks and H. O. Wirth. *J. Phys. Chem.* In press.
22. Th. Förster and K. Kasper. *Z. physik. Chem.* **1,** 275 (1954).

NEUTRON ACTIVATION ANALYSIS OF SAMPLES OF BIOLOGICAL AND ENVIRONMENTAL INTEREST. EVALUATION OF THE EXPERIMENTAL METHOD

D. N. Edgington and H. F. Lucas, Jr.

INTRODUCTION

The importance of trace elements in disease, nutrition, toxicology, ecology, and environmental pollution is generally recognized. In biological research the main interest centers on the recognition of those which are essential for life. In plants it appears that iron, copper, zinc, manganese, boron, sodium, chlorine, cobalt, molybdenum and vanadium are essential. For animals the list is almost as extensive, with the addition of iodine and selenium and the elimination of boron, sodium and vanadium. In addition fluorine, bromine, barium and strontium are probably essential for animals. The concentrations of these elements in animal or plant tissue varies from hundreds of parts per million for manganese in plants and zinc in animals, to a fraction of a part per million of molybdenum in either. In fact, as Allaway[1] states in a recent review "... Throughout the search for essential trace elements, the state of knowledge of the essentiality of elements in biology has never been far removed from the process of development of more sensitive and reliable analytical methods for the detection and measurement of trace elements."

The analysis of trace elements may be accomplished by many different experimental techniques. Tipton and coworkers[2] have looked for many trace elements in a wide variety of samples of soft tissue from different geographical regions using emission spectrography. While this is an elegant method for analyzing a large number of samples in a short time, in many instances the concentration of several of the trace elements of interest was less than the lowest detectable amount. More recently, atomic absorption has been employed to investigate the concentrations of trace elements in biological samples.[3] While it is recognized that all analytical techniques have their drawbacks as well as their well-documented advantages, it is reasonable to assert that of all methods currently available, neutron activation analysis using thermal neutrons from a nuclear reactor probably provides the research worker with the greatest possible sensitivity for many elements, though it may not necessarily be the most convenient method to employ on a routine basis. This sensitivity depends on the induced activity at the end of the irradiation, the degree of radiochemical purity, and the sensitivity of the detector. The induced activity, A, in disintegrations per minute is given by:

$$A = N\phi\sigma(1 - e^{-\lambda t}) \cdots \quad (1)$$

where N is the number of atoms of the isotope irradiated ($6.02 \times 10^{23} \times W \times f$, W being the weight of the element taken and f the fractional abundance of the particular isotope involved of the element), σ is the neutron cross section in barns (10^{-24} cm^2), ϕ is the thermal neutron flux (neutrons cm^{-2} min^{-1}), λ is the radioactive decay constant of the induced radionuclide, and t is the time of irradiation. It is clear that A attains a maximum value when $(1 - e^{-\lambda t}) \rightarrow 1$, or, in practical terms, after an irradiation time of six to ten half-lives. Sensitivities of detection for all possible isotopes produced by irradiation with thermal neutrons have been tabulated by Wing and Wahlgren,[4] some of which are reproduced in Table 34, together with sensitivities of detection obtainable using emission spectrography and atomic adsorption.

Neutron or other particle activation techniques have been widely utilized for the analysis of trace elements in biological samples.[5] These techniques fall into two general categories. Firstly, there are those which involve minimal sample preparation before or after irradiation in a nuclear reactor or a charged particle generator, followed by detection of the induced radiation by gamma spectrometry and some form of computer-based analysis of samples where the activation of the trace element provides the principal contribution to the resultant induced radioactivity.[7]

Secondly, there are the techniques where the sample is destroyed chemically after irradiation, a known concentration of inactive carrier added, and careful conventional wet chemical analyses carried out to isolate a radiochemically pure nuclide for determinatic with known chemical yield. These techniques are admirably exemplified by the work of Smales and coworkers.[8] Here, the use of gamma spectrometry is not

TABLE 34. COMPARISON OF LIMITS OF DETECTION BY EMISSION SPECTROSCOPY, ATOMIC ABSORPTION, AND NEUTRON ACTIVATION ANALYSIS (IN PARTS PER MILLION)

Element	Emission[a]	Atomic[b] absorption	Neutron activation[c]			
			Nuclide measured	20-Minute irradiation	1-Day irradiation	1-Week irradiation
Ag	0.01	0.02	Ag^{110m}	0.26	0.004	0.0005
As	1.0	1.0	As^{76}	0.0002		
Au	0.05	0.1	Au^{198}	8.3×10^{-5}		
Cd	1.0	0.01	Cd^{115}	0.01	0.002	2×10^{-5}
Co	0.01	0.15	Co^{60}	0.07	0.001	0.0001
Cr	0.02	0.01	Cr^{51}	0.03	0.0004	6×10^{-5}
Cu	0.02	0.005	Cu^{64}	0.0002	2×10^{-6}	
Fe	0.1	0.05	Fe^{59}	11	0.2	0.02
Hf			Hf^{181}	0.03	0.005	0.0005
Mn	0.02	0.01	Mn^{56}	7×10^{-6}		
Mo	1.0	0.2	Mo^{99}	0.03	0.0004	6×10^{-5}
Sb	0.2	0.2	Sb^{122}	0.001	0.0002	
			Sb^{124}	0.1	0.01	
Th			Pa^{233}	0.17	0.002	0.0003
U			Np^{239}	0.04	0.0006	8×10^{-5}
W			W^{187}	0.0003	4×10^{-5}	
Zn	1.0	0.005	Zn^{65}	1.0	0.01	0.002
			Zn^{69}	0.03	0.0004	6×10^{-5}
Zr	1.0		Zr^{97}	0.7	0.009	0.001

[a] D.C. arc, limits from superimposed spectra method, see Reference 6.

[b] Published limits of detection by Perkin Elmer.

[c] Calculated for a neutron flux of 2×10^{13} neutrons cm^{-2} sec^{-1} assuming a minimum sensitivity of 100 cpm above background and counting directly after irradiation.

essential, being used solely as a check on radiochemical purity.

In the former cases, the computer-based analysis of the gamma spectra was dependent on either spectrum stripping or some form of a least-squares solution of a set of simultaneous equations, the intensity of each radioactive nuclide present being the unknown quantity. In either case, a library of known, radiochemically pure gamma spectra is necessary. The spectrum stripping method of analysis is acceptable as long as the intensity of the induced radioactivity from the trace elements is of the same order as that produced in the matrix. For biological systems, where the major components (other than carbon, hydrogen and oxygen) are sodium, phosphorus, chlorine and calcium, all of which have large neutron absorption cross sections and, therefore, a high induced radioactivity, the activity from the trace elements of interest is frequently several orders of magnitude lower than that obtained from the irradiated matrix. Therefore, as long as the activity produced by the trace elements is greater than the statistical uncertainty in the activity of the matrix, only the least squares method will give acceptable results for the analysis.

The success of these computer-based methods is highly dependent on the stability of the nucleonic equipment and/or the ability to correct the data for drifts in zero-energy intercept and total system gain. They are also highly dependent on the variance of the standard spectra in the library.[7] In the least squares method, in particular, the observed counting rate is exceedingly important since chance coincidences distort the spectral shape (see Experimental Results).

In this paper, we shall describe the techniques which we have employed for the analysis of several trace elements in biological materials in which we combine the advantages of both chemical separation and computer-based reduction of the resultant gamma-ray spectra. After irradiation, the previously dry-ashed samples are dissolved in concentrated hydrochloric acid and separated into groups of elements by elution from an anion exchange column. The elution from the column is performed in such a way that essentially complete recovery of each nuclide of interest is achieved. The analysis is completed by obtaining the gamma ray spectrum of each group of elements. The spectra are finally fitted using a rigorous weighted least squares method. The computer program first of all corrects the data spectra for changes in gain and zero energy intercept due to electronic or temperature instability and then calculates the concentration and associated statistical counting error for each nuclide in the group by an iterative weighted least-squares method which allows for the counting statistics of each channel being

analyzed in both the data spectra and the library reference spectra.[9]

This paper describes the testing of the separation techniques and details of the computational methods.

SEPARATION METHODS

Ion-exchange chromatographic techniques are ideally suited for problems of separation associated with the highly radioactive products obtained from the neutron activation of biological materials. While many solvent extraction techniques have been devised which are specific for a certain element and can be completed within a few minutes, they involve considerable manipulation of the sample and the concomitant danger from contamination of personnel and equipment. Separations involving ion-exchange are much slower than those with solvent extraction and are not useful where the half-life of the induced radioactivity is less than a few hours. However, they involve the minimum of handling after dissolution and are readily adapted to automatic operation. This is exemplified in the elegant work of Samsahl where he devised a scheme for the complete separation of seventeen elements on six interconnected ion-exchange columns.[10]

Separation into groups rather than single element fractions, when combined with a least squares analysis of the resultant gamma-ray spectra, permits a simpler separation scheme to be utilized. In order to further reduce the problems associated with the handling of the highly radioactive samples after irradiation, all samples are ashed in platinum crucibles at 600° C for sixteen hours and then irradiated. The residue generally dissolves readily in a minimum volume of 9 *M* hydrochloric acid and is immediately ready for transfer to the ion-exchange column. This technique of ashing the samples prior to irradiation is open to criticism on two counts: first, contamination may be transferred to the sample for the crucible or furnace, and second, certain trace constituents may be lost by volatilization at this temperature, i.e. volatile elements like arsenic, selenium and iodine and volatile halides of transition metals. The latter problem will be investigated at a later date. At the present time there is little positive evidence of contamination from the platinum crucible or the furnace lining.

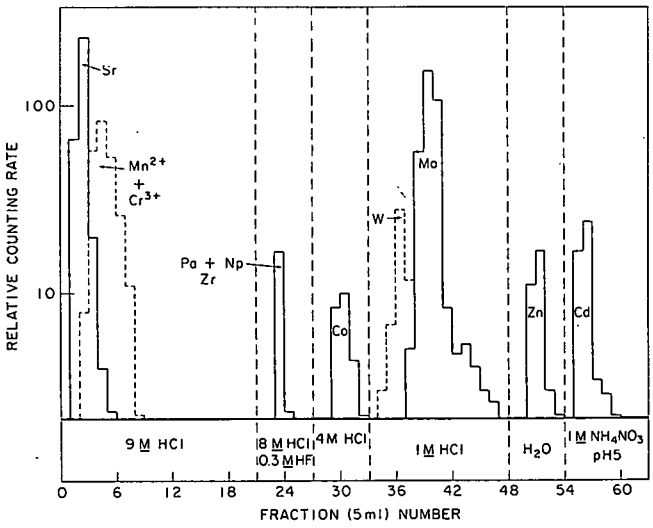

FIG. 46. Elution of several anionic species from Dowex 1-X8

By taking advantage of differences in their ability to form anionic chloride complexes, separations of many elements may be accomplished on anion-exchange columns. Their behavior may be predicted from the results presented in many papers by Kraus et al.[11] However, there may be differences in the elution pattern due to the experimental conditions. For example, the presence of a large concentration of phosphate ion from dissolved bone radically changed the adsorption behavior of protactinium and neptunium from nitric acid solution onto Dowex-1.[12]

In an earlier paper we have discussed in detail the separation of protactinium (Pa) and neptunium (Np) from samples of bone after irradiation and thereby the determination of thorium and uranium.[12] In that paper it was shown that a quantitative separation of Pa and Np could be made from the irradiated bone if the bone was dissolved in 9 *M* HCl, put on a column of Dowex-1, the column washed with 9 *M* HCl until the eluent contained no further activity, and then eluting with a mixture of 8 *M* HCl and 0.3 *M* HF. It was further shown that by eluting first with 4 *M* HCl and then water, a quantiative separation of cobalt and zinc may also be accomplished. The separation scheme shown in Figure 46 is essentially an extension of that used previously and includes several other elements of interest. The column was filled with Dowex-1-X8, 100–200 mesh in the chloride form and was made from polyethylene tubing (because of the use of HF) 6 mm in diameter and 35 cm long.

In view of the fact that these separations are used in conjunction with the least squares analysis of the resultant gamma-ray spectra, the presence of radiochemically pure nuclides is not necessary and only four eluents are generally used. They are (A) 9 *M* HCl, which elutes all cations and anions which are not adsorbed in the presence of a large concentration of chloride ions; (B) 8 *M* HCl and 0.3 *M* HF, which elutes protactinium and neptunium; (C) 1 *M* HCl, which elutes cobalt, ferric iron, molybdenum, and tungsten; and (D) 1 *M* NH_4NO_3 at pH 5, which elutes zinc and cadmium. Of a the common elements, copper is the only one which does not elute cleanly by this method. It is weakly adsorbed on the anion exchange column and appears in the 8 *M*

HCl + 0.3 *M* HF fraction with the Pa and Np. Elution of copper is complete with 4 *M* HCl and appears with cobalt. In some experiments, Pa, Np, Co and Cu were eluted together using 4 *M* HCl, 0.3 *M* HF. If it is desired to determine tin, this may be eluted finally using 2 *M* H_2SO_4. Antimony appears to be very strongly adsorbed to the column under all conditions and is presumably in the trivalent state.[13]

Zirconium and niobium elute under the same conditions as neptunium, while tellurium elutes together with cadmium. This latter behavior was elucidated from the behavior of the uranium fission products on the same anion-exchange column. This study was required to identify those fission products which are sufficiently abundant to require inclusion in the library of standard spectra for the least-squares program and which might contribute errors in the estimation of naturally-occurring isotopes when a significant concentration of uranium was present; e.g., both the fission of uranium and the neutron irradiation of zirconium produce the same nuclides of zirconium, Zr^{95}, Zr^{97}.

This anion exchange procedure gives a very efficient separation of the anionic species from the large concentration of calcium and phosphate. Preliminary studies have attempted to separate cations, i.e., rare earths, chromium, barium, etc. from these major constituents. A separation of the cations from the phosphate is readily accomplished by evaporating the initial 9 *M* HCl fractions from the Dowex-1 column to a small volume, adjusting the acidity to approximately 1 *M* and then putting this solution on a column of Dowex-50. Elution with 0.1 *M* EDTA buffered to pH 5 elutes the rare earths before the alkaline earths. Precipitation methods have also been attempted, but the tremendous difference in specific activity between the matrix and the desired trace elements (approximately 10^8) makes quantitative separations very difficult. Further studies are in progress.

ACCUMULATION AND QUANTITATIVE ANALYSIS OF GAMMA RAY SPECTRA

Gamma-ray spectrometry using pulse height analyzers in conjunction with computer resolution of the resultant spectra has proved to be a powerful analytical tool for the analysis of complex mixtures of radioactive nuclides. It is particularly useful in studying the induced radioactivity after the irradiation of material in a nuclear reactor. The technique has been exploited by many workers, notably by those devising completely automatic methods of analysis which involve no chemical separations.[14, 15] The quantitative analysis of a spectrum may be accomplished by a variety of methods, from that of simple subtraction of background and summing the residual counts in a particular band of channels, through the process of subtraction or stripping of known spectra, to the very sophisticated method of least squares.

Apart from the simplest of computational methods, the common requirements for computer-based methods of analysis are (1) the availability of a library of gamma spectra of all the radioactive nuclides (including β-emitters whose brehmsstrahlung contribute to the gamma spectrum at low energies) likely to be encountered in the complex spectrum and (2) an experimental system with good stability of gain and zero energy intercept over a long period of time.

The preparation of the library of standard spectra is of prime importance. The precision (and possibly the accuracy if the standards are calibrated absolutely) of the final answer depends entirely on these standards, and therefore, it is very important that the greatest care be taken to insure their radiochemical purity at the time of preparation. It is also very important that the geometry of these standards be identical in every way with the geometry of the samples which will be counted later because even small changes affect the spectral shape and will show up as an error in the least squares method (vide infra). The effort required for the preparation of this library of spectra is considerable and it is not practicable to duplicate it at frequent intervals such as would be required by lack of stability of the gamma spectrometer or changes in the geometry.

The long-term stability of a gamma spectrometer is dependent on good quality electronics, the temperature, and the line voltage variation under which it is operated. All control processes are cyclic, and these introduce short-term variations in temperature and voltage. These short-term variations can cause changes in the slope of the energy calibration (gain) and in the zero energy intercept. Further, a stable background counting rate and spectral shape simplify the analysis since an overnight counting interval may then be used for background determination or for samples with very low count rates.

The data reported in this paper were obtained using a 4″ × 2″ NaI(Tl) crystal with a thin aluminum window (Harshaw matched window) which has a resolution of 6% for Cs^{137} and a high linearity, high stability amplifier built by the Electronics Division at Argonne (LPA-9). The output of the amplifier was fed into a Nuclear Data 512-channel analyzer (ND 120). The gamma spectrometer was set up in the Radiological Physics Division vault,[16] where the room temperature is controlled at 74 ± 0.5° F over long periods of time, the line voltage is controlled to within ± 0.10 volts, and the concentration of radon in the atmosphere is less than 0.01 pCi per liter. The crystal and photomultiplier are mounted in an 8″ thick walled steel cave

which is lined with lead and having internal dimensions 14″ × 14″ × 28″. In order to minimize the effects of geometry, the samples, both standards, and experimental solutions are contained in ¾″ × 3½″ (15-ml) plastic tubes,* the volume of the solution being made up to 10.0 ± 0.1 ml. To insure that these tubes are placed in a reproducible position on the face of the crystal, a Lucite sample holder was fabricated. In order to prevent accidental contamination of the crystal, the ¾″ tubes are placed in a replaceable plastic tube 1″ in diameter. The data are read from the analyzer onto punched paper tape and then transferred to magnetic tape. This tape forms the data input for the least squares computer program. The gain of the linear amplifier was set such that 512 channels corresponds 3.2 MeV, a scale which includes virtually all nuclides produced in (n, γ) reactions.

A detailed description of the last squares computer program has been given in an earlier paper by Parr and Lucas and only a brief review will be given here.[9] The program calculates the intensities of up to twenty different components in a complex mixture, the precision of each intensity depending on the library standard, the counting statistics of the sample spectra, and the ability to compensate for instrumental drifts.

The first stage in the calculations corrects for instrumental instability. A standard spectrum was chosen and written into the library, in this case a sample of thorium ore, which has prominent peaks at both high and low energies. This spectrum is used to establish standard values of zero-energy intercept and gain against which all other spectra will be corrected and is one of the library of standard spectra. This correction is calculated by counting this same standard before and after each experimental spectrum (or at 30-minute intervals), determining the change in the two parameters for each sample count and assuming the average is the true value for the experimental spectrum. These values of zero-energy intercept and gain shifts are then used to modify the experimental spectrum. The shift in position of the low-energy peak reflects a change in zero-energy intercept and the shift of the high-energy peak a change in system gain. This correction is made by a method of linear interpolation between channels because the only true representation of the data is a histogram. This method of correction has the effect of smoothing the experimental data and introduces correlation between neighboring channels because the statistical variations are reduced as each channel is no longer statistically independent of all others. This effect is included in the estimate of the variance of the count in each channel.[17, 18]

In the method of least squares it is assumed that the count rate in any one channel of a complex spectrum is a linear combination of the counts from its constituent spectra together with a random error. The problem consists in minimizing the sum of the weighted squared residuals (the statistical function χ^2) across a specified range of channels of the spectrum. The residual in each channel, δ_j is

$$\delta_j = \sum_i a_{ij}x_i - a_{oj} \tag{2}$$

where a_{oj} is the count rate of the experimental spectrum, a_{ij} is the count rate of library spectrum i in channel j and x_i is the activity or weight of i in the unknown. The units of x_i depend on the calibration used in preparing the library. For the best least squares fit, the expression

$$\chi_F^2 = \sum_j w_j\delta_j^2/\text{variance } (\delta_j) \tag{3}$$

is a minimum, where w_j [= 1/variance (δ_j)] is a weighting factor dependent on the variance in channel j and F is the number of degrees of freedom in the system. Assuming that the count rates in each channel are statistically independent, it follows that

$$\text{variance } (\delta_j) = \sum_i x_i^2 \cdot \text{variance } (a_{ij}) + \text{variance } (a_{oj}). \tag{4}$$

It has been assumed (or minimized) by others that the first term in this expression is negligible in comparison to the second. The first term in this expression contains the unknown we wish to calculate, x_i. Therefore, in order to obtain a rigorous solution, an iterative method of calculation has to be used. For the first iteration the variance of the experimental spectrum is considered alone; this estimate of x_i is then used for all calculations until the values of x_i obtained are not significantly changed by further iterations.

For an ideal fit χ_F^2 should have a value of unity. A more convenient indicator of goodness of fit is the parameter s, where

$$s = \sqrt{2\chi_F^2} - \sqrt{2F - 1}. \tag{5}$$

For values of F greater than 30, s should be approximately normally distributed with zero mean and unit variance.[19]

In cases where a good fit is not obtained, these parameters are not a great help in distinguishing the source of error. In these cases the quantity

$$\text{DEL/SIGMA} = \delta_j/\sigma_j = \sigma_j/\sqrt{\text{variance } (\sigma_j)} \tag{6}$$

which has units of σ and may be called the normalized residual is particularly valuable for recognizing uncompensated instrumental changes, changes in spectral shape, or identifying nuclides present in the experi-

* Lermer Packaging Company, Chicago, Illinois.

mental spectrum but not included in the analysis. Generally $\chi^2_F \rightarrow 1$ and $-1 < s < 1$ when the residual in each channel is $\pm 3\ \sigma$ or less.

The following data are obtained for each case as part of the output from the computer program: the values of x_i and their standard errors, the values of χ^2_F and s, and a plot of the normalized residual DEL/SIGMA versus channel number.

As long as all the experimental precautions outlined above are taken, the analysis of gamma ray spectra by the method of least squares is a very powerful technique. There are a few other operational limitations which should be mentioned before describing some experimental results. The values of zero-energy intercept and gain are influenced by the counting rate. As long as the total counting rate is less than 10^5 cpm there was an observed change of less than 0.2 channels in zero intercept and a 0.1 % change in gain.[17] If the counting rate is greater than 10^5 cpm, the zero intercept and the gain changes more markedly. For least squares analysis which includes the low energy channels, the change in intercept is very important and the counting rate should be limited to approximately 5×10^4 cpm.[17] High counting rates also give rise to chance coincidences which affect the spectral shape. While the decrease in gain may be explained in terms of increased "noise" in the photomultiplier, the change in zero intercept is not understood.

The Radiological Physics Division underground counting facility is ideally suited for this type of study. The background counting rate is approximately 315 cpm over the energy range of 0.05 to 3.2 MeV and is stable within counting statistics as had been found by Corcoran and Markun for an $8'' \times 4''$ crystal.[20] In calculating the minimum sensitivities for neutron activation in Table 34, it was assumed that the minimum count rate detectable for any component is 100 cpm. It has been shown in a different system if the sample is counted long enough a lower minimum value may be attained.[21] The method of least squares can detect a component which accounts for only 0.1 % of the total count using a normal time of accumulation of the spectrum (i.e., 10 minutes and 10^6 counts total).[22] However, if longer count times are employed, this lower limit may be reduced.

EXPERIMENTAL RESULTS

Neutron activation is an instrumental method of analysis, and therefore, all results must be obtained elative to a known standard or standards. The intensity f the induced radioactivity is proportional to the mass of target element and the neutron flux integrated over the time of irradiation. Standardization of the system may be accomplished in two ways. A known mass of inactive standard is irradiated for a given time in an accurately calibrated neutron flux, and the induced radioactivity used as an absolute standard. The neutron flux for every other experiment is then measured using a flux monitor, such as gold foil. The other method, which is essentially the one used in this study, is to irradiate each time a set of standards in the same irradiation can as the experimental samples. The result is then obtained as a ratio independent of the neutron flux.

For the experiments described here solutions of pure elements* containing 10 mg per ml were prepared. From these individual solutions, a solution containing a mixture of ten elements of interest (20–200 μg per ml, depending on the thermal neutron cross section(s) of the element) was made up as a standard. Fifty microliter aliquot portions were pipetted into 2 dram polyethylene snap-top containers (Olympic Plastics) for irradiation. The samples were irradiated for twenty minutes in a standard position in the Argonne CP-5 reactor with a flux of 2×10^3 neutrons cm^{-2} sec^{-1}. After irradiation the solution was transferred into a counting vial and made up to the standard volume as explained previously. The gamma spectra were then accumulated and analyzed using the least squares computer program.

Evaluation of sensitivity and reproducibility is usually accomplished under nearly ideal experimental conditions. In real samples, however, the ratio of the counting rates may be expected to vary by more than a factor of 1000, and delays between irradiation and counting may vary between 24 and 48 hours. The measurements summarized in Table 35 were made on eight samples of a standard mixture which stimulates that expected for real samples. The counting rates for the various elements in the mixture vary over a wide range, while that for nuclides with a short half-life vary between samples.

Summarized in Table 35A are the results calculated in the least squares analysis of the gamma spectra obtained from the direct counting of the irradiated standard samples. The sensitivity computation assumes a net, uncorrected for decay, counting rate of 100 cpm, a neutron flux of 2×10^{13}n cm^{-2} sec^{-1} and a 10-minute counting period. These sensitivities ranging from 0.01 to 2 μg are attainable even in the presence of a large counting rate from other elements. Higher sensitivities are, of course, attainable for longer irradiation times or longer counting intervals. These values may be compared to those given in Table 34.

The parameters of goodness of fit (χ^2_F and s) in Table 35A exceed those normally obtained and indicate that at least one nonstatistical parameter is affecting the analysis. One of these was found to result from an error in the energy calibration of the library standard for Cu^{64}.

* Johnson Matthey, "Spec-Pure" materials.

TABLE 35A. OBSERVED COUNTING RATE FROM IRRADIATED STANDARD MIXTURE[a]

Element	Na	Co	Mo	Th	Mn	Zn	Zn	Cu	Cd	Cr	Total counts/ min	s	χ_P^2
Nuclide measured	Na^{24}	Co^{60}	Mo^{99}	Pa^{233}	Mn^{56}	Zn^{65}	Zn^{69}	Cu^{64}	Cd^{115}	Cr^{51}			
Micrograms added	5	10	10	5	1	10	10	5	10	10			
	counts/minute from least squares												
Experiment													
1	36109	4681	419	5639	151	N.F.[b]	522	16,300	1800	639	66260	2.41	1.16
2	13293	4645	303	6432	110	211	188	4,871	1791	454	32298	3.07	1.20
3	95044	4320	585	5475	7332	440	1361	43,992	2022	503	162820	1.99	1.42
4	96600	4267	577	5314	8040	N.F.[b]	1559	45,264	1997	701	166630	4.33	1.30
5	87020	4729	497	5705	6472	N.F.[b]	1444	44,433	2084	501	152865	2.80	1.20
6	55050	3007	504	3729	3801	234	907	28,230	1460	313	97235	0.54	1.03
7	44160	4570	299	5545	315	274	703	20,945	2115	491	79417	3.71	1.25
8	41060	4437	347	5139	172	131	643	19,445	1922	568	73864	3.26	1.22
Uncertainty from least squares	±0.3%	±6%	±32%	±3%	±2%–±32%	±50%	±6%	±0.5%	±11%	±23%			
Approximate sensitivity (μg)[c]	0.01	0.25	2.0	0.10	0.001–1.0	?	1.0	0.02	0.50	2.0			

[a] Other elements asked for in least squares determination were Fe^{59}, Cd^{115m}, W^{187}, Tc^{99m}.
[b] Not found.
[c] For a neutron flux of 2×10^{13} n cm^{-2} sec^{-1}, 20-minute irradiation, and 10-minute counting period.

TABLE 35B. REPRODUCIBILITY OF COMPLETE PROCEDURE

Sample	Na	Co	Mo	Th	Mn	Zn	Cu	Cd	Cr
1	1.03	0.94	0.92	0.99	—	1.04	1.00	0.98	0.84
2	1.01	0.98	1.01	0.85	—	0.96	0.98	0.74	1.14
3	0.92	1.05	0.80	1.04	1.22	1.05	1.02	1.11	1.09
4	0.93	1.06	0.82	1.06	1.17	0.95	1.02	1.25	0.78
5	0.98	0.95	0.94	1.00	1.13	0.97	0.98	1.97	1.09
6[a]	1.52	1.49	0.92	1.53	1.70	1.50	1.50	1.51	1.75
7	1.04	1.00	1.35	1.01	0.45	1.00	0.98	0.88	1.10
8	1.11	1.01	1.16	1.09	1.00	1.07	1.05	0.97	0.95
σ (±%)	7	5	20	8	26	5	3	16	14
$\sigma_{\bar{x}}$ (±%)	2.6	1.9	7.6	3.0	12	1.9	1.1	6.0	5.3

[a] Excluded in calculation of σ and $\sigma_{\bar{x}}$.

Figure 47A is a plot of the net spectra from experiment 3. Figure 47B is a plot of the normal residual DEL/SIGMA [equation (6)]. The sigmoid shaped curve between channels 50 and 100 is a unique characteristic for small errors in peak position. Since this curve is only associated with the prominent peak from Cu^{64}, this spectrum is the one in error. The error in peak position is less than 0.1 channel and is only apparent when the total counts from Cu^{64} are greater than 200,000. When the total number of counts is less than 50,000, a normal residual is obtained. A further smaller effect is caused by the change in photomultiplier gain of about 0.02% per minute which persists for about 10 minutes following a change in counting rate from 300 to 100,000 cpm.

The reproducibility and freedom from errors was evaluated as follows: The values obtained from the least squares analysis of the standard samples were corrected for decay since the end of irradiation. The ratios of these corrected values, including all statistical counting errors, normalized to a mean value of one, were then calculated. These values are summarized in Table 35B. Except for sample number six for which a portion of the standard was lost, the standard deviation varies between 3 and 26% for copper and manganese, respectively. The standard deviation of replicates for copper of ±3% is considerably greater than the uncertainty of about ±0.5% calculated in the least squares analysis. This results from the correlation coefficient of −0.42 with W^{187} and the previously mentioned problems with gain shift. On the other hand the large variation of ±7% for sodium, in contrast to the variation from the least squares of ±0.3%, is due, in the main, to contamination. In addition, experience to date indicates that statistical errors of less than ±1% are unrealistic in this present counting system. The larger uncertainties found in Table 35B correlate with counting statistics and could be reduced by a more realistic standard sample. This test, however, has clearly indicated a freedom from systematic errors.

An increase in sensitivity may also be accomplished by making the standards up in two sections, those with fairly short half-lives and high neutron cross section which contribute better than 90% of the total activity (i.e., Na, Cu, Mn), and the rest. For more accurate calibrations, concentrations greater than 10 μg may be

used for certain elements to normalize the number of cpm obtained at the time of counting. A precision of about ±10% is obtained for this rather rigorous test for the simultaneous determination of nine separate elements. This compares favorably with the ±3% found for a single element by a similar method.[23]

In addition to the ten nuclides given in Table 35A, four other nuclides were found in the standard samples and were included in the least-squares analysis. They are Fe^{59}, Cd^{115m}, W^{187}, and Tc^{99m}. The standard solution contained 10 μg of iron, but this concentration is too low to provide a significant counting rate for this study. Similarly, Cd^{115m} was not detectable. Tungsten-187 was found in all samples and was introduced as a trace contaminant in molybdenum. Technetium-99m is the daughter product of Mo^{99}:

$$Mo^{99} \xrightarrow[\beta]{67\ h} Tc^{99m} \xrightarrow{6.0\ h} Tc^{99} \xrightarrow{10^4\ years}$$

and grows in rapidly. If it were possible to wait long enough to allow this activity to grow into its equilibrium value, then measurement of Tc^{99m} would provide a more accurate method of determining molybdenum, as the specific activity of Tc^{99m} is approximately ten times greater than that of Mo^{99}.

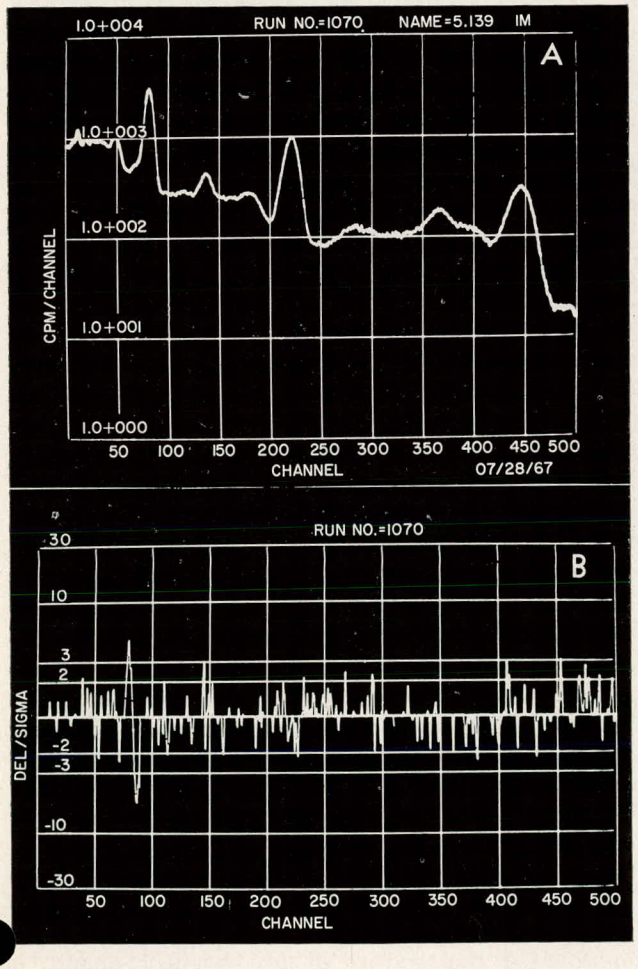

FIG. 47A. Gamma-ray spectra from mixed standards
FIG. 47B. Plot of δ/σ from least squares analysis of sample given in Figure 47A.

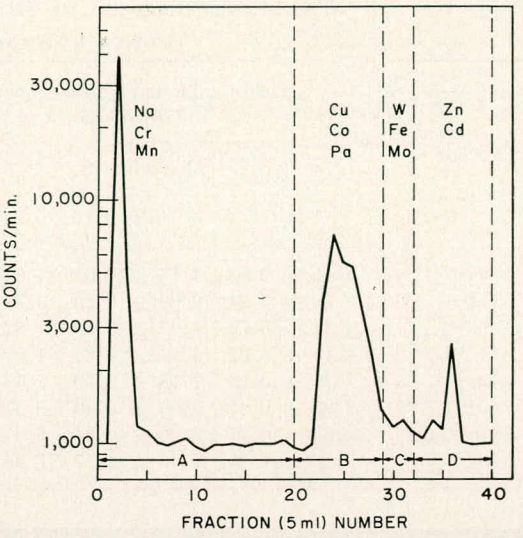

FIG. 48. Elution of irradiated mixed standard. Eluant A = 9 *M* HCl; B = 4 *M* HCl, 0.3 *M* HF; C = 1 *M* HCl; and D = 1 *M* NH_4NO_3, pH = 5.0.

The Efficiency of the Anion Exchange Process

In devising the separation scheme it has been tacitly assumed that the nuclides of interest will elute quantitatively. If this assumption is valid, then it will be unnecessary to add inactive carriers to each sample and determine the chemical yield for each element.

In order to test the efficiency of the chemical process an additional set of standards (prepared in the same manner as above) was irradiated. After irradiation the samples were added to 0.5 g calcium phosphate and dissolved with 5 ml 9*M* HCl. This resulting solution, which has approximately the same gross composition as most of the actual samples likely to be encountered, was put onto the anion exchange column of Dowex 1-X8 and then eluted using a series of four eluents. The eluent from the column was collected as fractions of 5 ml each, and then each fraction was counted. A plot of the elution histogram obtained for one of the samples is shown in Figure 48. The fractions were then either combined in pairs (i.e., 10 ml) or several pooled together and evaporated down to a volume of 10.0 ml, depending on the total count rate in each, and quantitatively transferred to vials for counting.

Table 36 summarizes the results obtained for a series of these standards. The experimental recoveries in micrograms are the values obtained from the least squares, corrected for radioactive decay between the end of

TABLE 36. Recovery of Several Nuclides on Elution from a Column of Dowex 1-X8 in the Presence of 0.5 g $Ca_3(PO_4)_2$

Nuclide	Yield total found by least squares program, μg			Average yield	Total μg added	Average recovery, %
	Experiment					
	A	B	C			
Na^{24}	4.44 ± 0.02	4.75 ± 0.02	4.63 ± 0.02	4.61 ± 0.10	5	92 ± 2
Co^{60}	8.71 ± 0.24	9.69 ± 0.25	9.99 ± 0.29	9.46 ± 0.39	10	95 ± 4
Pa^{233}	4.34 ± 0.09	4.97 ± 0.10	4.82 ± 0.10	4.71 ± 0.19	5	94 ± 4
Cu^{64}	4.49 ± 0.02	4.57 ± 0.02	4.91 ± 0.02	4.66 ± 0.13	5	93 ± 3
Zn^{69}	7.36 ± 0.50	7.18 ± 0.50	7.38 ± 0.51	7.31 ± 0.06	10	73 ± 4
Cd^{115}	8.07 ± 0.41	9.06 ± 0.46	8.57 ± 0.43	8.57 ± 0.29	10	86 ± 3
Cr^{51}	6.82 ± 0.77	6.00 ± 0.81	5.81 ± 0.77	6.21 ± 0.31	10	62 ± 6
Mo^{99}	7.18 ± 1.55	7.49 ± 1.77	7.45 ± 1.19	7.37 ± 0.09	10	74 ± 12

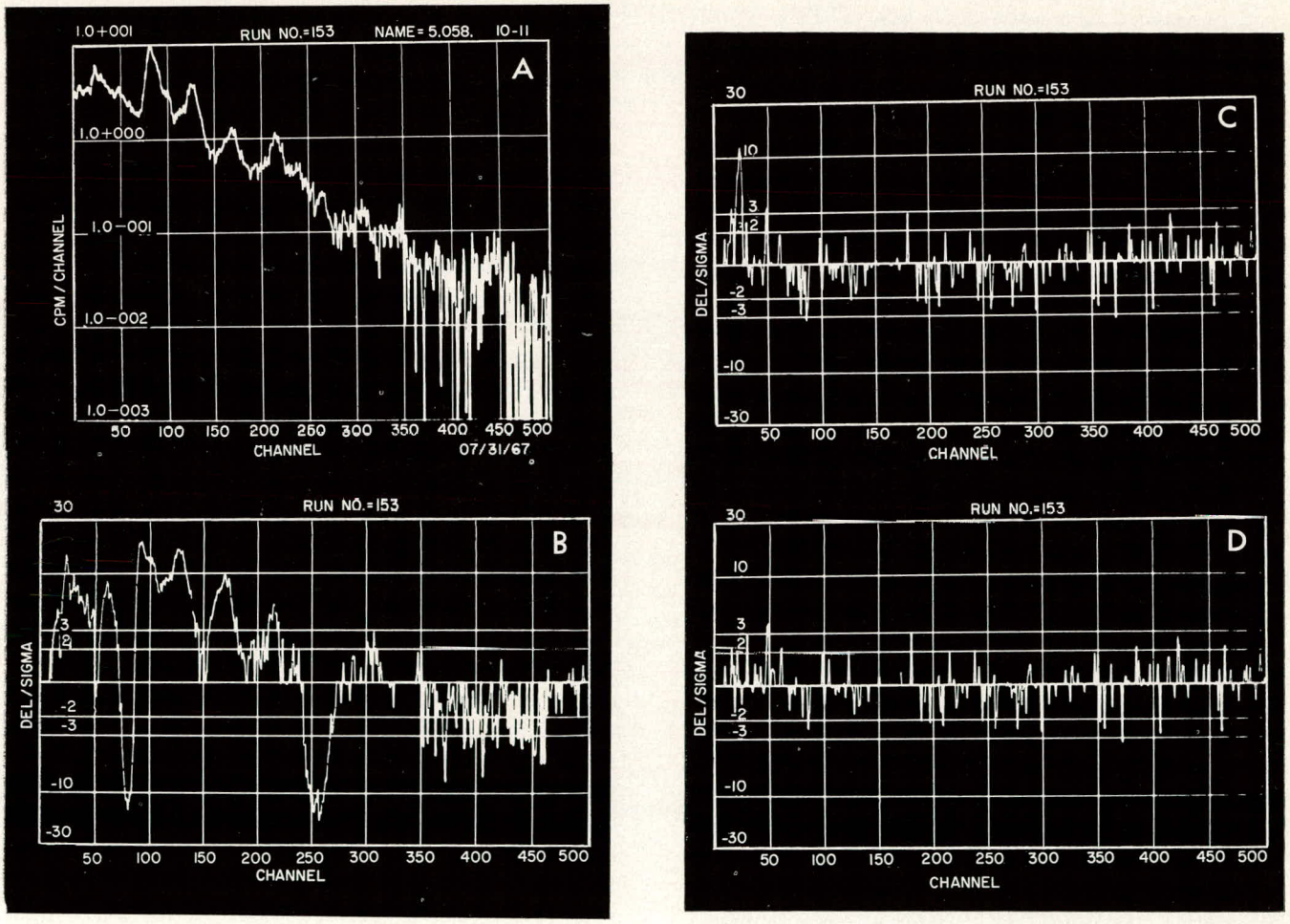

Fig. 49. A. Gamma-ray spectrum of 9 *M* HCl fraction 10 + 11. B, C, D. Normalized residuals obtained and used to identify Br^{82} and Sc^{47}.

irradiation and the time of counting, and any differences in the standardization (in cpm/μg) between the library reference spectra and the results from the analysis of the same standards irradiated at the same time but counted directly without any chemical separation. In the calculation of the average recovery it is necessary to consider both the standard deviation of the mean yield and the standard deviation of the individual values

TABLE 37. EFFECT OF MISSING NUCLIDE ON LEAST SQUARES ANALYSIS

Number	Na^{24}	K^{42}	La^{40}	Cu^{64}	Br^{82}	Sc^{47}	χ_F^2	s
	counts per minute							
1	40 ± 7	57 ± 10	118 ± 14	186 ± 10	N.A.[a]	N.A.[a]	33.5	148.3
2	9.3 ± 1.7	<6	12.1 ± 3.4	125 ± 3	408 ± 5	N.A.[a]	2.06	13.5
3	9.7 ± 1.2	<4	11.6 ± 2.4	122 ± 2	399 ± 4	16.2 ± 0.8	1.06	1.00

[a] N.A., not available for least squares analysis.

due to the counting errors in the standard library spectra and the spectrum analyzed. If the standard deviation due to counting statistics is greater than that of the mean value of the yield, then the former is used for the calculation of the error in average recovery. This corrects for correlation in the least squares.

Previous experiments with separate nuclides have shown that for all the nuclides listed in Table 35, a recovery of better than 95% was achieved for elution from the same anion exchange column. The recoveries given here vary from better than 90% for those nuclides which have the smallest statistical counting errors, to those which show large effects due to counting statistics and an apparently low recovery. The total counts available are comparable to those shown in Table 35A for the mixed standards and that discussion also applies.

This experiment was again conducted under far from ideal conditions and would be representative of a real experiment. Under these circumstances the average recoveries found are satisfactory. For example, the estimate for the determination of the recovery of molybdenum was based on a total of 156 cpm and zinc on a total of 157 cpm (10-minute count). The count rate for zinc is low because of a large time lapse between irradiation and counting and the short half-life of Zn^{69}. On the other hand, the values for cobalt are based on the recovery of 3645 cpm in the presence of 4722 cpm of Pa^{233} and 2191 cpm of Cu^{64}.

Unknown Nuclides

One of the problems encountered in neutron activation studies is the presence of unexpected and usually unknown nuclides in a sample. The effects on the statistical parameters χ_F^2 and s are readily apparent so that a problem is known. The identification of low counting rate contaminants is less obvious, however. The following example resulted during a test of the separation process in which 1.0 g of caribou bone had been irradiated and was processed as usual. The spectrum given in Figure 49A is that obtained for the 10th and 11th fraction of the 9*M* HCl eluate from the anion exchange column. The net counting rate was 563 cpm and the counting interval was 80 minutes. Normally one expects little or no radioactivity in these fractions since most of the Na^{24} and P^{32} (as phosphate) as well as other anions has been eluted.

The plots of the normalized residual (DEL/SIGMA) in Figures 49B, C and D are those obtained for analyses numbers 1, 2 and 3 in Table 37 respectively. In the first of these neither Sc^{47} nor Br^{82} was available so that a very poor fit was obtained. Since this is a weighted least squares, the inverted peaks in Figure 49B result from overestimation of Cu^{64} and K^{42}. The positive peaks in this figure correspond to the photopeaks of the missing nuclide. From this plot Br^{82} was identified. However, from the plot of DEL/SIGMA in Figure 49C, a peak corresponding to that from Sc^{47} was also found in this sample. When this final nuclide was added to the least squares calculation, χ_F^2 and s were reduced to normal values of 1.06 and 1.00, respectively. The counting rate attributed to Sc^{47} was only 16.2 cpm or 2.9% of the total, and the plot of DEL/SIGMA indicates a nearly perfect fit to the data. While the peak in channels 48 and 49 (0.30 MeV) occurs frequently and presumably corresponds to still another missing element, its intensity is too low for accurate identification.

REFERENCES

1. W. H. Allaway. *Trace Analysis—Physical Methods*, Ed. G. H. Morrison. Interscience Publr., New York, 1965, Ch. 3.
2. I. H. Tipton and M. J. Cook. *Health Phys.* **9**, 103 (1963).
3. F. Ronsselet. Atomic Adsorption Spectrophotometry Applied to Biology. Thesis. University of Paris, Faculty of Pharmacy (1966).
4. J. Wing and M. H. Wahlgren. Detection Sensitivities in Thermal-Neutron Activation. Argonne National Laboratory Report ANL-6953 (1965).
5. W. S. Lyon. *Guide to Activation Analysis*. Van Nostrand, New York, 1964, p. 158.
6. H. Kaiser. Optical and γ-ray Spectroscopy. *Trace Characterisation—Chemical and Physical*, Ed. W. W. Meinke and B. F. Scribner. National Bureau of Standards, Washington, D. C., Monograph No. 100 (1967).
7. J. I. Trombka. Jet-Propulsion Laboratory Report JPL-TR-32-373 (1962).
8. A. A. Smales, D. Mapper, and A. J. Wood. *Analyst* **82**, 75 (1957).
9. R. M. Parr and H. F. Lucas. *IEEE Trans. Nucl. Sci.* **NS-11** (3), 349–357 (1964).
10. K. Samsahl. Atomenergi Reports AE-159 (1964); AE-215, (1966).

11. K. A. Kraus and P. Nelson. *Proc. U. N. Conf. on Peaceful Uses of Atomic Energy* **7**, 13 (1955).
12. D. N. Edgington. *Intern. J. Appl. Radiation Isotopes* **18**, 11 (1967).
13. G. W. Smith and S. A. Reynolds. *Anal. Chim. Acta.* **12**, 151 (1966).
14. K. G. Neinen, G. Larrabee. *Anal. Chem.* **38**, 1853–1857 (1966).
15. R. E. Wainerdi and L. E. File. National Aeronautics and Space Administration Report NASA-CR-52997 (1963).
16. H. A. May, J. B. Corcoran, and P. Hess. Argonne National Laboratory Radiological Physics Division Annual Report July 1963 through June 1964. ANL-6938, pp. 194–205.
17. R. M. Parr. Argonne National Laboratory Radiological Physics Division Summary Report July 1962 through June 1963. ANL-6769, pp. 40–51.
18. H. F. Lucas, Jr. Argonne National Laboratory Radiological Physics Division Annual Report July 1964 through June 1965. ANL-7060, pp. 46–50.
19. A. Hald. *Statistical Theory with Engineering Applications*. John Wiley and Sons, Inc. New York, 1952, p. 258.
20. J. B. Corcoran and F. Markun. Argonne National Laboratory Radiological Physics Division Annual Report July 1964 through June 1965. ANL-7060, pp. 99–112.
21. H. F. Lucas, F. Markun, and J. Farnham. This report.
22. P. E. Brown and I. J. Davis. United Kingdom Atomic Energy Authority Report AERE-R-5272 (1966).
23. W. D. Ehmann. *Geochim. Cosmochim. Acta* **31**, 357–376 (1967).

DIVISION DELAY IN IRRADIATED GAMETES OF SEA URCHINS

Patricia M. Failla

Exposure to sufficient doses of ionizing radiation of either the eggs or sperm of sea urchins results in a delay in the time of first division of the fertilized eggs. Early experiments by Henshaw[1, 2] demonstrated recovery from this cleavage delay in eggs—but not in sperm—before fertilization. That is, there was a decrease in magnitude of the radiation-induced cleavage delay with the length of time that the eggs remained in sea water after irradiation but before fertilization. If entire urchins are irradiated and the gametes sampled and tested for cleavage delay at various times thereafter, recovery is again demonstrable in the eggs but not in the sperm.[3] In this case, however, the rate of recovery of the eggs when they remain in the urchin during the postirradiation period is much less (by a factor of 50–100) than when they are in a dish of sea water. This unexpected inhibitory effect of the maternal environment has not been explained.

A postfertilization recovery process has also been demonstrated—in this case for both irradiated eggs and sperm.[4, 5] This process involves a prolongation of the first division cycle by anoxia or D_2O exposure during which time the radiation effect is reduced. All the work described so far has been performed during summer months at Woods Hole, Massachusetts with the native sea urchin, *Arbacia punctulata*. In order to expand the opportunity to carry out this type of project, artificial sea water tanks have been set up at Argonne, and different species of sea urchins with various seasonal spawning periods are being utilized. Some of the observations made under these conditions are described below.

MATERIALS AND METHODS

Two 25-gallon refrigerated aquaria* were acquired which are designed to recirculate sea water continuously through a calcareous filtrant spread over the bottom of the tank. Artificial sea salts (Instant Ocean) are used as the medium. Various species of sea urchin have been maintained: *Arbacia punctulata*,† *Strongylocentrotus purpuratus*,‡ *Lytechinus pictus*,‡ and *Lytechinus variegatus*.§

Gametes were procured by electrical stimulation of the animals with an alternating potential. *Lytechinus pictus* and *Arbacia* gametes are released at about 8 volts. It was necessary, however, to use about 40 volts before gametes were released from *Strongylocentrotus purpuratus*. No gametes were ever procured from the *Lytechinus variegatus* urchins although they were reportedly in their spawning season when received.

Unless otherwise specified, the radiation exposure was delivered by an x-ray unit operating at 150 kV (CP) and 10 mA with 0.25 mm Cu and 0.5 mm Al filtration (HVL = 0.4 mm Cu). The gametes were generally exposed in small plastic Petri dishes (3 cm diameter) at a distance of 20.0 cm from the target to a dose rate of about 235 rads/min. The dishes used to irradiate sperm were placed in a larger plastic Petri dish containing chopped ice. This procedure was employed to conserve the motility of the sperm over the

* Supplied by Aquarium Systems, Inc., Wickliffe, Ohio.

† Supplied by Marine Biological Laboratory, Woods Hole, Massachusetts.

‡ Supplied by Pacific Biomarine Supply Co., Venice, California.

§ Supplied by Stanley Becker, Big Pine Key, Florida.

twenty-odd minute period required to deliver the desired dose (usually about 5000 R).

Since the first division of fertilized sea urchin eggs is ordinarily very synchronous, the estimation of the time when 50% of the eggs have cleaved was made visually. Under good conditions this time can generally be determined within ±1 minute. Cleavage delay times, therefore, are good to about ±2 minutes.

The lack of running sea water and the condition of the urchins after being shipped from one or the other coast constitute certainly less than ideal conditions. Consequently many experiments carried out previously at Woods Hole have been repeated to test the suitability of the artificial system at Argonne. It has been found that a large number of experiments have to be aborted because of imcomplete fertilization, lack of synchrony of cell division, or simply no cell division at all. In those instances where the behavior of the cells has been satisfactory, results of past experiments have been confirmed. This has inspired confidence in the results of new experiments.

RESULTS

Most of the successful experiments have been carried out with *Lytechinus pictus,* the hardiest species used and the one with the longest spawning season. The phenomenon of *in vitro* prefertilization recovery

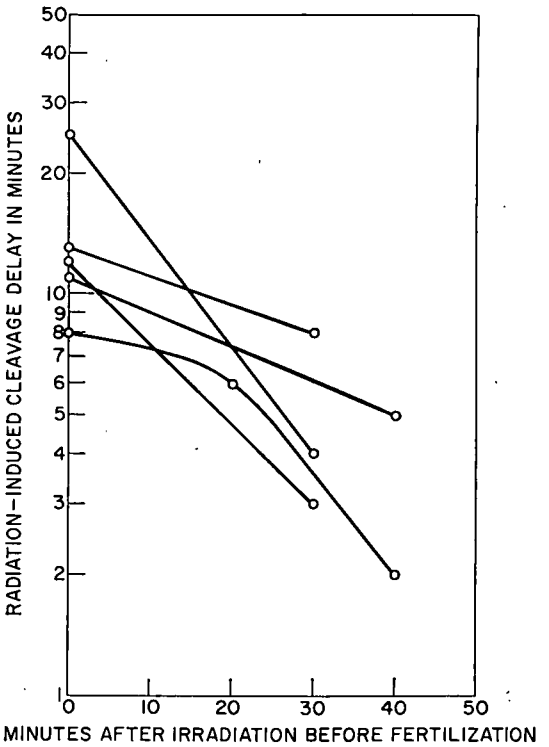

FIG. 50. Decrease in cleavage delay in *Lytechinus pictus* eggs exposed to 5000 R as a function of time they remain in Instant Ocean after irradiation but before fertilization.

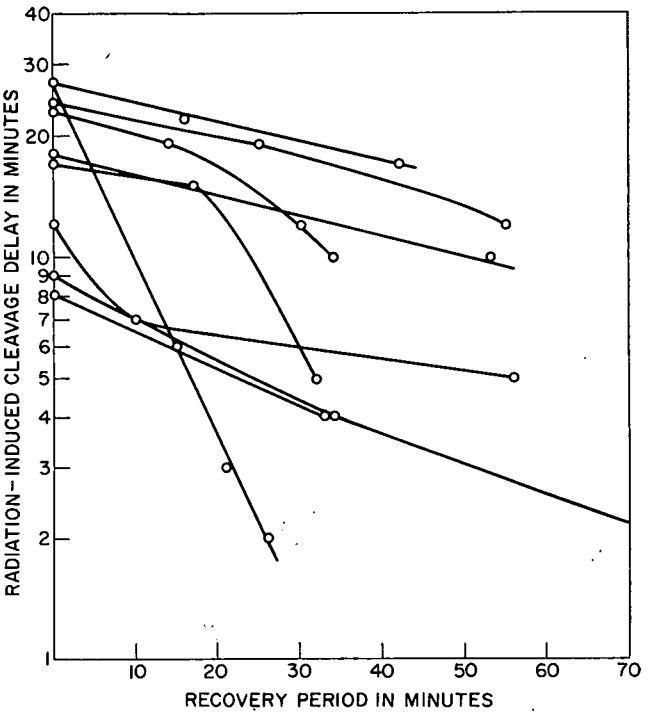

FIG. 51. Decrease in cleavage delay in *Lytechinus pictus* sperm exposed to 5000 R as a function of the time the post-fertilization control cell division cycle was prolonged by exposure to N_2.

of irradiated sea urchin eggs from radiation-induced cleavage delay has been confirmed and is shown in Figure 50. A decrease in cleavage delay is evident with the time that the eggs are allowed to stand in sea water after irradiation and before insemination with unirradiated sperm.

When the first division cycle is prolonged by the bubbling of nitrogen through the fertilized cell suspension, the recovery from cleavage delay in irradiated sperm first observed in *Arbacia punctulata*[4, 5] is also found with *L. pictus*. This is shown in Figure 51. The recovery period represents the length of time the first division cycle was prolonged by the nitrogen treatment.

It was decided to block the aerobic metabolism of the fertilized sea urchin eggs by a means other than anaerobiosis. Sodium azide has been shown to be a metabolic inhibitor that reversibly blocks the cleavage of fertilized sea urchin eggs.[6] Accordingly, eggs were put into a 3×10^{-5} *M* sodium azide solution shortly after being fertilized with irradiated or control sperm. This solution was replaced with ordinary Instant Ocean after various periods of time. The sodium azide solution was found to delay the first division cycle for approximately the length of time it was applied and during this time the radiation-induced cleavage delay was decreased. These results are shown

in Figure 52 where the recovery period represents the time the first division cycle was prolonged by the sodium azide treatment.

Colcemide was also tried as an inhibitor to prolong the first division cycle. A 0.01% solution was found in two experiments to delay the time of first cleavage when applied for periods up to one half hour—and in these experiments (with *L. pictus*) there was a decrease in the radiation-induced cleavage delay. In most cases, however, the colcemide-treated eggs appeared to break up into many units instead of dividing into two and it was impossible to determine the time of 50% cleavage. These experiments may be repeated with lower concentrations at times when the behavior of the cells is good.

Recently a cesium-137 gamma irradiator has been acquired which delivers a dose rate of about 1500 R/min. This has made it possible to irradiate fertilized eggs at various times during the first division cycle. The cleavage delay in *L. pictus* as a function of time of irradiation after fertilization is shown in Figure 53. The exposure time in each case was 4 minutes (about 5000 R); the position of each point on the abscissa is midway through the irradiation period. This curve is very similar to those published for *Arbacia punctulata*[1] and *Strongylocentrotus purpuratus*.[7] It is planned to study the fine structure of this type of curve more carefully and do some split-dose recovery studies similar to those carried out with mammalian cells.

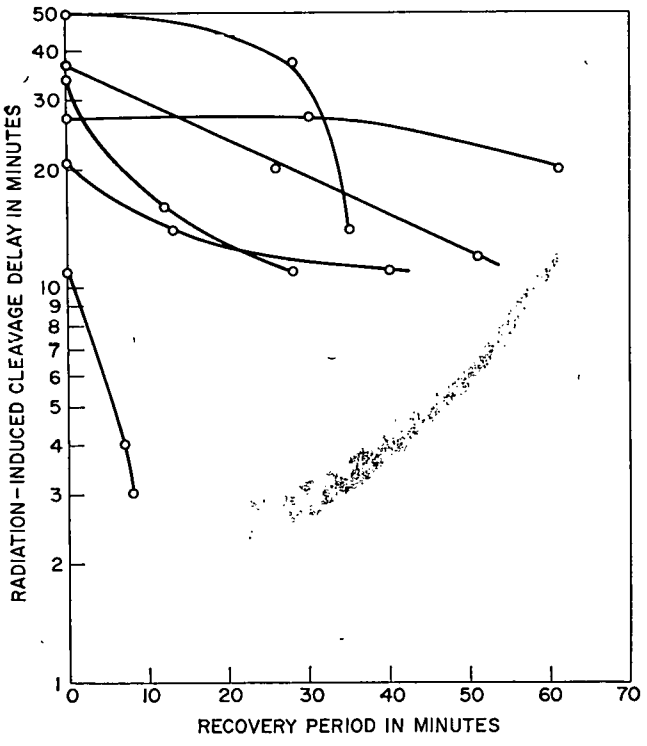

FIG. 52. Decrease in cleavage delay in *Lytechinus pictus* sperm exposed to 5000 R as a function of the time the post-fertilization control cell division cycle was prolonged by exposure to sodium azide.

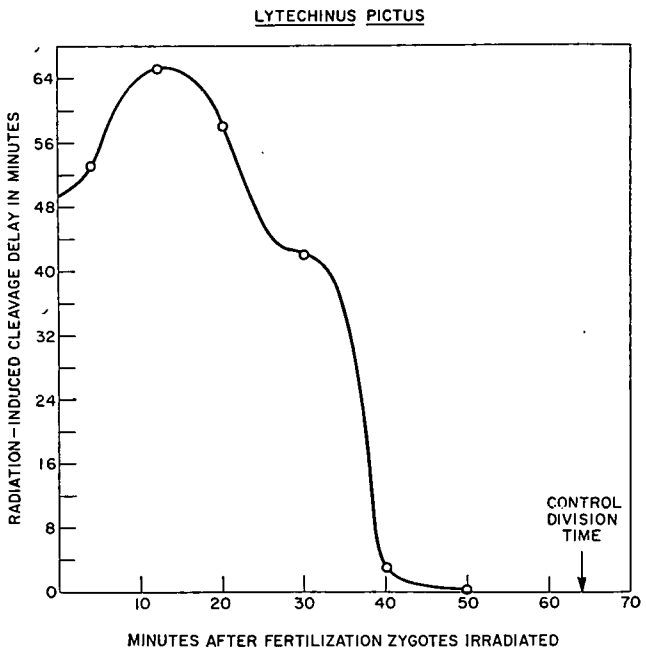

FIG. 53. Sensitivity to radiation-induced cleavage delay as a function of time after fertilization that the zygotes were exposed.

Temperatures of about 0° C have been shown to inhibit strongly the pre-[5] and postfertilization[5] recovery processes. Since a drop in temperature also increases the time to first division of fertilized eggs it seemed advisable to determine the effect of temperature on the cleavage delay produced by a certain dose of radiation. Accordingly, eggs of *L. pictus* fertilized with irradiated sperm were allowed to develop at 24°, 15°, and 8° C. The cleavage delay was found to be the same—independent of the temperature. It seems, therefore, that the increase in recovery that should result from the longer division cycle is compensated for by the reduced recovery rate.

DISCUSSION

It has been shown to be feasible to carry out research with sea urchin gametes almost throughout the year in a locality almost 100 miles from the nearest ocean. Admittedly the conditions are far from ideal, but it is hoped that many of the difficulties can soon be identified and overcome. Communication has bee established with other investigators who encounte similar difficulties working under similar conditions. It is hoped that this cooperation will help speed the solution of these mutual problems.

SUMMARY

Artificial sea water conditions have been established to permit year-round research with sea urchin gametes. A number of phenomena, such as pre- and postfertilization recovery from radiation-induced cleavage delay have been confirmed using a different species of urchin. Postfertilization recovery has been demonstrated during the time the division cycle is prolonged by treatment with sodium azide, an inhibitor of aerobic metabolism. Similar treatment with colcemide has given equivocal results.

The radiation-induced cleavage delay has also been shown to be independent of the temperature at which the fertilized eggs are allowed to develop (between 8° C and room temperature). This implies a compensation between the temperature-mediated increase in time for recovery and the reduced recovery rate. Finally, the variation in sensitivity to radiation-induced cleavage delay of developing zygotes of *Lytechinus pictus* during the first division cycle has been found to be similar to that exhibited by *Arbacia punctulata* and *Strongylocentrotus purpuratus*.

The assistance of Jean Robisch and Janet Prince in carrying out these studies is gratefully acknowledged.

REFERENCES

1. P. S. Henshaw. Further studies on the action of roentgen rays on the gametes of *Arbacia punctulata*. *Am. J. Roentgenol.* **43**, 899–933 (1940).
2. P. S. Henshaw. Studies of the effect of roentgen rays on the time of first cleavage in some marine invertebrate eggs. I. Recovery from roentgen-ray effects in *Arbacia* eggs. *Am. J. Roentgenol.* **27**, 890–898 (1932).
3. Patricia Failla. *In vivo* and *in vitro* recovery of irradiated gametes of *Arbacia punctulata*. *Radiation Res.* **17**, 767–773 (1962).
4. Patricia Failla. Recovery from radiation-induced delay of cleavage in gametes of *Arbacia punctulata*. *Science* **138**, 1341–1342 (1962).
5. Patricia Failla. Recovery from divison delay in irradiated gametes of *Arbacia punctulata*. *Radiation Res.* **25**, 331–340 (1965).
6. A. H. Whiteley and E. L. Chambers. Phosphate transport in fertilized sea urchin eggs. II. Effects of metabolic inhibitors and studies on differentiation. *J. Cell. Physiol.* **68**, 309–324 (1966).
7. Bhashini Rao. Analysis of x-ray induced mitotic delay in sea urchin eggs. University of California, Lawrence Radiation Laboratory Publication UCRL-10979 (1963).

EXCRETION OF ^{210}Pb AND ^{226}Ra BY RADIUM-DIAL PAINTERS*

Richard B. Holtzman and Henry F. Lucas, Jr.

The excretion of endogenous ^{210}Pb and its precursor, ^{226}Ra, were determined in 11 human subjects 30 to 40 years after exposure to ^{226}Ra. The total body burdens of ^{226}Ra in these subjects were sufficiently high, 0.12 to 2.4 μCi, to cause excretion of ^{226}Ra and ^{210}Pb in quantities much higher than normal. The measurements were corrected for the dietary content of these nuclides and for the ^{210}Pb grown from ^{226}Ra during storage of the samples.

For ^{226}Ra the daily fecal excretion rate averaged 0.008% of the retained burden; the comparable urinary rate was only about 1% of the fecal rate.

By contrast, the daily total excretion rate of the ^{210}Pb was only about 0.002% of the total body content of this nuclide (a rate about one-third that of the radium), and it was distributed nearly equally between the urinary and fecal routes.

* Abstract of paper presented at the Health Physics Society Annual Meeting, Washington, D. C., June 18–22, 1967.

CONCENTRATIONS OF THE NATURALLY-OCCURRING RADIONUCLIDES ^{210}Pb, ^{210}Po, AND ^{226}Ra IN AQUATIC FAUNA

R. B. Holtzman

INTRODUCTION

The concentrations and distributions of the radionuclides ^{210}Pb, ^{210}Po, and ^{226}Ra in the biosphere and more particularly in the human environment have been studied extensively. In addition to being among the oldest known radioisotopes and having been studied as industrial hazards, they are ubiquitous and contribute a substantial fraction of the natural radiation dose to humans[1-3] and to various biota.[4-6] Metabolic behavior of these nuclides is of interest because they are in the uranium-238 radioactive decay chain and may be considered as naturally-occurring tracers for the study of calcium metabolism in nature. The ^{210}Pb is also a tracer for lead which is of great toxicological interest in itself.

Although both the radium and lead are bone-seekers, and the ^{210}Pb is a decay product of the radium, their concentrations are not obviously correlated in the biosphere. As shown in the decay schemes in Figure 54, the ^{226}Ra decays to the 3.8-day ^{222}Rn, a noble gas which is easily translocated from its parent. The radon eventually decays through a series of short-lived daughters to the long-lived ^{210}Pb, which then is metabolized independently of the radium. Moreover, the ^{210}Po with its reasonably long half-life of 138 days is not necessarily correlated with its lead precursor because of their different chemistries and metabolic properties. The fate of the polonium is quite important because it contributes more than 95% of the biologically effective radiation dose of the ^{210}Pb-^{210}Bi-^{210}Po series. Thus, human populations consuming drinking waters with high levels of ^{226}Ra acquire relatively high concentrations of this nuclide,[1] but little excess ^{210}Pb.[2] In turn, caribou and reindeer in the Arctic acquire large amounts of the latter nuclide, but relatively little ^{226}Ra, a phenomenon attributed to the natural fallout of the ^{210}Pb onto their food base of slow-growing lichens.[7, 8] Finally, the ^{210}Po activities in the soft tissues of man and animals are usually several times those of its precursors.[3]

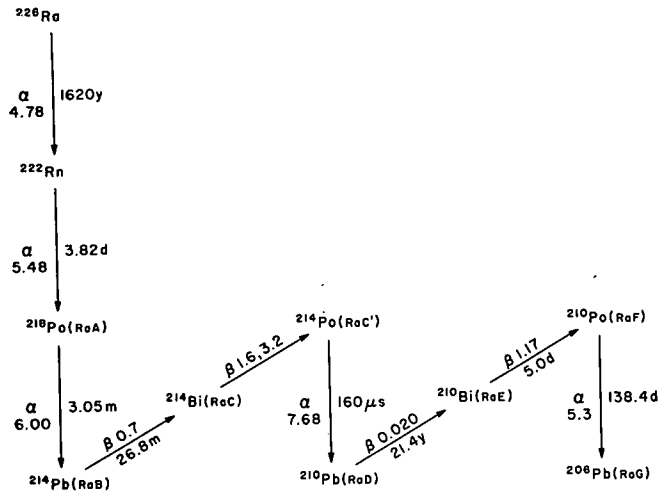

FIG. 54. Decay scheme for ^{226}Ra series

Although the distributions of these nuclides have been studied extensively in terrestrial environments such as food,[9] cattle,[4, 10] and humans,[2, 3] little is known of their concentrations in aquatic and, particularly, marine environments. The concentrations of ^{226}Ra and ^{210}Pb are well-characterized in potable waters,[11] but characterized less extensively in marine waters.[12] High concentrations of the polonium-210 have been reported in marine specimens, plankton, cockles, and crab,[9, 13] but the correlations between the various nuclides were not examined in detail. Such relationships are of importance since the marine life may constitute a large portion of the diets of some human populations. The lead-210 is of particular importance because it is long-lived and controls, in part, the availability of its two daughters.[14]

In addition to their usefulness in the estimate of background doses, such measurements may be of use in several ecological and biological problems, such as tracing food chains of animals and studying their metabolism.

Presented here is a preliminary survey of some relationships of these nuclides in a variety of aquatic fauna, many in the human food chain.

SAMPLING

The specimens under study came from several sources. The fish were obtained frozen from a local food store. Halibut and flounder were from off the Atlantic coast of the United States, pike was from the Great Lakes and herring (Silver Minch) from Scotland. Canned salmon and tuna were from the Pacific Ocean (near the U. S.), and the oysters and clam (canned) were from Japan. The specimens from Alaska, seal, salmon, pike and whitefish, were from the northern areas near Barrow. The data on these speci-

mens are taken from a previously published paper.[6] The samples of sperm whale tooth (No. II) and of baleen were obtained from a biological supply house and therefore of unknown origin. The other tissues, bone, tooth, muscle and food were from sperm whales from the Pacific Ocean near North America. Bone, muscle, kidney and blubber were from a fin whale caught at latitude 44° 6′ N, longitude 64° 8′ W.

The sea urchin (*Strongylocentrotus purpuratus*) was from the Pacific Coast near Los Angeles, California. In addition, several other specimens, representing part of the diets of whales were also measured: Krill (*Meganyciphanes norvegica*) were from the stomach of the fin whale, copepoda (*Calanus plumchrus*) were from the stomach of a 40-foot female sei whale, squid (*Anycholeuthis* sp.) was from a fur seal, but is a common species found in the stomachs of sperm whales; and finally, euphausia (*Euphausia pacifica*) were from the stomach of a 72-foot male blue whale. The dates of collection or estimates thereof are given with the results in Tables 38 and 39.

METHODS OF ANALYSIS

The ^{210}Po and its parent ^{210}Pb were determined by the previously described procedures in which the material was wet-ashed in nitric and perchloric acids and the nitrates were removed by fuming the perchloric acid.[2] After several additions of hydrochloric acid and further fuming, the ^{210}Po was removed from the solution of 0.5 *N* HCl at 95° C by plating onto a silver disk by the electrodisplacement method. The amount method. The amount of ^{210}Po was determined by counting the disk in an internal alpha counter.

The amount of ^{210}Pb present at the time of collection was calculated from the Bateman equations using the amount of ^{210}Po present at the time of the first counting and that grown into the solution four months after the first plating.

The ^{226}Ra was determined by the radon-emanation method of Lucas.[1]

The errors (95% confidence limits) are based on counting statistics only. ^{226}Ra was not measured in all specimens and ^{210}Po, because of its volatility and relatively short radioactive half-life, was not measured in some samples which had either been dry-ashed at 450° C or had been collected more than a year prior to measurement.

The data from bone and tooth are presented as concentration or specific activity in units of pCi/100g of sh content (or the equivalent $Ca_3(PO_4)_2$), on the asis that ^{226}Ra and ^{210}Pb are in the mineral phase of mineralized tissue. Moreover, use of these units tends to eliminate variations in wet weight of bone, which is very sensitive to methods of preparation such as drying, scraping and storage.[15] In other tissues the basis is pCi/100g wet tissue.

RESULTS AND DISCUSSION

The dates of collection and specific activities of the nuclides in the various specimens are listed in Tables 38 and 39 and the ^{226}Ra and ^{210}Pb activities are plotted in Figure 55. Included for comparison are the activities of these nuclides in human bone[2] and the activity of ^{210}Pb in U. S. cattle bone.[4] The ratios of the specific activities of ^{210}Po to those of ^{210}Pb in the various specimens are shown in Figure 56.

The origins of these nuclides and causes of variations of specific activities in the various groups are not clear from the available information, although some estimates are possible.

The bone of pelagic fish has a specific activity for ^{210}Pb of about 27 pCi/100g ash, a value about ⅓ that in bovine and about twice that in human bone. The specific activity of the ^{210}Po is about equal to that of the parent lead nuclide, but that of the ^{226}Ra is only 20% of the ^{210}Pb, 5.3 pCi/100g ash. This ^{226}Ra specific activity is about 4 times that found in humans drinking surface waters,[1] but only about 10% that in cattle.[4]

Fresh-water fish exhibit specific activities of these nuclides about ⅓ to ⅕ those in the pelagic specimens. These differences between the fresh water and pelagic data for ^{210}Pb appear to reflect dietary differences, since the concentrations reported in both salt and fresh water are nearly identical at about 0.1 pCi/1.[11, 12]

In mollusca (clams, oysters and squid), arthropoda and sea urchin, the concentrations of these nuclides are one to two orders of magnitude greater than in the soft tissues of fish, and they are comparable to those in the pelagic fish bone ash. Moreover, relative to the calcium content of the tissue, the lead-210 concentrations in the mollusca and arthropoda are 500 times those in fish bone.

Seals exhibit much lower concentrations of the lead-210 in bone than do the pelagic fish, but the concentration of ^{226}Ra, 6.9 pCi/100g, is about equivalent to that in fish. The concentrations of the lead in soft tissues are also equivalent to those in pelagic fish.

Variation of the relative distributions of these nuclides is shown in Figure 56 by the ratios of the specific activities of ^{210}Po to those of ^{210}Pb in the various groups of specimens. In bone and tooth (not shown) the ratio is about unity. However, in other tissues it ranges from 2 to 44. The non-bony hard tissues, such as urchin cctoskeleton and beak, and squid shell, also have ratios greater than in bone. Because of the large fraction of ^{210}Pb and consequently large fraction of

TABLE 38. ^{210}Pb, ^{210}Po AND ^{226}Ra IN TISSUES OF FRESHWATER AND MARINE ANIMALS

Sample (Date of collection)	Hard tissue (Bone, tooth, shell)				Soft tissue			
	^{210}Pb, pCi/100g ash	^{210}Po, pCi/100g ash	^{226}Ra, pCi/100g ash	Ratio $^{210}Po/^{210}Pb$	^{210}Pb, pCi/100g wet	^{210}Po, pCi/100g wet	^{226}Ra, pCi/100g wet	Ratio $^{210}Po/^{210}Pb$
Ocean fish								
Halibut 1 (8/10/64)	33.0 ± 3.1	29.5 ± 2.4	5.7 ± 0.8	0.89	0.044 ± 0.023	0.041 ± 0.02	0.22 ± 0.02	0.92
Halibut 2 (8/24/64)	8.2 ± 1.4	4.0 ± 0.2	5.0 ± 0.1	0.49	0.075 ± 0.033	0.059 ± 0.03	0.02 ± 0.01	0.78
Herring 1 (8/10/64)	38.8 ± 4.0	39.0 ± 3.2	4.3 ± 0.9	1.01	0.22 ± 0.04	1.50 ± 0.11*	0.04 ± 0.02	7.64
Herring 2 (8/1/64)	42.0 ± 4.0	59.1 ± 5.6	9.8 ± 1.1	1.41	0.23 ± 0.06	0.26 ± 0.08	0.03 ± 0.02	1.13
Flounder (8/24/64)	10.1 ± 1.8	25.2 ± 3.3	4.7 ± 0.9	2.48	0.09 ± 0.02	0.97 ± 0.18	0.51 ± 0.01	10.8
Ocean perch (fillet) (8/10/64)	—	—	—	—	0.09 ± 0.04	0.10 ± 0.03	0.00 ± 0.02	11.5
Salmon (canned) (8/1/64)	—	—	—	—	0.56 ± 0.08	0.30 ± 0.10	0.26 ± 0.03	0.53
Tuna (canned) (8/1/64)	—	—	—	—	0.13 ± 0.04	0.40 ± 0.13	0.06 ± 0.01	3.2
Salmon (Alaska) (8/1/62)	28.9 ± 2.4	—	2.4 ± 0.6	—	0.08 ± 0.02	—	0.27 ± 0.02	—
Averages ± S.D.	26.8 ± 14.4	31.4 ± 20.0	5.3 ± 2.5	1.2	0.17 ± 0.16	0.30 ± 0.32	0.16 ± 0.17	4.5
Freshwater fish								
Pike (Great Lakes) (8/24/64)	8.9 ± 1.3	1.2 ± 1.3	1.5 ± 0.5	0.13	0.03 ± 0.03	0.77 ± 0.08	0.02 ± 0.01	23.8
Pike (Alaska) (8/24/63)	4.7 ± 1.9	—	—	—	0.15 ± 0.04	—	—	—
Whitefish (Alaska) (7/1/63)	—	—	—	—	0.03 ± 0.02	—	—	—
	6.8							
Other sea animals								
Clams (canned, Japan) (8/1/64)					4.13 ± 0.20	12.4 ± 0.4	3.77 ± 0.09	3.01
Clams (juice) (8/1/64)					0.14 ± 0.04	0.03 ± 0.07	0.04 ± 0.02	
Oysters (canned, Japan) (7/20/65)					6.2 ± 0.2	21.2 ± 0.5	0.25 ± 0.03	3.43
Copepoda (*Calanus plumchrus*) (7/20/65)					12.1 ± 0.9	113.7 ± 3.4		9.42
Euphausia pacifica (6/1/65)					3.75 ± 0.33	26.7 ± 1.3		7.14 ± 0.10
Krill (*Megancyliphanes norvegica*) (8/25/65)					1.32 ± 0.02	5.29 ± 0.34		4.02
Squid (*Anycholeuthis* sp.) (beak)	15 ± 11	72 ± 36		4.7	0.92 ± 0.20	13.2 ± 0.9		14.4
Sea urchin (*Strongylocentrotus purpuratus*) (4/7/66)								
Shell	6.0 ± 0.5	12.2 ± 0.7		2.05				
Spines	5.0 ± 0.6	18.3 ± 0.9		3.63				
Fluids					0.19 ± 0.06	1.5 ± 0.11		7.89
Soft tissue					1.07 ± 0.27	15.1 ± 0.7		14.08
Jaws	3.7 ± 0.7	5.0 ± 0.7		1.36				
				2.3				11.0
Mammals								
Seals (Alaska)								
Spotted seal (7/8/63)	4.77 ± 0.07	—	7.4 ± 0.6	—	0.20 ± 0.07	—	—	—
Bearded seal 1 (7/25/63)	6.76 ± 1.03	—	6.4 ± 0.7	—	0.51 ± 0.13	—	—	—
Bearded seal 2 (7/25/63)	7.4 ± 1.0				0.26 ± 0.13			
Average ± S.D.	6.3 ± 1.4		6.9		0.32 ± 0.17			
Whales								
Fin (8/25/65)								
Blubber					0.02 ± 0.07	3.46 ± 0.26		
Dorsal muscle					0.23 ± 0.11	5.09 ± 0.37		21.6 ± 0.5
Kidney					0.55 ± 0.15	24.5 ± 0.8		44.2
Spine, dorsal	37.8 ± 4.0	35.2 ± 5.1		0.93				
Fluke, tail					0.077 ± 0.11	0.95 ± 0.21		12.3

TABLE 38. *Continued*

Sample (Date of collection)	Hard tissue (Bone, tooth, shell)				Soft tissue			
	^{210}Pb, pCi/100g ash	^{210}Po, pCi/100g ash	^{226}Ra, pCi/100g ash	Ratio ^{210}Po/^{210}Pb	^{210}Pb, pCi/100g wet	^{210}Po, pCi/100g wet	^{226}Ra pCi/100g wet	Ratio ^{210}Po/^{210}Pb
Baleen 1					4.3 ± 2.6 703 ± 0.53 (ash)			
Baleen 2					4.0 ± 0.7 373 ± 0.67 (ash)			
Sperm Whale (9/12/65)								
Whale I								
mandible	363 ± 15	326 ± 25		0.90				
muscle					~1	62.9 ± 1.2		
tooth (maxillary)	365 ± 18	290 ± 28		0.80				
Whales II to VI, see Table 39								

TABLE 39. ^{210}Pb, ^{210}Po AND ^{226}Ra IN BONE AND TEETH OF WHALES

Sample (Date of collection)	^{210}Pb, pCi/100g ash	^{210}Po, pCi/100g ash	^{226}Ra pCi/100g ash	Ratio ^{210}Po/^{210}Pb
Fin Whale				
Spine	37.8 ± 4.0	35.2 ± 5.1		0.93
Sperm Whales				
I. Mandible	363 ± 15	326 ± 25		0.90
Tooth	365 ± 18	290 ± 28		0.80
II. (Single Tooth)				
Base (outside)	302 ± 16			
Cementum (center)	319 ± 12			
Cementum (upper tip)	295 ± 11			
Core (near upper tip)	635 ± 3.6		10.1 ± 0.9	
Core (near upper tip)	465 ± 4.6			
Teeth:				
III. (age 65) (5/11/60)				
Tip	248 ± 16			
Base	416 ± 20			
IV. (age 38) (9/7/62)				
Tip	1220 ± 45			
Base	325 ± 18			
V. (age (19) (8/30/63)				
Tip	397 ± 17			
Base	261 ± 15			
VI. (age 31) (8/20/62)				
Tip (5 layers)	261 ± 40		52 ± 11	
Center (5 layers)	268 ± 34		74 ± 9	
Base (5 layers)	112 ± 20		63 ± 11	

^{0}Po in bone, this ratio in the total animal is unity in ertebrates, as represented by man.[14] The very low polonium-to-lead ratio observed in the pike may reflect lack of equilibrium in rapidly-growing specimens.

By contrast, in the invertebrates studied the ^{210}Po in the total animal is always many times that of its precursor. This indicates either a very high intake and retention of ^{210}Po relative to that of ^{210}Pb or that the life-span of the organism is short, that is, of the order of the half-life of ^{210}Po in the organism which is prob-

ably appreciably less than 138 days, the radioactive half-life of the nuclide. These high ratios may also indicate the mean residence time of lead in these organisms is short.

Consistent with previous estimates on man and Arctic biota,[2, 6, 7] most of the ^{210}Pb in the organisms examined here originates from sources other than the internally deposited ^{226}Ra, which is usually of much lower specific activity than the ^{210}Pb. Even in cases where the specific activities of the ^{226}Ra are comparable to those of the ^{210}Pb, the source must still be found elsewhere because the ^{210}Pb with its 22-year half-life grows in slowly, and, by analogy to the data cited by Mays et al.[16] on beagles, rats and man, 70% or more of the intermediate nuclide, ^{222}Rn, emanates from the animal.

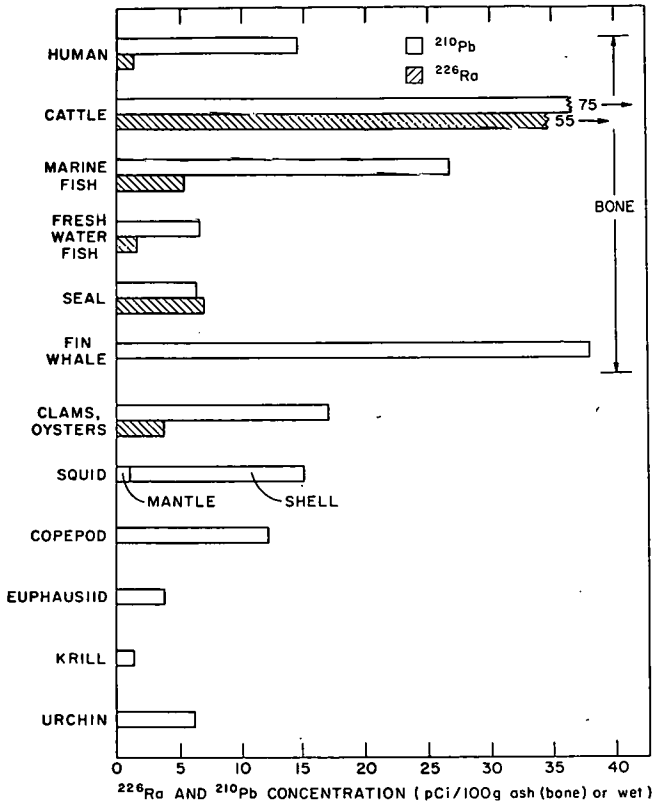

FIG. 55. Concentrations of ^{210}Pb and ^{226}Ra in the tissues of humans and the various fauna.

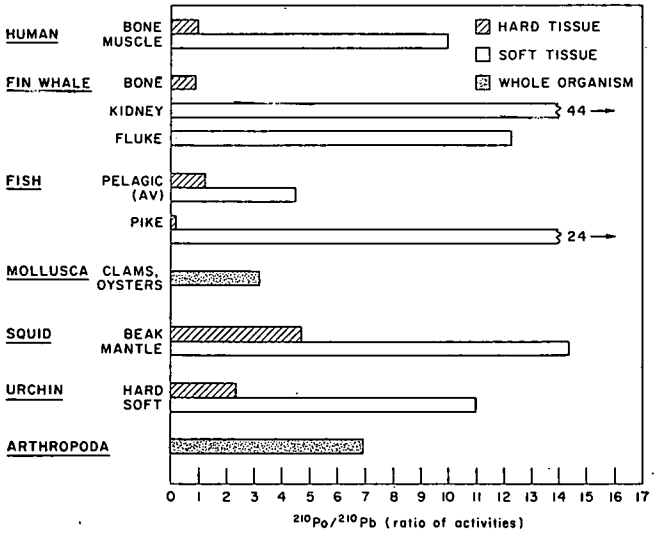

FIG. 56. Ratios of the specific activities of ^{210}Po to those of ^{210}Pb in tissues of humans and fauna.

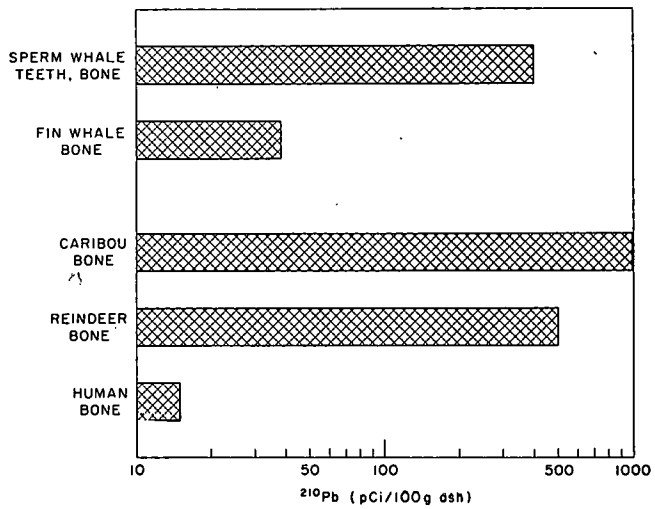

FIG. 57. Concentrations of ^{210}Pb in bones and teeth (higher level species and humans).

In whales the concentrations of these nuclides are higher than in fish, as shown in Tables 38 and 39. The ^{210}Pb concentrations are shown in Figure 57 on a logarithmic plot, and compared with human bone, and those from two species with the highest known levels, caribou and reindeer.

In the fin whale both the lead and polonium in bone are about 38 pCi/100g ash, each 50% greater than in pelagic fish and 3 times those in human bone. In the soft tissues these concentrations are much higher than in fish except for the tail fluke. That the kidney concentrates the ^{210}Po to the high levels comparable to those in bone, 24 pCi/100g wet, is a phenomenon consistent with that observed in sheep,[9] caribou,[17] and man.[3] The lead-210 is also concentrated, but to a much lesser extent.

Baleen, of unknown origin and species, is fairly high in the lead-210, about 4 pCi/100g. Further, relative to the ash content lead-210 is a quite high 500 pCi/100g ash.

By contrast to most animals, teeth from six differer sperm whales showed extremely high levels of lead-210, 100 to 600 pCi/100g ash. These levels are among the highest observed under natural exposures, com-

parable to the 1100 pCi/100g bone ash in Alaskan caribou.[5]

These high levels are also reflected in a few tissues from a single sperm whale (No. I) in which the concentrations in the mandible are identical to those in a mandibular tooth. Muscle showed high polonium-210 concentrations, even higher than the kidney of the fin whale but with little parent lead-210.

In addition to the estimation of the average amounts of Pb^{210} in teeth, more detailed measurements were also made, based on tooth structure and growth pattern. Thus, as shown in Figure 58, the sperm whale tooth consists of an outer layer of cementum and a core of dentin. The tooth growing from its base shows periodic (probably yearly) growth layers in both materials.[19, 20]

The concentrations of ^{210}Pb, shown in Table 39 and Figure 59 in Teeth IV and V of ages 38 and 19 years (laminae), respectively, show the tips to have concentrations of ^{210}Pb comparable to or greater than the base. In Tooth III, age 65, these results were inverted. In a more detailed experiment a tooth, VI, was sectioned longitudinally into about a 30μ thick section and the cementum was removed. Sections consisting of five layers each were removed from near the tip, the center, and the base, and each set was analyzed for ^{210}Pb and ^{226}Ra. The specific activity of ^{226}Ra was constant throughout the tooth, but for ^{210}Pb the tip and center sections were identical and significantly more active than the base. These relations are confirmed to some extent in Tooth II, a large one of unknown origin. In this case the concentrations in the tip are higher than those in the base. However, it should be noted that two adjacent, but otherwise apparently identical sections (d and e) differ significantly. The cementum appears to have a uniform distribution of the ^{210}Pb, the concentrations being essentially identical in sections of base, center and tip, possibly because of the large number of growth layers present in the samples taken.

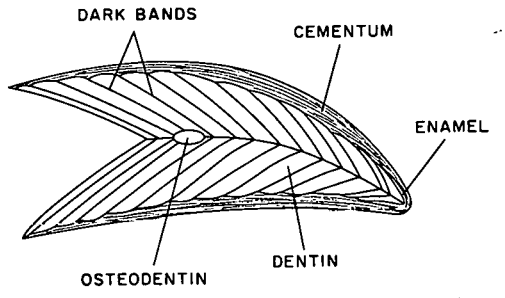

FIG. 58. Section of tooth of sperm whale (modified from Ref. 18).

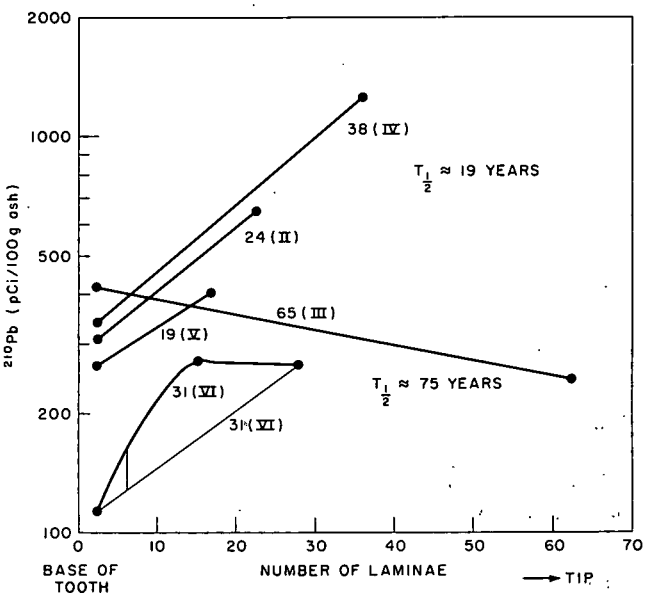

FIG. 59. Specific activity of ^{210}Pb in sperm whale teeth as a function of distance or number of laminae from base of each tooth. It is assumed that one lamina is formed per year.

It might be noted in Figure 59 in which the logarithm of the specific activity is plotted against the number of laminae, the slopes are fairly constant with about a 19-year half-life, but in the wrong direction; that is, except for the 65-year old specimen, the slopes increase instead of decrease. Moreover, there appears to be little difference between center and tip. Thus, these data indicate that either the ^{210}Pb intake varies with age, it being higher at earlier ages, or that there is a migration of the ^{210}Pb in the tooth. It is also possible that the ^{210}Pb may be added directly to the surfaces of the teeth during capture of food. However, because most of the teeth are maxillary and not exposed, the most probable explanation is that at earlier times the intake (or retention) of ^{210}Pb relative to calcium is greater than at later times. If the intake of nuclides were constant with time and there were no diffusion of the nuclides through the tooth, the specific activities of long-lived nuclides such as ^{226}Ra (1625 years) would be fairly constant from the base to the oldest parts of the tooth near the tip. On the other hand, the specific activity of ^{210}Pb, (which decays with a 22-year half-life) should decrease in this direction.

These results might help to confirm ideas as to the rate of formation of the layers, thought to be yearly, and are very important in estimating the actual age of the animals studied. The contradictions observed between these ideas and the data, on the other hand, could be valuable in estimating variations of intake with age.

The relatively high levels of ^{210}Pb in sperm whale

teeth could originate in the dietary constituents, as squid, with about 1 pCi/100g wet. Thus, on a basis of bone equivalent ash [$Ca_3(PO_4)_2$] content of about 0.3% (as in oysters)[21] the squid would contain about 300 pCi/100g ash, as do whale teeth. Tissues of squid other than the mantle (such as liver) might possibly contain more of this nuclide. Although copepoda and euphasia are not direct components of the whale diet, they do form part of the diet of the squid.

Although it appears that the fin whale ingests food of fairly high ^{210}Pb content relative to that of the sperm whale, final levels are quite a bit lower in the former. On the other hand, if copepoda, with their 12 pCi/100g wet, are actually ingested by the sperm whale, they could constitute a large source of ^{210}Pb.

The data presented here indicate that these nuclides provide a substantial fraction of the total environmental dose to the fauna. The dose from marine sources is about 130 mrem/year (90 from internal and external ^{40}K, about 10 from fission products, and zero to 30 from cosmic rays, depending on depth). If we assume a relative biological effectiveness (RBE) of 10 for alpha particles, the 5.3 MeV alpha particles from ^{210}Po would produce about 1 rem/year for each pCi/g of wet tissue.[22] Thus, mollusca receive about 100 to 200 mrem/year from the ^{210}Po alone. The arthropoda receive as high as 1000 mrem/year from this source.

The dose rate to sperm whales is about 700 mrem/year to soft tissue compared to about 100 mrem/year in man.[23] Ninety percent of this dose to whales is from the ^{210}Pb-^{210}Po series alone. Studies of somatic radiation effects at low levels might be of some interest although materials may be difficult to acquire.

The contributions of these nuclides to the human diet from aquatic fauna appear to be relatively small. Mollusca, and also arthropoda and whales, would contribute substantial amounts to the internal radiation of man if they were consumed in large quantities. It is possible that special populations do consume such quantities, and it may be worth while to search for such groups with the view of instituting pertinent epidemiological studies.

I wish to thank F. H. Ilcewicz for most of the analyses. For the specimens of whale material I am indebted to members of the Fisheries Research Board of Canada (D. E. Sergent for many of the arrangements, to C. W. Nicol for the fin whale specimens, to G. C. Pike for many of the sperm whale specimens), and to D. W. Rice of the United States Department of the Interior Fish and Wildlife Service for other sperm whale teeth. The Alaskan samples were collected by W. C. Hanson and sent by D. G. Watson of the Battelle Memorial Institute Pacific Northwest Laboratory.

REFERENCES

1. H. F. Lucas, Jr. Correlation of the natural radioactivity of the human body to that of its environment: Uptake and retention of Ra^{226} from food and water. Argonne National Laboratory Radiological Physics Division Semiannual Report, July through December 1960. ANL-6297, pp. 55–66.
2. R. B. Holtzman. Measurement of the natural contents of RaD(Pb^{210}) and RaF(Po^{210}) in human bone-estimates of whole-body burdens. *Health Phys.* **9**, 385 (1963).
3. R. V. Osborne. Lead-210 and polonium-210 in human tissues. *Nature* **199**, 295 (1963).
4. H. F. Lucas and E. R. Di Ferrante. The Ra^{226}, Po^{210} and Th^{228} in bovine bone and teeth. *Radiation Res.* **27**, 718 (1966).
5. R. B. Holtzman. Natural levels of lead-210, polonium-210 and radium-226 in humans and biota of the Arctic. *Nature* **210**, 1094 (1966).
6. R. B. Holtzman. Ra^{226} and the natural airborne nuclides Pb^{210} and Po^{210} in Arctic biota. Argonne National Laboratory Radiological Physics Division Annual Report, ANL-7220, pp. 51–58 (1966); also to be published in the Proc. First Intern. Congr. of Intern. Radiation Protection Assoc., Rome, 1966.
7. R. B. Holtzman. The Pb^{210} (RaD) concentrations of some biological materials from the Arctic. Argonne National Laboratory Radiological Physics Division Summary Report, July 1962 through June 1963. ANL-6769, pp. 59–65.
8. C. R. Hill. Inst. Cancer Res., Royal Cancer Hospital, Belmont, Surrey, England. Unpublished.
9. C. R. Hill. Identification of α-emitters in normal biological materials. *Health Phys.* **8**, 17 (1962).
10. E. R. Di Ferrante. The natural concentrations of Ra^{226} in bovine bones and teeth. *Health Phys.* **10**, 259 (1964).
11. R. B. Holtzman. Lead-210 (RaD) and polonium-210 (RaF) in potable waters in Illinois. *The Natural Radiation Environment.* University of Chicago Press, Chicago, 1964, pp. 227–237.
12. Rama, M. Koide, and E. D. Goldberg. Lead-210 in natural waters. *Science* **134**, 98 (1961).
13. R. D. Cherry. Alpha-radioactivity of plankton. *Nature* **203**, 139 (1964).
14. R. B. Holtzman. The source of unsupported Po^{210} (RaF) in tissue. *Health Phys.* **10**, 763 (1964).
15. R. B. Holtzman. Desirability of expressing concentrations of mineral-seeking constituents of bone as a function of ash weight. *Health Phys.* **8**, 315 (1962).
16. C. W. Mays, M. A. Van Dilla, R. L. Floyd, and J. S. Arnold. Radon retention in radium-injected beagles. *Radiation Res.* **8**, 480 (1958).
17. T. M. Beasley and H. E. Palmer. Lead-210 and polonium-210 in biological samples from Alaska. *Science* **152**, 1062 (1966).
18. S. Ohsumi, T. Kasuya, and M. Nishiwaki. Accumulation rate of dentinal growth layers in the maxillary tooth of the sperm whale. *Sci. Repts. Whale Res. Inst.* **17**, 17 (1963).
19. D. E. Sergeant. The biology of the pilot or pothead whale *Globicephala melaena* (trial) in Newfoundland waters. *Bull. Fish. Res. Board Canada*, No. 132 (1962).

20. N. A. Mackintosh. *The Stocks of Whales*. Fishing News, Ltd., London, 1965.
21. J. H. Harley. Health and Safety Laboratory Manual of Standard Procedures. U.S. Atomic Energy Commission Report NYO-4700 (Rev.). (1964) pp. E-38-01-10 and E-38-01-11.
22. Report of the International Commission on Radiation Protection Committee II on permissible dose for internal radiation. *Health Phys.* **3**, 1–380 (1960).
23. R. A. Dudley. Natural and artificial radiation background of man. *Low-Level Irradiation*. Am. Assoc. Advan. Sci., Washington, D. C., 1959, pp. 7–31.

A RAPID AND PRECISE METHOD FOR THE ANALYSIS OF CALCIUM IN BLOOD SERUM

Frank H. Ilcewicz and R. B. Holtzman

INTRODUCTION

Although serum calcium has been determined by many methods, few offer the advantages of simplicity, use of microquantities of samples, high precision and accuracy, and correction for sample aging. Small samples allow continuous sampling of small laboratory animals and, if done precisely, allow observation of slight changes in serum calcium levels. Volumetric titrations, which use a minimum of equipment, are usually the standard methods. However, they generally require large samples and a fair amount of manipulation. The more recent methods of atomic absorption spectrophotometry, although potentially rapid and reasonably accurate suffer from the need for fairly large samples and clogging of the jets by serum protein. On the other hand, differential absorption spectrophotometry, along with calcium specific indicators and stable spectrophotometers, appears to offer sensitive and precise methods of analysis. Thus, Spare[1] used this method with murexide to estimate calcium in serum directly. Others[2, 3] used glyoxal-bis (2-hydroxyanil) in similar procedures. These dyes, however, fade during analysis and are sensitive to changes in serums caused by aging and to interferences when used in other substrates.

This paper describes an adaption of the murexide process of Spare[1] which gives a highly precise analysis of calcium in small volumes of serum (as little as 0.01 ml). Compensation is made for fading, variations in types of serum or plasma, and for aging of the specimen.

EXPERIMENTAL

Spectrophotometer

The measurements were made on a Perkin-Elmer Model 350 double beam recording spectrophotometer ith 1.0-cm silica cells.

Reagents

Murexide. This solution is made up to 0.1 mg murexide per ml of 2% water in propylene glycol. Fifty mg of murexide are dissolved in 10 ml of hot water and immediately filtered through a fine sintered glass filter with a 10-ml hot propylene glycol wash and diluted to 500 ml with propylene glycol. The optical density is used as a check on the concentration of the dye; 1.5 ml of indicator in 2.5 ml 0.044 *M* KOH compared to a reference cell containing water should read approximately 1.4 absorbance units (A) at 545 mμ at a time five minutes after addition to the KOH solution. When not in use, the murexide solution stored in a polyethylene bottle equipped with Repipet* is kept refrigerated to retard fading; with daily use the indicator fades at a rate of approximately 0.01 absorbance units per day.

Stock Calcium Standard

2.5114 g of dried $CaCO_3$ are dissolved in 5 ml concentrated HCl and diluted to one liter to give a liter of 1.00 mg Ca per ml. The working calcium standard is the stock solution diluted one to ten with water to give a concentration of 100 μg Ca/ml.

Potassium Hydroxide (0.044 M)

2.831 g KOH (87.2%) are dissolved in one liter of H_2O and stored in a polyethylene bottle.

Versatol (Lot 0518065)

Diagnostic reagent, General Diagnostics Division, Warner Chilcott Laboratories, Morris Plains, New Jersey. Reconstituted with 5.0 ml distilled water. The calcium concentration is 10.5 mg%, a value which appears to be correct.[4]

PROCEDURES

General

2.50 ml of 0.044 *M* KOH are pipetted with a 5-ml graduated pipette to each of the two 7-ml self-capping polyethylene vials. A 10–15 μl sample is pipetted into

* Labindustries, Berkeley, California. (This pipet cannot be used with the KOH solution because of contamination from the glass.)

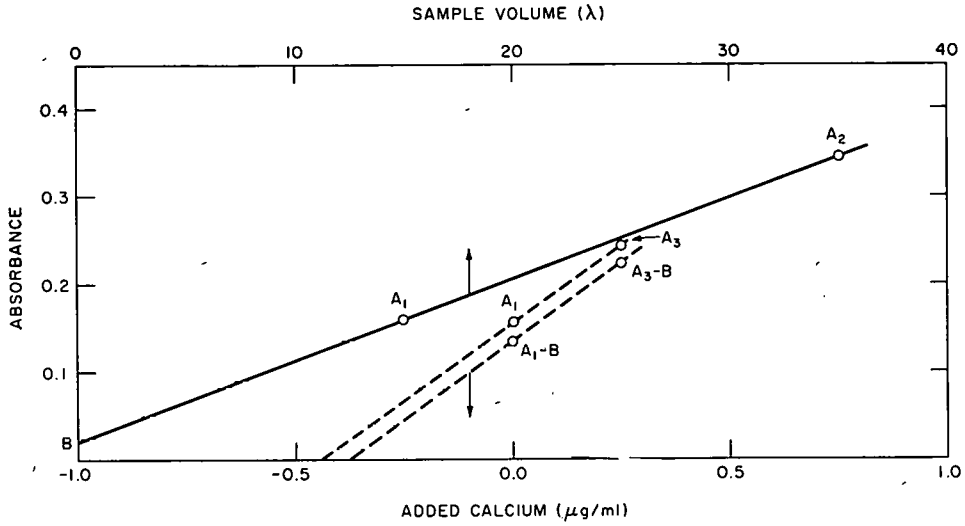

FIG. 60. Graphic solution for the method of additions

one of the vials and the pipette rinsed with the contained solution. The indicator (1.50 ml) is added to both bottles in rapid succession with a Repipet dispensing unit and the solutions mixed by repeated inversions in a manner slow enough to prevent foaming. The solutions are then charged into clean, dry cells, and the absorption peak of the sample solution read against the reagent blank at 497 mμ 5 minutes after the addition of the dye. The ratio of the absorbance of the sample to that of an equal volume of 0.1 μg Ca/μl calcium standard multiplied by ten equals the concentration of the calcium in the sample (mg %).

The rapidity of operations allows 3 samples and a reagent blank to be dispensed and run at one-minute intervals without affecting the accuracy of measurement. In this case the average time of dye addition is used. Although the absorbance measured was linear with volume of serum from 5 to 35 μl amounts of 10 mg percent serum samples, it was necessary to correct for the definite absorbance at zero volume as shown in Figure 60 (solid line). This intercept was partially instrumental, but it was also sample dependent. The correction (absorbance intercept) was determined by using 2 samples of different volumes from the same specimen, usually 10 and 20 μl of serum. The intercept B is then

$$B = A_2 - \frac{A_2 - A_1}{V_2 - V_1} V_2$$

where A_1 and A_2 are the absorbancies for sample volumes V_1 and V_2, respectively.

The sensitivity of the method for given samples was checked by the method of additions, as shown in the dashed line (upper line is one made without taking into account the intercept), Figure 60. The concentration of the Ca in mg % is

$$(\mathrm{Ca}) = \frac{C(A_2 - B)}{A_3 - A_1}\left(\frac{4 + V_2}{10V_2}\right)$$

where A_1, A_2, B and V_2 are as above. A_3 is the absorbance for sample of volume V_1 with added standard, and C is the μg Ca added per ml of solution in the cells.

The results of the analyses of serum samples are given in Tables 40 to 42. Analyses on the reconstituted serum Versatol of known Ca concentration showed a variation of about 1.4% (σ) from the mean, which, in turn, was within less than 0.1 mg % of that value stated to be in the sample. Similarly, the reproducibility of measurements on serum from freshly drawn blood from a dog and from 2 rats in this laboratory was 1 to 2%. Serum from Rat II was slightly hemolyzed. Analyses on 2 portions of a pooled rabbit serum* stored frozen for 5 months before analysis showed a standard deviation of 1.6%, even though the samples were thawed and refrozen several times over a period of several days. Further thawings resulted in excessively high absorbance intercepts and inconsistent results.

The accuracy of this method, as based on our results with the reconstituted serum, appears to be good. It was further substantiated by wet-ashing of the pooled rabbit serum before analysis. Ten ml of the serum, which had been refrigerated for 5 months was wet-ashed in a Teflon beaker with the minimum amounts of nitric and perchloric acids necessary to destroy the organic material. The results given in Table 43 are essentially identical with those on the unashed serum.

In order to determine the optimum conditions, various aspects of the procedure were studied, namely the effect of pH on sensitivity and fading, and the rates of

* Fisher Scientific Company, Chicago, Illinois.

fading under various conditions. The general procedure was followed. Equal volumes of Versatol and calcium standard were used along with different concentrations of potassium hydroxide; with 0.067 *M* KOH (pH 12.5), the solution containing Versatol faded at a slightly greater rate than did that with the calcium standard; with 0.044 *M* KOH (pH 12.3) the fading was reduced in both the Versatol and the calcium standard solutions; and with 0.023 *M* KOH (pH 12.1) the fading rate of neither sample was reduced, but the peak of the Versatol sample was slightly augmented and displaced to a lower wavelength, possibly because of interference from magnesium.[5] Therefore, the 0.044 *M* KOH solution appeared to be the optimum solution for this procedure.

The fading rates of the Ca-dye complex were somewhat greater than those of the pure dye and were also dependent on the sample. Relative to the reagent blank, 35 μl of Versatol and Ca standard faded at about 0.001 and 0.0005 A/min, respectively. The reagent blank, in turn, faded at about 0.003 A/min relative to a water reference. These rates are thus low enough that, with the use of automatic pipets and careful timing, one may run three samples at a time with a minimum of error.

Several precautions are necessary with this method

TABLE 40. Calcium Determination in Versatol
(Lot 0518065 = 10.5 mg % Ca, Reconstituted 3/9/67)

Date	Volume, μl	Intercept, A	Slope, A μg^{-1} ml^{-1}	Ca, mg %
3/14/67	10	0.010	0.345	10.3
	20	0.010	0.345	10.4
	35	0.010	0.345	10.4
3/28/67	10	0.010	0.349	10.7
4/10/67	15	0.018	0.345	10.4
	25	0.018	0.345	10.6
	35	0.018	0.345	10.4
Mean				10.46
S.D.				±0.14

TABLE 41. Calcium Determination in Different Plasma Samples
(Refrigerated Only)

Sample	Age, days	Volume, μl	Intercept, A	Slope, A μg^{-1} ml^{-1}	Ca, mg %
Dog	0	10	0.025	0.347	10.5
		25	0.025	0.347	10.6
		35	0.025	0.347	10.6
	11	15	0.024	0.333	10.8
	11	25	0.024	0.333	10.9
	11	35	0.024	0.333	10.9
Mean					10.7
S.D.					±0.2
Rat I	0	10	0.019	0.347	10.7
	0	15	0.019	0.347	10.6
	0	25	0.019	0.347	10.7
	0	35	0.019	0.347	10.8
Mean					10.7
S.D.					±0.1
Rat II	0	10	0.021	0.341	9.8
	0	15	0.021	0.341	9.7
	0	25	0.021	0.341	9.8
	1	10	0.020	0.338	9.7
	1	15	0.020	0.338	9.8
	1	25	0.020	0.338	9.8
Mean					9.8
S.D.					±0.1

TABLE 42. Precision of Calcium Determination in Frozen Rabbit Serum
(Aliquots Frozen 5 Months)

Sample	Thaw	Volume, μl	Intercept, A	Slope, A μg^{-1} ml^{-1}	Ca, mg %
Rabbit IA	2nd	10	0.021	0.334	12.8
		15	0.021	0.334	12.4
		20	0.021	0.334	12.8
	3rd	10	0.024	0.334	12.5
		10	0.024	0.334	12.2
		20	0.024	0.334	12.6
Rabbit IB	1st	10	0.025	0.325	12.8
		20	0.025	0.325	12.8
		15	0.025	0.341	12.2
		25	0.025	0.341	12.2
	2nd	10	0.025	0.325	12.7
		20	0.025	0.325	12.8
	3rd	10	0.023	0.338	12.8
		20	0.023	0.338	12.8
		15	0.017	0.353	12.5
		20	0.017	0.353	12.5
Mean					12.6
S.D.					±0.2

TABLE 43. Calcium in Wet-Ashed Rabbit Serum
(10 ml from Rabbit 1, Refrigerated for 5 Months, Diluted to 10 ml)

Volume, μl	Intercept, A	Slope, A μg^{-1} ml^{-1}	Ca, mg %
10	0.022	0.335	12.8
15	0.022	0.335	12.4
20	0.022	0.335	12.8
25	0.022	0.335	12.8
Mean			12.7
S.D.			±0.2

and checks on the quality of the analyses should be made. First, in order to dissolve the dye completely more water was used than in Spare's procedure (2% rather than 1%), and the dye solution was initially filtered. Second, because the die fades at the rate of about 0.01 absorbance unit per day it is good only for about a month. The quality of analysis may be checked by several methods. First, to check on the condition of the serum and pipetting accuracy the second sample A_3 (serum + calcium standard) was run against the first sample A_1 as reference (an equal volume of serum) after the initial readings (eight to nine minutes after dye addition). This absorbance should equal the absorbance of the same quantity of calcium standard measured against a reagent blank. Second, the recording spectrophotometer provides a check on the relative concentration of colorimetric agents in the solution. Thus, in the case presented here, there are two components. The differential absorption spectrum of Ca-sample versus reagent blank shows a negative peak near 545 mμ and a positive one around 497 mμ. When the initial concentrations of dye in sample and blanks are identical, the crossover point at about 535 mμ from negative to positive peak should occur near zero absorbance. Moreover, for samples identical, except for Ca content, this crossover or isosbestic point,[6] even if not at zero absorbance, should occur for all samples at the same point (wavelength and absorbance) regardless of the Ca content of the samples. The lack of such a point for three or more samples indicates a nonuniformity in the procedures.

Several potential interferences are present in serum relative to that in the Ca standard solution. For a given quantity of Ca, as the serum volume is increased the results deviate from Beer's law sooner than do the purely inorganic standard solutions, and the intercept is always higher than in the former case. Moreover, as the serum ages the absorbance intercept increases to about 0.030 absorbance units, where the reproducibility is impaired. The length of the linear portion of the plot of absorbance against volume also decreases with age of the sample.

Mager and Farese[2] attributed this decreased linearity in serum to the presence of phosphate and suggested that the Ca-P product should be limited. Bellinger and Campbell[3] suggest the aging effect might be due to binding at the glass surface or in protein which could be corrected by incubating at 37° C. However, the ability of our method to compensate for the aging and the recovery of the full amount of Ca on wet ashing is not consistent with this surface-effect explanation. The apparently lost Ca would be recovered from serum removed directly from the container without involving the container surfaces. We found their method to work for frozen rabbit serum, but not for those specimens which had only been refrigerated.

The sensitivity (slope) of the plot of absorbance versus volume determined by the method of additions was found to vary slightly for different samples and for repeated determinations of the same sample. In using a minimum number of 3 points to determine the slope and the blank, precautions should be taken that the capacity of the dye is not exceeded. The nonlinearity of both curves occurs gradually, and the interpretation of the curve is dependent on pipetting accuracy. The volumes of the serum and standard used should be well within the linear portion.

Because of the variations in intercept and slope, the method of additions and intercept determination should preferably be applied to each sample and repeated when values are obtained at different times. However, the corrections necessary on a given type of sample, such as freshly drawn blood from a given type of animal, remain fairly constant and a single measurement for each sample, rather than the 3 recommended, can be used after determination of the slope and intercept. These corrections should be determined daily and for different types of specimens.

In summary, the method proposed for the analysis of Ca in serum or plasma is very rapid, particularly if a large number of samples are to be processed. The precision and accuracy are about 1½% and could probably be improved through practice and modified techniques. A large part of the errors appears to be in the chemical manipulations, particularly pipetting. This method lends itself to checks in the reproducibility without using diagnostic reagents, the properties of which are not necessarily identical to those of serum. Finally, it is possible to correct for constituents in serum which cause changes in sensitivity with aging and deviations from Beer's law.

REFERENCES

1. Peter D. Spare. *Clin. Chem.* **10,** 726 (1964).
2. Milton Mager and Genvieve Farese. *Clin. Chem.* **12,** 234 (1966).
3. John F. Bellinger and Robert A. Campbell. *Clin. Chem.* **12,** 90 (1958).
4. Bernard Klein and Milton Weissman. *Clin. Chem.* **4,** 194 (1958).
5. Max E. Chilcote and Richard D. Wasson. *Clin. Chem.* **4,** 200 (1958).
6. Norman A. Share and Joseph I. Routh. *Anal. Chem.* **39** 414 (1967).

SURFACE/VOLUME RATIOS OF BONE DETERMINED BY COMPUTER ANALYSIS OF MICRORADIOGRAPHS

Elizabeth Lloyd, R. E. Rowland, Donald Hodges and J. H. Marshall*

INTRODUCTION

In a previous paper[1] the use of an automatic scanning device under the control of a computer was described for measuring the blackening of autoradiographs in order to examine the distribution of radioisotopes in microscopic areas of bone.

The present paper describes the use of the same system for obtaining surface/volume ratios by scanning microradiographs of bone sections.

Our interest in the surface/volume ratio of bone stems from the fact that some bone-seeking isotopes such as Pu^{239} and Am^{241} deposit specifically on bone surfaces. Calculations of the relative toxicity of these isotopes compared with those which deposit throughout the whole volume of bone (such as Ra^{226}) must include a factor for the surface/volume ratio. In addition autoradiographic studies have shown that at short times after the injection of a radioisotope of Ca, surface uptake predominates;[2] in order to assess its importance in calcium kinetic studies[3] it is important to know the surface/volume ratio for the whole skeleton.

Previously, the only methods available for determining surface/volume ratios involved tedious manual operations which were so time-consuming as to make representative sampling of a whole skeleton impracticable. In the present work a microradiograph of a cross section of bone could be scanned and a print-out of area and perimeter given within one minute. Knowing the thickness of each of the specimen samples of bone, this could be converted into total surface area and surface/volume ratio.

The use of some simple geometrical principles greatly simplified the computer programming.

EXPERIMENTAL METHODS

Individual bones from a complete adult human skeleton were cut into convenient sizes, usually about 5 cm in length, for embedding in methyl methacrylate. Sections 125 μ thick, and less than 1 inch square, were cut from these pieces. The sections were x-rayed using a Matchlett x-ray tube with a tungsten filament, operated at 5 kV and 20 mA. The section was mounted in close contact with a high contrast film (Eastman Kodak, fine grain, positive). This was loaded into a 35-mm camera attached to the exit port of the x-ray tube. A typical exposure for a section 125 μ thick was 4 minutes. The film was developed in a high contrast developer (dextrol, 1:1 dilution) for 1½ minutes. Figure 61 shows a typical microradiograph suitable for scanning.

The 35-mm film used here had several advantages over more conventional spectroscopic plates. First, scanning of the film to determine the perimeter and area was greatly facilitated by obtaining maximum contrast between the bone (white areas) and those where bone was absent (black areas). Second, 35-mm film made possible the automatic scanning of a large number of pictures on a roll of film: the computer program provided for film advance under the control of an on-line typewriter.

SCANNER

The automatic scanner (CHLOE) was designed for the study of spark chamber photographs. A detailed description of its design and operation is given elsewhere;[4, 5] for the sake of completeness, a very brief summary of the operation is included here.

A spot of light (about 25 μ in diameter) generated by a cathode ray tube is focused onto the film, and the transmitted light is detected by a photomultiplier. The light spot moves in discrete steps 28 μ apart in the x direction, then returns to make successive scans separated by 28 μ in the y direction. Thus the density of the film is effectively sampled in an area 28 μ square. All parameters of the scan including the rectangular

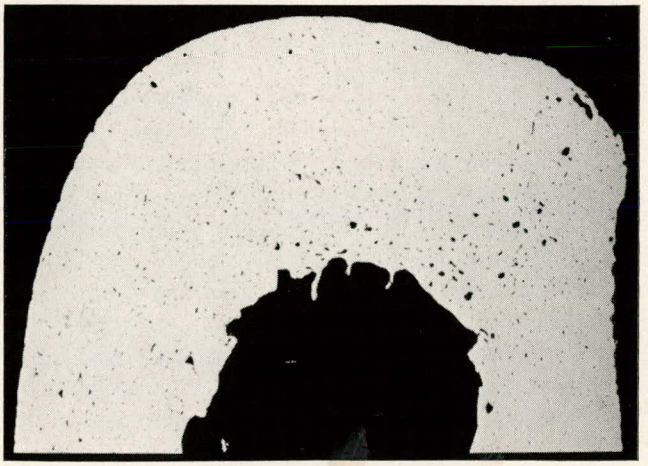

FIG. 61. Microradiograph of half of a cross section of cortical bone taken from the diaphysis of a human adult femur.

* Applied Mathematics Division.

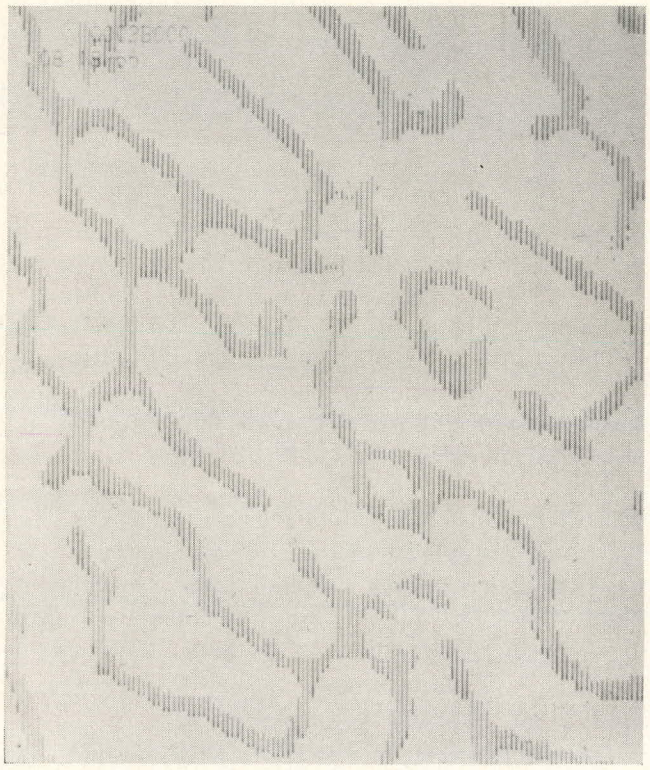

FIG. 62. Print-out of the line segments generated by the Computer Scanning Program over a small portion of trabecular bone.

boundaries of area scanned are under the control of the on-line typewriter. The scanner system records the coordinates of the point at which the light spot detects a change from black to white or from white to black. A pair of such points marks the beginning and end of a line segment parallel to the x axis, as shown in Figure 62. The equipment can be programmed so that the line segments lie over either white areas on a black background or black areas on a white background.

AREA

The area of bone is measured by taking the sum of the lengths of all line segments lying over the white area of a microradiograph (Figure 61) and multiplying by the vertical separation between scans. Figure 62 shows the line segments over a small portion of trabecular bone. The line segment length in each linear scan is obtained by subtracting the x coordinates of the beginning and end of each line segment when scanning in the x direction. These are summed for all of the line scans—about 1000 over the 1 inch square area. The scanning area is calibrated by using a 2-mm grid on 35-mm film and counting the number of scanning lines in each of the x and y directions corresponding to a known grid size.

Line segments which appear discontinuous because of interruptions by small vascular canals in bone (appearing as small black dots in Figure 61) are at present being linked if the separation in the x direction between successive line segments is less than 200 μ. This linking is used so that the measured area of bone includes all but the largest Haversian canals, but excludes large resorption cavities. A computer print-out of the area is shown in Figure 63. The uneven blackening of the line segments is an artifact in the DD80 printer. Only those cavities greater than 200 μ in width are seen because of the effect of the linking.

PERIMETERS

The perimeter of bone, P, is measured by counting the number of intersections, n, of the scan with bone surface and multiplying by $\pi d/2$, where d is the vertical separation between scans. The relationship $P = \pi nd/2$ has been shown to hold for both circular and random shapes.[6] It can be seen from the method of scanning described above that this simple relationship is especially suitable for use with the computer.

Periosteal Surface

The perimeter of cortical bone is measured by switching to the black-on-white mode and counting those line segments over the black portion surrounding the bone image (Figure 61) which do not have both ends on the scan boundaries. For periosteal perimeter, the computer is programmed to count only line segments with one end on a scan boundary. The scanning is done in both the x and y directions and a mean value obtained for the periosteal perimeter using the above formula.

When the bone approximates a semicircle, the pe-

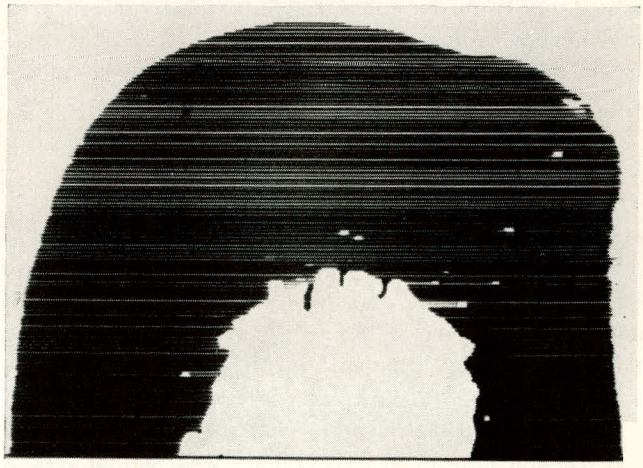

FIG. 63. A computer print-out of line segments seen over a cross section of bone. The outline is a good replica of that shown in the microradiograph in figure 61.

rimeter $P = \pi nd$, where n = number of line segments measured and d = distance between successive scans. However, if the shape were square the errors in perimeter using the above formula could be as much as 22%. This possible error due to the lack of randomness in the angles of the periosteal surface in a single bone section is easily reduced to <5% by placing the bone section at different angles relative to the x and y scanning directions.

Endosteal Surface

Measurements of the endosteal perimeter are made by again counting the number of line segments over the black area (Figure 61), but this time those line segments which start or end on the scan boundaries are excluded. In addition, black areas over the bone corresponding to small vascular channels can be excluded by imposing a minimum line segment length which is accepted by the computer. This length was set at 200 μ, which included large resorption areas in bone but excluded most of the Haversian canals.

RESULTS

Six cross sections of the diaphysis of the femur have been measured. These sections were taken at 1-cm intervals from portion 5 of the bone which was segmented as shown in Figure 64. In order to accommodate the section within a 1-in. square, the limit imposed by the scanning equipment, it was necessary to cut the cross sections in half longitudinally. Table 44 gives values obtained for the surface length of the periosteum and the endosteum. The area of bone and the surface to volume ratio are also given. It is interesting to note that in this segment of the diaphysis, where the number of trabeculations is small compared to the number in the metaphysis, the irregularity of the endosteal surface is sufficient to make its length almost the same as that of the periosteal surface, despite the fact that

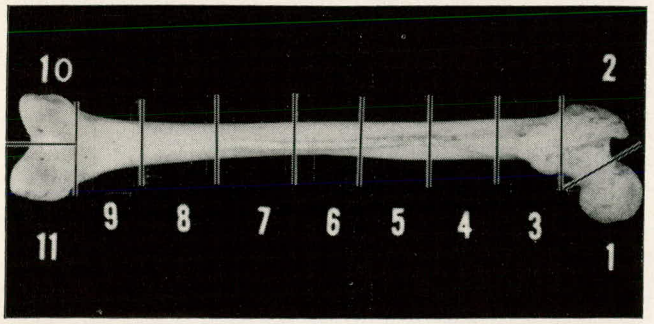

FIG. 64. Adult human femur, showing the cuts made before embedding each portion in methyl methacrylate. The bone was subsequently cut into sections 125 μ thick suitable for microradiography.

TABLE 44. PERIMETER AND AREA OF CROSS SECTIONS OF HUMAN FEMUR DIAPHYSIS

(*Segment 5*)

Section number	Periosteal perimeter, cm	Endosteal perimeter, cm	Area, cm^2	Periosteal perimeter/area, cm/cm^2	Endosteal perimeter/area, cm/cm^2	Periosteal + endosteal perimeter/area, cm/cm^2
1	8.7	10.8	4.1	2.1	2.6	4.7
2	8.8	9.6	4.1	2.2	2.4	4.5
3	9.0	8.3	4.2	2.1	2.0	4.1
4	9.0	7.5	4.2	2.1	1.8	3.9
5	9.1	8.1	4.3	2.1	1.9	4.0
6	9.1	8.7	4.2	2.2	2.0	4.2

TABLE 45. PERIMETER/AREA FOR CORTICAL AND CANCELLOUS BONE

Cortical, cm/cm^2	Cancellous, cm/cm^2	Reference
210	900	Jowsey[8]
—	100	Bromley et al.[10]

the diameter of the marrow cavity is about half the external diameter of the bone.

Inclusion of all the Haversian canals would increase the measurement of perimeter but would have little effect on area. When the contact microradiographs described above were used, the small canals were not resolved on CHLOE, but a study of a magnified image of the microradiograph is planned. Higher resolution scans may also be possible. In the segment of the diaphysis which has been measured, most of the Haversian canals were about 40 μ in diameter. This is close to the value of 50 μ in diameter reported by Johnson[7] and Jowsey[8] for adult man.

Values obtained by Jowsey[9] and Bromley et al.[10] for perimeter/area ratios are given in Table 45 for both cortical and cancellous bone. These values, unlike those in the present study, include all Haversian canals. Preliminary observations suggest that, even when allowance is made for Haversian canals and the smaller resorption cavities, our values given in Table 44 will not be increased by more than a factor of 5. This would place them at about 1/10th of those given by Jowsey.

Since only one skeleton was measured here, our values may be atypical, but the present investigation was primarily designed to study the variation between different bones and to assess a total perimeter/area ratio for the whole skeleton. Our system is ideally suited for the study of the more complex trabecular bone, which is very tedious by ordinary mechanical means. Measurements of cortical bone were carried out first to fa-

cilitate checking by ordinary map-measuring techniques. Trabecular bone studies are now in progress.

REFERENCES

1. E. Lloyd, J. H. Marshall, J. W. Butler, and R. E. Rowland. A Computer Programme for Automatic Scanning of Autoradiographs and Microradiographs of Bone Sections. *Nature* **211**, 661 (1966).
2. R. E. Rowland. Exchangeable Bone Calcium. *Clin. Orthoped.* **49**, 233–248 (1966).
3. J. H. Marshall and C. Onkelinx. Radial Diffusion from Canaliculi. An Explanation for the Retention of Alkaline Earths in Adult Bone. This report.
4. Donald Hodges. CHLOE—An Automatic Film Scanning Equipment, Hardware Reference Manual. Argonne National Laboratory Applied Mathematics Division Technical Memo Number 61, 1963. Unpublished.
5. Donald Hodges. The Liberator. Argonne National Laboratory Applied Mathematics Division Technical memo Number 127, 1966. Unpublished.
6. A. Henning. A Critical Survey of Volume and Surface Measurement in Microscopy. *Zeiss Werkzeitschrift* **30**, 78 (1958).
7. L. C. Johnson. Morphologic Analysis in Pathology: The Kinetics of Disease and General Biology of Bone. *Bone Biodynamics*, Ed. H. M. Frost. Little Brown and Company, Boston, 1964, p. 543.
8. J. Jowsey. Studies of Haversian Systems in Man and Some Animals. *J. Anat.* **100**, 857 (1966).
9. J. Jowsey, P. J. Kelly, B. L. Riggs, A. J. Bianco, D. A. Scholz, and J. Gershon-Cohen. Quantitative Microradiographic Studies of Normal and Osteoporotic Bone. *J. Bone Joint Surg.* **47-A**, 785 (1965).
10. R. G. Bromley, N. L. Dockum, J. S. Arnold, and W. S. S. Jee. Quantitative Histological Study of Human Lumbar Vertebrae. Research in Radiobiology, University of Utah Report COO-119-234 (1966) p. 191.

*A RADON REMOVAL SYSTEM FOR THE NASA LUNAR SAMPLE LABORATORY: DESIGN AND DISCUSSION**

Henry F. Lucas, Jr.

INTRODUCTION

The radon removal system required for the NASA Lunar Sample Laboratory should have excellent inherent reliability and good radon removal characteristics, even with complete loss of either water removal capabilities or loss of ability to cool the charcoal bed. From consideration of the normal operation (when loss of radon-free air is not important) and extrapolation to the condition following receipt of the lunar sample, a design has been developed for an extremely reliable radon removal system.

In general, failure of any individual components of the system does not immediately affect the radon removal characteristics of the system—or more importantly will have little or no effect on the radon level in the controlled air space of the counting facility for periods as long as 10 days. This system is shown schematically in Figure 65. Fortunately, the welded steel liner for the counting facility insures that the radon level without any input air flow will not change rapidly—as has occurred under certain conditions in the system originally constructed at the Argonne National Laboratory. Since repair or replacement of any individual component should not exceed one day, and the system is duplicated by a standby system, the probability of having no source of radon-free air is extremely small—and perhaps negligible. However, to cover even this potentiality, it is suggested that ten 300-ft^3 capacity cylinders of breathing air be stored and available to pressurize the counting space. For this, a flow rate of 0.2 SCFM is adequate.

The radon removal system described in this report should cost about $40,000.00 complete (2 units). It is designed to provide radon-free air (less than 10^{-16} Ci/liter) at a flow rate of 20 SCFM for more than 24 hours after complete loss of refrigeration to the charcoal bed. Similarly, operation will be unaffected for 24 hours after complete loss of air drier facilities so that air at 50% R.H. and 80° F dry bulb is used. Complete simultaneous loss of both the air drier and refrigeration capability is estimated still to provide radon-free air for more than 24 hours, but may be as little as 12 hours. This system includes all necessary controls and sensors required for normal and emergency situations. All research instrumentation previously described has been deleted. It has been assumed that the moisture content of the inlet air to the system is not greater than 50% R.H. at 80° F dry bulb. The measurements included in the discussion were selected from those available. A more complete discussion of the individual components follows.

* This report was prepared after repeated requests for isolated details of design and operation of the system in use at Argonne National Laboratory. The design presented here is not recommended for an ordinary whole-body counting facility.

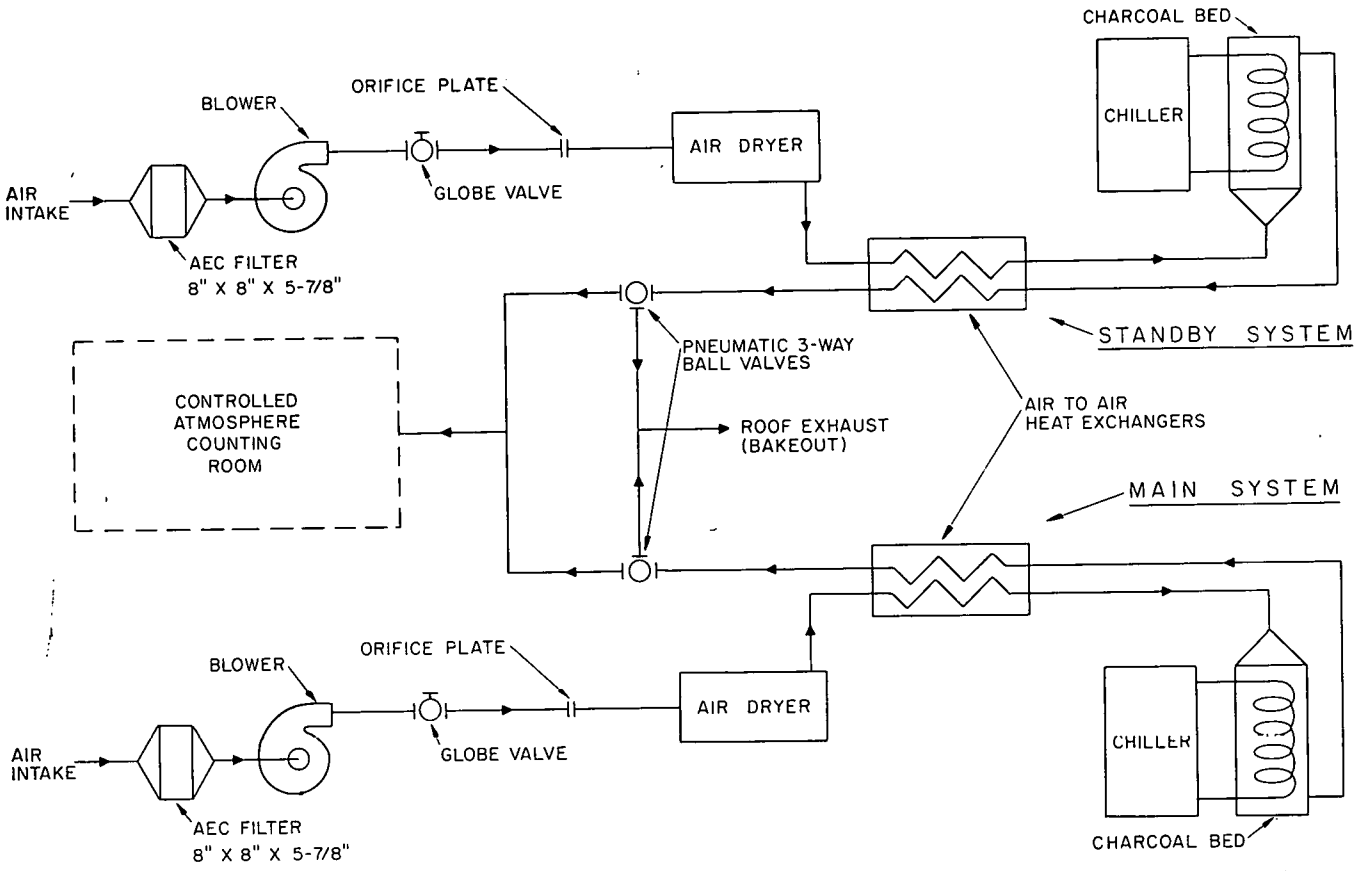

RADON REMOVAL SYSTEM FOR LUNAR SAMPLING LABORATORY

FIG. 65. Radon removal system for Lunar Sampling Laboratory

BLOWER

The blower (1)* gives about 70 SCFM of free air at 27 oz/in.^{2} in our system, which is more than sufficient. The original pulley on the blower turbine was only 3½ in. in diameter, and the old style thick belts would begin to squeal after 3 to 6 months. However, the present belts have been in use for nearly a year without any problem. We plan to increase the pulley size to 5 in. and replace belts annually. The blower has been in continuous operation for about 4 years.

AIR DRIER

Discussion

The air driers (2)* must be assembled as shown in Figure 66. (This figure was taken from the Lectrodryer General Instruction Book Number 1A and modified for the specific requirements of this system.) This system has been semiautomated for ease and simplicity of operation. This is accomplished by replacing valves A and B in Figure 66 with a pneumatic operated ball valve (3a).* For fail-safe operation, both valves must be open on loss of power to the pilot valves. With manual control of the reactivation cycle, the system will be attended and appropriate action taken if power failure occurs during this period. Power failure at any other time is of no consequence since either bed gives dry air.

The description of the operation of the Lectrodryer is given in the next section of this report. Since beds are operated to breakthrough, the time required to reactivate has been found to range from 6 to 7 hours. The temperature of the air from the preheater ranges from 675 to 725° F. Reactivation is not considered complete until the temperature at the reactivation outlet reaches 325° F. This high bed temperature means that any attempt to cool a bed quickly with water is slightly explosive unless extremely great care is taken. We, however, let each bed cool by standing, closing valves (E, F, G, H) and leaving both C and D open. The bed will cool below 100° C in about 10 hours, and cooling water may then be used to accelerate cooling, although the bed reaches room temperature in about 36 hours. We only use water cooling

* See list of possible suppliers at end of paper.

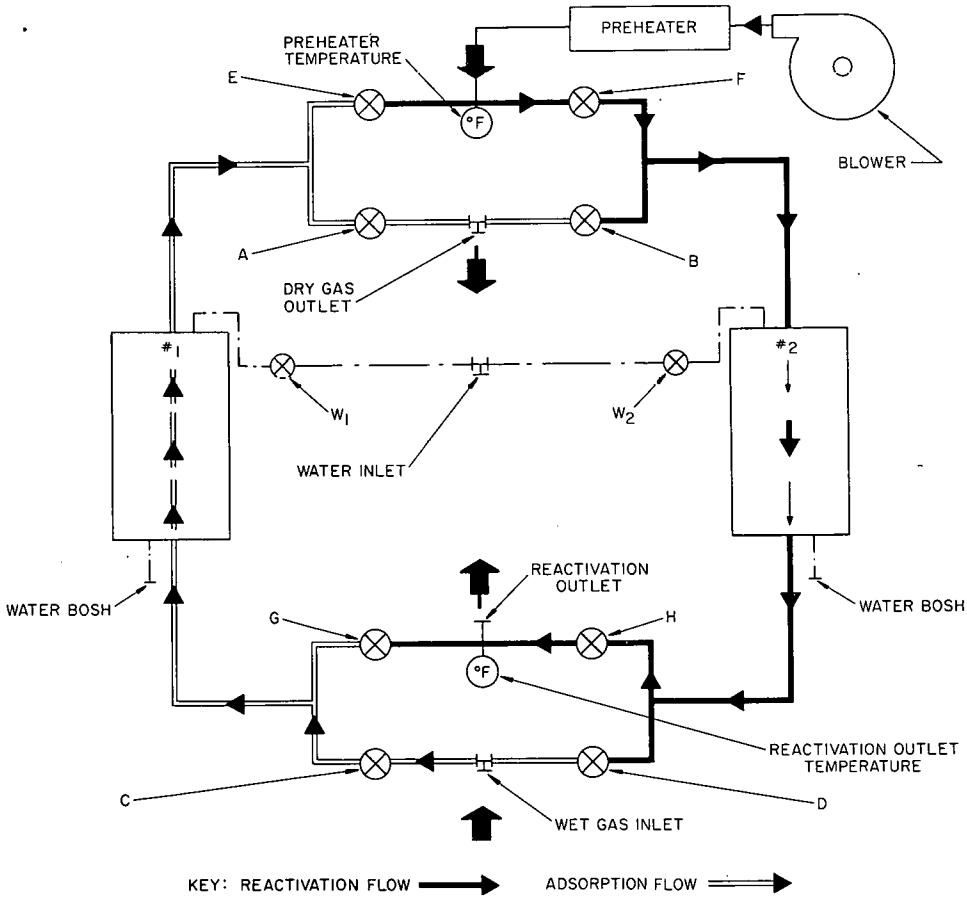

FIG. 66. Assembly of Lectrodryer

in an emergency. It should be noted that only valves E and F have high temperature requirements, and valves C, D, G and H could be ball valves similar to A and B, already described.

The reactivation exhaust must be vented to the outside and the piping insulated. If the length of the vent pipe (2 in.) exceeds 20 ft *or* has more than two 90° elbows, increase pipe size to 2¼ or 2½ in. This is essential.

Operating the Drier

1. Figure 66, shows the #1 absorber on drying service and #2 absorber on reactivation. Under this condition the valves A, F, C and H are open, and valves B, E, D and G are closed. Blower and preheater are on.

2. As a starting point visualize that #1 absorber is on drying service and that #2 absorber has been reactivated, cooled and is about to be switched to drying service. Before switching, the positions of the valves and controls are:

a. Valves A, C and D are open.
b. Valves B, E, F, G and H are closed.
c. Valves W_1 and W_2 are off except for a special reason to be discussed in text.
d. Preheater and blower are off.

3. To place #2 absorber on drying service instead of #1 absorber, open valve B and close valve A. These valves may be operated by an electropneumatic operator and automatically sequenced by a control circuit in the moisture analyzer.

4. Before beginning reactivation of absorber #1, the position of the valves are:

a. Valves B, C and D are open.
b. Valves A, E, F, G and H are closed.
c. Preheater and blower are off.

5. To reactivate absorber #1 while absorber #2 is on drying service, the position of the valves are:

a. Valves B, D, E and G are open.
b. Valves A, C, F and H are closed.
c. Then turn on preheater and blower.

6. Reactivation of absorber #1 will be comple after about 6 to 7 hours. Absorber #2 will continue drying service at least until absorber #1 has cooled. The valves and controls are:

a. Preheater and blower are off.

b. Valves B, C, and D are open.

c. Valves A, E, F, G and H are closed.

7. The sequencing of valves and controls described in 2 thru 5 above are summarized in Table 46, sequence 1 thru 4. Continued operation will place valves and controls in positions indicated in the table. Operation may be initiated at any sequence.

AIR-TO-AIR HEAT EXCHANGER

The two heat exchangers described in the earlier report[1] are not suitable for the present application since high humidity air from any failure of the Lectrodryer will quickly plug the unit. Further, with the other changes incorporated into this design, dual units are no longer required. The unit selected should maximize the surface area on which water or frost may accumulate. Thus, it is essential that the air from the drier enter the shell and the air from the charcoal enter the tubes of the heat exchanger (12).*

CHARCOAL BED

General Discussion

Radon is adsorbed onto the surface of the activated coconut charcoal. The activation energy is high so that the rate of migration through the charcoal bed under dynamic conditions is highly dependent on temperature. (The radon concentration in the outlet air from the charcoal bed is dependent on several variables of which both temperature and charcoal bed depth are important.) The outlet radon concentration for a bed 50 cm long at −60° C is equal to or less than 1.0×10^{-17} Ci/liter. This concentration is very much less (~1%) than that required for maintaining a "radon-free" counting facility. The limiting radon concentration is determined by the "emanating radium" in the equipment and personnel within the counting facility.

The charcoal bed shown in Figure 67 has been designed to provide an outlet radon concentration of less than 1.0×10^{-16} Ci/liter for a period of 24 hours after the loss of all refrigeration, loss of air drier or both. This could not be achieved except (1) the air-to-air heat exchanger is very efficient, (2) the heat capacity of the approximately 350 pounds of charcoal is large, (3) radon retention in a bed of this length is still high for a mean temperature of −20° C, and (4) the system has a high tolerance for water or frost. All calculations and extrapolations are conservative so that low radon concentrations may be obtained for even longer periods of time.

* See list of suppliers.

TABLE 46. OPERATION OF LECTRODRYER VALVES AND CONTROLS

Valve[b] or control	Operation cycle in each absorber[a]							
	Absorber No. 1							
	AB	OFF	BO	CL	AB	AB	AB	AB
	Absorber No. 2							
	OFF	AB	AB	AB	OFF	BO	CL	OFF
A	X	O	O	O	X	X	X	Same as Sequence 1
B	O	X	X	X	O	O	O	
C	X	X	O	X	X	X	X	
D	X	X	X	X	X	O	X	
E	O	O	X	O	O	O	O	
F	O	O	O	O	O	X	O	
G	O	O	X	O	O	O	O	
H	O	O	O	O	O	X	O	
Preheater	O	O	X	O	O	X	O	
Blower	O	O	X	O	O	X	O	
Sequence	1	2	3	4	5	6	7	

[a] OFF = a cool unused absorber; AB = absorber in service for dry air; BO = absorber being reactivated; CL = absorber being cooled after reactivation; X = This valve in Figure 66 is open or power is on; O = This valve in Figure 66 is closed or power is off.

[b] Valve number in Figure 66.

Carbon Dioxide

Carbon dioxide at concentrations of about 5% affects radon retention, while at normal atmospheric levels of 0.02 to 0.05%, no effect on radon retention can be measured. It should be noted that carbon dioxide is absorbed on the charcoal as is radon. However, carbon dioxide, unlike radon, does not undergo radioactive decay so that the concentration in the outlet air quickly reaches that of the inlet.

Water

Not all of the water in the air from the drier will be removed in the heat exchanger. In addition, this remaining water has a finite vapor pressure and will slowly migrate to the charcoal bed. It was originally thought that this water would accumulate in or on a charcoal bed located in the air stream between the heat exchanger and the entrance to the charcoal bed. However, recent measurements have shown that the temperature of the air leaving the heat exchanger ranges from −50° C to −70° C as the flow rate varies from 10 to 30 SCFM. Experiments have also shown that water (or frost particles) in air at this temperature accumulates at the points of turbulence which, in this case, is the face of the charcoal bed. The amount of water required to plug the charcoal has

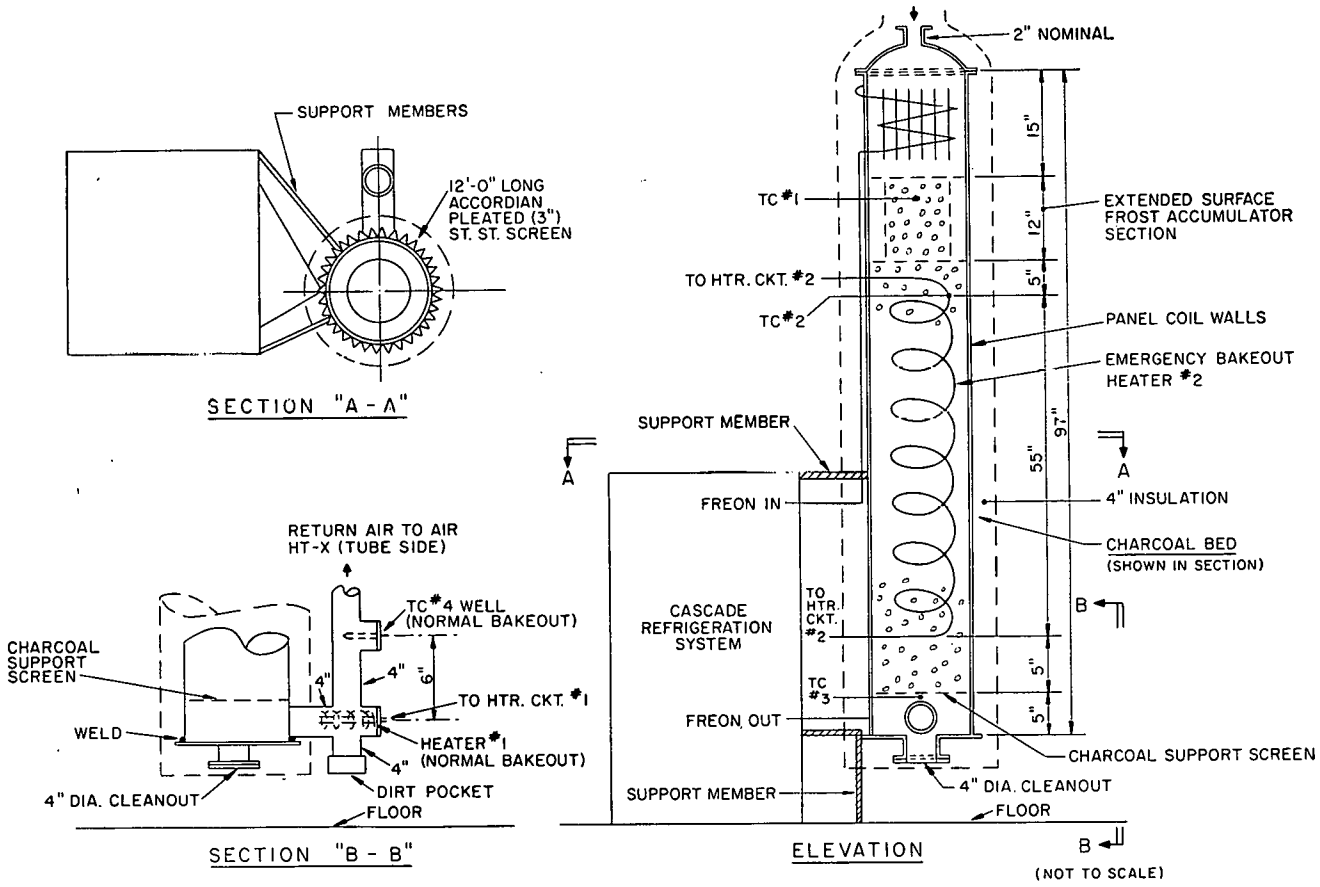

FIG. 67. Charcoal bed for Lunar Sampling Laboratory

been studied. While extrapolating from the much smaller system is subject to considerable error, the value of 300 g water/ft^2 of charcoal surface appears to be reasonably correct, since it is approximately equal to the pore volume in a loosely packed 6–8 mesh activated coconut charcoal bed. Our present charcoal bed has a fiberglass mat at the entrance. When the charcoal is compacted, the pore space is very small and plugging occurs with only about 60 g water/ft^2. From this, it is essential (1) that the previously suggested 300-pound charcoal bed prefilter be removed from consideration; and (2) that the surface area of the charcoal bed be as large as possible.

As shown in Figure 67, the exposed surface area of the proposed charcoal bed is essentially that of a 1′ 3″ wide by 12′ long accordian-pleated stainless steel screen. If one assumes that 12″ of the 15″ screen width is not covered by charcoal, then the 12 square feet of exposed charcoal should accumulate a total of about 3.6 kg or 8 pounds of water before plugging. This amount of water in addition to that removed by the air-to-air heat exchanger insures that plugging will not occur even with complete failure of the air dryer for periods of time in excess of 24 hours.

Chiller

The shell of the charcoal bed and the finned heat exchanger at the top of the charcoal bed in Figure 67 are both cooled by direct expansion of Freon-13. The capacity of the cascade refrigeration (13)* equipment is sufficient for flow rates to 40 SCFM in this system. For flow rates less than 20 SCFM, the temperature of the bed will approach −95° C. Continuous operation at temperatures below −85° C is not recommended and a timer or low pressure cutout should be included in the Freon-13 controls. A one hour timer, adjustable from 2 to 98% is recommended for reliability and freedom from "short cycle" problems. At 10 SCFM and 40% on time per hour, this system will give temperatures ranging from −60° C to −80° C at the inlet and less than −60° C at the outlet of the charcoal bed.

The system may be operated at flow rates as hig as 100 SCFM if the capacity of the Freon-13 system is

* See list of suppliers.

increased appropriately. However, this will result in a reduction in the time interval during which loss of refrigeration will have no effect on the radon concentration.

Assembly Sequence for Chiller-Charcoal Bed

1. The shell of the charcoal bed is formed from a single sheet of 43″ × 95″ carbon steel Panelcoil (4),* rolled and welded to give a cylinder having a nominal inside diameter of 13.7 in. Holes for the emergency heater bulkhead fittings, thermocouple fittings, 1″ wide heavy duty flange at the top, and the 2″ pipe at the bottom are to be all installed by the vendor.

2. The shell should be securely mounted to a support frame also containing the cascade refrigeration unit.

3. Check Panelcoil for leaks using Freon type leak detector.

4. The emergency heater is formed from a straight tube which has a heated length of 16′, and an unheated length on each end of 2′. This heater should dissipate 500 watts nominal at 115 volts AC, and should have a steel sheath. Beginning 2′ from each end, the heater is formed into an 8 turn 7″ diameter (nominal) coil. The unheated lengths on each end pass through the wall of the shell and should be bent such that their projection passes through the centerline of the coil, i.e., when installed, any point on the heater coil is equidistant from the wall of the shell. If the heater is constructed of ¼″ carbon steel tubing, iron wire spacers must be used to give nearly equal vertical distances between the coils. Install emergency heater (5)*

5. Install copper/constantan thermocouple number 2 (6).* This thermocouple must contact the heater coil approximately 4′ from its upper end or on the second coil. Wrap the heater coil and the thermocouple with iron wire to insure intimate contact.

6. Install charcoal bed support screen.

7. Weld bottom plate onto shell, leaving clean-out port open.

8. Install thermocouple number 3 at bottom of charcoal bed.

9. Install 1′ 3″ wide by 12′ long accordian-pleated screen used for extended surface frost accumulating section.

10. Install approximately 350 pounds of 6–8 mesh activated coconut charcoal (7)* by pouring and gently tamping. Fill to within 1″ of top of the pleated screen. Clean out dust from bottom of bed through port provided.

11. Install thermocouple number 1, bend tip until it is approximately on centerline of charcoal bed and 4″ below the top of the bed.

12. Install fin-tube heat exchanger at top of bed. Connect to Panelcoil. Check for leaks with Freon type leak detector.

13. Install normal bakeout heater number 1 (8)* and thermocouple number 4 in return air line.

14. Install gaskets (9)* and clean out port on bottom and on top cover.

15. Pressurize to 5 psi gauge, check gaskets and bulkhead fittings for leaks using a bubble solution. If leak free, system should show less than a 0.5 psi pressure drop in 24 hours.

16. Connect low temperature Freon lines, testing as required (usually done by vendor on chiller).

17. Insulate with double layer fiberglass. Note: In the event the required vertical height is not available, then use the 46″ wide Panelcoil (4),* while decreasing the height not more than 2 feet. The reduction in charcoal bed depth and weight will slightly reduce the time period over which loss of low temperature refrigeration will have no effect on outlet air radon concentration. Under normal conditions the shorter length will have no effect. It will be necessary to adjust emergency heater length. No other changes are needed.

Bakeout of Charcoal Bed

Bakeout of the charcoal bed is required only for water removal, and this is complete when the temperature at the exit end of the charcoal bed reaches 150° C. The temperature within the bed is limited to 225° C by the oil used in the refrigeration system. This temperature is much less than the charcoal autoignition point of 389° C.

Fire in the charcoal bed is prevented by placing the normal bakeout heater (10a)* (No. 1, Figure 67) in the pipe external to the bed and on the return air line. Heater placement at this point accelerates melting of any frost accumulated in the air-to-air heat exchanger, which further limits inlet air temperature to about 200° C—well below the autoignition point. The temperature of the air is measured by the adjacent thermocouple #4 and is maintained by the heat controller number 1 at a set point of 225° C. A nitrogen blanket or purge is not necessary since fire is extremely unlikely and can be put out by closing the air inlet valve or by cooling with the chiller.

In normal operation in which the moisture monitor automatically switches the drier absorbers when the water content reaches about 99 ppm, water accumulation by the charcoal is negligible, even over periods of several years. It is, therefore, possible that the bakeout heater will only be used at the time of

* See list of suppliers.

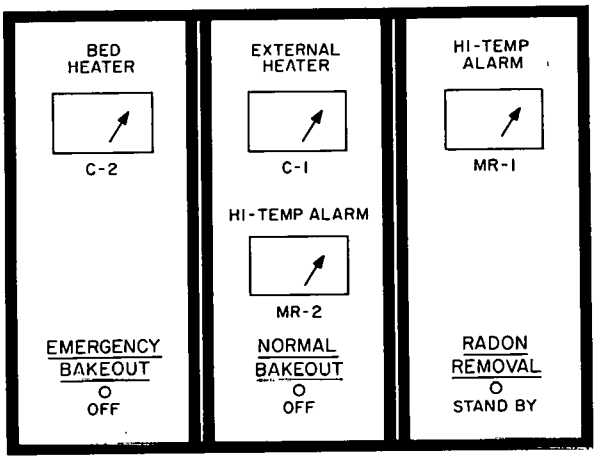

FIG. 68. Chiller-charcoal bed control panel

initial assembly. The only other time that bakeout will be required is when there has been an exceptional failure of the drier system. This failure must occur undetected for a substantial period of time since the outlet water concentration normally requires 3 to 30 hours to increase from 0.1 to 9 ppm and about 12 to 24 hours to reach 1000 ppm.

Consideration has been given to the emergency situation where a large amount of water has been accumulated in the system and a rapid bakeout is required. If more time were available, one would simply turn off the chiller, allow the charcoal bed to warm above 0° C and then initiate the normal bakeout. For the emergency situation, a second bakeout heater (№2, Figure 67) (10a)* is included. The temperature of the heating element is controlled by thermocouple number 2 and controller number 2 at a set point of 100° C.

The end of the bakeout cycle or excessive heat production within the charcoal from fire is sensed by thermocouple number 3 located at the exit of the charcoal bed. The temperature should be sensed by a locking coil meter relay (10b),* initiate an audio-visual alarm at a set point of 150° C, remove all power to the heaters, and turn blower off.

Restart of the chiller after bakeout of the charcoal is recommended only after it is allowed to cool by standing. In an emergency, the chiller may be restarted without any air flow (blower off), provided that trained personnel are present to monitor the power consumption of the chiller compressors and check that the proper cycling sequence is maintained.

Loss of refrigeration is noted by a temperature rise of thermocouple №1 which initiates an audio-visual alarm (10b).*

* See suggested list of suppliers at end of paper.

Electrical

Since the radon removal system may be operated by persons not very familiar with its design and hence its limitations, it is suggested that the chiller-charcoal bed control panel be of the form shown in Figure 68 in which the controls are grouped according to the three operating modes. In addition, the following conditions are suggested.

1. The master power switch to the control panel should be normally on.
2. The power switch for the radon removal section should be a multiple pole-double throw type so that power to the heater is only available when this switch is in the standby mode and, conversely, heater operation is prevented during chiller operation.
3. The power switch for the radon removal system should deactivate the audio-visual hi-temp alarm when it is in standby position. In addition, this switch should control power to the pilot relay on the 3-way ball valve (3b)* at the radon-free air outlet of the air-to-air heat exchanger. This valve prevents reverse flow of radon-free air through the system when the blower is off, and prevents flow of carbon monoxide, noxious gases or radon from entering the counting room during bakeout of the charcoal system.
4. The power for the emergency heater system should be available only when the "normal bakeout control" is on.
5. The blower must be on during bakeout of the charcoal bed.
6. The high temperature alarm (MR-2, Figure 68) during the bakeout cycle must remove power to the blower and bakeout heaters and provide audio-visual alarm.
7. Manual reset of audio-visual alarms in "normal bakeout" and in "radon removal" modes (MR-1 and MR-2, Figure 68) is essential.

MOISTURE MONITOR

The moisture content of the air leaving the drier beds should range from 0.2 to 2 ppm (by weight) under normal operating conditions. On occasion, incomplete bakeout of a drier bed may give moisture levels as high as 4 ppm. Usually, however, moisture levels greater than 2 ppm indicate either leaky valve packing, incompletely closed valves, or leaks in the air sampling line.

The moisture monitor is an extremely valuable addition since it can be used to check for improper drier operation and may be used to switch bed automatically as each absorber becomes saturated. This latter feature is a convenience only for a drier system having a manually controlled reactivation cycle. Under this mode of operation, each absorber in

the air drier is used until water breakthrough occurs. Thus, the time for this to occur will vary from about 2 to 3 days during hot, humid weather to as long as 12 days during cold, dry weather.

A fail-safe modification to the moisture monitor (11)* has been designed and incorporated into our system. A copy of the modified circuit diagram is available on request.

INSULATION

The insulation on the air-to-air heat exchanger, charcoal bed, and interconnecting piping must be applied as follows to avoid moisture problems.

Low Temperature Air System Insulation Application

1. Pipe or duct insulation should be applied in a minimum of two layers with vapor barrier between layers.
2. Pipe and duct insulation should be applied with the pipe at approximately room temperature.
3. The sectional and segmental pipe insulation and board insulation must be applied so that the ends of adjacent sections are butted tightly against each other.
4. The longitudinal seam of the vapor barrier must be sealed with a fire-resistive vapor barrier adhesive.
5. End joints are to be sealed with a 4″ wide barrier strip applied with a fire-resistive vapor barrier adhesive. All joints between layers shall be staggered.
6. Ends of pipe insulation should be sealed off with a fire-resistive vapor barrier adhesive at flanges, valves and fittings. The second layer of insulation at such seals should be stepped away a minimum of 4 in. to avoid conduction of heat through the mastic.
7. All flanges and fittings should be insulated with mitered segments of pipe insulation of a thickness equal to that of the insulation on the adjoining pipe, securely cemented and wired in place. Vapor seal treatment composed of 0.002-inch aluminum foil laid in and brushed over with a fire-resistive vapor barrier adhesive should be made over each layer of fitting insulation and carried at least 2 in. over adjoining pipe insulation. The seal at the outer layer of insulation should be further reinforced ith glass fabric tape wrapped around the flange or tting vapor barrier.
8. Insulation should not be applied until piping has been subjected to a hydrostatic or compressed air test as specified.

Materials and Equipment

1. Piping insulation materials should be as follows:
   a. Piping insulation should be sectioned of segmental form or a combination of both, except as specified herein.
   b. Pipe insulation for the low temperature air system is to be fine fiberglass wool or fine fiber mineral wool molded to conform to the pipe. Density of the fiberglass must be a minimum of six (6)* pounds per cubic foot and the mineral wool 16 pounds per cubic foot. The thermal conductivity (k) may not be greater than 0.31 BTU/hr/ft^2/degree F/inch of thickness at a mean temperature of 40° F. Minimum insulation thickness shall be 4 in.
   c. Insulation for the low temperature air system should have a vapor barrier comprised of laminate of aluminum foil (minimum thickness of foil 0.001 inch) sandwiched between two layers of kraft paper for the piping.
2. Duct insulation materials are to be as follows:
   a. Duct insulation for the low temperature air system should be rigid board made of fiberglass or mineral wool. Insulation must have a minimum weight of 6 pounds/cubic foot and have a maximum heat transfer coefficient (k) of 0.31 BTU/hr/ft^2/degree F/inch thickness at a mean temperature of 40° F. Minimum thickness shall be 4 inches.
   b. Duct insulation for the low temperature air system shall have a vapor barrier comprised of laminate of aluminum foil (minimum thickness of foil 0.001 inch) sandwiched between two layers of kraft paper.

SPARE PARTS

The following list of spare parts has been found sufficient to provide continuous operation for periods in excess of one year. Most of the following can be replaced in less than 8 hours, which is well within the time period in which no increase in radon can be detected in the air from the radon removal system or in the underground counting facility.

Blower
1. Fan belts
2. Motor
3. Fan assembly complete with bracket and including shaft.

Lectrodryer
1. Preheater element

Low temperature refrigeration
1. Freon-13, 5-lb cylinder

* See list of suppliers.

2. Compressor
Moisture monitor
1. Electrolytic cell
Fuses for all units

POSSIBLE SUPPLIERS

Disclaimer: The use of particular equipment or suggested supplier does not constitute an endorsement or recommendation. All suggested vendors appear for one or more of the following reasons: (1) They are the first vendors to respond to a request for information. (2) Catalogues appear to describe equipment having the desired specifications. (3) The vendor appears from catalogue to have required capability to modify an existing product to the required specifications. (4) Representatives were willing to discuss modifications to their normal product line. (5) This product is currently in use.

1. Spencer Turbine Company drive turbo compressor (Cat. No. B-70-24TC), 53 West Jackson Boulevard, Chicago, Illinois.

2. #BWC-500-F-SP (CIBIEI) Lectrodryer. Designed for 100 psig and to include not less than 500 lbs of Molecular Sieve type 5A-1/16" pellets in each absorber bed. Unit shall have electric regeneration and manual switch over. Regeneration and absorption cycles shall be countercurrent. Pittsburgh Lectrodryer Division, Pittsburgh, Pennsylvania.

3. a. Ball Valves, 2", carbon steel type A22 with Teflon seats, Cat. #AHV 22TT, complete with Model ST 50 pneumatic operators and pilot valve.

b. Ball Valves, 2", carbon steel, three way type DM 150 FD-22 (2 position) with Teflon seats and seals. Complete with pneumatic operators and pilot valve.

Smith-Schrader Company, Inc., 1032 South La-Grange Road, LaGrange, Illinois, 60525.

4. Panelcoil, Dean Products Co., 1042 Dean Street, Brooklyn, New York 11238.

5. Tru Heat Corporation, 700 Grand Street, Allegan, Michigan.

6. All thermocouples are copper/constantan, Cat. #2082-2024, available from API Instruments Co., Chesterland, Ohio 44026.

7. Activated coconut charcoal, 6–8 mesh, Fisher Scientific Company, Chicago, Illinois.

8. Heater is 500-watt, 115V AC, steel sheath, similar to Cat. #CWA-50 except that unheated portion extends 8" to 10" from pipe plug. Pipe plug must be less than 2" NPT. Tru Heat Corporation, 700 Grand Street, Allegan, Michigan.

9. Gaskets are to be cut from a single piece of 1/16" thick silicone rubber. COHR lastic 500 sheet, Connecticut Hard Rubber Co., 407 East Street, New Haven, Connecticut.

10. a. Temperature controller, copper/constantan thermocouple, range to include −100° C to +250° C, Compac I, on/off model 603 K, single set point.

b. Locking Coil relay, copper/constantan thermocouple, range to include −100° C to +250° C, Model 160Z-C, single set point. API Instrument Company, Chesterland, Ohio.

11. Model W Electrolytic Moisture Analyzer, Manufacturers Engineering Equipment Corporation, 250 Titus Avenue, Warrington, Pennsylvania.

12. Air-to-air heat exchanger. 5" diameter shell with 1161/4" tubes about 8' long. Nonferrous high transfer. Fractional bypass and number of baffles to be determined. Pro-Quip, Inc., 418 Shawmut Avenue, LaGrange, Illinois 60525.

13. Air chiller, Murphy and Miller Model SVO-6W-90 or equivalent to condition 30 SCFM at 0° F D.B. and −110° F dew point to −80° F D.B. and −110° F dew point. Murphy and Miller, Chicago, Illinois.

REFERENCE

1. H. F. Lucas, Jr. Argonne National Laboratory Radiological Physics Division Annual Report, July 1963 through June 1964. ANL-6938, p. 91.

RADON IN COAL MINE AIR. Part II

Henry F. Lucas, Jr.

Measurements of the radon concentration in coal mine air have been continued with samples from an additional 9 mines in West Virginia, Kentucky, and Tennessee. Mine air samples (~95 cc) were obtained as in the earlier study[1] by filling a previously evacuated alpha scintillation radon counting chamber to atmospheric pressure. The chamber was returned to Argonne National Laboratory, where the radon concentration was determined. All values include correction for radioactive decay between collection and analysis. The radon concentrations for this final series are summarized in Table 47. The radon concentra-

TABLE 47. RADON IN COAL MINE AIR: WEST VIRGINIA, KENTUCKY AND TENNESSEE

Mine	Key[a]	Radon, pCi/l ± E[b]
A	beh	63.6 ± 7.1
	aeg	2.3 ± 0.4
	aeg	2.2 ± 0.4
B	aeg	0.3 ± 0.2
	beg	11.7 ± 0.9
C	aeg	1.5 ± 0.4
	adeg	7.9 ± 0.7
D	afg	1.1 ± 0.5
	befg	112.6 ± 7.1
E	aceh	79.1 ± 3.6
F	adeg	0.9 ± 0.4[c]
G	aeg	0.4 ± 0.2
	bcdeh	1108.7 ± 47.7
H	aeg	1.5 ± 0.4
I	aeh	70.8 ± 5.2
	bdfh	813.3 ± 27.5[c]

[a] Key: a. moving air; b. still air; c. seeping gas noted; d. water; e. mine operating; f. mine idle; g. no rock exposed (high coal or rock dusted); h. rock exposed and/or new cave-in.

[b] 0.90 Statistical counting error.

[c] An error in matching sample identification numbers may have caused interchange of these two samples.

tion of 1100 pCi/l exceeded the previous maximum value of 147 pCi/l.[1] However, the significance of these values is unknown since only 0.4 ± 0.2 pCi/l was found in a sample from another portion of Mine G, and good ventilation reduced the radon concentration in all cases. Consequently, because of the method of sampling, this survey has only established that high radon levels may occur in coal mines at least occasionally. Since any radiation hazard requires exposure at high levels for long periods of time, any further study should evaluate the mean radon daughter levels in the working areas during the normal work day.*

REFERENCE

1. H. F. Lucas, Jr. and A. F. Gabrysh. Radon in Coal Mines. Argonne National Laboratory Radiological Physics Division Annual Report, July 1965 through June 1966. ANL-7220, pp. 58–60.

* The samples were collected by A. F. Gabrysh, U. S. Bureau of Mines, 4800 Forbes Street, Pittsburgh, Pennsylvania.

EXCRETION AND RETENTION OF LEAD-210 IN RATS

*Henry F. Lucas, Jr. and James E. Stanford**

INTRODUCTION

Lead is one of the more important elements in the field of toxicology. The retention and excretion of lead in experimental animals has thus been the subject of considerable investigation. Due to the lack of sensitivity in chemical detection methods, however, this work has generally been limited to experiments of less than ten days' duration.

The use of radioactive lead isotopes has greatly extended the range of these experiments. Recent research has shown that approximately 40% of an injected dose of lead is excreted from an animal in the first ten days, while the remainder is held mostly in the skeleton and is removed very slowly.[1, 2] In another study on the long-term retention and excretion of Sr^{85} and Ra^{226} by the chinchilla,[3] an enhanced fecal excretion rate was observed between 30 and 120 days postinjection. Similar variations in this ratio with time have been observed in mice, rats and rabbits.[4, 5] Since lead, like the alkaline earths, is a bone-seeking element, and since the cause of the enhanced fecal excretion rate was unknown, a study was undertaken to determine the long-term retention and excretion of lead.

Compared to the mean life of rodent erythrocytes (60 days) the previous studies on lead in blood[6, 7] had been of short duration. Therefore, the possibility of a changing distribution of lead between the plasma and the cellular fractions of blood with time postinjection is also of interest.

MATERIALS AND METHODS

Three two-month-old female rats (SD/ANL-SPF) weighing from 200 to 225 grams each were used for the experiment. The rats were kept in cylindrically shaped individual stainless steel metabolism cages 8 in. in diameter and 8 in. tall. The cages had floors constructed of 0.062-inch diameter stainless steel wire having a mesh of 5 × 5 in a 2-in. square. The animals were supplied with the Rockland Rat/Mouse Diet (complete) and distilled water ad libitum. Custom built urine-feces separators were installed under the cages.

Before the injection, samples from each animal were processed to determine the levels of elemental lead. The analysis was by the standard method,[8] which

* ACM Student, 1967.

consisted of extracting the lead, forming a lead-dithizone colored complex, and measuring its absorbance at 515 mμ in a Perkin Elmer 350 spectrophotometer. Feces and urine were found to contain 18 and 0.06 μg/g, respectively. Food and water samples were similarly processed and found to contain 8.4 and 3 μg/g, respectively. Total intake and excretion was about 70 μg Pb/day.

To prepare the injection solution, a 0.500-ml aliquot of a Pb^{210} solution* was washed into a test tube with two rinses of 1. *N* HNO_3. This aliquot was evaporated to dryness and brought into solution twice with 0.100 *N* HCl. It was then evaporated and brought into solution with 0.100 *N* HCl again, to a final volume of 10.0 ml. Three 500-μl aliquots (10.44 μCi ± 0.09 μCi) of this solution were then pipetted onto separate parafilm sheets, and the pipettes were rinsed once with distilled water and once with 0.100 *N* NaOH. Each of the resulting injection doses was mixed well to form a slightly acidic saline solution of $PbCl_2$. Each injection dose was drawn into a disposable syringe and injected without anesthesia into the lateral tail vein of the rat.

Following the injection of each rat, all spillage, the syringe, needle, washings from the animal's tail and other sources of activity loss were collected into a 500 ml beaker. Concentrated HCl (100 ml) was added and the resultant mixture was boiled for 4 hr and then brought to a 500-ml volume with distilled water. A 100-μl aliquot was taken from each solution and plated onto a 1.5″ diameter stainless steel counting planchet. These planchets were then counted to determine the fractions of the original doses that were not successfully injected.

Blood specimens were collected from each rat at intervals over a 100-day period (see data). The blood samples were collected in weighed 200-μl heparinized blood sample tubes.† Initially the terminal centimeter of the rat's tail was cut off and allowed to bleed. The scab was cut off for successive collections. "Milking" the tail speeded the process of bleeding. The tubes of blood, and centrifuged for 10 min at approximately 2000 rpm. After centrifugation, the tubes were scored and broken near the cell-plasma line. The contents were washed into 5-ml beakers with distilled water, were washed into 5-ml beakers with distilled water, special care being taken to avoid cell contamination of plasma. The cell and plasma samples were heated to dryness with concentrated HNO_3 and then brought into solution three times under an infrared lamp. The samples were then plated onto 1.5″ stainless steel planchets with two concentrated HNO_3 washes of the beakers. The hematocrit was measured on each blood collection and was used for calculation of cell and plasma activity. The average hematocrit was found to be 0.49; however, individual values ranged from 0.34 to 0.62 under unusual conditions (deviations from 10-min centrifugation or during a period when two of the animals experienced swollen inflamed tails).

The urine and feces samples were collected at one-day intervals for the first seven days postinjection and at weekly intervals thereafter. When the specimens were collected, all the solid material (food particles and feces) that fell through the apparatus was counted as feces. The apparatus was then rinsed with 0.5 *N* HNO_3 and the urine-soaked food particles and hair which had adhered to the sides of the funnel and separator were counted as urine. The samples from rat C were processed immediately, while those from rats A and B were, for convenience, set aside and processed later.

Urine and feces samples up to day 82 postinjection were boiled to dryness three times with concentrated nitric acid. Because several samples were lost, the procedure was changed to slowly heating the samples to dryness three times without boiling. This reduced the danger of sample loss due to bumping. As the reaction was accompanied by large quantities of foam, the oxidation of fecal samples was carried out in 1-liter Erlenmeyer flasks. Minimum foaming occurred when the initial oxidation in concentrated HNO_3 was allowed to take place at room temperature. The urine and fecal residues after oxidation were brought up to 100-ml volume with 1 *N* HNO_3. Five hundred microliter aliquots of these 100-ml solutions were plated onto stainless steel planchets with two washes of the 500-μl pipets using concentrated HNO_3. The residues on the planchets were dried under an infrared lamp. The remainders of the 100-ml solutions were rinsed into 250-ml polyethylene bottles for storage.

After 50 days postinjection, rat A was sacrificed by an intraperitoneal injection of Nembutal and a whole body count for Pb^{210} was taken. The rat was boiled in 700 ml of distilled water for 6 hr, by which time the tissues were largely dispersed through the solution. Five hundred ml of concentrated HNO_3 were added slowly, and the resulting solution was heated and allowed to evaporate to 200 ml. With the oxidation of the organic matter nearly complete at that point, the solution was transferred to a volumetric flask and taken up to one liter of volume with distilled water. Twelve 500-μl aliquots were taken from this solution and plated on planchets. These were then

---

* Radiochemical Centre, Amersham, England, Cat. No. RBS.1, 4 mCi/ml, 3*N* HNO_3, 30 μg Pb/ml.

† Micro Blood Collecting Tubes distributed by Scientific Products, Division of American Hospital Supply Corporation, Evanston, Illinois.

counted, once in each of the four chambers of the beta counter. The lead retention of 73% of that calculated by difference was expected since, for this animal, recovery of spillage was known to be incomplete and a portion of several excretion samples had been lost. It is, however, 10–15% lower than expected. A second rat is being processed for which we had fewer accidents.

Each of the twelve aliquots was counted in each of the four counting chambers. The efficiency of each was found to be within ±1%. The counting rate of the individual sample varied ±2%, a direct result of variations in self-absorption resulting from variations in plated areas.

The stainless steel counting planchets were cleaned in hot nitric acid, and a ring was painted around the edge on one surface with Zapon* varnish to contain liquids in the center. The planchets were weighed before and after plating to determine the weights of the sample residues for self-absorption corrections. The residue weights were found to range up to 30 mg/cm^2, which required corrections for self-absorption of up to 30%. The plated planchets were wrapped in one layer of aluminum foil (D = 5.13 mg/cm^2) to filter out the alpha-emitting isotopes.

The activity measured was that of the 1.17 MeV, 5.0 day half-life bismuth-210 daughter of lead-210. At least six half-lives (thirty days) were allowed to elapse between plating and counting. By this time the growth and decay of bismuth-210 had come within 98.4% of equilibrium, and therefore, the beta count of bismuth-210 was representative of the amount of lead-210 in the sample.

The activity of the samples was measured in a custom-made four-chambered "pancake" type flow-gas Geiger counter.[9] The background counting rate in each of the chambers was less than 0.4 cpm, and the efficiency for these samples was 50% (0.5 c/d). Samples were counted for sufficient time to give a statistical counting error (σ) of less than 3% except in the case of low level blood plasma, where an error of 5% was tolerated.

The percent dose retained and percent dose excreted per day were computed by taking the ratio of counting rates, thereby avoiding the need for absolute calibration. All calculations and plotting of data were performed by a CDC 3600 computer and a Calcomp plotter using a program previously prepared by one of us (HFL).

DISCUSSION

The rate of fecal and urinary excretion for the three rats is summarized in Table 48. One-day samples were collected for the first 8 days with essentially 7-day samples thereafter. The fecal-to-urinary excretion ratio (F/U) was calculated for each of the 51 samples in Table 48 and was found to range from 0.6 to 3.5. The means for the three animals were 1.5, 1.2 and 1.2, with a grand mean of 1.34. This compares to the values of 1.2 and 2.2 found previously.[1, 10] The cumulative fecal plus urinary excretion was 28% of the injected doses at 6 days postinjection, which is somewhat less than the 44% found previously.[1] The cumulative excretion was 36% at 14 days postinjection, which is also less than the 52% found in another study.[10] The ages of the rats in the other studies were not given.[1, 10] However, our rats were injected at 65 days of age, which has been found to give a greater strontium retention than injection at ages of less than 40 or more than 120 days.[11]

The uptake of radioelements by the rodent incisor with subsequent loss by the normal process of attrition is well known.[12, 13] This mechanism has recently been found to be the cause of the enhanced fecal excretion at about 60 days postinjection in the chinchilla[3] and presumably for rats, mice and rabbits.[4, 5]

The failure to observe the variation in the fecal-to-urinary ratio as the incisors were lost by attrition was at first attributed to a possible radiation dose effect. Rabbit incisor growth rates were found to be retarded at doses of 600 μCi/kg Sr^{90}.[14] The absorbed dose from the 36 μCi/kg of Pb^{210} plus Bi^{210} and Po^{210} daughters would be nearly equal to that for the rabbits, especially if the quality factor for the alpha radiation is included. However, when animal B was sacrificed at 110 days postinjection, the concentration of Pb^{210} in the incisors of 0.019 ± 0.001 μCi/g was much less than the 0.20 ± 0.01 μCi/g for pooled femur, tibia and fibula.

This implies the normal growth process with loss by attrition, since accretion rates for rat incisors are equal to or greater than for tibias.[12] In addition, the concentration of Sr^{85} in the chinchilla incisor was 4 times that for the skeleton at 28 days postinjection.[3]

The Pb^{210} retained in the 4 rat incisors at 110 days postinjection was 0.06% of the injected dose or 0.15% of the body content. This is very much less than the 5.5% found for Ca^{45} in rats,[12] as well as the 2–3% for Sr^{90} estimated from data by Thompson.[5] Since the concentration of Ca^{45} at t = 1 day in rat whole blood of 0.02%/g is twice that of $Sr^{89\text{-}90}$,[5, 16] uptake by the incisor may be directly related to the blood concentration. With this assumption and the observed Pb^{210} concentration at 1 day of 0.007 to 0.009% dose/g plasma, only 0.5% of the injected dose would be expected in the incisors. Uptake by the incisors at this level would not be detectable in the excretion or re-

* Zapon Division, Atlas Powder Company, North Chicago, Illinois.

TABLE 48. Pb^{210} EXCRETION BY THE YOUNG RAT AFTER SINGLE I.V. INJECTION

Mid-time, days	Rat A			Rat B			Rat C		
	Feces, % dose/day	Urine, % dose/day	F/U	Feces, % dose/day	Urine, % dose/day	F/U	Feces, % dose/day	Urine, % dose/day	F/U
0.5	7.3	4.2	1.72	3.4	4.7	0.73	7.8	6.8	1.16
1.5	5.5	2.0	2.73	9.2	2.6	3.52	4.9	2.9	1.67
2.5	2.5	1.3	1.91	2.3	1.6	1.42	2.9	2.0	1.44
3.5	0.95	0.65	1.44	[a]	0.9	—	0.67	0.91	0.73
4.5	1.42	0.83	1.71	1.3	1.0	1.25	1.7	1.5	1.16
5.5	0.46	0.53	0.86	0.61	0.68	0.89	0.76	0.82	0.92
6.5	0.53	0.34	1.55	0.51	0.47	1.08	0.31	0.52	0.59
7.5	0.28	0.25	1.13	0.29	0.30	0.98	[a]	0.47	—
10.0	0.38	0.14	2.65	0.35	0.20	1.64	0.26	0.26	1.01
15.0	0.18	0.14	1.29	0.18	0.16	1.11	0.21	0.16	1.31
22.0	0.12	0.096	1.24	0.16	0.14	1.17	0.13	0.085	1.57
29.0	0.10	0.084	1.17	0.10	0.11	0.90	0.094	0.099	0.95
36.0	0.082	0.070	1.17	0.09	0.09	1.00	0.092	0.046	2.00
43.0	0.080	0.064	1.25	0.08	0.07	1.13	0.074	0.044	1.68
48.0	0.080	0.072	1.10	—	—		—	—	
50.0				0.07	0.07	1.06	0.052	0.055	0.94
57.0				0.06	0.05	1.04	0.069	0.046	1.50
64.0				0.05	0.03	0.66	0.053	0.033	1.62
71.0				0.03	0.03	1.00	0.034	0.038	0.88
78.0				0.03	0.03	1.17	0.041	0.038	1.08
Mean			1.51			1.21			1.23

[a] Sample lost.

TABLE 49. Pb^{210} IN CELLULAR AND PLASMA FRACTIONS OF RAT BLOOD

Days postinjection	Rat A			Rat B			Rat C		
	Cells, % dose/g	Plasma, % dose/g	C/P	Cells, % dose/g	Plasma, % dose/g	C/P	Cells, % dose/g	Plasma, % dose/g	C/P
0.11	[a]	4.1×10^{-2}	—	1.69	3.2×10^{-2}	53	1.97	4.7×10^{-2}	42
0.25	1.70	2.0	82	1.34	1.6	81	1.01	2.4	45
0.50	0.51	1.5	34	0.68	1.3	51	0.48	1.0	73
1.0	0.39	[a]	—	0.54	1.1	52	0.41	5.6×10^{-3}	57
2.0	0.22	4.2×10^{-3}	51	0.32	4.0×10^{-3}	79	0.27	4.7	68
3.0	0.074	4.1	18	0.17	1.9	88	0.17	2.4	18
5.0	0.078	3.4	23	0.097	2.1	45	0.082	4.6	48
8.0	0.059	3.8	15	0.051	5.8×10^{-4}	89	0.064	1.3	21
12.0	0.035	7.7×10^{-4}	45	0.043	3.9	108	0.040	1.9	86
16.0	0.018	2.1	87	0.022	1.9	117	0.025	2.9×10^{-4}	106
20.0	0.019	1.9	97	0.016	1.8	90	0.019	1.8	125
23.0	0.017	2.8	62	0.015	1.8	82	—	—	—
27.0	0.015	1.0	143	0.013	1.0	117	0.018	1.5	147
30.0	0.015	1.8	83	0.012	0.7	168	0.017	1.2	94
36.0	0.016	1.1	151	0.013	0.9	149	0.015	1.6	127
43.0				0.010	0.6	154	0.014	1.1	80
50.0				0.0094	0.7	130	0.013	1.7	61
57.0				0.0085	0.7	114	0.0097	1.6	171
64.0				0.0088	0.7	126	0.0093	0.5	
78.0				0.0096	0.6	163	0.0050	0.5	96
Mean			69			106			82

[a] Sample lost.

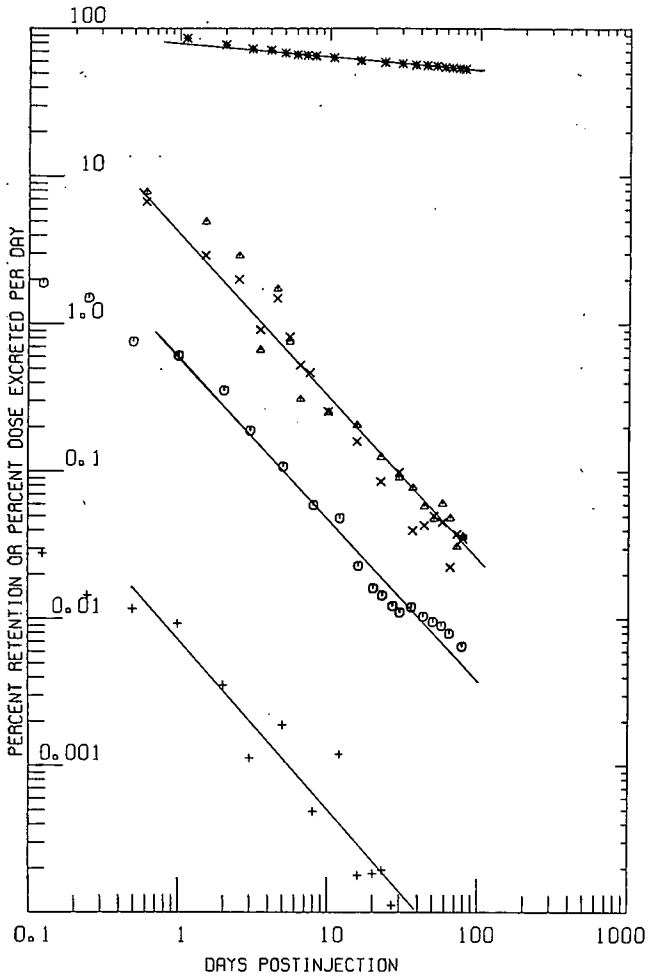

FIG. 69. Rat B: * = Whole-body retention (% dose); △ = fecal excretion (% dose/day); × = urinary excretion (% dose/day); ○ = activity in blood cells (% dose/g); + = activity in blood plasma (% dose/g).

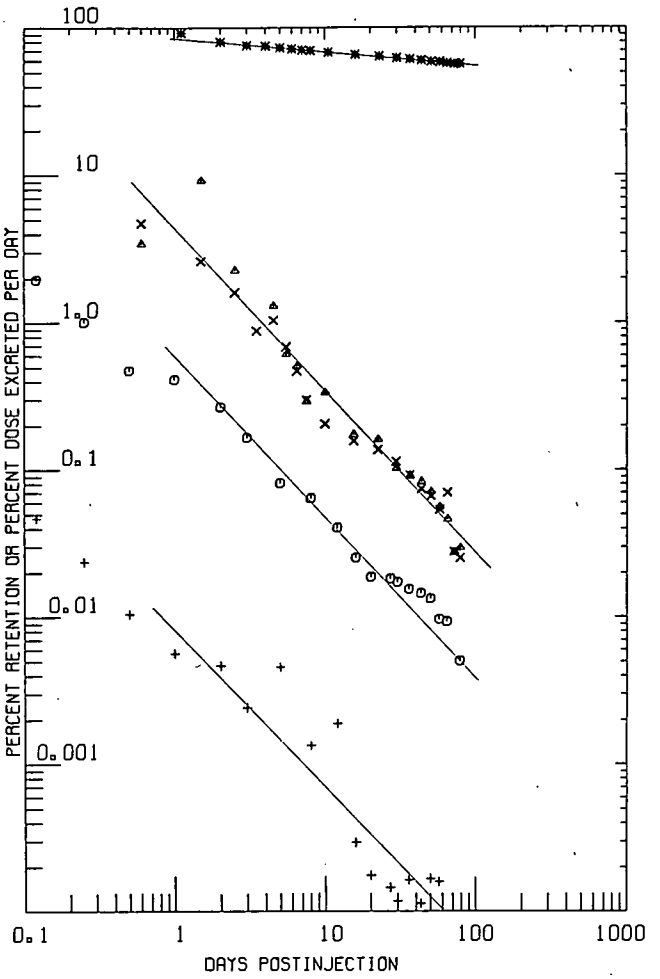

FIG. 70. Rat C.: * = Whole-body retention (% dose); △ = fecal excretion (% dose/day); × = urinary excretion (% dose/day); ○ = activity in blood cells (% dose/g); + = activity in blood plasma (% dose/g).

tention curves. Further studies are in progress to confirm the amount of uptake by the incisors at early times.

The concentration of Pb^{210} in the cellular and plasma fractions of blood are summarized in Table 49. The ratio of concentration in the cells to that in the plasma was found to increase by about a factor of two throughout the 80-day period for which samples were processed. In agreement with others,[1, 2] it was found that more than 90% of the lead in the blood was in the erythrocytes. Since it is very difficult to avoid hemolysis and obtain cell-free plasma, the ratio of activities varied over a wide range. The small difference in the cell-to-plasma ratio observed at times ess than or greater than the mean cell lifetime of 60 days[15] should be verified. The relative stability of the cell-plasma ratio implies that the rate of lead uptake and loss by the erythrocytes is fast compared to the decrease in the blood content.

The urinary and fecal excretion rate in percent dose per day, the percent dose per gram of erythrocytes and plasma, and the whole body retention estimated by subtraction of cumulative excretion are given for rat B in Figure 69 and rat C in Figure 70. The slopes in both these figures are nearly identical and the lines drawn through the data give the following:

$$R_t = 0.80\ (t)^{-0.086}$$
$$F_t = 0.1\ (t)^{-1.09} \qquad t \geq 1 \text{ day.}$$

A line with the same slope of $t^{-1.09}$ was drawn through the erythrocytes and plasma data. Urinary clearance corresponds to 80 g plasma per day. Fecal clearance probably would be derived from both the erythrocytes and the plasma and is not estimated.

REFERENCES

1. N. Castellino and S. Aloj. *Brit. J. Ind. Med.* **21**, 308 (1964).
2. R. D. Lloyd and W. Fisher. University of Utah College of Medicine Report COO—224 (1961).

3. H. F. Lucas, F. Markun, and J. Farnham. To be published.
4. M. Fujita and J. Iwamoto. *Health Phys.* **11,** 271 (1965).
5. R. C. Thompson and P. L. Hackett. Paper presented at International Symposium on Some Aspects of Strontium Metabolism, Annan, Scotland, 5–6 May 1966. Private communication.
6. R. A. Mortensen and K. E. Kellogg. *J. Cell. Comp. Physiol.* **23,** 11 (1944).
7. K. K. Reddi. *Arkiv Kemi* **6,** 147 (1954).
8. *Official Methods of Analysis of the Association of Official Agricultural Chemists*, Association of Official Agricultural Chemists, Washington, D. C., 1965.
9. H. F. Lucas. Argonne National Laboratory Radiological Physics Division Semiannual Report, January through June, 1959. ANL-6049, p. 117.
10. J. Schubert and M. R. White. *J. Lab. Clin. Med.* **39,** 260 (1952).
11. T. W. Speckman and W. P. Norris. *Radiation Res.* **23,** 461 (1964).
12. G. C. H. Bauer, A. Carlsson, and B. Lindquist. *Mineral Metabolism: An Advanced Treatise*, Ed. C. L. Comar and F. Bronner. Academic Press, New York, 1961, Vol. 1, Part B, p. 624.
13. B. J. Sessle. *J. Dental Res.* **45,** 1571 (1966).
14. M. A. Rushton, M. Owen, W. Holgate, and J. Vaughan. *Arch. Oral Biol.* **3,** 235 (1961).
15. N. I. Berlin, T. A. Waldmann, and S. M. Weissman. *Physiol. Rev.* **39,** 577 (1959).
16. W. P. Norris and W. E. Kisieleski. Comparative Metabolism of Radium, Strontium and Calcium. *Cold Spring Harbor Symp. Quant. Biol.* **13,** 164–172 (1948).

*RADIAL DIFFUSION FROM CANALICULI: AN EXPLANATION FOR THE RETENTION OF ALKALINE EARTHS IN ADULT BONE**

John H. Marshall and Claude Onkelinx

The retention of alkaline earth radioisotopes in skeletal systems can be approximated by the power function t^{-b}, where t is the time after a single injection and b is a positive fraction between 0.0 and 0.5.[1] It has been shown[2] that the time derivative of this expression, which contains t^{-b-1}, is also a good approximation to curves of plasma specific activity. Several explanations have been suggested as possible physiological bases of these power function expressions. The most common is that a large number of mineral compartments with different sizes and different turnover times somehow give rise to a series of exponential terms that approximate a power function.[3] Another possibility is that the turnover rate of a single, dominant compartment for some reason decreases in inverse proportion to the time since injection.[4] Still a third possibility is provided by the stochastic model of recrystallization suggested by Edgington.[5] The purpose of this note is to suggest another possible explanation for power function retention, one that may be particularly applicable to normal, adult metabolism in animals or man.

Consider the problem of diffusion of alkaline earth ions from blood into bone. At short times after tracer injection, the fall of plasma specific activity is dominated by the equilibration of the short-term pool, the rapidly exchangeable calcium. A considerable fraction of this exchangeable calcium resides at bone surfaces[6] so that the diffusing ion is presented initially with a large, almost plane surface in contact with extracellular fluid. The problem of diffusion at these external bone surfaces is similar to that for an instantaneous source of tracer at the plane surface of a semi-infinite solid. The expression for plasma specific activity[7] would be approximately $t^{-0.5}$, not far from actual observations for times less than a day in dog[8, 9] and in man.[10]

At times later than a day or so in adult animals, the tracer activity at bone surfaces drops rapidly and builds up in the volume of existing bone. This low-intensity, volume deposit of alkaline earth tracers has been called the diffuse component. The rapid uptake and long retention of tracer in a volume of mineral which is approximately in steady state has not been explained, though it has been described operationally as long-term exchange.[11] Its magnitude in man relative to other processes of calcium transfer such as the apposition and resorption of bone has not been definitely established, but in fully adult dogs and rabbits it is probably the dominant process of long-term calcium transfer.[12, 13]

Now, if the build-up and retention of tracer activity in the diffuse component is considered as a problem of diffusion, there is an important difference from the earlier diffusion into plane bone surfaces. The tracer must reach the volume of the bone by passing through tiny canals. Subsequent diffusion outward from these canals will take place in cylindrical geometry rather than in plane geometry. The

* The following paper, Calcium Pools and the Power Function, was prepared six months before this paper and provides the background for the present development.

diffusion problem is similar to an instantaneous source of tracer along the axis of a cylinder at $t = 0$.

Consider a long cylinder of bone with a tiny canal running along the cylinder axis. If a diffusible tracer is distributed uniformly along the canal at time zero, the amount of tracer remaining in the canal as a function of time can be calculated by solving the diffusion equation in cylindrical coordinates:

$$\frac{\partial V}{\partial t} = D\left(\frac{\partial^2 V}{\partial r^2} + \frac{1}{r}\frac{\partial V}{\partial r}\right) \qquad (1)$$

where V is the concentration of tracer as a function of time t at any radius r, and D is the coefficient of diffusion.[14] It has been assumed that there is no variation of tracer concentration with angle within the cylinder or with distance parallel to the axis. For the initial conditions given above, the solution of equation (1) for tracer concentration at $r = 0$ is

$$V = \frac{q'}{4\pi Dt} \qquad (2)$$

where q' is the quantity of tracer per unit length deposited along the axis at $t = 0$.[7] Notice that the quantity of activity remaining in the canal depends exactly upon the power function t^{-1}. If a finite canal diameter is assumed, V remains finite at time zero.

Now, what would happen if the radial diffusion equation, expression (1), were perturbed by applying a small drain on the axial canal after instantaneous labeling? Such a drain might result from the flow of calcium down canaliculi to blood vessels and thence to excretory outlets in urine and feces. The effect of a drain was tested by setting up an eighteen-compartment approximation to the radial diffusion equation on the PACE analogue computer. The model consisted of a series of compartments whose sizes were proportional to the areas between a set of 18 concentric, equally-spaced circles. The rate of calcium transfer in each direction between neighboring compartments was proportional to the circumference of the corresponding circle. The differential equations for such a series model reduce to equation (1) as the number of compartments becomes large. The solution with a drain does not appear to be expressible in terms of tabulated functions.[14] When the drain was set equal to zero, the theoretical t^{-1} dependence for axial activity resulted, as in expression (2). This provided a check on the model. When the drain was increased to values consistent with the known endogenous excretion rates for the different alkaline earths, a series of urves for axial activity versus time was produced which could be approximated by a set of power function expressions varying continuously from $t^{-1.0}$ to $t^{-1.5}$. This is similar to curves of plasma specific activity. Since plasma specific activity is proportional to the time derivative of retention,[2] the corresponding retention curve could be given by t^{-b} with b between 0.0 and 0.5.

Now at what level of organization might one find a cylinder of bone which would satisfy the conditions of this solution of the retention problem? The first choice might be the osteon, but this level appears to be eliminated by the observation that the tracer taken up in newly-formed bone does not diffuse radially throughout the osteon. Rowland[15] has observed that Ra^{226}, even forty years after ingestion, remains localized in the lamellae laid down at the time of tracer intake.

The second choice of a level with cylindrical geometry might be the bone crystals themselves, but at that level the diffusion would have to be inwards from the circumference of each crystal and not outwards from the axis. That initial condition does not result in even approximate power function retention for crystals of a size comparable to those in bone.[16-18]

The remaining choice appears to be the cylindrical territory surrounding canaliculi, the tiny canals that connect osteocyte lacunae. It could not be radial diffusion outwards in all directions from the point sources represented by lacunae, because diffusion from an instantaneous source at the center of a sphere[7] yields the solution $t^{-1.5}$. If we assume that the rate-controlling process in normal, adult bone is radial diffusion in canalicular territory, then we have the first simple explanation both for the diffuse component and for approximate power function retention. Of course, this could not be the whole story, and we expect to have to modify the solution for more exact initial conditions and for the effects of apposition and resorption when they are important.

We picture this radial diffusion from each canaliculus into its surrounding territory of calcified matrix as involving penetration of alkaline earth ions through the collagen, water, ground substance, amorphous component, and embedded bone crystals. A random walk through this heterogeneous calcified matrix should, when viewed from a higher level, be equivalent to a process of diffusion through a continuous medium with a single, effective coefficient of diffusion (Figure 71). When the analogue computer model is set to conform to the radii of the typical canaliculus and of its territory, as measured through the electron microscope in mouse bone by Baud,[19] a resulting solution for canalicular specific activity, S, as a function of time is shown in Figure 72. This result was produced by a canalicular drain comparable to that expected from the urinary and fecal endogenous excretion rate in dogs.

To calculate the canalicular drain from the known excretion rates, we have assumed that the specific activity of the plasma corresponds closely to canalicular specific activity. This is a reasonable assumption because one can estimate from the magnitude of the uptake of tracer in the diffuse component that the calcium in the fluid within canaliculi must be cleared by bone many hundreds of times a day.[6]

The problem of recycling and translocation of tracer via the plasma is accounted for by the present theory, because an ion which diffuses from bone into one canaliculus, then moves into the blood and enters another canaliculus somewhere else in the skeleton, is equivalent to an ion which spends the time of translocation in the original canaliculus. This follows from our assumption that all the calcium of the initial pool is in a rapid exchange with the axial compartment of the diffusion model. Similarly, we have accounted for ions which diffuse in bone from one canaliculus to another, because such a path is equivalent to a path within the original canalicular territory together with a reflection at its outer boundary (Figure 71).

Since the specific activity of plasma should be equal to that within canaliculi, at least a day or more after injection, the curve of whole-body retention versus time, R, which would result from this process of radial diffusion can be calculated from the excretion postulate,[2] which can be written

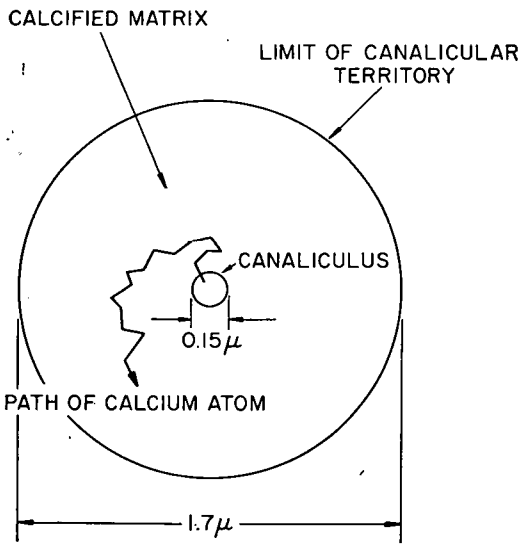

FIG. 71. Diagram of the diffusion of an atom of calcium or other alkaline earth from a canaliculus into the calcified matrix within canalicular territory. The dimensions are taken from the electron microscope work of Baud.[19] The diffusion problem is essentially that of an instantaneous source of tracer distributed along the axis of a cylinder at time zero.

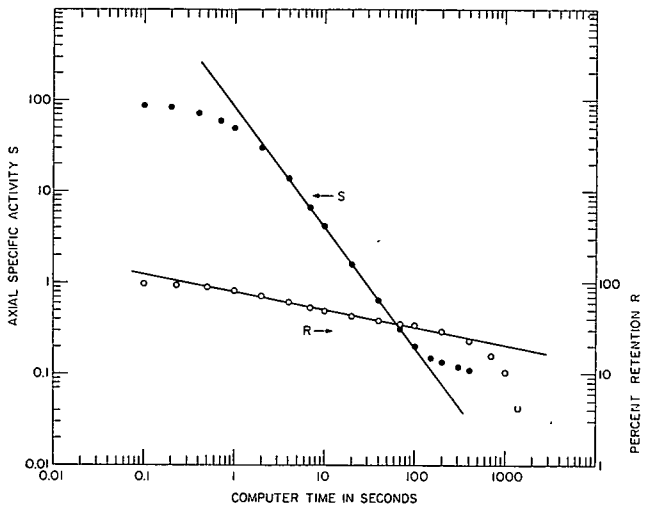

FIG. 72. One of the analogue computer outputs for plasma specific activity, S, and whole-body retention, R, from an eighteen-compartment representation of the diffusion equation in cylindrical coordinates. The effective coefficient of diffusion is about 10^{-16} cm^2/sec. The excretion rate, ηk, has been chosen to simulate the data for Ra^{226} in adult dogs.[8] One second of computer time is approximately equal to one day of real time. In this run (No. 22), 25% of the calcium in canalicular territory was assumed to be available, representing only that calcium lying close to crystal surfaces. The S curve is approximated by $t^{-1.3}$, the R curve by $t^{-0.2}$. At long times, equilibration of the model requires final exponentials for both R and S. Equilibration is delayed if all the calcium within canalicular territory is considered available.

$$R = 1 - \frac{\eta k}{q} \int_0^t S dt, \qquad (3)$$

where k is the endogenous excretion rate in grams calcium per day, η is the factor by which the excretory clearance of an alkaline earth exceeds that of calcium, q is the tracer activity in the initial pool at time zero, and S is either plasma or canalicular specific activity. This is simply an equation of tracer conservation: the tracer retained is equal to that injected minus that excreted. The value of ηk used in expression (3) must, of course, be the same as the canalicular drain which perturbs the diffusion equation, expression (1). The result for bodily retention R is shown in Figure 72. The results for both R and S are quite similar to the retention and plasma specific activities observed in adult dogs for different alkaline earths.[2]

The slope of the best power function line through the curve for plasma specific activity, S, is not exactly one unit greater than that through the curve for retention, R. However, real data often show a simila behavior.[8] According to the excretion postulate, expression (3), S must be proportional to the time derivative of R, but R need not be proportional to

the time integral of S because a constant of integration is involved. Furthermore, although the model fits the data well for three decades of time, the very long term retention has not yet been fitted closely.

This diffusion mechanism is sufficient to explain the rapid uptake of tracer in the diffuse component as well as the long retention. Note that thick-section autoradiographs of Ca^{45} have a resolution of only 10–100 μ so that the diffuse component includes the tracer activity within the canaliculi as well as that within canalicular territory. Therefore, diffuse uptake can be fast because it involves flow through the liquid within canaliculi. The subsequent retention is very long because the ions diffuse outwards into the almost solid calcified matrix and exchange with a large mass of mineral. Furthermore, retention is enhanced by the geometry of the cylinder, because once an ion has left the cylinder axis it is very improbable for it to return by a random walk.

The coefficient of diffusion corresponding to the present solution, when fit to typical alkaline earth data, is the order of 10^{-16} cm^2/sec. On this basis it should take almost a year for tracer to diffuse from a canaliculus to the border of canalicular territory. This is over a billion times slower than diffusion through a liquid and only twenty times faster than diffusion of Na in crystalline NaCl when extrapolated to body temperature.[20] The theory, therefore, represents a marked departure from the common hypothesis that the typical bone crystal is bathed by extracellular fluid which is in fairly rapid exchange with the blood. The theory is in agreement with the view of Neuman and Neuman[21] when they say that fully calcified matrix is "diffusion-locked." It is diffusion-locked by comparison with the *in vitro* situation which involves diffusion in the liquid phase. However, due to the extremely small separation between canaliculi, this very low coefficient of diffusion would be capable of producing a large two-way flow of calcium between blood and bone.

The rate of calcium uptake in the diffuse component varies widely as a function of animal age and species.[22] We expect the corresponding coefficient of diffusion to show similar variation and, in addition, to depend upon the element. The central position of the osteocyte and the location of one of its processes in each canaliculus[19, 23, 24] strongly suggests that this diffusion process of calcium transfer is in some way dependent on cellular activity.

It should be possible to test this theory of the slow, radial diffusion of alkaline earth ions in canalicular territory by means of carefully-timed electron microscope autoradiography.

Note: A new hypothesis involving two random walks separated by a gate has been proposed[25] to explain the power function nature of the plasma specific activity curve at times less than a day. This portion of the curve describes the equilibration of the initial pool which in the present work is assumed to have taken place *before* the times of consequence for the diffusion of tracer into canalicular territory. The approximate time of separation between these two phenomena is given by the time epsilon of the power function model for retention.[2]

We thank J. A. Yaeger for bringing to our attention a concept of the possible function of the osteocyte and of its canalicular processes.[23]

REFERENCES

1. W. P. Norris, S. A. Tyler, and A. M. Brues. *Science* **128**, 456 (1958).
2. J. H. Marshall. *J. Theoret. Biol.* **6**, 386 (1964).
3. J. H. Marshall. *Compartments, Pools, and Spaces in Medical Physiology*, Proc. Symp. held at Oak Ridge, October 24-27, 1966, USAEC Symp. Ser. 11, Report CONF-661010, pp. 451–468; see also this report.
4. J. H. Marshall. Argonne National Laboratory Radiological Physics Division Semiannual Report July through December, 1958. ANL-5967, p. 78.
5. D. N. Edgington. Argonne National Laboratory Radiological Physics Division Annual Report July 1965 through June 1966. ANL-7220, p. 42.
6. R. E. Rowland. *Clin. Orthoped.* **49**, 233 (1966).
7. R. M. Barrer. *Diffusion in and through Solids*. Cambridge University Press, New York, 1951, pp. 45–46.
8. M. A. Van Dilla, B. J. Stover, R. L. Floyd, D. R. Atherton, and D. H. Taysum. *Radiation Res.* **8**, 417 (1958).
9. J. Cohen, C. J. Maletskos, J. H. Marshall, and J. B. Williams. *J. Bone Joint Surg.* **39A**, 561 (1957).
10. J. Anderson, E. W. Emery, J. M. McAlister, and S. B. Osborn. *Clin. Sci.* **15**, 567 (1956).
11. J. H. Marshall, R. E. Rowland, and J. Jowsey. *Radiation Res.* **10**, 258 (1959).
12. E. Lloyd. *Calcified Tissues*. University of Liege, Liege, 1965, p. 381.
13. R. E. Rowland. *Radiation Res.* **15**, 126 (1961).
14. H. S. Carslaw and J. C. Jaeger. *Conduction of Heat in Solids*. Clarendon Press, Oxford, 1959, pp. 188 and 262.
15. R. E. Rowland. *Clin. Orthoped.* **28**, 193 (1963).
16. J. H. Marshall and R. E. Rowland. Argonne National Laboratory Radiological Physics Division Semiannual Report, January through June 1958. ANL-5919, p. 35.
17. J. C. Reynolds. Argonne National Laboratory Radiological Physics Division Semiannual Report January through June, 1958. ANL-5967, p. 81.
18. J. H. Marshall. Argonne National Laboratory Radiological Physics Division semiannual Report July through December, 1958. ANL-5967, p. 99.
19. C. A. Baud. *Acta Anat.* **51**, 209 (1962).
20. W. Jost. *Diffusion in Solids, Liquids, Gases*. Academic Press, New York, 1952, p. 205.
21. W. F. Neuman and M. W. Neuman. *The Chemical Dynamics of Bone Mineral*. University of Chicago Press, Chicago, 1958, pp. 101–106.

22. J. H. Marshall. *Bone as a Tissue*. McGraw-Hill, New York, 1960, p. 149.
23. F. Wasserman and J. A. Yaeger. *Z. Zellforsch.* **67**, 636 (1965).
24. R. R. Cooper, J. W. Milgram, and R. A. Robinson. *J. Bone Joint Surg.* **48A**, 1239 (1966).
25. J. Anderson, R. W. S. Tomlinson, S. B. Osborn, and M. E. Wise. *Lancet* **I**, 930 (1967).

CALCIUM POOLS AND THE POWER FUNCTION*

John H. Marshall

INTRODUCTION

There is now an extensive literature on calcium kinetics using ^{47}Ca and ^{85}Sr for medical purposes.[1] Heaney has provided a valuable review of the current interpretation of calcium kinetic data.[2] A recent paper[3] describes the use of a digital computer program to fit a two-compartment open model to ten days of ^{47}Ca data in man. Rather than reviewing the data from these excellent and practical approaches to calcium pools, I should like to take a broader view and try to see whether, by considering the data from autoradiography and tetracycline labeling as well as all the alkaline earth tracer data, one can delineate the mechanisms of calcium transfer and fit them into the whole-body system. This undertaking is not complete. The following is the situation as it appears today.

Calcium metabolism is complex both because there are a number of interacting mechanisms of calcium transfer and because there is an extremely wide range of calcium turnover times. There has been much research on the mechanisms at the level of bone crystals and at the microscopic level, but there is as yet no close relationship between these physiological mechanisms and whole-body models. To represent the known physiological mechanisms accurately, one would be forced to use so complex a model that its many parameters could not be derived from existing data. To represent simply the whole-body retention of calcium-like isotopes, without attention to mechanism, it has been found that one needs about one compartment for each factor of ten in the time period over which data are to be fitted, and some of the compartments in such a set find little physiological correlation. I suspect that one could choose many different sets of compartmental turnover times and get just as good a fit to the data, depending upon which time one chose to terminate the data collection. If the fit is made by computer, the decision as to where the compartmental time constants will fall on the time scale is largely made when one chooses the number of compartments and when one places lower and upper limits on the time after injection over which data are entered. This complication arises from the fact that bone, at least over the longer periods of time, represents a continuous system for calcium deposition and removal without the clumping of turnover times into groups that would suggest a particular compartmental representation. Furthermore, data are now available that cover five and six orders of magnitude of time, from minutes after injection of a radioisotope to many years, and five- and six-compartment systems are probably too unwieldly to provide much insight into mechanisms.

For calcium one needs both a simpler and a more powerful approach to supplement compartmental analysis, an approach which treats the body as a continuous system without the assumption of particular pools. Such an approach is made by the power function model, a model which provides approximations to blood and body specific activities under different physiological conditions and yields quite complex predicted behavior under changes of any one of its three parameters. I will briefly describe this power function model and then go on to a generalized compartmental model which provides one way to relate the physiological mechanisms to the essentially power-function behavior of the system as a whole. But first, let me review the mechanisms of calcium transfer on the microscopic level as observed by autoradiography and microradiography of bone.

MECHANISMS ON THE MICROSCOPIC LEVEL

Figure 73 shows four autoradiographs of a cross section through the midshaft of the radius of two beagle dogs injected with ^{45}Ca at one year of age. The bone samples were obtained at four different times after injection, 5 hours, 4 days, 28 days, and 372 days. The first two times refer to the first dog, the last two to the second dog. The 5-hour and 28-day autoradiographs were obtained by amputating a foreleg just below the knee. The 4-day and 372-day autoradiographs

* Presented at Symp. on Compartments, Pools and Spaces in Medical Physiology, Oak Ridge, October 24–27, 1966. USAEC Symp. Ser. 11, Report CONF-661010, pp. 451–468.

This paper was presented six months before the preceding paper, Radial Diffusion from Canaliculi, was written and provides the background for that development.

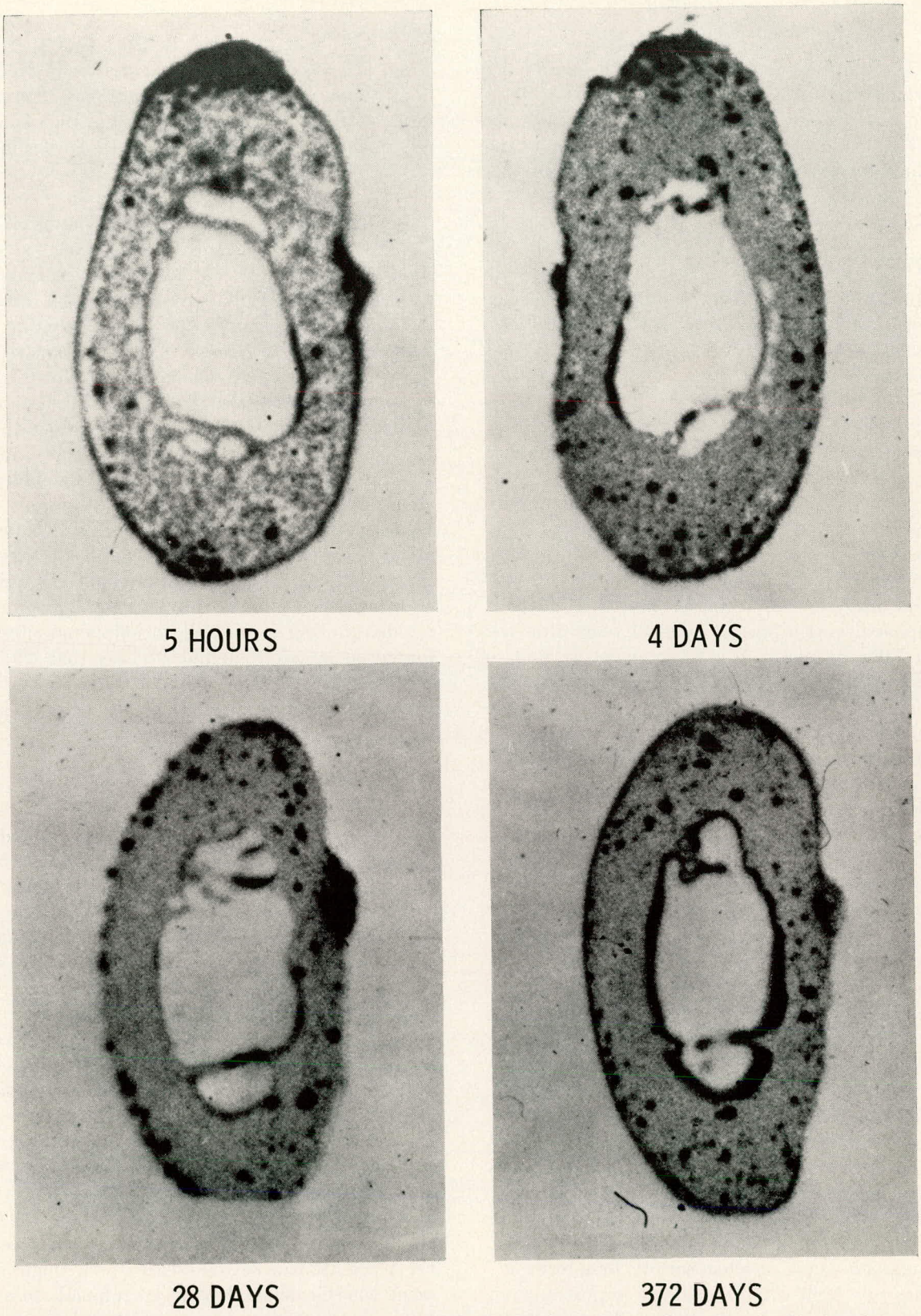

FIG. 73. Calcium-45 autoradiographs of a cross section through the midshaft of the radius of two beagle dogs injected with 44 μCi/kg at one year of age. The times under each picture refer to the time the bone sample was taken. The upper two refer to one dog, the lower two to the other. Eastman No Screen (2) Film exposed for 19 days beginning 13 months after injection. All four autoradiographs were exposed and developed together for identical times. Note the black band at the endosteal surface of the 372-day autoradiograph which corresponds to new bone growth which must have been a strengthening reaction to the amputation of the opposite leg. The pictures show the buildup and retention of the diffuse component.

were made from the same location in the remaining foreleg which was taken at the time of sacrifice. This procedure was chosen so that in the comparison of the two early and the two late autoradiographs the dogs could serve as their own controls. The ^{45}Ca injections and the exposure times were the same for each autoradiograph.

Long-Term Exchange

Probably the most prominent feature of the calcium transfer of adult bone is associated with the gray area, which indicates a relatively uniform ^{45}Ca uptake and which is described as the diffuse component. At five hours this diffuse component is not quite uniform. The ^{45}Ca activity has not yet reached the mineral most remote from the blood supply. By four days, however, the white areas are practically all filled. The remarkable thing is that the activity can be picked up rapidly and yet is held with little loss for long periods of time. By densitometer, the specific activity of the diffuse component in the second dog was only 10 to 20 percent less at one year than it was at one month. The diffuse component is still present even 40 years after the intake of ^{226}Ra in man.[4] Whatever model we find to describe it, we know that it is a very long term phenomenon. The activity shows little tendency to equilibrate with the activity of the blood. One would naturally suppose that this activity is taken up in a one-way flow of calcium from blood to bone, but surprisingly, this is not the case. To explain the observed ^{45}Ca uptake, we would need a rate of increase of mineral density of 20 to 30 percent per year. Although there is some *secondary mineralization* going on in these locations, the rate of increase of mineral density is much too low to account for the observed rate of calcium transfer. Furthermore, in fully mineralized canine bone, which according to serial x-ray measurements is not increasing in mineral density, there is still a diffuse component of almost the same magnitude as shown here.[5] The diffuse component, therefore, represents primarily a two-way transfer of calcium between blood and bone. Operationally, we describe it as long-term exchange. Because it is a two-way process, one must expect that alkaline earth tracers will be lost by exchange back again from bone to blood, and this has now been observed over long periods of time in several laboratories.[6]

The submicroscopic mechanism of long-term exchange has not been established, but it probably involves turnover of calcium by recrystallization or by diffusion in the solid phase. Furthermore, bone crystals are extremely small, probably roughly cylindrical, and averaging 50 angstroms in diameter,[7] so that they have a tremendous surface-to-volume ratio. From this shape and diameter it follows that 20% of body calcium is within 3 angstroms of crystal surfaces, so that a large calcium compartment may be in relatively close communication with extracellular fluid.

Bone Formation: Apposition

Another mechanism of calcium transfer between blood and bone is indicated by the black spots, or hot-spots in Figure 73. In a number of experiments we have directly measured the amount of ^{45}Ca activity associated with regions of new bone formation, and we find that the more intense ^{45}Ca depositions represent a one-way transfer of calcium from blood to newly-forming bone crystals. Since bone formation occurs by the addition of thin layers of new bone to existing bone surfaces, it may be conveniently called apposition. The rate of apposition as observed by double tetracycline labeling agrees within 10 to 20 percent with the value one calculates from the observed ^{45}Ca activity at about a week after injection divided by the time integral of the blood specific activity. However, this close agreement holds only if one limits oneself to rapidly-growing animals or to individual sites of bone formation in adult animals.[8] Less than 20% of the ^{45}Ca in the cortical bone of older adult dogs is deposited by bone formation.[5] Most of the activity is due to long-term exchange.

Resorption

The inverse process to bone formation is resorption, which involves local removal of both mineral and its supporting bone matrix. Until recently it has been thought that resorption could take place only at bone surfaces. Now Bélanger[9] and others have shown that it is possible for an osteocyte within bone to erode the wall of its lacuna, a process which they term osteolysis.

Short-Term Exchange

Finally a mechanism of calcium transfer which can be called short-term exchange has recently been investigated by Rowland.[10] Shortly after injection there is a rapid uptake of ^{45}Ca on all bone surfaces near the blood supply, surfaces of trabeculae, cortex, and the walls of haversian canals. Only the crystals which lie near these bone surfaces appear to be involved. This ^{45}Ca activity reaches a maximum at about 0.6 day in adult dogs and then falls with the specific activity of the blood. It can be represented as a single compartment whose calcium content corresponds to a layer of bone mineral 2000 angstroms thick. When extrapolated to the whole skeleton using an estimate of the tota surface-to-volume ratio of bone, this compartment contains an amount of calcium which is close to that obtained by whole-body kinetic measurements of the

short-term pool. The rapidly-exchangeable calcium of the mineral phase has, therefore, been located at bone surfaces. It does *not* lie primarily in regions of young or lowly-mineralized bone as had been thought until quite recently, and it does not involve the surfaces of crystals at more than a few microns from the blood supply.

In summary, the process of calcium uptake can be described as of four types: short-term exchange on bone surfaces; bone formation which leads to the more intense hotspots; secondary mineralization, the slow approach to full bone density; and, perhaps for adult bone the most important, long-term exchange with the calcium of existing bone. The rate of long-term exchange is known to decrease slowly with local bone age.[11] Furthermore, in the adult, there are often quite different rates of bone formation and resorption in different bones and in different parts of the same bone. We are, therefore, faced with a mixed model situation. Calcium can be incorporated by the formation of new bone and it can be removed by resorption. It can be incorporated and removed by long-term exchange. Calcium incorporated by bone formation can be lost by long-term exchange, and conversely, calcium that has been deposited by long-term exchange can subsequently be lost by resorption. Finally, over 80% of the calcium lost from bone by any process will will be carried by the blood and will be redeposited somewhere else.* What is the best way to represent such a system?

THE POWER FUNCTION MODEL

The most successful *simple* way of representing the retention of alkaline earth tracers has been by the use of the power function. It has been profitable to base a model on this observed retention function in order to derive a number of relations between blood and body specific activities. The specific activity of the blood is closely related to that of extracellular fluid, which provides the microscopic environment for the bone mineral. The feedback between the many processes of calcium transfer throughout the body probably occurs primarily by way of the blood. With a representation of blood specific activity under different conditions one can construct *local* compartmental and stochastic models that use forced, rather than free-running, functions for blood specific activity. In this way one can isolate *in vivo* the separate local processes of calcium transfer, comparing the predictions of local models with direct observations of tracer concentration by quantitative autoradiography.

In order to derive a curve of blood specific activity from a power function type of retention curve, one must first insure that the boundary conditions on retention make sense mathematically. In other words, the retention of tracer in the body at the instant of injection must be unity. This can be done by modifying the power function by the addition of a small time ϵ and using as coefficient ϵ^b. The retention R as a function of time t is then

$$R = \epsilon^b (t + \epsilon)^{-b} \qquad (1)$$

This is not an exact representation of alkaline earth retention curves, but it is the closest simple approximation to the true situation.

If one postulates that all the tracer activity which leaves the body must be carried to an excretory outlet by way of the blood, and if the rate of excretory blood clearance is constant, then the specific activity of the blood, S, as a function to time, t, can be derived[12] from the time derivative of the retention function:

$$S = -\left(\frac{q}{\eta k}\right)\frac{dR}{dt} \qquad (2)$$

where q is the activity injected, k is the total endogenous excretion rate of calcium (urinary plus fecal) and η is a factor to describe the excretion of other alkaline earth tracers relative to calcium ($\eta = 1$ for calcium, $\eta \sim 3$ for strontium, and $\eta \sim 30$ for radium). If one uses the power function expression for R given above, (1), then expression (2) fits within 20 to 30% a wide range of data for ^{45}Ca, ^{90}Sr, and ^{226}Ra in dogs, one example of which is shown in Figure 74. I must emphasize that the

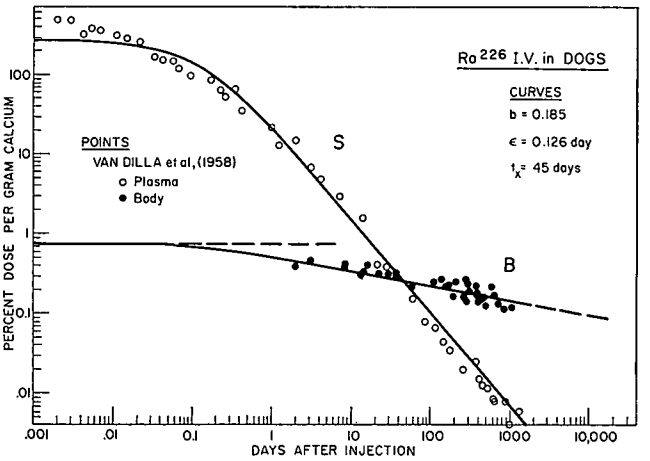

FIG. 74. Log log plot of $^{226}Ra/Ca$ ratio in the blood plasma and the body of beagle dogs injected at 1.3 years of age.[13] The body data were obtained from retention data by dividing by the measured average body calcium, c = 135 g Ca. The retention was measured for four different injection groups (levels 2–5, a factor of 27 in dose) and no effect of dose level was observed. Almost all plasma samples were from 4- and 5-level dogs. Curves S and B are the best fits of the power function model.[12]

* This follows from the power function model[12] expression $A_0 = \eta k/b$ with the typical value of $b = 0.2$.

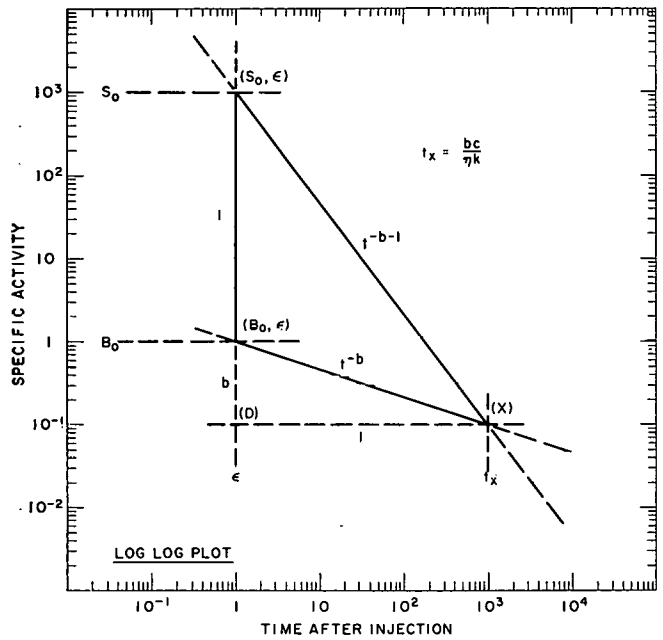

FIG. 75. The power function triangle. This construction is used to demonstrate the behavior of the specific activities of the body, $B \sim t^{-b}$, and blood, $S \sim t^{-b-1}$, under changes in accretion and excretion rates according to the power function model.[12] Compare with Figure 74. The time ϵ is the time of intersection of the extrapolated power function lines with the zero time asymptotes of S and B.

fit is not perfect. Curve S is the $^{226}Ra/Ca$ ratio in blood plasma. Curve B is the body retention curve R multiplied by the activity injected, q, and divided by body calcium, c. The points are data.[13] The curves are theory. There is often a tendency for the data to "ess" slightly about the power function line, though here it is barely perceptible. This power function expression for blood specific activity has been found to be approximately correct even forty years after the time of radium intake in man,[14] and it also provides a good approximation to radiocalcium blood curves over the period soon after injection.[12]

At short times there is a bend in the log log plot of blood specific activity at about the time ϵ, which in Figure 74 is 0.1 days. At times shorter than ϵ, the data appear to follow another straight line with a slope much less than unity.[13, 15] Expressions (1) and (2) do not fully represent these early times, though the discrepancy is not large. Two straight lines with an intersection at about ϵ might be better if there were a way to write such an expression analytically. It follows from the power function model that ϵ is the turnover time of an initial calcium pool.[12] The time ϵ is closely related to the time of appearance of a straight section in a semilog plot of S, because a curve which is bending downwards on a log log plot can for a short time be represented as a single exponential.

Now, how do the power function slope b and the time ϵ vary under different metabolic conditions? Expressions (1) and (2) lead to finite values of B and S, as time approaches zero, which we can designate B_0 and S_0, respectively. Note that B_0 is simply q/c. Let us look at the obtuse triangle formed by the points (S_0, ϵ), (B_0, ϵ), and the crossover point (X) on a log log plot of serum specific activity S and body specific activity B, Figure 75. Point (X) determines a crossover time t_x. The dashed lines complete two right triangles with their right angle at (D). Now, if we let the actual distance on the graph paper between points (D) and (X) be 1 inch, then the distance between (D) and (B_0, ϵ) will be b inch. That is what is meant by the power function expression, $B \sim t^{-b}$. Similarly, the distance between points (D) and (S_0, ϵ) is $b + 1$ inches because, being the time-derivative of t^{-b}, $S \sim t^{-b-1}$. Therefore, it follows that the distance between points (B_0, ϵ) and (S_0, ϵ) is always equal to the distance between points (D) and (X) (one inch). Equal distances on a log log plot mean equal ratios, so that the ratio S_0/B_0 is equal to the ratio t_x/ϵ. The values B_0 and S_0 are the specific activities one obtains at zero time by considering the injected activity either to be divided by total body calcium, c, or by the calcium of an initial pool, E_0, respectively. Now, initial pool calcium should be a fairly constant proportion of total body calcium, so that we can consider $S_0/B_0 = c/E_0 = t_x/\epsilon$ to be a constant of calcium metabolism that can be determined from existing data. The value of c/E_0 that so far gives the best fit to most data[12] is roughly the order of 300.

Now what would a constant ratio, t_x/ϵ, imply about the shape of blood specific activity curves under different metabolic conditions? By equating the power function expressions for S and B and solving for t, one finds a simple expression for crossover time:

$$t_x = \frac{bc}{\eta k} \qquad (3)$$

where ηk is the calcium excretion rate as defined above, c is body calcium, and b is the slope of power function expression for retention. Suppose that one holds the rate of calcium excretion constant but increases the rates of calcium transfer between blood and bone. The initial effect after injection of a tracer is to increase tracer retention in the body, because tracer is more rapidly transferred out of the blood to the bone. If it is no longer in the blood, it cannot be excreted as rapidly as it was before. Therefore, increased rates of calciu transfer between blood and bone reduce the value of In particular, larger accretion rates require smaller values of b.[12] Now from the formula for crossover time, expression (3), it is clear that for constant excretion

rate, ηk, smaller values of b lead to smaller values of t_x. And since the ratio t_x/ϵ is constant, smaller values of t_x imply smaller values of ϵ.

The model is telling us that increased rates of calcium transfer between blood and bone shift the whole triangle to the left. Also it says that the blood specific activity curve becomes *less steep* on a log log plot (b is less)—a remarkable result. One might expect a steeper drop in S when the rate of tracer transfer from blood is greater. What happens is that lower values of S at any given time are produced by a movement of the triangle to the left accompanied by a decrease in the slope of the power function. This is actually observed. For example, for ^{45}Ca in normal, adult man ϵ is two to three days. For adult dog, $\epsilon = 0.3$ day. For a growing puppy $\epsilon = 0.03$ day, less than an hour.[12] This means that one would have to look as early as an hour or so after injection to find the straight section in a semilog plot of S for a growing puppy, whereas one finds it at several days in man. The parameter ϵ is two orders of magnitude smaller in a rapidly-growing animal than it is in adult man. This agrees with the observations of Anderson in man[15] and rats.[16]

Data for other species, different rates of growth, and other alkaline earth isotopes have so far fallen between these two extremes. This complex and fairly realistic shift in position of the power function triangle suggests that it should be informative to consider tracer data with relation to the times ϵ and t_x. Physiologically, such shifts in time scale imply that the rates of many different processes are all changing together.

Exchangeable Mass and the Time t_y

Of course, *if* one is dealing with a steady state system, one knows that an increased rate of calcium transfer between blood and bone must eventually have the opposite effect to that described above: tracer that was initially picked up more rapidly must finally be released more rapidly. *If* the function R is age-invariant, (which is less restrictive than the steady state assumption) this effect can be taken into account in the model by calculating a later time t_y, at which the tracer must begin leaving the body at a rate faster than that predicted by the power function. This calculation is based on the requirement that the area under the retention curve be no greater than the area under the blood specific activity curve.[12] I mention this point here because Bergner[17] has presented essentially the same relationship, a ratio of the time integral of the body specific activity to the time integral of the blood specific activity, as a method for measuring the exchangeable mass. There are now enough data to suggest that the method would run into difficulty if applied to calcium metabolism. We are beginning to find that in several cases the power function retention curves continue beyond the time t_y, which means that the area under the retention curve will exceed that expected if all body calcium were exchangeable. All body calcium probably *is* exchangeable according to Bergner's definition; that is, if one could wait long enough one would find that practically all of body calcium had at some time transferred from bone to blood either by resorption or by long-term exchange. It has been suggested that the excess area may be due to partial failure of age-invariance,[12] or in the case of ^{133}Ba, to the deposition of activity at much higher than the specific activity of the blood.[18]

THE CLOCK MODEL

Now what physiological mechanism(s) are responsible for the essentially power-function retention of the alkaline earths? There are a number of kinds of models that have some elements of truth to them. Stochastic models of recrystallization and mineral remodelling are promising. Non-steady state models which incorporate a rate of calcium transfer which decreases with the age of the bone element are probably part of the story: we know that the rate of long-term exchange does decrease with bone age[11] and that an inverse dependence upon time would give rise to a power function retention whose slope depended upon the rate of exchange at a given age.[15, 19] However, there seems to be no evidence as yet that the over-all behavior of alkaline earth isotopes in man is strongly dependent on the age at injection after adulthood has been reached. Perhaps the reduction in the rate of long-term exchange with bone age is compensated by the continual creation of new bone by haversian remodelling.

When one considers compartmental models which yield power function retention, it is difficult to decide whether a series model or a parallel model will best approach the known complexity of the system. Several multicompartmental models of the series type have been tried which represents a diffusion of calcium from the blood into extracellular fluid and into the deepest layers of bone crystals.[20] Most compartmental models, however, have represented only a small fraction of body calcium, being primarily attempts to describe the short-term exchangeable pool. I would like to describe here another compartmental model which may provide a little insight into the problem.

It is an open parallel model with an indefinitely large number of compartments connected directly to a central pool, as shown in Figure 76. The central pool is assigned a mass of calcium E_0 which corresponds to the initial pool of the power function model, as described above. E_0 is essentially the blood calcium plus

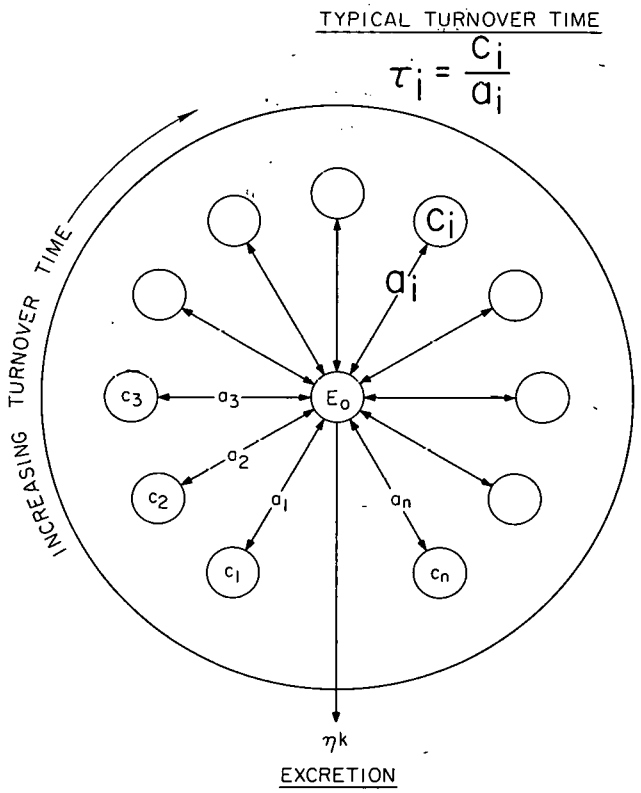

FIG. 76. The clock model. A parallel, open model represent ing body calcium by an indefinitely large number of peripheral compartments with predetermined turnover times spaced at even geometric intervals over the full range of possible turnover times. The model is fitted to particular retention and blood data by finding the corresponding set of values c_i.

all other calcium which can equilibrate with the blood calcium within the time ϵ. Each of the peripheral compartments is assigned a mass of calcium c_i and a two-way rate of transfer a_i (mass of calcium per unit time) in such a way as to maintain a predetermined set of turnover times (c_i/a_i).

Now if one wishes to represent the data of alkaline earth tracer retention by a series of exponentials, one needs about one exponential term for each decade of time after tracer injection. One can easily use more than one term per decade. Therefore, if the turnover times of the peripheral compartments are distributed geometrically, and two or three compartments are assigned to each decade of turnover time, a generalized parallel model results which for obvious reasons is called the clock model. The range of turnover times can be made large enough to cover the whole possible span from an hour to a hundred years. The model can then be made to fit a wide variety of retention curves simply by choosing different sets of values for c_i, the amount of calcium to be associated with each turnover time. This calcium distribution can then be expressed as a function of turnover time without reference to individual compartments.

In particular, the PACE analogue computer was used to determine which sets of calcium values are associated with different power function retentions. The resulting specific activities of several different peripheral compartments and that of the central pool are shown in Figure 77. In this plot, $\epsilon = 1$ unit of time and $b = 0.2$. Thus the pool specific activity S is made to fall according to the function $(t + 1)^{-1.2}$. Curves for compartments with turnover times of 0.1, 10, and 1000 ϵ are shown. Note that the overshoot of the specific activity of these peripheral compartments after their maximum, increases with turnover time. Thus, estimates of pool size from the parameter E of the Bauer-Carlsson-Lindquist[12] equation grow more rapidly with time than the actual size of the pool. (The E value includes the overshoot or transient equilibrium factor in its representation of exchangeable or equilibrated activity, ES.) It is also significant for the understanding of models that the time of maximum specific activity of each compartment is later than its turnover time τ if that turnover time is less than ϵ, and is progressively earlier with respect to turnover time as turnover time increases. In Figure 77, the curve for the longest term compartment peaks at 1/10 of its turnover time. For the runs with $b = 0.5$, one of the long-term compartments peaked at 1/100 of its turnover time.

Given a model of this type, there is only one smooth distribution of calcium with respect to turnover time that yields a given power function retention. This calcium distribution is shown in Figure 78, in which the

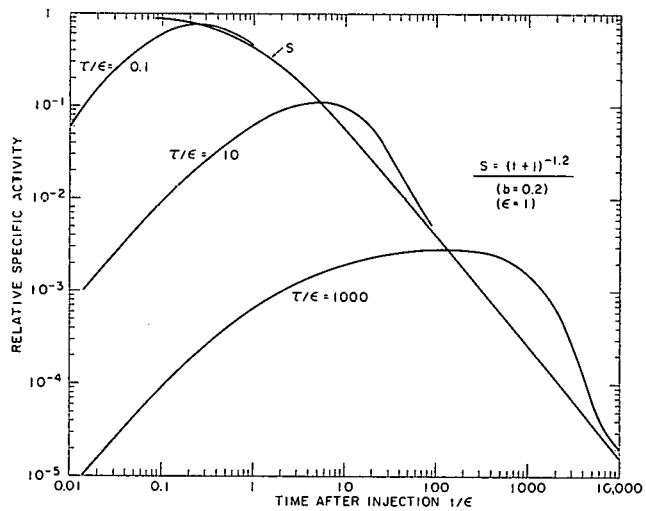

FIG. 77. Analogue computer traces for several peripher compartments and for the central pool, S, of the clock mod with the calcium values c_i so chosen that power function retention with $\epsilon = 1$ and $b = 0.2$ was obtained. Fifteen peripheral compartments were actually used, though five would have given almost as smooth a curve for S.

fraction of body calcium with turnover time less than or equal to a time τ is plotted versus τ/ϵ. The ordinate represents the sum of the masses of calcium contained in all the peripheral compartments from the shortest term compartment at seven o'clock in Figure 76 up to any given turnover time τ. It does not include the calcium of the central pool E_0, and this must be added to the values for peripheral calcium to give the total exchangeable pool.* Since a conversion factor from analogue computer time to real time is necessary, it is convenient to express the turnover times along the abscissa in units of the time ϵ, the turnover time of the initial pool. As was suggested by the power function model, it is interesting to relate the kinetic data for a particular animal or isotope to the time ϵ, which determines the position of the power function triangle. When this is done with the analogue computer data, it is found that the calcium distributions are not very different for a slope of $b = 0.2$ (typical of most data) and the slope of $b = 0.5$ (which occurs for ^{226}Ra in man).

This implies that the calcium distribution with respect to turnover time in units of ϵ does not depend very strongly on the particular slope b, but is primarily a property of power function retention. Different slopes are then primarily indicative of different excretion rates, ηk. This conclusion may not hold for very long turnover times: the analogue computer solution was not accurate beyond times of 1000 ϵ owing to the four to five orders of magnitude in the falling specific activity of the central pool which had to be followed. However, if one takes $\epsilon = 1$ day as a representative value for adult man, one finds that the calcium distribution in Figure 78, when extrapolated upwards to the right, reaches total body calcium at roughly 100 years. The most slowly-remodelling regions of human bone probably do have turnover times of this order of magnitude.

Approximately the same relative distribution of calcium with respect to turnover time is not unreasonable for rapidly-growing animals, provided one remembers that then ϵ is much smaller and that the time scale must be shifted to the left by two orders of magnitude.

Perhaps different metabolic states can be represented primarily as a shift in time scale. The physiological meaning of such a representation would be that metabolic shifts normally result in proportionate changes in all the rates of calcium flow in the various processes. This would explain the observed correlation between A_t and E_t, the accretion rate and exchangeable pool.[1, 12] When ϵ is lowered, A_t is raised because the

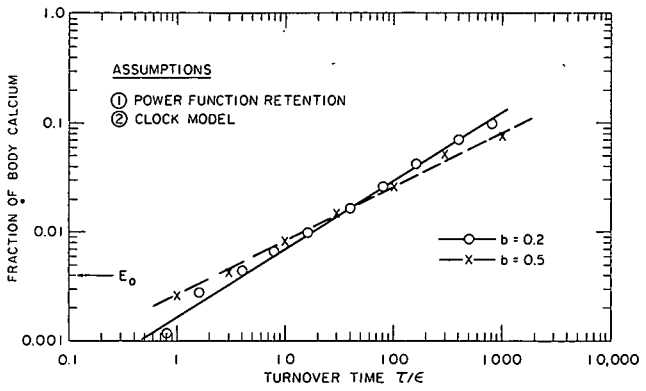

FIG. 78. Data from the PACE analogue computer for the values of c_i versus turnover time τ_i when the clock model is fitted to power function retention with either $b = 0.2$ or $b = 0.5$. The ordinate was obtained by taking the sum of the calcium contents of the peripheral compartments from c_1 up to c_i with a turnover time τ_i, dividing that sum by body calcium, and plotting the result at turnover time τ_i. The ordinate is, therefore, independent of the number of compartments and represents the fraction of body calcium with turnover time less than or equal to τ. The turnover time τ along the abscissa has been normalized by dividing it by ϵ. The time ϵ was 0.1 second in computer time. Note that the fraction of body calcium per unit turnover time increases roughly as the square root of turnover time.

constituent rates of calcium transfer are higher. The corresponding shift of the whole calcium distribution to shorter turnover times raises E_t, because then more calcium can equilibrate within the given time t. The time-scale-shift explanation is needed more than ever now that Rowland[10] has shown that the rapidly-exchangeable pool is not associated histologically *either* with regions of new or lowly-mineralized bone *or* with the diffuse component, which together give rise to A. If A and E are unrelated in location, they must be related in time scale. They correlate because the rates of the different processes change together.

We, therefore, have a broad picture of the turnover time distribution of calcium in the body. It may be significant that this distribution is not far from an amount of calcium per unit of turnover time which rises with the square root of the turnover time. Such a relation seems suggestive of stochastic or diffusion processes, but as yet we do not have a detailed explanation.

It must be remembered that there is no proof that the parallel model is really closer to the truth than series models or microscopically time-variant models. Is there a wide enough distribution in the rates of apposition and resorption in different volumes of bone to account for the calcium distribution in Figure 78? It hardly seems likely. But then, if the processes of long-term exchange are predominant in adult bone, one

* The value for the size of the initial pool used in the computer runs, $E_0 = 0.4\%$ of body calcium, may be a little too high for some data. The time period over which the computer solution remained accurate was extended by making E_0 as large as possible.

would have to associate the whole clock model with individual regions of bone so that the central pool could be visualized as the fluid environment of the bone crystals. If that is the case, a better model might be approached from a series configuration. We need to know more about the processes of calcium transfer on the submicroscopic level of bone crystals before the matter can be decided.

SUMMARY

Calcium metabolism appears to be a continuous system. The calcium pool expands as time after tracer injection increases due to the fact that one includes larger and larger calcium turnover times due both to apposition-resorption and to long-term exchange. This pool expansion has a change of character at about the time ϵ, and it may prove useful to consider metabolic data in relation to this time. Thereafter, according to a parallel model, the amount of calcium per unit of turnover time increases approximately as the square root of turnover time. It may be possible to visualize widely different rates of metabolism both in different species and at different ages as a shift in time scale, which would imply a proportionate change in all the rates of calcium transfer between blood and bone. Such a shift provides an explanation for the often observed correlation between A and E, the calcium accretion rate and exchangeable pool.

REFERENCES

1. *Medical Uses of ^{47}Ca: Second Panel Report*, Technical Reports Series No. 32 International Atomic Energy Agency, Vienna, 1964.
2. R. P. Heaney. Evaluation and Interpretation of Calcium-Kinetic Data in Man. *Clin. Orthoped.* **31**, 153–183 (1963).
3. S. H. Cohn, S. R. Bozzo, J. E. Jesseph, C. Constantinides, D. R. Huene, and E. A. Gusmano. Formulation and Testing of a Compartmental Model for Calcium Metabolism in Man. *Radiation Res.* **26**, 319–333 (1965).
4. R. E. Rowland and J. H. Marshall. Radium in Human Bone: The Dose to Microscopic Volumes of Bone. *Radiation Res.* **11**, 301 (1959).
5. J. H. Marshall, R. E. Rowland, and J. Jowsey. Microscopic Metabolism of Calcium in Bone. *Radiation Res.* **10**, 243–270 (1959).
6. E. L. Lloyd. Quantitative Autoradiography of ^{45}Ca in Bone. *Calcified Tissues*, Second European Symposium. University of Liege, Liege, 1965, pp. 381–390; see also, K. A. Sears, W. S. S. Jee, and C. W. Mays. Radium Dosimetry. *University of Utah Radiobiology Report* COO-226 (September 30, 1962), pp. 86–94.
7. F. C. McLean and M. R. Urist. *Bone. An Introduction to the Physiology of Skeletal Tissue*. University of Chicago Press, Chicago, 1962, p. 46.
8. W. R. Lee, J. H. Marshall, and H. A. Sissons. Calcium Accretion and Bone Formation in Dogs, an Experimental Comparison between the Results of ^{45}Ca Kinetic Analysis and Tetracycline Labeling. *J. Bone Joint Surg.* **47B**, 157–180 (1965).
9. L. F. Bélanger, J. Robichon, B. B. Migicovsky, D. H. Copp, and J. Vincent. Resorption without Osteoclasts (Osteolysis). *Mechanisms of Hard Tissue Destruction*. A. A. A. S. Publication No. 75, Washington, 1963, pp. 531–556.
10. R. E. Rowland. Exchangeable Bone Calcium. *Clin. Orthoped.* **49**, 233–248 (1966).
11. J. H. Marshall. Microscopic Metabolism of Calcium in Bone. *Bone as a Tissue*, Ed. K. Rodahl et al. McGraw-Hill, New York, 1960, pp. 144–155.
12. J. H. Marshall. Theory of Alkaline Earth Metabolism, *J. Theoret. Biol.* **6**, 386–412 (1964).
13. M. A. VanDilla, B. J. Stover, R. L. Floyd, D. R. Atherton, and D. H. Taysum. Radium and Radon Metabolism in Dogs. *Radiation Res.* **8**, 417–437 (1958).
14. H. F. Lucas, Jr., J. H. Marshall, and L. A. Barrer. The Level of Radium in Human Blood Forty Years after Ingestion. Argonne National Laboratory Radiological Physics Division Summary Report, July 1962 through June 1963. ANL-6769, pp. 75–78.
15. J. Anderson, R. W. S. Tomlinson, and S. B. Osborn. An Interpretation of Radioisotope Turnover Data. *Lancet.* **I**, 949–950 (1962).
16. J. Anderson and R. W. S. Tomlinson. The Distribution of ^{47}Ca in the Rat. *J. Physiol.* **182**, 664–670 (1966).
17. P. F. E. Bergner. Exchangeable Mass: Determination without the Assumption of Isotopic Equilibrium. *Science* **150**, 1048–1050 (1965); also paper presented at Symp. on Pools in Medical Physiology, Oak Ridge, Tennessee, October 27, 1966.
18. T. M. Domanski, D. Depczyk, and J. Liniecki. A Test of the Theory of Alkaline Earth Metabolism by the Behavior of ^{133}Ba in Rats. *Phys. Med. Biol.* **11**, 461–470 (1966).
19. J. H. Marshall and R. E. Rowland. Microscopic Metabolism of Calcium in Bone, Addendum Concerning the Power Function Behavior of Radioisotope Retention. Argonne National Laboratory Radiological Physics Division Semiannual Report, July through December 1958. ANL-5967, pp. 78–79.
20. C. J. Maletskos. A Study of the Dynamics of Calcium Metabolism in Dogs, Ph.D. Thesis Massachusetts Institute of Technology (1954) and *Radioactivity Center Annual Progress Report* (May 12–16, 1955); see also J. H. Marshall and R. E. Rowland. Calculation of the Possible Effects of Calcium Diffusion in Bone Crystallites. Argonne National Laboratory Radiological Physics Division Semiannual Report, January through June 1958. ANL-5919, pp. 35–46.

AUTORADIOGRAPHY OF RADIUM BONE SECTIONS BY MEANS OF POLAROID FILM

R. E. Rowland

Autoradiography of bone sections from the radium cases has been of great value, not only for an understanding of the microdosimetry which exists in these bones, but also for the information that has been developed regarding the normal metabolism of bone. In our laboratory gross autoradiographs of these bone sections have routinely been made on Eastman Kodak Autoradiographic Type A plates.

In recent years our interests have turned toward those cases whose body content has been relatively low, of the order of 0.5 μCi or less. A question of considerable significance concerns the alteration of bone mineral metabolism as a consequence of the radium burden. Are the autoradiographs we have obtained, and the information derived from them regarding bone turnover, altered as a consequence of the radiation dose experienced by the bone?

We have, in the past, restricted our gross autoradiographic studies to bone sections obtained from cases with terminal burdens greater than 1 μCi Ra^{226}. This restriction has been due to the time required for satisfactory autoradiography. In general, sections from cases containing about 1 μCi Ra^{226} require an exposure of about one year on the Type A plates. Thus, extension of autoradiography to cases containing only 0.1 μCi would require exposures of the order of 10 years, clearly an unacceptably long time.

A solution to this impasse was presented by the article by Hsieh, Hungate and Wilson,[1] which described a technique for registering alpha particle autoradiographs on Polaroid film by means of a zinc sulfide screen. The transformation of alpha particle energy into light proved to be an effective method of utilizing the alpha particles from bone to produce gross autoradiographs.

The bone section to be autoradiographed is mounted on a 2″ × 3″ glass microscope slide and covered with the zinc sulfide phosphor. We have employed a silver-activated phosphor which is coated on a Mylar film.*

The slide, bone section, and phosphor, taped together as a unit, are pressed in contact with the Polaroid film for a suitable exposure period. Two films have been employed, Type 57 and the very fast Type 510. Type 57 has given the most satisfactory results in terms of visual appearance.

Figure 79 shows a Type A autoradiograph and a Polaroid Type 57 autoradiograph of the same bone section. The Type A autoradiograph was exposed for 15 months, the Polaroid for only 7 days. This reduction in exposure time, of the order of a factor of 60, is typical of our experience with this film.

Figure 80 shows the results from a low-level radium case, the terminal burden here is 0.074 μCi (Case

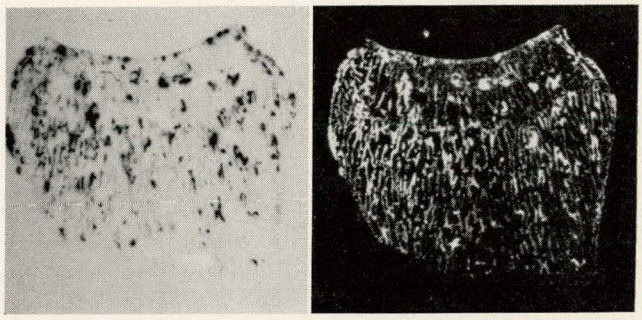

FIG. 79. Two autoradiographs of the same bone section. On the left the film is Eastman Kodak Autoradiographic Type A, exposed for 15 months; on the right Polaroid Type 57 exposed to the zinc sulfide screen and bone section for 7 days. This distal tibia section came from case 03-210, which contained terminally 1.2 μCi Ra^{226} acquired 29 years earlier.

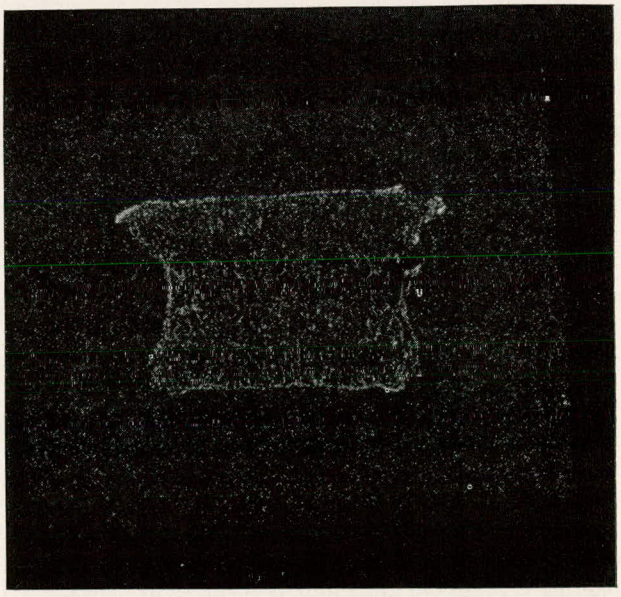

FIG. 80. A 153-day exposure of a bone section from the first lumbar vertebra of case 01-456. The body content was 0.074 μCi, the lumbar vertebrae contained 0.82 times the skeletal average in terms of μCi Ra^{226} per gram of bone. The radium was acquired over a 3-month period at age 50, 20 years before death.

* Type AST-3, obtained from W. B. Johnson and Assoc., Inc., P. O. Box 415, Mountain Lakes, New Jersey.

01-456, section from the first lumbar vertebra). This is also Type 57 film; the exposure was for 153 days.

When exposures as long as this are employed, a very noticeable background is apparent, as can be seen in Figure 80. It is of interest to evaluate the magnitude of this background and to determine its origin. To attempt this, it is necessary to have a feeling for the efficiency of this system for the detection of alpha particles.

By means of a plaster of Paris radiator containing a known quantity of Ra^{226} and daughters the efficiency has been determined for the two Polaroid films. Comparing the number of recognizable white spots on the positive print (the largest of which was 130 μ in diameter) with the number of alpha particles emitted from the surface of the radiator, the efficiency was found to be of the order of 60% for Type 510. The Type 57 film detected about 40% of the emitted alpha particles.

Counting the background spots over the region on the print corresponding to the area where the zinc sulfide was in contact with the glass microscope slide, we obtained 6.0 spots cm^{-2} day^{-1} for Type 510, and 3.3 spots cm^{-2} day^{-1} for Type 57. Correcting for efficiency, these correspond to emission rates of the order of 10 and 8 alpha particles cm^{-2} day^{-1}, respectively.

It is of interest to note that figures of the order of 4 alpha particles cm^{-2} day^{-1} are quoted for the emission rates for the glass used for nuclear track plates.[2] It would thus appear that a significant portion of the background is due to the glass plates on which our sections have been mounted.

Close examination of Figure 80 will show that the background is somewhat lower immediately adjacent to the image of the bone. In this region the material in contact with the phosphor is the embedding medium, methyl methacrylate. In this autoradiograph the background over the methyl methacrylate is 2 alpha particles cm^{-2} day^{-1}, corresponding to an emission rate of about 5 alpha particles cm^{-2} day^{-1}. If this alpha activity originated entirely within the methacrylate, this would indicate about 6×10^{-13} Ci of alpha activity per gram of material. On the other hand, radon is constantly escaping from the bone section and will also contribute to the observed background.

It would appear that if care were taken to mount the bone section on a material known to be low in alpha activity, exposures of the order of one year would prove feasible. This would allow these gross autoradiographs to be made from bone sections obtained from cases with terminal body contents as low as 0.02 μCi Ra^{226}.

REFERENCES

1. J. J. C. Hsieh, F. P. Hungate, and S. A. Wilson. Autoradiography: Technique for Drastic Reduction of Exposure Time to Alpha Particles. *Science* **150,** 1821–1822 (1965).
2. S. Deutsch and E. C. Dodd. Specific Radioactivity of Ilford Plates for Nuclear Research. *Nuovo Cimento* **10,** 858–861 (1953).

RICKETS IN RATS. A PROGRESS REPORT

David J. Simmons

Rickets is a disorder of growing bone.[1, 2] The skeletal parts are soft and the long bones have very thick epiphyseal cartilages. The disorder exists because the normal processes of endochondral ossification fail. The cells in the epiphyseal growth cartilages continue to proliferate, but the tissue does not mineralize normally, and vascular invasion lags or proceeds irregularly. The general features of human rickets and rickets in rats appear similar histologically. However, whereas rickets in children is caused by a lack of dietary vitamin D, simple D deficiency alone will not produce rickets in laboratory animals. In these experiments, we have employed a low phosphorus, vitamin D-free rachitogenic diet. High resolution autoradiography with tritiated thymidine labeling was used to follow the development and healing of the disorder.

MATERIALS AND METHODS

Male weanling rats, 40–50 g body weight (Sprague-Dawley Strain) were maintained on a rachitogenic high calcium (1.2%), low phosphorus (0.1%), vitamin D-free diet for 17 days.* Control weanling rats were fed Wayne Laboratory Chow (calcium = 1.2%, phosphorus = 0.99%). At the end of this period, 5 rats fed the experimental diet and an equal number of control animals were injected with 1 μCi H^3-thymi-

* The optimum dietary phosphorus requirement for normal rat growth is 0.56–0.69%.[3]

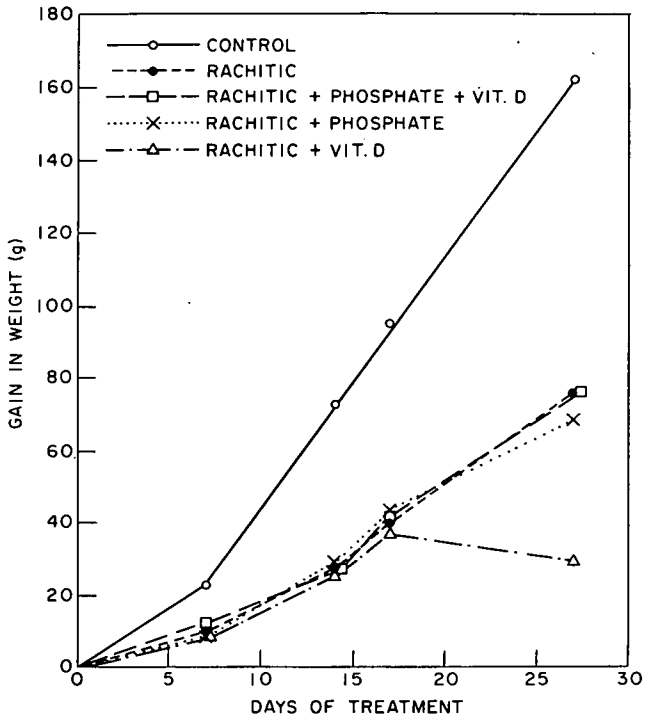

FIG. 81. Effect of diet on growth of rats

dine/g body weight* intraperitoneally, and they were sacrificed an hour later. A third group of rats was continued on the rachitogenic diet for an additional 10 days, but the basal ration fed other groups during this time was modified either by the addition of 10 I.U. of vitamin D_2 (Drisdol) per g diet, or by the addition of NaH_2PO_4 (calcium-phosphorus ratio 1.4:1), or by the addition of both NaH_2PO_4 and vitamin D_2. Groups of 5 rats fed the basal rachitogenic ration and each of the supplemented diets for 19 days (27th day of the experiment) were injected with H^3-thymidine an hour before sacrifice. The rats were killed by decapitation. At autopsy, the bones from the left side were fixed in 10% neutral formalin, decalcified in 10% EDTA (pH 7.4–7.6), embedded in paraffin and sectioned on a rotary microtome at 5 μ. The sections were dipped in Kodak NTB-2 liquid emulsion, exposed in a freezer for 10 days and developed for 5 minutes in Kodak D-19. The slides were then stained through the emulsion with hematoxylin and eosin.

The long bones from the right side were stripped free of soft tissues, x-rayed, and measured with a vernier caliper. One bone from each group was embedded undecalcified in methyl methacrylate and sectioned longitudinally on a high speed rotary saw at 100 μ. These sections were microradiographed on Kodak 649-0 spectroscopic plates. The remaining 4 bones were defatted, dried and weighed, and ashed at 600° to determine the ratio of mineral to organic matter.

The animals were weighed daily during the experiment, but no attempt was made to estimate the amount of food consumed by the different groups.

* New England Nuclear Corporation, Lot No. 235-118A-6*. Specific activity, 12.5 Ci/mM.

RESULTS

Body Weight

Figure 81 shows that the rats on the rachitogenic diet grew only half as much as the chow-fed control rats. The weight gain of the rats fed the deficient diet was not significantly different from that experienced by the rats fed the basal diet supplemented with phosphate alone or phosphate in combination with vitamin D_2 during the last 10 days of the experiment. However, the rats raised on the D-supplemented diet lost weight. The phosphorus content of the food is, then, a critical factor, for rats raised on a low phosphate diet eat less.[4, 5] We did not measure food intake, but we attempted to provide a supply of food in excess of expected consumption. Nevertheless, the animals frequently ate all the food provided before the dishes could be replenished, and these rats must be considered at least partially starved. The only rats which found their diets unpalatable or voluntarily starved were those fed the vitamin D_2 supplements.

Bone Growth

The lengths of the femurs were estimated as a measure of bone growth. The data have been compiled in Table 50. The femurs from rats maintained

TABLE 50. THE EFFECT OF A LOW PHOSPHATE, VITAMIN D-FREE DIET ON FEMUR LENGTH

Days	Group	Length, cm[a]	% Change (17–27 days)
17	Control (4)	2.68 ± 0.07	—
	Rachitic (4)	2.46 ± 0.09	—
		$p < 0.02$	
27	Control (5)	2.93 ± 0.07	+8.5
	Rachitic (5)	2.75 ± 0.19	+10.6
		$p < 0.01$	
17–27	R + P + D (4)	2.76 ± 0.08[b]	+10.9
	R + P (4)	2.68 ± 0.03[c]	+8.3
	R + P (4)	2.50 ± 0.05[d]	+1.6

[a] Mean ± S.D.
[b] $p < 0.2$ compared to 27-day control.
[c] $p < 0.1$ compared to 27-day control.
[d] $p < 0.5$ compared to 27-day rachitic control.
( ) Number of rats.

on the rachitogenic diet for 27 days were shorter than the controls. There was good agreement between the weight gain data and bone length. During the final 10 days, when the animals were fed the supplemented regimen, the bones from the rats fed either phosphorus alone or phosphorus and vitamin D_2 grew as well as the bones from the rats continuously maintained on the rachitogenic diet. The poorest growth was observed in the vitamin D_2 supplemented rats.

It is instructive to compare the percent change in femur length from day 17 to day 27. By this method (Table 50), it is difficult to distinguish any meaningful difference attributable to diet alone, with the sole exception of the rats fed the vitamin D_2-supplemented diet.

Ash and Dry Weight of Bone

The dry and ash weights of the bones from rats maintained on the basal rachitogenic diet for 27 days were less than the controls (Table 51). However, while the ash/dry weight ratio was subnormal after 17 days, as might be expected, the ratio was surprisingly similar to the control value after 27 days. It seems probable that there had been spontaneous healing of rickets in this group, perhaps due to intermittent starvation during the final 10 days of the experiment. On the other hand, the ratios of ash/dry were higher than normal.

Changes in the Thickness of the Proximal Tibial Cartilage

The cartilages from rats maintained on the low phosphate rachitogenic diet for 17 days were thicker (30%) than the control cartilages because of the increased numbers of hypertrophic cells (Table 52). At 27 days, the cartilages from the group fed the deficient diet were still thicker, but the difference from the controls was not nearly as large (20%). On the other hand, the cartilages from rats fed the supplemented diets were thinner than the control plates. This would have been expected had the rachitic lesions healed (and if the rats had been partially starved). The thickness of the proliferating zones of cartilage cells [Dodds:[6] Zones 2–3] is a useful index to the severity of the rachitic state. Whereas the zones normally occupy half the thickness of the cartilage, they were narrower in the rachitic bones and contributed only a third to the full thickness of the plate. In the rats fed the "healing" diets from 17–27 days, normal relationships between the growth and mature zones of cartilage were reestablished (Table 52).

During the development of rickets and healing, the epiphyseal marrow cavities became very fatty. The most fat occurred in the bones of rats fed the vitamin D_2 supplements, and the least fat occurred in the controls and in the rats fed both phosphate and vitamin D_2. Zipkin et al.[7] suggested that fat deposition was related to phosphorus deficiency and not to any lack of vitamin D. We noted that the metaphyseal trabeculae in the groups fed phosphate or vitamin D_2 supplements (17–27 days) were very short, presumably due to increased osteoclastic bone resorption (Table 53); the shortest trabeculae occurred in the D_2 supplemented group. Unresorbed nodules of cartilage were also present in the epiphyseal marrow cavities of one or two animals from each group. While this did not seem related to dietary regimen, the nodules were always much smaller in the control and rachitic rats than in the rats fed the healing diets. The largest nodules were observed in the bones of animals fed the phosphate or the vitamin D_2 supplemented food.

Tritiated-Thymidine Labeling of Epiphyseal Cartilage

The percent of cells in the growth cartilages of rats maintained on the rachitogenic diet the nuclei

TABLE 51. Effect of a Low Phosphate, Vitamin D-Free Diet on Rat Femurs

Days	Group	Dry weight, g	Ash weight, g	Ratio: Dry weight/ Ash weight	Ratio: Ash weight/ Dry weight
17	Control (5)	0.181 ± 0.016	0.094 ± 0.007	1.929 ± 0.021	0.519
	Rachitic (4)	0.128 ± 0.018	0.048 ± 0.006	2.528 ± 0.100	0.375
	p	<0.01	<0.01	<0.01	
27	Control (5)	0.260 ± 0.014	0.154 ± 0.006	1.683 ± 0.039	0.592
	Rachitic (5)	0.161 ± 0.037	0.095 ± 0.020	1.763 ± 0.032	0.590
	p	<0.01	<0.01	<0.02	
17–27	R + P + D (5)	0.194 ± 0.017	0.129 ± 0.007	1.500 ± 0.070	0.664
	R + P (5)	0.158 ± 0.025	0.106 ± 0.014	1.482 ± 0.047	0.671
	R + D (5)	0.123 ± 0.012	0.082 ± 0.006	1.496 ± 0.056	0.666

( ) Number of rats.

TABLE 52. THE THICKNESS OF THE PROXIMAL TIBIAL CARTILAGE PLATE IN RATS ON VARIOUS DIETS

Day of sacrifice	Group	Entire cartilage		Proliferating cell zones		
		Thickness,[a] mm	% Decrease in thickness from 17–27 days	Thickness, mm	% of Total cartilage thickness	% Change from 17–27 days
17	Control (5)	0.57 ± 0.018	—	0.28 ± 0.026	49.1	—
	Rachitic (4)	0.83 ± 0.230 p < 0.02	—	0.26 ± 0.006 N.S.	31.3	—
27	Control (5)	0.52 ± 0.06	8.0	0.27 ± 0.02	51.9	+5.4
	Rachitic (4)	0.65 ± 0.11 p N.S.	21.7	0.20 ± 0.05 <.05	30.8	−1.6
27	Rachitic + Vit. D + Phosphate (5) (10 days)	0.44 ± 0.06[b]	47.0	0.21 ± 0.04[b]	47.7	+34.4
	Rachitic + Phosphate (5) (10 days)	0.35 ± 0.04[c]	57.8	0.19 ± 0.01[d]	54.2	+42.3
	Rachitic + Vit. D (5) (10 days)	0.31 ± 0.06[c]	62.7	0.16 ± 0.01[d]	51.6	+39.3

[a] Mean ± S.D.
[b] $p < 0.05$ compared to 27-day control.
[c] $p < 0.05$ compared to rachitic + phosphate + Vitamin D.
[d] $p < 0.01$ compared to 27-day control.
[e] $p < 0.01$ compared to 27-day rachitic.
( ) Number of rats.

of which could be flash labeled with H^3-thymidine was always less than in the controls (Table 54). In the controls, approximately 11% of the chondrocytes were labeled an hour after tracer injection. In the rachitic animals, only 9.3% of the cells could be flash labeled after 17 days, and this value decreased ($p < 0.01$) to 7.1% after 27 days. The group which has been placed on the phosphate + vitamin D_2 supplemented diet from 17 to 27 days showed complete "healing," and the percent labeled cells in the cartilages were similar to the controls. However, the percent of labeled cells in the cartilages of rats fed only the phosphate or the vitamin D_2 supplemented food was not significantly different from the value obtained from rachitic cartilages. In spite of the fact that there were fewer labeled cells in the cartilages from the rachitic rats and those fed the phosphate enriched basal diet, there were no real differences in the number of exposed silver grains over labeled nuclei (Table 54). Fewer than the normal numbers of exposed silver grains were detected only in the cartilages from rats fed the basal diet supplemented with vitamin D_2. These data seemed to explain why the growth cartilages in the rats raised on the basal rachitogenic diet and the diet enriched with either phosphate or vitamin D_2 (17–27 days) were thinner than normal and why, then, the bones from these groups failed to elongate normally during "healing."

TABLE 53. NUMBER OF OSTEOCLASTS IN THE TIBIAL METAPHYSIS IN RATS ON VARIOUS DIETS

Day of sacrifice	Group	Number of osteoclasts/ $4 \times 10^4 \mu^2$ [a]
17	Control (5)	2.1 ± 0.2
	Rickets (4)	2.3 ± 0.4
	p	N.S.
27	Control (5)	2.6 ± 0.2
	Rickets (5)	2.6 ± 0.5
	p	N.S.
17–27	Rachitic + Vit. D + Phosphate (5) (10 days)	3.7 ± 0.3[b]
	Rachitic + Phosphate (5) (10 days)	3.4 ± 0.3[b]
	Rachitic + Vit. D (5) (10 days)	3.3 ± 0.5[b]

[a] Mean ± S.E.
[b] $p < 0.01$ compared to 27-day control rats.
( ) Number of rats.

DISCUSSION

The results of these experiments are not entirely satisfactory. We are haunted by the spectre of spontaneous healing in the rats raised on the low phosphate, vitamin D-free rachitogenic diet. This was apparent in the ash/dry weight ratios at 27 days, but not at 17 days. We have attributed this to intermittent starvation because the animals frequently

TABLE 54. PERCENT CHONDROCYTES LABELED IN THE TIBIAL EPIPHYSEAL CARTILAGE IN RATS ON VARIOUS DIETS

Sacrifice day	Group	% Labeled nuclei[a]	% Change from 17–27 days	Grain counts per nucleus
17	Control	11.4 ± 0.1 (4)	—	28.7 ± 1.8 (5)
	Rachitic	9.3 ± 0.8 (4) $p < .01$	—	29.4 ± 2.1 (4)
27	Control	11.0 ± 0.3 (5)	−2.3	25.2 ± 3.2 (4)
	Rachitic	7.1 ± 0.2 (5)[b] $p < .01$	−23.7	25.1 ± 1.5 (5)
	Rachitic + Phosphate + Vit. D (10 days)	11.1 ± 0.5 (5)	+16.2	26.1 ± 0.9 (5)
	Rachitic + Phosphate (10 days)	7.8 ± 0.6 (4)[c]	−16.2	21.5 ± 1.4 (5)
	Rachitic + Vit. D (10 days)	7.5 ± 0.3 (4)[c]	−19.4	17.6 ± 1.5 (5)[d]

[a] Mean ± S.E.
[b] $p < 0.02$ compared to 17-day rachitic rats.
[c] p not significantly different from 27-day rachitic rats.
[d] $p < 0.01$ compared to 27-day control and rachitic rats.
( ) Number of rats.

ate all the food provided before the dishes could be replenished. Day and McCollum[8] found that there was a very extensive transfer of phosphorus from bone to soft tissues during the development of low phosphorus rickets. It is, therefore, probable that the reverse situation obtains during starvation. If, for instance, soft tissue stores of phosphorus were mobilized, it would serve to raise the Ca × P product in the blood to a level which would support calcification of cartilages (and bone).[5, 9] It was earlier proposed by Albright et al.[10] that rickets in children was characterized by a low Ca × P product in serum, and that the low concentrations of calcium absorbed from the gut (lack of vitamin D) would stimulate the parathyroid hormone release to increase further the excretion of phosphate by decreasing reabsorption by kidney tubules. This appears true for rats as well, although there are important biochemical differences between human and rat rickets.[11-13] While chemical analyses were not performed on the bones in this series, the rats made rachitic by Harrison's[11] low phosphate, vitamin D-free diet had low bone calcium and phosphorus values. These authors, and Thomson[5] earlier, noted that rickets may heal normally in animals when starved or given vitamin D (and citrate) supplements in their diets. Thomson[5] reported low calcium but normal phosphorus values for bone ash of rats made rachitic on a Steenbock-Black Diet; he noted that the Steenbock-Black Diet had deficiencies which prevent the restoration of normal weight gain and bone mineralization, even if phosphate and vitamin D are supplied. Because our control rats were fed a Wayne Lab Block diet, while the experimental rats were fed a noncommercial regimen, it was not possible entirely to relate suppressed weight gain and cartilage growth as did Harrison et al.[11] However, in a subsequent study (unpublished) in which we restricted the dietary intake of the controls to the amount and type of food consumed by the rats developing rickets, the controls still gained more weight.

There seems to be little doubt that vitamin D can promote the intestinal absorption of calcium and its deposition in the skeleton, but it appears to have a negligible effect on these parameters of phosphorus metabolism.[14] It is also known that rachitic rat bone accumulates more vitamin D than normal bone.[15-17] We observed that the healed bones had more ash than normal, even when the diets had the same calcium concentrations and a nearly equivalent Ca/P ratio. Moreover, Hiltibran and his coworkers[18] reported similar results on feeding vitamin D to rachitic rats. Hypermineralization might be expected to follow phosphate or vitamin D feeding if a more effective utilization of phosphorus had developed in the skeletons of rachitic animals. Morgareidge and Manly,[14] for instance, produced calcification of rachitic tissue with a tracer dose of P^{32} which was too low to affect serum phosphorus concentrations. In a more recent acute experiment, Robinson and Sheldon[19] found that injections of phosphate (or vitamin D) produced lines of calcification in uncalcified rachitic bone matrix during the time that blood phosphorus was temporarily adequate. Failure of the newly elaborated skeletal tissue of rachitic rats to mineralize has been noted by poor staining with the von Kossa technique as

well as by impaired tetracycline[20] and radiotracer fixation studies [Ca^{45},[5] P^{32},[21] $Sr^{89, 90}$[22]].

While Harrison et al.[11] found histologic evidence of bone healing in rats after a single injection of vitamin D (100 units), the smaller dietary doses employed by Kunin and Krane[23] also effectively increased the mineral content of the tissues. In concert with the results of the present study, phosphate supplements alone or with vitamin D_2 were even more effective. The percent of cartilage cells which would be flash labeled with tritiated thymidine was also in accord with colorimetric measurement of DNA in rats rendered rachitic and healed by Kunin and Krane,[23] who maintained their rats on diets nearly identical to the ones employed in this study. Therefore, we suspect that the deleterious effects of intermittent starvation were experienced by rats fed the rachitogenic and vitamin D_2 supplemented basal ration from 17–27 days. It is probable that phosphate rather than vitamin D is required for normal DNA synthesis in cartilage cells, even though both agents seemed necessary to reestablish the normal percent of cells functioning in this respect. On the other hand, vitamin D has been localized in the cytoplasm of proliferating chondrocytes by high resolution autoradiography,[24] and it seems to be required to reverse the abnormalities in glucose utilization, lactate production, and citrate metabolism existing in rachitic cartilage.[23] These observations have led to the concept that a hormone may function in biochemical processes to produce an organic matrix which can calcify under normal physiologic conditions.

We have confirmed the observation by Rohr[25] that there are fewer cells capable of synthesizing DNA in rachitic cartilage. However, it is not possible to intercompare the severity of the changes strictly since Rohr[25] used a diet markedly deficient in both calcium and phosphorus (0.03% of each). It is important to note that the level (and rate?) of DNA synthesis per cell was not generally affected by the dietary regimen low in phosphorus. The preliminary nature of these experiments does not permit interpretation of the low levels of DNA synthesis per cell in the rickets healed by vitamin D_2 per se.

SUMMARY

Laboratory rats were rendered rachitic by maintaining them on a low phosphate-Vitamin D-free diet for 17 days. The animals were then fed the basal ration enriched with either phosphate or vitamin D_2 alone, or in combination. The ability of these diets to produce and heal rickets was measured histologically, by ash weight determinations, and by high resolution autoradiography with H^3-thymidine.

1. The cartilages of rats fed the rachitogenic diet for 17 days were thicker than normal owing to increased numbers of hypertrophic cells. Fewer cells than normal could be labeled with H^3-thymidine, so that total DNA synthesis was impaired. Phosphate or vitamin D_2 supplements alone were ineffective and the percent labeling at 27 days remained at rachitic level. Complete healing was afforded by a combination of phosphate and vitamin D_2. The diets did not alter the level of DNA synthesis per cell in any group except in the rats fed vitamin D_2 supplements, where the grain counts were appreciably lower.

2. Severe loss of appetite (voluntary starvation) was noted in rats maintained on the vitamin D_2 enriched basal ration (17–27 days). Intermittent starvation also occurred in rats fed the low phosphate rachitogenic diet.

3. Ash weights were low in rachitic rats, but the bones of animals fed phosphate and vitamin D_2 supplements had more ash than normal.

The author wishes to express his appreciation for the technical assistance provided by Mrs. Helen Cummins and to Dr. A. S. Kunin who supplied the diets used in this experiment.

REFERENCES

1. W. C. Russell, M. W. Taylor, and M. T. Duncan. Bone Development in Normal and Rachitic Rats. *J. Nutr.* **18,** 27–33 (1939).
2. R. D. Coleman, H. Becks, K. F. Van Nouhuys, and D. H. Copp. Skeletal Changes in Severe Phosphorus Deficiency of the Rat. I. Tibia, Metacarpal Bone, Costochondral Junction, Caudal Vertebra. *Arch. Path.* **50,** 209–232 (1950).
3. R. M. Bethke, C. H. Kick, and W. Wilder. The Effect of the Calcium-Phosphorus Relationship on Growth, Calcification, and Blood Composition of the Rat. *J. Biol. Chem.* **98,** 389–403 (1932).
4. R. D. Ray, D. E. Stedman, and N. K. Wolff. Bone Metabolism. III. The Effect of Various Diets on the Mobilization of Strontium From the Rat Skeleton. *J. Bone Joint Surg.* **38-A,** 637–654 (1956).
5. D. L. Thomson. The Effect of Age and Low Phosphorus Rickets on the Metabolism of Calcium-45 in Rats. University of California Radiation Laboratory Report UCRL-2302 (1953).
6. G. S. Dodds. Row Formation and Other Types of Arrangements of Cartilage Cells in Endochondral Ossification *Anat. Rec.* **46,** 385 (1930).
7. I. Zipkin, R. C. Likins, and F. J. McClure. Deposition of fluoride, calcium and phosphorus in experimental low-phosphorus rickets. *J. Nutr.* **67,** 59–67 (1959).
8. H. G. Day and E. V. McCollum. Mineral Metabolism, Growth, and Symptomology of Rats on a Dict Extremely Deficient in Phosphorus. *J. Biol. Chem.* **130,** 269–283 (1939).
9. R. Robinson and K. M. Soames. The Possible Significance

of Hexosephosphoric Esters in Ossification. VIII. Calcification *in vitro*. *Biochem. J.* **24**, 1922–1926 (1930).
10. F. Albright, A. M. Butler, and E. Bloomberg. Rickets Resistant to Vitamin D Therapy. *Am. J. Dis. Child.* **54**, 529 (1937).
11. H. C. Harrison, H. E. Harrison, and E. A. Park. Vitamin D and Citrate Metabolism. Inhibition of Vitamin D Effect by Cortisol. *Proc. Soc. Exptl. Biol. Med.* **96**, 768–773 (1957).
12. H. E. Harrison and H. C. Harrison. The Interaction of Vitamin D and Parathyroid Hormone on Calcium, Phosphorus, and Magnesium Homeostasis in the Rat. *Metabolism* **13**, 952–958 (1964).
13. G. W. Engstrom, H. F. Deluca, J. W. Cramer, and H. Steenbock. Vitamin D and Urinary Amino Acid Excretion in the Rat. *Proc. Soc. Exptl. Biol. Med.* **108**, 105–108 (1961).
14. K. Morgareidge and M. L.-F. Manly. Simultaneous Appearance of a Positive Line Test and Radioactive Phosphate Deposition in the Rachitic Rat Metaphysis. *J. Nutr.* **18**, 411–421 (1939).
15. E. Kodicek. Turnover and Distribution of Vitamin D and Its Mode of Action. *The Transfer of Calcium and Strontium Across Biological Membranes*, Ed. R. H. Wasserman. Academic Press, New York, 1963, pp. 185–196.
16. R. K. Callow, E. Kodicek, and G. A. Thompson. Metabolism of Tritiated Vitamin D. *Proc. Roy. Soc.*, **B.164**, 1–20 (1966).
17. A. W. Norman and H. F. DeLuca. The Preparation of H^3-Vitamin D_2 and D_3 and Their Localization in the Rat. *Biochemistry*, **2**, 1160–1168 (1963).
18. R. C. Hiltibran, F. C. Hoecker, and R. C. Mills. Effect of Vitamin D on Retention of Radium by the White Rat. *Proc. Soc. Exptl. Biol. Med.* **95**, 772–774 (1957).
19. R. A. Robinson and H. Sheldon. Crystal-Collagen Relationships in Healing Rickets. *Calcification in Biological Systems*, Ed. R. F. Sognnaes. Am. Assoc. Advan. Sci., Washington, D. C., 1960, pp. 261–279.
20. R. Steendijk. Studies on the Mechanism of the Fixation of Tetracyclines to Bone. *Acta Anat.* **56**, 368–382 (1964).
21. L. H. Weissberger and L. S. Harris. A Possible Vitamin D Assay Technique with Radiostrontium. *J. Biol. Chem.*, **144**, 287 (1942).
22. D. H. Copp, J. G. Hamilton, D. C. Jones, D. M. Thompson, and C. Cramer. The Effect of Age and Low Phosphorus Rickets on Calcification and the Deposition of Certain Radioactive Metals in Bone. *Conf. Metab. Interrelations., Trans.* **3**, 226 (1951).
23. A. S. Kunin and S. M. Krane. Utilization of Citrate by Epiphyseal Cartilage of Rachitic and Normal Rats. *Biochim. Biophys. Acta* **111**, 32–39 (1965).
24. E. Kodicek and G. A. Thompson. Autoradiographic Localization in Bones of (1-^{3}H) Cholecalciferol. *Structure and Function of Connective and Skeletal Tissue*. Butterworths, London, 1965, pp. 369–372.
25. H.-P. Rohr. Autoradiographishe Untersuchungen über das Knorpel/Knochen-Langenwachstum bei der experimentellen Rattenrachitis. *Z. Gesamte Exp. Med.* **137**, 248–255 (1963).

*SKELETAL CHANGES IN MURINE RUNT DISEASE**

David J. Simmons and Richard L. Simmons†

Runt disease was produced in neonatal F_1 hybrid mice by the injection of spleen cells from a mature donor of the parental strain. Clinically apparent runting appeared after the tenth day. Mice were serially sacrificed when 11–19 days old, and their long bones were examined histologically and histochemically. In runt disease, development of the epiphyseal secondary centers of ossification was retarded. The cells and protein polysaccharides did not mature normally, and the tissue contained acellular cartilage. Accumulations of hypertrophic chondrocytes signified impaired endochondral ossification. While the osteogenic cells in the medullary spaces had been replaced largely by mononuclear lymphoid cell infiltrates, bone collagen was present on unremodeled metaphyseal trabeculae, which possessed wide cartilage cores. The intertrabecular spaces were moderately fibrotic. Large remnants of unossified unresorbed cellular cartilage were frequently observed in the metaphysis. It appeared that the generalized graft-versus-host reaction induced by the spleen cell "grafts" was extended to the skeleton but that the changes in the cartilage and bone tissue had occurred largely before the onset of clinical runting.

* Abstract of paper published in *Am. J. Anat.* **121**(1), 15–27 (July 1967).

† Columbia University College of Physicians and Surgeons.

OBSERVATION ON THE DEPOSITION OF THOROTRAST IN RAT TISSUE

*David J. Simmons, Helen Cummins, and Edwin Nirdlinger**

INTRODUCTION

The colloidal form of thorium dioxide (Thorotrast) had been employed extensively from 1930–1945 as a medical diagnostic radiopaque dye, especially in angiography, and to visualize the liver, spleen, and kidney. Thorotrast consists of 24–26% thorium dioxide stabilized by dextrin to which is added methylparahydroxybenzene (0.15%) as a preservative. It is well known that the material is rapidly filtered from the blood and "permanently" sequestered by cells of the reticuloendothelial system. Thorotrast has been detected in the tissues of human subjects many decades following treatment, and there are numerous clinical observations relative to long term tissue damage at the sites of deposition in liver, spleen and kidney, and other organs. Excellent reviews of the medical literature have been published in recent years by Looney[1] and Faber.[2] The mechanism by which the material produces its effects is presently obscure. It is not known, for instance, whether the histopathological events are due to chemical changes, such as those which might follow extravasation of Thorotrast at the sites of injection (thorotrastomas), or whether they are specifically induced by the radioactive nature of the parent thorium-232 and/or by its complex series of decay products which are alpha, beta, and gamma emitters. Because it is recognized that all the tissues of the body contain reticuloendothelial cells which accept Thorotrast following parenteral administration, it is important, for estimates of radiation dose, to know the whole-body distribution of the material, and the degree of disequilibria of the daughters in different organs, as well as their rates of translocation within and excretion from the body.[3, 4] The present study was performed to determine the microscopic sites of Thorotrast deposition in rats at various times after a single intravenous injection. Some of the material was harvested from rats used for gamma spectrometric analysis of the equilibrium states of the thorium daughter isotopes in this laboratory.[3] In particular, we were interested in the occurrence of histopathological changes in the soft tissues, in the skeleton, and the effects of Thorotrast on the growth nd development of the long bones. Autoradiographic echniques were applied to localize aggregates of colloidal thorium dioxide and to quantitate their distribution in tissues. Short-term studies using radiostrontium (Sr^{85}) were also employed to estimate the effect of Thorotrast on mineral metabolism.

* CSUI-ANL Honors Research Student, 1967.

MATERIALS AND METHODS

Adult (4-month-old) male, Sprague-Dawley strain albino rats, 300-g body weight, were injected with 0.50–0.75 ml Thorotrast (Testagar Corporation Lot #13098) via the tail vein.† The animals were sacrificed at various intervals thereafter—6 hours, 3, 23, 50, and 80 days, 7.5, 8.5, and 14 months. A younger group of rats, 100g body weight, were similarly injected with 0.40 ml and sacrificed at intervals of 1, 3, 6, and 12 weeks. On the day of sacrifice, the animals were radiographed to visualize major sites of Thorotrast deposition and to determine if any of the injected material could be visualized in the tail at the site of injection owing to extravasation. The rats were killed by ether anesthesia, and tissue samples were taken from most of the organs. The tissues were fixed in 10% neutral formalin, embedded in paraffin, and sectioned at 5μ on a rotary microtome. The sections were stained with hematoxylin and eosin, PAS, or by the von Kossa technique to establish sites of ectopic calcification.

Longitudinal sections of formalin-fixed femora, tibias and mandibles (left side) were made following decalcification in 10% EDTA (pH 7.4–7.6) and paraffin embedding. The bone sections were stained by the methods cited above.

The long bones from the right side were stripped of soft tissues. They were measured with a vernier caliper, embedded in methyl methacrylate without prior decalcification, and sectioned longitudinally at 100μ on a high-speed rotary saw. These sections were microradiographed (10 kV, 20 ma, 10 min) using Kodak Spectroscopic Plates No. 649-0 for comparison with the histologic material.

Autoradiography

The soft tissues and decalcified bone sections were autoradiographed by the dipping technique of Messier and Leblond.[5] The slides were immersed in Kodak liquid NTA emulsion for a few seconds, dried, and

† In this experiment, the Thorotrast solution was one in which the radioactive daughters had not attained radioactive equilibrium with their parent Th^{232}. The injected material contained the following activities: Th^{232}, 17.6 mμCi; Ra^{228} and Ac^{228}, 3.2 mμCi; Th^{228} and its daughters, 4.4 mμCi.

stored in lightproof boxes in a freezer. This emulsion records chiefly the alpha emissions from the daughters of Th^{232}. Following an exposure period of 6 months, the slides were developed for 5 minutes in Kodak D-19, fixed, washed, and stained through emulsion with hematoxylin and eosin. In certain instances, alternate sections were stained by the PAS method prior to autoradiography, and they were counterstained with hematoxylin after exposure and development.

Contact autoradiographs of the undecalcified methacrylate embedded bones were made using Kodak NTA plates which are sensitive to both alpha and beta emissions. It was necessary to expose the plates for 30 months. The autoradiographs were analyzed by microdensitometry to obtain a relative measure of the activity in the different regions of bone. The same sections were autoradiographed by the method of Hsieh et al.[6] which employs a zinc sulfide coated plastic film intensifier interposed between the bone section and a fast Polaroid Land Type 57 film. Gross autoradiographs were obtained by this method after short exposure periods—1 to 2 weeks, and the image is largely the result of alpha emissions. The beta-ray contribution is negligible owing to the lesser energy deposition.

Analysis of Liquid Emulsion Autoradiographs

While doses could not be easily measured, the degree to which the aggregates of Thorotrast were distributed within tissues and the variation of size of the individual deposits with time after injection were of interest. The size of the aggregations was estimated microscopically in 50 fields, each 4×10^{-4} μ^2, using dark field illumination. Average values were computed for liver, adrenal, and lung. The number of alpha tracks per aggregate of Thorotrast was also measured as an index to the uniformity of dose delivered to these tissues. Autoradiographs of bone were subjected to similar analysis. In a single specimen sacrificed 50 days after injection, we measured the proximity of the aggregations of Thorotrast to the endosteal (inner diaphysis) and trabecular surfaces (metaphysis), for this would be the skeletal tissue at risk.

Retention of Radiostrontium

The 24-hour retention of strontium-85 was measured in the alcohol-fixed femurs and tibias obtained from rats which had previously received Thorotrast and from an equal number of rats in the control series. The level of radiostrontium delivered to the groups of rats 1, 3 and 6 weeks following Thorotrast administration varied from 0.2 to 1.0 μCi. Because the same tissues were used for microradiography and autoradiography, they could not be dried or ashed. Therefore, the data were expressed simply as cpm/100 g tissue weight. Counting was performed in a well-type scintillation crystal.

RESULTS

Distribution of Thorotrast in Soft Tissues

Reticuloendothelial System.—Liver: Thorotrast particles were found in the Kupffer cells lining the central veins of the lobules. A few small aggregates were also found in the parenchymal cells at the peripheral regions of lobules. The largest deposits were on the order of 30 to 50μ in diameter. Small areas of hemorrhage and disrupted cellular architecture occurred by 3 days after injection, but these bore little topical relation to the sites of Thorotrast deposition. Obvious parenchymal cell damage occurred infrequently as judged by the tissue reaction to the von Kossa stain. The number and distribution of cells containing Thorotrast in the liver was estimated by dark field microscopy. The data in Table 55 suggest that the diameter and number of alpha tracks emanating from each deposit did not change appreciably from 6 hours to 8.5 months following injection. The amount of Thorotrast administered was small, so that the changes, if any, might have passed undetected by the method employed. However, the number of Thorotrast-laden macrophages per unit area tends to decrease with time.

Previous electron microscopic studies in rats[7, 8] have shown that a dose of Thorotrast nearly equivalent to that utilized in this study can label nearly all the Kupffer cells by 4 hours. Large and small aggregates of Thorotrast particles 70 Å in diameter were found within cytoplasmic vacuoles in the Kupffer cells and also within intracellular vacuoles of occasional hepatic parenchymal cells near bile canaliculi (a major route of excretion).

Spleen: Thorotrast was found largely within macrophages of the red pulp. There was a tendency for these cells to coalesce at the margins of the white pulp (lymphocyte generative regions) by 50 days. While the bulk of the material remained in the red pulp, the numbers of phagocytic reticular cells or fixed macrophages containing Thorotrast in the white pulp increased with time. It was, therefore, difficult to estimate the size of the individual aggregations of Thorotrast. Aggregates in the red pulp were as larg as 90 μ in diameter, and occasionally greater tha 120×60 μ in the white pulp.

Thymus: Thorotrast particles were concentrated by the reticular cells in the interlobular connective tis-

TABLE 55. AGGREGATE SIZE AND NUMBER OF ALPHA TRACKS FROM THOROTRAST IN LIVER

Sacrifice time	Rat No.	No. of deposits[a] per field ($4 \times 10^4\ \mu^2$)	Liver aggregate size,[a] μ	No. of alpha tracks per aggregate[c]	Ratio: aggregate size/No. of alpha tracks	No. of alpha tracks/μ^2 (10^{-6})
6 hr	23998	—	11.4 ± 0.5[a]	10.9 ± 0.6	1.045	2040
6 hr	24000	—	—	—	—	2996
8 d	Th 1, 2, 4	13.2 ± 2.2	13.2 ± 2.2	10.9 ± 0.6	1.211	—
21 d	Th 5–8	10.3 ± 1.5[b]	—	—	—	—
30 d	Th 15	7.8 ± 0.4	—	—	—	—
42 d	Th 23, 25, 27	7.5 ± 0.9[b][b]	—	—	—	—
50 d	23995	—	14.5 ± 0.97	18.8 ± 1.4	0.792	2345
80 d	23985	—	12.9 ± 0.8	17.8 ± 1.5	0.724	581
7.5 mo	23986	—	17.7 ± 1.2	14.4 ± 1.1	1.224	686
	23991	—	20.5 ± 1.3	15.7 ± 1.3	1.310	1020
8.5 mo	23987	—	15.8 ± 1.3	24.6 ± 0.6	0.642	1270

[a] Data based on counts of 50 cells or 50 fields. Values expressed as Mean ± S.E.
[b] $p < 0.05$ compared with 8-day Thorotrast rats Th 1, 2, 4.
[c] Dose normalized to 0.5 ml and an exposure time of 400 days.

sue, and occasional alpha tracks were observed emanating from cortical and medullary tissue as early as 6 hours after injection.

Lymph Nodes (Cervical): Thorotrast was acquired by isolated macrophages or by small groups of cells during the first 80 days. The deposits averaged 12μ in diameter. After 7.5 months, however, Thorotrast particles were concentrated in larger aggregates 110μ in diameter. Compared to those in the liver, the Thorotrast-laden cells were irregularly distributed.

Respiratory System.—Lung: Thorotrast aggregates were located in some cells in the epithelial lining of the alveoli 6 hours after injection. Deposits of 5 to 10 μ in diameter were also found in the submucosal layer of the bronchi. The size of the individual inclusions within lung cells estimated in a few rats sacrificed 80 days to 8.5 months did not appear to change with time (Table 56). The numbers and distribution of alpha tracks from these cells proved similar in all animals as well.

Trachea: Large accumulations of Thorotrast were found in the macrophages of the loose connective tissue surrounding the glandular mucosa adjacent to the tracheal cartilages 6 hours after injection. The cells containing Thorotrast particles were approximately 15 μ long.

Digestive System.—Esophagus: Thorotrast-laden cells (6 to 17 μ) were concentrated in the lamina propria and submucosa of the esophagus in the region of the thyroid glands 6 hours after injection and at all subsequent sacrifice times. Some alpha tracks also appeared to originate in the circular muscle. However, sections taken within the cardiac region of the stomach showed no histochemical (PAS) or autoradiographic evidence of Thorotrast.

Stomach and Intestines: Thorotrast cells were found very infrequently in the tunica propria, submucosa and mucosal layers of the gut at all sacrifice times.

TABLE 56. AGGREGATE SIZE AND NUMBER OF ALPHA TRACKS FROM THOROTRAST IN LUNG TISSUES

Sacrifice time	Rat No.	Aggregate size,[a] μ	No. of alpha tracks[a] per aggregate	No. of alpha tracks per μ^2 (10^{-6})[b]	Ratio: aggregate size/No. of alpha tracks
6 hr	23998	—	—	77.0	—
6 hr	24000	—	—	110.0	—
80 d	23985	7.6 ± 0.26	7.5 ± 0.53	141.0	1.01
7.5 mo	23986	9.2 ± 0.32	10.5 ± 0.91	212.0	0.88
7.5 mo	23991	12.6 ± 0.87	7.2 ± 0.64	199.0	1.75
8.5 mo	23987	11.3 ± 1.11	24.6 ± 1.75	—	0.46

[a] Data (Mean ± S.E.) based on a count of 50 cells.
[b] Dose normalized to 0.5 ml and an exposure time of 400 days.

Pancreas: Occasional masses of Thorotrast particles were observed in the acinar cells at all times after injection; the possibility of contamination cannot be excluded. The septal connective tissue cells and the macrophages of the loose connective tissue binding the pancreas to the stomach unequivocally contained Thorotrast particles. No Thorotrast was observed in the islets of Langerhans. The cells containing the Thorotrast were approximately 15 to 20 μ long.

Excretory System.—Kidney: Little Thorotrast was found in the kidney. Thorotrast aggregates were found in some cells of the glomerular epithelium after 80 days, and at this time the cells in Bowman's capsule were somewhat enlarged. The tubular epithelium appeared to be degenerating in certain areas.

Urinary Bladder: Scattered Thorotrast-laden mac-

rophages were found among the mucosal epithelial cells at all times after injection. The largest concentrations of Thorotrast were in the lamina propria and submucosa.

Reproductive System.—Testes: Cells with Thorotrast inclusions were always found in the interstitial connective tissue between the seminiferous tubules.

Accessory Reproductive Structures: No Thorotrast was ever detected in the ductus deferens. However, Thorotrast-laden cells were identified in the connective tissue surrounding seminal vesicles and epididymis; their distribution remained unchanged with time.

Endocrine System.—Adrenal: Aggregations of Thorotrast particles, 5 to 10μ in diameter, were concentrated in the cells lining the sinusoids—particularly in the zona reticularis—at all sacrifice times. Deposition in the other zones of the adrenal was spotty. Thorotrast was present in the regions of the medulla contiguous with the zona reticularis. The size of the inclusions of Thorotrast was estimated in a few rats sacrificed 50 days to 8.5 months. The data in Table 57, based upon counts of 50 Thorotrast-laden cells under dark field microscopy, indicates that the deposits in the zona reticularis do not change size with time. Neither was there any significant difference in the area distribution of alpha tracks.

Thyroids and Parathyroids: The histology of the glands was normal at all times. Thorotrast was seen infrequently in the cells of the interfollicular connective tissues of the thyroid at all sacrifice times, but no Thorotrast was present in the parathyroids.

Exocrine System.—Salivary Glands: (Mandibular, Parotid): Thorotrast cells were present in the investing loose connective tissue 6 hours after injection and at all subsequent sacrifice times.

TABLE 57. AGGREGATE SIZE AND NUMBER OF ALPHA TRACKS FROM THOROTRAST IN ADRENAL TISSUE[a]

Sacrifice time	Rat No.	Zona glomerulosa	Zona fasciculata	Zona reticularis		
		No. of alpha tracks per μ^2 (10^{-6})[b]	No. of alpha tracks per μ^2 (10^{-6})[b]	Aggregate size, μ	No. of alpha tracks per deposit	No. of alpha tracks per μ^2 (10^{-6})
50 d	23995	67	289	6.3 ± 0.3	4.9 ± 0.4	1170
7.5 mo	23991	262	266	5.0 ± 0.2	6.0 ± 0.3	1093
8.5 mo	23987	—	—	7.3 ± 0.5	8.5 ± 0.8	—

[a] Data based on counts in 50 fields or from 50 aggregates of Thorotrast.

[b] Dose normalized to 0.5 ml and an exposure time of 400 days.

Adipose Tissue: Thorotrast cells were always found in the connective tissue surrounding fat cells but never in the fat cells per se.

Thorotrast in Skeletal Tissue

Distribution of Thorotrast in Bone.—In the long bones, aggregates of Thorotrast particles were detected in the macrophages and reticular cells of the marrow and in the tissue between the metaphyseal and epiphyseal trabeculae. Thorotrast was also found in periosteal and endosteal cells, and these regions of bone are clearly outlined in contact autoradiographs (Figure 82B). In the jaw, Thorotrast aggregates as large as 20μ were found in some cells in the connective tissue between the bone and periodontal membrane. The Thorotrast-laden cells could be identified by their strong PAS staining reaction, and, in liquid NTA preparations, by overlying concentrations of alpha tracks. In the high-resolution autoradiographs, occasional alpha tracks could be seen over bone and cartilage. Tiny aggregates of Thorotrast particles were occasionally present in the lacunae of hypertrophic cartilage cells. However, because these tissues had been fixed in formalin and decalcified, we may be dealing with an artifact due to the solubility and translocation of Th^{228}. Despite these reservations, it seemed possible to estimate the uniformity of dose delivered to marrow cells by counting the alpha tracks originating from the discrete aggregates of Thorotrast particles.

Determinations of the number of alpha tracks/μ^2 were made from the high resolution autoradiographs (liquid NTA emulsion) of femurs from rats sacrificed during the first 50 days after injection. Analysis was restricted to the mid-shaft marrow and to the intertrabecular tissue 0–200 μ below the distal epiphyseal cartilage. The data have been compiled in Table 58. The distribution of alpha tracks in each region appeared quite similar after 6 hours. After 21 days, however, it was evident that there was much more activity in the mid-shaft marrow. The alpha counts were quite variable, perhaps because of differential retention of Thorotrast in the tail following perivascular extravasation of the material at the site of injection. While animals were excluded only when there was sufficient Thorotrast in their tails to be visible radiographically, there may be reason to question the precision of injection in other rats as well, even when x-rays were negative. The change in distribution may be due to factor other than technique. Our data indicate that the long bones were growing during the periods in question. If, for instance, Thorotrast had been sequestered in "fixed" macrophages at the ossification front as the



FIG. 82. Microradiograph (A) and autoradiographs (B = Type A; C = Polaroid Type 57) of an undecalcified section of a femur from a rat sacrificed 50 days after a single intravenous injection of 0.75 ml Thorotrast. Note the intense deposition of Thorotrast activity in the marrow transversely across the proximal tips of the metaphyseal trabeculae.

bones were growing in length, it is likely that these marked cells would later appear at a site regionally distinct from their original "niche." On the other hand one would not expect the level of activity in the nongrowing mid-shaft marrow to change appreciably. The data in Table 58 suggest that this supposition is true, and the thesis will be discussed below.

The autoradiographs (liquid NTB-2 emulsion) also revealed that Thorotrast-laden cells were more highly concentrated within 100μ of the endosteal surfaces than in the middle of the marrow cavity. Figure 83 represents only mid-shaft counts from a single rat (※23995) sacrificed 50 days postinjection. The data indicate that 40% of the cellular Thorotrast inclusions are within 30μ of the endosteum and that 57% lie within a distance of 40μ. This nonuniform deposition in marrow which is concentrated at endosteal

surfaces would provide a higher alpha radiation dose than had previously been expected.[4] We further attempted to analyze the concentrations of the different alpha-emitting daughter isotopes of Th^{232} by measuring track lengths in the emulsion according to the methods of Rotblat and Ward;[9, 10] however, these efforts were abandoned because the emulsion applied to the sections was too thin.

The contact autoradiographs of undecalcified sections of femurs from the 50-day sacrifice (Rat ※23995) showed that nearly all periosteal and endosteal surfaces of bone were labeled (Figure 82B). Yet, very little radioactivity had been incorporated in the cortical bone of the shaft. The epiphyseal and diaphyseal medullary cavities were diffusely labeled. Comparison with a microradiograph of the identical section (Figure 82A) reveals little activity in the distal metaphysis per se, but a band of high activity traversed the diaphyseal ends of the trabeculae. The data in Table 55 indicate that the long bones of rats injected at 30 days of age were growing at a rate of 0.67 mm/wk or nearly 0.1 mm/day; therefore, the femurs should have elongated 5 mm during the 50 days before sacrifice. This is, in fact, the value obtained by comparing the length of the metaphyseal trabeculae in the microradiographs and the length of the "negative" autoradiographic image under the epiphyseal plate. It is also of some interest to compare (qualitatively) the autoradiographic density in the metaphysis and mid-shaft regions with the marrow alpha track counts from decalcified sections (Table 58). While these tracks cannot be translated directly into dose for reasons mentioned previously, the activity in these regions was similar at 6 hours and different thereafter. We suggested that Thorotrast was contained in fixed macrophages. That growth had occurred subsequent to Thorotrast injection was indicated also by the diagonal trail of silver grains passing from the endosteum to the periosteum. Presumably this is due to the incorporation of translocated thorium and radium daughters in a region of active endosteal bone growth, i.e., the "funnel effect" of Enlow.[11] Because the soft tissue covering the periosteal surface of the bone was stripped thoroughly prior to embedding, the periosteal outline undoubtedly represents appositional growth. However, the line marking the endosteum at the mid-shaft was probably produced in part by alpha and beta particles originating from the cellular inclusions of Thorotrast and does not reflect a growth process.

A quantitative estimation of the activity in the contact autoradiograph was performed by microdensitometry (Figure 84). The densities varied from 0.06 to 0.25 in the bone. The marrow in the epiphyseal medullary cavity, the marrow at the proximal tip of the metaphyseal trabeculae and the growing peri-

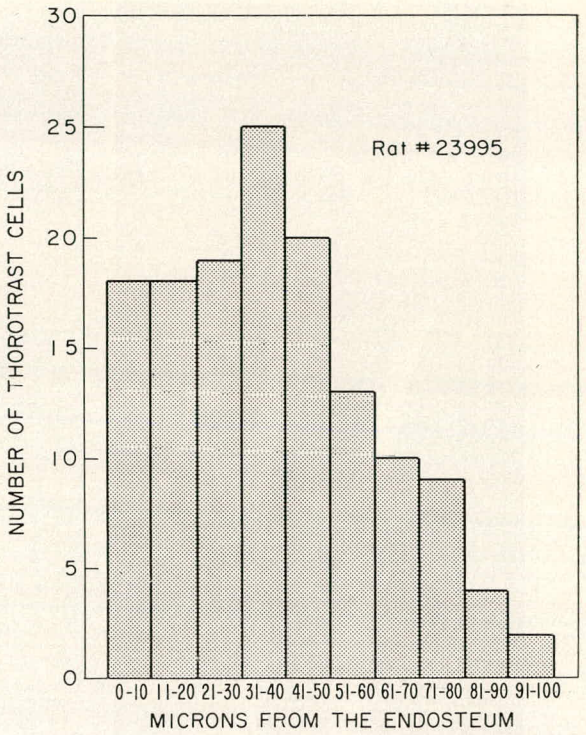

FIG. 83. Graph showing the proximity of Thorotrast-laden cells to the endosteal surfaces (NTB-2 autoradiographs) of a femur from a rat sacrificed 50 days following a single intravenous injection of 0.75 ml Thorotrast.

TABLE 58. DISTRIBUTION OF ALPHA TRACKS FROM THOROTRAST IN BONE MARROW

Sacrifice time following injection	Rat No.	Bone	No. of tracks/μ^2 (10^{-6})[a]		
			Distal metaphysis "marrow" (DM)	Mid-shaft (marrow) (MS)	Ratio DM/MS
6 hrs	24000[b]	Femur	599	719	0.833
21 days	Th 5	Femur	110	280	0.393
	Th 7	Femur	370	1583	0.233
	Th 8[c]	Femur	139	830	0.167
23 days	23997[b]	Femur	399	358	0.897
28 days	Th 15	Femur	215	1666	0.129
42 days	Th 24	Tibia	129	1268	0.102
	Th 27	Femur	105	928	0.113
		Tibia	110	1062	0.104
50 days	23995[b]	Femur	398	1666	0.662

[a] Autoradiographs (NTB-2) exposed for 6 months. Dose normalized to 0.5 ml and an exposure time of 400 days.

[b] Animals 4 months old at time Thorotrast was injected.

[c] Very slight retention of Thorotrast at the site of injection.

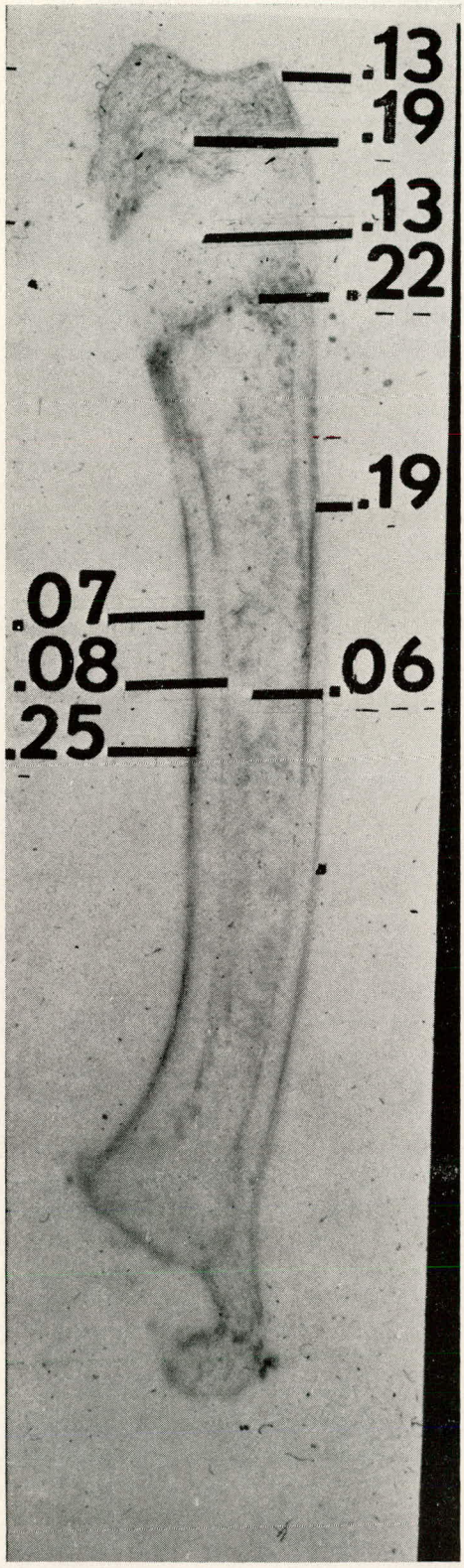

FIG. 84. A microdensitometric analysis of a Type A autoradiograph of an undecalcified section of a femur from a rat sacrificed 50 days after a single intravenous injection of 0.75 ml Thorotrast.

osteal surfaces all had approximately the same density averaging 0.19. Where the endosteum was not growing but yet contained intracellular aggregates of Thorotrast particles, the activity was approximately the same as that of the marrow (0.07). The level of activity in mid-shaft cortical bone was as low as in the mid-shaft marrow, probably because the cortical bone of rodents undergoes only appositional growth and rarely has foci of internal remodelling to trap activity.

Additional information about the disposition of Thorotrast in bone was afforded by Polaroid autoradiography (Figure 82C). This method is very fast owing to image intensification by a ZnS screen interposed between the bone and emulsion. However, resolution suffers because (a) the tissue and film are not in close apposition and (b) the exposed grains of Polaroid 57 film are on the order of 100 μ compared to 0.5 μ in Type A emulsions.[12] The image recorded by the two methods is nevertheless in good accord, although the definition permitted by Type A plates is to be preferred for analytic and esthetic reasons. The position of the transverse band of high activity in the metaphysis of the femur (distal) and tibia (proximal) relative to the epiphyseal cartilage plate was measured by vernier calipers. The results

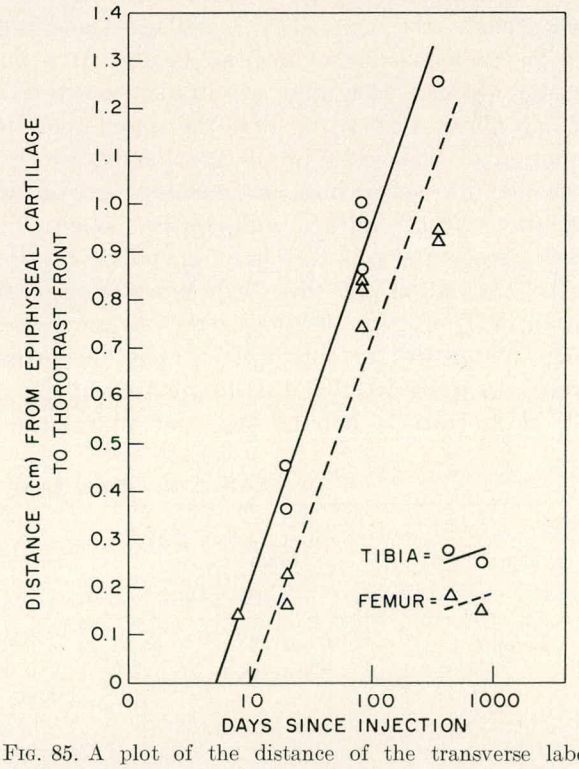

FIG. 85. A plot of the distance of the transverse labeled band of Thorotrast in the marrow from the epiphyseal cartilages of femurs (distal) and tibias (proximal) vs. days following a single intravenous injection of Thorotrast (Polaroid Type 57 autoradiographs). Compare with Figure 86

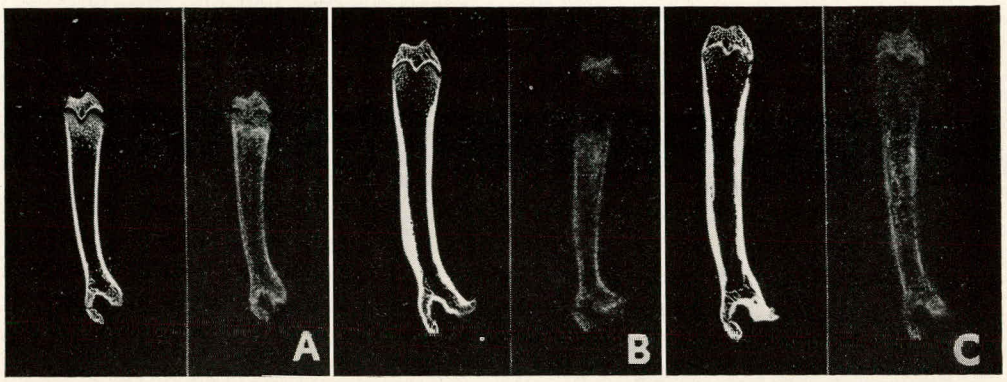

FIG. 86. Comparison of microradiographs (left) with Polaroid Type 57 autoradiographs (right) of femurs from rats which had received a single intravenous injection of 0.4–0.75 ml Thorotrast at 1 month of age. A, sacrifice after 8 days; B, sacrifice after 12 weeks; C, sacrifice after 1 year. Note that the position of the labeled Thorotrast front in the marrow is progressively displaced from the distal epiphyses of the femurs as the bones grow in length.

have been plotted in Figure 85. The graph and Figure 86 show that this activity band moves away from the growth cartilage with time after injection, and that the displacement is roughly equivalent to the rate at which the bones were growing in length. These pictures appear to confirm the interpretation given to the Type A autoradiograph. It seems likely that the macrophages at the ossification front filter out the Thorotrast brought via the capillary loops which invade the epiphyseal cartilages, and that these macrophages do not migrate further. It is possible, for instance, that they are fixed in position by reticular fibers. It may be that the undifferentiated population of bone cells in the metaphysis which is responsible for generating new macrophages at the ossification front during subsequent longitudinal growth, or new macrophages may repopulate the zone via the circulation. In these experiments, then, the position of Thorotrast particles serves as an indirect marker for growth in length. It is more important, however, to recognize that the distribution of Thorotrast in marrow is nonuniform, and that sites in marrow and its quantity destined for radiochemical analysis must be chosen with great care.

Histopathology of Bone Due to Thorotrast.—Epiphyseal Cartilage: Demonstrable histopathologic changes occurred in the bones of rats treated with 0.40 ml Thorotrast at 42 days of age. The thickness of the epiphyseal cartilages was normal at all experimental periods. Although there was perhaps a slight reduction in the height of the columns of cartilage cells, longitudinal growth of bone was unimpaired (Table 59). One week following Thorotrast (0.40 ml), the cartilages of 2 rats (Th 1, Th 4) showed transverse rents between the zones of proliferating and hypertrophic cells which were similar to the defect occurring in osteolathyrism (Figure 87).[13] Three weeks after injection, nodules of cartilage were observed in the epiphyseal marrow cavity (Th 11, Th 28), and plugs of acellular degenerate cartilage matrix were present in the zones of resting and proliferating cells (Figure 88). The aberrant tissue stained deep red by the PAS method as did the normally calcified intercolumnar matrix and the calcified cores of metaphyseal trabeculae.

TABLE 59. BONE LENGTH IN THOROTRAST-TREATED RATS[a]

Bone	Group	Weeks of treatment			
		1	3	6	12
Femur	Control	3.20 ± 0.04 (4)	3.44 ± 0.05 (4)	3.75 ± 0.10 (3)	3.94 ± 0.02 (3)
	Thorotrast	3.11 ± 0.03 (4)	3.37 ± 0.05 (4)	3.69 ± 0.06 (4)	4.02 ± 0.09 (3)
	p	N.S.	N.S.	N.S.	N.S.
Tibia	Control	3.63 ± 0.04 (4)	3.81 ± 0.04 (4)	4.14 ± 0.04 (3)	4.20 ± 0.08 (3)
	Thorotrast	3.53 ± 0.05 (4)	3.84 ± 0.06 (4)	4.05 ± 0.05 (4)	4.10 ± 0.21 (3)
	p	N.S.	N.S.	N.S.	N.S.

[a] In cm (mean ± S.E.).
( ) Number of rats.

Microradiographs also showed that the plugs were heavily calcified (Figure 89). Six to 21 weeks after injection, cartilage nodules were found between the growth plate proper and the transverse epiphyseal bone. Moreover, the wide plugs extended through the full thickness of the cartilage and were continuous with the cartilage in the primary spongiosa and trabeculae (Figure 88). Plugging became somewhat more severe in the tissues examined 6 months after Thorotrast injection. They could not be seen in the cartilages of rats sacrificed after 14 months; at that time, the growth apparatus was very thin, its cells irregularly disposed, and it was sealed off by a transverse subchondral bony plate in the metaphysis. Certain areas of the older cartilages contained masses of cells which had not been removed by vascular invasion in the normal fashion.

Endochondral Ossification: The appearance of the ossification front reflected the development of defects in the cartilage plate. While vascular invasion proceeded evenly across the metaphyseal face of the cartilage at early times, the front became less regular 3–6 weeks after injection, apparently because the acellular cartilage plugs were not resorbed. Similarly,



FIG. 87. Photomicrograph of a lesion in the proximal tibial epiphyseal cartilage plate from a rat sacrificed 8 days after a single intravenous injection of 0.5 ml Thorotrast. Hematoxylin, eosin and Azure II.

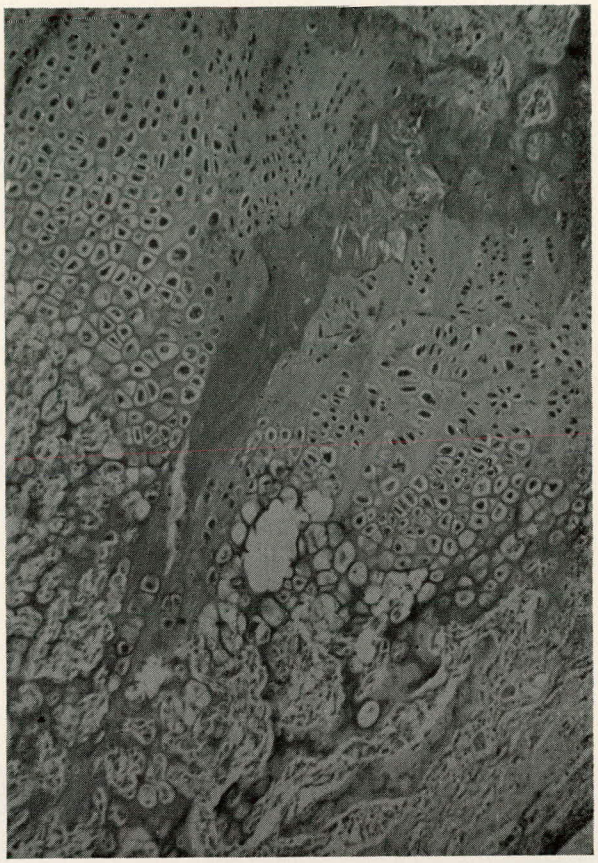

FIG. 88. Photomicrograph of a plug of degenerate cartilage in the distal femoral epiphyseal cartilage of a rat sacrificed 1 week after a single intravenous dose of 0.5 ml Thorotrast. Note that the plug contains a tongue of cellular matrix which projects into the metaphysis. The rows of chondrocytes adjacent to the plug are disorganized. PAS stain. Compare with Figure 89.

while the metaphyseal trabeculae which formed in the process of endochondral ossification appeared normal at first, they subsequently became more massive and longer than those in control bones (owing to the inclusion of broad plugs). The abnormal length of the trabeculae was probably due to a failure of resorption. The trabeculae in the Thorotrast-injected rats, then, contained more cartilage, and this was also true for the compact bone of the shaft, i.e., some trabeculae became incorporated at the endosteum as the bones grew in length. Few trabeculae persisted at mid-shaft level after the older cartilage plates became sealed off. Normal numbers of osteoclasts lined the surfaces of the trabeculae and endosteum in the first 12 weeks of treatment, but they became less abundant after 6 months; however, there was some residual remodelling.

The microradiographs of the undecalcified sections served to confirm plugging and thickened trabeculae, and revealed intracellular particles of Thorotrast

along the endosteum and in the marrow cavity. These could be distinguished from artifacts (dust or impurities in the emulsion) since they did not change their positions when sections were microradiographed a second time. Gross radiographs of femurs from 2 rats (23989, 23999) sacrificed 14 months after Thorotrast treatment suggested that the thickness of the cortices had become quite irregular (Figure 90). The femur alone appeared mottled; the tibias appeared normal. The microradiographs and histologic preparations indicated that the irregularities were due to hypertrophy of endosteal bone. The endosteal ridges ran irregularly along the length of the bone.

Effect of Thorotrast on Bone Growth: The lengths of the femurs and tibias of rats sacrificed during the first 12 weeks after an intravenous dose of Thorotrast (0.40 ml) were not significantly different from those of the uninjected controls. The average values from groups of 3 to 5 rats have been summarized in Table 59.

24-Hour Retention of Radiostrontium: The data in Table 60 show that the bone burden of Thorotrast has no important effect upon the 24-hour retention of Sr^{85}. Inasmuch as the sequential high resolution autoradiographic studies by Hammerström and his coworkers[14] on Sr^{85} rats have shown that most of the activity is in the cortex 24 hours after injection, our findings indicate that Thorotrast does not affect the activities of the bone cells governing formation and resorption during the first 6 weeks.

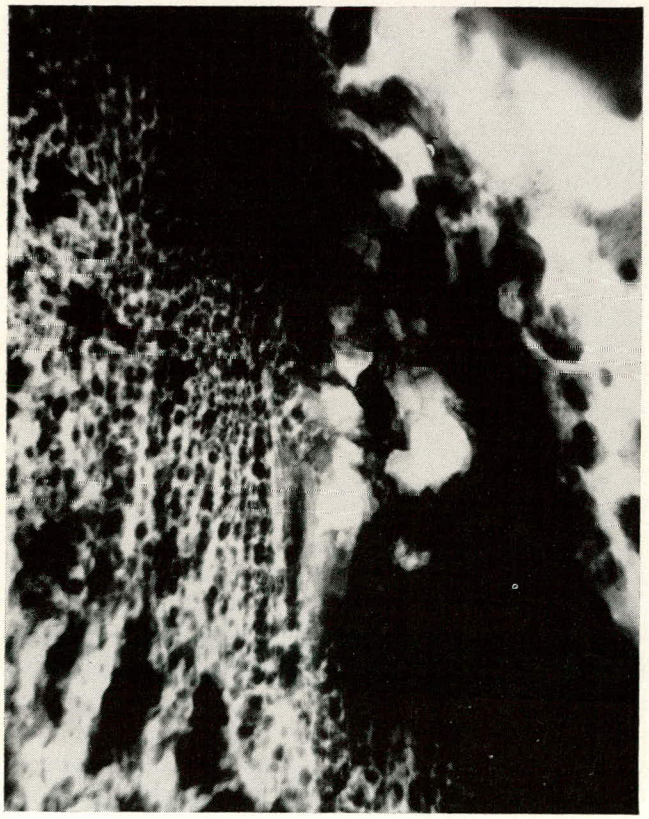

FIG. 89. Microradiograph of an irregular plug of degenerate cartilage in the distal femoral epiphyseal cartilage of a rat sacrificed 3 weeks after a single intravenous dose of 0.5 ml Thorotrast. Note that the plug is heavily calcified (compare with Figure 88).

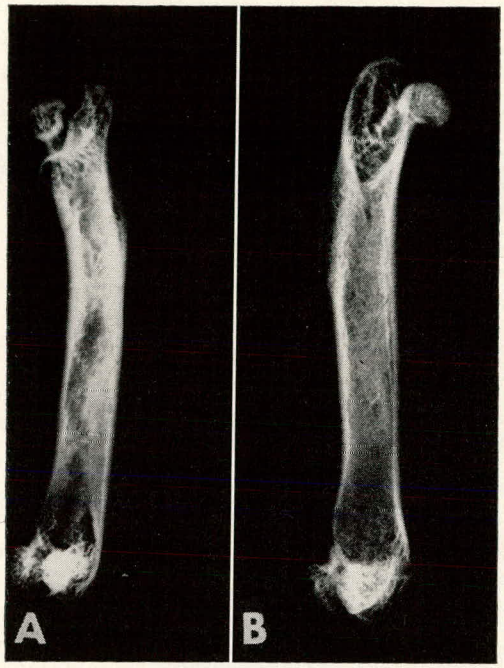

FIG. 90. Gross radiographs of femurs from two rats sacrificed 14 months after Thorotrast injection. A, Thorotrast-injected; B, control.

DISCUSSION

The fact that Thorotrast remains in tissues long after deposition is not a new observation. Tissue surveys in man and experimental animals have given similar results. It has also been recognized that the inclusions of the parent Th^{232} within cells of the reticuloendothelial system provide a source from which there is a constant infusion of alpha, beta, and gamma emitters into the body. Each of these emitters may then be translocated to favored anatomical sites. Little is known about the residence time or the time at which radioactive equilibria of these daughters are achieved in different tissues. This is, of course, dependent in part, upon the age of the Thorotrast preparation administered. While in this study the microscopic pattern of Thorotrast deposition in soft tissues was quite similar to that previously reported, the dose of Thorotrast administered was much less than the amount injected by other in-

TABLE 60. 24-HOUR RETENTION OF STRONTIUM-85 IN FEMURS AND TIBIAS[a]

Bone	Group	Weeks of treatment		
		1[b]	3[b]	6[c]
Femur	Control	4113 ± 177 (3)	1835 ± 92 (3)	229 ± 11 (3)
	Thorotrast	3914 ± 207 (4)	2090 ± 235 (4)	215 ± 15 (4)
	p	Y.S.	N.S.	N.S.
Tibia	Control	3303 ± 331 (3)	1355 ± 101 (4)	186 ± 31 (3)
	Thorotrast	2984 ± 206 (4)	1686 ± 281 (4)	179 ± 26 (4)
	p	N.S.	N.S.	N.S.

[a] Cpm/100 g body weight (mean ± S.E.).
[b] Administered dose of Sr^{85} = 1.0 μCi/100 g body weight.
[c] Administered dose of Sr^{85} = 0.02 μCi/100 g body weight.
( ) Number of Rats.

vestigators who have induced pathologic changes in diverse organs. In general, the histology of the tissues was unaffected by the dose employed. We did not experience tumors of liver or spleen.[15-17] However, thrombohemorrhagic lesions were found in liver and kidney 3 days after injection, and anomalies of this type were reported by Gabbiani et al.[18] within the same time period. The fibrotic changes observed in the spleen of man[19, 20] were not present in our rats. It would, in fact, have been quite unusual if extensive soft tissue changes had been found in this study. Pathology has not ordinarily been experienced until 6 to 10 months after injection in laboratory rodents. Our observations rarely extended beyond 6 months.

Interest in this study focused upon the effects of Thorotrast on skeletal development. Marinelli and Lucas[4] estimated that bone from human Thorotrast cases contained approximately 0.5% of the body content of Th^{232}. Since there is virtually no excretion of thorium dioxide or translocation to bone from the reticuloendothelial system, the amount of the injected Th^{232} in these rat bones was probably on the order of 0.088 mμCi. Perhaps only 2% of the injected Th^{228} is deposited in bone immediately after injection, for along with Ra^{228}, the bulk of these long-lived isotopes are bound to the Thorotrast particles and are sequestered in the liver and spleen. It has further been estimated[3] that most of the Th^{228} (half-life = 1.91 years) found in bone at times long after injection is born from bone-bound Ra^{228} (half-life = 5.7 years). Paar[3] noted that a large proportion of the Ra^{224} produced from Th^{228} in the liver and spleen is either excreted or incorporated into the skeleton, but Ra^{224} has a short half-life (3.64 days) and could not be expected to exert a significant effect on skeletal metabolism. We found that Thorotrast had little effect on the rate of longitudinal growth (femurs and tibias) at the dose employed. Because the cells in the epiphyseal growth cartilages (growth apparatus) govern the rate at which a bone may elongate, one may conclude that Thorotrast had little influence over the mitotic potential of chondrocytes. This assumption appears to be true in general for liver cells as well, where Thorotrast is concentrated and more ubiquitously distributed.[16] However, Lübke[21] reported a slight increase in liver cell mitoses 3 days after Thorotrast injection and described the discharge of "thorium nuclei" from dividing cells. While alpha tracks were occasionally found over dividing cartilage cells, only electron microscopy could tell us if there were any Thorotrast particles remaining in the cells. It is most likely that we were dealing solely with the deposition of translocated daughters of Th^{232}. Barnett and Palfrey[22] introduced Thorotrast into rabbit knee joints and were unable to find thorium in chondrocytes by electron microscopy. Some chondrocytes in the superficial zones showed degenerate changes within hours after injection, and the cartilage matrix tended to fray and slough off. Thorotrast penetrated 3 μ into the matrix 24 to 38 hours after administration, but degenerative cell and matrix changes occurred in advance of the physical penetration of thorium. Because the calculated alpha dose delivered to the cells appeared too small to account for degradative phenomena, the authors suggested that thorium interfered with the passage of nutrients from the synovial fluid required for tissue viability. Zedgenidze and Amosov[23] administered repeated large doses of Thorotrast (40–50 ml/2 months) to young growing rabbits intravenously. "Rapid and massive deposition of thorium in the growth zones" occurred, causing acute radiation lesions of the epiphysis and knee joints, wide foci of bone dissolution in the growth zones, epiphyseolysis and pathological fractures

within the first month. Osseous damage seemed to be directly related to the amount of absorbed thorium.

The extensive lesions incurred in a few of the rat cartilages during the first week after Thorotrast injection did not appear due to faulty tissue nutrition. Radiation damage also seemed unlikely. We administered 0.1 g (1 mg/g body weight) thorium to young rats (100 g) compared to the 11 g (5.5 mg/g body weight) injected by Zedgenidze and Amosov,[23] and the alpha dose to the skeleton would have been correspondingly smaller. Moreover, we have demonstrated that the major reservoir of activity in the growth zones (metaphysis) becomes more remote from the growth cartilage with time in a growing animal. Relative to nutrition of cartilage, joint nutrition is apparently dependent upon the flux of synovial fluid in and out of articular cartilage by intermittent pressure and by diffusion from the underlying bony endplate.[24] The same cannot be said for growth cartilage which is nourished by vessels entering the marrow cavity at the proliferative epiphyseal end of the cell columns. If blood flow through these vessels were impeded, we would have anticipated derangement of cell columns (and perhaps cell death). This did not occur. However, a few columns of hypertrophic cells did project into the primary spongiosa after several months, perhaps indicating minimal damage to metaphyseal vessels.[25]

The principal skeletal anomalies detected early in this study were (a) wide calcified plugs of degenerate acellular cartilage in the growth apparatus, (b) faulty endochondral ossification owing to the presence of the plugs which failed to resorb and (c) thickened confluent trabeculae in the metaphysis. After 6 months, ridges formed on the endosteum. Thus, the skeletal changes became apparent at a time when soft tissue changes were negligible. The late overgrowth of the endosteum in rats may be compared to the longitudinal striations seen radiographically by Looney[1] in human bone 10 to 19 years after Thorotrast injection.

While no Thorotrast-related tumors were found in this study, we have reviewed the literature to determine if any of the skeletal anomalies could be considered pretumorous changes. Selbie[26] reported an osteosarcoma in a mouse (group of 60 animals) 9 months after two subcutaneous injections of Thorotrast (each 0.1 ml). It is possible that this osteosarcoma developed quite independently of Thorotrast, for the bulk of the injected activity would probably have been retained in the soft tissue. Zak and his coworkers[27] observed an osteolytic fibrosarcoma of the 9th thoracic vertebra in a patient 21 years after Thorotrast treatment; the tumor contained Thorotrast-laden macrophages, but the adjacent intervertebral discs were normal. Hasterlik and Finkel[28] note that resorptive lesions in human bone are rather typical of the radiation damage induced by radium. Tsuya et al.[29] reported an osteogenic sarcoma (with liver metastases) in the pelvis of a 40-year-old male 19 years after an injection of Thorotrast for hepatolienography. While Thorotrast was seen in the marrow, the tissue was not fibrotic. Because the isotope retention in the bone was small and liver metastases were present, there is always the possibility that this was a bone tumor quite unrelated to Thorotrast. Osteolysis of long bones of Thorotrast rabbits with changes resembling fibrotic osteodystrophy was recorded by Zedgenidze and Amosov.[23] In rabbits, the pretumorous changes were related to the amount of absorbed Thorotrast, and tumors developed at sites where thorium was concentrated maximally. Radiation necrosis developed in 2 weeks after a single massive dose of 5 ml Thorotrast. Both Wenz[30] and Zedgenidze and Amosov[23] noted Thorotrast deposition in blood vessel walls, and studies by others suggest that Thorotrast increases capillary permeability.[31, 32] Damage to the vascular system appears to be a function of the suspending medium (dextran) alone. Particles of thorium dioxide are sequestered in vesicles within endothelial cells and subendothelial spaces, but they do appear to alter the ultrastructure of endothelial cells within 48 hours after injection.[32] Wenz[30] cited a more direct relationship between an intravenous injection of Thorotrast (0.025–1.0 g thorium) and the incidence of skeletal tumors. However, this conclusion was based on a relatively small sample, i.e., 4 rats from a group of 84 animals. Three were illustrated with data relative to dose and latency time:

Tumor	Dose of thorium, g	Latency time, years
Lower sacral vertebrae	0.125	2.25
Right scapula	0.025	1.75
Femur osteosarcoma	0.125	2.00

Moreover the number of rats developing tumors of all kinds was not related to dose.

However, the fact that survival at high doses was shorter than at low doses may explain why no bone tumors appeared with 0.25, 0.5 and 1.0 g administered thorium.

The etiology of the damage to the endosteum in this experiment is uncertain. It is difficult to compare the apparent effects of radiation incurred by human bones which were generally not growing (in length) at the time Thorotrast was administered and the damage incurred by those of the rats which were

growing. If in the rats, some of the tiny capillaries supplying the endosteum were either plugged by Thorotrast particles or destroyed by radiation, sufficient collateral circulation must have existed to maintain normal histology in the first year after injection. If vascular damage became more severe with time, the resultant malnutrition (hypoxia) might have stimulated the formation and activity of osteoblasts.[33-35] Alternately, in view of Thorotrast-augmented capillary permeability, Bassett[36] has shown that the combination of compaction and high oxygen tension *in vitro* can also lead to bone formation. A third possibility is that the skeletal changes observed in the rats treated with Thorotrast are due to a chemical interaction between Th^{232} and the organic components of bone. When administered in a citrate buffer solution, Th^{228} binds to collagen and/or mucopolysaccharides.[37] However, in the present study, we administered a very small mass of Th^{228} relative to Th^{232}; most of the Th^{228} was bound to the particles of Thorotrast and could, therefore, be expected to have a very different pattern of distribution. At least in the period of time this experiment was performed, there did not appear to be any specific radiation-induced changes in the skeletons.

SUMMARY

Young growing rats were injected intravenously (tail vein) with colloidal thorium dioxide (Thorotrast, 0.4–0.75 ml), and the disposition of the material in the body was traced at various times after injection by autoradiographic techniques. In bone, the injected material was filtered from the blood and sequestered by macrophages in the marrow and intertrabecular regions. The distribution of these cells was nonuniform, and the autoradiographic pattern seemed to reflect growth processes. In the metaphysis of the long bone, the labeled cells (in fixed macrophages?) formed a band of high activity which became further removed from the epiphyseal cartilages with time due to continued endochondral ossification. The rate at which the bones of the Thorotrast-treated rats grew in length was normal. Nevertheless, irregular foci of endochondral bone formation were observed due to the formation of plugs of degenerate cartilage in the growth cartilages during the first 6 weeks, and focal hypertrophy of endosteal bone occurred by 12 months. The etiology of the histologic change is obscure.

The authors wish to express their appreciation to H. F. Lucas, Jr. and L. D. Marinelli for their encouragement and useful counsel.

REFERENCES

1. W. B. Looney. An Investigation of the Late Clinical Findings Following Thorotrast (Thorium Dioxide) Administration. *Am. J. Roentgenol.* **83,** 163–184 (1960).
2. M. Faber. Thorotrast in Man—The Carrier State and the Sequelae. *Some Aspects of Internal Irradiation,* Ed. T. F. Dougherty. Pergamon Press, New York, 1962, pp. 473–496.
3. R. M. Paar. The Relative Activities of Thorium Daughter Isotopes in the Tissues of Thorotrast Patients. A Progress Report. Argonne National Laboratory Radiological Physics Division Annual Report, July 1963 through June 1964. ANL-6938, pp. 127–139.
4. L. D. Marinelli and H. F. Lucas. Translocation of Thorium Daughters to Bone. *Some Aspects of Internal Irradiation,* Ed. T. F. Dougherty. Pergamon Press, New York, 1962, pp. 499–516.
5. B. Messier and C. P. Leblond. Preparation of Coated Radioautographs by Dipping Sections in Fluid Emulsion. *Proc. Soc. Exptl. Biol. Med.* **96,** 7–10 (1957).
6. J. J. C. Hseih, F. P. Hungate, and S. A. Wilson. Autoradiography: Technique for Drastic Reduction of Exposure Time to Alpha Particles. *Science* **150,** 1821–1822 (1965).
7. J. C. Hampton. An Electron Microscope Study of the Hepatic Uptake and Excretion of Submicroscopic Particles Injected into the Blood Stream and into the Bile Duct. *Acta Anat.* **32,** 262–291 (1958).
8. J. Wiener, D. Spiro, and W. Margaretten. An Electron Microscopic Study of Reticuloendothelial System Blockade. *Am. J. Path.* **45,** 783–803 (1964).
9. J. Rotblat and G. Ward. The Radioactivity from Thorotrast and Its Retention in Tissues. *Phys. Med. Biol.* **1,** 125–137 (1956).
10. J. Rotblat and G. Ward. Analysis of the Radioactive Content of Tissues by Track Autoradiography. *Phys. Med. Biol.* **1,** 57–70 (1956).
11. D. H. Enlow. Principles of Bone Remodeling. C. C Thomas Publ., Springfield, Ill., 1963.
12. R. E. Rowland. Personal Communication, 1967.
13. D. J. Simmons, A. M. Pankovich, and A. M. Budy. Osteolathyrism in Mice and Inhibition of the Endosteal Bone Reaction in Estrogen-Treated Mice by Aminoacetonitrile. *Am. J. Anat.* **116,** 387–400 (1965).
14. L. Hammarström, A. Nilsson, and S. Ullberg. Distribution of Radiostrontium in Developing Bones and Teeth. *Acta Radiol.* **3,** 183–192 (1965).
15. G. Grampa and A. Severini. Tumori epatici da thorotrast nel ratto. *Boll. Soc. Ital. Patol.* **8,** 12–14 (1963–1964).
16. J. P. Guimares and L. F. Lamerton. Further Experimental Observations on the Late Effects of Thorotrast Administration. *Brit. J. Cancer* **10,** 527–532 (1956).
17. E. S. Gaidova and H.-S. Yen. Morphological Changes in the Lungs and Other Organs of Rats following Intratracheal Administration of ThO_2. *Med. Nauk S. S. S. R.* **No. 4,** 58–72 (1964) [Abstract in *Nucl. Sci. Abstr.* **19,** 2026 (1965)].
18. G. Gabbiani, H. Selye, and B. Tuchweber. Adrenal Localization of Thrombohemorrhagic Phenomenon. *Endocrinology* **77,** 177–182 (1965).
19. R. Baserga, H. Yokoo, and G. C. Henegar. Thorotrast-Induced Cancer in Man. *Cancer* **13,** 1021–1031 (1960).
20. W. B. Looney, J. S. Arnold, H. Levi, and W. S. S. Jee. Autoradiographic and Histopathological Studies of

Thorium Dioxide Patients. *Arch. Path.* **60**, 173–178 (1955).
21. A. Lübke. Über den Einfluse und der Blockade des Retikuloendothelialen Systems durch Thorotrast auf die Vitamin und die Entstehung der Maul- und Klauenseuche (MKS)—Myokarditis. *Zentr. Veterinarmed.* **10**, 449–458 (1963).
22. C. H. Barnett and A. J. Palfrey. Absorption into the Rabbit Articular Cartilage. *J. Anat.* **99**, 365–375 (1965).
23. G. A. Zedgenidze and I. S. Amosov. Radiation Changes in Bone Tissue Inducted by Chronic Internal Irradiation. *Acad. Med. Sci. U. S. S. R.* 3-8 (1965).
24. H. Mankin. The Structure, Chemistry and Metabolism of Articular Cartilage. *Bull. Rheumatic Dis.* **17**, 447–452 (1967).
25. J. Trueta. The Role of the Vessels in Osteogenesis. *J. Bone Joint Surg.* **45B**, 402–418 (1963).
26. F. R. Selbie. Tumors in Rats and Mice following Injection of Thorotrast. *Brit. J. Exptl. Path.* **19**, 100–107 (1938).
27. F. Zak, F. Stryhal, A. Sosna, J. Burnianek, and D. Buchalova. Trvale Poskozeni Lidskeho Organismu Thorotreastem. *Universitas Carolina Med.* (1956), pp. 330–335.
28. R. J. Hasterlik and A. J. Finkel. Diseases of Bones and Joints with Intoxication by Radioactive Substances, Principally Radium. *Med. Clin. N. Am.* **49**, 285–296 (1965).
29. A. Tsuya, T. Tanaka, T. Mori, T. Hashizume, and Y. Kato. Four Cases of Thorotrast Injury and Estimation of Absorbed Tissue Dose in Critical Organs. *J. Radiation Res.* **4**, 126–145 (1963).
30. W. Wenz. Thorotrasttumoren. Quantitativ Untersuchungen über das Dosis-Wirkungs-Problem bei der Thorotrastose. *Ergeb. Chir. Orthopäd.* **46**, 6–166 (1964).
31. D. A. Rowley. Mast Cell Damage and Vascular Injury in the Rat. An Electron Microscopic Study of a Reaction Produced by Thorotrast. *Brit. J. Exptl. Path.* **44**, 284–290 (1963).
32. W. J. S. Still and P. R. Prosser. The Reaction of Aortic Endothelium of the Rabbit to Hyperlipemia and Colloidal Thorium. *J. Artherosclerosis Res.* **4**, 517–526 (1964).
33. J. L. Shaw and C. A. L. Bassett. Improved Method for Evaluating Osteogenesis *in vitro*. *Anat. Rec.* **149**, 57–66 (1964).
34. P. Goldhaber. Effect of Hyperoxia on Bone Resorption in Tissue Culture. *Arch. Path.* **66**, 635–641 (1958).
35. L. W. Gorham and W. T. West. Circulatory Changes in Osteolytic and Osteoblastic Reactions. *Arch. Path.* **78**, 673–680 (1964).
36. C. A. L. Bassett. Current Concepts of Bone Formation. *J. Bone Joint Surg.* **44A**, 1217–1244 (1962).
37. M. A. Van Dilla, B. J. Stover, and J. S. Arnold. On the Retention and Translocation of Ra^{224} (Th X) in Dogs. *Am. J. Roentgenol.* **77**, 503–510 (1957).

LEAD AND LEAD-210 IN RAINWATER

G. L. Ter Haar, R. B. Holtzman, and H. F. Lucas, Jr.*

There is a continuing interest in the possible toxicity to man and animals from the present and future levels of lead in the environment. The importance of environmental lead was emphasized by Monier-Williams in 1938,[1] and has resulted in numerous studies in the interim.[2-4]

Lead exists in the atmosphere as an aerosol which contributes to the body content of man.[4] Knowledge of the mean residence time of the lead aerosol is important since for any given set of meteorological conditions and a fixed rate of injection, the concentration will be an inverse function of the residence time.

^{210}Pb has a half-life of 21.4 years and would be an ideal tracer for stable lead, if lead and ^{210}Pb were acted on by the same forces. Since the mean residence time of the ^{210}Pb can be estimated from the ratio of its specific activity to that of one of its decay products, ^{210}Bi or ^{210}Po,[5-8] then this residence time would also apply to stable lead. There are both differences and similarities in the mode of injection of lead and ^{210}Pb into the atmosphere; ^{210}Pb is derived from the decay of ^{222}Rn (a noble gas) which escapes from the soil and is dispersed throughout the atmosphere by winds and convection, while lead aerosols originate from automobile exhaust, from smelting, or from other industrial operations. The source of both stable lead and ^{210}Pb is at, or very near, the earth's surface. Except for regional differences in the rates of injection of lead and ^{210}Pb, the sites of injection seem very similar, so that both may experience the same meteorological conditions. Both are returned to earth mainly by the cleansing action of rainfall from altitudes between 1 and 10 km.[9]

Although fairly extensive measurements of the concentrations of ^{210}Pb in rainwater have been reported,[5-8, 10] little is known of the concentrations of stable lead.[11] Moreover, the concentrations of lead and ^{210}Pb have not been reported from the same samples.

It is the purpose of this study to evaluate the relationship between lead and ^{210}Pb in the atmosphere Rainwater was selected since it samples a large volume of air at high altitudes and thereby minimizes effects from local sources.

Samples of rainwater were collected on the roof of

* Industrial Trainee from Ethyl Corporation Research Laboratories, Ferndale, Michigan.

the Physics building at Argonne National Laboratory, and on a farm in Ottawa County, Michigan. The first site is located in a semirural area 25 miles west of Chicago, while the second is located in an area of farms 125 miles northeast of the Argonne site. This latter site was located 1200 feet from the nearest roadway and 15 miles from the nearest city (population 25,000). Consecutive samples of rainwater were collected at Argonne from July 1 to September 14, 1966. All samples were collected in porcelain-coated steel pans which had been cleaned of dirt and dust immediately prior to collection of the rainwater. These samples, ranging in volume from 1 to 6 liters, were filtered through a fritted glass filter before analysis. Analyses of both portions of the sample showed that less than 10% of the lead was in the solids retained on the filter. The data in Tables 61 and 62 are for the materials in the soluble portion of the rainwater. The samples were stored in acid-cleaned polyethylene bottles for shipment. Loss of lead to the walls is negligible under these conditions.

Lead analysis and reagent purification were by the standard A.O.A.C. spectrophotometric dithizone method.[12] Reagent blanks were less than 0.4 μg. Triplicate analyses were performed with each sample containing at least 4 μg of lead. Under these conditions, the standard deviation of a single determination was $\pm 5\%$.

The ^{210}Pb was determined from the beta count rate of its ^{210}Bi daughter. These samples were prepared by evaporating the dithizone solution on a 1.5″ diameter stainless steel planchet, covering it with a 5 mg/cm^2 aluminum foil, and allowing the sample to age for 30 days to attain radioactive equilibrium. The aluminum foil prevented the variable amounts of the alpha-emitting activity of ^{210}Po, which accompanied the ^{210}Pb, from being counted. The samples were counted in a four-section, low-background, end-window, gas-flow, Geiger counter.[13] Background counting rates were about 0.25 cpm and the counting efficiency for these samples was 50%. Samples of known ^{210}Pb concentrations showed that the procedure gave a chemical yield of 93 $\pm$ 5%. Samples were counted for sufficient time to give a statistical counting error (σ) of less than 5%.

The concentrations of the stable lead and ^{210}Pb and the amount and type of rainfall in the various samples of rainwater for the Argonne and Michigan sites, are summarized in Tables 61 and 62, respectively. The arithmetic mean lead concentration of 18.9 μg/l at Argonne is essentially identical to the 17.4 μg/l in Michigan. Similarly, the mean concentrations of the ^{210}Pb were 1.26 and 1.78 pCi/l at the Argonne and Michigan sites, respectively. These values for ^{210}Pb are a little lower than the average of 2.3 pCi/l found by King et al.[7] and by Glöbel et al.[10] in Germany.

TABLE 61. Lead and Lead-210 in Rainwater at Argonne National Laboratory during the Summer of 1966

Date	Precipitation,[a] mm	Pb, μg/l	^{210}Pb, pCi/l	Specific activity, pCi/g $\times 10^{-4}$
July 1	18.—S	10.6	1.08	10.2
July 11	15.—S	9.2	0.63	6.8
July 13	10.—S	4.6	0.28	6.1
July 26–27	106.—S	4.0	0.51	12.8
August 2	6.—S	6.3	0.10	1.6
August 8	9.—S	13.2	0.62	4.7
August 10	9.—R	44.3	3.10	7.0
August 21	11.—TS	3.8	0.28	7.5
September 14 (total)	9.	71.1	4.68	6.6
September 14 (early interval)	7.—TS	87.4	5.84	6.7
September 14 (last interval)	2.—TS	20.6	1.05	5.1

[a] R signifies a rain of an even, slow character; S signifies a shower (rapid, brief rainfall varying in intensity); TS signifies a thunderstorm.

TABLE 62. Lead and Lead-210 in Rainwater in Western Michigan during the Summer of 1966

Date	Precipitation,[a] mm	Pb, μg/l	^{210}Pb pCi/l	Specific activity, pCi/g $\times 10^{-4}$
August 1	13.—R	29.2	2.90	9.9
August 10	8.—S	6.2	0.33	5.3
August 15	25.—TS	6.5	0.93	14.3
August 21	51.—R	27.5	2.96	10.8

[a] R signifies a rain of an even, slow character; S signifies a shower (rapid, brief rainfall varying in intensity); TS signifies a thunderstorm.

Although the amount of data is limited, there appears to be a correlation between the type of rain and the concentrations; a shower (S) (rapid, brief rainfall varying in intensity) had lower concentrations than a slow, even rainfall (R). Thundershowers (TS) usually had lower concentrations, but they also could be very high. There does not appear to be a correlation between lead concentration and the length of time between rains. However, weather preceding a rain may affect the lead concentrations. Thus, the September 14 rain, with its high values, was preceded by a thermal inversion for the 7 days prior to precipitation. In this case the lead and ^{210}Pb aerosols appear to have been formed at the usual rates, but they were confined to a relatively small atmospheric volume over this long period of time.

The rates of deposition at Argonne are estimated at about 1 μg cm^{-2} yr^{-1} for the lead and 0.08 pCi cm^{-2} yr^{-1} for the ^{210}Pb. These estimates are based on this series, representing 20% of the measured rainfall at this site during 1966, a mean weighted lead content of 10.6 μg/l (each result multiplied by its respective depth of rainfall) and mean weighted ^{210}Pb content of 0.83 pCi/l. The contribution of these materials to those already present in the soil is thus small. A brief study near Argonne showed that soil contained about 20 μg of lead and 1.5 pCi of ^{210}Pb per gram of dry material. This lead concentration is similar to Swaine's estimate of 16 μg/g world wide.[14] The ^{210}Pb concentration is probably also of the same order as the world average. With these values for lead and ^{210}Pb and a soil density of 2 g/cm^3, the contribution of both lead and ^{210}Pb to the top 15 cm (6″) of soil would be 0.2% per year. This neglects leaching of the lead from the soil or run-off of the rainfall before it can enter the soil.

The specific activities of the lead (pCi ^{210}Pb/g Pb) are also shown in Tables 61 and 62. These values for the two series are much more nearly constant and give average values of 6.7 and 10.4 $\times$ 10^4 pCi/g at the Argonne and Michigan sites, respectively. Student's t test indicates the specific activities to be significantly different ($p < 0.01$). The correlation coefficients for concentration of lead and ^{210}Pb in the two series of data were 0.98 ($p < 0.0001$) at the Argonne and 0.63 ($p < 0.1$) for the Michigan samples. The lower level of significance of the latter is probably because of the small number of samples.

These data show that there is good mixing of lead and ^{210}Pb in the atmosphere before they are returned to the earth in rainfall. Thus ^{210}Pb will be a valid tracer for stable lead in the atmosphere, and it appears that the meteorological conditions which affect the concentrations of lead and ^{210}Pb do not appear to substantially affect their relative mean residence times in the atmosphere. A similar result was noted by Kuroda[15] in an analysis of fallout from weapons testing, i.e., the concentrations of several radioisotopes in rainwater varied over a wide range, but the ratios of their concentrations were amazingly uniform, varying only as a function of decay rates. The mean residence times established from ^{210}Pb daughter assay may also apply to the total lead in these same samples. Burton and Stewart[5] found a mean residence time of 29 days for ^{210}Pb in the total atmosphere, and 22 days for the troposphere. Lehmann and Sittkus[6] reported 33 and 14 days from rain and air samples, respectively. Fry and Mennon[8] estimated the mean residence time to be about one week. This lower value may be due to the high frequency of rainfall in the area studied. From these data and from the correlation between lead and ^{210}Pb established in this study, a mean residence time for stable lead of about one month is indicated.

The lack of correlation between lead and ^{210}Pb in air samples from about 1 meter above the ground[16] suggests that atmospheric mixing at low altitudes does not eliminate local variations in the rate of injection of one or the other of these materials. Consequently, it appears that the radioactive isotope is an adequate tracer for estimation of the residence time of stable lead only in rainwater or perhaps in air from higher altitudes.

The authors gratefully acknowledge the technical assistance of David Masters.

REFERENCES

1. G. W. Monier-Williams. *Lead in Food*, Reports on Public Health and Medical Subjects, No. 88. His Majesty's Stationery Office, London, 1938.
2. H. A. Schroeder and J. J. Balassa. *J. Chronic Dis.* **14**, 408 (1961).
3. C. C. Patterson. *Arch. Environ. Health* **11**, 344 (1965).
4. R. A. Kehoe. *J. Roy. Inst. Pub. Health* **24**, 81 (1961).
5. W. M. Burton and N. G. Stewart. *Nature* **186**, 584 (1960).
6. L. Lehmann and A. Sittkus. *Naturwissenschaften* **46**, 1 (1959).
7. R. King, L. B. Lockhart, Jr., R. A. Baus, R. L. Patterson, Jr., H. Friedmann, and I. H. Blifford, Jr. *Nucleonics* **14**(6), 78 (1956).
8. L. M. Fry and K. K. Mennon. *Science* **137**, 994 (1962).
9. B. B. Hicks, D. M. Nelson, S. S. Brar. Argonne National Laboratory Biological and Medical Research Division Annual Report, 1966. ANL-7278, pp. 307–310.
10. B. Glöbel, H. Muth, and E. Oberhausen. *Strahlentherapie* **131**, 218 (1966).
11. M. B. Ettinger. *Symposium on Environmental Lead Contamination*. Public Health Service Bulletin No. 1440, March 1966.
12. *Official Methods of Analysis of the Association of Official Agricultural Chemists*. Assoc. Official Agricultural Chemists, Washington, D. C., 1965.
13. H. F. Lucas, Jr. Argonne National Laboratory Radiological Physics Division Semiannual Report, January through June, 1959. ANL-6049, p. 117.
14. D. J. Swaine. Technical Communication No. 48 of the Commonwealth Bureau of Soil Science. Rothanstead Experimental Station, Harpenden, 1955.
15. P. K. Kuroda. Argonne National Laboratory Report ANL-5920 (October 1958).
16. S. S. Brar, D. M. Nelson, and S. E. Muniak. Argonne National Laboratory Biological and Medical Research Division Annual Report, 1966. ANL-7278, p. 312.

AIR, WATER, AND SOIL AS SOURCES OF LEAD IN PLANTS

G. L. Ter Haar, R. R. Dedolph,† R. B. Holtzman, and H. F. Lucas, Jr.*

Consideration of the possible toxicity of environmental lead as well as lead from industrial exposure was expressed by Monier-Williams in 1938.[1] In a recent review, it was suggested that primordial man's lead uptake and absorption was much less and resulted in a much smaller body burden than that of modern man.[2] This increase in modern man was attributed to environmental contamination from man's industrial and agricultural activities. In order to examine these ideas, the metabolic pathways of lead into man must be considered. Since the major source of lead in man is his food,[3-5] the sources of lead in food are of great importance.

The lead content of fruits and vegetables, as well as meats, may be derived from soil, air, rainwater and food processing. This study was designed to investigate the relative contributions of soil, air, and water to the lead content of plants.

Uptake and retention of lead by perennial rye grass (*Lolium perenne*) and radishes (*Raphanus sativus* c.v. Early Scarlet Globe) were determined from the lead content of the plant parts, grown in specially constructed chambers located in a green house. This chamber, shown in Figure 91, was constructed from an epoxy-coated galvanized tub covered with an acrylic hemisphere.‡ Air leaks were prevented by a water seal.

The alluvial black loam soil used was obtained 1–2 feet below the surface from a five-foot square area about 250 feet from a secondary roadway. This plot is part of a four-acre tract which has not been cultivated since the turn of the century and may be virgin. About one ton of this soil was prepared for use in all experiments by sifting through a copper screen. It was mixed by the standard method to insure uniformity and had a lead content of 26.8 ± 1.3 μg/g dry soil.§

The experiment was designed with eight discrete combinations of conditions each of which was replicated. Filtered or unfiltered air was passed over

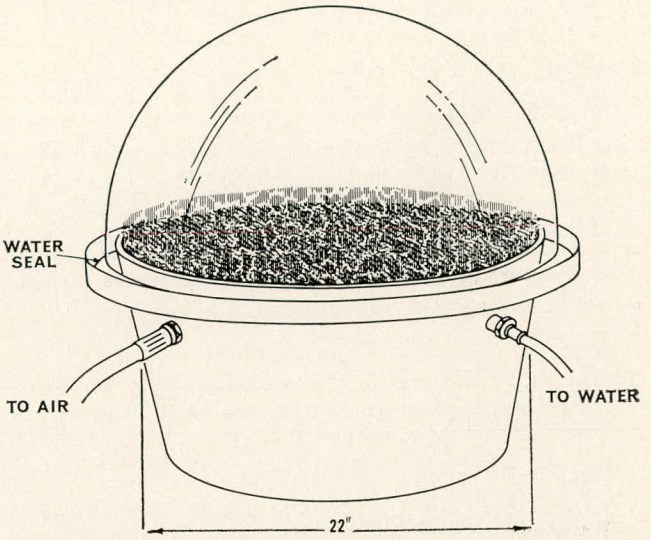

FIG. 91. Growth chamber

the plants. The water used was either distilled or lead-containing water and was applied either as a spray on the foliage or directly on the soil. The metered (0.06 m^3/min) ambient air stream was either passed through a Flanders "absolute" filter before entering the chambers or was taken in directly. The mean lead content of the filtered air of 0.03 ± 0.01 $\mu g/m^3$ was determined by analysis of a 1 *N* solution of hydrochloric acid used to scrub the air. The lead content of 0.96 $\mu g/m^3$ in the unfiltered air was determined by analysis of the residue on an asbestos filter (H.V. 70) placed at the exit to the system. This concentration is similar to that reported for a suburban environment.[6] Plants were watered when necessary, either with distilled water or water containing 40 μg Pb/l (as $PbCl_2$).

Grass samples were harvested by cutting with a scissors at least 2 or 3 cm above the soil when sufficient crop was present to allow accurate lead determination. Six sequential harvests were obtained with sample size ranging from 0.57 to 3.63 grams after drying at 110°C. Radishes, harvested as they attained edible maturity, yielded three crops. The tops ranged from 4.77 to 11.84 grams dry weight, the edible portion 0.85 to 2.30 grams dry weight.

All foliar samples were rinsed briefly in distilled water to remove surface dust. The edible portions were scrubbed with a brush until clean. All samples were wet ashed by dissolving in nitric and perchloric acids. Lead determination and reagent purification

* Industrial Trainee from Ethyl Corporation Research Laboratories, Ferndale, Michigan.

† Division of Biological and Medical Research.

‡ The lead-free paint was obtained from Devoe and Raynolds Paint Co., the tubes from McMaster Can Supply Co., Chicago, Illinois, and the hemispheres from Consolidated Plastics Co., Chicago, Illinois.

§ Errors for soil and air determinations are standard deviations. Four samples of soil, 6 of filtered air and 10 of unfiltered air were analyzed.

TABLE 63. THE EFFECT OF LEAD SOURCE ON THE LEAD CONTENT OF GRASS LEAVES[a]

Water supply	Water application	Air supply	
		Filtered, 0.03 μg Pb/m³	Unfiltered, 0.96 μg Pb/m³
Distilled	Foliar	2.55	5.43
	Soil	2.39	5.50
Lead-containing (40 μg Pb/l)	Foliar	2.79	5.45
	Soil	2.46	4.48
Mean		2.54	5.21

[a] Data are μg Pb/g dry weight of grass leaves; n = 12; δ error of mean = 0.51; L.S.D. (0.05) = 1.42; L.S.D. (0.01) = 1.86.

TABLE 64. THE EFFECT OF LEAD SOURCE ON THE LEAD CONTENT OF HYPOCOTYLS AND LEAVES OF RADISHES[a]

Water supply	Water application	Air supply			
		Filtered, 0.03 μg Pb/m³		Unfiltered, 0.96 μg Pb/m³	
		Leaves	Hypocotyls	Leaves	Hypocotyls
Distilled	Foliar	2.35	1.64	3.27	1.80
	Soil	1.73	2.80	3.55	1.91
Lead-containing (40 μg Pb/l)	Foliar	2.83	1.44	1.22	1.27
	Soil	2.21	2.09	2.74	2.43
Mean		2.28	1.99	2.70	1.85

[a] Data are μg Pb/g dry weight; n = 3; δ error of mean = 0.86; L.S.D. (0.05) = 2.49.

were based on the dithizone method of A.O.A.C.[7] The blank averaged 0.4 μg lead per sample. The reproducibility of replicate analyses was ±10%. Samples were coded by one of the authors (R. D.) and analyzed "blind."

Lead concentration data from 96 grass samples were subjected to variance analysis. Probability statements in the text refer to the probability that the difference or lack of differences cited are due to chance as determined by the "F" test criterion.[8] Prior covariance analysis using sample weights as the covariate disclosed no covariance of lead content with sample weight. This clearly implies that the chemical analysis was unaffected by the sample weights. The concentrations of lead in grass affected by all combinations of the three discrete variables, air, water, and water application, are summarized in Table 63.

It is readily apparent that the lead concentration in the air was the only significant variable. The mean lead concentration of grass grown in filtered air was 2.54 μg/g, while that grown in unfiltered air was 5.21 μg/g. These values are significantly different at the 1% level.

Conversely, none of the other experimental treatments affected the concentration of lead in grass. The mean lead concentration of grass grown with distilled water was 3.97 μg/g; with lead-containing water 3.80 μg/g; under foliar application of water, 4.05 μg/g; and under soil application of water 3.71 μg/g. All of these values do not differ significantly at the 5% level. Lead concentrations found in these studies compare favorably to literature values of 4.9 and 3.5 μg/g for lead in grass.[9, 10]

The concentration of lead in grass grown in the unfiltered air was about twice that of grass grown in the filtered air. However, since substantial amounts of lead were present in the grass grown in filtered air and watered with distilled water, uptake of lead by grass from the soil is clearly shown (Table 63).

Radishes were grown under identical conditions. Lead concentration data were statistically analyzed by the same method used in studying lead contents of grass. The concentrations of lead in the leaves and edible portion (expanded hypocotyles) of the radishes from the various combinations of the three discrete variables are summarized in Table 64.

The lead concentrations in radishes, regardless of treatment, did not differ greatly. The ability to discern differences statistically was less than in the grass study, as fewer samples were available. Main effect comparisons, using averages of 12 analyses for each plant part showed no significant differences at the 5% level. For example, the concentration of lead in radish leaves grown in filtered air was 2.28 μg/g; in unfiltered air 2.70 μg/g; with distilled water 2.73 μg/g; with lead-containing water 2.25 μg/g; under foliar application of water 2.25 μg/g; and under soil application of water 2.73 μg/g. Likewise the hypocotyl had a consistent concentration of lead regardless of treatment. The lead concentration of those grown in filtered air was 1.99 μg/g; in unfiltered air 1.85 μg/g; in distilled water 2.04 μg/g; in lead-containing water 1.81 μg/g; under foliar application of water 1.54 μg/g; and under soil application 2.31 μg/g. All of these means are not significantly different at the 5% level. It is interesting to note that the lead concentration of radishes was the same as that of grass grown in filtered air. These data indicate that half of the lead content in grass and all of that in radishes was obtained from the soil rather than from the air with little or no significant absorption from simulated rainfall. This differs from estimates and assumptions made elsewhere.[2]

While this study has been too limited in scope to

define the relative contribution of soil and air-borne lead to the human body burden, it has indicated that a substantial fraction of the lead in man's food may be obtained from the soil. Variables other than those studied may be of importance. These include the effect of soil type and pH, natural lead concentration of the soil, and plant type. A seasonal effect should also be considered since the lead content of grass increases substantially during its dormant season.[11]

The authors gratefully acknowledge the technical assistance of David Masters.

REFERENCES

1. G. W. Monier-Williams. *Lead in Food*, Reports on Public Health and Medical Subjects, No. 88, Ministry of Health. Her Majesty's Stationery Office, London, 1938.
2. C. C. Patterson. *Arch. Environ. Health* **2**, 344–360 (1965).
3. R. A. Kehoe. *J. Roy. Inst. Public Health* **24**, 81–203 (1961).
4. H. A. Schroeder and J. J. Balassa. *J. Chronic Dis.* **14**, 408 (1961).
5. R. B. Holtzman. Argonne National Laboratory Radiological Physics Division Semiannual Report, July through December, 1960. ANL-6297, pp. 67–80.
6. R. T. P. DeTreville. *Arch. Environ. Health* **8**, 212–221 (1964).
7. *Official Methods of Analysis of the Association of Official Agricultural Chemists*. Assoc. Official Agricultural Chemists, Washington, D. C., 1965.
8. G. W. Snedecor. *Statistical Methods*, 5th Ed. Iowa State College Press, Ames, Iowa, 1965.
9. J. S. Jones and M. B. Hatch. *Soil Service* **60**, 277–287 (1945).
10. G. C. Marten and P. B. Hammond. *Agron. J.* **58**, 553–554 (1966).
11. R. L. Mitchell and J. W. S. Reither. *J. Sci. Food Agr.* **17**, 437–440 (1966).

METEOROLOGICAL STUDIES

DEWPOINT TEMPERATURE INVERSIONS

W. C. Ashby, Harry Moses, and Mary A. Bogner*

INTRODUCTION

Water vapor is a variable constituent of the atmosphere. The amount present at any one time depends upon the type of air mass, the nature of the terrain over which the air mass has traveled, radiation conditions, turbulence structure, and other factors. Ordinarily, especially during clear daytime conditions, the moisture content decreases with height. During nighttime conditions with clear skies when the air is relatively moist and the winds are light, a reversal in the moisture gradient often occurs, that is, the moisture increases with height in the first several hundred feet above ground.

A number of investigators have obtained data on the variation of moisture with height in the lower atmospheric layers. Robinson,[1] for example, conducted such measurements in Greenland to study the meteorological conditions related to fog formation. Best et al.[2] carried out an extensive set of temperature and humidity measurements at four levels up to a height of 106.7 meters over a 3-year period. These data were obtained for use in atmospheric refractive index determinations necessary for work involving the propagation of radio and radar signals. Many measurements of the variation of moisture with height have been made in connection with agricultural work.

Absolute humidity, specific humidity, mixing ratio, wet-bulb temperature, relative humidity, vapor pressure, or dewpoint may be used to describe atmospheric moisture content. Authors have used those measures most appropriate to their studies. Since the dewpoint was measured directly, it is the primary measure of moisture used in this work.

The vertical flux of water vapor in the atmosphere is given by

$$F = -K_s \rho \frac{dq}{dz}, \qquad (1)$$

where F is the flux of water vapor in grams per square centimeter per second K_s the eddy diffusion coefficient for moisture in centimeters squared per second, ρ the air density in grams per cubic centimeter, q = the specific humidity in grams of water vapor per gram of moist air, and z = the height in centimeters. Any other consistent system of units may be used.

When the moisture content decreases with height, the flux of moisture is directed upward and is considered positive. Similarily, when moisture increases with height, the vapor flux is directed downward.

* Associate Professor of Botany, Southern Illinois University, Carbondale.

The vapor pressure e is related to the specific humidity q by the following equation

$$q = 0.622 \frac{e}{p - 0.378e}, \qquad (2)$$

where e is the vapor pressure in millibars, p the atmospheric pressure in millibars, and q is defined as above.

The dewpoint temperature T_d and the vapor pressure e have a one-to-one correspondence and are related by the Clapeyron-Clausius equation which may be expressed as

$$\frac{de}{dT_d} = \frac{Le}{RT_d^2}, \qquad (3)$$

where e is the vapor pressure in millibars or other consistent units, T_d the dewpoint temperatures in °K, L the heat of vaporization in calories per gram and assumed constant for temperature above 0°C, and R the gas constant for water vapor in calories per gram per degree.

Upon integration, one obtains the relation between the vapor pressure over water and dewpoint temperature as

$$\ln e = 1.81 + 19.9\left(\frac{t_d}{t_d + 273}\right), \qquad (4)$$

where t_d = the dewpoint temperature in °C.

If an unsaturated parcel of air is lifted adiabatically, its dewpoint temperature will fall even though the moisture content (grams water vapor/grams moist air) remains constant. The fall will be at a rate of about 0.17 times the dry adiabatic lapse rate of 10°C per kilometer. The dewpoint thus will fall at the rate of about 1.7°C per kilometer ascent. Making use of this information and that contained in equations (1–4), one can determine the vertical gradient of moisture content from measurements of dewpoint temperatures at two or more levels. It is of interest to point out that zero dewpoint gradients correspond to a reversal in the normal gradient of moisture concentration and to a water vapor flux directed downward.

INSTRUMENTATION AND AVAILABLE DATA

Objectives of this study are to present data on the climatography of vertical dewpoint profiles as determined by dewpoint temperature differences for the 1.2- and 9.4-ft levels and the 1.2- and 131-ft levels; and to investigate the relations between the variation of dewpoint with height and the associated meteorological conditions. Five years of hourly observations, from December 1, 1960 through December 31, 1965, made at the Argonne National Laboratory have been used. Data on solar radiation and net radiation flux, air and dewpoint temperatures, relative humidity, soil temperatures, wind speed and direction, and pressure have been examined to establish the influence of meteorological variables on the variation of dewpoint temperature with height.

At the Argonne National Laboratory meteorological installation, approximately 40 meteorological variables are measured each hour.[3] The data are recorded not only on pen and ink charts, but also on paper punch tape and on a teletype printout. The paper punch tape is converted into IBM cards and magnetic tape for computer processing. The Control Data Corporation (CDC) 3600 computer compiled the tables used in this paper.

Dewpoint measurements used in the present study were obtained by Foxboro Dewcels (Conover[4]) at 1.2, 9.4 and 131 feet on the Argonne meteorological tower. These instruments have an absolute accuracy of about 3°F and a greater relative accuracy. Dewpoints at each level were recorded for two minutes each, five times per hour and punched on tape once an hour.

Vertical temperature gradient measurements were obtained by copper-constantan thermocouples measuring the difference between temperatures at 5.5 and 144 feet. The temperature differences for this layer were integrated with a contact-closure type ball and disc integrator over a 2-minute period each hour. Hourly relative humidity values were computed from the 5.5-ft ambient air temperatures and the 4.7-ft dewpoint values. Net radiation flux measurements were obtained with a Beckman and Whitley radiometer located at 6 feet above the ground. The hourly values represent the integrated value of net radiation flux ending on the hour indicated. Belfort Corporation three-cup anemometers were used for measuring wind speed on a pole 19 feet high located 200 feet east of the meteorology tower. The meteorology tower itself is unsuitable for measuring wind speed at this height because of the wind shadow effect.[5] The wind speed readings represent 10-minute averages for each hour. The instrumentation for meteorological measurements used in this report which receive only secondary emphasis are described by Moses and Kulhanek.[3]

CLIMATOLOGICAL FEATURES OF DEWPOINT INVERSIONS

Frequency of Dewpoint Inversions

Dewpoint inversions are a fairly common occurrence. In winter as many as 41% of the hourly readings showed a dewpoint inversion between the 131- and 1.2-ft levels. In summer and fall 22 and

21% of the observations respectively showed inversion conditions. Further, the average number of days per month during which inversions occur ranges from a minimum of 18 in October to a maximum of 26 in January (Table 65) This table shows also that the dewpoint inversion occurs in a substantial number of hours. Table 66 presents the frequency distribution of the dewpoint temperature differences between the 131- and 1.2-ft levels for each season and for the entire year. Winter was taken as December, January and February; spring as March, April, May, etc.

A 20-degree range, i.e., from minus 10 to plus 10 degrees Fahrenheit brackets over 98% of the values (1% were missing due to malfunction at one or both levels). In winter 73% but in summer 48% of the dewpoint temperature differences fell within ±2 degrees. In each season more than one half of the observations showed hydrolapse conditions in the 0 to −3.9°F range.

Figure 92 shows the percentage frequency distribution of the dewpoint temperature differences per 100 feet based on data for the layer from 1.2 to 9.4 ft as well as that from 1.2 to 131 ft. The curves are reasonably symmetrical, but it is evident that most of the change in dewpoint temperature takes place in the 1.2 to 9.4-ft layer.

Diurnal Variation of Dewpoint Temperatures

In general, the dewpoint temperature rises during the daytime and falls at night. The hourly values shown in the upper part of Figure 93, provide a picture of the diurnal variation. It is evident that when vegetation is present the amplitude of the diurnal wave is appreciably greater than during the winter months. The double maximum described by Geiger[6] may be seen for the months of October and November.

The lower portion of Figure 93 shows the diurnal variation of the dewpoint temperature difference for the 9.4- to 1.2-ft and 131- to 1.2-ft levels. The large differences observed during the daylight hours for months when vegetation is present, i.e., May through October, are noteworthy. During these months

TABLE 65. Periods with Inverted Dewpoint Temperature Difference, 131- Minus 1.2-Foot Levels, December 1960 to November 1965

Month	Average number of hours per day			Number of days per month		
	Highest monthly average	5-Year average	Lowest monthly average	Highest	5-Year average	Lowest
December	16	10	4	31	25	12
January	18	11	5	31	26	19
February	18	9	4	29	24	17
March	15	9	4	31	25	17
April	16	7	2	30	21	12
May	12	6	1	30	21	7
June	11	6	3	29	23	16
July	7	6	4	28	23	18
August	6	5	3	25	23	19
September	6	5	1	26	21	5
October	7	4	2	22	18	10
November	14	7	3	30	21	14

TABLE 66. Percentage Frequency Distribution of the Dewpoint Gradient, December 1960 to November 1965

Dewpoint temp. difference, 131- minus 1.2-ft, °F	Season				Annual
	Winter	Spring	Summer	Fall	
<−10.0	0.2	0.8	0.7	0.6	0.6
−9.9 to −8.0	0.2	1.4	1.6	1.3	1.1
−7.9 to −6.0	0.7	3.9	5.8	4.3	3.7
−5.9 to −4.0	2.7	9.0	13.6	10.5	9.0
−3.9 to −2.0	10.6	17.8	23.0	20.0	17.9
−1.9 to −0.0	44.1	38.9	32.1	41.6	39.2
0.1 to 2.0	29.2	22.4	15.7	14.2	20.4
2.1 to 4.0	7.6	4.0	4.6	3.7	4.9
4.1 to 6.0	2.5	0.9	1.2	1.6	1.5
6.1 to 8.0	0.8	0.3	0.2	0.8	0.5
8.0 to 10.0	0.3	0.1	—	0.3	0.2
>10.0	0.3	—	—	0.1	0.1
Missing	0.8	0.6	1.6	1.0	1.0
Percent lapse	58.5	71.8	76.8	78.3	71.5
Percent inversion	40.7	27.7	21.7	20.7	27.6

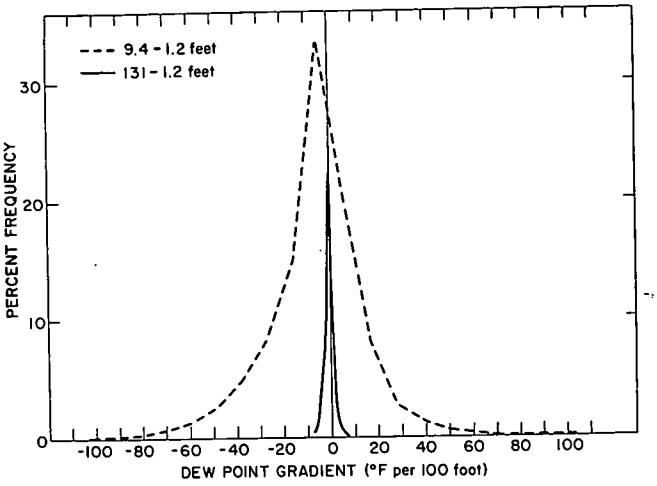

Fig. 92. Percent frequency distribution of the dewpoint gradient.

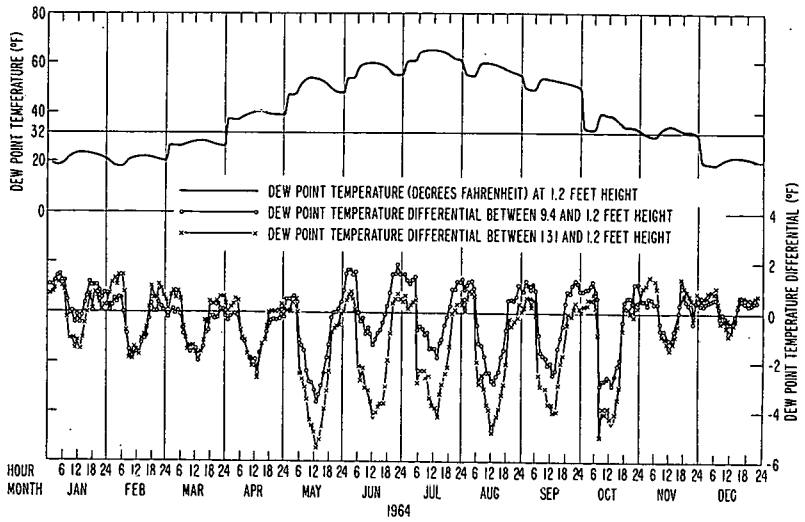

FIG. 93. Average hourly dewpoint temperature at 1.2 feet and average hourly dewpoint temperature difference between 131 and 1.2 feet, and 9.4 and 1.2 feet for each month of 1964.

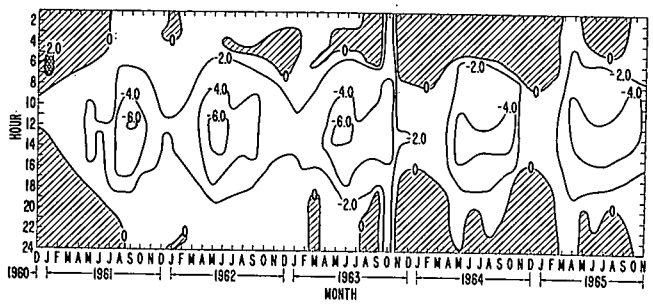

FIG. 94. Isopleths of average hourly dewpoint temperature difference for month versus hour charts for December 1960 to November 1965.

the largest positive, as well as negative, gradients are observed. Note that the curves do not cross over during these months. In strong hydrolapse conditions the average humidity decreases monotonically but during dewpoint inversion conditions the increases with height are not monotonic, since the dewpoint difference between 9.4- and 1.2-ft levels is greater than the difference between the 131- and 1.2-ft levels. Thus, the average dewpoint inversion profile indicates that a maximum exists between the 1.2- and 131-ft levels. The recurrence of this pattern in other years as well confirms its validity.

The average hourly dewpoint temperature differences between 131- and 1.2-ft levels for each month of each year for the period December 1, 1960 to November 30, 1965 are presented in Figure 94. The strong daytime hydrolapse pattern during the growing season is clearly shown. Inversion conditions appear as hatched areas. This figure shows again that dewpoint inversions are nighttime phenomena.

Since the dewpoint inversion occurs more frequently at night, one would expect its onset to be around sunset and its disappearance shortly after sunrise. Figure 95 shows this to be so. This figure shows the annual average frequency of onset and disappearance of the dewpoint inversion for each hour of the day. It is evident that the maximum frequency of onset occurs in the late hours of the afternoon or early evening and the most frequent hour for ending occurs at about sunrise. The maxima are broadened because all of the data for the year were used. In similar charts, drawn for each season, the relation between disappearance and appearance with sunrise and sunset are more distinct. Charts drawn for the 9.4- to 1.2-ft levels show more clearly the beginning and end of the dewpoint inversion with dusk and dawn.

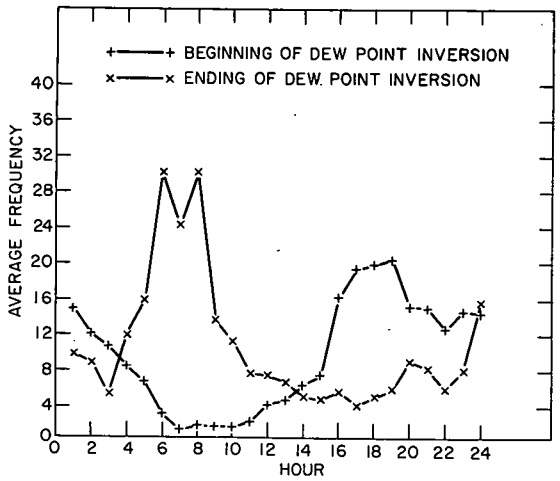

FIG. 95. Annual average frequency of the beginning and ending of dewpoint inversion (two or more hours' persistence) by hour for the period December 1960 to November 1961.

RELATION BETWEEN THE VERTICAL DEWPOINT PROFILE AND ASSOCIATED METEOROLOGICAL VARIABLES

The observed variation of dewpoint temperature with height is markedly affected by conditions which lead to condensation on or evaporation from the ground surface. It is also possible for advective processes to contribute to the changes of dewpoint temperature with height, but for this study advection is not taken into account although in some cases it may be important.

A dewpoint inversion will develop if the ground acts as a sink to remove water vapor. The ground does act as a sink whenever it cools to a point where condensation will take place or if it is hygroscopic. Condensation may be expected during clear nighttime conditions when the ground radiates strongly to outer space and cools to below the dewpoint temperature. One should expect appreciable condensation to take place during times when the relative humidity is high and when the net radiation flux is directed outward, which in turn leads to a strong surface inversion. During windy conditions the lower layers of the atmosphere are well mixed, thus preventing strong cooling in the lower layers because warmer air is continually brought down from above. Thus, dewpoint inversions would be expected to form more frequently under light wind conditions, all other factors being equal.

Dewpoint Case Studies

The relation between the 131- and 1.2-ft dewpoint temperature difference and the aforementioned and other meterological variables are presented in the two case studies of Figures 96 and 97. Figure 96 is based on measurements for the 120-hour period beginning at 0100, August 7, 1963, and ending at 2400,

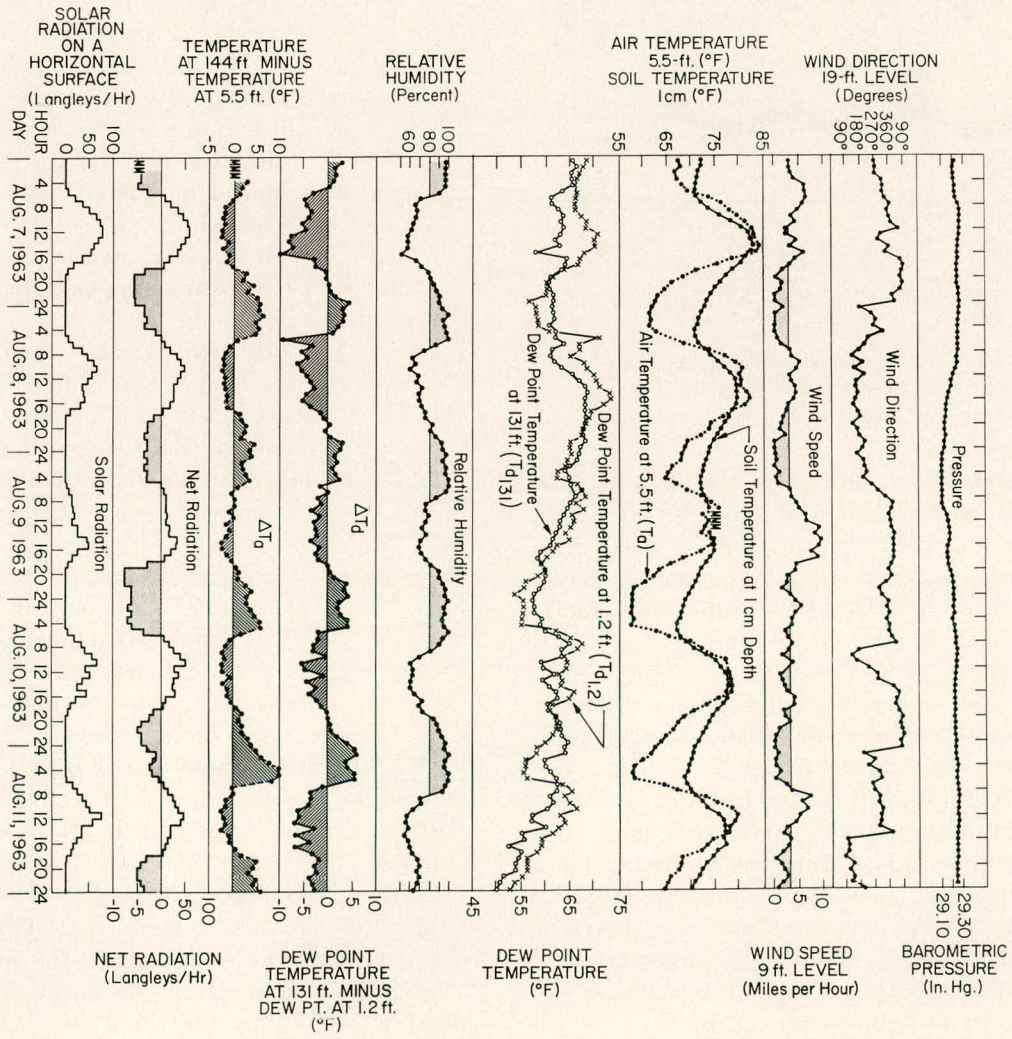

FIG. 96. Time series of hourly dewpoint temperature differences between 131 and 1.2 feet and related meteorological variables for the period 7–11 August, 1963.

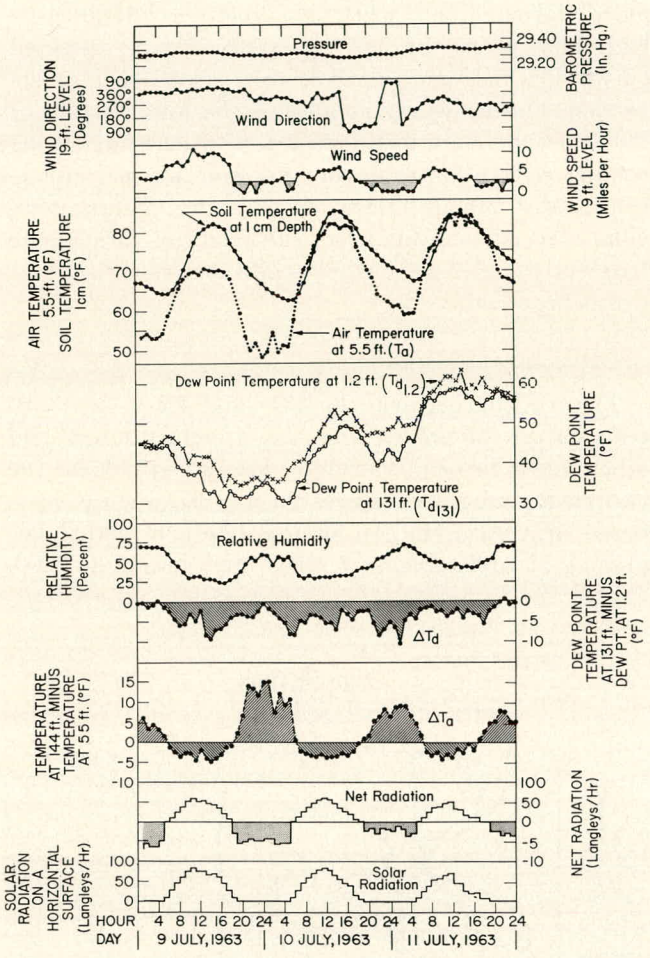

FIG. 97. Time series of hourly dewpoint temperature differences between 131 and 1.2 feet and related meteorological variables for the period 9–11 July, 1963.

August 11, 1963. Figure 97 shows the data for the 72-hour period beginning at 0100, July 9 and ending at 2400, July 11, 1963. In the August case, dewpoint inversions occurred for a substantial period during each of the five nights. In the July study, dewpoint inversions occurred in only two isolated nighttime hours.

A study of these meteorological variables and their relationships throws light on the processes involved in producing downward fluxes of water vapor. The curves for net radiation flux, ambient air and dewpoint temperature, and wind speed are similar in that a maximum occurs during the daytime and a minimum during the night. Approximately 180° out of phase with these curves are those for dewpoint temperature difference, air temperature difference, and relative humidity. The soil temperature changes are similar to those of air temperature.

The August period is characterized by marked dewpoint inversions. The amplitude of the day-night dewpoint temperature changes at 1.2 feet is markedly greater than at 131 feet during this period. The following factors contributed to a decrease in dewpoint temperature at 1.2 feet and the development of a dewpoint inversion:

a) Outgoing radiation for approximately 12 hours each night, with maximum values of 4 to 8 langleys per hour.

b) Temperature inversions for 12 or more hours which reached maximum values of 4 to 10 degrees. The stability of the lower atmosphere during inversion periods suppressed vertical mixing. As a result the air near the earth's surface was not replaced with warmer air from above, and the lowermost layers continued to cool to the dew-point temperature. This, of course, allowed condensation at the ground.

c) Low wind speeds, under 5 mph at night. It is likely that an optimum range of wind speed exists for the development of dewpoint inversions. If the winds are too strong, mixing prevents the lower layers from cooling with the result that condensation is impeded. If the winds are too light so that the flow is nearly laminar, the vertical water vapor flux becomes markedly reduced. Thus, there must be a range of wind speeds for each combination of relative humidity, net radiation flux and stability which are effective in bringing about dewpoint inversions.

During the July period, wind speed, net radiation flux, and the air temperature difference were favorable for the development of a dewpoint inversion, but the relative humidity was too low. An inversion was recorded in only two isolated observations. The following features characterize the July case:

a) Nighttime periods of outgoing radiation were somewhat shorter and the magnitude was somewhat less than in August. During one night (9th–10th), however, greater values were observed than on two of the nights in the August period. Dewpoint inversions were not observed on that night.

b) Greater temperature inversions in July than in August. On the night of the 9th–19th a difference of over 15°F was observed. The relative dryness of the air no doubt contributed to this large temperature gradient.

c) Relative humidity values of less than 75%. Air temperature remained more than 9°F higher than dewpoint temperature throughout the period.

d) Nighttime wind speeds under 5 mph. On the night of 10–11 July the winds were less than 2 mph or calm.

Joint Frequency Distributions of Dewpoint Temperature and Associated Meteorological Variables

Joint frequency distributions are presented in Tables 67–70 for differences in dewpoint temperature between the 131- and 1.2-ft levels and each of the variables: net radiation flux, air temperature difference, relative humidity and the 19-foot wind speed.

The relation between the net radiation flux and the dewpoint temperature difference is shown in Table 67. Inversions as large as 6.0°F were found

TABLE 67. JOINT PERCENTAGE FREQUENCY DISTRIBUTION OF THE DEWPOINT GRADIENT AND NET RADIATION FLUX, DECEMBER 1960 TO NOVEMBER 1965

Dewpoint temp. difference 131- minus 1.2-ft, °F	Net radiation in tenths of langleys per hour						Total
	≦ −50	−49 to −25	−24 to 0	1 to 99	100 to 799	Missing	
<−10.0	—	—	—	0.1	0.4	—	0.6
−9.9 to −8.0	—	—	0.1	0.1	0.8	—	1.1
−7.9 to −6.0	0.1	0.1	0.2	0.3	2.9	0.2	3.7
−5.9 to −4.0	0.2	0.4	0.5	0.9	6.6	0.4	9.0
−3.9 to −2.0	1.2	1.4	2.2	3.6	8.2	1.3	17.9
−1.9 to −0.0	7.1	6.5	9.6	5.9	4.4	5.7	39.2
0.1 to 2.0	6.6	4.5	3.9	1.6	0.7	3.1	20.4
2.1 to 4.0	2.2	1.7	0.4	0.1	0.2	0.3	4.9
4.1 to 6.0	0.6	0.7	0.1	—	—	0.1	1.5
6.1 to 8.0	0.2	0.3	—	—	—	—	0.5
8.1 to 10.0	0.1	0.1	—	—	—	—	0.2
>10.0	—	0.1	—	—			0.1
Missing	0.1	0.2	0.1	0.1	0.2	0.2	1.0
Total	18.4	16.0	17.1	12.7	24.4	11.4	100.0
Cumulative total	18.4	34.4	51.5	64.2	88.6	100.0	100.0
Percent lapse	8.6	8.4	12.6	10.9	23.3	7.6	71.5
Percent inversion	9.7	7.4	4.4	1.7	0.9	3.5	27.6

TABLE 68. JOINT PERCENTAGE FREQUENCY DISTRIBUTION OF THE DEWPOINT GRADIENT AND AIR TEMPERATURE DIFFERENCE, DECEMBER 1960 TO NOVEMBER 1965

Dewpoint temp. difference 131- minus 1.2-ft, °F	Air temperature difference 144- minus 5.5-ft, °F								Total
	≦ −3.0	−2.9 to −2.0	−1.9 to −1.0	−0.9 to −0.0	0.1 to 1.0	1.1 to 3.0	≧ 3.1	Missing	
<−10.0	0.1	0.2	0.1	—	—	—	0.1	0.1	0.6
−9.9 to −8.0	0.2	0.4	0.2	0.1	—	—	0.1	0.1	1.1
−7.9 to −6.0	0.8	1.4	0.6	0.4	0.1	0.1	0.2	0.3	3.7
−5.9 to −4.0	1.7	3.1	1.6	1.0	0.2	0.3	0.5	0.6	9.0
−3.9 to −2.0	1.7	3.7	3.7	3.6	1.0	1.1	1.3	1.8	17.9
−1.9 to −0.0	0.5	2.2	4.0	13.0	5.1	5.0	3.6	5.7	39.2
0.1 to 2.0	0.1	0.4	1.1	5.1	3.3	4.3	3.4	2.6	20.4
2.1 to 4.0	0.1	0.1	0.1	0.3	0.4	1.3	2.5	0.3	4.9
4.1 to 6.0	—	—	—	—	—	0.2	1.2	0.1	1.5
6.1 to 8.0	—	—	—	—	—	—	0.4	—	0.5
8.1 to 10.0	—	—	—	—	—	—	0.2	—	0.2
>10.0	—	—	—	—	—	—	0.1	—	0.1
Missing	—	0.1	0.1	0.1	0.1	0.2	0.2	0.2	1.0
otal	5.1	11.6	11.4	23.7	10.2	12.6	13.6	11.7	100.0
umulative total	5.1	16.7	28.1	51.8	62.0	74.6	88.2	99.9	100.0
Percent lapse	5.0	11.0	10.2	18.1	6.4	6.5	5.8	8.6	71.5
Percent inversion	0.2	0.5	1.2	5.4	3.7	5.8	7.8	3.0	27.6

TABLE 69. JOINT PERCENTAGE FREQUENCY DISTRIBUTION OF THE DEWPOINT GRADIENT AND RELATIVE HUMIDITY, DECEMBER 1960 TO NOVEMBER 1965

Dewpoint temp. difference 131- minus 1.2-ft, °F	Relative humidity, %									Total
	21 to 30[a]	31 to 40	41 to 50	51 to 60	61 to 70	71 to 80	81 to 90	91 to 100	Missing	
<−10.0	—	0.2	0.1	0.1	—	—	—	—	—	0.6
−9.9 to −8.0	0.1	0.2	0.3	0.2	0.1	0.1	—	0.1	—	1.1
−7.9 to −6.0	0.2	0.6	1.1	0.8	0.5	0.2	0.1	0.1	—	3.7
−5.9 to −4.0	0.2	1.0	1.8	2.3	1.7	1.0	0.5	0.4	—	9.0
−3.9 to −2.0	0.2	0.8	2.1	3.3	4.1	3.6	2.4	1.3	0.1	17.9
−1.9 to −0.0	0.1	0.6	1.8	3.4	5.8	8.2	8.6	10.4	0.3	39.2
0.1 to 2.0	—	0.2	0.5	1.2	2.0	3.4	5.2	7.7	0.1	20.4
2.1 to 4.0	—	—	0.1	0.2	0.3	0.6	1.2	2.4	0.1	4.9
4.1 to 6.0	—	—	—	—	—	0.1	0.3	1.0	—	1.5
6.1 to 8.0	—	—	—	—	—	—	0.1	0.4	—	0.5
8.1 to 10.0	—	—	—	—	—	—	—	0.2	—	0.2
>10.0	—	—	—	—	—	—	—	0.1	—	0.1
Missing	—	—	0.1	0.1	0.1	0.1	0.1	0.1	0.4	1.0
Total	0.8	3.6	7.9	11.6	14.6	17.3	18.5	24.2	1.0	100.0
Cumulative total	0.8	4.4	12.3	23.9	38.5	55.8	74.3	98.5	99.5	100.0
Percent lapse	0.8	3.4	7.2	10.1	12.2	13.1	11.6	12.3	0.4	71.5
Percent inversion	—	0.2	0.6	1.4	2.3	4.1	6.8	11.8	0.2	27.6

[a] Zero values prevailed for 1–10 and 11–20% relative humidity.

TABLE 70. JOINT PERCENTAGE FREQUENCY DISTRIBUTION OF THE DEWPOINT GRADIENT AND 19-FT WIND SPEED, DECEMBER 1960 TO NOVEMBER 1965

Dewpoint Temp. difference 131- minus 2.1-ft, °F	Wind speed, mph							Total
	Calm	1 to 3	4 to 7	8 to 12	13 to 18	≧19	Missing	
<−10.0	0.1	0.1	0.2	0.1	—	—	—	0.6
−9.9 to −8.0	0.1	0.2	0.4	0.3	0.1	—	—	1.1
−7.9 to −6.0	0.1	0.5	1.4	1.2	0.4	0.1	—	3.7
−5.9 to −4.0	0.2	1.1	3.1	3.1	1.2	0.2	—	9.0
−3.9 to −2.0	0.4	2.4	6.4	5.7	2.5	0.5	—	17.9
−1.9 to −0.0	0.8	5.0	14.5	12.4	5.3	0.9	0.2	39.2
0.1 to 2.0	0.7	3.7	8.4	5.4	1.8	0.2	0.1	20.4
2.1 to 4.0	0.5	1.8	2.0	0.5	0.1	—	—	4.9
4.1 to 6.0	0.3	0.6	0.5	0.1	—	—	—	1.5
6.1 to 8.0	0.1	0.2	0.1	—	—	—	—	0.5
8.1 to 10.0	—	0.1	—	—	—	—	—	0.2
>10.0	—	0.1	—	—	—	—	—	0.1
Missing	—	0.1	0.4	0.3	0.1	—	—	1.0
Total	3.4	15.8	37.7	29.2	11.6	2.0	0.3	100.0
Cumulative total	3.4	19.2	56.9	86.1	97.7	99.7	100.0	100.0
Percent lapse	1.7	9.3	26.0	22.8	9.5	1.7	0.2	71.5
Percent inversion	1.6	6.5	11.0	6.0	1.9	0.2	0.1	27.6

only with outgoing radiation. Steep hydrolapse conditions were found with incoming radiation. With incoming radiation of 10 or more langleys per hour the hydrolapse frequency is overwhelmingly greater than the inversion frequency. Inversion frequencies exceeded hydrolapse frequencies whenever the outgoing radiation amounted to 5 or more langleys per hour.

The relation between dewpoint inversions and temperature inversions is given in Table 68. Under temperature lapse conditions no dewpoint inversion gradients greater than 4 degrees are found. The rela-

tively few observations (0.1%) of dewpoint inversion with temperature lapse conditions may be due to transitional observations, i.e., from night to day, or possible instrumental inadequacy. Large air temperature and dewpoint temperature inversions are associated, as are lapse and hydrolapse conditions.

A clear and marked relationship between relative humidity and dewpoint gradient was observed (Table 69). Only hydrolapse conditions occurred at humidities below 30%. With increasing relative humidity the ratio of the frequency of occurrence of hydrolapse to inversion cases diminishes. For the highest humidity class, 91–100%, large values of inversion were more frequent than large values of lapse conditions.

The relation between wind speed and dewpoint temperature differences is shown in Table 70. Increasing wind speed decreases the temperature differences observed. The proportion of hydrolapse to inversion increases with increasing wind speed. Dewpoint inversions, however, are found even in the highest wind speed groupings shown in the table.

TABLE 71. PERCENT FREQUENCY OF OCCURRENCE OF OUTGOING NET RADIATION FLUX, TEMPERATURE INVERSION, DEWPOINT TEMPERATURE INVERSION, AND RELATIVE HUMIDITY RELATED TO SEASON, DECEMBER 1960 TO NOVEMBER 1965

Season	Outgoing radiation[a]	Temperature inversion[a] 144-minus 5.5-ft	Dewpoint inversion[b] 131-minus 1.2-ft	Relative humidity ≧81%	Wind speed at 19 ft <4 mph
Winter	62	29	41	55	13
Spring	45	31	28	38	12
Summer	44	42	22	39	28
Fall	56	44	21	40	23
Annual	52	36	28	43	19

[a] Approximately 10% of the frequency distribution values are missing due to instrument malfunction during periods of rain.

[b] Approximately 1% of the frequency distribution values are missing due to instrumentation malfunction.

Frequency of Conditions Contributing to Dewpoint Inversions

The frequency of occurrence of those conditions which contribute to the development of dewpoint inversions are shown in Table 71 for each season. Strong outgoing net radiation, temperature inversions, relative humidity exceeding 80% and light winds all contribute. The frequency of air temperature inversions increases from winter to spring, summer and fall. Just the opposite is true for dewpoint temperature inversions. Each of the other variables has different frequency distribution patterns.

Multivariate Charts Relating Dewpoint Inversions with Other Meteorological Variables

The relation between the variables, net radiation flux, relative humidity and 19-ft wind speed, and the occurrence of dewpoint inversion are shown in Figure 98. This presentation makes it possible to examine the frequency of simultaneous occurrence of any one of these variables and dewpoint inversion with the other two held constant. For example, in Figure 98a

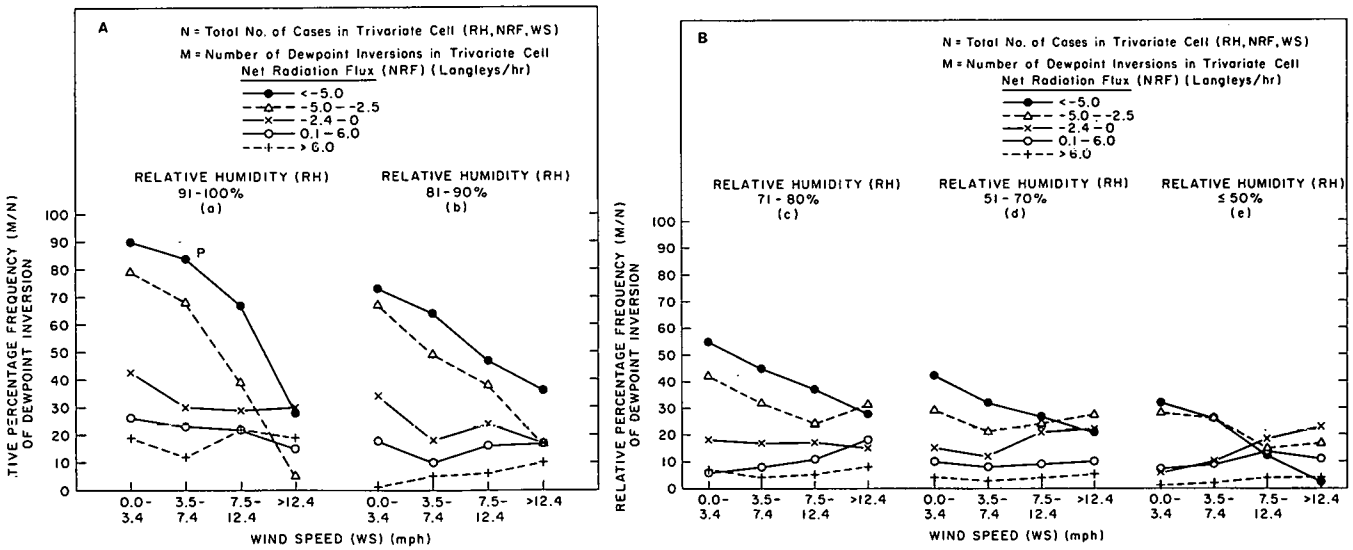

FIG. 98. Relative percentage frequency of dewpoint temperature inversion as a function of net radiation flux, relative humitity and wind speed.

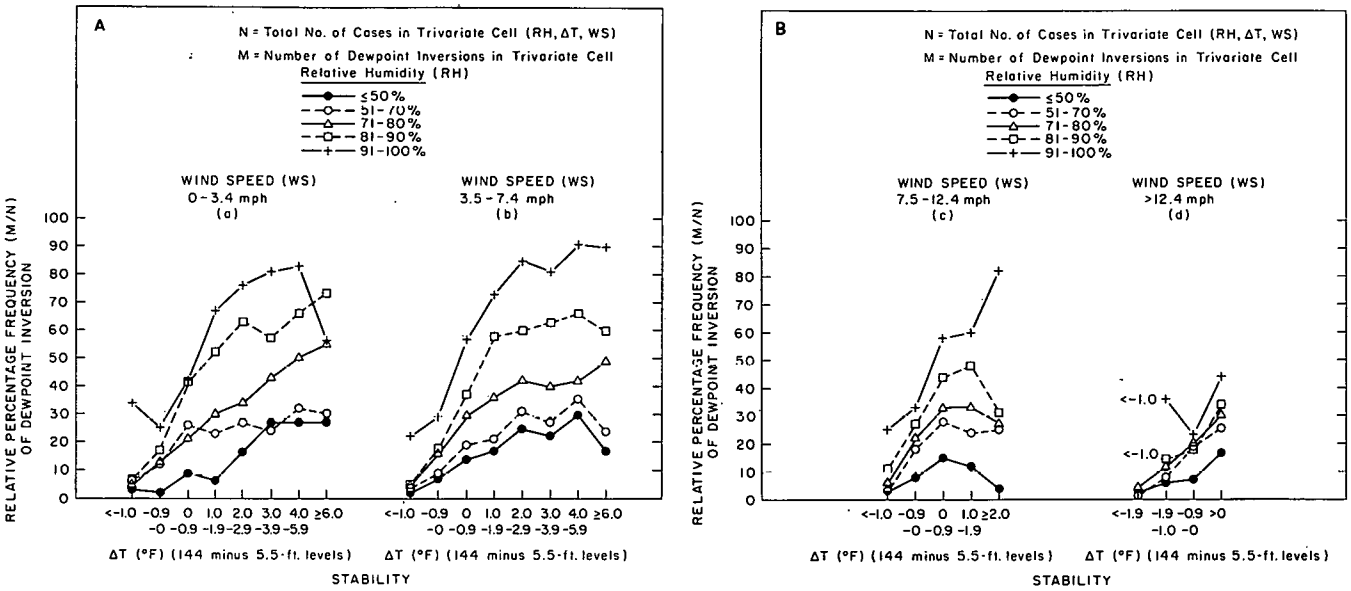

FIG. 99 Relative percentage frequency of dewpoint temperature inversions as a function of stability, relative humidity, and wind speed.

the relative humidity is in the range of 91–100%. Separate curves are drawn relating the relative percentage frequency of dewpoint inversion and wind speed holding the net radiation flux within a specified interval. Thus, along any of these curves the net radiation flux is constant. Since the relative humidity is also constant, within limits, one may observe how the relative frequency of dewpoint inversion changes with wind speed under these conditions.

The relative percentage frequency refers to the percentage of the total number of observations in a particular category (i.e., having a particular combination of wind speed, relative humidity and net radiation flux) which appears as dewpoint inversion reading. For example, point P shows a value of 84%. There were actually 1025 cases of relative humidity between 91 and 100%, of wind speed between 3.5 and 7.4 mph and of net radiation flux less than −5.0 langleys per hour. Of the 1025 cases in this category, 865, or 84%, were dewpoint inversions.

These graphs show clearly the high probability of dewpoint inversion existing under conditions of high relative humidity, strong outgoing radiation and relatively light winds. Of interest are the 30–40% inversion frequency values for low relative humidities with strong outgoing radiation. This must mean that the surfaces have cooled to very low levels and pronounced temperature as well as dewpoint temperature gradients exist. It is to be noted that the relative humidities measured are at 5 feet above ground. At short distances above the surface, i.e., millimeters, the relative humidity values are undoubtedly appreciably higher.

Figure 99 shows the relation between the occurrence frequency of dewpoint inversions and the three variables: wind speed at 19 ft, relative humidity, and stability as determined by the temperature difference between the 144- and 5.5-ft levels. In constructing the charts, the data were first divided into four wind speed groups, i.e., 0–3.4, 3.5–7.4, 7.5–12.4 and >12.4 meters per hour. For each wind speed category, the data were subdivided by group intervals of relative humidity. The individual charts representing the data for a given wind speed class, e.g., 99a, contain curves relating relative percentage frequency of dewpoint inversion and atmospheric stability for each relative humidity grouping. The relative percentage frequency of dewpoint inversion is defined above in the discussion of Figure 98.

The uppermost curve representing conditions of 91–100% relative humidity (Figure 98) and to a lesser extent the second curve from the top representing 81–90% are affected by precipitation and by ground fog, especially the patchy variety. When rainfall occurs, the copper-constantan thermocouples used for measuring stability become wet and often indicate readings of greater than actual atmospheric instability. Although a serious attempt was made to eliminate this error, the effect is probably still present. Evidence for this is shown in Figure 99a where the relative percentage frequency of 34% is shown for a stability value of <−1.0°F but falls to 25% for tl stability value of 0 to −0.9°F. This effect also aj pears on the other charts. The same effect may be due to patches of ground fog moving over one of the thermal or dewpoint elements and not the other.

The tendency for the relative percentage frequency of dewpoint inversions to fall during intense air temperature inversions, when the relative humidity is above 80%, appears to be real (see Figure 99). In Figure 99a, the 81–90% curve also shows a downward slope for intense inversions when the stability categories are divided into finer class intervals. The processes giving rise to this phenomenon warrant further investigation.

In Figures 99c and d it was necessary to combine data in the extreme categories because of the small number of cases in these intervals. With strong winds and pronounced vertical mixing the lapse rate tends toward the adiabatic, thus accounting for the few cases of strong inversion or superadiabatic lapse rates.

Figure 99 brings out clearly the relation between the occurrence frequency of dewpoint inversions and the other relevant variables—wind speed, relative humidity, and stability. The relatively little overlap of the relative humidity curves is marked but not unexpected; however, the change in slope of these curves with increase in stability is noteworthy.

Implications of Dewpoint Inversion

Evapotranspiration is a major component of the hydrologic cycle. Favorable conditions for evaporation and transpiration are present when the atmosphere serves as a moisture sink and an upward flux of water exists. During periods of inverted water vapor flux, an atmospheric restriction exists for evaporation and for plant water loss. Transpirational stresses are thereby relieved.

The implications of fluxes of downward flowing water vapor to agricultural problems have been discussed by Ramdas,[7] Thornthwaite,[8] and Monteith.[9] Best *et al.*,[2] Möller,[10] and Robinson[1] have considered this process from a general meteorological standpoint. A valuable discussion of the distribution of atmospheric moisture as a function of time and space is presented by Geiger.[6]

If the flux of downward-flowing water vapor is sufficiently great, dew, frost, or fog may form. Monteith[9] has discussed the formation of dew with a reversal in vertical dewpoint temperature differences. He points out that distillation-evaporation together with condensation, which may take place simultaneously on adjacent surfaces because of differences in vapor pressure, may give the appearance of dew during a period when transpiration is still possible. For example, upper- versus lower-leaf, water, and ground surfaces may have unlike radiation characteristics, different temperatures, and appropriately varied water vapor pressures.

Knowledge of the timing and persistence of downward-directed fluxes may be of great importance in estimating evapotranspiration and in assessing climates for plant production or introduction of plants into a new locale. As shown in the present paper, prediction of atmospheric restrictions on evaporation and plant water loss and of dew formations can be related to net radiation flux, air temperature differences at two heights, relative humidity, and wind speed. Of these, relative humidity and wind speed data are widely available. Temperature inversion measurements are being obtained more frequently, primarily in connection with air pollution problems, and the existence of outgoing net radiation flux leading to cooling of ground surfaces and of the immediately overlying atmosphere can be estimated from prevailing meteorological conditions especially solar radiation and sky cover.

Additional restrictions to plant water loss may be present. The escape of water molecules and consequent vapor pressure over a leaf surface is determined by the leaf temperature, by the concentration of solutes in the leaf sap, by the curvature of the evaporating surfaces—convex surface having a higher vapor pressure than a plane surface—and by the degree of stomatal opening. Stomatal closure reduces greatly the contribution of a leaf to enrichment of the adjacent air with moisture by reducing vapor movement. It does not alter equilibrium states. The major variable influencing the vapor pressure over leaf fluids is leaf temperatures. Leaf and air temperatures both vary day to night, creating continuously altering vapor pressure gradients.

The foliage cycle in northern Illinois is that of leafing in late April and shedding of leaves in October. During this 6-month period large transpiration surfaces are present. Dewpoint inversions occur, primarily at night, during this period. These recurring atmospheric restrictions on evapotranspiration may be of crucial importance in enabling the restoration of a favorable plant water balance and of cell turgor, which is a component of plant growth processes. The greater prevalance of dewpoint inversions during the dormant season for most plant species is of lesser importance for their growth and survival. It may be of hydrological significance in recharge of soil moisture and of importance to evergreen species which are, however, of very limited occurrence in northern Illinois.

Assessment of atmospheric restrictions on water loss for a locality in which dewpoint inversion data are not available may be based on the four meteorological variables here discussed. Unlikely times for dewpoint inversion are those in which wind speeds are greater than 8 mph, in which air temperatures

decrease with height, the net radiation is directed upward, and the relative humidity is below 80%. An appreciation of these relations will contribute greatly to hydrological and ecological understanding of climatic regimes.

We are indebted to Frank C. Kulhanek and Gunther A. Zerbe for maintaining the instrumentation and processing of the climatological data, and to Martin Kraimer and C. Williams for computer programming and analyses. L. D. Marinelli encouraged and assisted the studies, and Dr. James E. Carson commented on several aspects of the meteorological measurements.

REFERENCES

1. E. Robinson. Atmospheric water vapor measurements on the Greenland ice cap. Final Report Atmospheric Sciences Laboratory, U. S. Army Electronics Command (1965). [Contract DA-28-043-AMC-00130 (E)].
2. A. C. Best, E. Knighting, R. H. Pedlow, and K. Stormonth. Temperature and humidity gradients in the first 100 m over southeast England. *Geophys. Mem.* **No. 89.** Meteorological Office, Air Ministry, London, 1952.
3. H. Moses and F. C. Kulhanek. Argonne automatic meteorological data processing system. *J. Appl. Meteorol.* **1,** 69–80 (1962).
4. J. H. Conover. Tests and adaptation of the Foxboro dewpoint recorder for weather observatory use. *Am. Meteorol. Soc. Bull.* **31,** 13–22 (1950).
5. H. Moses and H. G. Daubek. Errors in wind measurements associated with tower-mounted anemometers. *Am. Meteorol. Soc. Bull.* **42,** 190–194 (1961).
6. R. Geiger. *The Climate Near the Ground.* Harvard University Press, Cambridge, Mass., 1965. (Translation of the 4th German Ed.)
7. L. A. Ramdas. The microclimates of plant communities. *Indian Ecologist* **1,** 1–20 (1946).
8. C. W. Thornthwaite. Micrometeorology of the surface layer of the atmosphere. Interim Report No. 10, Laboratory of Climatology, Johns Hopkins University, Seabrook, New Jersey (1950).
9. J. L. Monteith. Dew. *Roy. Meteorol. Soc. Quart. J.* **83,** 322–341 (1957).
10. F. Möller. Über den täglichen Gang des Dampfdruckes und seiner interdiurnen Veränderlichkeit. *Meteorol. Ztschr.* **54,** 124–133 (1937).

MODIFICATIONS OF CUP ANEMOMETER DESIGN TO IMPROVE THE MEASUREMENT OF MEAN HORIZONTAL WIND SPEEDS IN TURBULENCE

Paul Frenzen

INTRODUCTION

Were it not for a well-known predisposition to overspeed in turbulent conditions, the inherent stability, linearity, and ease of time integration afforded by the cup anemometer would make it an ideal instrument for many purposes. Indeed, these advantages frequently override less favorable considerations when wind sensors are chosen for micrometeorological investigations, for most wind profile data reported in the literature continue to be derived from cup anemometer measurements. But since the instruments so used are all subject in some degree to overspeeding in convectively turbulent conditions, it is not surprising that disagreement between profile theory and observation tends to increase with increasing thermal instability.

Determinations of micrometeorological parameters involving the surface stress or the rate of turbulent dissipation are particularly sensitive to instrumental errors of this kind when one relies upon a cup anemometer placed close to the ground to evaluate the friction velocity through the logarithmic profile. For, as shown in the previous report in this series,[1] significant overspeeding by cup anemometers can occur below the 1-m level in unstable conditions, the percentage error continuing to increase the nearer the instrument is placed to the ground. Since stress and turbulent dissipation vary with the square and cube of the friction velocity, respectively, small velocity errors introduced in this way can lead to serious misinterpretations. Certainly, if cup anemometers are to continue to be used to meet these and other of the more demanding requirements of meteorological measurement, significant improvement of their performance in unsteady winds must be attained.

Four kinds of error affecting measurements of mean speeds in turbulent winds have been summarized by MacCready.[2] One termed the "DP" or data-processing error is not due to any particular instrumental fault. Rather, it results from a misinterpretation of the total run of a meandering horizontal flow, however recorded, as a measure of the magnitude of a mean vector wind whose direction has been averaged over the same long period. Several consequences of this kind of error along with a means to correct for it have recently been discussed by

Bernstein.[3] Nevertheless, for many purposes (the important case of profile measurement for flux-gradient experiments among them), it actually is the *total* run of horizontal wind at one or more levels that is required. This being the case, the purely instrumental aberrations listed by MacCready as "*u*, *v*, and *w*" errors* are usually of greater consequence. Moreover, each of these affects the performance of cup anemometers of ordinary design; therefore, to improve these otherwise dependable sensors one must

a) correct their limited ability to smooth fluctuations in horizontal velocity by simple averaging, and

b) provide them with some measure of a hitherto markedly deficient capacity to distinguish between horizontal and vertical components of winds fluctuating in three dimensions.

MODIFICATIONS TO REDUCE OVERSPEEDING IN HORIZONTAL FLUCTUATIONS

Overspeeding in horizontal gusts results from the fact that cup rotors invariably accelerate more rapidly than they decelerate. This behavior is illustrated schematically in Figure 100 where a square-wave forcing wind $\bar{U} + u'$ is shown as a solid line, while a dashed line traces two mirror-image, rising and falling exponentials representing the symmetrical response of a sensor (such as a hot wire) having identical lag characteristics for both increasing and decreasing inputs. During accumulation of a long period mean, an ideal device of this kind will lose some portion of the signal (area A in the figure) by lagging behind the input during the accelerating phase of each cycle; but this loss is precisely compensated by an equivalent amount (area B) added through overshooting during each subsequent deceleration. A cup rotor, however, inherently decelerates more slowly, the rate of rotation characteristically following a less steeply sloped descending exponential similar to the dotted line in the drawing. As a result a net excess represented by the area C is erroneously contributed to the total integrated signal during each acceleration-deceleration cycle that a cup rotor undergoes.

Fundamentally, the comparatively slow deceleration of a cup rotor is caused by the relatively smaller aerodynamic drag presented as a braking surface by the reverse, convex sides of cups after inertia has caused the rotor to overshoot following a sudden reduction in wind speed. This less-than-ideal behavior can never be entirely eliminated. It is, in fact, a price paid in order that cup assemblies will rotate at all; for of course, it is this difference between front and back cup drag coefficients that enables a net rotational torque to develop.

It has long been appreciated that overspeeding in horizontal gusts can be reduced by decreasing a rotor's moment of inertia. If the aerodynamics of the cup assembly remains unchanged, decreasing inertia reduces both lagging and overshooting in the same proportion; therefore, the difference representing the overrun accumulated in each cycle will be diminished as well. Less obviously, similar over-all improvement in the ability of a rotor to track a fluctuating input can be obtained by placing the cups closer to the axis of rotation. Since driving torque increases linearly with the length of cup arms whereas inertia increases with the square of this dimension, shortening the arms increases the ratio of the one to the other and thus improves the dynamic response of the instrument. The potential contribution of each of these structural changes to the reduction of anemometer overspeeding has been apparent for many years in the theoretical analysis due to Schrenk[4] and summarized in Deacon.[5] But only inertia reduction has been used to any great extent.

One reason for the less frequent use of shorter cup arms is the fact that higher shaft speeds result and consequently greater wear is imposed upon the bearings. Furthermore, there is a practical limit to the tactic since, as cups approach the central axis, each increasingly interferes with the flow directed upon the next downwind. A lightweight three-cup rotor equipped with arms equal to the cup radius (i.e., with cups centered one cup diameter from the shaft,

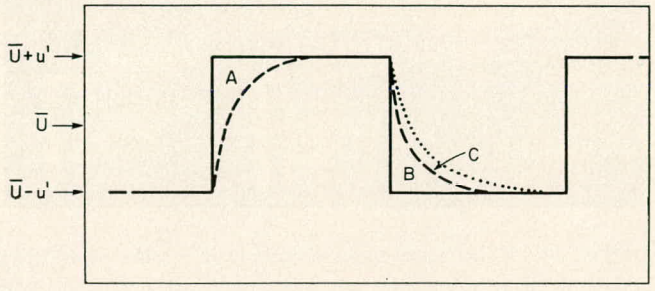

FIG. 100. Schematic representation of the response of a cup anemometer to a square-wave wind forcing function.

* The *v*-error (originally defined by MacCready as a consequence of lagging directional adjustments exhibited by vane-oriented sensors) is listed here in the sense that undirected, purely speed-sensitive cup rotors make no distinction between longitudinal or *u*-fluctuations in mean velocity and transverse or *v*-fluctuations associated with periodic changes in mean direction. For the present discussion, the *u* and *v* types will simply be collectively termed "horizontal fluctuation errors."

only about two-thirds the distance usually employed) visibly accelerates and decelerates three times during each revolution. Such pulsations are caused not only by increased cup shading, but also by the decreased ability of the low inertia rotor to damp angular oscillations of higher frequency. To utilize the favorable dynamic response properties of shorter cup arms without introducing an artificial oscillation in the recorded signal, the increased tendencies for rotors to pulsate can be countered by constructing them in the six-cup, staggered arrangement shown in Figure 101. Although originally suggested as a means to smooth anemometer output many years ago,[6] configurations of this kind have only come into common use in recent years with the marketing of a commercial rotor of "staggered-six" design by Beckman and Whitley, Mountain View, Calif. By superimposing an additional pulsed output of opposite phase upon that of a single three-cup assembly, the staggered, two-decked array reduces the amplitude of individual cup pulses and doubles their frequency. This serves to reduce errors contributed by the pulsations to short-period wind measurements and makes it easier to eliminate the pulses entirely by filtering if so desired. It should be remarked that, since both driving torque and inertia are doubled by this modification (neglecting shaft inertia), the ratio of the two remains essentially unchanged; consequently, the distance constant of a staggered-six assembly will not differ significantly from that of a three-cup rotor of otherwise similar construction.

The fact that the magnitude of overspeeding in horizontal gusts basically results from the size of the front-to-back cup drag difference suggests a further structural change to improve anemometer performance. By making the drag coefficient of the back of the cups more nearly equal to that of the front, the moment of the unbalanced aerodynamic forces which act to restore a rotor to its proper speed whenever it turns too rapidly for a given wind will be increased. At the same time, the net force available for accelerating the rotor whenever it turns more slowly than the prevailing wind will remain essentially unchanged. In terms of the Schrenk analysis,[4] the parabolic dependence of the net aerodynamic force would be made more nearly linear. From this it can be shown that the so-called Schrenk parameter for the rotor will be increased; consequently, overspeeding of the instrument in horizontal gusts will decrease.

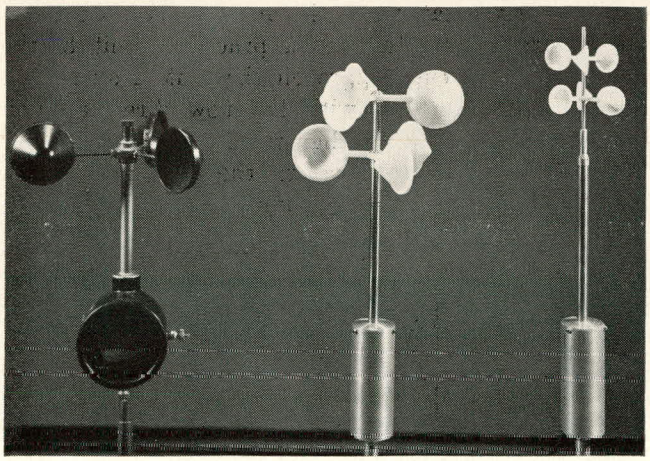

FIG. 101. Three anemometers compared in this study. The relatively heavy, 3-cup Casella on the left has a distance constant of 2.2 m, while the 6-cup LIHT instruments shown have constants between 0.3 and 0.4 m. The rotor of the center LIHT has 2-inch cups mounted in a closely spaced array while that of the instrument on the right has 1-inch cups, vertically spaced for optimum cosine response in nonhorizontal flow.

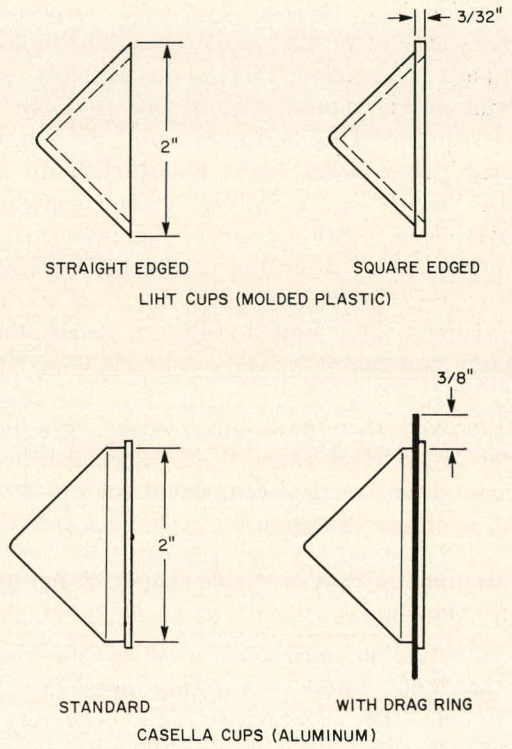

FIG. 102. Cup edge modifications designed to reduce overspeeding in horizontal wind fluctuations by reducing front-to-back drag coefficient differences.

To obtain the desired decrease in drag coefficient difference, squared trailing edges were included on the reverse side of each LIHT rotor cup as illustrated in Figure 102. Note that this increases the effective frontal area presented to the flow by the rear of each cup while that of the front remains unchanged. In the notation of Figure 100, these square-edged cups decrease the net overrun area C by reducing the excess signal contributed during overshooting by a relatively larger amount than they increase the losses

accumulated during acceleration. The over-all ability of the sensor to track a fluctuating input is somewhat reduced, but its response during acceleration and deceleration is made more symmetrical. Paradoxically, this relative drag coefficient modification reduces anemometer over-speeding while actually *increasing* the instrument's average distance constant. A secondary result of some practical value arises from the fact that cups modified in this way turn a rotor more slowly in any wind, a characteristic that partially alleviates the problem of high shaft speeds and excess bearing wear introduced by short cup arms.

EXPERIMENTAL RESULTS

Each of the foregoing modifications was incorporated in the LIHT anemometer shown in the center of Figure 101. First, low-inertia cup assemblies were molded in expanded polystyrene; six such cups, each two inches in diameter, weigh but 3.5 grams with their supporting arms attached. Second, short cup arms placed the inner edge of each cup only one cup radius from the axis of rotation. Third, the rotors were assembled in six-cup, staggered arrays to reduce pulsing. And finally, net overrun in each gust cycle was reduced by increasing the drag coefficient of the backs of the cups as sketched in Figure 102.

The improved anemometer performance obtained through these modifications can be seen in the results of pulsed wind tunnel tests summarized in Table 72. A series of more-or-less identical, abrupt changes in wind speed were generated in a 21-inch diameter calibration wind tunnel by manually swinging an opposed-blade, damper-type speed control between fixed stops at intervals of one second. Of course, true square-wave inputs were not achieved since the air column within the tunnel required an appreciable time to change its velocity. Nevertheless, gust sequences of sufficiently reproducible average amplitude and duration were evidently obtained, for the results obtained will be seen to be fairly systematic.

The first four experiments in the pulsed tunnel compare absolute overruns accumulated by a relatively heavy, three-cup anemometer (Casella, distance constant 2.2 m) to those recorded by a six-cup LIHT instrument (distance constant 0.4 m) incorporating both lightweight rotor construction and short cup arms, but without square-edged cups. These instruments were, in fact, the same two compared in the field experiments of the previous report[1] and shown here on the left and center of Figure 101. In he table it will be seen that under similar gust conditions the heavier Casella overruns very nearly three times as much as the "straight-edged" LIHT. Further, other things remaining equal, the amount

TABLE 72. PERCENT OVERRUN EXHIBITED BY SEVERAL ANEMOMETER CONFIGURATIONS IN A PULSED WIND TUNNEL

Exp. No.	$\bar{U} \pm u'$,* mps	3-cup Casella		6-cup LIHT	
		Unmodified	W/drag rings	Straight edges	Square edges
1	2.4 ± 1.3	15.7		5.4	
2	3.9 ± 1.3	6.9		2.2	
3	5.0 ± 1.4	3.1		1.2	
4	9.9 ± 1.3	1.0		0.1	
5	2.0 ± 0.6			2.6	2.0
6	4.2 ± 1.6			0.3 (?)	0.5
7	4.0 ± 1.5	10.5 (?)	7.0 (?)		
8	6.0 ± 1.5	2.2	1.0		
9	4.1 ± 1.4	6.3			0.6
10	4.2 ± 1.4		2.7		0.6
for $\bar{U} \pm 1.5$		$\sim(90/\bar{U}^2)$	$\sim(40/\bar{U}^2)$	$\sim(30/\bar{U}^2)$	$\sim(10/\bar{U}^2)$

* $\bar{U} \pm u'$ represents the mean speed and half amplitude of approximate square-wave wind forcing at a frequency of 0.5 cps.

each instrument overruns varies inversely with the square of the mean wind speed, roughly according to the relations entered at the foot of each data column. Evidently, the numerical constants in these relations depend upon the intensity and frequency of the gusts as well as the character of the instrument. In the notation of Figure 100, the constant varies with the size and frequency of occurrence of the net overrun areas C. Therefore, the values given are only appropriate to the conditions of these particular experiments, namely, for approximate square-wave forcing at 0.5 cps with a peak-to-peak amplitude of about 3 mps.

Experiments 5 and 6 compare the performance of a LIHT rotor equipped with straight-edged cups to that of an instrument similar in every respect except that squared trailing edges have been added to the back of each cup. Since these trials used different forcing amplitudes, the additional improvement obtained by increasing the aerodynamic drag available for deceleration in this fashion may best be seen in the three-fold reduction in the value of the constant shown in the approximate overrun relations at the bottom of the last two columns of the table. Further indication of the effect of this small change upon the front-to-back, cup drag coefficient difference lies in the fact that the slope of the calibration curve for the instrument was reduced from 0.8 to 0.6 rev per meter of wind after the square edged cups were installed.

Similar slowing of rotation occurs when beads are installed around the outer edges of thin metal anemometer cups, a modification ordinarily made to improve linearity by insuring fully turbulent flow in

the lee of the cups at lower speeds and, secondarily, to strengthen the cup shells. This suggested that exaggerating the beading procedure might moderate overspeeding tendencies as well. To test the idea, the cups of a standard Casella rotor were equipped with ⅜-inch wide external drag rings as sketched at the bottom of Figure 102. From results of trials 7 through 10 and the favorable changes in the constants in the appropriate overrun relations at the foot of Table 72, it will be seen that overspeeding of the Casella was more than halved by this modification. Paradoxically, the rings add even more mass to the already heavy rotor. On the other hand, their presence reduces the relative lengths of the cup arms by making them equal to the new larger cup radius defined by the ring. At all events, the installation of the rings reduced the rate at which the Casella turned in a given wind to less than half its former value; therefore, the reduction of front-to-back drag coefficient difference effected by the rings is evidently the principal cause of the decreased overspeeding in horizontal gusts observed.

Installation of similar rings upon heavy anemometer rotors is, of course, not to be recommended as a routine procedure. For one thing, the associated increase in cup shading of an instrument so drastically modified must seriously complicate its behavior in winds that depart from the horizontal. Conceivably, however, the use of drag rings could be of value as a temporary expedient when accurate measurements of average wind speeds in gusty conditions very close to the ground are required, but only an instrument equipped with a relatively high inertia rotor is available.

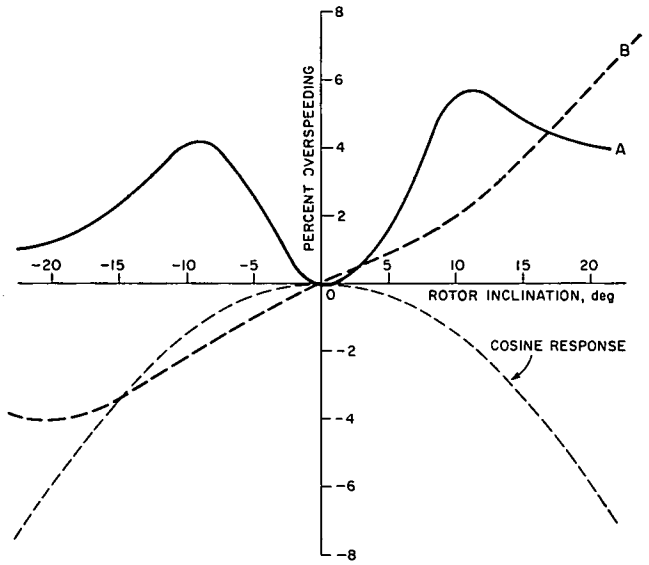

FIG. 103. Percent overspeeding exhibited by two anemometers placed in a wind tunnel with their rotor planes tilted at various angles relative to horizontal flow; curve A represents the behavior of the close-mounted LIHT instrument shown in the center of Figure 101, while curve B represents data given by MacCready[2] for a standard 3-cup instrument.

OVERSPEEDING IN VERTICAL WIND FLUCTUATIONS

At higher elevations in unstable conditions over level surfaces (or for that matter, at any height in any stability near large obstacles or over hilly terrain), the wind frequently departs from the horizontal. This leads to further deterioration in the performance of cup anemometers through the effect which MacCready termed the "*w*-error." Again, this flaw will cause an anemometer rotor systematically to overspeed, this time as a result of the intermittent relaxation of cup shading effects whenever the wind departs from the plane of the cups' rotation.

In winds that remain parallel to the rotor plane, the average rate of rotation realized by an ordinary cup assembly is limited by the fact that each cup periodically interferes in some measure with the wind flow affecting one or the other of its neighbors. On the other hand, when the wind deviates from the plane of the rotor, shading is reduced since more of the wind directed against a given cup during each revolution remains relatively unimpeded, passing above or below the other cups recurrently located in previously effective blocking positions. In many atmospheric circumstances the total wind continually fluctuates through appreciable vertical angles; consequently, significant anemometer overruns can accumulate as a result of the reductions in cup shading that periodically occur. For example, in winds with an rms vertical fluctuation of 20 deg (not uncommon at moderate heights in strong instability), MacCready[2] has shown that a cup anemometer can report an average wind speed as much as 6 percent greater than the true average horizontal velocity.

Figure 103 shows the percentage overspeeding exhibited by several cup anemometers placed in wind tunnels with their rotor planes inclined at various angles to the air stream. Since ideally the instruments should only sense flow components normal to their shafts, the curve labeled "cosine response" represents the behavior desired. Curve A shows the performance of a LIHT rotor similar in every respect to that illustrated in the center of Figure 101 save that all dimensions have been reduced by one-half. Since this assembly of 1-inch cups on ½-inch arms occupies less volume than a 3-inch cube, tests of a tilted rotor are reasonable even in the comparatively small 21-inch Argonne tunnel, at least for inclinations of 20 deg or less. For purposes of comparison, curve B reproduces the response of a 3-cup instrument equipped with "standard small cups" previously given by MacCready. It will be seen that

the small six-cup LIHT rotor exhibits an even stronger tendency to overspeed in nonhorizontal flow, especially in winds inclined between 10 and 15 deg. Approximate graphical integration of the curve indicates that in winds with a relatively modest rms vertical fluctuation of 10 deg, this version of the LIHT anemometer would accumulate an error of about 2.5 percent, almost twice that computed in similar fashion by MacCready for a standard 3-cup instrument. Fortunately, two simple changes in the configuration of the six-cup rotor effect a remarkable improvement in the response of the LIHT anemometer to nonhorizontal flow, for all intents and purposes giving the instrument a cosine response characteristic in a fluctuating, three-dimensional wind.

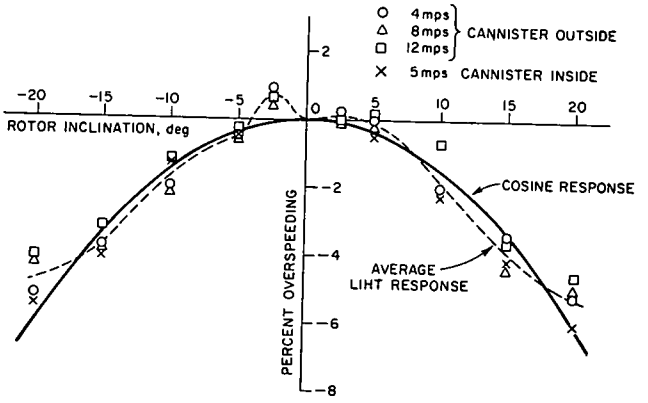

FIG. 104. Percent overspeeding exhibited in tilted rotor wind tunnel tests by an instrument tuned for optimum cosine response; data are for the LIHT anemometer equipped with a false upper shaft extension and 1-inch cups separated vertically by 1/16 of an inch as shown on the right of Figure 101.

MODIFICATIONS TO REDUCE OVERSPEEDING IN VERTICAL FLUCTUATIONS

Attempts to construct a cup anemometer that would respond solely to horizontal flows were begun by simply changing the shapes of rotor components. Among others the trials included cups in the form of long, thin half cylinders and turbine blades with right-angled sections in both 3- and 6-element assemblies. In retrospect, efforts along these lines seem foredoomed to fail. For the principal factor that causes the response of an assembly of wind-driven elements to depart from the desired cosine characteristic in vertically fluctuating winds is the variation of cup shading outlined above; and these effects always come into play at the ends of open rotors of finite size, whatever the shape of the individual rotor components. Installation of horizontal discs intended to restrict these end effects invariably seemed to overcompensate for them; overspeeding was eliminated, but the response of anemometers so equipped tended to fall off even more rapidly than the cosine of the angle of wind inclination. Nevertheless, the trials did lead to the discovery of a means by which the shading effects within a "staggered-six" rotor could be put to use, rather than avoided, in order to approximate the desired cosine response.

One problem presented by a double-decked rotor installation is the large horizontal drag which must be sustained by a comparatively long unsupported shaft extending above the upper bearing. To minimize the resultant bending moment, it is logical to assemble the two decks as compactly as possible by placing the lower edges of the upper cups and the upper edges of the lower cups in the same plane as in the LIHT rotor in the center of Figure 101. On the other hand, close mounting in this fashion leads to particularly severe overspeeding in vertically inclined winds (Figure 103), evidently through the introduction of new shading effects between cup assemblies in addition to those already present within each deck alone. It turns out, however, that by abandoning the fully compact arrangement, good use can be made of the fact that the strength of these additional shading effects varies with the spacing between decks. As will be seen in the results of tilted rotor tests plotted in Figure 104, it becomes possible to tune a six-cup rotor to a fair approximation of cosine response simply by adjusting the vertical distance between the three-cup subassemblies. In the special case of the LIHT rotors (which for reasons given earlier are equipped with unusually short arms), the best approximation to cosine behavior in flows inclined between plus and minus 20 deg occurs when the upper and lower cup assemblies are separated by between one half and three fourths of a cup radius. The optimum spacing for any combination of arm length and cup diameter can, of course, be determined by a similar series of wind tunnel tests.

One further modification of the LIHT rotor assembly makes the response of these instruments more nearly equivalent to fluctuations on either side of horizontal. As has been found by others,[7, 8] the inclusion of a false shaft extending above a wind driven assembly rotating in a horizontal plane gives it an aerodynamically similar appearance to both ascending and descending flows of small inclination. In this way, essentially symmetrical response is obtained up to the point where the winds are of sufficiently large inclination to be affected by the presence of the lower canister. To isolate the latter effect and to prevent it being magnified by the wall effects of the small tunnel, all of the inclined rotor tuning experiments were carried out with an extension shaft arrangement that made it possible to center the cup assembly in the tunnel for all trials while the canister remained outside. With relative

flow inclinations between plus and minus 20 deg, however, it makes little difference to the smallest LIHT rotor whether the canister is in or out of the tunnel, a fact which can be seen in the data compared in Figure 104.

SUMMARY AND CONCLUSIONS

Since all of the features designed to improve cup anemometer performance in three-dimensional turbulence that are discussed in this paper have been incorporated in the smallest LIHT rotor shown on the right in Figure 101, listing the characteristics of this unit will serve to summarize the presentation.

To reduce overspeeding in horizontal velocity fluctuations:

a) The rotor inertia has been minimized by fabricating entire three-cup subassemblies in expanded polystyrene, the two units using 1-inch cups in the smaller LIHT rotor weighing a total of 0.8 g.

b) The ratio of driving torque to rotor inertia has been maximized by locating the inner cup edges one cup radius from the axis of rotation.

c) The cup-to-cup pulsations introduced as a result of modifications a) and b) were decreased in amplitude and doubled in frequency by assembling the cups in a "staggered-six" array.

d) The net overrun contributed during each gust cycle was reduced by increasing the drag coefficients of the reverse sides of the cups by means of squared trailing edges (Figure 102).

To reduce overspeeding in vertical fluctuations:

e) The six-cup rotor was tuned for optimum shading between decks in order to obtain approximate cosine response in flows inclined between plus and minus 20 deg, the critical deck spacing appearing to be around 15 percent of the rotor wheel diameter measured between cup centers.

f) A false shaft extension was installed above the upper cup deck to improve the symmetry of response to flows inclined on either side of the horizontal.

The small LIHT rotor illustrated was primarily intended to record the short-period turbulent fluctuations themselves rather than long-term means. For this purpose, the instrument was equipped with a 60-slot photochopper that produces pulses at a rate of one for each 1.40 cm of wind. In average wind speeds, this relatively high resolution results in an audiofrequency signal that is recorded on magnetic tape for subsequent integration and spectral analysis.[9] The small wheel diameter of the 1-inch cup assembly is also advantageous to the recording of turbulent fluctuations, since the resulting rapid rotation in a given wind both improves resolution and increases the cup-pulse frequency to the point where it is largely removed by simple averaging during integration. By the same token, however, such small cups mounted on short cup arms sacrifice driving torque; consequently, the 1-inch LIHT rotor has a poor starting speed of about 0.5 mps. LIHT rotors using 2-inch cups on 1-inch arms and primarily intended for mean speed measurements fare better in this regard; these exhibit threshold velocities near 0.3 mps.

The turbulent energy density spectrum $[\overline{(u')^2}]$ obtained with this instrument and shown in the next article in this report demonstrates the suitability of the small LIHT anemometer to the task for which it was designed, that of recording a useful fraction of the inertial subrange at an operationally convenient height above the ground.[10] It remains for further field tests to show whether the utilization of these same principles of design in instruments better suited to the task of accumulating long term means will be able to provide sufficiently consistent measurements to reduce the uncertainty in wind profiles in unstable conditions. Experiments of this kind using the larger LIHT anemometers equipped with single pulse photochoppers are planned.

REFERENCES

1. P. Frenzen. Argonne National Laboratory Radiological Physics Division Annual Report, July 1965 through June 1966. ANL-7220, pp. 100–103.
2. P. B. MacCready, Jr. Mean wind speed measurements in turbulence. *J. Appl. Meteorol.* **5**, 219–225 (1966).
3. A. B. Bernstein. A note on the use of cup anemometers in wind profile experiments. *J. Appl. Meteorol.* **6**, 280–286 (1967).
4. O. Schrenk. *Z. Tech. Phys.* **10**, 57 (1937).
5. E. L. Deacon. The overestimation of cup anemometers in fluctuating winds. *J. Sci. Instr.* **28**, 231–234 (1951).
6. S. P. Fergusson and R. N. Covert. The measurement of the wind. *Bull. Am. Meteorol. Soc.* **4**, 41–44 (1923).
7. A. J. Dyer, B. B. Hicks, and K. M. King. The Fluxatron—a revised approach to the measurement of eddy fluxes. *J. Appl. Meteorol.* **6**, 408–413 (1967).
8. J. I. P. Jones. A portable sensitive anemometer with proportional dc output. *J. Sci. Instr.* **42**, 414–417 (1965).
9. P. Frenzen. Argonne National Laboratory Radiological Physics Division Annual Report, July 1964 through June 1965. ANL-7060, pp. 134–136.
10. P. Frenzen. Determination of turbulence dissipation by Eulerian variance analysis. *Quart. J. Roy. Meteorol. Soc* **91**, 28–34 (1965).

INSTRUMENTATION FOR ATMOSPHERIC TURBULENCE STUDIES. IV.

Paul Frenzen and Richard L. Hart

As reported in the previous contribution to this series[1] an initial effort to collect turbulent temperature fluctuation data of sufficiently high frequency to evaluate the vertical flux of heat by the method of variance reduction analysis failed because of the excessive response time of the thermistor sensor employed. During the past year an improved temperature measuring device has been completed, and promising results have been obtained in the field.

As diagrammed in Figure 105, the new apparatus uses an open coil of ½-mil nickel wire as a resistance thermometer in an unbalanced bridge circuit. The very small thermal mass per unit length of the fine wire gives this sensor a response time significantly less than 0.05 sec, the latter period representing the practical lower limit of our recording equipment's ability to track a stepped input. Sensor resistance changes very nearly one ohm per degree; but since the bridge current must be limited to very low values in order to minimize resistance heating (principally to avoid the possibility that the sensor will act like a hot-wire anemometer), only very small variations in bridge voltage result. It is, therefore, necessary to amplify these with a wide-band, differential "data amplifier" (Hewlett-Packard, model 2470A) in order to modulate the output of the voltage-to-frequency converter with the desired resolution and accuracy. With component values shown, the system produces a frequency modulated pulse train centered on 1 kc that shifts approximately 2 cps for each 0.01 deg change in sensor temperature. Since these pulsed signals are fully compatible with all components of the "Varedan" system,[2] including the computer program, temperature fluctuation spectra and variance reduction data are obtained without modification of existing procedures.

It may be noted that both the temperature dependence of the resistance of nickel wire and the error-signal voltage produced by a resistance bridge operated in the unbalanced mode are slightly nonlinear. However, in any one experiment, the system is operated around a point where the local slope of the calibration curve is known, while the small turbulent temperature fluctuations that are of principal interest do not cause the system to depart sufficiently from that set point to change the calibration significantly. Consequently, the effects of these nonlinearities are entirely negligible.

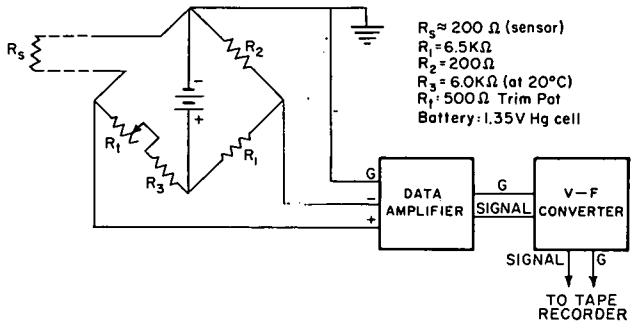

FIG. 105. Schematic representation of fast response system for the measurement of temperature fluctuations in the inertial subrange. Current through resistance thermometer R_s is less than 6.2 mA.

Figure 106 shows simultaneous spectra of fluctuations in temperature and horizontal wind speed, one of a number of such spectrum pairs obtained during a recent comparative experiment on the field site of the University of California at Davis, California.* Because of the limited extent of truly uniform wind fetch available at the Davis site, and because of the need to operate at heights compatible with other measurements being recorded simultaneously, observations were taken at a comparatively low elevation of 2.8 m. As will be seen in the spectra shown, this resulted in inertial subrange regimes ($-\frac{5}{3}$ slopes) that did not extend very far in the lower frequencies, especially in the case of temperature fluctuations. For the particular run shown, the ratio of mean wind speed to height (a figure generally considered to afford some measure of the lowest frequency of the inertial subrange) exhibits the relatively high value of 1.8. Previous field experience has indicated that $\bar{U}/z$ magnitudes nearer to unity are to be desired for our relatively long, data-averaging times. Nevertheless, the horizontal wind speed spectrum obtained under these relatively unfavorable conditions does show a well-marked $-\frac{5}{3}$ region extending from 0.4 to nearly 1.0 cps. Thus, the combination of the improved characteristics of the LIHT anemometer (described elsewhere in these pages) and the fact that the statistical character of the *horizontal* component of the inertial subrange tends to extend to lower frequencies than expected, appears to make it possible to evaluate

* Cooperative Field Experiment sponsored by Atmospheric Sciences Laboratory, U. S. Army Electronics Command, Fort Huachuca, Arizona.

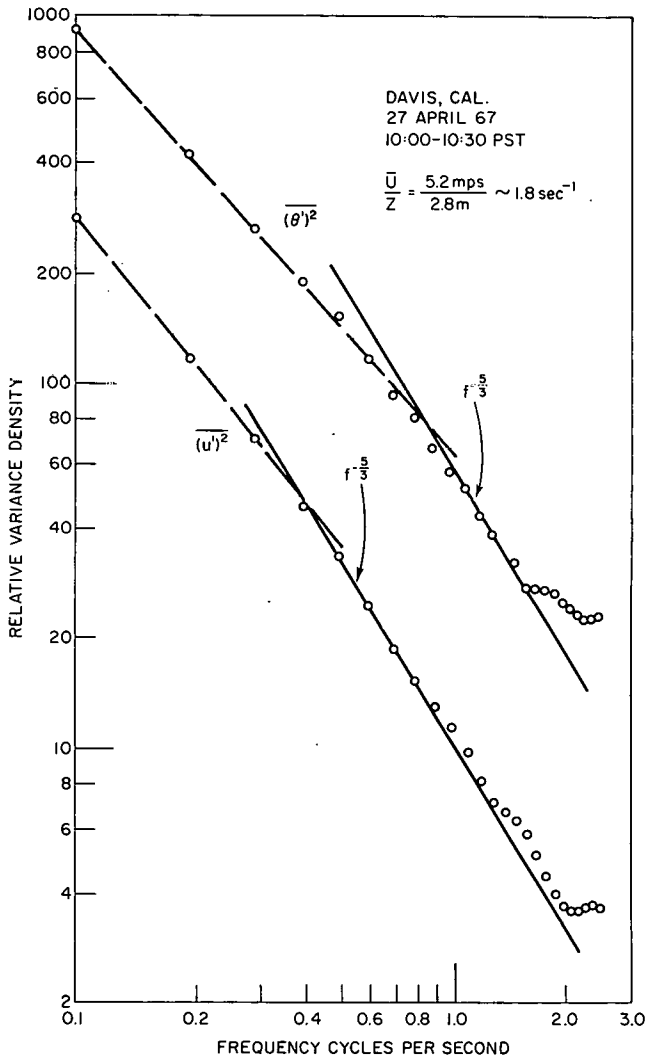

FIG. 106. Simultaneous spectra of temperature $\overline{(\theta')^2}$ and horizontal wind velocity $\overline{(u')^2}$ obtained at Davis, California during cooperative field experiments.

momentum flux by the Varedan method even at elevations so low that $\bar{U}/z$ approaches 2 sec^{-1}.

Unfortunately, the same circumstances do not obtain for the case of heat flux determinations from fast-response temperature measurements. Since the turbulent temperature field is largely controlled by vertical wind fluctuations, temperature fluctuations are correspondingly more sensitive to the presence of a rigid lower boundary. Consequently, inertial subrange portions of the temperature fluctuation spectra tend to follow the $\bar{U}/z$ criterion more closely; their properties do not extend into frequencies as low as do horizontal wind spectra. But, as will be seen in the figure, there are indications in this run (and, in fact, in almost all runs taken at Davis) that the new temperature system did begin to detect inertial subrange data around 1 cps. In the very near future, tests will be conducted at higher elevations (4 to 6 m) with essentially the same equipment, but which now includes some minor improvements designed to reduce noise in the higher frequencies. Independent estimates of the heat flux will be made from measurements of the 1- to 4-meter temperature difference in the manner suggested by Dyer.[3] Of course, considerably more accurate heat flux measurements will be required to evaluate the numerical constant in the Varedan heat flux relation with the accuracy desired.[4] Initially, at least, this requirement will be met by further participation in cooperative field experiments with other research groups. Eventually, the completion of an eddy-correlation apparatus now under construction will supply our own comparison standard for this and other turbulent flux determinations.

Finally, it should be noted that the evaluation of the constant in the Varedan heat flux relation is tantamount to the evaluation of the constant in the Kolmogoroff relation for the spectrum of temperature fluctuations in the inertial subrange. The Varedcn method merely introduces a particularly simple bandpass filter for the requisite evaluation of fluctuation variance density within the subrange. Since a number of research workers in various laboratories are now engaged in similar efforts, a number of estimates of the constant can be expected to appear shortly.

REFERENCES

1. P. Frenzen. Argonne National Laboratory Radiological Physics Division Annual Report, July 1965 through June 1966. ANL-7220, p. 103.
2. P. Frenzen. Argonne National Laboratory Radiological Physics Division Annual Report, July 1964 through June 1965. ANL-7060, p. 134.
3. A. J. Dyer. *Quart. J. Roy. Meteorol. Soc.* **91**, 151 (1965).
4. P. Frenzen. Argonne National Laboratory Radiological Physics Division Annual Report, July 1964 through June 1965. ANL-7060, p. 130.

STACK DESIGN PARAMETERS INFLUENCING PLUME RISE*

Harry Moses and James E. Carson

INTRODUCTION

In order to estimate downwind concentrations resulting from the emission of a gaseous stack effluent, the effective height of the stack must be known. The effective stack height is usually defined as the actual stack height plus the rise of the plume centerline above the stack due to the buoyancy and momentum of the effluent. Plume rise information is also needed in other diffusion calculations, such as the minimum stack height which prevents groundlevel concentrations from rising above a permissible level.

The state of the art of predicting height-of-rise from meteorological and stack data at present is quite poor. The number of formulas for calculating plume rise appears to vary inversely with our understanding of the processes involved: over fifteen such formulas (Moses, Storm and Carson, 1964) have been proposed, and at least one or two new ones appear annually. Some are based on theoretical consideration including dimensional analysis and others on empirical grounds. None is universally accepted, primarily because it has been impossible to establish the validity of any from the quality and quantity of available plume rise and meteorological data.

The paucity of acceptable height-of-rise data is due in large measure both to the inherent difficulties in carrying out satisfactory plume rise measurements and to the unwillingness of industry to release such data for fear of possible litigation. Plume rise measurements are ordinarily made by photographic, visual, or tracer sampling techniques. All of these methods are fraught with experimental difficulties; none is inexpensive or easy.

The meaning of the term plume rise has been defined differently by various authors presenting data, for example, Davidson,[1] Holland,[2] Bosanquet,[3] and Danovich and Pashkovskiy.[4] This lack of agreement on the definition of plume rise reduces the comparability of the various sets of data and produces more than a desirable amount of scatter about any fitted plume rise formula.

FACTORS CONTROLLING PLUME RISE

Three sets of factors control the behavior of a stack smoke plume ejected into the atmosphere. These are 1) engineering design parameters of the stack, 2) environmental conditions, and 3) the nature of the effluent itself.

Many of the expressions relating plume rise with stack and environmental parameters are of the form

$$\Delta h = f(V_s, d, U, Q_h)$$

where Δh is plume rise, V_s is stack effluent velocity, U is wind speed, Q_h is heat emission rate and d is stack diameter.

The stack parameters are V_s, d, and Q_h. Some authors have included H, the stack height (Stone and Clarke[5]). Of importance but not included in the formulas are such factors as the shape of the stack, whether it be circular, square or elliptical, and the location of the stack with respect to both the building it services and the other structures nearby. The aerodynamic effects produced by stack and building geometry may have a significant effect on plume rise or downwash near the stack.

The relation between the plume rise, Δh and V_s, d and Q_h is considered linear by Holland[2] but nonlinear by others.[3, 6, 7] Perhaps the most lively disagreement centers about the heat emission rate term (Q_h), with $\Delta h \sim Q_h^{C_3}$. The exponent C_3 has been given values of 0.25,[8, 9] 0.50 and 0.58,[10] and 1.[2] The relative merits of each of these values are examined in a later section.

The meteorological parameters which influence plume rise are the horizontal wind speed (U) and stability, as denoted by the vertical temperature or potential temperature gradient. Wind speed appears in virtually all of the formulas, but stability does not. Bosanquet's[3] technique includes the stability explicitly, and Sutton's[11] only implicitly. Also of importance is the wind direction if the terrain surrounding the stack is not uniform. Under such conditions the turbulence intensity will depend upon wind direction. With high turbulent intensities, rapid mixing of the plume takes place, thus destroying the effects of plume buoyancy and momentum.

Another factor influencing plume rise by its effect on turbulence intensity is the intensity of solar radiation and the distribution and type of cloudiness. Even over terrain which is quite smooth, cumulus clouds will cause patchy ground heating to set up large thermal eddies with appreciable vertical components. Under such conditions plumes from even tall stacks may be brought to the ground.

* Presented at the 60th Ann. Mtg. of the Air Pollution Control Assoc., Cleveland, Ohio, June 14, 1967.

The nature of the effluent itself influences its rise characteristics. Plumes containing particulates with mean diameters substantially exceeding 20 microns will have a settling component. The density of the plume gases in thermal equilibrium with the atmosphere is also important. Other factors, such as thermal conductivity, specific heat, viscosity, or the release of latent heat of condensation, such as in steam plumes, must also be considered.

DATA USED IN STUDY

A fairly comprehensive set of data was used to carry out a regression study relating plume rise with stack and meteorological variables. Ten stacks were used, with plume rises and heat emission rates ranging over about three and four orders of magnitude respectively. A total of 710 individual observations were used.

Table 73 presents a summary of the sources of data. Two sets of measurements were based on those obtained from the Argonne Meteorology Stack.[12, 13] Three industrial stacks in England,[14] a stack at Harwell, England,[15] two stacks from Germany (the Gernsheim and the Duisberg stacks[8]), and three stacks of the TVA complex—Widow's Creek, Gallatin and Paradise[16] are the sources of data upon which this investigation was based. In this analysis, only data from single stacks were used.

There was appreciable nonuniformity among the data from the ten stacks. For example, averaging times of the plume rise measurements differed—from 1.5 to 2.5 minutes for the German data, 4 minutes for the Argonne measurements, and up to 120 minutes for the TVA data. Plume rise definitions and techniques of measurement varied; wind measuring levels and procedures were not always comparable. For the purpose of this study all winds were corrected to represent the wind speed at the top of the stack.

Table 74 shows the ranges of meteorological and stack parameters which prevailed during the data acquisition period. This table provides a picture of the scope of the total set of data.

In Table 73, the data are subdivided according to atmospheric stability. The criterion for stability classification is given in Table 75, where $\partial\theta/\partial z$ is the lapse rate of potential temperature, θ.

No attempt was made to apply weights to the data, in spite of the differences on averaging periods. Among the data there are numerous instances where consecutive readings were taken and each is considered as an independent measurement. Where consecutive readings are correlated, the assumption of independence is, o course, invalid. In spite of these shortcomings, the data do bring out clearly some of the relations between plume rise and meteorological stack design parameters.

TABLE 73. SUMMARY OF DATA USED

Station	Atmospheric stability			
	Stable	Neutral	Unstable	Total
Argonne I	19	10	6	35
Argonne II	26	6	102	134
Harwell	8	27	11	46
Duisberg	51	328		379
Gernsheim	10	33		43
Bosanquet		7		7
TVA				
Widow's Creek	1	9		10
Gallatin	2	24		26
Paradise	4	26		30
Totals	121	470	119	710

TABLE 74. RANGES OF STACK AND METEOROLOGICAL PARAMETERS

Station	Wind speed, m/sec	Stack effluent velocity, m/sec	Heat emission rate, kilocal/cal	Plume rise, m	Stack height, m	Stack dia., m
Argonne I	7.3–1.0	13.2–4.7	12.7–2.0	16.9–1.4	34	0.44
Argonne II	10.3–3.1	14.0–4.56	34.4–3.3	34.3–0.2	34	0.44
Harwell	11.7–3.0	9.90	1215–1215	116–18	61	3.46
Duisberg	10.5–1.6	12.1–3.5	2475–979	112–9.0	125	3.50
Gernsheim	9.2–1.5	5.3–2.2	1003–384	78.0–21.0	75	2.30
Bosanquet	10.0–3.1	10.8–8.5	1530–72	61.0–14.0	?	2.5; 1.25
TVA						
Widow's Creek	6.6–1.5	24.5–22.9	$1.79–1.57 \times 10^4$	356–73	153	6.34
Gallatin	8.2–1.6	16.4–14.8	$1.77–1.50 \times 10^4$	476–81	143	7.63
Paradise	11.3–2.3	19.2–15.3	$2.46–1.70 \times 10^4$	457–64	183	7.93

TABLE 75. *A* FACTORS AND STABILITY CLASSES

		A Factor
Stable	$\delta\theta/\delta z \geqq 0.85$°K/100 m	2.65
Neutral	$-0.22 \leqq \delta\theta/\delta z < 0.85$°K/100 m	1.08
Unstable	$\delta\theta/\delta z < -0.22$°K/100 m	0.68

REGRESSION STUDIES

The purpose of these studies is to investigate the basic relations between plume rise and such factors as the momentum of the stack effluent, the buoyancy, and weather parameters. Insight into the basic processes is necessary to develop a sound technique for calculating plume rise from stack and meteorological data.

A general equation which takes into account both buoyancy and momentum components is

$$\Delta h_{calc} = C_5 + C_2 \left(\frac{V_s}{U}\right)^{C_1} d + C_4 \frac{(Q_h)^{C_3}}{U}, \quad (1)$$

where

Δh_{calc} is the calculated plume rise (meters)
C_1, C_2, C_3, C_4, and C_5 are regression coefficients and exponents
V_s is the stack effluent velocity (meters/sec)
U is the wind speed (meters/sec)
Q_h is the heat emission rate (kilocal/sec)
d is the stack diameter (meters).

Throughout this paper $C = 1$. The form of this equation was suggested by the Holland equation:

$$\Delta h_{calc} = 1.5\, d \frac{V_s}{U} + 0.04 \frac{Q_h}{U}. \quad (2)$$

In the selection of a criterion for a prediction equation, the accuracy to which it can predict is, of course, most important. Other considerations are simplicity or ease of computation, applicability to a wide range of conditions, and the availability of the necessary stack and meteorological measurements.

In previous investigations by the authors and from the results of this study, it was found that when stacks which vary over a wide range of heat emission rates, diameters, etc., are compared, a useful guide to the average height attained by the plume may be obtained from an equation of the form

$$\Delta h_{calc} = C_2\, d \frac{V_s}{U} + C_4 \frac{\sqrt{Q_h}}{U}. \quad (3)$$

A least squares fit of the data to this equation, where $C_5 = 0$, yields

$$\Delta h_{calc} = -0.029 \frac{V_s}{U} d + 5.35 \frac{\sqrt{Q_h}}{U} \quad (4)$$

The data were then further subdivided into the three stability classifications given in Table 75 and regression equations were calculated. The results are:

$$\text{Unstable} \quad \Delta h_{calc} = 3.47 \frac{V_s}{U} d + \frac{10.53\sqrt{Q_h}}{U} \quad (5)$$

$$\text{Neutral} \quad \Delta h_{calc} = 0.35 \frac{V_s}{U} d + \frac{5.41\sqrt{Q_h}}{U} \quad (6)$$

$$\text{Stable} \quad \Delta h_{calc} = -1.04 \frac{V_s}{U} d + \frac{4.58\sqrt{Q_h}}{U} \quad (7)$$

These results are summarized in Table 76. This table also provides the standard error of estimate, which for equation 4 is 29.7 meters. Standard errors of estimate for the equations representing the unstable, neutral and stable classes are 9.1, 30.2 and 23.4 meters, respectively.

With a single equation based on all data, such as equation (4), it is possible to apply a correction factor A to compensate for differences in stability. Thus only one equation would be necessary. The factor A is determined by minimizing the sum of the squares of the differences between the observed plume rise and that calculated by equation (4) but using the data in a particular stability class. The following expression was used:

$$\text{Standard error} = \left[\frac{\sum(\Delta h_{obs} - A\Delta h_{calc})^2}{N_s - 2}\right]^{1/2} \quad (8)$$

The standard error is minimized if

$$A = \frac{\sum \Delta h_{obs} \times \Delta h_{calc}}{\sum \Delta h_{calc}^2}, \quad (9)$$

where Δh_{obs} is the observed plume rise (meters) and N_s is the number of cases in the particular stability class.

TABLE 76. PLUME RISE REGRESSION PARAMETERS, AS RELATED TO STABILITY

Stability class	C_2	C_4	N	A	Standard error of estimates				Multiple correlation coefficient	
					S.E. #1	S.E. #2	S.E. #3	S.E. #4	R	R^2
All data	−0.029	5.35	710	—				29.7	0.82	0.67
Unstable	3.47	10.53	119	2.65	17.3	9.1	9.1			
Neutral	0.35	5.41	470	1.08	30.9	30.3	30.2			
Stable	−1.04	4.58	121	0.68	34.6	23.4	23.4			

N = sample size; A = A factor; C_2 and C_4 = regression coefficients; S.E. #1 = standard error without A factor, calculated from all-data formula and applied to data in stability class; S.E. #2 = standard errors with A factor, calculated from all-data formula and applied to data in stability class; S.E. #3 = standard error, calculated from equations for indicated stability class; S.E. #4 = standard error, calculated from all-data equation.

Then

$$\Delta h_{\text{corrected}} = A\left[-0.029\,\frac{V_s}{U}\,d + \frac{5.35\sqrt{Q_h}}{U}\right]. \quad (10)$$

$\Delta h_{\text{corrected}}$ represents the calculated plume rise computed by a single equation and the appropriate A factor. Table 76 shows the A factors as well as their effectiveness. The column headed S.E. # 1 gives the standard error without the A factor and the column headed by S.E. # 2 shows the change due to applying the A corrections.

To study the effect of varying the exponent of the heat emission terms, three sets of regression calculations were made; the results are shown in Tables 77–79. In the first table, C_5 was set equal to zero and C_3 was given successive values of ¼, ⅓, ½, ¾ and 1. In the second set, C_5 was computed as a regression coefficient and C_3 again took on the above set of values. In the last table, C_2 and C_5 were both set equal to zero and C_3 was allowed to vary the same way. In all cases $C_1 = 1$.

TABLE 77. MULTIPLE REGRESSION PARAMETERS, ALL DATA

$$\Delta h_{\text{calc}} = C_2 d\left(\frac{V_s}{U}\right)^{C_1} + C_4\,\frac{(Q_h)^{C_3}}{U}$$

C_3	C_1	C_2	C_4	Standard error
¼	1	3.75	18.4	29.9
⅓	1	+2.93	12.2	29.7
½	1	−0.029	5.35	29.7
¾	1	6.14	−0.039	32.1
1	1	7.76	−0.016	31.6

TABLE 78. MULTIPLE REGRESSION PARAMETERS, ALL DATA

$$\Delta h_{\text{calc}} = C_2 d\left(\frac{V_s}{U}\right)^{C_1} + C_4\,\frac{(Q_h)^{C_3}}{U} + C_5$$

C_3	C_1	C_2	C_4	C_5	Standard error
¼	1	4.69	4.38	13.0	29.2
⅓	1	4.12	4.87	11.3	29.1
½	1	1.96	3.06	11.0	28.6
¾	1	0.570	0.376	19.5	28.5
1	1	3.08	0.014	19.6	29.0

TABLE 79. MULTIPLE REGRESSION PARAMETERS, ALL DATA

$$\Delta h_{\text{calc}} = C_4\,\frac{(Q_h)^{C_3}}{U}$$

C_3	C_4	Standard error
¼	47.3	36.05
⅓	23.7	32.0
½	5.32	29.6
¾	0.487	33.6
1	0.0418	38.3

In Table 77 one observes that as C_3, the exponent of Q_h, increases, C_4 compensates by decreasing, while C_2 (the coefficient of the momentum term) decreases to a minimum and then increases. Of interest is the relative invariance of the standard error about the regression planes. This quantity has a minimum for $C_3 = ½$, as seen when more than three significant figures are considered.

In Table 78 are presented the regression calculations for equation (1) with C_5 as a calculated regression constant and C_3 allowed to vary from ¼ through 1 as previously. The standard error is reduced only slightly, and the $C_4 - C_2$ behavior pattern is similar to that of the previous set.

Table 79 shows the regression study for cases where $C_2 = C_5 = 0$. This equation is similar in form to the Lucas, Moore, and Spurr[9] and Rauch[8] formulas. Of interest here is that the standard error is a minimum for $C_3 = ½$.

CONCLUSIONS

From the standpoint of goodness of fit and ease of computation one is inclined to suggest equation (11),

$$\Delta h_{\text{calc}} = A\left[-0.029\,\frac{V_s}{U}\,d + \frac{5.35\sqrt{Q_h}}{U}\right], \quad (11)$$

as the preferred plume rise equation. Corrections for stability are made by using the A factors of 2.65, 1.08, and 0.68 for unstable, neutral, and stable conditions, respectively.

It should be emphasized that these equations were not designed nor tested for day-to-day operation with a single stack. They are to be used for general design considerations.

As more data are accumulated it is quite possible that the regression coefficients C_2 and C_4 will change. Further, the recommended value of $C_3 = ½$ and $C_1 = 1$ may also be adjusted as a result of further study and measurements.

Since the equation recommended is an empirical equation, it is important to caution that it only be used over the range upon which it is based. It is also essential to realize that these results apply to relatively smooth terrain without the undue influence of buildings.

The equations, however, do represent a least squares fit that should serve as a useful tool in building stack design.

The authors wish to acknowledge the assistance provided by Frank C. Kulhanek, Gunther A. Zerbe and

Miss Linda Rogers of the Argonne Meteorology Group. For assistance in programing the calculations for the computers, the contribution of Mr. Anthony J. Strecok is noted.

REFERENCES

1. W. F. Davidson. The Dispersion and Spreading of Gases and Dust from Chimneys. *Trans. Conf. on Industrial Wastes*, 14th Ann. Mtg. Ind. Hyg. Found. Am., 1954 pp. 38–55.
2. J. Z. Holland. A Meteorological Survey of the Oak Ridge Area. U. S. Atomic Energy Commission Report ORO-99 (1953), pp. 554–559.
3. C. H. Bosanquet. The Rise of a Hot Waste Gas Plume. *J. Inst. Fuel* **30**(197), 322–328 (1957).
4. A. M. Danovich and A. S. Pashkovskiy. Determining the Effective Stack Height Using Experimental Data. Dept. Commerce Joint Publication Research Service Translation 28, 188, p. 170. (From Vaprosy Trubulentnoy Diffuzii v Prizemnom Sloye Atmosfery, Trudy, Vypusk 18, Leningradskiy Gidrometeorologicheskiy Institut, 1963.)
5. G. N. Stone and A. J. Clarke. British Experience with Tall Stacks for Air Pollution Control on Large Fossil-Fuelled Power Plants. Paper presented at American Power Conf., Chicago, April 1967. Proceedings in press.
6. H. Stumke. Vorschlag einer empirischen Formel für die Schornsteinüberhöhung im Anschlusz und eine Überprüfung bekannter Formeln mit zusätzlichem Beobachtungsmaterial. II der VDI-Kommission "Reinhaltung der Luft" vorgelegt als wissenschaftliches Gutachten. Institut für Gasstromungen der Technischen Hochschule, Stuttgart, 1963.
7. G. A. Briggs. A Plume Rise Model Compared with Observations. *J. Air Pollution Control Assoc.* **15**(9), 433–438 (1965).
8. H. Rauch. Zur Schornstein Überhöhung. Bericht des Meteorologischen Institutes an der Technischen Hochschule, Darmstadt, 1962.
9. D. H. Lucas, D. H. Moore, and G. Spurr. The Rise of Hot Plumes from Chimneys. *Intern. J. Air Water Pollution* **7**, 473–500 (1963).
10. K. G. Brummage et al. The Calculation of Atmospheric Dispersion from a Stack. Stichting CONCAWE, The Hague, The Netherlands, August 1966.
11. O. G. Sutton. The Dispersion of Hot Gases in the Atmosphere. *J. Meteorol.* **7**(5), 307–312 (1950).
12. H. Moore and G. H. Strom. A Comparison of Observed Plume Rises with Values Obtained from Well-Known Formulas. *J. Air Pollution Control Assoc.* **11**(10), 455–466 (1961).
13. J. E. Carson and H. Moses. Analysis of Smoke Plume Photographs. Argonne National Laboratory Radiological Physics Division Annual Report, July 1965 through June 1966. ANL-7220, pp. 89–96.
14. C. H. Bosanquet, W. F. Carey, and E. M. Halton. Dust Deposition from Chimney Stacks. *Proc. Inst. Mech. Engrs.* (*London*) **162**, 355–368 (1950). (Seven unpublished appendices.)
15. N. G. Stewart, H. J. Gale, and R. N. Crooks. The Atmospheric Diffusion of Gases Discharged from the Chimney of the Harwell Pile (BEPO). A.E.R.E. Report HP/R 1452 (1954).
16. S. B. Carpenter, J. A. Frizzola, M. E. Smith, J. M. Leavitt, and F. W. Thomas. Report on Full-Scale Study of Plume Rise at Large Electric Generating Stations. Paper presented at Air Pollution Control Association 60th Annual Meeting, June 1967.

THE INFLUENCE OF METEOROLOGICAL CONDITIONS UPON RADIATION DOSES DUE TO INHALATION FOLLOWING A MAXIMUM CREDIBLE REACTOR ACCIDENT

Harry Moses, Mary A. Bogner, Cynthia Chamot,† and Frank C. Kulhanek

INTRODUCTION

Pollutants injected into the atmosphere are diluted by mixing with clean air. Wind speed, wind direction, turbulence intensity, and stability are the major meteorological parameters which determine how rapidly concentrations of materials are reduced through this process. Also of importance is the character of the underlying surface. Flat terrain, a hill-valley complex, a body of water or a forested area markedly influence the mixing process.

Ordinarily, in evaluating the hazards associated with a maximum credible reactor accident, one assumes a pessimistic set of meteorological conditions, for example, a wind speed of two meters per second, inversion conditions, and a constant wind direction for the entire period of evaluation. Previously this has been necessary because appropriate weather data have been unavailable or in a form where their utilization was prohibitively expensive. More realistic results are obtained by using actual measurements of wind speed, wind direction, and stability.

This paper describes a technique which utilizes hourly measurements of meteorological data for evaluating potential inhalation doses due to radiations arising from a reactor accident and compares the results with those obtained from the frequently assumed pessimistic meteorological conditions. This technique was devised for the Preliminary Safety Analysis Report (PSAR) for

† Applied Mathematics Division.

the Argonne Advanced Research Reactor (AARR) at the Argonne National Laboratory.

MODEL ASSUMPTIONS AND SOURCES OF DATA

The AARR reactor is designed to use the High Flux Isotope Reactor (HFIR) core developed at the Oak Ridge National Laboratory and is to operate at a power level of 100 megawatts. In ascertaining the effect of the assumed maximum credible accident it was postulated that the reactor containment building would not be violated and would leak at a rate of 1% per day.

The PSAR postulates that the air leakage is 1% per day at design overpressure (7.5 psig), and it is proportional to the square root of the pressure at lower overpressures following the accident. The PSAR analysis does account for the time-dependent leak rate.

All of the equations developed in this report depend upon the model: the source is a continuous, ground-level point source; and the time to reach distance d is short by comparison with the half-lives of the inhaled isotopes, and the decay of the isotopes enroute to the receptor is ignored. The approximation of zero decay enroute is acceptable for calculations of this type for most isotopes of importance to the evaluation of reactor siting.

The wind speed and direction data were obtained by cup anemometers and aerovanes located at 150 feet and 19 feet above ground at the Meteorology Site, which is one-half mile from the AARR site. The wind instruments at 150 feet were located on the Meteorology Tower, but those at 19 feet were mounted on a pole 200 feet to the east of the tower. Stability measurements were obtained by copper-constantan thermocouples located at 144 and 5.5 feet above ground. The Meteorology Tower served as the platform for the upper thermocouple; a mast 150 feet west of the tower served as the support for the lower one.

TABLE 80. VALUES OF $\sigma_y(d)$ $\sigma_z(d)$

Distance, meters	Stability class, s			
	Unstable, category C	Neutral, category D	Stable, category F	Stable, category E
100	1.12×10^2	4.00×10	8.00×10^0	2.40×10
300	7.90×10^2	3.00×10^2	8.40×10	1.62×10^2
500	2.16×10^3	7.60×10^2	1.60×10^2	4.20×10^2
800	4.95×10^3	1.68×10^3	3.72×10^2	9.00×10^2
1500	1.53×10^4	4.20×10^3	9.90×10^2	2.32×10^3
2000	2.60×10^4	7.60×10^3	1.54×10^3	3.80×10^3
4800	1.08×10^5	2.55×10^4	5.60×10^3	1.32×10^4
8000	2.52×10^5	5.50×10^4	9.65×10^3	2.55×10^4
20,000	1.12×10^6	1.96×10^5	2.95×10^4	8.50×10^4

TABLE 81. DEFINITION OF STABILITY CLASSES

Gifford-Pasquill category	Stability class	Temperature difference, °F (144- minus 5.5-foot temperature)
C	Unstable	<-2.0
D	Neutral	-2.0–0.0
F	Stable	>0.0

GENERAL METHOD FOR CALCULATING INHALATION DOSES

Calculations show that the inhalation doses provided by the isotopes of iodine 131–135 in the assumed AARR maximum credible accident determine the three critical distances: 1. exclusion radius, 2. low population zone radius, and 3. population center distance.[1] For this reason, the calculations are based on these isotopes, but the method is applicable to any radioactive isotope.

The dose for any hour at any distance from the reactor due to the inhalation of the iodine isotopes 131–135 is calculated by the method given in Reference 1. For the sake of completeness and clarity the procedure is outlined briefly.

$A_{t_1,t_2,r}$, the amount of radioactive isotope, r, in curies inhaled from a passing cloud between time t_1 and time t_2 is given by

$$A_{t_1,t_2,r} = \frac{RP_0Q_{t_1,t_2,r}}{\pi[u\sigma_y(d)\sigma_z(d)]_{s,t_1,t_2}}, \qquad (1)$$

where

R is the breathing rate, taken as 2.32×10^{-4} cubic meters per second (20 cubic meters per day),

P_0 is the power level in megawatts, taken as 100,

$Q_{t_1,t_2,r}$ is the number of curies of isotope r per megawatt power in the total cloud passing a point d meters from the reactor downwind between time t_1 and time t_2,

u is the mean wind speed in meters per second,

$[u\sigma_y(d)\sigma_z(d)]_{s,t_1,t_2}$ is the product of wind speed and the standard deviations of the concentration of an isotope at a distance d, assuming a Gaussian distribution within the cloud in the y and z directions for the Gifford-Pasquill stability class s (see Tables 80 and 81), which is assumed to characterize atmospheric stability between time t_1 and time t_2,

π is $3.14\cdots$

t_1 and t_2 are times after the reactor accident in seconds.

The number of curies of radioactive isotope r per megawatt of power, which passes the observer in time t_2 minus t_1, is given by the equation

$$Q_{t_1,t_2,r} = F_p F_b \left(\frac{q_{t_0,r}}{P_0}\right) \int_{t_1}^{t_2} \lambda_1 e^{-(\lambda_1+\lambda_r)t}\, dt$$
$$= F_p F_b \left(\frac{q_{t_0,r}}{P_0}\right) \frac{\lambda_1}{\lambda_1+\lambda_r} \qquad (2)$$
$$[e^{-(\lambda_1+\lambda_r)t_1} - e^{-(\lambda_1+\lambda_r)t_2}],$$

where

F_p is the fraction of radioactive material released from the reactor pressure vessel to the building and is taken as 0.5,

F_b is the fraction of radioactive material released to the building which becomes airborne and is available for emission into the atmosphere and is taken as 0.5,

λ_1 is the building leakage rate taken as 1% per day or 1.16×10^{-7} per second,

λ_r is the radioactive decay constant for isotope r,

$q_{t_0,r}/P_0$ is the reactor inventory of isotope r per megawatt after t_0 seconds of reactor operation.

$$\frac{q_{t_0,r}}{P_0} = \frac{3.2 \times 10^{16}\, \alpha_r (1 - e^{-\lambda_r t_0})}{3.7 \times 10^{10}} \qquad (3)$$
$$= 0.865 \times 10^6 \alpha_r (1 - e^{-\lambda_r t_0}).$$

where

α_r is the total fission yield for isotope r,

t_0 is the number of seconds of operation of the reactor,

3.2×10^{16} is the number of fissions per second per megawatt,

3.7×10^{10} is the number of disintegrations per second per curie.

For short-life emitters or long operating periods, the given isotope will reach saturation in the reactor. We then have

$$\frac{q_{t_0,r}}{P_0} \simeq \frac{q_{\infty,r}}{P_0} = 0.865 \times 10^6 \alpha_r . \qquad (4)$$

The dose to the thyroid due to inhalation of the passing cloud may be determined from

$$D_{t_1,t_2,r} = C_r A_{t_1,t_2,r} , \qquad (5)$$

where C_r is a constant for a given isotope, r, which has the same magnitude as $D_\infty/A_{t,r}$ of Reference 1; C_r is given in Table 82 for each of the five isotopes of iodine considered, and $A_{t_1,t_2,r}$ may be calculated from Eqs. (1–4) and the data given in Tables 80 and 82.

INHALATION DOSE CALCULATIONS USING ACTUAL METEOROLOGICAL DATA

In the equations developed above, varying atmospheric-stability conditions and wind speed are accounted for, but the effect of varying wind direction is not included. In the remainder of this report, the reduction in calculated dose rate due to varying wind direction is discussed.

An indication of the degree of conservatism of typical analyses of inhalation doses to the public following a reactor accident is provided by calculations of a "dose ratio," below. In these particular calculations, the simplifications are made that the ground-level point source is constant and that the isotope inhaled is long-lived.

TABLE 82. DECAY CONSTANT, FISSION YIELD, SATURATION INVENTORY, AND DOSE TO THYROID PER CURIE INHALED FOR IODINE ISOTOPES[a]

Iodine isotope	Decay constant, λ_r, sec^{-1}	Saturation inventory, curies per megawatt ($q_{\infty,r}/P_0$)	Fission yield (α_r), atoms per fission	Dose to thyroid, rads per curie, (C_r)
131	9.96×10^{-7}	2.51×10^4	2.9	1.48×10^6
132	8.26×10^{-5}	3.81×10^4	4.4	5.35×10^4
133	9.20×10^{-6}	5.63×10^4	6.5	4.0×10^5
134	2.20×10^{-4}	6.58×10^4	7.6	2.5×10^4
135	2.86×10^{-5}	5.10×10^4	5.9	1.24×10^5

[a] This table is adapted from Reference 1.

Inhalation Doses Due to Iodine

To perform the dose calculations, the area surrounding the reactor was divided into 18 contiguous 20° sectors centered at 15, 35, 55, and every 20° thereafter through 355°. One-day and thirty-day dose calculations for the inhalation of iodine isotopes were made for each of the distances: 100, 300, 500, 800, 1500, 2000, 4800, and 20,000 meters for each of the 20° sectors.

Two-hour dose calculations are not presented in this study since the usually assumed unchanging meteorological conditions for the two-hour period are realistic.

The infinite-time dose to the thyroid was determined for each hour at each of the 9 distances and 18 direction sectors. During any one hour only the direction sector over which the wind blew received a dose; the dose over the other sectors was counted as zero. Thirty-day doses were computed by summarizing the doses received at each point representing the center line of the sector at each distance for 720 consecutive hours. These compu-

TABLE 83. TABLE OF ISOTOPE CONSTANTS

r	Isotope	λ_r (sec^{-1})	K_r
1	I^{131}	9.96×10^{-7}	1.167×10^7
2	I^{132}	8.26×10^{-5}	1.045×10^4
3	I^{133}	9.20×10^{-6}	1.031×10^6
4	I^{134}	2.20×10^{-4}	3.195×10^3
5	I^{135}	2.86×10^{-5}	9.409×10^4

tations were performed for consecutive, overlapping 720-hour intervals beginning with each hour from 0100 January 1, 1959 for a period of about 5½ years. A total of 47,620, 720-hour dose calculations were made, and these were used to form cumulative percentage frequency distributions. The 5, 10, 20, 40, 50, 70, 80, 90, 95, 98, and 100 percentile doses were determined. A 90 percentile dose of 50 rem at a particular distance and direction sector, for example, indicates that 90% of the calculations for the 720-hour period show a dose value of 50 rem or less.

The dose from inhalation of isotope r, at distance d and in sector $\Delta\theta$, for a one-hour exposure starting h-1 hours after the beginning of the accident is

$$\hat{D}_{h,r}(\Delta\theta, d) = \frac{K_r[e^{-(\lambda_1+\lambda_r)3600(h-1)} - e^{-(\lambda_1+\lambda_r)3600h}]}{[u\sigma_y(d)\sigma_z(d)]_{s,h}} \quad (6)$$

where

$$K_r = C_r \frac{RP_0}{\pi} F_p F_b \left(\frac{q_{i_0,r}}{P_0}\right) \frac{\lambda_1}{\lambda_1 + \lambda_r}$$

and the notation

$[u\sigma_y(d)\sigma_z(d)]_{s,h}$ denotes the appropriate average value of the product between h-1 and h hours after time zero.

K_r and λ_r are coefficients obtained from Table 83;

u is the 19-foot wind speed, in meters per second, in hour h,

$\Delta\theta$ is the particular 20° sector indicated by the 19-foot wind direction during hour h, with the reactor located at the vertex,

λ_1 is 1.16×10^{-7} per second—the leakage rate of 1% per day,

$\hat{D}_{h,r}(\Delta\theta, d)$ is assumed to be 0 for all sectors except the one indicated by the wind direction in hour h.

The 30-day dose from a particular isotope, r, to a receptor in sector $\Delta\theta$ and at distance d, is given by

$$\tilde{D}_{720,r}(\Delta\theta, d) = \sum_{h=1}^{720} \hat{D}_{h,r}(\Delta\theta, d) \quad (7)$$

and the 30-day total iodine dose is given by

$$\mathfrak{D}_{720,I}(\Delta\theta, d) = \sum_{r=1}^{5} \tilde{D}_{720,r}(\Delta\theta, d). \quad (8)$$

Similarly iodine inhalation doses for 24-hour periods were computed based on approximately 6 years of data beginning January 1, 1959.

Dose Ratios

In this section the inhalation dose to a receptor from a long-lived isotope, r, in the plume from a constant, continuous, ground-level point source is examined. A comparison is made between the dose based upon actual meteorological conditions and the dose based upon assumed constant meteorological conditions, namely, constant wind speed (2 meters per second), constant wind direction (directly toward the receptor), and constant atmospheric-stability parameters (category E).

With the assumptions that the isotope, r, is long-lived and the source is constant, Eq. (6) becomes

$$\hat{D}_{h,r}(\Delta\theta, d) = \frac{C_r R S_r}{\pi} \frac{g_h(\Delta\theta)}{[u\sigma_y(d)\sigma_z(d)]_{s,h}}, \quad (6')$$

where

S_r is the constant emission rate of isotope r from the point source, in curies per hour,

$g_h(\Delta\theta)$ is the Dirac δ-function: $g_h(\Delta\theta) = 1$ when the wind direction is toward sector $\Delta\theta$, and $g_h(\Delta\theta) = 0$ otherwise,

and the other terms are as defined earlier.

For this case, for N hours of exposure, the total inhalation dose of isotope, r, by a fixed receptor at distance d in sector $\Delta\theta$ is obtained from Eq. (7):

$$\tilde{D}_{N,r}(\Delta\theta, d) = \frac{C_r R S_r}{\pi} \sum_{h=1}^{N} \frac{g_h(\Delta\theta)}{[u\sigma_y(d)\sigma_z(d)]_{s,h}}. \quad (9)$$

If the wind conditions and atmospheric-stability category (E) are constant, the inhalation dose in N hours is:

$$\bar{\tilde{D}}_{N,r}(\Delta\theta, d) \equiv \frac{C_r R S_r}{\pi} \frac{N}{[2\sigma_y(d)\sigma_z(d)]_{E,h}}. \quad (10)$$

The dose ratio, $\mathfrak{R}_{N,r}(\Delta\theta, d)$, at distance d and in sector $\Delta\theta$ is defined as the ratio of these two doses:

$$\begin{aligned} \mathfrak{R}_{N,r}(\Delta\theta, d) &\equiv \frac{\tilde{D}_{N,r}(\Delta\theta, d)}{\bar{\tilde{D}}_{N,r}(\Delta\theta, d)} \\ &= \frac{[2\sigma_y(d)\sigma_z(d)]_{E,h}}{N} \sum_{h=1}^{N} \frac{g_h(\Delta\theta)}{[u\sigma_y(d)\sigma_z(d)]_{s,h}}. \end{aligned} \quad (11)$$

Dose ratios were calculated for the periods 1, 2, 4, 8, 16, and 30 days for the nine distances and 18 20-degree sectors. To illustrate, for the 4-day or 96-hour calculations, inhalation doses due to one-hour exposure for each sector and each distance using actual wind speed, direction, and stability data were summed for 96 hours. This sum was divided by the dose calculated assuming constant meteorological conditions to provide the dose ratio. Dose ratios were computed over the overlapping 96-hour periods beginning with each hour for 34,946 hours, etc., i.e., for about a 4-year period, beginning with 0100 January 1, 1959.

Thus, the dose ratio calculations are similar to those of the iodine inhalation dose distributions. Similarly, a cumulative percentage frequency distribution was constructed showing the 5, 10, 20, 40, 50, 70, 80, 90,

TABLE 84. Estimation of Wind Speed at 19-Foot Level if Those Data are Missing

Stability	n	Multiply wind speed at 150-ft by
Unstable	0.20	0.794
Neutral	0.25	0.743
Stable	0.50	0.500

95, 98, and 100 percentile dose ratios for each distance and sector.

Handling Missing Data

To calculate a 30-day dose, an unbroken sequence of 720 hourly observations is needed. From time to time observations are missing because of instrument servicing, maintenance requirements, or some malfunction. With the computation of a moving summation, one hour of missing data resulted in 720 incomplete calculations, since each observation was used 720 times. It, therefore, became necessary to make reasonable substitutes for missing data. On the whole, the equipment worked quite well, so that the number of substitutions necessary was tolerable. The procedures for handling missing data are as follows:

Wind Speed Substitutions.—If in a given hour the 19-foot wind speed observation was missing, the 150-foot wind speed corrected by the exponential law was substituted (see Table 84). The exponential law is given as

$$\frac{u_1}{u_2} = \left(\frac{Z_1}{Z_2}\right)^{n/(2-n)}, \qquad (12)$$

where

u_1, u_2 are wind speeds at 19 and 150 feet

Z_1, Z_2 are heights, 19 and 150 feet, respectively, and

n is a Sutton diffusion parameter.

The value of n was taken as 0.20, 0.25, or 0.50, depending upon whether unstable, neutral, or stable conditions were present.

TABLE 85. Definition of Daylight Hours

Month	Daylight hours (CST)
January	0800–1600
February	0700–1700
March	0700–1800
April	0600–1800
May	0500–1900
June	0500–1900
July	0500–1900
August	0600–1900
September	0600–1800
October	0700–1700
November	0700–1600
December	0800–1600

Wind Direction Substitutions.—The wind direction at 19 feet determines which of the 18 20-degree sectors surrounding the reactor received the radiation dose for that hour. If the 19-foot level direction was missing, the 150-foot level was used. If both were missing, then the direction of the previous hour was used again.

Stability Substitutions.—The stability category was determined by ΔT, the difference in temperature (°F) between the 144- and the 5.5-ft levels above ground. The stability was classified according to Table 81. If ΔT was missing the stability was determined in the following manner: It was considered neutral, category D, during the daytime. The hours classified as day or night are given in Table 85. At night stability was considered neutral if precipitation was occurring; otherwise, it was considered stable, category F.

The Gaussian Correction

It is common practice to assume that the concentration about the plume center line forms a bivariate Gaussian distribution, and that the plume boundary is located on a surface where the concentrations are one tenth that at the center line. Since the plume meanders,

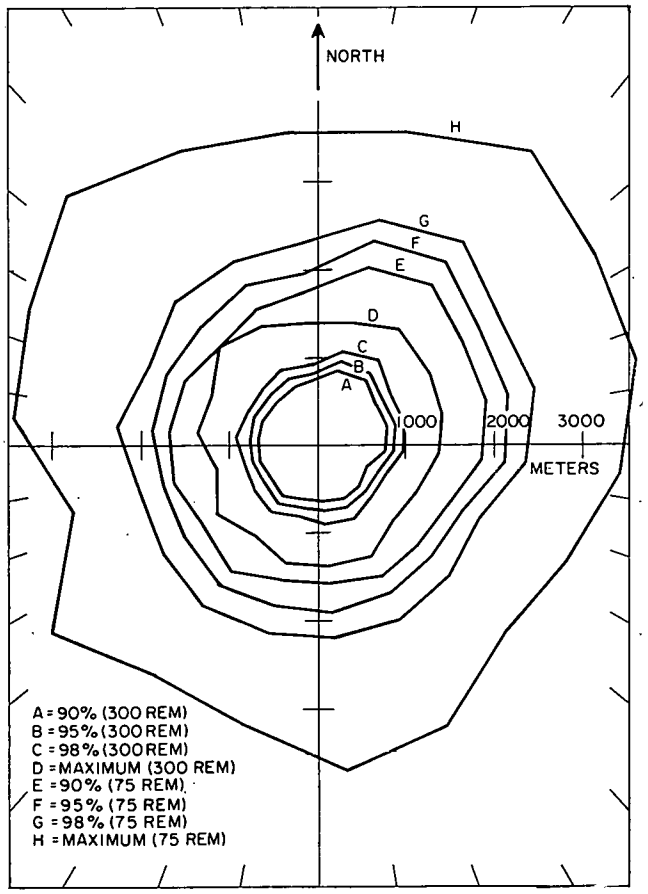

Fig. 107. Isopleths showing minimum distances at which the 30-day dose is equal to or less than the indicated value 90, 95, 98, and 100 percent of the time.

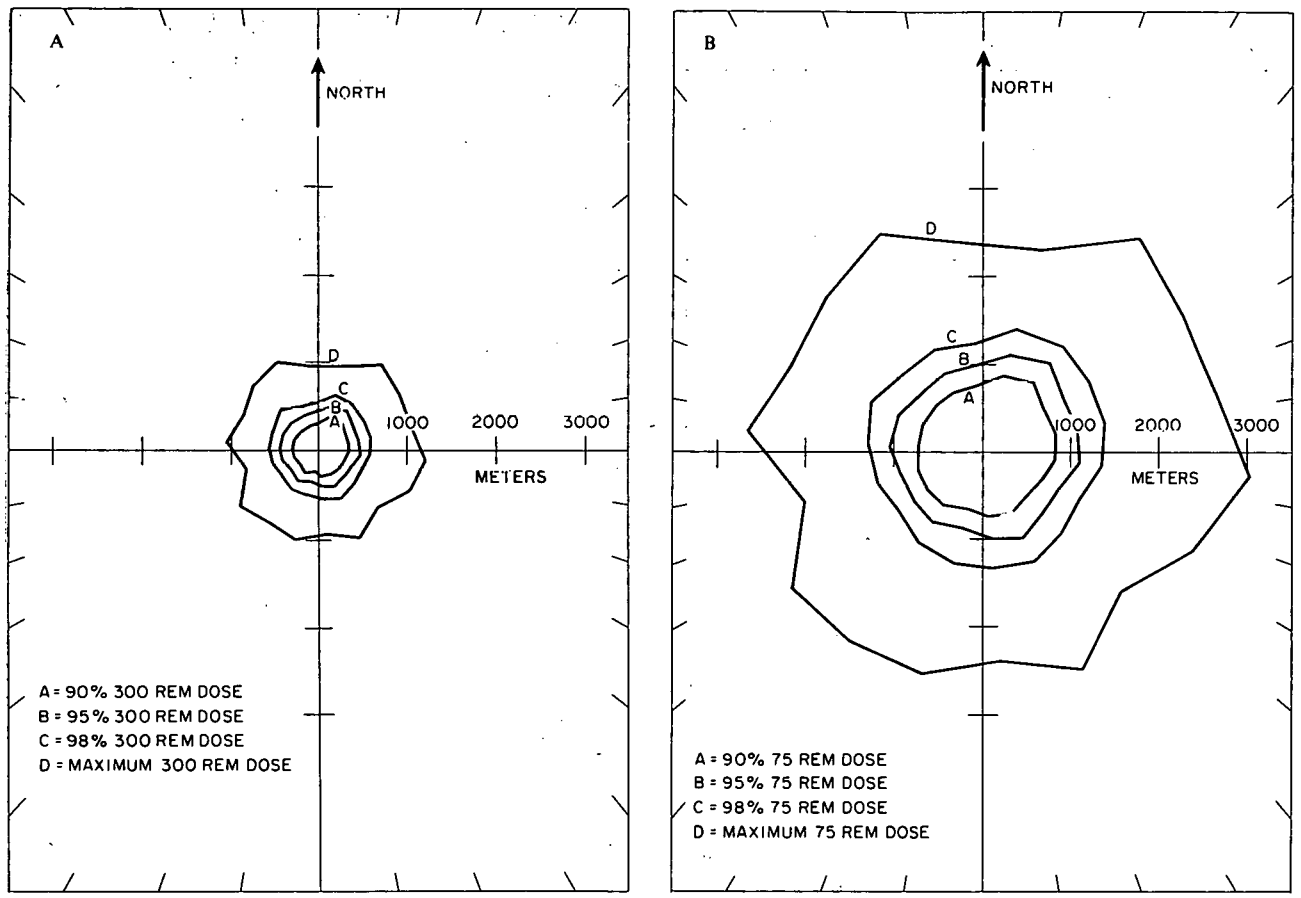

FIG. 108. Isopleths showing minimum distances at which the 24-hour dose is equal to or less than: a, 300 rem 90, 95, 98 or 100 percent of the time; b, 75 rem 90, 95, 98 or 100 percent of the time.

concentrations registered at a point on the ground are less than that of the center line. If the meandering angle is large compared to the angle subtended by the plume itself and if one assumes that the center line of the plume has an equal probability of being over any point on an arc of the circle centered at the reactor, then the average concentration is 0.57 times the center line or maximum concentration. In these calculations a factor of 0.6 was applied to the center-line values to correct for plume meander.

Building Wake Correction

To improve the accuracy of the dose calculations, it is possible to take account of the added dilution caused by building turbulence. This may be accomplished by modifying equation (1) to read

$$A_{t_1,t_2,r} = \frac{RP_0Q_{t_1,t_2,r}}{\pi[u\sigma_y(d)\sigma_z(d)]_{s,t_1,t_2} + cAu}, \qquad (13)$$

where A is the vertical cross sectional area of the building and c is a constant whose value varies from ½ to 2. This formulation for the building wake factor was suggested by Fuquay and described by Gifford.[2] In the calculations presented below this correction was not made.

ANALYSIS OF DATA

Iodine Inhalation Dose Calculations

The results of the iodine inhalation dose calculations for a given period may be expressed by the four variables: 1) dose magnitude, 2) cumulative percentage frequency or dose frequency percentile, 3) distance from the reactor, and 4) direction from the reactor.

Thirty-day dose data are given in Figure 107. Curves A through D represent 90, 95, 98 and 100 percentile isopleths showing distances at which a dose of 300 rem or less is received. Corresponding isopleths for a 75-rem dose are given in curves E through H. To illustrate, curve A is a plot of the distance from the reactor in each direction sector at which an iodine inhalation dose of 300 rem or less will be received in 90% of the 720-hour consecutive, overlapping periods beginning with each hour during a 5½-year period. The information presented in Figure 107 is essential for determining the low population zone distance, i.e., the greatest distance at which a 300 rem dose occurs in a 30-day period.

Figure 107 shows that the isopleths for the 90, 95 and 98 percentiles are relatively parallel. The 100 percentile curve representing the extreme for each direction shows

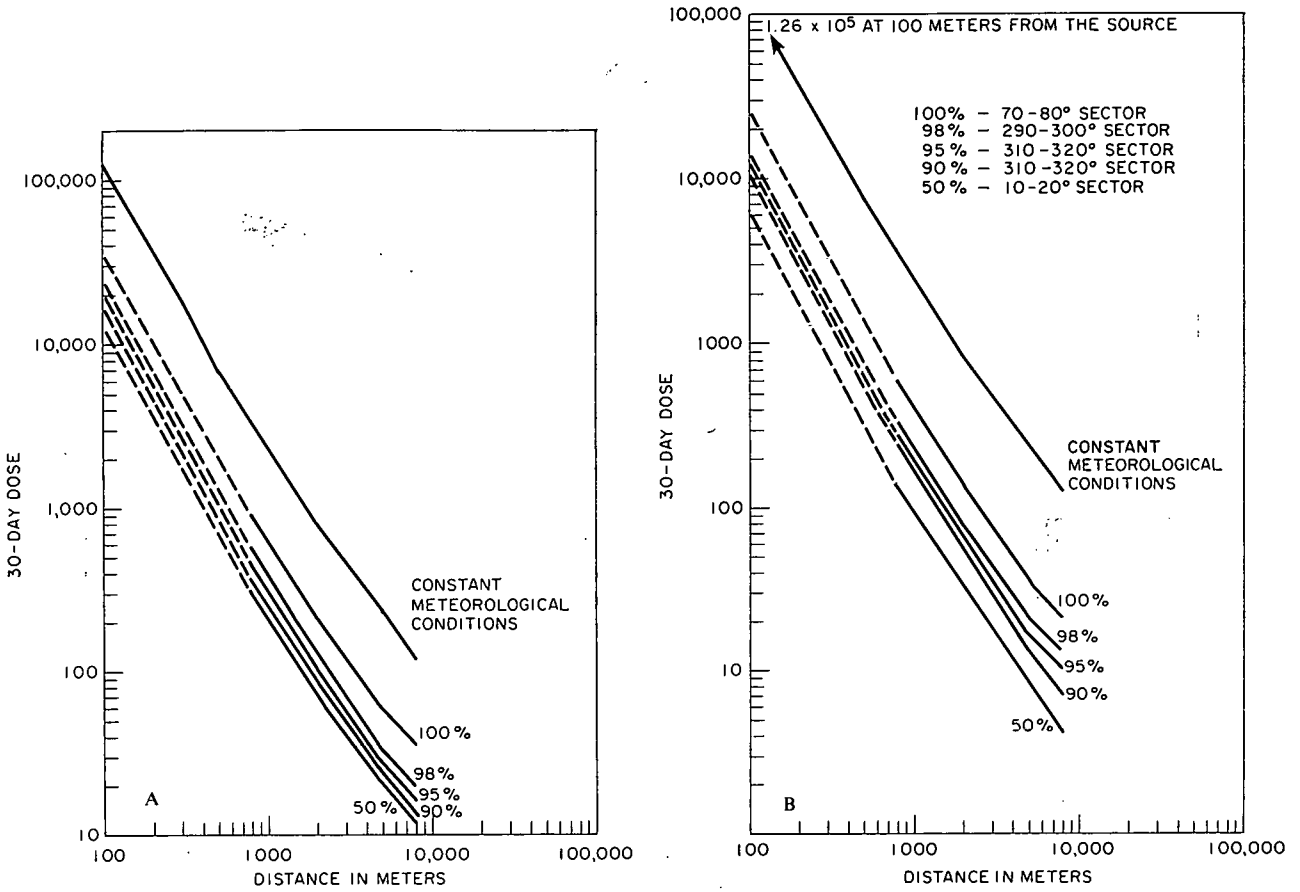

FIG. 109. a. Maximum dose vs. distance curves for indicated percentiles and for constant meteorological conditions—stability category E, constant wind direction, 2 meters/second wind speed; b. minimum dose vs. distance curves for indicated percentiles and for constant meteorological conditions—stability category E, constant wind direction and 2 meters/second wind speed.

more variation. The 90 percentile, 300-rem isopleth varies from about 700 to 900 meters. The maximum distance occurs in the northeast sector corresponding to southwesterly winds. (In meteorology the wind direction is that from which the wind blows.)

According to Figure 107, the southeast sector is the most favorable and the northeast least favorable with respect to a 30-day iodine inhalation dose. Should a reactor accident of sufficient magnitude to give a 300 rem dose at slightly less than one-half mile occur, it is likely that no one will be allowed to remain at this location for any length of time.

Figure 108 shows the percentile isopleths for 24-hour 75- and 300-rem doses on the same scale used in Figure 107. The patterns are quite similar, but the distances are smaller as is to be expected.

Figure 109 allows a comparison of the doses calculated under constant meteorological conditions—stability category E and constant wind and those calculated under actual meteorological conditions. Table 86 summarizes the results shown in these figures. The dose versus distance curves for the percentile values 50, 90, 95, 98 and 100 in Figure 109a represent the doses received in the sector giving the highest values. These were determined by examining the dose calculations in each sector at 1500 meters. The minima given in Figure 109b were determined the same way.

TABLE 86. MAXIMUM, MINIMUM, AND AVERAGE DOSE RATIOS AT 1500 METERS

Dose percentile	30-Day iodine inhlalation dose ratios			1-Day iodine inhalation dose ratios		
	Max.	Min.	Ave.	Max.	Min.	Ave.
100	0.265	0.161	0.213	1.077	0.648	0.862
98	0.154	0.093	0.124	0.388	0.250	0.319
95	0.125	0.076	0.101	0.281	0.173	0.227
90	0.106	0.065	0.085	0.189	0.097	0.143

The dose ratio for each percentile can be determined by dividing the dose obtained from the actual meteorological data by that obtained using constant conditions. The degree of pessimism resulting from use of constant meteorological conditions is well illustrated. For example, at the 90 percentile level the 30-day inhalation dose in the sector giving the highest doses is

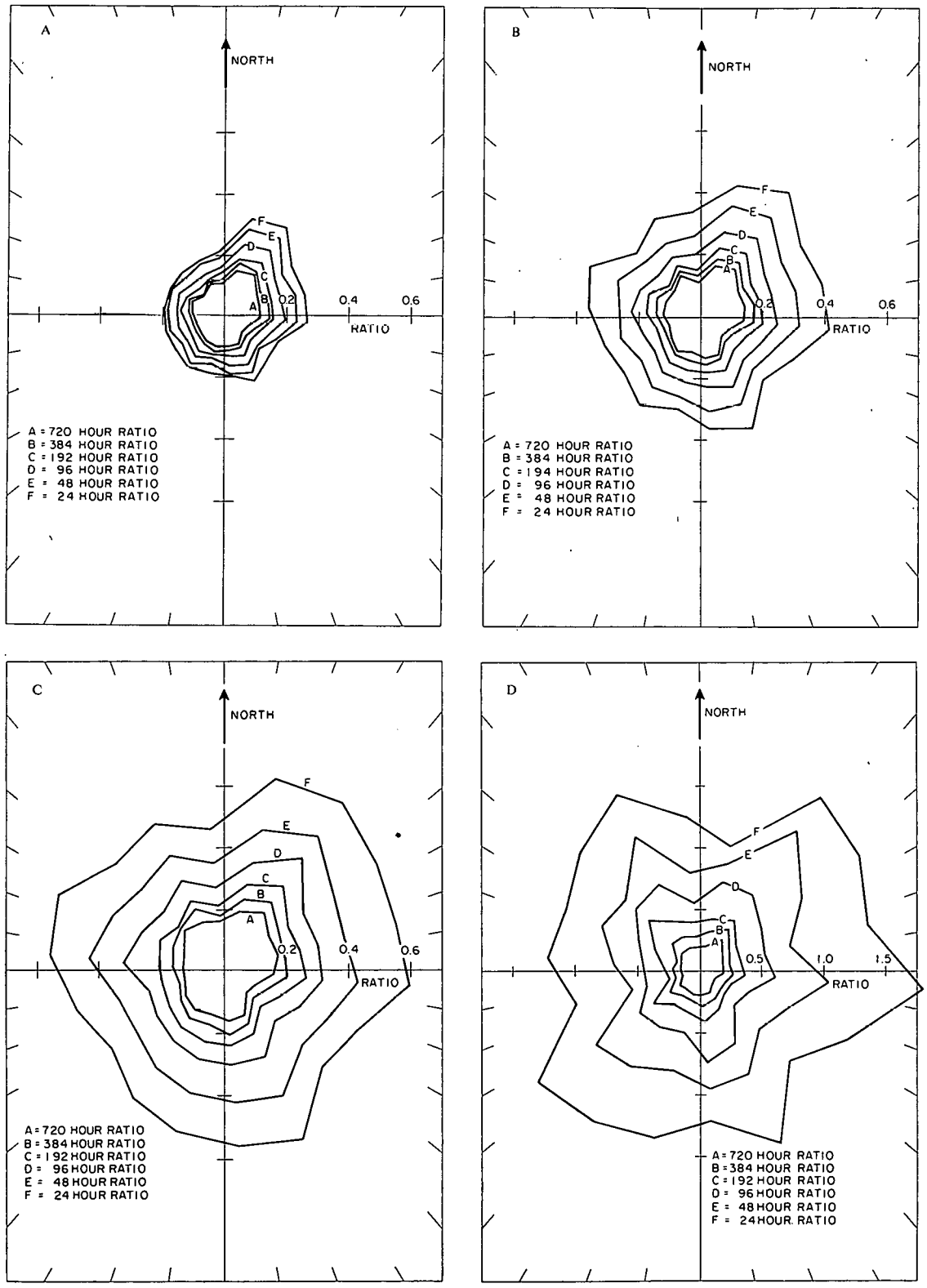

FIG. 110. Dose ratio = calculated dose using actual meteorological conditions/calculated dose using constant wind and stability. a. 90 Percentile values of dose ratios due to meteolorogical factors; b. 95 percentile values of dose ratios due to meteorological factors; c. 98 percentile values of dose ratios due to meteorological factors; d. 100 percentile values of dose ratios due to meteorological factors.

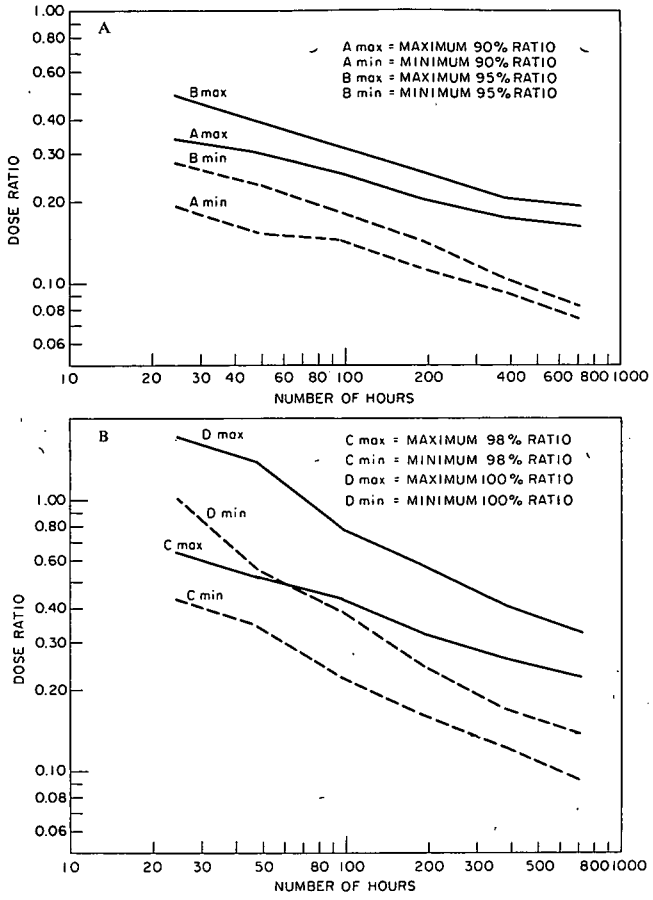

FIG. 111. Maximum and minimum of 20° sectors; dose ratios due to meteorological factors.

only $\frac{1}{10}$ of that calculated using the constant meteorological conditions. Correspondingly reduced values are shown at the other percentile values and also for the 24-hour doses. Thus, the use of actual meteorological conditions makes a significant difference in calculating iodine inhalation doses.

Dose Ratios

The dose ratio previously described represents the ratio of the inhalation dose calculated from actual meteorological data to that which would have been obtained if a constant speed of 2 meters per second, a constant wind direction and stability category E prevailed. The results of these calculations are shown in Figure 110. For this figure the percentile value was held constant and isopleths for each of the 6 exposure periods, 1, 2, 4, 8, 16, and 30 days, were drawn on a polar diagram, the radii of which represent the dose ratio in the angular sector indicated. The dose ratio is nearly invariant with distance. Therefore, only dose ratios at 1500 meters are presented.

Although these results are characteristic of long-lived emitters, they are similar to the 30-day inhalation iodine doses. Corresponding curves for radioisotopes having half-lives of minutes or seconds would be different in appearance. The northeast sector has the highest values, indicating the effects of the high frequency of winds from the southwest. The 90, 95, and 98 percentile curves have been drawn to the same scale; it is readily seen that the areas enclosed increase with the percentile value. The 100 percentile curves are drawn on a reduced scale.

In some cases the dose ratio exceeded one for the one- and two-day exposure period on the 100 percentile chart. This is due to persistent wind speeds of less than two meters per second and stability in category F.

Figure 111 shows the variation of the meteorological dose ratio with the exposure period. The highest and lowest values of the 90, 95, 98 and 100 percentile ratios

TABLE 87. CONSTANT EMISSION RATE INHALATION DOSE RATIOS FOR LONG-LIVED EMITTERS AT 1500 METERS

Exposure period, days		Dose percentile			
		100	98	95	90
1	Max.	1.835	0.655	0.495	0.345
	Min.	1.025	0.435	0.285	0.195
2	Max.	1.365	0.525	0.295	0.305
	Min.	0.555	0.335	0.235	0.155
4	Max.	0.775	0.435	0.315	0.255
	Min.	0.395	0.225	0.185	0.145
8	Max.	0.575	0.325	0.255	0.205
	Min.	0.245	0.165	0.145	0.115
16	Max.	0.415	0.265	0.215	0.175
	Min.	0.175	0.125	0.105	0.095
30	Max.	0.325	0.225	0.195	0.165
	Min.	0.135	0.095	0.085	0.075

TABLE 88. COEFFICIENTS OF REGRESSION CURVE RELATING DOSE RATIO AND EXPOSURE PERIOD

Curve No.[a]	a	b	Approximate equation
A—90% Max.	0.34	−0.221	$F = \frac{1}{3}\ T^{-1/4}$
A—90% Min.	0.19	−0.254	
B—95% Max.	0.49	−0.303	$F = \frac{1}{2}\ T^{-1/3}$
B—95% Min.	0.28	−0.326	
C—98% Max.	0.64	−0.315	$F = \frac{5}{8}\ T^{-1/3}$
C—98% Min	0.43	−0.434	
D—100% Max.	1.70	−0.491	$F = \frac{5}{3}\ T^{-1/2}$
D—100% Min.	1.00	−0.650	

[a] See Figure 111.

are plotted on these figures as a function of exposure time. Table 87 provides the tabular data on which Figure 111 is based. Values greater than one appear for the 1- and 2-day maximum readings for the 100 percentile curve. However, the ratios decrease with increasing exposure time and, of course, with decreasing percentile values.

Best-fitting straight lines using the equal area method were drawn by inspection. For the sake of simplicity in the calculations the line was drawn through the 1-day point. The equations of the lines may be expressed as $F = aT^b$, where F is the dose ratio, T is the exposure period in hours, and a and b are regression coefficients. The regression coefficients a and b are presented in Table 88.

The value of the coefficient a increases with percentile value as expected, but the behavior of b is not so obvious. Of interest is that the absolute value of b for the minimum curve was in each case larger than that for the maximum curve and that the b value increased steadily with the percentile value. The approximate equations relating the dose rate and exposure period given in the last column of Table 88 are simple in form and useful as "rule of thumb" estimates for the Argonne site.

CONCLUSIONS

Doses calculated from actual meteorological observations are significantly lower than those obtained from the assumption of constant wind direction, 2 meters per second wind speed and category E stability. For the 30-day iodine inhalation dose the 90th percentile dose ratio is 0.1 and the 95th percentile dose ratio is in the range one-eighth to one-thirteenth. For the 1-day dose a reduction to one-fourth or one-fifth may be expected.

For the long-lived inhalation doses, reduction factors are one-sixth to one-thirteenth on the 90th percentile level and one-fifth to one-twelfth on the 95th percentile value level.

The direction of the observer or monitoring station with respect to the reactor makes appreciable difference. For the same distance the probability of high doses is greater in the direction northeast of the reactors.

The data provided in this report may be used for comparison with other assumed constant meteorological conditions such as a different constant wind speed or stability category or constant parameters in the Sutton difference equation.

Although the information presented here is characteristic of the Argonne site, the magnitude of the dose factors would be quite similar in other middle latitude stations having similar wind rose and inversion frequency patterns. A study for a number of stations, however, is necessary before general conclusions can be drawn. At any rate, the study does show that for this station significant reductions are obtained when the actual meteorological data are used. For a 30-day dose it is reasonable to expect that the dose calculated using actual meteorological conditions would be approximately one-tenth of the dose calculated with the usual conservative, constant meteorological conditions.

The authors acknowledge the assistance provided by Michael T. Matthies, John R. Gabriel, and Marian Howe of the Applied Mathematics Division in programing the calculations for the CDC 3600 computer. Helpful discussions and assistance were provided by James E. Carson, Gunther A. Zerbe, and Linda S. Rogers.

REFERENCES

1. J. J. DiNunno, F. D. Anderson, R. E. Baker, and R. L. Waterfield. Calculation of Distance Factors for Power and Test Reactor Sites. U.S. Atomic Energy Commission Report TID-14844 (1962).
2. F. A. Gifford. Atmospheric Dispersion Calculations Using the Generalized Gaussian Plume Model. *Nucl. Safety* **2**(4), 47-51 (1961).

ARTICLES PUBLISHED BY THE RADIOLOGICAL PHYSICS DIVISION STAFF DURING THE PERIOD JULY 1966–JUNE 1967

Ashby, W. C., J. M. Beggs, J. Kastner, B. G. Oltman, and Harry Moses. Ecological Dosimetry: Radiation Levels Influenced by Plant Growth. *Science* **155,** 1430 (March 17, 1967).

Berlman, I. B. Fluorescence Studies Related to a Hidden Transition in Biphenyl and Substituted Biphenyls. *Proc. Intern. Conf. on Luminescence,* Budapest, Ujpest 1 Pf. 76, Hungary, Book of Preprints, August 1966, p. 79.

Edgington, D. C. The Estimation of Thorium and Uranium at the Submicrogram Level in Bone by Neutron Activation. *Intern. J. Appl. Radiation Isotopes* **18,** 11 (January 1967).

Failla, P. M. and D. J. Simmons. Strontium Retention in Mice Treated with Thyroid Hormones. *Health Phys.* **12,** 1249 (September 1966).

Frenzen, Paul. Some Meteorological Model Experiments of Several Scales. Simulation Colloquium Notes VIV: National Center of Atmospheric Research, NCAR-TN-22, (November 1966), p. 99.

Holtzman, R. B. and Frank Ilcewicz. Po^{210} and Pb^{210} in the Skeletal and Lung Tissues of Cigarette Smokers. *Science* **153,** 1259–1260 (September 1966).

Holtzman, R. B. Discussion of article Po^{210} in Bronchial Epithelium of Cigarette Smokers. *Science* **155,** 607 (February 3, 1967).

Inokuti, M. and F. Hirayama. Some Theoretical Aspects of Energy Transfer by the Exchange Mechanism. *Proc. Intern. Symp. on Luminescence,* Munich, Germany, Sept. 5–9, 1965. Verlag Karl Thiemig, KG, Munich, 1966, pp. 107–108.

Inokuti, M. Excitation of the Hydrogen Atom by Fast Electrons in the Ochkur Approximation. *J. Phys. Soc. Japan* **22**(4), 971 (April 1967).

Inokuti, M. The Oscillator Strength Distribution of Atoms and Molecules. *BUTURI* (Japanese journal) **22**(4), 196 (April 1967).

Kastner, J., H. Berger, and I. R. Kraska. LiF Thermoluminescence for Neutron Image Storage. *Nucl. Appl.* **2,** 252–253 (June 1966).

Kastner, J., R. Hukkoo, and B. G. Oltman. LiF Thermoluminescence Dosimetry for Beta-Rays. *Proc. Intern. Conf. on Luminescence Dosimetry,* USAEC Symp., Series 8, April 1967, pp. 482–489.

Kastner, J., B. G. Oltman, and P. Tedeschi. LiF Thermoluminescence Response to Fast Neutrons. *Health Phys.* **12,** 1125–1128 (August 1966).

Kastner, J., S. L. Halverson, Harry Moses, T. V. Banfield, E. A. Mueller, and G. E. Stout. Gamma Ray and Radar Interaction. *Radioisotopes for Aerospace. Part I: Advances and Techniques.* Plenum Press, New York, 1966, pp. 414–422.

Kastner, J., D. Eggenberger, A. Longnecker, D. King, and D. Schutt. UV Laser Excitation for Ultrasensitive Photoluminescent Dosimetry. *Symposium on Solid State and Chemical Radiation Dosimetry in Medicine and Biology.* Intern. Atomic Energy Agency, Vienna, 1967, pp. 115–120.

Lloyd, Elizabeth, J. H. Marshall, J. W. Butler and R. E. Rowland. A Computer Programme for Automatic Scanning of Autoradiographs and Microradiographs of Bone Sections. *Nature* **211,** 661–662 (August 1966).

Lucas, H. F., Jr., N. J. Petersen, L. D. Samuels and Simon P. Abrahams. An Epidemiological Approach to Low-Level Ra^{226} Exposure. *Public Health Reports* **81**(9), 805 (September 1966).

Marinelli, L. D. Geometrical Parameters in Whole-Body Gamma-Ray Spectrometry Measurements. *Proc. XI Intern. Congress of Radiology,* Rome, Italy, Sept. 22–28, 1965, pp. 1221–1231.

Marinelli, L. D. Review of *Assessment of Radioactivity in Man, Vols. I and II.* IAEA, Vienna, 1964. *Health Phys.* **12**(5), 722 (May 1966).

Rowland, R. E. Exchangeable Bone Calcium. *Clin. Orthoped.* **49,** 233 (Nov.–Dec. 1966).

ABSTRACTS

Bowe, J. C. and R. K. Langs. Drift Velocity and the Elastic Collision Cross Section for Electrons in Helium. *Bull. Am. Phys. Soc.* **12,** 232 (February 1967).

Carson, J. E. and Harry Moses. Calculation of Effective Stack Height. 47th Mtg. of Am. Met. Soc., New York, January 23–26, 1967. *Bull. Am. Meteorol. Soc.* **47,** 901 (November 1966).

Holtzman, R. B. Ra^{226} and the Natural Airborne Nuclides Pb^{210} and Po^{210} in Arctic Biota. *Health Phys.* **12**(12), 1807 (December 1966), Abstract #143.

Holtzman, R. B. and Henry F. Lucas, Jr. Excretion of ^{210}Pb and ^{226}Ra by Radium Dial Painters. Program of Health Phys. Soc. Annual Mtg., Washington, D. C. June 18–22, 1967, p. 15.

Inokuti, M., Yong-Ki Kim and R. L. Platzman. A Sum Rule for the Bethe Inelastic Cross Section and Its Application to the Helium Atom. Proc. Physical Society of Japan Mtg., Oct. 12–16, 1966, Nigita, Japan, p. 15.

Kastner, J., D. N. Eggenberger, A. A. Longnecker, David King and Dale Schutt. UV Laser Excitation for Ultrasensitive Photoluminescent Dosimetry. Abstracts of papers for the 15th Annual Mtg. of the Radiation Res. Soc., San Juan, Puerto Rico, May 7–11, 1966, p. 92.

Kastner, J., Harold Berger and I. R. Kraska. A Thermoluminescent Image Detection Method for Neutron Radiography. Proc. 5th International Conference on Nondestructive Testing, Montreal, Canada, May 21–26, 1967.

Lucas, H. F., Jr., Frank Markun and J. Farnham. Retention and Excretion of Sr^{85} by the Chinchilla. Radiation Res. Soc. Mtg., May 7–11, 1967, San Juan, Puerto Rico. Abstracts of Mtg., p. 9.

Marshall, John H. The Modified Power Function Model of Alkaline Earth Metabolism. 11th Annual Health Phys. Soc. Mtg., Houston, Texas. *Health Phys.* **12**(8), 1161 (August 1966).

Moses, Harry and William C. Ashby. Atmospheric Restrictions on Plant Water Loss. AAAS Meeting. *Bull. Ecol. Soc. Am.* (December 1966), p. 198.

Moses, Harry and William C. Ashby. Dewpoint Temperature Inversions. American Meteorological Society Conference on Physical Processes of the Lower Atmosphere, Ann Arbor, Michigan, March 20–22, 1967. *Bull. Am. Meteorol. Soc.* **48,** 23 (January 1967).

Moses, Harry and John E. Pearson. Atmospheric Radon Meteorology. International Congress of Biome-

teorology, Rutgers University, New Brunswick, New Jersey, Aug. 26–Sept. 2, 1966.

B. G. Oltman, J. Kastner and P. Tedeschi. The Effects of Fast Neutron Exposure on the LiF Thermoluminescent Response to Gamma-Rays. Program booklet for the Symp. of Health Phys. Soc., Chicago, January 20–February 2, 1967, p. 24.

Rehfeld, C. E., J. Kastner, B. G. Oltman, H. M. Rosenberg and D. E. Doyle. Thermoluminescent Microdosimetry in Dental Radiology. I. Technique. Abstracts of papers, International Assoc. for Dental Research, 45th General Mtg. and North American Division ISDR, March 16–19, 1967, Washington, D. C., p. 169; II. Clinical Application, p. 170.

PAPERS ACCEPTED FOR PUBLICATION

Berlman, I. B. Factors Relevant to a Short Fluorescence Lifetime of an Aromatic Molecule: Empirical Data. *Molecular Crystals.*

Kastner, J., Ramesh Hukkoo, B. G. Oltman, and Y. Dayal. Thermoluminescent Internal Beta-Ray Dosimetry. *Radiation Res.*

Oltman, B. G., J. Kastner, and P. Tedeschi. The Effects of Fast Neutron Exposure on the LiF Thermoluminescent Response of Gamma-Rays. *Health Phys.*

Rehfeld, C. E., J. Kastner, B. G. Oltman, H. M. Rosenberg and D. E. Doyle. Thermoluminescent Microdosimetry in Dental Radiology. I. Technique; II. Clinical Application. To be published as a proposal for the Starved Rock Conf., June 11–14, 1967, Profile of a Dental Faculty.

Marinelli, L. D. Dosimetry: D. Relevance of Doses from Thorotrast and Migrated Descendants to Other Irradiation Conditions; E. Critique of Dosimetry—What Information is Missing and How it Might be Obtained. *Proc. IAEA Panel on Dosimetry and Toxicity of Thorotrast,* Vienna, October 4–8, 1965.

Marinelli, L. D. Review of book *Radioisotopes for Internal Application in Diagnosis and Therapy* by Laconi, Cafferelli and Melfi. *Health Phys.*

Marinelli, L. D. Dosimetrie. *Handbook of Medical Radiology.* Springer-Verlag, Heidelberg, Vol. II, Chapter III-I.

Marinelli, L. D., J. F. Loutit, Dame Janet Vaughan, A. M. Brues, and F. W. Spiers. A Review of the Radiosensitivity of the Tissues in Bone; Report of a Task Group. ICRP 67/Cl-5/1, 1967

Marinelli, L. D. Problemi Inerenti alla Determinazione Delle Dosi Massime Ammissibili per L'Uomo. Atti Academia Medica Lombarda, Milan, Italy.

May, H. A., L. D. Marinelli and J. B. Corcoran. *In vivo* Counting of Thorium Dioxide Patients: Special Techniques and Preliminary Results. *Ann. N. Y. Acad. Sci.,* Proc. Conf. on Late Effects of Thorium Dioxide, April 20, 1966.

Marshall, J. H. Calcium Pools and the Power Function. ORINS Symp. on Compartments, Pools and Spaces in Medical Physiology, Oak Ridge, October 27, 1966.

Marshall, J. H. Measurements and Models of Skeletal Metabolism. *Calcium Metabolism, Mineral Metabolism,* Vol. 5. Eds. Comar and Bronner, Academic Press.

Moses, Harry, Elmer Robinson, M. E. Smith, G. C. Gill, E. M. Wilkins, and C. R. Dickson. Meteorology and Atomic Energy. *Meteorological Instruments for Use in the Atomic Energy Industry,* Ed., David H. Slade, Ch. 6.

Parr, R. M., H. F. Lucas, and M. L. Griem. Metabolism of ^{232}Th Decay-Series Isotopes in Man and Other Animals Following Intravascular Administration of Thorotrast. *Health Phys.*

Rowland, R. E. Studies on Bone-Seeking Radioisotopes. *Proc. XI Intern. Congress of Radiobiology,* Rome, Italy, 1965.

Simmons, D. J. and Richard L. Simmons. Skeletal Changes in Murine Runt Disease. *Am. J. Anat.*

Simmons, D. J. and Arthur S. Kunin. Autoradiographic and Biochemical Investigations of the Effect of Cortisone on the Bones of the Rat. *Clin. Orthoped.*